CMS Draft Analysis Note

The content of this note is intended for CMS internal use and distribution only

2020/11/11
Archive Hash: b9cc180-D
Archive Date: 2020/11/11

Analysis of the Higgs CP state in τ decays

Michal Bluj[1], Guillaume Bourgatte[2], Andrea Cardini[3], David Colling[4], Albert Dow[4], Máté Zoltán Farkas[5], Oleg Filatov[3], Elisabetta Gallo[3], Ulrich Goerlach[2], Clément Grimault[2], MohammadHassan Hassanshahi[4], Alexis Kalogeropoulos[6], Anne-Catherine Le Bihan[2], Teresa Lenz[3], Vinay Krishna[7], Mareike Meyer[3], Thomas Müller[5], Arun Nayak[7], Alexander Nikitenko[8], Claudia Pistone[5], Alexei Raspereza[3], Merijn van de Klundert[3], Diwakar Vats[7], Yiwen Wen[3], Lucas Wiens[5], Daniel Winterbottom[4], and Alexander Zotz[5]

[1] National Centre for Nuclear Research (PL)
[2] Institut Pluridisciplinaire Hubert Curien (FR)
[3] Deutsches Elektronen-Synchrotron (DE)
[4] Imperial College (UK)
[5] III. Physikalisches Institut B, RWTH Aachen University (DE)
[6] Princeton University (USA)
[7] Institute of Physics, Bhubaneswar (IN)
[8] Institute for Theoretical and Experimental Physics (RU)

DRAFT

Abstract

This study pursues a measurement of the CP quantum numbers of the Higgs boson in its decay to τ leptons via an analysis of the angular correlation between the τ decay planes.
The analysis targets the full Run 2 data set of proton-proton collisions at $\sqrt{s} = 13$ TeV, amounting to 137 fb^{-1}. It adopts as closely as possible the event selection, background estimation, and categorisation as used in the measurement of the Higgs couplings to τ decays analysis with ML techniques.
The analysis aims to include a subset of the hadronic and semileptonic decay modes. For the hadronic channel, the $\{\pi^{\pm}, \rho^{\pm}, \mathrm{a}_1^{\pm}\} \times \{\pi^{\mp}, \rho^{\mp}, \mathrm{a}_1^{\mp}\}$ decay modes are pursued, while for the semileptonic channel the $\mu^{\pm} \times \{\pi^{\mp}, \rho^{\mp}, \mathrm{a}_1^{\mp}\}$ and $\mathrm{e}^{\pm} \times \{\pi^{\mp}, \rho^{\mp}, \mathrm{a}_1^{\mp}\}$ decays are foreseen (in which the mesons decay as $\rho^{\pm} \to \pi^{\pm}\pi^{0}$ and $\mathrm{a}_1^{\pm} \to \pi^{\pm}\pi^{\mp}\pi^{\pm}$)
Different analysis techniques are deployed to reconstruct the τ decay planes, and various techniques have been designed to optimise the significance of the measurement. A BDT was developed to improve the discrimination between the decay modes. The primary vertex resolution was optimised using beamspot information and excluding the visible τ decay products. A helical track extrapolation was developed to estimate the impact parameters and their significance.
The observed (expected) full Run-2 significance to separate between CP-even and CP-odd states is 3.0σ (2.6σ). The observed (expected) mixing angle $\phi_{\tau\bar{\tau}}$ was was found to be -1 ± 18 $(0 \pm 21)^{\circ}$ at 68% CL, and -1 ± 39 $(0 \pm 47^{\circ})$ at 95% CL. These results are obtained when combining $\tau_e\tau_h$, $\tau_\mu\tau_\mathrm{h}$ and $\tau_\mathrm{h}\tau_\mathrm{h}$ channels. The results are consistent with predictions for the standard model Higgs boson.

DRAFT

This box is only visible in draft mode. Please make sure the values below make sense.

PDFAuthor:	Michal Bluj, Guillaume Bourgatte, Andrea Cardini, David Colling, Albert Dow, Mate Zoltan Farkas, Oleg Filatov, Elisabetta Gallo, Ulrich Goerlach, Clement Grimault, Mohammad Hassan Hassanshahi, Alexis Kalogeropoulos, Anne-Catherine Le Bihan, Teresa Lenz, Vinay Krishna, Mareike Meyer, Thomas Mueller, Arun Nayak, Alexander Nikitenko, Alexei Raspereza, Merijn van de Klundert, Diwakar Vats, Yiwen Wen, Lucas Wiens, Daniel Winterbottom, Alexander Zotz
PDFTitle:	Analysis of the Higgs CP state in tau decays
PDFSubject:	CMS
PDFKeywords:	CMS, physics, Higgs, tau

Please also verify that the abstract does not use any user defined symbols

Contents

1 Introduction . . . 3
2 Analysis strategy and CP sensitive observables . . . 5
2.1 Impact parameter method . . . 6
2.2 Decay plane method . . . 8
2.3 Polarimetric method . . . 10
2.4 Summary . . . 10
3 Datasets and simulated samples . . . 12
3.1 Datasets . . . 12
3.2 Monte Carlo samples . . . 12
3.3 Embedded samples . . . 13
4 Object reconstruction . . . 20
4.1 Muons . . . 20
4.2 Electrons . . . 20
4.3 Taus . . . 22
4.4 Jets and b-tagging . . . 23
4.5 Missing transverse energy . . . 24
4.6 Primary vertex reconstruction . . . 24
4.7 Impact parameter reconstruction . . . 28
4.8 Tau decay mode identification with BDT . . . 30
4.9 Polarimetric vectors . . . 35
5 Corrections . . . 40
5.1 Tau ID scale factors . . . 40
5.2 Residual $\mu \to \tau_{\mathrm{h}}$ fake rate corrections. . . . 43
5.3 Residual e $\to \tau_{\mathrm{h}}$ fake rate corrections. . . . 43
5.4 Tau trigger scale factors . . . 43
5.5 Impact parameter significance corrections . . . 47
6 Triggers and filters . . . 65
6.1 Event selection in the $\tau_\mu \tau_h$ channel . . . 65
6.2 Event selection in the $\tau_e \tau_h$ channel . . . 65
6.3 Event selection in the $\tau_h \tau_h$ channel . . . 66
7 Event Selection . . . 68
7.1 Introduction . . . 68
7.2 General event criteria . . . 68
7.3 Selection criteria in the $\tau_\mu \tau_h$ final state . . . 69
7.4 Selection criteria in the $\tau_e \tau_h$ final state . . . 70
7.5 Selection criteria in the $\tau_h \tau_h$ final state . . . 71
7.6 Pair selection . . . 71
7.7 Matching offline reconstructed objects to trigger objects . . . 71
8 Background estimation . . . 74
8.1 The fake factor method . . . 74
9 Control plots . . . 120
9.1 $\tau_\mu \tau_h$ channel . . . 120

DRAFT

9.2 $\tau_e\tau_h$ channel . . . 120
9.3 $\tau_h\tau_h$ channel . . . 120
10 Categorisation . . . 157
10.1 $\tau_h\tau_h$ channel . . . 157
10.2 $\tau_\mu\tau_h$ channel . . . 161
10.3 $\tau_e\tau_h$ channel . . . 164
11 Smoothing of background templates . . . 166
12 Systematic uncertainties . . . 171
12.1 Normalization Uncertainties . . . 171
12.2 Shape uncertainties . . . 172
12.3 Correlations between MC and embedded uncertainties . . . 177
13 Results . . . 178
13.1 Results in the $\tau_\mu\tau_h$ channel . . . 178
13.2 Results in the $\tau_e\tau_h$ channel . . . 180
13.3 Results in the $\tau_h\tau_h$ channel . . . 185
13.4 Observed impacts in the $\tau_\mu\tau_h$ and $\tau_h\tau_h$ channel . . . 186
13.5 Combined results . . . 190
14 Summary . . . 196
A Jacobi Matrices for Impact Parameter Significance . . . 197
B Plots of all categories used in the final fit . . . 199
C Plots of background categories split by MVA-DM . . . 217
C.1 Unrolled plots in the *ZTT* category . . . 217
C.2 Unrolled plots in the *fakes* category . . . 237
D Control plots using MC to model $Z \to \tau\tau$ . . . 257
D.1 Results in the $\tau_\mu\tau_h$ hannel . . . 257
D.2 Results in the $\tau_e\tau_h$ hannel . . . 269
D.3 Results in the $\tau_h\tau_h$ hannel . . . 282
E Fake factor fits . . . 288
E.1 Raw fake factor fits in the $\tau_h\tau_h$ channel . . . 288
E.2 Raw fake factor fits in the $\tau_\mu\tau_h$ channel . . . 291
E.3 Raw fake factor fits in the $\tau_e\tau_h$ channel . . . 298
E.4 Closure corrections in the $\tau_h\tau_h$ channel . . . 298
E.5 Closure corrections in the $\tau_\mu\tau_h$ channel . . . 298
E.6 Closure corrections in the $\tau_e\tau_h$ channel . . . 308
E.7 QCD DR→AR extrapolation corrections in the $\tau_\mu\tau_h$ channel . . . 308
E.8 W+jets DR→AR extrapolation corrections in the $\tau_\mu\tau_h$ channel . . . 308
E.9 $t\bar{t}$ DR→AR extrapolation corrections in the $\tau_\mu\tau_h$ channel . . . 308
E.10 QCD DR→AR extrapolation corrections in the $\tau_e\tau_h$ channel . . . 308
E.11 W+jets DR→AR extrapolation corrections in the $\tau_e\tau_h$ channel . . . 308
E.12 $t\bar{t}$ DR→AR extrapolation corrections in the $\tau_e\tau_h$ channel . . . 315
F CP measurement in the $a_1^{3pr} - a_1^{3pr}$ channel using the polarimetric vector method 316

DRAFT

1 Introduction

In the Standard Model the electroweak symmetry breaking is mediated via the Brout-Englert-Higgs mechanism [1–3]. The mechanism predicts the existence of a CP-even scalar boson, the Higgs boson. The Higgs boson was discovered simultaneously by the ATLAS [4] and CMS [5] collaboration using the LHC Run 1 collision data in 2012. Since 2012, amongst others, the coupling of the Higgs boson to tau leptons was established [6, 7].

The CP quantum number of the Higgs boson is an observable of paramount interest, since a deviation from a pure scalar (CP-even state) would directly indicate new physics. The aim of this analysis is bifold. At one hand, the analysis aims to assess the potential mixing between a scalar and pseudoscalar (CP-odd state) tau Yukawa coupling via the τ decay planes. The manifest advantage of this method is that it is fully model-independent. At the other hand, the analysis aims to compare and contrast the various methods available to extract the τ decay planes.

This is the first CMS analysis using the τ decay planes to measure the Higgs CP quantum numbers. The analysis aims to interpret the results in terms of BSM physics models, and compare the methods to predictions. For example, in [8] a prediction on the precision of the mixing angle for an LHC measurement was found to be 15° (9°) for 150 (500) fb^{-1} proton-proton (p + p) collisions. Furthermore, the ATLAS collaboration pursued a Phase 2 projection study, limited to the $\tau \to \rho$ channel [9].

The ATLAS and CMS collaborations already deployed various studies of anomalous couplings, including tests of CP violation, of the Higgs boson to vector gauge bosons; we refer to [10–15] and [16–21], respectively. These studies are focussed on deviations in the Higgs boson production though. Although it was already excluded that the Higgs boson is a pure CP-odd state (pseudoscalar), it has not yet been excluded that the Higgs boson is a mixed CP state.

More precisely, the tau Yukawa coupling can be decomposed as [22]:

$$\mathcal{L}_Y = -\frac{m_\tau}{\mathrm{v}}\kappa_\tau(\cos(\phi_{\tau\bar{\tau}})\bar{\tau}\tau + \sin(\phi_{\tau\bar{\tau}})\bar{\tau}i\gamma_5\tau)h. \tag{1}$$

In this equation v has a value of 246 GeV, κ_τ is the the reduced Yukawa coupling strength, and $\phi_{\tau\bar{\tau}}$ represents the mixing angle. For $\phi_{\tau\bar{\tau}}$ =0($\pi/2$) the state of the boson is a scalar(pseudoscalar). For any other value of $\phi_{\tau\tau}$ the Higgs boson is in a mixed state and CP violation occurs, and the CP violation is maximal at the so-called maxmix value of $\pi/4$. It should be noted that a measurement of CP violation in the tau Yukawa coupling is fully complementary to measurements of, for example, CP violation in the Yukawa top coupling, and such measurements are also pursued at CMS (HIG-19-013). We refer to analysis note AN-2019/186.

The decay of a (speudo)scalar boson into 2 fermions can be written as [23]:

$$\Gamma(h \to f\bar{f}) \propto 1 - s_z\bar{s}_z \pm s_\perp\bar{s}_\perp, \tag{2}$$

in which the transversal term has a different sign depending on whether h is scalar or pseudoscalar.

The transverse tau polarisation configuration affects the angular distribution of the di-tau decay topology. For τ decay to a charged pion and neutrino (the simplest $1 \to 2$ τ decay configuration), the transverse momentum components of the charged pions are anti-aligned for a scalar decay, and aligned for a pseudoscalar, as displayed in Fig. 1. As a result, the angle between the decay planes of the tau leptons is sensitive to the CP state of the Higgs boson.

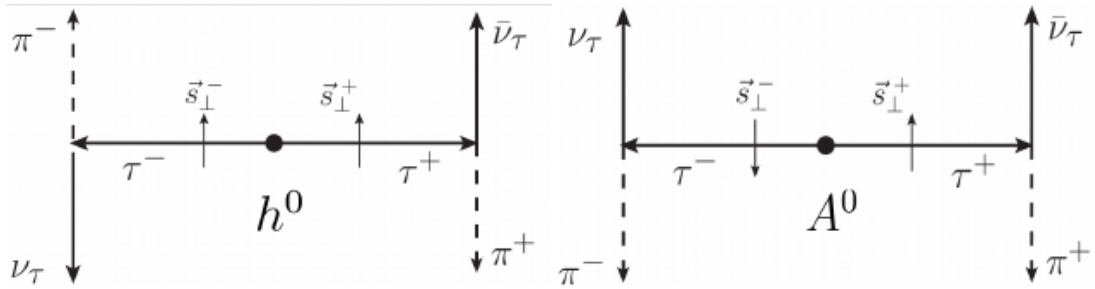

Figure 1: Left: the decay topology of a scalar boson, with the decay products anti-parallel. Right: the decay of a pseudoscalar, with parallel decay products. Fig. courtesy of [24]

To obtain optimal sensitivity to the Higgs boson CP state, this analysis aims to include the full 137 fb^{-1} obtained during Run 2. Therefore, we follow as much as possible the objects and selections as used in the Run 2 analysis of Higgs couplings in $h \to \tau\tau$ decays. As a result, throughout this note we will refer often to the relevant analysis notes for their descriptions.

The analysis targets to include the most sensitive decay modes, which are the $\tau_\mathrm{h}\tau_\mathrm{h}$ channel (with both τ leptons decaying hadronically), $\mu\tau_\mathrm{h}$ channel (with one τ lepton decaying hadronically, while the other decays via a muon) and eτ_h (with one τ lepton decaying hadronic ally, while the other decays via an electron). The publication foresees, besides an estimate of $\phi_{\tau\bar{\tau}}$, to compare and contrast between different analysis techniques available for different decay modes. However, a preliminary result is anticipated including only the most sensitive methods.

This analysis note is organised as follows. First, the strategy and CP sensitive observables of the measurement are outlined, as well as the various methods to extract the angle between the decay planes. Partially, this section is also intended to serve as a reference for future measurements by the CMS Collaboration. Thereafter, the datasets and simulated samples are described. Subsequently, the object identification is discussed, and in this section we also discuss various methods that were developed dedicatedly for this analysis. It is followed by a chapter on corrections needed to obtain good agreement between data and simulated events. This is followed by a chapter on the event selection. Special data-driven methods are used to obtain data-driven estimates of the backgrounds. The so called fake-factor method is used as well as embedded event samples. We give an overview of the methods and refer to relevant references. It should be noted that for this analysis dedicated fake factors needed to be derived (in the so-called determination region), since we make use of a dedicated tau decay mode algorithm. The analysis chains for the $\tau_\mu\tau_h$, $\tau_e\tau_h$ and $\tau_\mathrm{h}\tau_\mathrm{h}$ channels are discussed separately. It should be noted that this analysis uses machine learning techniques for event categorisation, and the techniques per channel are discussed. Subsequently, the systematic uncertainties are discussed.

In the final section the most significant value of $\phi_{\tau\bar{\tau}}$ is extracted with a combined template fit to all channels, using the optimal method for each individual decay mode. A separate paragraph with a dedicated analysis of the sensitivity of the different methods is included.

DRAFT

2 Analysis strategy and CP sensitive observables

In this section we outline the different methods at our disposal to reconstruct the τ decay planes. We define ϕ_{CP} as the angle between the decay planes (we'll elaborate below how ϕ_{CP} is projected on a range $[0, 2\pi]$). We start with reviewing the shapes of ϕ_{CP} for the signals and backgrounds. In Fig. 2 we display generator-level distributions of the angle ϕ_{CP} for both taus decaying to a charged pion and neutrino. We observe that a phase shift occurs in the distributions of ϕ_{CP} for the scalar, speudoscalar, and maximally mixed state (with $\phi_{\tau\bar{\tau}} = \pi/4$), which allows to extract $\phi_{\tau\bar{\tau}}$ from a measurement of ϕ_{CP}. We emphasise that the phase shift in the distribution of ϕ_{CP} equals $\phi_{\tau\bar{\tau}}/2$. It is of paramount importance to observe that the distribution of ϕ_{CP} of a decaying vector boson (an irreducible background) is flat.

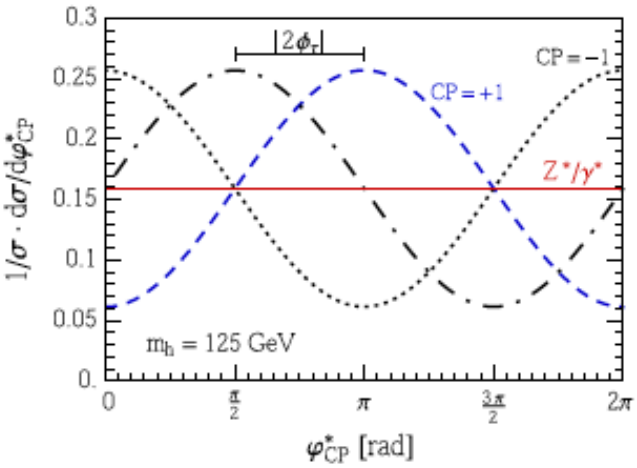

Figure 2: The normalised distribution of ϕ_{CP} between the τ decay planes, for both τ leptons decaying to a charged pion and a neutrino. The state of the decaying particle is scalar (blue), pseudoscalar (black dotted), maximally mixed scalar/pseudoscalar (black dashed), and vector boson (red). Fig. from [8].

The observable ϕ_{CP} has been introduced decades ago [23, 25]. It was originally foreseen to be applied in e^+e^- collisions, where the Higgs boson and rest frames can be relatively well reconstructed. Since then, the methods have been extended and optimised for hadronic collisions, we refer to [8] and the numerous references within.

A few general remarks are in order though. Optimal sensitivity would be obtained by boosting in the Higgs rest frame, and directly calculating the angle between the decay planes from the momenta of the charged decay products. However, in $p + p$ collisions this is not trivial when the Higgs boson decays into τ leptons, since the neutrinos invoke missing transverse momentum. Thus, usually the charged tau decay products are used to define a zero-momentum frame (ZMF); this still enhances the sensitivity w.r.t. calculating ϕ_{CP} in the lab frame. Furthermore, the methods outlined below generally do not reconstruct the actual τ decay plane, but rather a plane that is correlated to it (except for the polarimetric method).

In table 1 we briefly recall the different τ decay modes and their decay fractions.

Table 1: The τ decay modes with their percentages. The leptonic decay products are accompanied by two neutrinos, while the hadronic modes involve one neutrino

$e\nu\nu$	$\mu\nu\nu$	$\pi^\pm\nu$	$\rho^\pm\nu \to \pi^\pm\pi^0\nu$	$a_1{}^\pm\nu \to \pi^\pm\pi^0\pi^0\nu$	$a_1{}^\pm\nu \to \pi^\pm\pi^\mp\pi^\pm\nu$	kaonic/rare
17.5%	17.5%	10%	25%	10%	10%	10%

Various methods are available to extract ϕ_{CP}. In the paragraphs below we describe how the decay planes η^+ and η^- can be reconstructed for different decay topologies and their (dis)advantages. Since the methodology for the polarimetric vector reconstruction is rather different, this is explained in a separate paragraph.

In this section we restrict ourselves to a discussion mainly on generator level. We summarise the section with an overview of the qualitative differences observed on generator level.

2.1 Impact parameter method

To obtain the decay planes for 1-prong decays, the impact parameter method exploits the finite decay time of the τ lepton. The impact parameter $\mathbf{j}^{\pm}$ is the vector between the primary vertex and the point of closest approach (PCA) between the primary vertex and extrapolated charged particle track. We define the decay plane by the impact parameter vector (alternatively, one may take the vector orthogonal to the plane spanned by the impact parameter vector and the charged particle vector). The impact parameter is graphically depicted in Fig. 3. Below we discuss a few characteristics of the impact parameter method.

Only for the decay to a neutrino and single charged pion, the vectors $\mathbf{j}^{\pm}$ represent the genuine tau decay planes in the laboratory frame. These already have sensitivity to the Higgs CP state. However, better sensitivity to ϕ_{CP} can be obtained by boosting to the ZMF [26] (indicated with *).

To this purpose, we take unit vectors $\hat{\mathbf{j}}^{\pm}$. This are 3-vectors though; we construct four vectors in the lab frame as $\eta^{\pm} = (0, \hat{\mathbf{j}}^{\pm})$. These are boosted in the ZMF and denoted $\eta^{*\pm}$ (and thus in the ZMF these vectors do not represent the genuine decay planes anymore). We also boost the respective charged pion also to the ZMF, denoted $q^{\pm *}$.

Subsequently, we take the transverse component of $\eta^{*\pm}$ w.r.t. $q^{\pm *}$. We obtain $\hat{\eta}_{\perp}^{*+}$ and $\hat{\eta}_{\perp}^{*-}$. From these vectors we reconstruct the angles O^* and ϕ^* as:

$$\begin{aligned} \phi^* &= \arccos(\hat{\eta}_{\perp}^{*+} \cdot \hat{\eta}_{\perp}^{*-}) \\ O^* &= \hat{q}^{*-} \cdot (\hat{\eta}_{\perp}^{*+} \times \hat{\eta}_{\perp}^{*-}), \end{aligned} \tag{3}$$

From O^* and ϕ^* we reconstruct ϕ_{CP} on a domain $[0, 2\pi]$ as:

$$\phi_{\mathrm{CP}} = \begin{cases} \phi^* & \text{if } O^* \geq 0 \\ 2\pi - \phi^* & \text{if } O^* < 0 \end{cases} \tag{4}$$

For a more detailed description we refer to [8] and references within.

We outline a few characteristic features of the impact parameter method:

- Since this method relies solely on the kinematics of a charged particle, it can be applied to all τ decay modes.
- The impact parameter method relies in particular crucially on the reconstruction of the primary vertex.
- The sensitivity of this method strongly varies between the different decay modes:
    - For the decay $\tau^{\pm} \to \pi^{\pm}\nu$, the sensitivity is optimal, i.e. on generator-level this decay mode yields the best intrinsic CP sensitivity. With this statement we mean more precisely that the spectral function is constant and maximal (1). For a more in-depth discussion of the spectral functions we refer to [27].

DRAFT

- For the decay via the $\rho^{\pm}\nu \rightarrow \pi^{\pm}\pi^{0}\nu$ mode, different regions of the decay phase space contribute with a different sign in the spin-momentum correlation, leading to negative interference. This can be avoided by introducing a p_{T} cutoff of approx. 40 GeV on the charged pion. The decays above this cutoff have a spin resolving power that is deteriorated w.r.t. single pion decays though, and the cutoff severely limits the statistics.
- For the decay $\mathrm{a}_1{}^{\pm}\nu \rightarrow \pi^{\pm}\pi^{0}\pi^{0}\nu$ the same arguments hold as for $\rho^{\pm}\nu \rightarrow \pi^{\pm}\pi^{0}\nu$, and the spin resolving power is lower than for ρ decay.
- For decays to charged leptons, also two parts of the phase space contribute with a different phase. These can be approximately separated by a p_{T} cutoff of 20 GeV (which conveniently corresponds quite well to experimental reconstruction limits). However, also for the leptons the resolving power is reduced w.r.t. the decay to a single pion. Furthermore, the region above 20 GeV has a flipped phase w.r.t. a single pion decay

- Theoretically, the interfering spin-momentum contributions above and below the p_{T} cutoffs may be analysed separately. In practise, this may rather be feasible for $\mathrm{e}^{+}\mathrm{e}^{-}$ collisions.

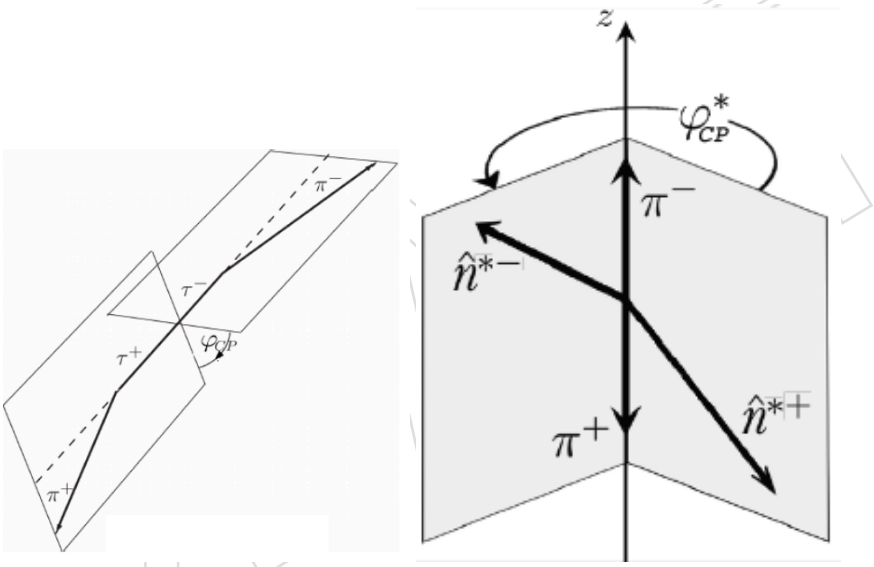

Figure 3: Left: illustration of the angle ϕ_{CP} and the τ decay planes (TODO insert reference for figure). Right: illustration of the impact parameter method to extract the decay planes for $\tau \rightarrow \pi\nu$ decays. The charged pion tracks are extrapolated to derive the PCA w.r.t. the primary vertex. The vector between the primary vertex and PCA yields the impact parameter. Fig. from [22].

2.1.1 Impact parameter method for 3-prong decays

For 3-prong decays, the method can be applied as well. Instead of extrapolating a track to obtain the impact parameter, instead one obtains this vector as the difference between the primary and secondary vertex, and the pion momentum is replaced by the momentum of the sum of the charged pions. However, due to contributions with a different a_1 polarisation this method has approx. no sensitivity in this channel. This could potentially be further pursued by applying a categorisation to distinguish the polarisation on an even-by-event basis; this direction has not yet been further pursued though.

2.2 Decay plane method

This method can be applied to hadronic decay channels involving more than one outgoing hadron. We first discuss the method for the 1-prong decay modes [28, 29]. Instead of using the impact parameters $\mathbf{j}^{\pm}$, here η is given by the momentum of the π^0, or the sum of the two neutral pions. The procedure for calculating ϕ_{CP} is analogue to the procedure of the impact parameter, except that to avoid negative interference from differently polarised states, one needs to introduce a new variable:

$$\begin{aligned} y^{\tau^-} &= \frac{E_{\pi^-} - E_{\pi^0}}{E_{\pi^-} + E_{\pi^0}}\,, \\ y^{\tau^+} &= \frac{E_{\pi^+} - E_{\pi^0}}{E_{\pi^+} + E_{\pi^0}}\,, \\ y^{\tau} &= y^{\tau^-} y^{\tau^+}. \end{aligned} \tag{5}$$

If y^{τ} is negative, ϕ_{CP} is obtained via the shift $2\pi - \phi_{\mathrm{CP}}$. The method is graphically depicted in Fig. 4 (left).

We outline a few features of the decay plane method below:

- The method may be applied to decays involving a ρ or a_1
- A particular advantage of the decay plane method is that it does not rely on the reconstruction of the primary vertex. Also, no cutoff on the charged pion p_{T} needs to be introduced
- This method only reconstructs a plane correlated to the τ decay plane
- The sensitivity of this method varies between the different decay modes:
    - For the decay via the ρ channel the sensitivity on generator level is roughly comparable with the impact parameter applied to a lepton (NEEDS TO BE CHECKED). However, the dependence on the p_{T} of the charged outgoing particle is negligible (TO DO citation needed), and thus no cuts in the phase space need to be applied
    - For the decay $\tau^{\pm} \to a_1{}^{\pm}\nu \to \pi^{\pm}\pi^0\pi^0\nu$ the same arguments hold, except for that the resolving power is significantly lower than for decay via a ρ (IC: please commend if you do something different instead?)

2.2.1 Decay plane method for 3-prong decays

The decay plane method can also be successfully applied to the 3-prong decays. We illustrate in Fig. 4 (right) the decay chain for a 3-prong decay. Firstly, we select the oppositely charged pion pair with invariant mass closest to a neutral ρ^0. This neutral ρ^0 is then treated in the same way as a charged neutral ρ with the method explained in Section 2.2.

(TO DO: replace right fig. with descent resolution figure..)

2.2.2 Mixed scenarios

Naturally, for the decay configuration of, for example, $\tau^{\mp} \to \mu^{\mp} + \nu$ and $\tau^{\pm} \to \pi^{\pm}\pi^{\mp}\pi^{\pm} + \nu$, a mixture of the reconstruction methods needs to be applied. This does not impose any obstructions, since the decay planes are reconstructed individually. The procedures carry over without any loss of generality when the vectors $\eta^{\pm}$ are derived via different methods.

DRAFT

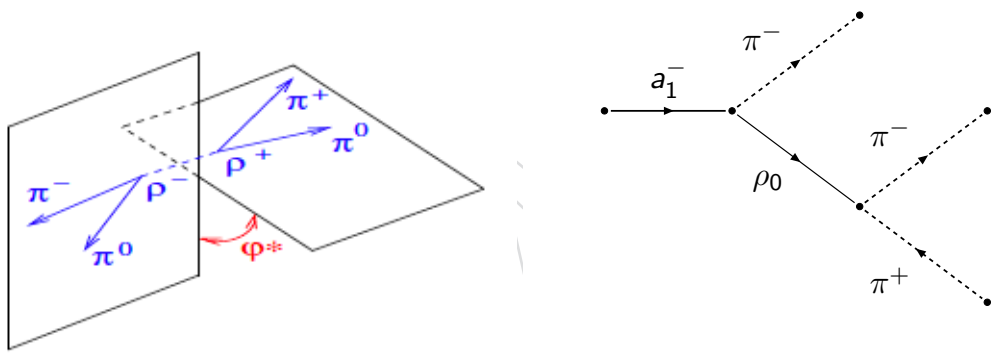

Figure 4: Left: the neutral and charged pion momentum together span the τ decay plane. Fig. from [30]. Right: the decay chain for a 3-prong decay.

2.3 Polarimetric method

To characterise tau transverse spin correlations, to whose the Higgs CP angle is sensitive to, one can rely on so called polarimetric vectors. The polarimetric vector ($\vec{h}$) of a given tau is given by the hadron momenta and the decay model of the resonance mediating the decay. It can be seen as the most probable direction of the tau spin ($\vec{s}$) in the tau rest frame. The tau partial decay width depends indeed on the product of the polarimetric vector and the spin vector: $d\Gamma \propto (1 + \vec{h} \cdot \vec{s})$. $d\Gamma$ is hence maximal for $\vec{h}$ oriented along $\vec{s}$, and $\vec{h}$ hence most likely points in the direction of $\vec{s}$. The acoplanar angle between the planes, defined each by the tau direction and the polarimetric vector, in the Higgs boson rest frame, shows a very good sensitivity to the CP angle, as established in [31].

The polarimetric vector method can be used in final states in which at least one tau lepton decays to a_1. The reconstruction of the tau secondary vertices to three charged pions allows to reconstruct the full tau momenta (including neutrino momenta), thanks to global kinematic event fit methods (GEF) [32]. In this analysis, the polarimetric vector method has been investigated for the a_1-a_1 final state as described in section 4.9. The a_1 resonance model is taken from *TAUOLA* [33–35], including the parameters measured by the CLEO collaboration. The three pion momenta are needed, as well as the estimated tau momentum, to compute $\vec{h}$. For each tau, a plane is hence defined by the direction of the reconstructed polarimetric vector and reconstructed tau momentum. The acoplanar angle is then defined by the angle spanned between the two planes:

$$\phi^* = \arccos(\vec{k}_1 \cdot \vec{k}_2) \tag{6}$$

with $\vec{k}_{1,2} = \frac{\vec{h}_{1,2} \times \vec{n}_{1,2}}{|\vec{h}_{1,2} \times \vec{n}_{1,2}|}$,
$\vec{n}_{1,2}$ the unit vector of the tau direction in the Higgs boson rest frame, and

$$\phi_{\mathrm{CP}} = \begin{cases} \phi_{\mathrm{CP}} = \phi_{\mathrm{CP}}, & \text{if } (\vec{h}_1 \times \vec{h}_2) \cdot \vec{n}_1 \leq 0, \\ \phi_{\mathrm{CP}} = 2\pi - \phi_{\mathrm{CP}}, & \text{if } (\vec{h}_1 \times \vec{h}_2) \cdot \vec{n}_1 > 0. \end{cases} \tag{7}$$

2.4 Summary

We outlined different methods to reconstruct ϕ_{CP} for the different decay modes. In Fig. 5 we display generator level distributions for ϕ_{CP} in various decay modes, for a scalar and pseudoscalar decay. We make some rudimentary assessment of the resolution power by studying the amplitude divided by the baseline of the sinusoidal fit.

In Fig. 5 we observe that the resolving power on generator level is maximal for the decay to single charged pions (TO BE INSERTED!); a consequence of the optimal spectral functions. Replacing one pion decay plane by a muon decay plane, we observe the phase flip. We further observe that the resolving power is substantially reduced. When studying the $\mu + \rho$ channel in the decay plane method, we observe that the resolving power is reduced by approx. 30% w.r.t. the pionic case.

We may also study the $\mu + \rho$ channel using the impact parameter method. In Fig. 6 we study the resolving power above and below the 40 GeV cutoff. We observe that the events below the cutoff have no relevant resolving power. The method, when applied above the p_{T} cutoff, seems

DRAFT

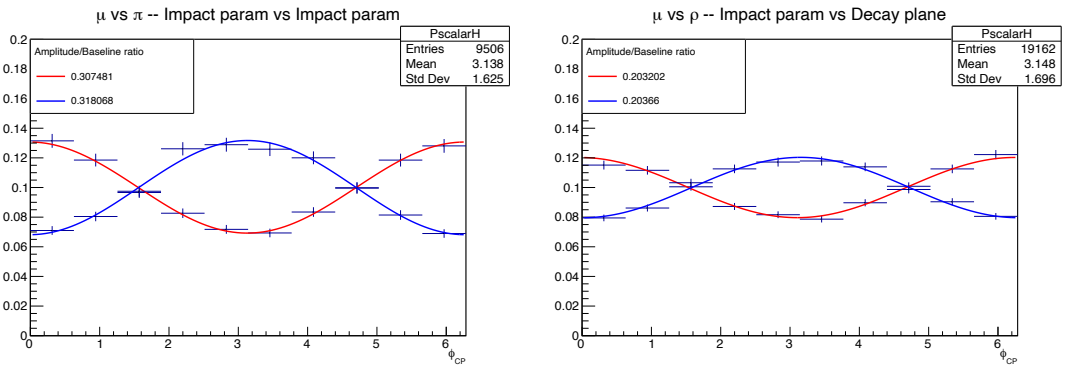

Figure 5: Left: the $\mu + \pi$ channel using the impact parameter method. Right: the $\mu + \rho$ method, using the decay plane method

to perform a bit worse that the decay plane method, while the decay plane method further has the advantage of enhanced statistics.

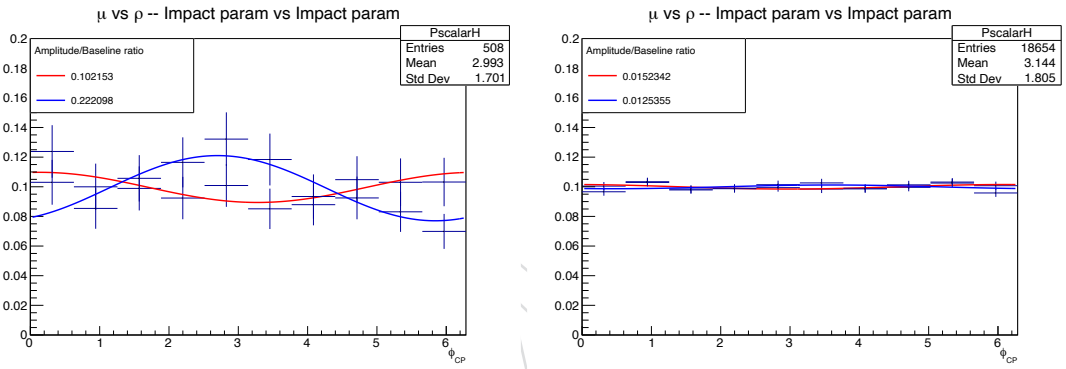

Figure 6: Left: the $\mu + \rho$ channel using the impact parameter method, where a cutoff of $p_T > 40\,\text{GeV}$ was applied to the charged pion. Right: the $\mu + \rho$ channel using the impact parameter method, where a cutoff of $p_T < 40\,\text{GeV}$ was applied to the charged pion. Right: the $\mu + \rho$ method, using the decay plane method

In conclusion, we reviewed various methods to analyse the various decay modes. From a generator level study it appears that the decay plane method is to be preferred over the impact parameter method; the latter should only be used for leptonic or single pion decays, for which no alternative exists (TO DO elaborate conclusions once have pi pi and 3 prong, possibly with polarimetric, also). In the following sections we will review in more detail the experimental smearing effects that play a role, and assess the performance of the methods on simulated data.

TO DO: this needs to be complemented by pion-pion plot still, and pref. done with higher statistics! TO DO: include polarimetric vector gen level and 3-prong gen-level results for comparison!

3 Datasets and simulated samples

3.1 Datasets

For this analysis the full 2016 (legacy 94X), 2017 and 2018 datasets collected at the CMS experiment are used. These correspond to 13 TeV data with an integrated luminosity of 35.9 fb^{-1} (2016), 41.8 fb^{-1} (2017) and 59.7 fb^{-1} (2018). A summary of the datasets and their associated run ranges and integrated luminosities is given in Table 2, Table 3 and Table 4. This data is fully certified by the CMS collaboration and is selected using the following JSON files: `Cert_271036-284044_13TeV_23Sep2016ReReco_Collisions16_JSON.txt` (2016), `Cert_294927-306462_13TeV_EOY2017ReReco_Collisions17_JSON_v1.txt` (2017) and `Cert_314472-325175_13TeV_17SeptEarlyReReco2018ABC_PromptEraD_Collisions18_JSON.txt` (2018).

Channel	Dataset	Run range	Integrated Luminosity
$\mu\tau_h$	/SingleMuon/Run2016B-17Jul2018-ver2-v1/MINIAOD	272007–275376	5.788 /fb
$\mu\tau_h$	/SingleMuon/Run2016C-17Jul2018-v1/MINIAOD	275657–276283	2.573 /fb
$\mu\tau_h$	/SingleMuon/Run2016D-17Jul2018-v1/MINIAOD	276315–276811	4.248 /fb
$\mu\tau_h$	/SingleMuon/Run2016E-17Jul2018-v1/MINIAOD	276831–277420	4.009 /fb
$\mu\tau_h$	/SingleMuon/Run2016F-17Jul2018-v1/MINIAOD	277772–278808	3.102 /fb
$\mu\tau_h$	/SingleMuon/Run2016G-17Jul2018-v1/MINIAOD	278820–280385	7.540 /fb
$\mu\tau_h$	/SingleMuon/Run2016H-17Jul2018-v1/MINIAOD	280919–284044	8.606 /fb
$e\tau_h$	/SingleElectron/Run2016B-17Jul2018-ver2-v1/MINIAOD	272007–275376	5.788 /fb
$e\tau_h$	/SingleElectron/Run2016C-17Jul2018-v1/MINIAOD	275657–276283	2.573 /fb
$e\tau_h$	/SingleElectron/Run2016D-17Jul2018-v1/MINIAOD	276315–276811	4.248 /fb
$e\tau_h$	/SingleElectron/Run2016E-17Jul2018-v1/MINIAOD	276831–277420	4.009 /fb
$e\tau_h$	/SingleElectron/Run2016F-17Jul2018-v1/MINIAOD	277772–278808	3.102 /fb
$e\tau_h$	/SingleElectron/Run2016G-17Jul2018-v1/MINIAOD	278820–280385	7.540 /fb
$e\tau_h$	/SingleElectron/Run2016H-17Jul2018-v1/MINIAOD	280919–284044	8.606 /fb
$\tau_h\tau_h$	/Tau/Run2016B-17Jul2018-ver2-v1/MINIAOD	272007–275376	5.788 /fb
$\tau_h\tau_h$	/Tau/Run2016C-17Jul2018-v1/MINIAOD	275657–276283	2.573 /fb
$\tau_h\tau_h$	/Tau/Run2016D-17Jul2018-v1/MINIAOD	276315–276811	4.248 /fb
$\tau_h\tau_h$	/Tau/Run2016E-17Jul2018-v1/MINIAOD	276831–277420	4.009 /fb
$\tau_h\tau_h$	/Tau/Run2016F-17Jul2018-v1/MINIAOD	277772–278808	3.102 /fb
$\tau_h\tau_h$	/Tau/Run2016G-17Jul2018-v1/MINIAOD	278820–280385	7.540 /fb
$\tau_h\tau_h$	/Tau/Run2016H-17Jul2018-v1/MINIAOD	280919–284044	8.606 /fb

Table 2: List of 2016 (legacy 94X) datasets included in the analysis. Re-miniAOD is used for data.

3.2 Monte Carlo samples

The signal and background Monte Carlo samples used in this analysis are summarised in Table 6 and 7 (2016 signal and background), Table 8 and 9 (2017 signal and background) and Table 10 and 11 (2018 signal and background). The signal samples are produced using POWHEG with the tauspinner package [36] to allow for reweighting to different Higgs boson CP scenarios, whereas the other background MC samples are produced with several packages.

Tauspinner can inprinciple produce weight corresponding to any CP scenario. However, only three weights and corresponding differential distributions are needed to form templates for all CP scenarios, namly the pure CP-even ($\phi_{\tau\bar{\tau}} = 0^o$), the pure CP-odd ($\phi_{\tau\bar{\tau}} = 90^0$), and a mixed CP weight (chosen to be $\phi_{\tau\bar{\tau}} = 45^o$). The differential distributions for these three contributions

Channel	Dataset	Run range
$\mu\tau_h$	/SingleMuon/Run2017B-31Mar2018-v1/MINIAOD	297047–299329
$\mu\tau_h$	/SingleMuon/Run2017C-31Mar2018-v1/MINIAOD	299368–302029
$\mu\tau_h$	/SingleMuon/Run2017D-31Mar2018-v1/MINIAOD	302030–302663
$\mu\tau_h$	/SingleMuon/Run2017E-31Mar2018-v1/MINIAOD	303818–304797
$\mu\tau_h$	/SingleMuon/Run2017F-31Mar2018-v1/MINIAOD	305040–306460
$e\tau_h$	/SingleElectron/Run2017B-31Mar2018-v1/MINIAOD	297047–299329
$e\tau_h$	/SingleElectron/Run2017C-31Mar2018-v1/MINIAOD	299368–302029
$e\tau_h$	/SingleElectron/Run2017D-31Mar2018-v1/MINIAOD	302030–302663
$e\tau_h$	/SingleElectron/Run2017E-31Mar2018-v1/MINIAOD	303818–304797
$e\tau_h$	/SingleElectron/Run2017F-31Mar2018-v1/MINIAOD	305040–306460
$\tau_h\tau_h$	/Tau/Run2017B-31Mar2018-v1/MINIAOD	297047–299329
$\tau_h\tau_h$	/Tau/Run2017C-31Mar2018-v1/MINIAOD	299368–302029
$\tau_h\tau_h$	/Tau/Run2017D-31Mar2018-v1/MINIAOD	302031–302663
$\tau_h\tau_h$	/Tau/Run2017E-31Mar2018-v1/MINIAOD	303824–304797
$\tau_h\tau_h$	/Tau/Run2017F-31Mar2018-v1/MINIAOD	305040–306460

Table 3: List of 2017 datasets included in the analysis.

Channel	Dataset	Run range
$\mu\tau_h$	/SingleMuon/Run2018A-17Sep2018-v2/MINIAOD	
$\mu\tau_h$	/SingleMuon/Run2018B-17Sep2018-v1/MINIAOD	
$\mu\tau_h$	/SingleMuon/Run2018C-17Sep2018-v1/MINIAOD	
$\mu\tau_h$	/SingleMuon/Run2018D-PromptReco-v2/MINIAOD	
$e\tau_h$	/EGamma/Run2018A-17Sep2018-v2/MINIAOD	
$e\tau_h$	/EGamma/Run2018B-17Sep2018-v1/MINIAOD	
$e\tau_h$	/EGamma/Run2018C-17Sep2018-v1/MINIAOD	
$e\tau_h$	/EGamma/Run2018D-PromptReco-v2/MINIAOD	
$\tau_h\tau_h$	/Tau/Run2018A-17Sep2018-v1/MINIAOD	
$\tau_h\tau_h$	/Tau/Run2018B-17Sep2018-v1/MINIAOD	
$\tau_h\tau_h$	/Tau/Run2018C-17Sep2018-v1/MINIAOD	
$\tau_h\tau_h$	/Tau/Run2018D-PromptReco-v2/MINIAOD	

Table 4: List of 2018 datasets included in the analysis.

are summed according to the formular

$$\frac{d\sigma}{dx}(\phi_{\tau\bar{\tau}}) = \left(\cos^2\phi_{\tau\bar{\tau}} - \cos\phi_{\tau\bar{\tau}}\sin\phi_{\tau\bar{\tau}}\right)\cdot\frac{d\sigma}{dx}^{\text{CP-even}} + \left(\sin^2\phi_{\tau\bar{\tau}} - \cos\phi_{\tau\bar{\tau}}\sin\phi_{\tau\bar{\tau}}\right)\cdot\frac{d\sigma}{dx}^{\text{CP-odd}} + 2\cos\phi_{\tau\bar{\tau}}\sin\phi_{\tau\bar{\tau}}\cdot\frac{d\sigma}{dx}^{\text{CP-mix}} \tag{8}$$

Additionally, the signal samples are filtered at generator level with filter efficiencies indicated in Tables 6 – 10. The GEN-level filter removes events based on the visible p_T and $|eta|$ of the leptons in the di-τ system in the corresponding $\tau\tau$ channel that is being generated. This is useful for this analysis since many of the selection cuts, such as the trigger selection in $\tau\tau$ analyses, remove a lot of events at analyser level. The cuts are chosen as 10% (20%) lower than the offline cuts for the leptons (taus) and are displayed in Table 5.This way the GEN filter effectively increases the number of available events for analysis by a factor 4, making the simulation process more computationally efficient as well.

3.3 Embedded samples

The list of embedded samples used in this analysis is summarised in Table 12, Table 13 and Table 14. Embedded samples are used in 2016, 2017 and 2018, and are employed for the data-

DRAFT

Table 5: Generator-level selection on simulated $\mathrm{H} \to \tau\tau$ samples.

Channel	$p_{\mathrm{T}}^{\mathrm{lepton1}}$ (GeV)	$p_{\mathrm{T}}^{\mathrm{lepton2}}$ (GeV)	$\lvert\eta\rvert_{\mathrm{lepton1}}$	$\lvert\eta\rvert_{\mathrm{lepton2}}$
$\tau_\mu\tau_h$	> 19	> 16	< 2.5	< 2.7
$\tau_h\tau_h$	> 33	> 33	< 2.5	< 2.5

Signal Monte Carlo samples				
Dataset Description	Dataset Name	Cross-section [pb] ($\times\mathcal{B}_{\tau\tau}$ NNLO)	Events	Filter Eff.
ggH $h \to \tau\tau$	/GluGluHToTauTauUncorrelatedDecay_Filtered_M125_TuneCUETP8M1_13TeV-powheg-pythia8 [1]	3.046	20156550	0.2455
VBF $h \to \tau\tau$	/VBFHToTauTauUncorrelatedDecay_Filtered_M125_TuneCUETP8M1_13TeV-powheg-pythia8 [1]	0.237	18671016	0.2727
$W^+h \to \tau\tau$	/WplusHToTauTauUncorrelatedDecay_Filtered_M125_TuneCUETP8M1_13TeV-powheg-pythia8 [1]	0.0527	2735246	0.2425
$W^-h \to \tau\tau$	/WminusHToTauTauUncorrelatedDecay_Filtered_M125_TuneCUETP8M1_13TeV-powheg-pythia8 [1]	0.0358	1884919	0.2596
$Zh \to \tau\tau$	/ZHToTauTauUncorrelatedDecay_Filtered_M125_TuneCUETP8M1_13TeV-powheg-pythia8 [1]	0.0594	3557541	0.2546

[1] `/RunIISummer16MiniAODv3-PUMoriond17_94X_mcRun2_asymptotic_v3-v1/MINIAODSIM`

Table 6: List of 2016 Monte Carlo samples used to model $\mathrm{gg} \to h \to \tau\tau$ signal.

driven estimation of the $Z \to \tau\tau$ and some $t\bar{t}$/di-boson/single-top background. The embedding method is described more thoroughly in section 8.

DRAFT

Background Monte Carlo samples		
Dataset Description	Dataset Name	Cross-Section [pb]
$t\bar{t}$	/TT_TuneCUETP8M1_13TeV-powheg-pythia8[1]	831.76
Single top	/ST_tW_antitop_5f_inclusiveDecays_13TeV-powheg-pythia8_TuneCUETP8M1[2]	35.6
	/ST_tW_top_5f_inclusiveDecays_13TeV-powheg-pythia8_TuneCUETP8M1[2]	35.6
	/ST_t-channel_top_4f_leptonDecays_13TeV-powheg-pythia8_TuneCUETP8M1[1]	136.02
	/ST_t-channel_antitop_4f_leptonDecays_13TeV-powheg-pythia8_TuneCUETP8M1[1]	80.95
$Z \to LL$	/DYJetsToLL_M-50_TuneCUETP8M1_13TeV-madgraphMLM-pythia8[3,4]	6077.22 (NNLO)
$Z+1$jet	/DY1JetsToLL_M-50_TuneCUETP8M1_13TeV-madgraphMLM-pythia8[1]	1012.5 (LO)
$Z+2$jets	/DY2JetsToLL_M-50_TuneCUETP8M1_13TeV-madgraphMLM-pythia8[1]	332.8 (LO)
$Z+3$jets	/DY3JetsToLL_M-50_TuneCUETP8M1_13TeV-madgraphMLM-pythia8[1]	101.8 (LO)
$Z+4$jets	/DY4JetsToLL_M-50_TuneCUETP8M1_13TeV-madgraphMLM-pythia8[1]	54.8 (LO)
Low mass $Z \to LL$	/DYJetsToLL_M-10to50_TuneCUETP8M1_13TeV-madgraphMLM-pythia8[1]	18610
W+jets	/WJetsToLNu_TuneCUETP8M1_13TeV-madgraphMLM-pythia8[1,4]	61526.7 (NNLO)
$W+1$jet	/W1JetsToLNu_TuneCUETP8M1_13TeV-madgraphMLM-pythia8[1]	9644.5 (LO)
$W+2$jets	/W2JetsToLNu_TuneCUETP8M1_13TeV-madgraphMLM-pythia8[1,2]	3144.5 (LO)
$W+3$jets	/W3JetsToLNu_TuneCUETP8M1_13TeV-madgraphMLM-pythia8[1,2]	954.8 (LO)
$W+4$jets	/W4JetsToLNu_TuneCUETP8M1_13TeV-madgraphMLM-pythia8[1,2]	485.6 (LO)
EWK $W^+ + 2$jets	/EWKWPlus2Jets_WToLNu_M-50_13TeV-madgraphMLM-pythia8[1,2,4]	25.62 (LO)
EWK $W^- + 2$jets	/EWKWMinus2Jets_WToLNu_M-50_13TeV-madgraphMLM-pythia8[1,2,4]	20.25 (LO)
EWK $Z+2$jets	/EWKZ2Jets_ZToLL_M-50_13TeV-madgraphMLM-pythia8[1,2]	3.987 (LO)
VV	/VVTo2L2Nu_13TeV_amcatnloFXFX_madspin_pythia8[1,2]	11.95
ZZ	/ZZTo2L2Q_13TeV_amcatnloFXFX_madspin_pythia8[1]	3.22
ZZ	/ZZTo4L_13TeV_amcatnloFXFX-pythia8[1,2]	1.212
WW	/WWTo1L1Nu2Q_13TeV_amcatnloFXFX_madspin_pythia8[1]	49.997
WZ	/WZJToLLLNu_TuneCUETP8M1_13TeV-amcnlo-pythia8[1]	4.708
WZ	/WZTo2L2Q_13TeV_amcatnloFXFX_madspin_pythia8[1]	5.595
WZ	/WZTo1L3Nu_13TeV_amcatnloFXFX_madspin_pythia8[1]	3.05
WZ	/WZTo1L1Nu2Q_13TeV_amcatnloFXFX_madspin_pythia8[5]	10.71

[1] /RunIISummer16MiniAODv2-PUMoriond17_80X_mcRun2_asymptotic_2016_TrancheIV_v6-v1/MINIAODSIM
[2] /RunIISummer16MiniAODv2-PUMoriond17_80X_mcRun2_asymptotic_2016_TrancheIV_v6-ext1-v1/MINIAODSIM
[3] /RunIISummer16MiniAODv2-PUMoriond17_80X_mcRun2_asymptotic_2016_TrancheIV_v6-ext1-v2/MINIAODSIM
[4] /RunIISummer16MiniAODv2-PUMoriond17_80X_mcRun2_asymptotic_2016_TrancheIV_v6-ext2-v1/MINIAODSIM
[5] /RunIISummer16MiniAODv2-PUMoriond17_80X_mcRun2_asymptotic_2016_TrancheIV_v6-v3/MINIAODSIM

Table 7: List of 2016 Monte Carlo samples used to model $Z/\gamma^* \to ee, Z/\gamma^* \to \mu\mu, Z/\gamma^* \to \tau\tau$, W + jets, $t\bar{t}$, single top and di-boson (WW, WZ, ZZ) backgrounds. UPDATE TO LEGACY POSTFIXES

Signal Monte Carlo samples				
Dataset Description	Dataset Name	Cross-section [pb] ($\times \mathcal{B}_{\tau\tau}$ NNLO)	Events	Filter Eff.
ggH $h \to \tau\tau$	/GluGluHToTauTauUncorrelatedDecay_Filtered_M125_TuneCUETP8M1_13TeV-powheg-pythia8 [1]	3.046	19420205	0.2447
VBF $h \to \tau\tau$	/VBFHToTauTauUncorrelatedDecay_Filtered_M125_TuneCUETP8M1_13TeV-powheg-pythia8 [1]	0.237	20397834	0.2697
$W^+h \to \tau\tau$	/WplusHToTauTauUncorrelatedDecay_Filtered_M125_TuneCUETP8M1_13TeV-powheg-pythia8 [1]	0.0527	2640112	0.2394
$W^-h \to \tau\tau$	/WminusHToTauTauUncorrelatedDecay_Filtered_M125_TuneCUETP8M1_13TeV-powheg-pythia8 [1]	0.0358	1986464	0.2567
$Zh \to \tau\tau$	/ZHToTauTauUncorrelatedDecay_Filtered_M125_TuneCUETP8M1_13TeV-powheg-pythia8 [1]	0.0594	2477724	0.2514

[1] /RunIIFall17MiniAODv2-PU2017_12Apr2018_94X_mc2017_realistic_v14-v1/MINIAODSIM

Table 8: List of 2017 Monte Carlo signal samples used to model $gg \to h \to \tau\tau$ signal.

DRAFT

Background Monte Carlo samples		
Dataset Description	Dataset Name	Cross-Section [pb]
$t\bar{t} \to LL\nu\nu$	/TTTo2L2Nu_TuneCP5_13TeV-powheg-pythia8[8]	88.29
$t\bar{t} \to$ hadronic	/TTToHadronic_TuneCP5_13TeV-powheg-pythia8[11]	377.96
$t\bar{t} \to$ semi-leptonic	/TTToSemiLeptonic_TuneCP5_13TeV-powheg-pythia8[8]	365.34
Single top	/ST_tW_antitop_5f_inclusiveDecays_TuneCP5_13TeV-powheg-pythia8[2]	34.97
	/ST_tW_top_5f_inclusiveDecays_TuneCP5_13TeV-powheg-pythia8[2]	35.85
	/ST_t-channel_top_4f_inclusiveDecays_TuneCP5_13TeV-powhegV2-madspin-pythia8[8]	136.02
	/ST_t-channel_antitop_4f_inclusiveDecays_TuneCP5_13TeV-powhegV2-madspin-pythia8[2]	80.95
$Z \to LL$	/DYJetsToLL_M-50_TuneCP5_13TeV-madgraphMLM-pythia8[5,6]	6077.22 (NNLO)
$Z+1$jet	/DY1JetsToLL_M-50_TuneCP5_13TeV-madgraphMLM-pythia8[8,7]	877.8 (LO)
$Z+2$jets	/DY2JetsToLL_M-50_TuneCP5_13TeV-madgraphMLM-pythia8[1,9]	304.4 (LO)
$Z+3$jets	/DY3JetsToLL_M-50_TuneCP5_13TeV-madgraphMLM-pythia8[1,9]	111.5 (LO)
$Z+4$jets	/DY4JetsToLL_M-50_TuneCP5_13TeV-madgraphMLM-pythia8[10]	44.03 (LO)
Low mass $Z \to LL$	/DYJetsToLL_M-10to50_TuneCP5_13TeV-madgraphMLM-pythia8[1,1a]	18610
W+jets	/WJetsToLNu_TuneCP5_13TeV-madgraphMLM-pythia8[2,2a]	61526.7 (NNLO)
$W+1$jet	/W1JetsToLNu_TuneCP5_13TeV-madgraphMLM-pythia8[12]	9644.5 (LO)
$W+2$jets	/W2JetsToLNu_TuneCP5_13TeV-madgraphMLM-pythia8[13]	3144.5 (LO)
$W+3$jets	/W3JetsToLNu_TuneCP5_13TeV-madgraphMLM-pythia8[1]	954.8 (LO)
$W+4$jets	/W4JetsToLNu_TuneCP5_13TeV-madgraphMLM-pythia8[11]	485.6 (LO)
EWK $W^+ + 2$jets	/EWKWPlus2Jets_WToLNu_M-50_TuneCP5_13TeV-madgraphMLM-pythia8[11]	25.62 (LO)
EWK $W^- + 2$jets	/EWKWMinus2Jets_WToLNu_M-50_TuneCP5_13TeV-madgraphMLM-pythia8[11]	20.25 (LO)
EWK $Z+2$jets	/EWKZ2Jets_ZToLL_M-50_TuneCP5_13TeV-madgraphMLM-pythia8[11]	3.987 (LO)
ZZ	/ZZTo2L2Q_13TeV_amcatnloFXFX_madspin_pythia8[1]	3.688
ZZ	/ZZTo2L2Nu_13TeV_powheg_pythia8[1]	0.6008
ZZ	/ZZTo4L_13TeV_amcatnloFXFX-pythia8[8,14]	1.325
WW	/WWTo2L2Nu_NNPDF31_TuneCP5_13TeV-powheg-pythia8[1]	11.08
WW	/WWToLNuQQ_NNPDF31_TuneCP5_13TeV-powheg-pythia8[8]	45.99
WZ	/WZTo2L2Q_13TeV_amcatnloFXFX_madspin_pythia8_v2[1]	6.331
WZ	/WZTo1L3Nu_13TeV_amcatnloFXFX_madspin_pythia8_v2[1]	3.293
WZ	/WZTo1L1Nu2Q_13TeV_amcatnloFXFX_madspin_pythia8[2]	11.66
WZ	/WZTo3LNu_13TeV_amcatnloFXFX_madspin_pythia8_v2[8]	5.052
WZ	/WZTo1L1Nu2Q_13TeV_amcatnloFXFX_madspin_pythia8[2]	11.66

[1] /RunIIFall17MiniAODv2-PU2017_12Apr2018_94X_mc2017_realistic_v14-v1/MINIAODSIM

[1a] /RunIIFall17MiniAODv2-PU2017_12Apr2018_94X_mc2017_realistic_v14_ext1-v1/MINIAODSIM

[2] /RunIIFall17MiniAODv2-PU2017_12Apr2018_94X_mc2017_realistic_v14-v2/MINIAODSIM

[2a] /RunIIFall17MiniAODv2-PU2017_12Apr2018_94X_mc2017_realistic_v14_ext1-v2/MINIAODSIM

[3] /RunIIFall17MiniAODv2-PU2017_12Apr2018_94X_mc2017_realistic_v14-v3/MINIAODSIM

[4] /RunIIFall17MiniAODv2-PU2017_12Apr2018_94X_mc2017_realistic_v14-v4/MINIAODSIM

[5] /RunIIFall17MiniAODv2-PU2017RECOSIMstep_12Apr2018_94X_mc2017_realistic_v14-v1/MINIAODSIM

[6] /RunIIFall17MiniAODv2-PU2017RECOSIMstep_12Apr2018_94X_mc2017_realistic_v14_ext1-v1/MINIAODSIM

[7] /RunIIFall17MiniAODv2-PU2017_12Apr2018_v3_94X_mc2017_realistic_v14_ext1-v2

[8] /RunIIFall17MiniAODv2-PU2017_12Apr2018_new_pmx_94X_mc2017_realistic_v14-v1

[9] /RunIIFall17MiniAODv2-PU2017_12Apr2018_new_pmx_94X_mc2017_realistic_v14_ext1-v2

[10] /RunIIFall17MiniAODv2-PU2017_12Apr2018_v2_94X_mc2017_realistic_v14-v2

[11] /RunIIFall17MiniAODv2-PU2017_12Apr2018_new_pmx_94X_mc2017_realistic_v14-v2

[12] /RunIIFall17MiniAODv2-PU2017_12Apr2018_94X_mc2017_realistic_v14-v3

[13] /RunIIFall17MiniAODv2-PU2017_12Apr2018_94X_mc2017_realistic_v14-v4

[14] /RunIIFall17MiniAODv2-PU2017_12Apr2018_94X_mc2017_realistic_v14_ext2-v1

Table 9: List of 2017 Monte Carlo samples used to model $Z/\gamma^* \to ee$, $Z/\gamma^* \to \mu\mu$, $Z/\gamma^* \to \tau\tau$, W + jets, $t\bar{t}$, single top and di-boson (WW, WZ, ZZ) backgrounds.

DRAFT

Signal Monte Carlo samples				
Dataset Description	Dataset Name	Cross-section [pb] ($\times \mathcal{B}_{\tau\tau}$ NNLO)	Events	Filter Eff.
ggH $h \to \tau\tau$	/GluGluHToTauTauUncorrelatedDecay_Filtered_M125_TuneCUETP8M1_13TeV-powheg-pythia8 [1]	3.046	20283379	0.2446
VBF $h \to \tau\tau$	/VBFHToTauTauUncorrelatedDecay_Filtered_M125_TuneCUETP8M1_13TeV-powheg-pythia8 [1]	0.237	24065183	0.2695
$W^+h \to \tau\tau$	/WplusHToTauTauUncorrelatedDecay_Filtered_M125_TuneCUETP8M1_13TeV-powheg-pythia8 [1]	0.0527	2716402	0.2397
$W^-h \to \tau\tau$	/WminusHToTauTauUncorrelatedDecay_Filtered_M125_TuneCUETP8M1_13TeV-powheg-pythia8 [1]	0.0358	1876352	0.2563
$Zh \to \tau\tau$	/ZHToTauTauUncorrelatedDecay_Filtered_M125_TuneCUETP8M1_13TeV-powheg-pythia8 [1]	0.0594	3049541	0.2513

[1] /RunIIAutumn18MiniAOD-102X_upgrade2018_realistic_v15-v1/MINIAODSIM

Table 10: List of 2018 Monte Carlo signal samples used to model gg $\to h \to \tau\tau$ signal.

Background Monte Carlo samples		
Dataset Description	Dataset Name	Cross-Section [pb]
$t\bar{t} \to LL\nu\nu$	/TTTo2L2Nu_TuneCP5_13TeV-powheg-pythia8[1]	88.29
$t\bar{t} \to$ hadronic	/TTToHadronic_TuneCP5_13TeV-powheg-pythia8[1]	377.96
$t\bar{t} \to$ semi-leptonic	/TTToSemiLeptonic_TuneCP5_13TeV-powheg-pythia8[1]	365.34
Single top	/ST_tW_antitop_5f_inclusiveDecays_TuneCP5_13TeV-powheg-pythia8[3]	34.97
	/ST_tW_top_5f_inclusiveDecays_TuneCP5_13TeV-powheg-pythia8[3]	35.85
	/ST_t-channel_top_4f_inclusiveDecays_TuneCP5_13TeV-powhegV2-madspin-pythia8[1]	136.02
	/ST_t-channel_antitop_4f_inclusiveDecays_TuneCP5_13TeV-powhegV2-madspin-pythia8[1]	80.95
$Z \to LL$	/DYJetsToLL_M-50_TuneCP5_13TeV-madgraphMLM-pythia8[1]	6077.22 (NNLO)
$Z+1$jet	/DY1JetsToLL_M-50_TuneCP5_13TeV-madgraphMLM-pythia8[2]	877.8 (LO)
$Z+2$jets	/DY2JetsToLL_M-50_TuneCP5_13TeV-madgraphMLM-pythia8[2]	304.4 (LO)
$Z+3$jets	/DY3JetsToLL_M-50_TuneCP5_13TeV-madgraphMLM-pythia8[2]	111.5 (LO)
$Z+4$jets	/DY4JetsToLL_M-50_TuneCP5_13TeV-madgraphMLM-pythia8[1]	44.03 (LO)
Low mass $Z \to LL$	/DYJetsToLL_M-10to50_TuneCP5_13TeV-madgraphMLM-pythia8[2]	18610
W+jets	/WJetsToLNu_TuneCP5_13TeV-madgraphMLM-pythia8[2]	61526.7 (NNLO)
$W+1$jet	/W1JetsToLNu_TuneCP5_13TeV-madgraphMLM-pythia8[2]	9644.5 (LO)
$W+2$jets	/W2JetsToLNu_TuneCP5_13TeV-madgraphMLM-pythia8[2]	3144.5 (LO)
$W+3$jets	/W3JetsToLNu_TuneCP5_13TeV-madgraphMLM-pythia8[2]	954.8 (LO)
$W+4$jets	/W4JetsToLNu_TuneCP5_13TeV-madgraphMLM-pythia8[2]	485.6 (LO)
EWK $W^+ + 2$jets	/EWKWPlus2Jets_WToLNu_M-50_TuneCP5_13TeV-madgraphMLM-pythia8[1]	25.62 (LO)
EWK $W^- + 2$jets	/EWKWMinus2Jets_WToLNu_M-50_TuneCP5_13TeV-madgraphMLM-pythia8[1]	20.25 (LO)
EWK $Z+2$jets	/EWKZ2Jets_ZToLL_M-50_TuneCP5_13TeV-madgraphMLM-pythia8[1]	3.987 (LO)
ZZ	/ZZTo2L2Q_13TeV_amcatnloFXFX_madspin_pythia8[1]	3.688
ZZ	/ZZTo2L2Nu_13TeV_powheg_pythia8[4,5]	0.6008
ZZ	/ZZTo4L_13TeV_amcatnloFXFX-pythia8[4,5]	1.325
WW	/WWTo2L2Nu_NNPDF31_TuneCP5_13TeV-powheg-pythia8[1]	11.08
WW	/WWToLNuQQ_NNPDF31_TuneCP5_13TeV-powheg-pythia8[1]	45.99
WZ	/WZTo2L2Q_13TeV_amcatnloFXFX_madspin_pythia8_v2[1]	6.331
WZ	/WZTo1L3Nu_13TeV_amcatnloFXFX_madspin_pythia8_v2[1]	3.293
WZ	/WZTo1L1Nu2Q_13TeV_amcatnloFXFX_madspin_pythia8[1]	11.66
WZ	/WZTo3LNu_13TeV_amcatnloFXFX_madspin_pythia8_v2[1,4]	5.052
WZ	/WZTo1L1Nu2Q_13TeV_amcatnloFXFX_madspin_pythia8[1]	11.66

[1] /RunIIAutumn18MiniAOD-102X_upgrade2018_realistic_v15-v1/MINIAODSIM

[2] /RunIIAutumn18MiniAOD-102X_upgrade2018_realistic_v15-v2/MINIAODSIM

[3] /RunIIAutumn18MiniAOD-102X_upgrade2018_realistic_v15-ext1-v1/MINIAODSIM

[4] /RunIIAutumn18MiniAOD-102X_upgrade2018_realistic_v15-ext1-v2/MINIAODSIM

[5] /RunIIAutumn18MiniAOD-102X_upgrade2018_realistic_v15-ext2-v2/MINIAODSIM

Table 11: List of 2018 Monte Carlo samples used to model $Z/\gamma^* \to ee$, $Z/\gamma^* \to \mu\mu$, $Z/\gamma^* \to \tau\tau$, W + jets, $t\bar{t}$, single top and di-boson (WW, WZ, ZZ) backgrounds.

DRAFT

Channel	Dataset Name
$\tau_e\tau_h$	/EmbeddingRun2016B/ElTauFinalState[4]
$\tau_e\tau_h$	/EmbeddingRun2016C/ElTauFinalState[4]
$\tau_e\tau_h$	/EmbeddingRun2016D/ElTauFinalState[4]
$\tau_e\tau_h$	/EmbeddingRun2016E/ElTauFinalState[4]
$\tau_e\tau_h$	/EmbeddingRun2016F/ElTauFinalState[4]
$\tau_e\tau_h$	/EmbeddingRun2016G/ElTauFinalState[4]
$\tau_e\tau_h$	/EmbeddingRun2016H/ElTauFinalState[4]
$\tau_\mu\tau_h$	/EmbeddingRun2016B/MuTauFinalState[1]
$\tau_\mu\tau_h$	/EmbeddingRun2016C/MuTauFinalState[1]
$\tau_\mu\tau_h$	/EmbeddingRun2016D/MuTauFinalState[1]
$\tau_\mu\tau_h$	/EmbeddingRun2016E/MuTauFinalState[1]
$\tau_\mu\tau_h$	/EmbeddingRun2016F/MuTauFinalState[1]
$\tau_\mu\tau_h$	/EmbeddingRun2016G/MuTauFinalState[1]
$\tau_\mu\tau_h$	/EmbeddingRun2016H/MuTauFinalState[2]
$\tau_h\tau_h$	/EmbeddingRun2016B/TauTauFinalState[1]
$\tau_h\tau_h$	/EmbeddingRun2016C/TauTauFinalState[1]
$\tau_h\tau_h$	/EmbeddingRun2016D/TauTauFinalState[1]
$\tau_h\tau_h$	/EmbeddingRun2016E/TauTauFinalState[1]
$\tau_h\tau_h$	/EmbeddingRun2016F/TauTauFinalState[1]
$\tau_h\tau_h$	/EmbeddingRun2016G/TauTauFinalState[1]
$\tau_h\tau_h$	/EmbeddingRun2016H/TauTauFinalState[3]

[1] -inputSep16DoubleMu_mirror_miniAOD-v2/USER
[2] -inputPromptDoubleMu_mirror_miniAOD-v2/USER
[3] -inputPromptDoubleMu_mirror_miniAOD-v3/USER
[4] -inputDoubleMu_94X_Legacy_miniAOD-v5/USER

Table 12: List of 2016 embedded samples.

Channel	Dataset Name
$\tau_e\tau_h$	/EmbeddingRun2017B/ElTauFinalState[4]
$\tau_e\tau_h$	/EmbeddingRun2017C/ElTauFinalState[4]
$\tau_e\tau_h$	/EmbeddingRun2017D/ElTauFinalState[4]
$\tau_e\tau_h$	/EmbeddingRun2017E/ElTauFinalState[4]
$\tau_e\tau_h$	/EmbeddingRun2017F/ElTauFinalState[4]
$\tau_\mu\tau_h$	/EmbeddingRun2017B/MuTauFinalState[1]
$\tau_\mu\tau_h$	/EmbeddingRun2017C/MuTauFinalState[1]
$\tau_\mu\tau_h$	/EmbeddingRun2017D/MuTauFinalState[1]
$\tau_\mu\tau_h$	/EmbeddingRun2017E/MuTauFinalState[1]
$\tau_\mu\tau_h$	/EmbeddingRun2017F/MuTauFinalState[1]
$\tau_h\tau_h$	/EmbeddingRun2017B/TauTauFinalState[1]
$\tau_h\tau_h$	/EmbeddingRun2017C/TauTauFinalState[1]
$\tau_h\tau_h$	/EmbeddingRun2017D/TauTauFinalState[1]
$\tau_h\tau_h$	/EmbeddingRun2017E/TauTauFinalState[1]
$\tau_h\tau_h$	/EmbeddingRun2017F/TauTauFinalState[1]

[1] -inputDoubleMu_94X_miniAOD-v2/USER
[4] -inputDoubleMu_94X_Legacy_miniAOD-v2/USER

Table 13: List of 2017 embedded samples.

DRAFT

Channel	Dataset Name
$\tau_e\tau_h$	/EmbeddingRun2018B/ElTauFinalState[4]
$\tau_e\tau_h$	/EmbeddingRun2018B/ElTauFinalState[4]
$\tau_e\tau_h$	/EmbeddingRun2018C/ElTauFinalState[4]
$\tau_e\tau_h$	/EmbeddingRun2018D/ElTauFinalState[4]
$\tau_\mu\tau_h$	/EmbeddingRun2018A/MuTauFinalState[1]
$\tau_\mu\tau_h$	/EmbeddingRun2018B/MuTauFinalState[1]
$\tau_\mu\tau_h$	/EmbeddingRun2018C/MuTauFinalState[1]
$\tau_\mu\tau_h$	/EmbeddingRun2018D/MuTauFinalState[1]
$\tau_h\tau_h$	/EmbeddingRun2018A/TauTauFinalState[1]
$\tau_h\tau_h$	/EmbeddingRun2018B/TauTauFinalState[1]
$\tau_h\tau_h$	/EmbeddingRun2018C/TauTauFinalState[1]
$\tau_h\tau_h$	/EmbeddingRun2018D/TauTauFinalState[1]

[1] -inputDoubleMu_102X_miniAOD-v1/USER
[4] -inputDoubleMu_102X_miniAOD-v1/USER

Table 14: List of 2018 embedded samples.

DRAFT

4 Object reconstruction

4.1 Muons

Identification
Muons are required to be reconstructed as muon by the particle flow reconstruction.

For muons selected in the $\tau_e\tau_\mu$ and $\tau_\mu\tau_h$ channels additional *Medium muon* requirements [**?**], as recommended by the Muon POG, are applied. These requirements are:

- The muon is reconstructed by the *tracker* or *global* muon reconstruction algorithm.
- The impact parameters d_{xy} and d_z between the muon track ('best track') and the primary vertex are restricted as $d_{xy} < 0.045$ cm and $d_z < 0.2$ cm to ensure the muon is associated with the primary vertex
- At least 49% of the tracker hits have to be valid (at least 80% of the tracker hits have to be valid) in 2016 data from runs B–F (2016 data from runs G–H, 2017 data runs B–F, or MC)

In addition, either of the following two sets of criteria must be satisfied:

- The muon is reconstructed by the *global* muon reconstruction algorithm.
- The χ^2/ndof of the global track fit is smaller than 3
- The χ^2 of the tracker-standalone position match is smaller than 12
- The χ^2 of the track kink finder is less than 20
- The muon segment compatibility is > 0.303

or:

- The muon segment compatibility is > 0.451

Finally the impact parameters d_{xy} and d_z between the muon track and the primary vertex are restricted as $d_{xy} < 0.045$ cm and $d_z < 0.2$ cm to ensure the muon is associated with the primary vertex

Isolation
To reduce the contamination from muons originating from heavy-flavoured quark decays in jets or decays in flight, selected muons are required to be isolated. The isolation is based on photon and neutral/charged hadron particle flow candidates within a cone size of $\Delta R < 0.4$ of the selected muon. A relative combined isolation variable is defined as:

$$I^{\mu}_{rel} = \frac{\Sigma P_T(\text{charged}) + \max(\Sigma E_T(\text{neutral}) + \Sigma E_{\text{T}}(\text{photon}) - \Delta\beta\Sigma E_{\text{T}}(\text{PU}), 0)}{P^{\mu}_{\text{T}}}, \tag{9}$$

where $P_T(\text{charged})$ corresponds to the P_T of all charged hadronic candidates, $E_T(\text{photon, neutral})$ to the transverse energy of all photon and neutral hadron candidates, and $\Delta\beta$ is the energy estimate of neutral particles due to pileup, which is taken to be 0.5.

In the $\tau_\mu\tau_h$ channel the requirement on muon isolation is $I_{\text{rel}} < 0.15$.

4.2 Electrons

Identification
Electrons are required to be reconstructed as electron by the particle flow reconstruction. In addition, electrons are required to pass an identification variable based on a Boosted Decision

DRAFT

Tree (BDT) discriminator which uses track quality, shower shapes and kinematic quantities as input. The following variables are used as input to the BDT: [**?**]

- Cluster shape variables $\sigma_{i\eta,i\eta}$ and $\sigma_{i\phi,i\phi}$, with $i\eta$ and $i\phi$ the integer label of the η and ϕ calorimeter cell. The circularity = $1 - \frac{E1\times5}{E5\times5}$, with $E1 \times 5$ and $E5 \times 5$ the energies in a 1×5 and a 5×5 grid around the super cluster seed, respectively. Shape variable R9 = $\frac{E3\times3}{E_{SC}}$, with $E3 \times 3$ the energy in a 3×3 grid of cells around the super cluster seed and E_{SC} the raw energy of the super cluster.
- The number of valid hits in the track fit, the χ^2 of the track fit and the χ^2 of the GSFTrack fit
- The number of GSFtrack hits, the number of expected missing inner hits and the result of the conversion vertex fit
- The distance $\Delta\eta$ and $\Delta\phi$ between the reconstructed super cluster and the associated track at the position of the primary vertex, and the distance in η between the super cluster and the track at the calorimeter surface.
- H/E, the ratio of the hadronic energy over the electromagnetic energy in the super cluster and E/P, the ratio of the super cluster energy over the momentum of the track associated with the electron
- The ratio of the energy of the electron cluster and the momentum of the associated track, evaluated at the electron cluster, and $1/E_e - 1/P_e$, with E_e the energy of the electron candidate and P_e its momentum.

The BDT was trained on a Z/γ^* Monte Carlo sample generated with `MadGraph 5`, in 3 η bins for electrons with $p_{\mathrm{T}} > 10$ GeV. This analysis uses the version of the ID BDT without the isolation included in the training, instead using an additional cut on the electron isolation. This was shown to give similar performance to the version of the ID including the isolation and makes defining side-band regions used for estimation of backgrounds simpler.

For electrons selected in the $\tau_e\tau_\mu$ and $\tau_e\tau_h$ channels we require the electron to pass the 90% efficiency working point. To avoid event overlap, events passing the $\tau_\mu\tau_h$ and $\tau_h\tau_h$ selections are vetoed if they contain electrons passing the 90% efficiency working point.

Finally electrons are also subject to the same impact parameter cuts as the muons: the impact parameters d_{xy} and d_z between the electron track and the primary vertex are restricted as $d_{xy} < 0.045$ cm and $d_z < 0.2$ cm to ensure the electron is associated with the primary vertex.

Isolation

The isolation used is based on photon and neutral/charged hadron particle flow candidates within a cone size of $\Delta R < 0.3$ of the selected electron but used a different method to estimate the neutral particles due to pileup, namely the rho–effective-area method. The pileup in this method is estimated as $PU = \rho \cdot \mathrm{EA}$, where ρ is the event-specific average pile-up energy density per unit area in the ϕ-η plane and the EA is the effective area specific to the given type of isolation. The rho–effective-area subtracted relative combined isolation variable is defined as:

$$I^{\mathrm{e}}_{rel} = \frac{\Sigma P_T(\mathrm{charged}) + \max(\Sigma E_T(\mathrm{neutral}) + \Sigma E_T(\mathrm{photon}) - \rho \cdot \mathrm{EA}, 0)}{P^e_T}, \tag{10}$$

where the EA is measured in bins of η as listed in Table 15.In both the $\tau_e\tau_h$ and $\tau_e\tau_\mu$ channels the requirement on electron isolation is $I_{rel} < 0.15$.

DRAFT

η range	EA
$0.0 \leq \eta < 1.0$	0.1440
$1.0 \leq \eta < 1.479$	0.1562
$1.479 \leq \eta < 2.0$	0.1032
$2.0 \leq \eta < 2.2$	0.0859
$2.2 \leq \eta < 2.3$	0.1116
$2.3 \leq \eta < 2.4$	0.1321
$2.4 \leq \eta < 5.0$	0.1654

Table 15: Electron effective areas used for the rho-corrected isolation computation.

4.3 Taus

Hadronic tau decays are reconstructed using the `hadrons plus strips` (HPS) algorithm [**? ?**], which uses particle flow candidates to reconstruct and identify hadronic tau decays. In the reconstruction step, particle-flow charged and neutral particles are grouped into combinations compatible with specific hadronic tau decay modes, and the 4-momentum of the candidates is computed. In the identification step, discriminators that separate hadronic taus from quark and gluon jets and from electrons and muons are evaluated. Taus in the hadrons plus strips algorithm are seeded by jets clustered with the anti-k_{T} algorithm with a distance parameter $\Delta R = 0.4$.

To reconstruct the energy deposits π^0 candidates leave in the ECAL, photon and electron constituents of the jet that seeds the τ reconstruction are clustered into strips. The e or γ with highest p_{T} that is not yet included in a strip is used to build a new strip. The η and ϕ of this candidate determine the initial position of the strip, the next highest p_{T} e or γ within an $\eta \times \phi$ window centred on the strip location is added to the strip and the position is recomputed as the energy-weighted average of the electron/photon constituents in the strip. This procedure is repeated until there are no more electrons or photons with $p_{\mathrm{T}} > 0.5$ GeV within the strip window. The $\Delta\eta$ and $\Delta\phi$ of the strip are varied based on the p_{T} or E_{T} to be added to the strip and on the energy the strip already has, as

$$\begin{aligned} \Delta\eta &= f(p_{\mathrm{T}}^{e/\gamma}) + f(p_{\mathrm{T}}^{\mathrm{strip}}) \\ \Delta\phi &= g(p_{\mathrm{T}}^{e/\gamma}) + g(p_{\mathrm{T}}^{\mathrm{strip}}), \end{aligned} \tag{11}$$

where $p_{\mathrm{T}}^{e/\gamma}$ is the transverse momentum of the candidate to be added to the strip and $p_{\mathrm{T}}^{\mathrm{strip}}$ is the transverse momentum of the strip before merging a new candidate in. In addition, the strip size is bounded as $0.05 < \Delta\eta < 0.15$, $0.05\Delta\phi < 0.3$.

The functions $f(p_{\mathrm{T}})$ and $g(p_{\mathrm{T}})$ are defined as

$$\begin{aligned} f(p_{\mathrm{T}}) &= 0.2 \cdot p_{\mathrm{T}}^{-0.66} \\ g(p_{\mathrm{T}}) &= 0.35 \cdot p_{\mathrm{T}}^{-0.71}. \end{aligned} \tag{12}$$

If the Σp_{T} of the strip is at least 2.5 GeV, it is considered as a π^0 candidate. To reconstruct hadronic taus, charged particles and strips are combined into different signatures which are compatible with a certain decay mode if the set of cuts listed below is satisfied. If a candidate satisfies more than one of the hypotheses, the one that maximises the p_{T} is retained.

The decay modes (with decayModeFindingNewDMs) considered for reconstructing taus are:

DRAFT

- **One prong, 0 π^0 :** One charged particle, no strips.
- **One prong, 1 π^0 :** One charged particle + one strip with mass $0.3 < m_\tau < 1.3\sqrt{p_\mathrm{T}/100}$ GeV. The mass window upper limit is constrained to lie between 1.3 and 4.2 GeV.
- **One prong, 2 π^0 :** One charged particle + two strips. The τ_h mass should be $0.4 < m_\tau < 1.2\sqrt{p_\mathrm{T}/100}$ GeV. The upper limit on the mass window is constrained to lie between 1.2 and 4.0 GeV.
- **Two prong, 0 π^0 :** Two charged particle + no strips.
- **Two prong, 1 π^0 :** Two charged particle + one strips.
- **Two prong, 2 π^0 :** Two charged particle + two strips.
- **Three prong, 0 π^0:** Three charged particles with mass $0.8 < m_\tau < 1.5$ GeV. The tracks are required to originate within $\Delta z < 0.4$ cm of the same vertex.
- **Three prong, 1 π^0:** Three charged particles + one strip.

Isolation
Requiring the reconstructed τ_h to be isolated reduces the jet$\rightarrow$ τ_h fake rate. Both a cut-based discriminator and MVA-based ones are available, in this analysis we make use of the deepTau discriminator [37].

The deepTauv2p1 discriminator is a DNN-based algorithm that gives three outputs: tau vs jets, tau vs electrons and tau vs muons [**?**], where the anti-lepton discriminators provide reduction in $e \rightarrow \tau_h$ and $\mu \rightarrow \tau_h$ fake rates. In the analysis for the hadronic tau we require the medium working point for the anti-jet score. In the $\mu\tau_h$ channel in addition to the vs jet discrimination, we require the vvloose WP on the vs electron discriminator and the tight WP for the vs muon discriminator. In the $e \rightarrow \tau_h$, on the other hand, we require the vs electron discriminator to be tight and the vs muon discriminator vloose. Finally in the all-hadronic channel the two τ_h are required to have pass the medium vs jet, the vvloose vs electron, and the vloose vs muon discriminators.

4.4 Jets and b-tagging

For the classification of events according to different Higgs boson production mechanisms, jets are used. These are clustered from all particle flow candidates using the anti k_T algorithm [**?**] with a cone size R=0.4. To reduce the contribution of jets that originate from pile–up vertices, charged hadrons that are not associated with the hard–scattering primary vertex are removed from the particle flow candidates that form the input to the anti-k_T-algorithm (charged hadron subtraction).

Practically, this means we use the "slimmedJets" collection from the miniAOD dataformat, where the jet-energy corrections from global tags

`94X_mcRun2_asymptotic_v3` (mc) and
`94X_dataRun2_v10` (data) are reapplied for (legacy) 2016 and the jet-energy corrections from global tags
`102X_mc2017_realistic_v6` (mc) and
`102X_dataRun2_v8` (data) are reapplied for 2017.

`102X_upgrade2018_realistic_v20` (mc) and
`102X_dataRun2_v12` (data) are reapplied for 2018. In MC events, we reapply correction levels L1Fastjet, L2Relative and L3Absolute, whereas for data events L1Fastjet, L2Relative, L3Absolute and L2L3Residual levels are reapplied.

DRAFT

The jets are required to pass the tight working point of the PF jet ID discriminator provided by the jetMET POG [38]. To exclude selected e, μ, τ_h candidates from the jet collection, the jets are required to be separated from the selected di-τ candidate by $\Delta R > 0.5$. Jets with a corrected $p_{\mathrm{T}} > 30$ GeV and $|\eta| < 4.7$ are considered.

High endcap ECAL noise in 2017 led to large amounts of noise in reconstructed jets [39]. To mitigate the noise issue, jets reconstructed on 2017 data also used a veto of jets with raw $p_t < 50$ and $2.65 < |\eta| < 3.139$.

For determining information about the b-tagging status of the jets, the `deepCSV` algorithm is used. Jets with $p_{\mathrm{T}} > 20$ and $|\eta| < 2.4$ are considered b-tagged if their deepCSV discriminator value is larger than 0.6321, 0.4941 or 0.4184 in the 2016, 2017 or 2018 analysis, respectively. This corresponds to the medium working point provided by the b-tag POG [**?**]/ [**?**].

4.5 Missing transverse energy

The missing transverse energy in the event is reconstructed using the PUPPI algorithm [40], which is more robust towards pileup compared to PF MET, which tends to increase for Run 2 analyses. This algorithm is an extension of the PFCHS algorithm an assigns weights to PF candidates based on the probability that they come from pileup or the primary vertex. Type-I corrections are applied to correct the MET estimated in this way for over- or underestimation due to inefficiencies in the detector. These corrections entail the propagation of the JECs to the MET as

$$\vec{E}_{\mathrm{T}}^{\mathrm{miss,corr}} = \vec{E}_{\mathrm{T}}^{\mathrm{miss}} - \Sigma_{\mathrm{jets}}(\vec{p}_{\mathrm{T}}^{\mathrm{corr}} - \vec{p}_{\mathrm{T}}). \tag{13}$$

4.6 Primary vertex reconstruction

Precise determination of the location of pp interaction vertex (primary vertex) is essential for this analysis as it employs impact parameter of the charged decay products of the τ lepton to reconstruct the CP discriminating observable (see also the definition in paragraph 2.1). The impact parameter of the tracks from the charged decay products are measured with respect to the primary vertex. At CMS the pp interaction vertices in an event, that includes the hard-scatter (signal) vertex as well as any vertcies from pileup collisions, are reconstructed by clustering tracks using the so-called *deterministic annealing* algorithm [41]. The candidate vertex with the largest value of $\sum p_{\mathrm{T}}^2$ of physics objects is considered to be the primary pp interaction vertex, where the physics objects refer to jets reconstructed from tracks assigned to candidate vertices, and the associated missing transverse momentum, which is taken as the negative vector sum of the p_{T} of those jets.

The primary vertex reconstruction algorithm assumes all tracks to be originating from primary vertices. However, given its lifetime, τ lepton travels a certain distance before its decay. Thus, the decay products of the τ leptons originate from secondary vertices. Including tracks of the charged decay products of the τ leptons in the primary vertex reconstruction can lead to incorrect estimation of the primary vertex position, thereby leading to incorrect measurement of impact parameter vectors. To remove such bias in the estimation of primary vertex position we proceed as follows. We take the collection of reconstructed tracks that are associated with the candidate primary vertex. The tracks that match with the tracks from the decay products of the pair of selected τ leptons are removed from the collection. The remaining tracks in the collection are refitted together using an *adaptive vertex fitter* [42] to re-compute the best estimate of the vertex parameters, includig its x, y, and z position. The removal of the tracks belonging to the decay products of pair of τ leptons changes the position of the primary vertex as seen in Fig 7. However, the resolution of the primary vertex position remains almost un-

affected, which can be seen in Fig. 8, despite reduction in the number of tracks in the vertex fitting. The steps for the refitting of a collection of tracks using *adaptive vertex fitter* to estimate the primary vertex position and its uncertainty are summarized here. An initial (prior) estimation of the vertex position is obtained using the so-called fraction of sample mode with weights (FSMW) method [42] and a large initial uncertainty is assigned to the prior position. The tracks are sorted based on their distance from this prior position. Tracks are added one by one to the vertex and the vertex position is updated by the Kalman Filter algorithm [43]. After all the available track candidates are added the updated vertex position is compared to that of the position obtained in the privious iteration. If the vertex position moved significantly with respect to the position obtained in previous iteration the tracks are then reweighted based on their compatibility with the updated vertex position, computed by the Kalman Filter compatibility estimator. The vertex fitting steps are repeated with the collection of reweighted tracks, again starting with the prior vertex position and uncertainties. The iterations are repeated untill the displacement in the vertex position is small in successive iterations or a maximum number of iterations has been attained. The position and uncertainty obtained in the last iteration is considered to be the final vertex position and uncertainty.

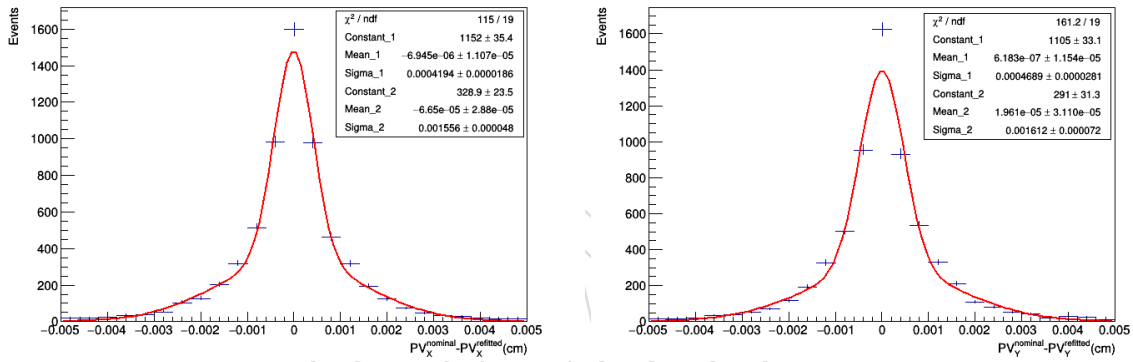

Figure 7: The difference in the position of the primary vertex, in x (left) and y (right) directions, with nominal vertex reconstruction and with the removal of tracks belonging to τ lepton decay products. A MC simulated sample consisting of $\mathrm{H} \to \tau\tau \to \mu\tau_{\mathrm{h}}$ events are used in these plots. The distributions are fitted with a double Gaussian function to understand the nature of the displacement.

To make a further improvement in the estimation of the primary vertex position an additional constraint is imposed in the reftting of tracks by the *adaptive vertex fitter* from the estimation of LHC beam spot. The beam spot represents a 3-D profile of the luminous region, where the LHC beams collide in the CMS detector. The parameters of the beam spot are determined from an average over many events, as described in Ref. [41]. In case of a beam spot constraint the beam spot position is taken as the prior vertex position, instead of obtaining it using FSMW method. The covariance matrix of the beam spot is used as uncertainty of the prior vertex instead of assigning a large uncertainty. Since the beam spot is measured quite precisely it gets larger weight in the fit procedure, and the uncertainties on the track parameters are unable to move the primary vertex position significantly. Thereby, the overall uncertainties in the vertex position are dominated by the uncertainty in beam spot position, at least in the transverse plane. The rest of the steps in the successive iterations of the vertex fitting remain similar to that of fitting without beam spot constraint. The constraint from the beam spot significantly improves the resolution of the primary vertex position in x and y direction, as seen in Fig 8, while the z position remains almost unchanged.

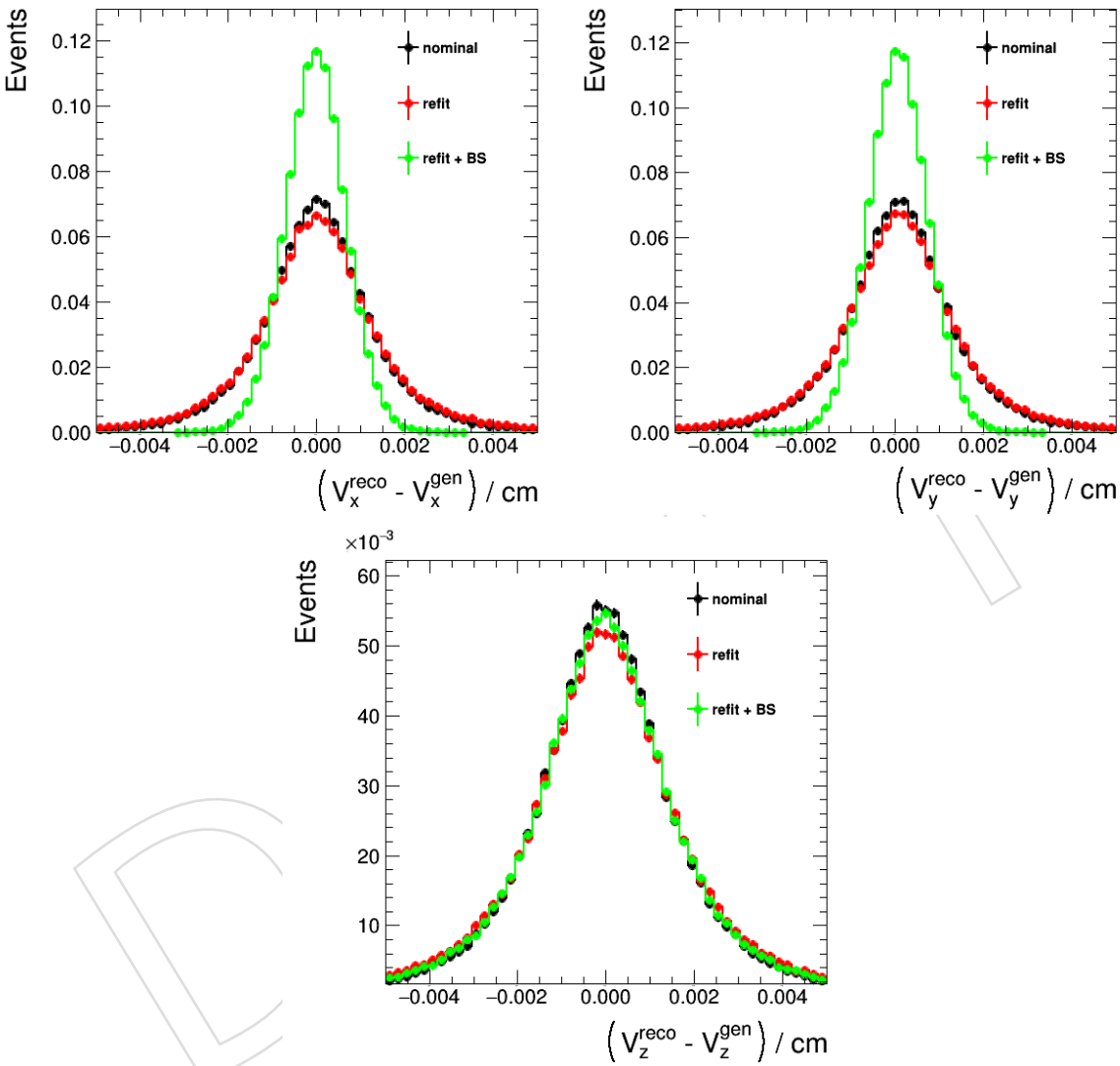

Figure 8: The difference between the generated position of the primary vertex and its reconstructed position with three different approach: (1) nominal vertex reconstruction, (2) refitting of tracks to determine primary vertex position after exclusion of tracks belonging to the decay products of the pair of τ leptons, and (3) applying beam spot constraint during refitting with exclusion of tracks belonging to the τ leptons. A MC simulated sample consisting of $H \to \tau\tau \to \mu\tau_h$ events are used in these plots.

4.6.1 Effect of the track removal and beamspot corrections

There are essentially two smearing effects that smear the ϕ_{CP} angle, being the tracking and PV smearing effects. For the $\mu\pi$ and $\pi\pi$ modes, in which the impact parameter method is used for both τ leptons, the vertex smearing effects lead to a correlated effect on the IP vectors.

The PV smearing effect may be subdivided still in statistical smearing effects and the pull effect due to the displaced tracks of the τ leptons. The statistical effects of smearing the PV were reviewed on particle-level in [8]. It was found that effectively the distance between the vertex and the tracks increases. As a result, the angles around 0 and 2π are enhanced.

In Fig 9 (left) we display the Drell-Yan spectrum for $\mu\pi$ decays (after a rudimentary event selection) with the refitted beamspot-corrected PV. We observe that indeed the angles at 0 and 2π are enhanced, as expected.

However, when we include the tau tracks in the vertex fit, we observe that the Drell-Yan spectrum instead exhibits a peak at $\phi_{\mathrm{CP}} = \pi$. For such configurations, the primary vertex is pulled to be located in between the tau tracks, by which their impact parameters become oppositely directed instead. Thus, incorporating the beamspot reduces the statistical smearing effects, while removing the tau tracks from the vertex fit removes the pull effect. It may also be seen from Fig 9 that these effects only play a significant role for decay modes involving two impact parameters; since the decay plane method does not rely on the primary vertex, the smearing barely doesn't affect the ϕ_{CP} distributions.

For completeness we display the same distributions for the signals in Fig. 10 for refitted beamspot-corrected verices (left) and beamspot-corrected vertices for a scalar boson. We observe the expected convolution of the PV smearing effects and the signal shapes.

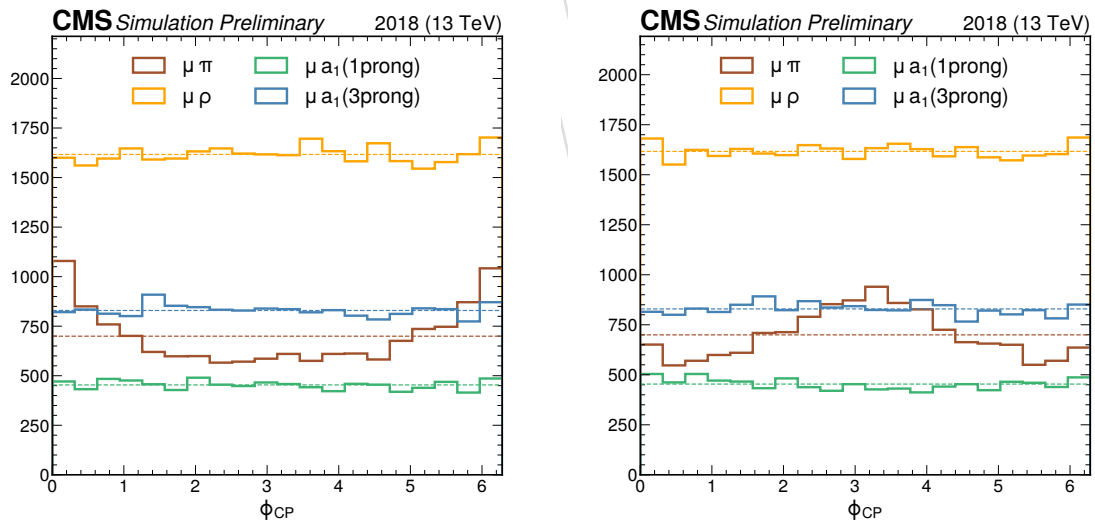

Figure 9: The distribution of $Z \to \tau_\mu \tau_{\mathrm{h}}$ for various τ_{h} decay modes. Left: the refitted beamspot-corrected primary vertex with tau tracks removed was used. Right: the beam-spot corrected vertex without removed tau tracks was used. For the $\mu\pi$ channel we observe that the PV smearing effects induce substantial correlations between the impact parameters, while the decays with a single impact parameter are barely affected.

throughout this analysis, the refitted beamspot corrected vertex is used.

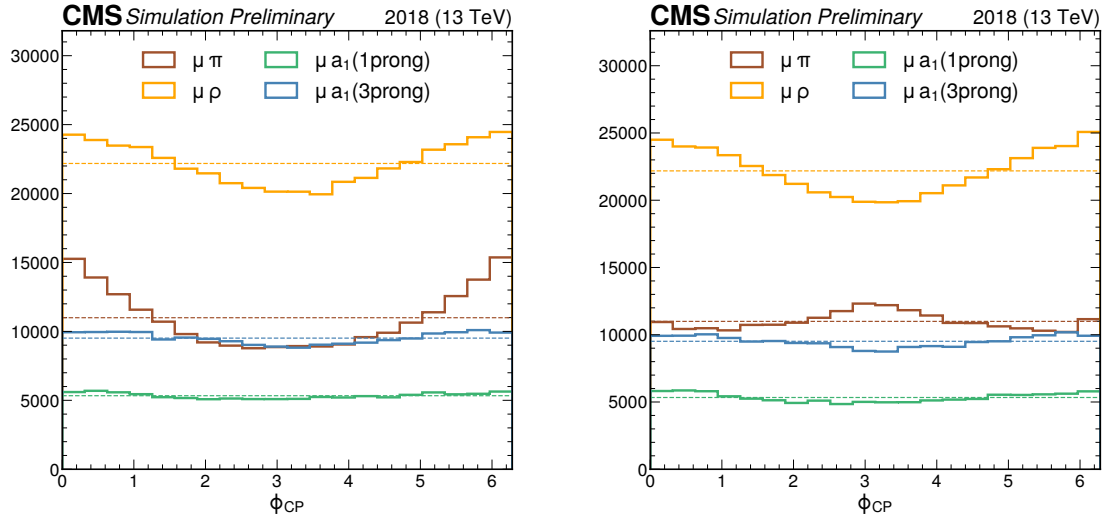

Figure 10: The distribution of $H \to \tau_\mu \tau_h$ for various τ_h decay modes. Left: the refitted beamspot-corrected primary vertex with tau tracks removed was used. Right: the beam-spot corrected vertex without removed tau tracks was used. For the $\mu\pi$ channel we observe that the PV smearing effects induce substantial correlations between the impact parameters, while the decays with a single impact parameter are barely affected.

4.7 Impact parameter reconstruction

The impact parameters can be reconstructed with a finite precision. By careful extrapolation of both track and primary vertex uncertainties, we can derive a significance of the impact parameter incorporating both uncertainties. This allows to discard events with poorly reconstructed impact parameters, which dilute the sensitivity of the analysis. This section describes how the significance of the impact parameter can be calculated.

However, the impact parameters, which are input to the ip significance calculations, are not well described by MC. In Section 5.5 the procedure to calibrate the impact parameters in MC and embedded samples is outlined, as well as the propagation of their new uncertainties in the ip significance.

The CMSSW track parameters only provide a measure for the transverse impact parameter, which describes the minimal distance from the track to a specified point in the projection onto the xy-plane. For the measurement of the ϕ_{CP} angle however the three-dimensional impact parameter vector has to be determined. To obtain it, the particle's trajectory is parameterised by a helix in the form of

$$\vec{x}(t) = \vec{o} + \begin{pmatrix} r\cos(\omega t - \varphi_1) \\ -r\sin(\omega t - \varphi_1) \\ v_z t \end{pmatrix}. \tag{14}$$

In this formalism, t is the curve parameter, r is the radius of the helix, φ_1 is a phase setting the orientation of the helix (as shown in Fig. 11), v_z is the longitudinal velocity and $\vec{o}$ is the vector from the CMS coordinate centre to the axis of the helix O'.

For $t = 0$ one can set without the loss of generality

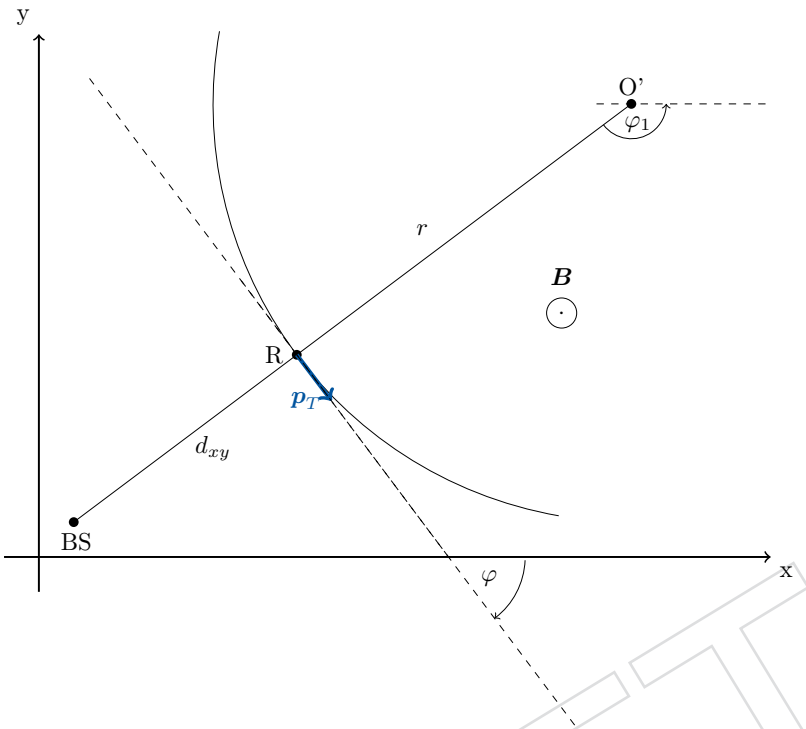

Figure 11: A visualisation of the parameters of the helical curve projected on to the xy-plane.

$$\vec{o} = \vec{x}(t=0) - \begin{pmatrix} r\cos(-\varphi_1) \\ -r\sin(-\varphi_1) \\ 0 \end{pmatrix}. \tag{15}$$

Eq. 14 can be rewritten using $t' = \omega t$ and the CMSSW track parameter convention as

$$\vec{x}(t') = \vec{R} + \begin{pmatrix} \frac{\cos\lambda}{B\cdot\frac{q}{p}} \cdot \mathrm{sgn}\left(\frac{q}{p}\right) \cdot [\sin\phi(1-\cos t') + \cos\phi\sin t' \\ \frac{\cos\lambda}{B\cdot\frac{q}{p}} \cdot \mathrm{sgn}\left(\frac{q}{p}\right) \cdot [\sin\phi\sin t' - \cos\phi(1-\cos t') \\ \frac{\sin\lambda}{B\cdot\frac{q}{p}} \cdot \mathrm{sgn}\left(\frac{q}{p}\right) \cdot t' \end{pmatrix}. \tag{16}$$

Here, B is the magnetic field, q is the charge of particle, p is the 3-momentum magnitude and ϕ, λ its polar and azimuthal angles at the reference point $\vec{R}$, respectively. The latter is given by

$$\vec{R} = \vec{BS} + \begin{pmatrix} -d_{xy}\sin\varphi \\ d_{xy}\cos\varphi \\ \frac{d_{sz}}{\cos\lambda} \end{pmatrix} \tag{17}$$

with $\vec{BS}$ indicating the vector to the beamspot, and d_{xy}, d_{sz} two helix parameters. In order to obtain the impact parameter vector, the expression

$$\delta(t') = |\vec{V} - \vec{x}(t')| \tag{18}$$

DRAFT

has to be minimized, with $\vec{V}$ being the vector to the primary vertex. At the minimum $\vec{x}(t'_{min})$ represents the point on the track at which the distance to the primary vertex is minimal. The impact parameter vector therefore is

$$\vec{n} = \vec{x}(t'_{min}) - \vec{V}. \tag{19}$$

4.7.1 The IP-significance

The uncertainty on the parametrisation vector $\vec{x}$ (see Eq. 16) can be calculated analytically via uncertainty propagation:

$$\mathbf{\Sigma}_{\vec{x}} = \mathbf{J}_{\vec{x}} \mathbf{\Sigma}_{\text{Helix}} \mathbf{J}_{\vec{x}}^{\mathsf{T}}, \tag{20}$$

with $\mathbf{\Sigma}_{\text{Helix}} \in \mathbb{R}^{5\times5}$ being the covariance matrix of the helix parameters and $\mathbf{J}_{\vec{x}} \in \mathbb{R}^{3\times5}$ being the Jacobian matrix of the parametrisation vector $\vec{x}$. With $\Sigma_{\vec{n}}$ the uncertainty on the impact parameter vector can be calculated similarly:

$$\mathbf{\Sigma}_{\vec{n}} = \mathbf{J}_{\vec{n}} \begin{pmatrix} \mathbf{\Sigma}_{\vec{x}} & 0 \\ 0 & \mathbf{\Sigma}_{\text{PV}} \end{pmatrix} \mathbf{J}_{\vec{n}}^{\mathsf{T}}. \tag{21}$$

$\mathbf{\Sigma}_{\text{PV}} \in \mathbb{R}^{3\times3}$ is the covariance matrix of the primary vertex and $\mathbf{J}_{\vec{n}} \in \mathbb{R}^{3\times6}$ the Jacobian matrix connected to the impact parameter vector. The uncertainty on the impact parameter $|\vec{n}|$ is then

$$\sigma_{|\vec{n}|} = \frac{\vec{n}^{\mathsf{T}}}{|\vec{n}|} \mathbf{\Sigma}_{\vec{n}} \frac{\vec{n}}{|\vec{n}|}, \tag{22}$$

where the Jacobian matrix is given in its explicit form due to its simplicity. An impact parameter significance is defined as

$$\sigma_{\text{IP}} = \frac{|\vec{n}|}{\sigma_{|\vec{n}|}}. \tag{23}$$

The parametrisation of all other Jacobian matrices used in this method can be found in the appendix A.

The contribution of the uncertainties coming from the primary vertex and the helix parameters to the total uncertainty on the impact parameter are shown in Fig. 12 for muon and single charged pion decays. Additionally the effects of the different primary vertex reconstruction algorithms introduced in 4.6 are compared. It can be noted that both uncertainty sources have a comparable impact on the total uncertainty and therefore neither can be neglected.

4.8 Tau decay mode identification with BDT

The Hadron-Plus-Strip (HPS) [44] algorithm is currently used in CMS to reconstruct and identify the hadronic decays of τ (τ_{h}). Starting from Particle Flow (PF) jets, the HPS algorithm clusters electrons, positrons and photons which are close enough to the jet into what is called a "strip". If the charged particles in the jet, together with the strips (if any) pass certain cuts then it is reconstructed as a τ_{h}. The strips should represent the decay products of π^0s. Depending on the number of strips and charged particles in τ_{h}, the reconstructed decays are labeled with

DRAFT

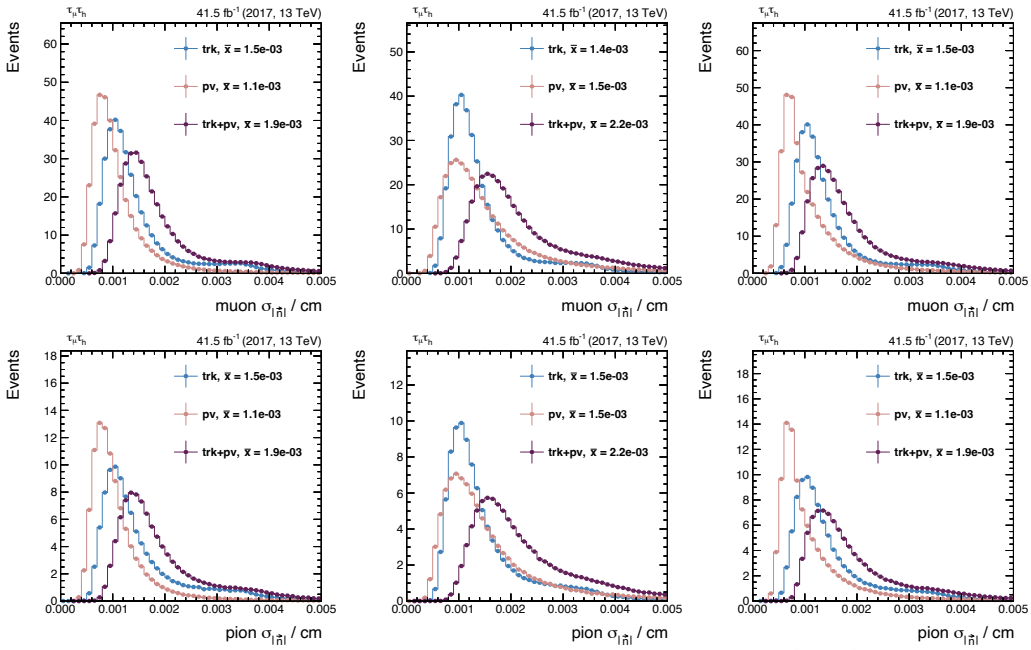

Figure 12: The top plots show the uncertainty on the magnitude of the impact parameter ($\vec{n}$) of signal muons, while the bottom ones show the same distribution for the signal pions for the VBF $h \to \tau\tau$ signal sample. The uncertainties are shown for three different reconstructions of the primary vertex, from left to right, namely for the nominal primary vertex including tracks of tau decay products, the primary vertex obtained through adaptive vertex fitting ("the refitted primary vertex"), and the refitted primary vertex with the beamspot constraint. Each plot shows the distribution of the uncertainty split into the contributions from the primary vertex (labelled *pv*), track paramaters (labelled *trk*) and the full uncertainty including both (labelled *trk+pv*).

a number, called *decay mode* (DM). The DM labels are defined as $5.(N_c - 1) + N_p$ in which N_c is the number of charged particles and N_p is the number of strips.

In the measurement of the Higgs CP using $\mathrm{H} \to \tau\tau$, since the decay channels of τ_h have different CP sensitivity, it is crucial to correctly identify these channels. Fig 13 shows an example of how impurities in DM 1 affects the CP separation between a scalar and pseudoscalar Higgs scenarios. In order to enhance the identification power of the τ_h decay channels, we performed a multi-class Multivariate Analysis (MVA) with the Boosted Decision Tree (BDT) algorithm using XGBoost library on top of the HPS algorithm. We trained the MVA for the 1 charged prong decays and 3 charged prong decays separately, which will be elaborated on below.

As the input data for the MVA, we used $\mathrm{H} \to \tau\tau$ events where the Higgs are produced through ggH and VBF processes and the taus are required to decay through $\mu\tau_\mathrm{h}$ or $\tau_\mathrm{h}\tau_\mathrm{h}$ channels. After that, we collected all τ_h and treated them independent of their production process. The 2017 setup is used to produce MC samples. All τ_h in the $\tau_\mathrm{h}\tau_\mathrm{h}$ ($\tau_\mu\tau_\mathrm{h}$) channel are required to have $p_\mathrm{T} > 40$ (20) GeV to match the selections used in the analysis.

4.8.1 1-prong τ_h decay classification

As shown in table 16, the main 1-prong decays of τ_h are $\tau \to \pi\nu$, $\tau \to \rho \to \pi\pi^0\nu$ and $\tau \to \mathrm{a}_1 \to \pi 2\pi^0\nu$. The HPS algorithm reconstructs these decays into DM 0, DM 1 and DM 2, respectively. However, almost all of the $\tau \to \mathrm{a}_1 \to \pi 2\pi^0\nu$ events are reconstructed in DM 0 or DM 1 since the HPS algorithm cannot disentangle the two π^0s in the final state efficiently.

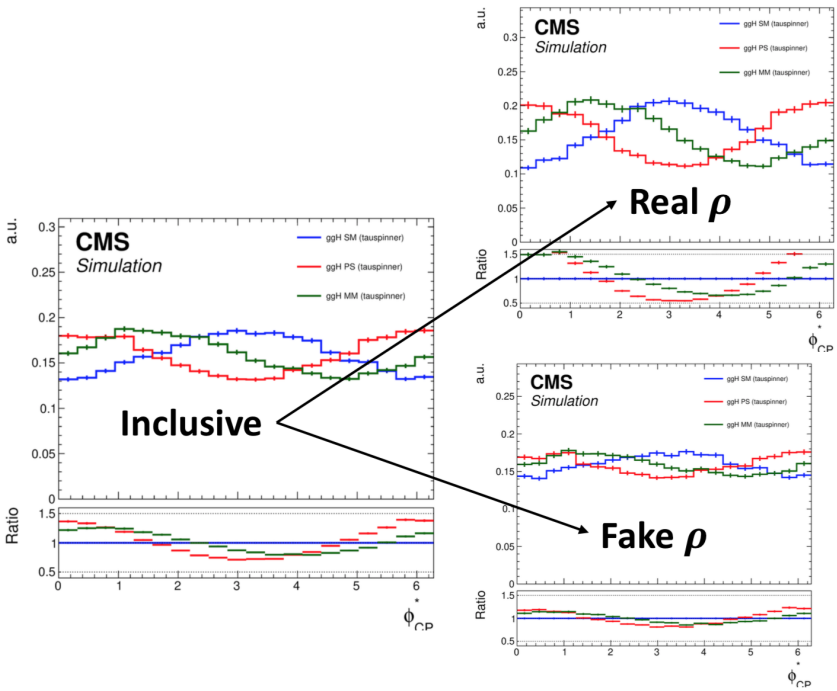

Figure 13: The distribution of ϕ_{CP} for the Standard Model (blue), pseudoscalar (red) and maximum mixing (green) scenarios is shown using all events which passed HPS DM 1 (left). The CP sensitivity increases when considering only real $\tau_h \to \rho \to \pi\pi^0$ decay in HPS DM 1 (top right). The non-ρ events in HPS DM 1 shows significantly less separation between CP scenarios (bottom right).

The reason is that the ECAL deposits from the individual π^0s are very close together in the detector, often they can be clustered into a single PF gamma candidate, and even in cases where multiple PF gammas candidated are reconstructed it is inpractical to allocate the PF gammas to the individual π^0s. Therefore, the HPS algorithm tends to group them all into a single strip.

Table 16: The τ^- hadronic decay channels with B.F.> 2%.

Decay channel	Branching fraction (%)	Main resonance
$\pi^-\nu_\tau$	10.82	-
$\pi^-\pi^0\nu_\tau$	25.49	ρ^-
$\pi^-2\pi^0\nu_\tau$	9.26	$a_1^- \to \pi^0\rho^-$
$\pi^-\pi^-\pi^+\nu_\tau$	8.99	$a_1^- \to \pi^-\rho^0$
$\pi^-\pi^-\pi^+\pi^0\nu_\tau$	2.74	-

In order to purify the reconstructed 1-prong τ_h decay channels, we collected all events in DM 0, 1 and 2 and looked at the distribution of discriminating variables using Gen-Level information. As can be seen in Fig. 14, the decay channels cannot be sufficiently separated with simple cuts on the variables. Therefore, an MVA is used to this end, as mentioned before. The output of the MVA includes four classes corresponding to the final states $\pi\nu$, $\pi\pi^0\nu$, $\pi 2\pi^0\nu$ and the "other" category which means none of the mentioned decays. Very loose MVA isolation cuts are performed on τ_h.

The variables used in the MVA are:

- Mass of ρ and π^0 (strip)

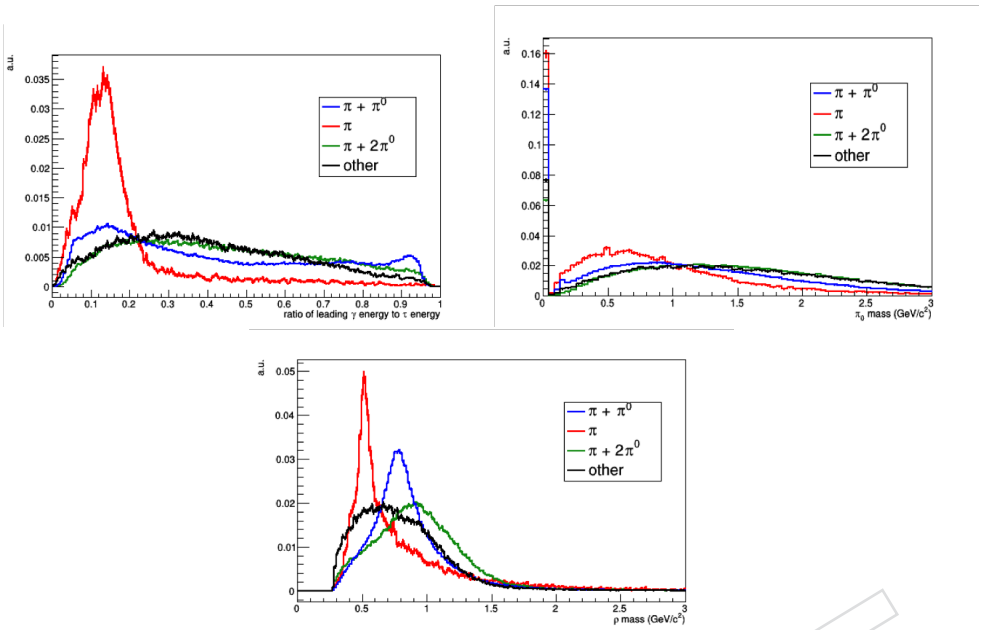

Figure 14: Comparison between variables discriminating τ_h 1-prong decays. The distributions are normalized. π^0 mass is defined as the invariant mass of the strips constituents and ρ mass is the invariant mass of the strips and the charged prong.

- $E_\gamma / E_{\tau_{\text{vis}}}$ for the leading photons
- η and p_{T} of τ_{vis}
- The angular variables (ΔR, $\Delta\phi$ and $\Delta\eta$) between the two leading photons (also multiplied by the sum of their energies)
- The angular variables between π^0 and π (also multiplied by the sum of their energies)
- E_π and E_{π^0} (also dividing by $E_{\tau_{\text{vis}}}$)
- $< \Delta R^2 > = \frac{\Sigma_i \Delta R_i^2 p_{T_i}^2}{\Sigma_i p_{T_i}^2}$ ("i" goes over τ_{h} visible constituents)
- HPS τ decay mode

The MVA allocates four scores to each event showing how likely the event belongs to each of the classes. We assigned each event to the class with the maximum score. This assignment defines new reconstructed τ_{h} decay channels which we call it *MVA DM*.

In order to compare the MVA DM with the HPS DM, we defined purity and efficiency for MVA/HPS DM "i" as:

$$\text{purity} = \frac{\#\text{events[(genuine decay "i") \quad \& \quad (Reco. as "i")]}}{\#\text{events[(Reco. as "i")]}} \tag{24}$$

$$\text{efficiency} = \frac{\#\text{events[(genuine decay "i") \quad \& \quad (Reco. as "i")]}}{\#\text{events[(genuine decay "i")]}} \tag{25}$$

We used the $\mu\tau$ channel to compare MVA and HPS DM. As mentioned in tables 17 and 18, the MVA DM reconstructs 14% purer $\tau_{\text{h}} \to \pi$ events at the cost of losing 8% efficiency. For the $\tau_{\text{h}} \to \pi\pi^0$ sample, both purity and efficiency increase by 12 and 6%, respectively. The MVA

DRAFT

DM can additionally reconstruct 39% of the $\tau_{\mathrm{h}} \to \pi 2\pi^0$ decays in a 55% pure sample where there is (almost) no reconstruction with HPS DM, as mentioned before.

4.8.2 3-prong τ_h decay classification

The 3-prong τ decay through a_1 resonance, $\tau \to a_1 \to \rho^0\pi \to 3\pi$, is also a CP sensitive channel which is considered in this analysis. Similar to the 1-prong decays, there are contamination from other decay channels (mostly $\tau \to 3\pi\pi^0$) which decreases the CP sensitivity. Therefore, we performed a similar MVA but with three classes: $\tau \to 3\pi$, $\tau \to 3\pi\pi^0$ and "other" category. There are two main features that differentiate the above decays. Firstly, one of the decays occur through mass resonances ($a_1 \to \rho^0\pi \to 3\pi$). This is the reason why the mass variables (Fig. 15) were more discriminant than the other variables we used. And secondly, the extra π^0 in the $\tau \to 3\pi\pi^0$ can help us identifying the channels using a strip reconstruction. We performed the HPS algorithm to reconstruct strips for each event. In our experience, working with the leading e/γ in a strip usually yielded more robust results, especially when the strip energy is low (which is the case for the 3-prong a_1 decay). Therefore, after the HPS strip reconstruction, the leading strip is chosen (prioritizing the strips inside the signal cone) and the properties of the leading e/γ in the strip is utilized in the MVA variables.

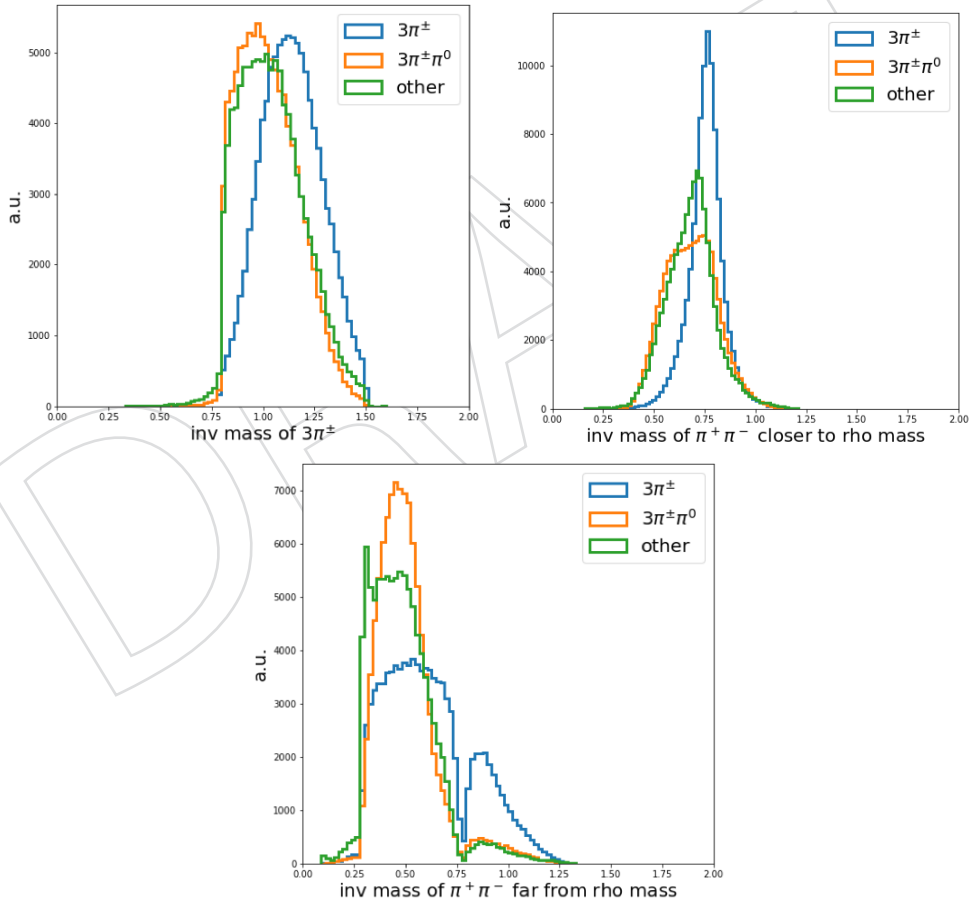

Figure 15: The figures show comparison between some variables which discriminate τ_h 3-prong decays. In these decays, two out of the three pions have same electric charge. Since it is not clear which of the two $\pi^+\pi^-$ pairs originate from a ρ^0, we defined two mass variables depending on which pair have closer invariant mass to ρ^0 mass.

We collected DM 10 and DM 11 as the input events for the MVA. The variables used in this

MVA are:

- Invariant mass of charged pion pairs
- Energy fraction carried by each charged pion
- Angular variables between charged pion pairs (also multiplied by sum of the energies of the pair)
- Energy, p_{T} and η of τ_{vis}
- Strip energy and p_{T} as well as the angle between the strip and a_1 (sum of charged pions)

Similar to the 1-prong decays, we defined MVA DM using MVA scores and calculated the new purity and efficiency using equations 24 and 25. As can be seen in tables 17 and 18, the purity of the 3-prong a_1 decay increased by 15% with more or less the same efficiency. The MVA also improves the purity and efficiency of $\tau_h \to 3\pi\pi^0$ channel by 16% and 12%, respectively.

Table 17: Comparing purity of the HPS and MVA DM.

	π	$\pi\pi^0$	$\pi 2\pi^0$	3π	$3\pi\pi^0$
HPS DM	56%	56%	0%	67%	55%
MVA DM	70%	68%	55%	82%	71%
Gain	14%	12%	55%	15%	16%

Table 18: Comparing efficiency of the HPS and MVA DM.

	π	$\pi\pi^0$	$\pi 2\pi^0$	3π	$3\pi\pi^0$
HPS DM	91%	73%	0%	89%	53%
MVA DM	83%	79%	39%	87%	65%
Gain	−8%	6%	39%	−2%	12%

As the MVA model is trained on the 2017 CMS data, the performance of the model was tested by applying it separately to the data from 2016, 2017 and 2018. A comparison of the MVA DM purity and efficiency confusion matrices for applying the model to these years are shown in Fig. 16 and 17. Overall, the model has similar performance in all years.

The MVA decay mode classification of τ_h and the corresponding ID and trigger scale factor corrections were presented [45] in Tau POG and blessed by the conveners.

4.9 Polarimetric vectors

In this analysis note, the polarimetric vector method has been investigated for the a_1-a_1 final state, that allows to reconstruct the full tau momenta (including neutrino momenta), thanks to the reconstruction of the tau secondary vertices to three charged pions. An adaptation of the global kinematic event fit method (GEF) [46], has been used to reconstruct the tau momenta. The GEF method is considered instead of SVFit, even though the obtained tau momenta resolutions are accurater using SVFit, as can be seen of figure 19. SVFit uses the visible tau momenta and the transverse missing momentum imbalance (and associated covariance matrix) to constrain the full tau momenta. The information from the primary and secondary vertices information is not exploited. The tau decay mode matrix element and missing momentum imbalance precision are varied to find the tau 4-momenta. This leads the estimated 4-momenta to

DRAFT

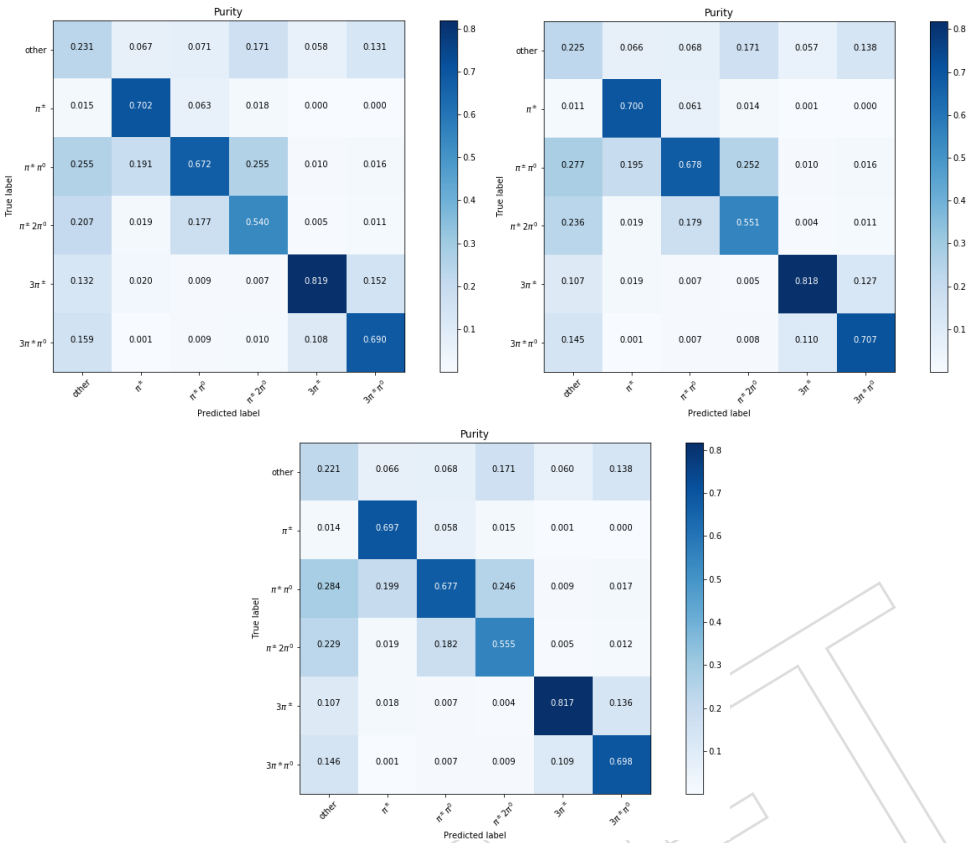

Figure 16: The purity confusion matrices of MVA DM for data from 2016 (top left), 2017 (top right) and 2018 (bottom). Although the model is trained on 2017 data, the performance is preserved when applying to other years.

be close to the visible momenta, and the angular directions to be less precise (figure 20).

The decay channel of the tau lepton into three charged pions and a neutrino can be treated as a two-body decay considering the a1 resonance. Starting from the momentum-energy conservation in the laboratory rest frame and assuming the tau lepton mass known, one can obtain the magnitude of the tau momenta, depending on the a1 momenta and Gottfried-Jackson angle θ_{GJ}. The Gottfried-Jackson angle is defined as the angle between the tau flight direction and the a1 direction, as depicted on figure 18.

$$P_\tau = P_{a1} + P_\nu \leftrightarrow m_\tau^2 = m_{a1}^2 + 2E_{a1}\sqrt{|\vec{p}_\tau|^2 + |\vec{p}_{a1}|^2 - 2|\vec{p}_\tau||\vec{p}_{a1}|} - 2|\vec{p}_{a1}||\vec{p}_\tau|\cos\theta_{GJ} + 2|\vec{p}_{a1}|^2 \tag{26}$$

$$|\vec{p}_\tau| = |\vec{p}_\tau|(m_{a1}, |\vec{p}_{a1}|, \theta_{GJ}) = \frac{(m_{a1}^2 + m_\tau^2)|\vec{p}_{a1}|\cos\theta_{GJ} \pm \sqrt{(m_{a1}^2 + \vec{p}_{a1}^2)((m_{a1}^2 - m_\tau^2)^2 - 4m_\tau^2\vec{p}_{a1}^2\sin^2\theta_{GJ})}}{2(m_{a1}^2 + \vec{p}_{a1}^2\sin^2_{\theta_{GJ}})} \tag{27}$$

In equations 26, 27, the tau momenta are given by the knowledge of the primary and secondary vertices positions: $\overrightarrow{SV - PV}$. Two solutions are then possible: a_1 emitted in the same direction

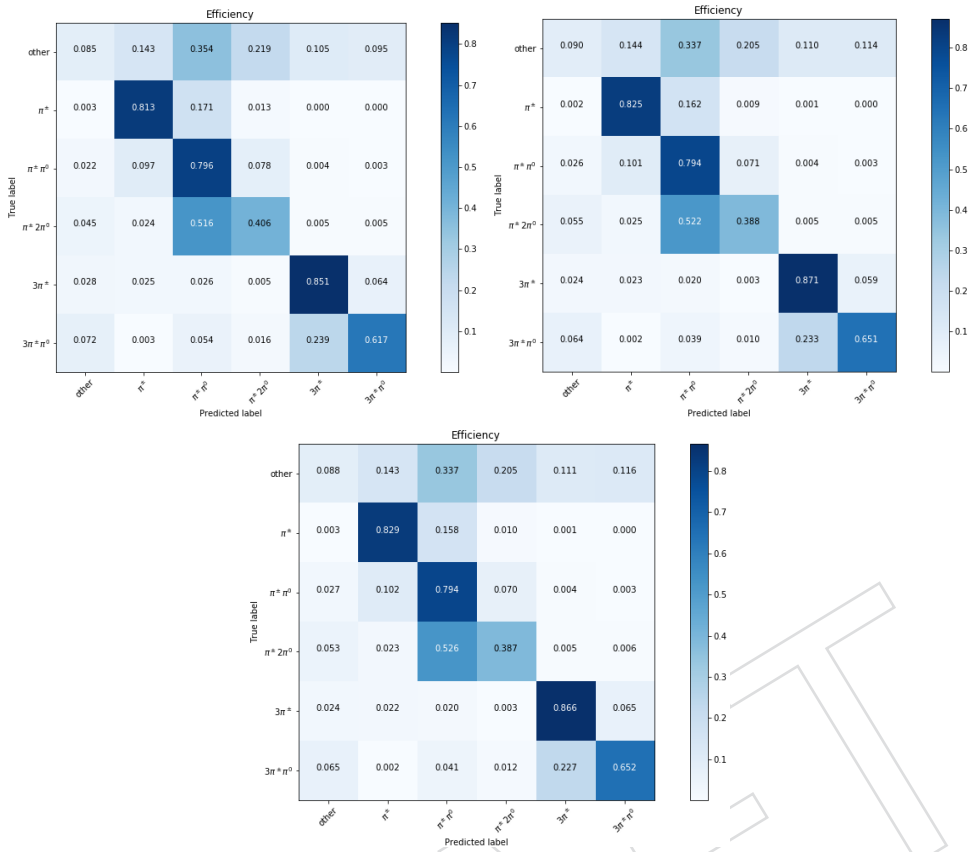

Figure 17: The efficiency confusion matrices of MVA DM for data from 2016 (top left), 2017 (top right) and 2018 (bottom). The efficiencies are similar in all years.

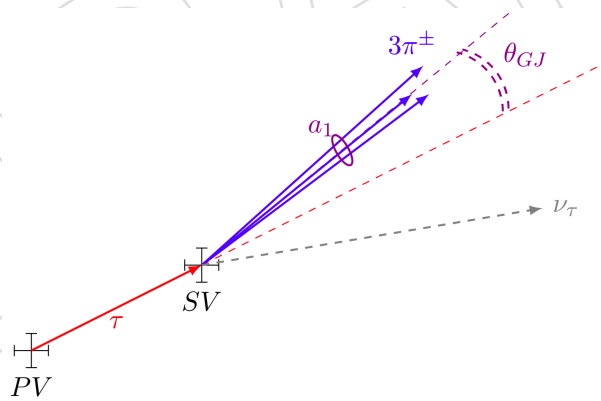

Figure 18: Tau decay sketch, representing the Gottfried-Jackson angle.

as the tau flight direction (lower tau momentum), or a_1 direction opposite to the tau flight direction (higher tau momentum). The ambiguity is settled when the square root in 27 is zero. This condition allows to determine the maximum value for the Gottfried-Jackson angle.

$$(m_{a1}^2 + \vec{p}_{a1}^2)\left((m_{a1}^2 - m_\tau^2)^2 - 4m_\tau^2\vec{p}_{a1}^2\sin^2\theta_{GJ}\right) = 0 \leftrightarrow \theta_{GJ}^{max}(m_{a1}, |\vec{p}_{a1}|) = \arcsin\left(\frac{m_\tau^2 - m_{a1}^2}{2m_\tau|\vec{p}_{a1}|}\right)$$

Since the measured Gottfried-Jackson angle has to be smaller of equal to θ_{GJ}^{max}, one sets the

measured values exceeding θ_{GJ}^{max} (due to inaccuraties in the SV and PV positions) to θ_{GJ}^{max}. The pair of possible solutions in each event is chosen to be the one closest to Higgs boson mass.

Figure 21 shows the worse separation, quantified by the a/b ratio with "a" the amplitude and "b" the baseline, obtained estimating the tau momenta with SVFit. The MVA decay mode 10 and the presence of a reconstructed secondary vertex are required for both taus. The usual tau identification criteria are applied in addition. The use of the MVA decay mode allows to increase the purity of the selection. As for the other investigated channels, the primary vertex is refitted by keeping particles stemming from the tau decays and exploiting the beam spot constraint.

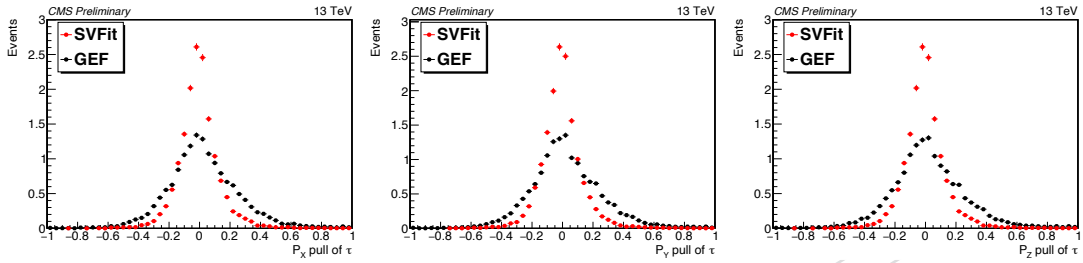

(a) τ_{P_X} (b) τ_{P_Y} (c) τ_{P_Z}

Figure 19: Comparison of momentum resolutions obtained with GEF (black) and SVFit (red).

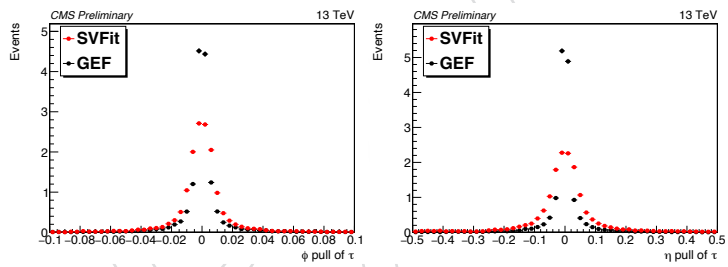

(a) τ_ϕ (b) τ_η

Figure 20: Comparison of angular resolutions obtained with GEF (black) and SVFit (red).

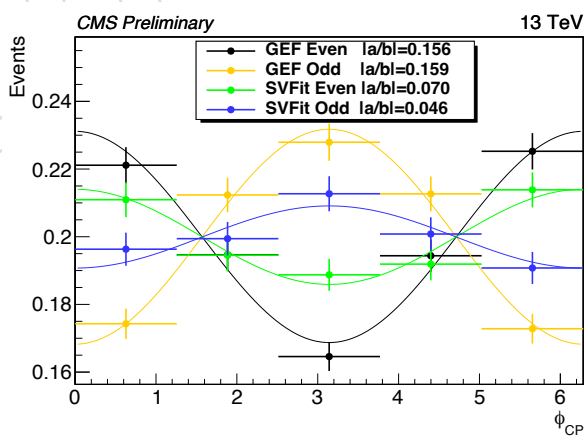

Figure 21: Comparison of the acoplanar angle computed using the GEF method and SVFit with signal from 2016.

Figures 22-24 show the separation with the polarimetric vector (black) and the decay plane (blue) method using signal samples. The presence of the secondary vertex is required for both

methods in order to compare same events. Because of a different convention between these two methods, extrema are shifted by π. The polarimetric vector method has a better separation than the decay plane method in all years.

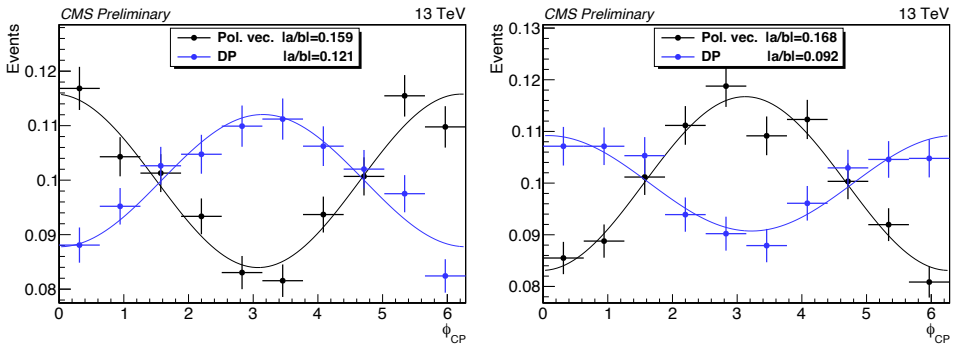

(a) Even (b) Odd

Figure 22: Comparison of the acoplanar angle with 2016 signal samples computed using the GEF method for the polarimetric vector method.

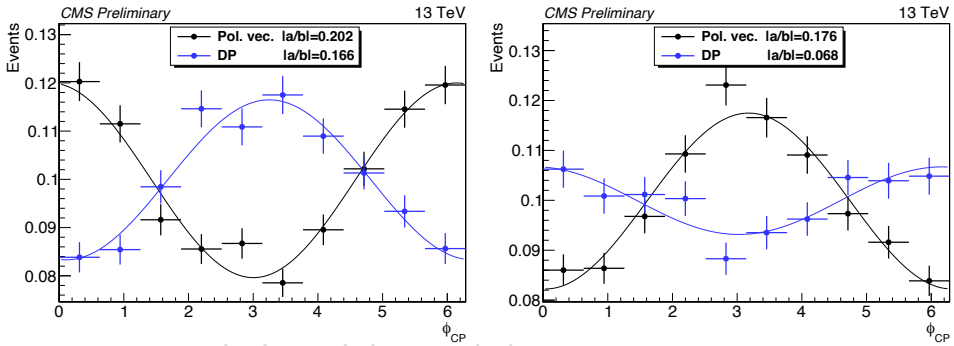

(a) Even (b) Odd

Figure 23: Comparison of the acoplanar angle with 2017 signal samples computed using the GEF method for the polarimetric vector method.

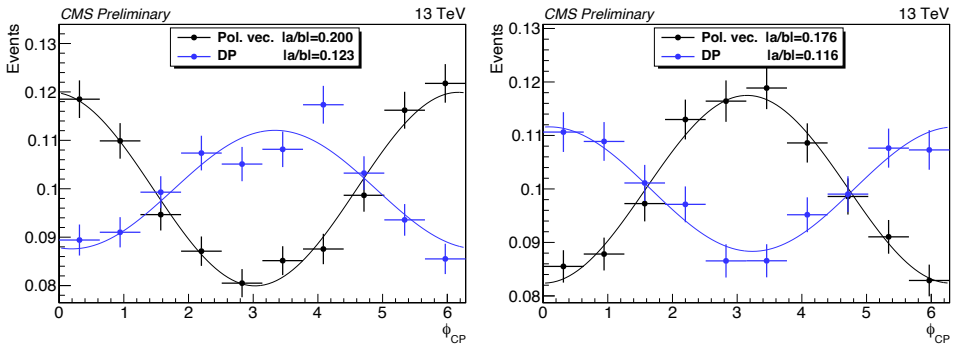

(a) Even (b) Odd

Figure 24: Comparison of the acoplanar angle with 2018 signal samples computed using the GEF method for the polarimetric vector method.

5 Corrections

The corrections applied to MC and embedded events to improve the description of the data follow closely those used for the SM coupling analysis [47]. The changes with respect to Ref. [47] (v6 of AN-2019-019) are:

- The use of hadronic tau ID scale factors in bins of MVA-DM instead of HPS-DM - the measurement of these scale factors will be described in 5.1.
- The use of hadronic tau trigger scale factors in bins of MVA-DM instead of HPS-DM - the measurement of these scale factors will be described in 5.4.
- Corrections applied to the impact parameter length and significance.
- Residual corrections for the $\mu \to \tau_{\mathrm{h}}$ fake rate in bins of MVA-DM.

The corrections applied to to the MC include:

- Pileup reweighting
- Electron/muon tracking/ID/isolation/trigger scale factors (see Ref. [48] for details about scale factor measurements)
- Hadronic tau ID and trigger corrections
- $\ell \to \tau_h$ fake rate corrections
- Hadronic tau energy scale corrections (for genuine taus and $\ell \to \tau_h$ fakes)
- Electron smear and scale corrections (from EGamma POG)
- MET recoil corrections (for Z, W, and Higgs samples)
- Btag efficiency corrections
- Z p_{T}-mass reweighting (for DY+jets MC)
- Top p_{T} reweighting (for $\mathrm{t\bar{t}}$ MC)

For the embedded samples some of these corrections are not required as it is estimated directly from data. The correction applied for the embedded samples are:

- Electron/muon tracking/ID/isolation/trigger scale factors (see Ref. [48] for details about scale factor measurements)
- Hadronic tau ID and trigger corrections
- Electron smear and scale corrections (from EGamma POG)

Note that no corrections are applied to the nominal hadronic tau energy scale in this case, but variation in the energy scale are included as uncertainties.

The corrections that differ from Ref. [47] will be described in detail below.

5.1 Tau ID scale factors

Corrections are applied to taus to account for data/simulation differences in the efficiencies for hadronic taus to pass the tau reconstruction algorithm and identification discriminants.

These corrections are necessarily different to those provided by the tau POG as we require scale factors measured in bins of the MVA-DM. The corrections provided by the tau POG are only measured in bins of the HPS-DM for taus with $p_{\mathrm{T}} > 40$ GeV, and in bins of p_{T} for taus with $p_{\mathrm{T}} < 40$ GeV.

The corrections derived specifically for this analysis are measured in two p_{T} bins ($p_{\mathrm{T}} < 40$ GeV

DRAFT

and $p_T > 40$ GeV) and 5 MVA-DM bins (0,1,2,10,11). The procedure used to measure the scale factors is described below.

A sample enriched in $Z/\gamma^* \to \tau_h\tau_\mu$ events is selected. For the 2016 (2017/2018) measurement the following selections are imposed:

- The muon is required to pass the `Medium` ID, have $I_{rel} < 0.15$, have $p_T > 23$ (28) GeV, and pass the single-muon trigger.
- The hadronic tau candidate must have $p_T > 20$ GeV and pass the HPS algorithm, the `Medium` working point of the deepTau vs jets discriminator, the `Tight` working-point of the deepTau vs muon discriminator, and the `VVVLoose` working-point of the deepTau vs electron discriminator.
- The muon and tau should have opposite charge and be separated by $\Delta R > 0.5$. If more than one pair meet this requirement the most isolated pair is retained.
- The transverse mass $m_T(\mu, E_T^{miss})$, which is defined as

$$m_T(i,j) = \sqrt{2p_T^i p_T^j (1 - \cos\Delta\phi_{ij})}, \tag{28}$$

  must be smaller than 40 GeV.
- Events with additional electrons or muons or with b-jets are vetoed.

A sample of $Z/\gamma^* \to \mu\mu$ events is also selected in order to ensure the fit is able to differentiate between shifts in the $Z/\gamma^* \to \tau_h\tau_\mu$ due to the tau ID scale factor, and other effects such as a shift in the cross-section - where the former would only shift up/down the $Z/\gamma^* \to \tau_h\tau_\mu$ yield, whereas the latter should simultaneously shift $Z/\gamma^* \to \tau_h\tau_\mu$ and $Z/\gamma^* \to \mu\mu$.

The $Z/\gamma^* \to \mu\mu$ event selections are purposefully kept as similar to the $Z/\gamma^* \to \tau_h\tau_\mu$ as possible. The following selections are imposed for 2016 (2017/2018):

- The events must contain two muons passing the *medium* ID with $I_{rel} < 0.15$, and $p_T > 10$ GeV.
- The leading muon is additionally required to have $p_T > 23$ (28) GeV, and pass the single-muon trigger.
- The di-muon pair should have opposite charge and be separated by $\Delta R > 0.5$. If more than one pair meet this requirement the most isolated pair is retained.
- The invariant mass of the di-muon pair must be between 70 and 120 GeV.
- Events with additional electrons or muons or with b-jets are vetoed.

In the $\tau_\mu\tau_h$ category the invariant mass of the muon and hadronic tau is used as the discriminating variable. The $\mu\mu$ category is included as a single bin category to constrain the Drell-Yan yield. A common rate parameter is included to simultaneously scale the $Z/\gamma^* \to \tau_h\tau_\mu$ and $Z/\gamma^* \to \mu\mu$ yields in each category. An additional rate parameter which corresponds to the tau ID scale factor and therefore scales only the $Z/\gamma^* \to \tau_h\tau_\mu$ yield is also included. Simultaneous maximum-likelihood fits of the $\mu\mu$ and $\tau_\mu\tau_h$ categories are then performed to extract the tau ID scale factors.

The following background processes are considered when performing these fits: $t\bar{t}$, di-boson, single-top, W+jets, QCD. When the embedded scale factors are measured the small fraction of Drell-Yan events in the $\tau_\mu\tau_h$ channel not covered by the embedded samples is also treated as background - these correspond to Drell-Yan events where the tau is faked by a muon or a jet. All background processes except QCD are modelled using MC simulation. The QCD is

DRAFT

estimated using same-sign data scaled by a constant factor = 1.12 to account for different rates in same-sign and opposite-sign QCD production. The W+jets yield is also estimate using a data-driven method - this method normalises the yield to the data in the high m_{T} side-band region ($m_{\mathrm{T}} > 70$ GeV) which is very pure in W+jets events.

The fits are performed separately for MC and embedded samples. For the latter the $\mu\mu$ channel is modelled using a sample of embedded Z$\rightarrow$ $\mu\mu$ events which is produced using the same procedure as for the Z$\rightarrow$ $\tau\tau$ samples except in this case the muons selected in data are removed and replaced with simulated muons rather than taus.

The following systematic uncertainties affecting the normalisations and shapes of the signal and background templates are also included when performing the fits:

Normalisation uncertainties:

- **Luminosity:** The luminosity uncertainty amounts to 2.5%. This uncertainty is applied to all processes where the yield is estimated from MC.
- **Muon ID/isolation efficiency:** The uncertainty on the muon ID/isolation efficiency is 1% per muon.
- $\boldsymbol{j \rightarrow \tau_h}$ **fake-rate:** A 20% uncertainty is applied for all processes containing a $j \rightarrow \tau_h$ fake where the yield is estimated from MC.
- $\boldsymbol{\mu \rightarrow \tau_h}$ **fake-rate:** A 20% uncertainty is applied to the Z$\rightarrow$ $\mu\mu$ process in the $\tau_\mu\tau_{\mathrm{h}}$ channels where one of the muons fakes a hadronic tau.
- **Trigger efficiency:** The uncertainty on the single-muon trigger efficiency amounts to 2%.
- **B-jet efficiency:** The uncertainty on the b-tagging efficiency due to the b-jet veto is applied for di-boson and $\mathrm{t\bar{t}}$ events only, the size of the uncertainty is $\approx$ 5%.
- **Background normalisation uncertainties:**
  - A 4% uncertainty on the embedded Z$\rightarrow$ $\mu\mu$ and Z$\rightarrow$ $\tau\tau$ yields.
  - A 2% uncertainty on the MC Z$\rightarrow$ $\mu\mu$ and Z$\rightarrow$ $\tau\tau$ yields to account for the uncertainty on the Drell-Yan cross section.
  - A 5% uncertainty is on the diboson and single-top yields to account for the uncertainties on the production cross sections.
  - A 4.2% uncertainty is on the $\mathrm{t\bar{t}}$ yields to account for the uncertainties on the production cross section.
  - A 10% uncertainty on the W+jets yield to account for the extrapolation from the high to low m_{T} regions when estimating the W yields.
  - A 10% uncertainty on the QCD yield to account for the uncertainties on the measure OS/SS ratio.
  - Only when fitting the embedded scale factors an additional uncertainty due to the tau ID scale factors in MC amounting to 15% which affects only the MC events not covered by the embedding procedure (i.e a fraction of the di-boson and $\mathrm{t\bar{t}}$ events).

Shape uncertainties:

- **Hadronic tau energy scale:** Four uncorrelated uncertainties each that affect only one of the three tau decay modes. Each uncertainty varies the hadronic tau energy scale by $\approx$ 1–1.5%.

DRAFT

- **μ energy scale:** The uncertainty on the muon energy scale varies as a function of η and ranges between 0.4–2.7%
- **Statistical uncertainties:** Limitations in the statistical sizes of the signal and background templates are accounted for by the Barlow-Beeston method [49, 50].
- **Top p_{T} reweighting:** Uncertainty between no and twice the correction on the reweighting applied to $\mathrm{t\bar{t}}$ events.
- **Drell-Yan Z p_{T} reweighting:** Uncertainty between $\pm$ 10 % of the p_{T}-mass correction on the reweighting applied to MC Z$\to \mu\mu$ and Z$\to \tau\tau$ events.
- Uncertainties on the $E_{\mathrm{T}}^{\mathrm{miss}}$ resolution and scale which are estimated by varying the recoil correction by the recommended uncertainties.

Examples of the post-fit data/background comparisons for the $p_{\mathrm{T}} > 40$ GeV bins in 2018 are shown in Figures 25 and 26 for the MC and embedding measurements respectively. Good agreement with the data is observed. The results of the maximum likelihood fits of the scale factors are shown in Figures 27 – 28.

5.2 Residual $\mu \to \tau_{\mathrm{h}}$ fake rate corrections.

The $\mu \to \tau_{\mathrm{h}}$ fake rate corrections provided by the tau POG are measured inclusively in decay mode. Since we split events based on MVA-DM an additional correction is derived to account for the dependence on the MVA-DM. These residual corrections are applied on top of the POG corrections and are extracted from the post-fit values of the pulls on the $\mu \to \tau_{\mathrm{h}}$ fake rate nuisance parameters for the fits used to extract the tau ID scale factors de scribed in the previous section. Thus they are measured in the same p_{T} and MV A-DM bins as the tau ID scale factors.

The size of the corrections depends on the MVA-DM and year. Typically for MVA-DM is it O(30%), whereas for MVA-DM 1 and 2 it can be as large as about 15%. For MVA-DM 10 and 11 the $\mu \to \tau_{\mathrm{h}}$ backgrounds are very small and therefore the post-fit values of the pulls give scale factors consistent with 1. In this case no additional residual corrections are applied.

5.3 Residual e $\to \tau_{\mathrm{h}}$ fake rate corrections.

For the $\tau_e\tau_h$ channel a relevant contribution to the background processes comes from the $Z \to$ ee process. This is due to an electron being misidentified as a hadronically decaying tau lepton. To correct the misidentification rate in simulation to better reproduce real data, scale factors are applied to the simulated sample of the $Z \to$ ee process. Since for this analysis the decay mode of the tau is fundamental in determining the method used to reconstruct the relevant observables, scale factors used have been measured, together with the e $\to \tau_h$ energy scale, exclusively in decay mode.

5.4 Tau trigger scale factors

The τ_{h} trigger scale factor provided by Tau POG is calculated in bins of HPS-DM and may not be accurate enough for our analysis which is based on MVA-DM. We therefore calculated the MVA-DM binned trigger SF for $\tau_{\mathrm{h}}\tau_{\mathrm{h}}$ and $\tau_\mu\tau$ channels. For this measurement, the tag and probe (TAP) method is utilized using $\tau_\mu\tau_{\mathrm{h}}$ events.

The background is estimated using the standard method in which W+jet is normalized to data using high m_T ($m_T > 70$ GeV) region. Then the following conditions are performed:

- muon passed single-muon trigger
- muon isolated with 0.15 cut

DRAFT

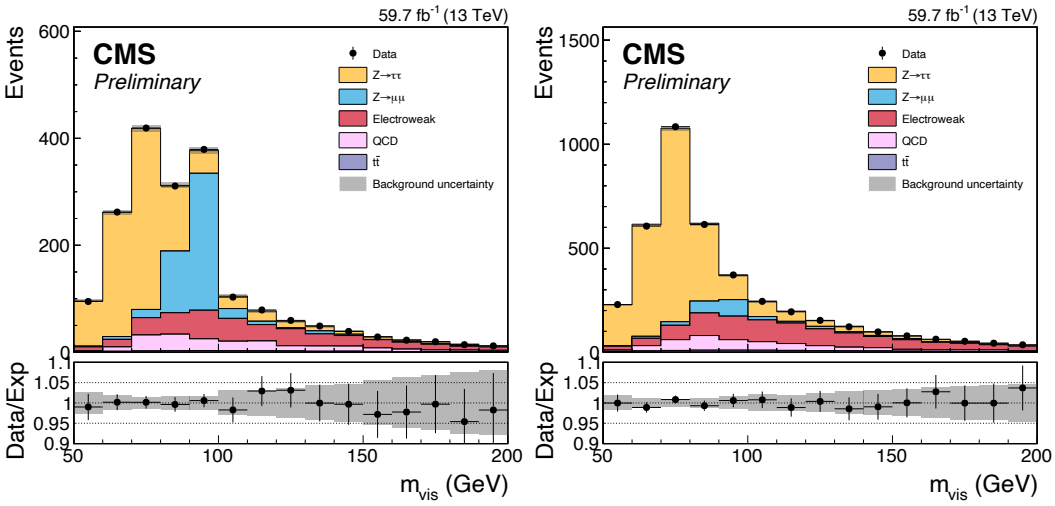

(a) MVA-DM = 0

(b) MVA-DM = 1

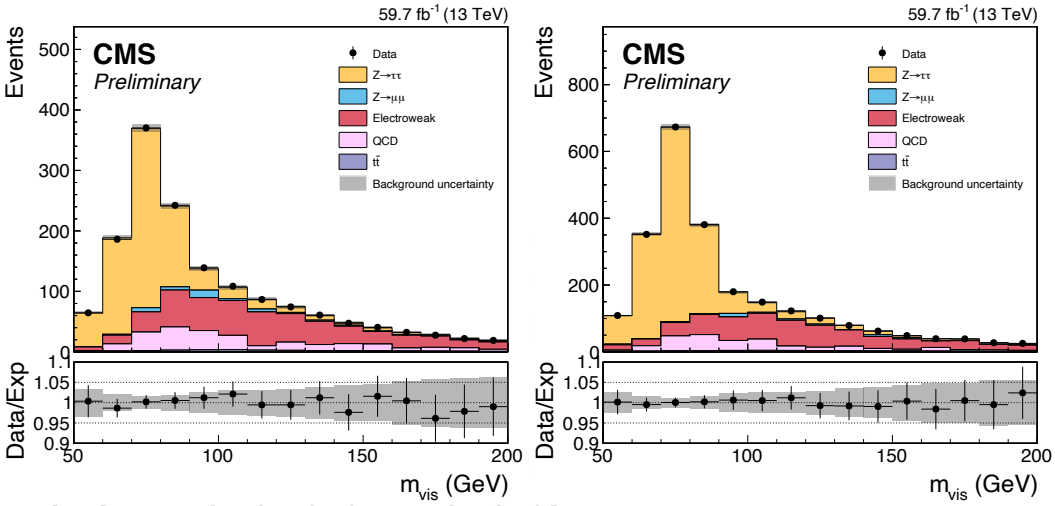

(c) MVA-DM = 2

(d) MVA-DM = 10

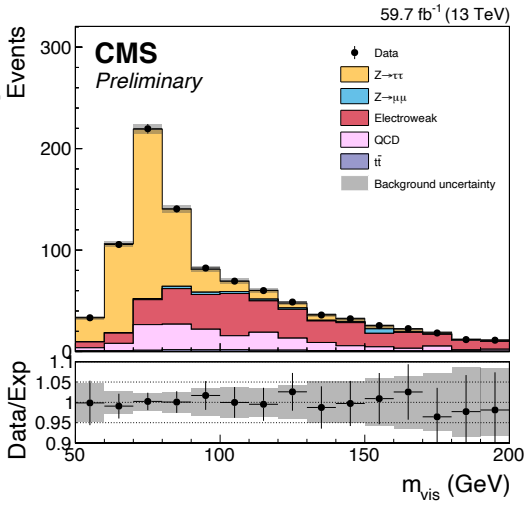

(e) MVA-DM = 11

Figure 25: The post-fit distributions showing the post-fit data/background-prediction agreement for the $p_T > 40$ GeV MVA-DM bins in which the MC tau ID scale factors are measured. The uncertainty band shown in shaded grey includes both systematic and statistical uncertainties.

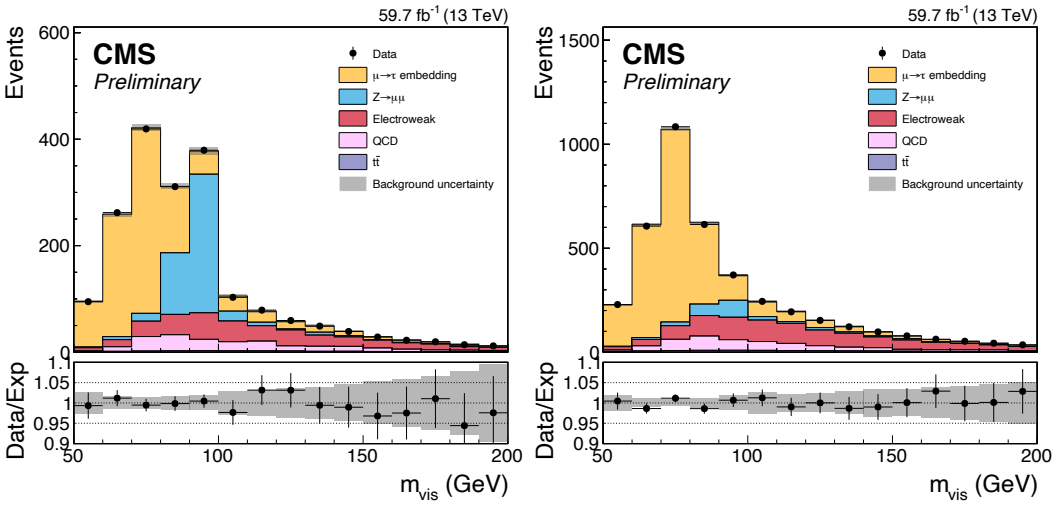

(a) MVA-DM = 0

(b) MVA-DM = 1

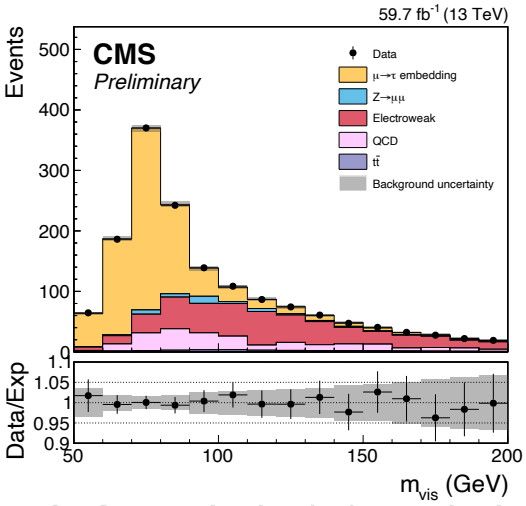

(c) MVA-DM = 2

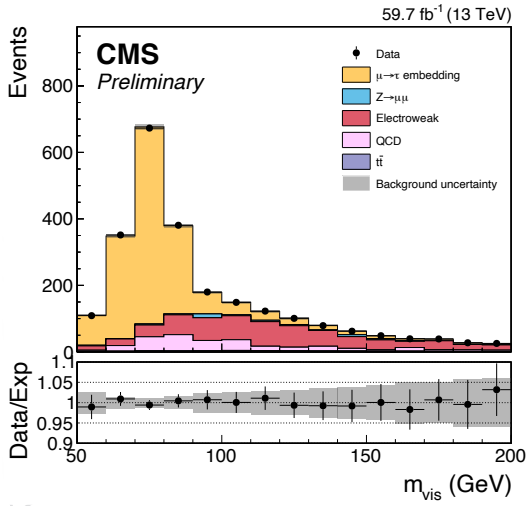

(d) MVA-DM = 10

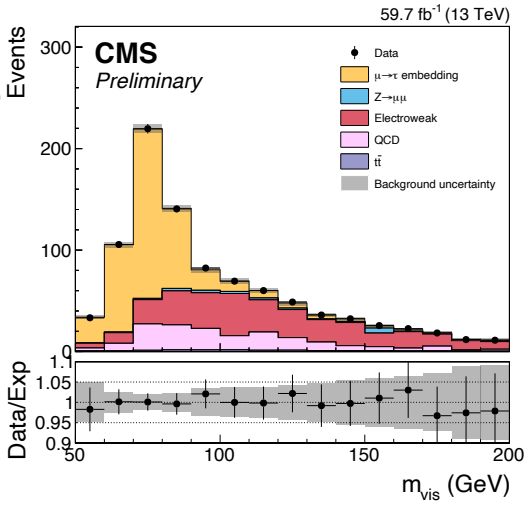

(e) MVA-DM = 11

Figure 26: The post-fit distributions showing the post-fit data/background-prediction agreement for the $p_T > 40$ GeV MVA-DM bins in which the embedding tau ID scale factors are measured. The uncertainty band shown in shaded grey includes both systematic and statistical uncertainties.

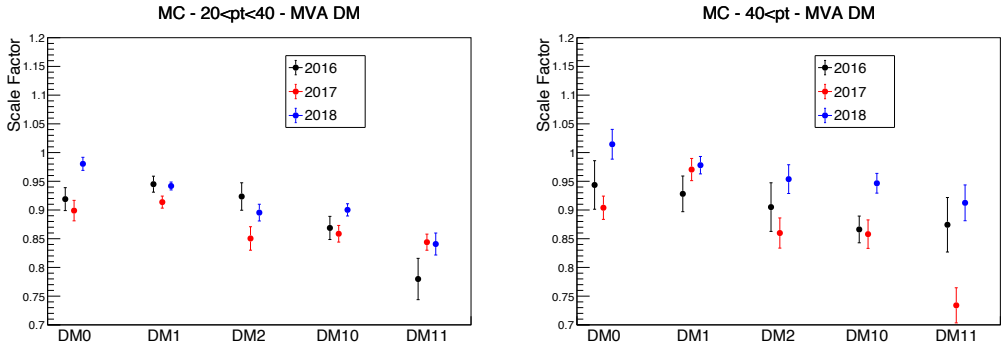

(a) $p_T < 40$ GeV (b) $p_T > 40$ GeV

Figure 27: The best fit values of the MC tau ID scale factors are shown for the $p_T < 40$ GeV (left) and $p_T > 40$ GeV (tight) bins.

DRAFT

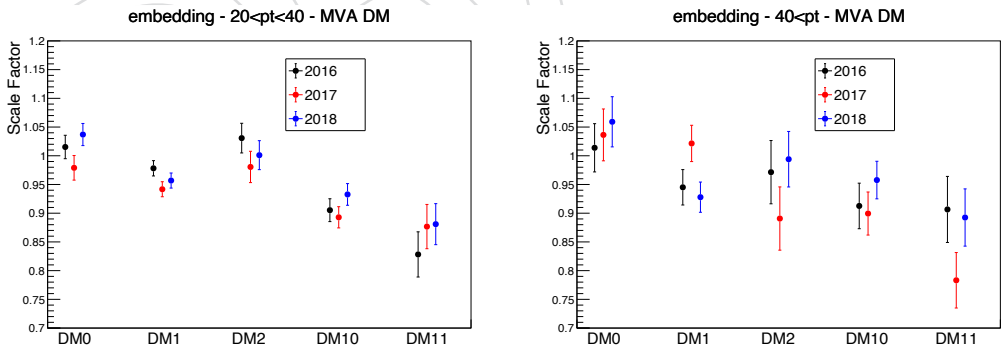

(a) $p_T < 40$ GeV (b) $p_T > 40$ GeV

Figure 28: The best fit values of the embedded tau ID scale factors are shown for the $p_T < 40$ GeV (left) and $p_T > 40$ GeV (tight) bins.

- DeepTau discriminator against jets, electrons and muons with Medium, VVVLoose and Tight working points, respectively
- events with additional leptons are vetoed
- muon passed $p_T > 25$ GeV for 2016 and $p_T > 29$ GeV for 2017 and 2018
- veto events with b-jets
- $m_T < 40$ to decrease the background from W+jets
- 50 GeV $< m_{vis} <$ 90 GeV

The triggers used on the τ_{h} leg are shown on tables 19 and 20 for the $\tau_{\mathrm{h}}\tau_{\mathrm{h}}$ and $\tau_\mu\tau$ channels, respectively. In order to measure the efficiency of the triggers, the p_T of τ_{h} is binned as [20,21,22,23,24,26,28,30,35,40,50,60,75,110,410] GeV and the efficiency in each bin is defined as the fraction of events which pass the trigger.

To fit the efficiency graphs, we inherited a method recently used for trigger SF measurement in TauPOG [51]. This method utilizes Gaussian Process (GP) to fit the graphs with a non-parametric continuous function. In the high-p_T region (plateau) of each graph a constant kernel is used, whereas in the low-p_T region, the constant kernel is multiplied by a Matern kernel (with parameter $\nu = 1$) to be flexible for fitting the turn-on. The bin uncertainties are included in the fit using a White Noise kernel for both p_T region. A tanh function smoothens the intersection of the high and low p_T regions.

The scale factor is calculated by dividing the fitted function of data by that of MC(or embedding), and the uncertainty is derived with the standard error propagation. Figures 29 and 30 show examples of the fits to the efficiency and scale factor graphs.

5.5 Impact parameter significance corrections

Essential ingredient of the analysis is the impact parameter (IP) significance of tracks originating from decays of τ candidates. Cuts on the IP significance considerably improve sensitivity of the analysis in channels where decay plane of one or both τ candidates is constructed using the IP vectors. This quantity is not perfectly described by simulation and needs proper calibration. Calibration of the IP significance is performed with the sample of Z decays into a pair of muons, $Z \to \mu\mu$, and consists of two steps

- correction of the IP vector;
- correction of the IP covariance matrix.

Calibration is performed separately for simulated and embedded samples.

Figure 31 shows the distribution of cartesian coordinates of the IP vector in the sample of selected $Z \to \mu\mu$ events. The 2017 dataset is chosen as a representative example. Data are compared to the uncalibrated MC simulation in the left plots and to uncalibrated embedded $Z \to \mu\mu$ sample in the right plots. Figure 32 shows distributions of uncalibrated IP significance for the 2017 dataset.

To compensate for discrepancies between data and MC simulation in the distributions of the cartesian coordinates of the IP vector, the simulated (embedded) distributions are matched to data via the quantile mapping method. In this procedure the cumulative distribution of the uncalibrated simulated (embedded) sample is compared to the cumulative distributions of data, and corrected value of the ith coordinate of the IP vector (IP_i, $i = x, y, z$) is computed using the formula

DRAFT

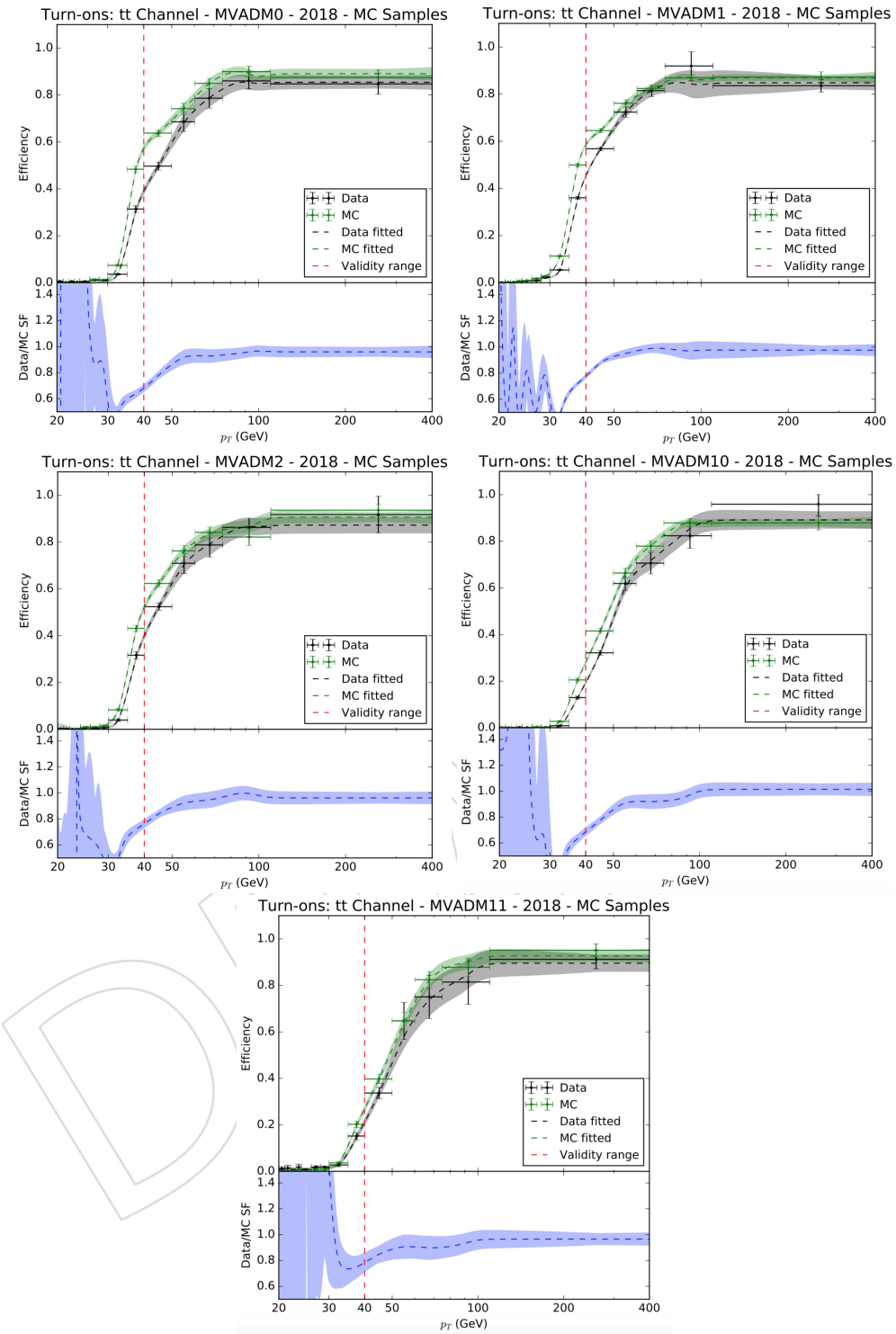

Figure 29: The data and MC efficiency and scale factor graphs and the fits corresponding to them for $\tau_h\tau_h$ channel and 2018 data set for different MVA DM.

$$IP_i^{\text{corr}} = F_{\text{data}}^{-1}(F_{\text{MC(emb)}}(IP_i)), \tag{29}$$

with IP_i^{corr} and IP_i being the corrected and uncorrected coordinates of the IP vector, respectively, $F_{\text{MC(emb)}}$ - cumulative distribution function of the respective IP coordinate in MC (embedded) sample, and F_{data}^{-1} - quantile function (inverse cumulative distribution function) of the

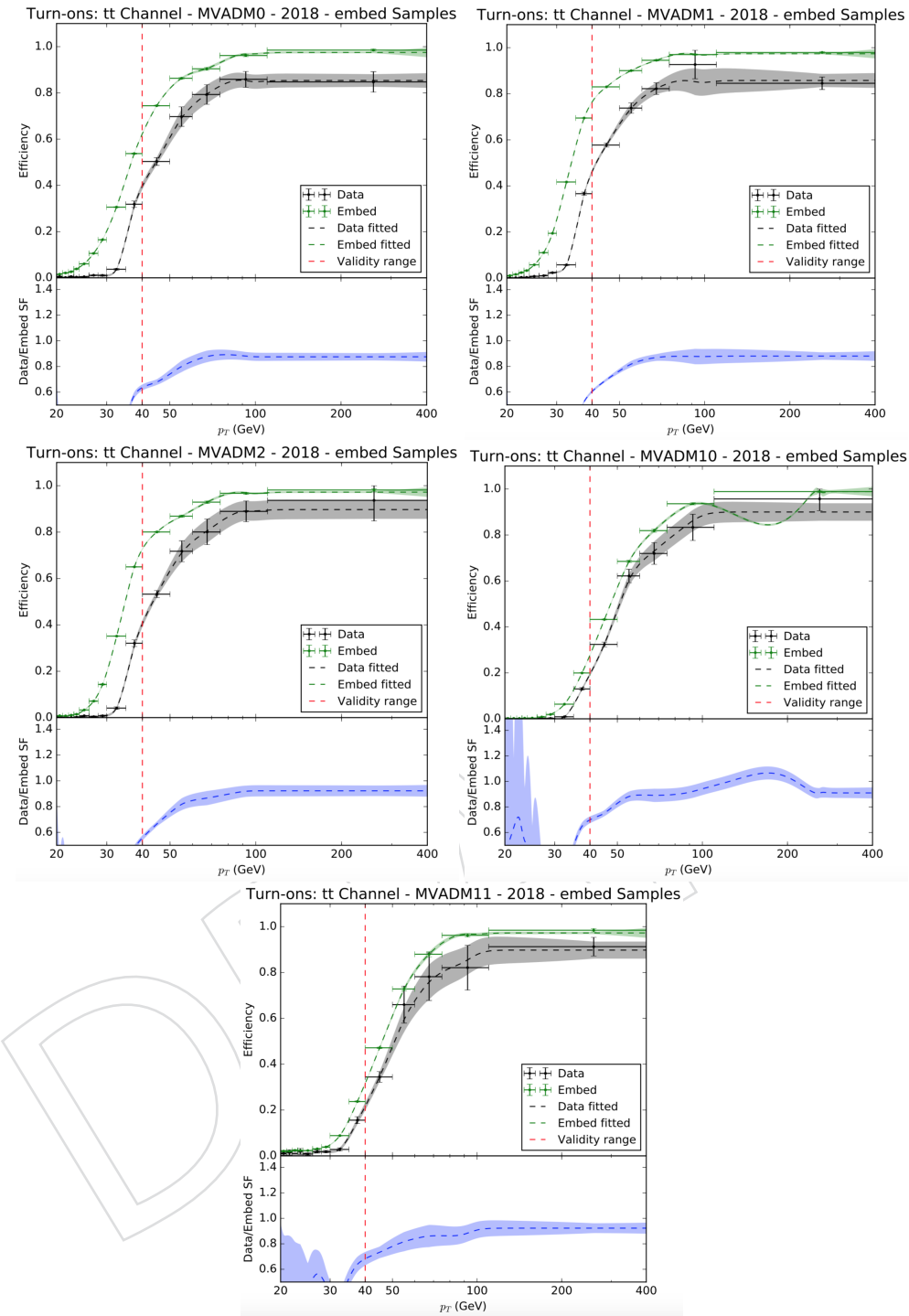

Figure 30: The data and embedding efficiency and scale factor graphs and the fits corresponding to them for $\tau_h\tau_h$ channel and 2018 data set for different MVA DM.

respective IP coordinate in data. Given dependence of the IP resolution on the pseudorapidity of track (η), the correction is performed differentially in η bins:

- $|\eta| < 0.9$,
- $0.9 < |\eta| < 1.2$,
- $1.2 < |\eta| < 2.1$,

- $2.1 < |\eta| < 2.4$.

For each of these bins corresponding quantile function for data and cumulative function for the simulated (embedded) events is derived and used in quantile mapping procedure.

Distributions of the calibrated cartesian coordinates of the IP vector are shown in Figure 33 for the $Z \to \mu\mu$ sample in 2017. By construction, distribution in data matches that of simulated (embedded) events.

Calibration of the IP significance includes also corrections to the IP covariance matrix. The error estimates for the IP vector components (σ_i^{IP}, $i = x, y, z$) are related to diagonal elements of the IP covariance matrix (V_{ii}) as

$$\sigma_i^{\mathrm{IP}} = \sqrt{V_{ii}}. \tag{30}$$

They are corrected differentially in bins of the track pseudorapidity using the aforementioned quantile mapping technique. The same η binning is used as for the IP vector calibration. As an example Figures 34 and 35 show the IP error estimate distributions for the z component in bins of η before and after calibration, respectively, for the 2017 dataset.

The corrected covariance matrix is then computed as

$$V_{ij}^{\mathrm{corr}} = \alpha_i \alpha_j V_{ij}, \tag{31}$$

where V_{ij} (V_{ij}^{corr}) are components of the uncorrected (corrected) covariance matrix and α_i is the ratio of the corrected value of the error estimates for the ith coordinate of the IP vector to its uncorrected value

$$\alpha_i = \sigma_i^{\mathrm{IP,corr}} / \sigma_i^{\mathrm{IP}}. \tag{32}$$

The procedure of correcting the IP covariance matrix accounts for differences in error estimates for the IP vector components between data and simulated (embedded) events, but retains correlation coefficients from the original (uncorrected) IP covariance matrix.

The calibrated IP vector and covariance matrix are then used to compute corrected value of the IP significance. The distributions of the IP significance in the $Z \to \mu\mu$ before and after calibration procedure are shown in Figure 36 and 37 for the MC simulation and embedded samples, respectively. Agreement between data and modeling is significantly improved for the MC simulation. For the embedded events residual discrepancy is observed in the tail of the IP significance distribution even after calibration. The discrepancy in tail of the distribution, however, will have minor impact on the results, as the analyses in $\mu\tau_h$ and $\tau_h\tau_h$ channels don't use the IP significant variable in the multivariate-based categorization of events, and only loose cuts on the IP significance of the muon and pion are applied in the $\tau \to \mu$ and $\tau \to 1-$prong decay modes to select those events in the signal region, which have good quality of the IP vector reconstruction.

A quarter of the correction is regarded as a systematic uncertainty in the corrected value of the IP significance. The systematic-shifted values of the IP significance are computed as

$$\begin{aligned} IP_{\mathrm{sig}}^{\mathrm{down}} &= IP_{\mathrm{sig}}^{\mathrm{corr}} - 0.25(IP_{\mathrm{sig}}^{\mathrm{corr}} - IP_{\mathrm{sig}}^{\mathrm{uncorr}}) \\ IP_{\mathrm{sig}}^{\mathrm{up}} &= IP_{\mathrm{sig}}^{\mathrm{corr}} + 0.25(IP_{\mathrm{sig}}^{\mathrm{corr}} - IP_{\mathrm{sig}}^{\mathrm{uncorr}}) \end{aligned} \tag{33}$$

DRAFT

where $IP_{\text{sig}}^{\text{corr}}$ is the corrected value of the IP significance, and $IP_{\text{sig}}^{\text{uncorr}}$ - its uncorrected value. The assigned uncertainty covers variations in the distribution of the IP significance in the sample of selected $Z \to \mu\mu$ events between simulated (embedded) events and data in the range of the IP significance up to ≈ 4. The uncertainty is treated as uncorrelated across different data taking periods.

It should be noted, that the events used for the fake factors do not need any calibration, since here the IP vectors are taken from data already.

Calibration of the IP vector for non-prompt particles, including those resulting from decays of τ candidates, involves generator level information. The corrected IP vector is computed as

$$IP_i^{\text{corr}} = IP_i^{\text{gen}} + F_{\text{data}}^{-1}(F_{\text{MC(emb)}}(IP_i - IP_i^{\text{gen}})), \tag{34}$$

where IP_i^{gen} is the ith component of the IP vector at the generator level. The quantile and cumulative distribution functions of the IP vector components are those derived differentially in track η from the $Z \to \mu\mu$ sample as described above. The IP covariance matrix is corrected using η-dependent quantile and cumulative distribution functions of the error estimates for the IP vector components, derived from the $Z \to \mu\mu$ control sample. The correction is performed based on Eqs. 31 and 32.

The calibration of the IP significance is validated with the sample of $Z \to \tau\tau$ events with one τ decaying muonically and the other - hadronically. The effect of applying corrections to muon from the τ decay is illustrated in Figures 38 and 39 for the MC simulation and embedding, respectively.

The impact parameter and its significance for electrons are calibrated in similar way using the samples of the $Z \to$ ee decays.

The calibration of the IP significance is validated with the sample of $Z \to \tau\tau$ events with one τ decaying into an and the other - hadronically. The effect of applying corrections to electron from the τ decay is illustrated in Figures 40 and 41 for the MC simulation and embedding, respectively.

A 40% of the correction is regarded as a systematic uncertainty in the corrected value of the electron IP significance. The assigned uncertainty covers variations in the distribution of the IP significance in the sample of selected $Z \to \tau_{\text{e}}\tau_{\text{h}}$ events between simulated (embedded) events and data in the range of the IP significance up to ≈ 10. The uncertainty is treated as uncorrelated across different data taking periods.

DRAFT

Table 19: Summary of the probe trigger requirements used to measure trigger efficiencies for $\tau_h\tau_h$ channel.

Year	HLT path(s)	Filter(s) to match for data/MC	Filter(s) to match for embedding	Extra	Notes
2016	HLT_IsoMu19_eta2p1_MediumIsoPFTau32_Trk1_eta2p1_Reg_v	hltOverlapFilterIsoMu19MediumIsoPFTau32Reg	hltPFTau32Reg	35 GeV HLT p_T cut	–
2016	HLT_IsoMu19_eta2p1_MediumCombined IsoPFTau32_Trk1_eta2p1_Reg_v	hltOverlapFilterIsoMu19MediumCombinedIso PFTau32Reg	hltPFTau32Reg	35 GeV HLT p_T cut	–
2017	HLT_IsoMu24_eta2p1_TightCharged IsoPF-Tau35_Trk1_TightID_eta2p1_Reg_CrossL1	hltSelectedPFTau35TrackPt1Tight ChargedIsolation AndTightOOSCPhotonsL1HLTMatchedReg	hltSingleL2IsoTau26eta2p2	32 GeV (isolated) L1 p_T cut	–
2017	HLT_IsoMu24_eta2p1_MediumChargedIso PFTau35_Trk1_TightID_eta2p1_Reg_CrossL1	hltSelectedPFTau35TrackPt1Medium ChargedIsolation AndTightOOSCPhotonsL1HLTMatchedReg	hltSingleL2IsoTau26eta2p2	32 GeV (isolated) L1 p_T cut	–
2017	HLT_IsoMu24_eta2p1_TightCharged IsoPF-Tau35_Trk1_eta2p1_Reg_CrossL1	hltSelectedPFTau35TrackPt1Tight ChargedIsolation L1HLTMatchedReg	hltSingleL2IsoTau26eta2p2	40 GeV HLT p_T cut & 32 GeV (isolated) L1 p_T cut	–
2018	HLT_IsoMu24_eta2p1_TightCharged IsoPF-Tau35_Trk1_TightID_eta2p1_Reg_CrossL1	hltSelectedPFTau35TrackPt1Tight ChargedIsolation AndTightOOSCPhotonsL1HLTMatchedReg	hltSingleL2IsoTau26eta2p2	32 GeV (isolated) L1 p_T cut	Not used in MC
2018	HLT_IsoMu24_eta2p1_MediumChargedIso PFTau35_Trk1_TightID_eta2p1_Reg_CrossL1	hltSelectedPFTau35TrackPt1Medium ChargedIsolation AndTightOOSCPhotonsL1HLTMatchedReg	hltSingleL2IsoTau26eta2p2	32 GeV (isolated) L1 p_T cut	Not used in MC
2018	HLT_IsoMu24_eta2p1_TightCharged IsoPF-Tau35_Trk1_eta2p1_Reg_CrossL1	hltSelectedPFTau35TrackPt1Tight ChargedIsolation L1HLTMatchedReg	hltSingleL2IsoTau26eta2p2	40 GeV HLT p_T cut & 32 GeV (isolated) L1 p_T cut	Not used in MC
2018	HLT_IsoMu24_eta2p1_MediumCharged IsoPFTauHPS35_Trk1_eta2p1_Reg_CrossL1_v	hltHpsSelectedPFTau35TrackPt1Medium ChargedIsolation L1HLTMatchedReg	hltSingleL2IsoTau26eta2p2	32 GeV (isolated) L1 p_T cut	–

Table 20: Summary of the probe trigger requirements used to measure trigger efficiencies for $\tau_\mu \tau_\mathrm{h}$ channel.

Year	HLT path(s)	Filter(s) to match for data	Filter(s) to match for MC	Filter(s) to match for embedding
2016	HLT_IsoMu19_eta2p1_LooseIsoPFTau20_SingleL1_v	hltPFTau20TrackLooseIsoAgainstMuon	hltPFTau20TrackLooseIsoAgainstMuon	hltPFTau20
2016	HLT_IsoMu19_eta2p1_LooseIsoPFTau20_v	hltPFTau20TrackLooseIsoAgainstMuon	hltPFTau20TrackLooseIsoAgainstMuon	hltPFTau20
2017	HLT_IsoMu20_eta2p1_LooseChargedIsoPFTau27_eta2p1_CrossL1_v	hltSelectedPFTau27LooseChargedIsolationAgainstMuonL1HLTMatched	hltSelectedPFTau27LooseChargedIsolationAgainstMuonL1HLTMatched	hltL1sMu18erTau24erIorMu20erTau24er
2018	HLT_IsoMu20_eta2p1_LooseChargedIsoPFTau27_eta2p1_CrossL1_v	hltSelectedPFTau27LooseChargedIsolationAgainstMuonL1HLTMatched	–	–
2018	HLT_IsoMu20_eta2p1_LooseChargedIsoPF-TauHPS27_eta2p1_CrossL1_v	hltHpsSelectedPFTau27LooseChargedIsolationAgainstMuonL1HLTMatched	hltHpsSelectedPFTau27LooseChargedIsolationAgainstMuonL1HLTMatched	hltL1sBigORMu18erTauXXer2p1

DRAFT

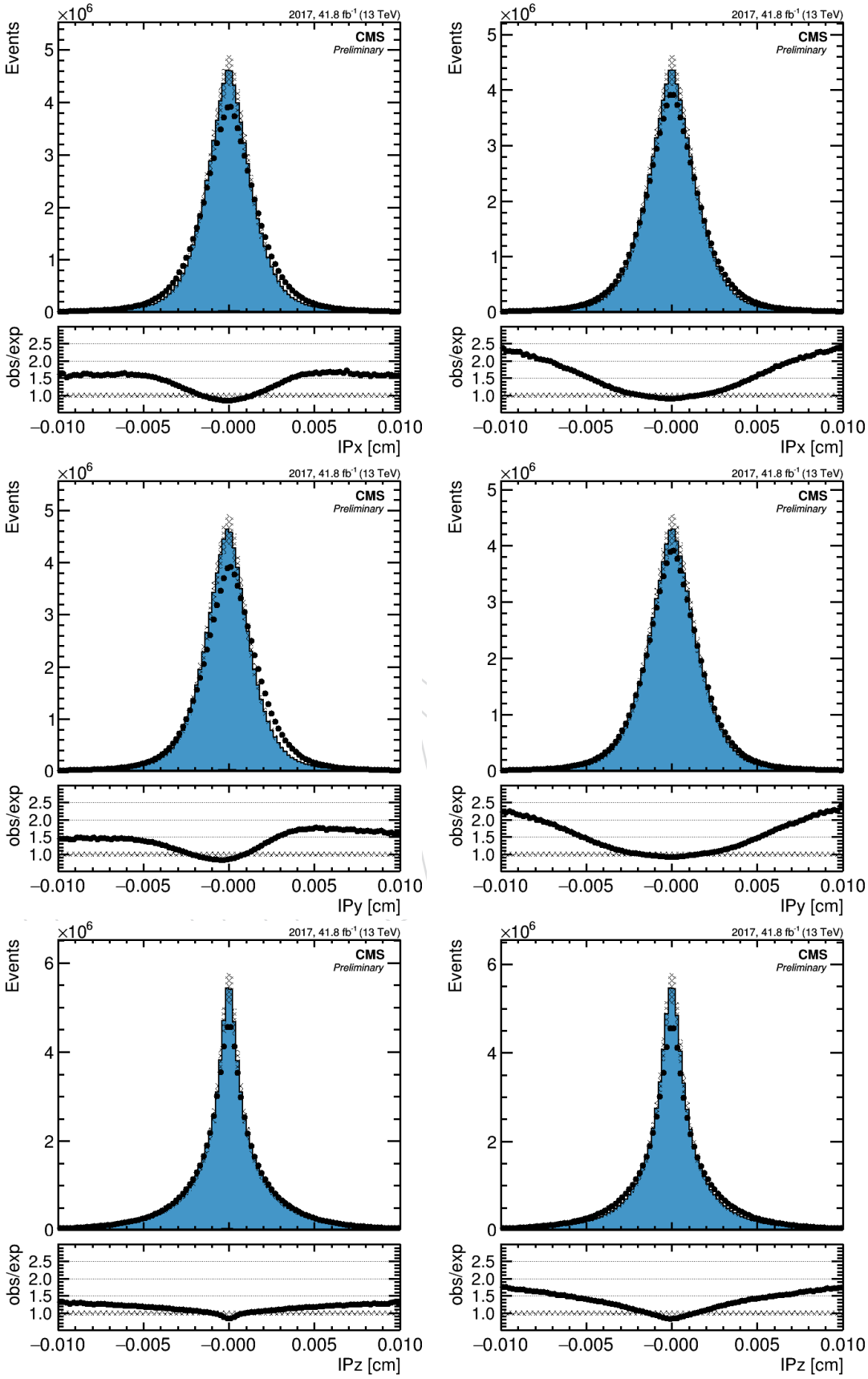

Figure 31: Distribution of cartesian coordinates of uncalibrated IP in the $Z \to \mu\mu$ sample. Left plots : data are compared to MC simulation. Right plots : data are compared to $Z \to \mu\mu$ embedded samples. The 2017 dataset is chosen as a representative example.

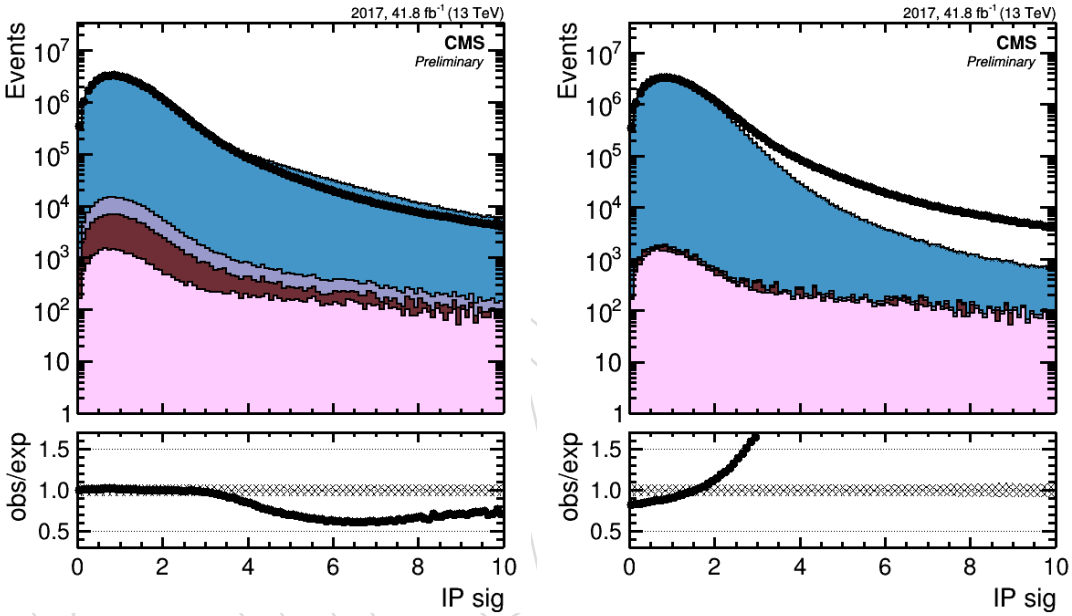

Figure 32: Distribution of uncalibrated IP significance in the $Z \rightarrow \mu\mu$ sample. Left plots : data are compared to MC simulation. Right plots : data are compared to $Z \rightarrow \mu\mu$ embedded samples. The 2017 dataset is chosen as a representative example.

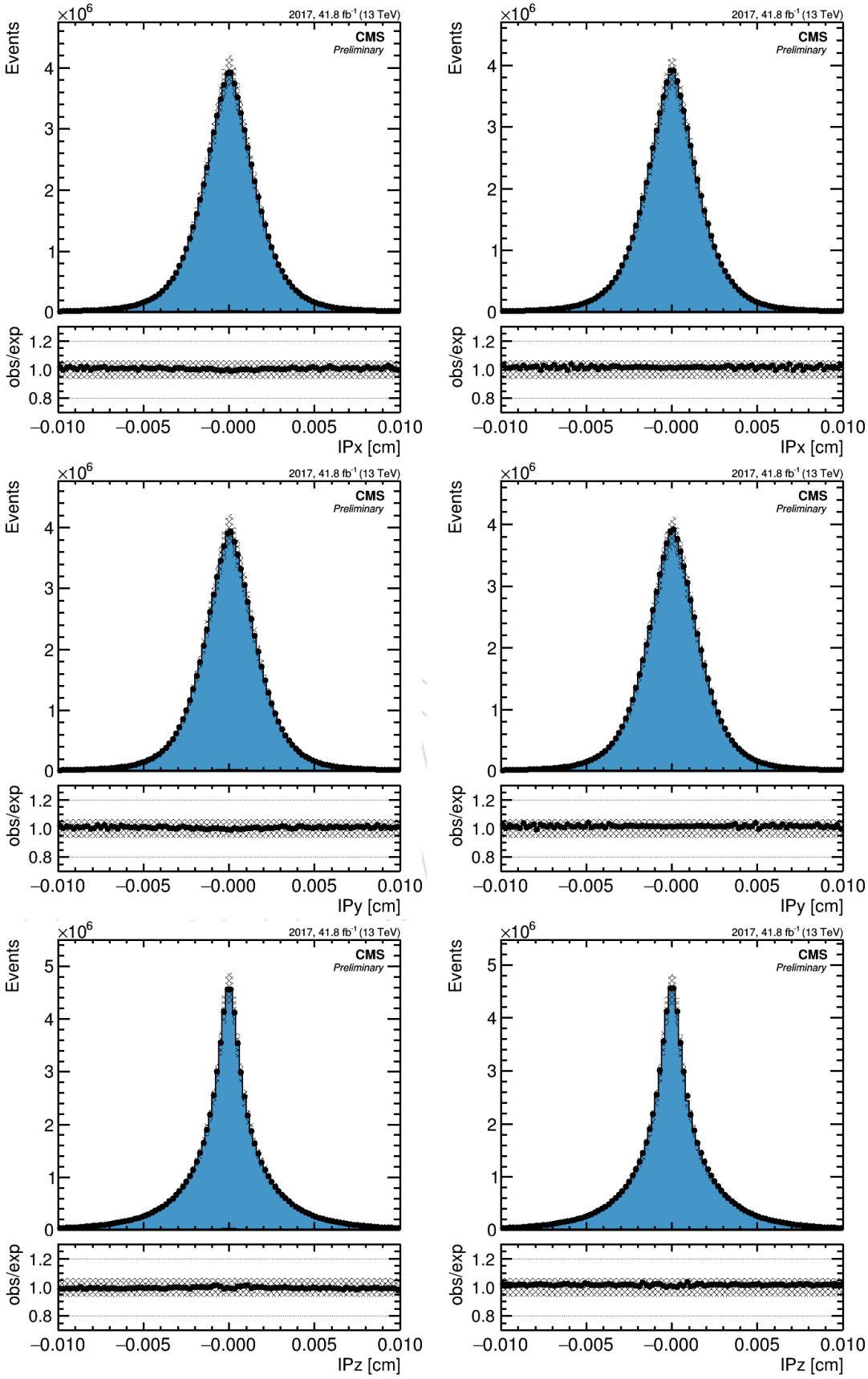

Figure 33: Distribution of cartesian coordinates of calibrated IP vector in the DY control region. In left plots data are compared to MC events. In right plots - to embedded events. The 2017 dataset is chosen as a representative example.

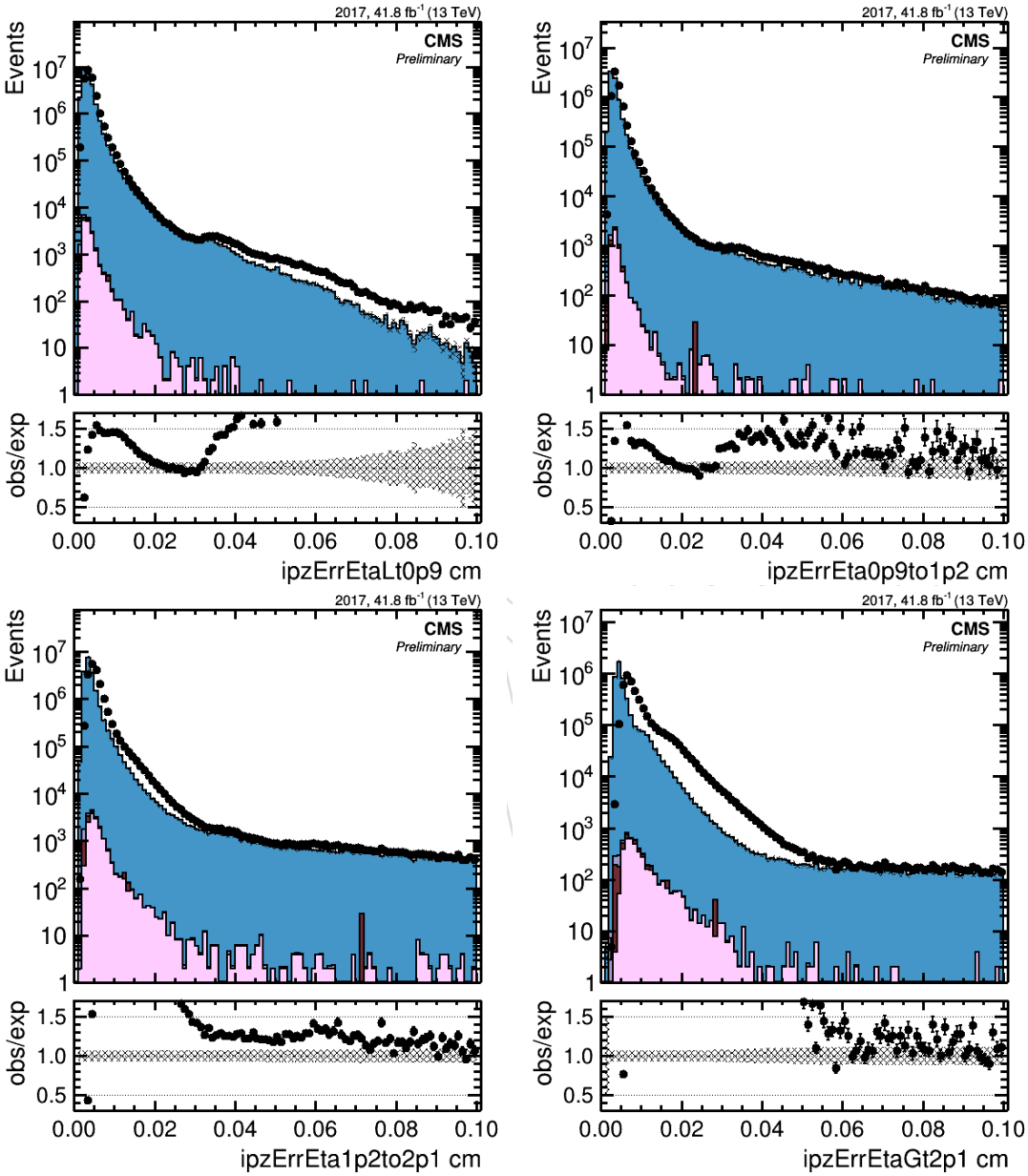

Figure 34: Uncalibrated distribution of the IP error estimate for the z component in bins of η of the muon in the sample of $Z \to \mu\mu$ events. The 2017 dataset is chosen as a representative example. Embedded sample is used to model $Z \to \mu\mu$ process.

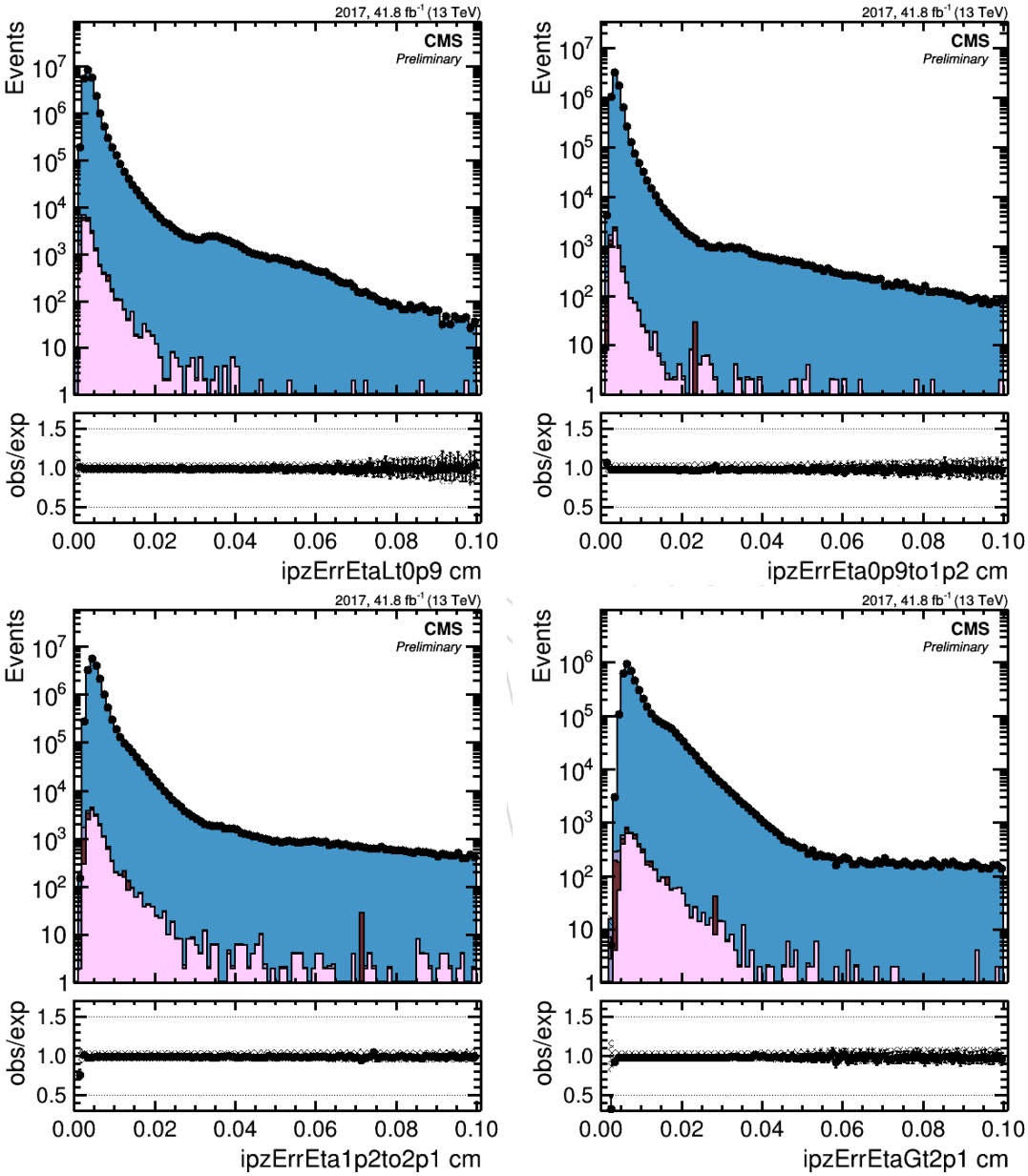

Figure 35: Calibrated distribution of the IP error estimate for the z component in bins of η of the muon in the sample of $Z \to \mu\mu$ events. The 2017 dataset is chosen as a representative example. Embedded sample is used to model $Z \to \mu\mu$ process.

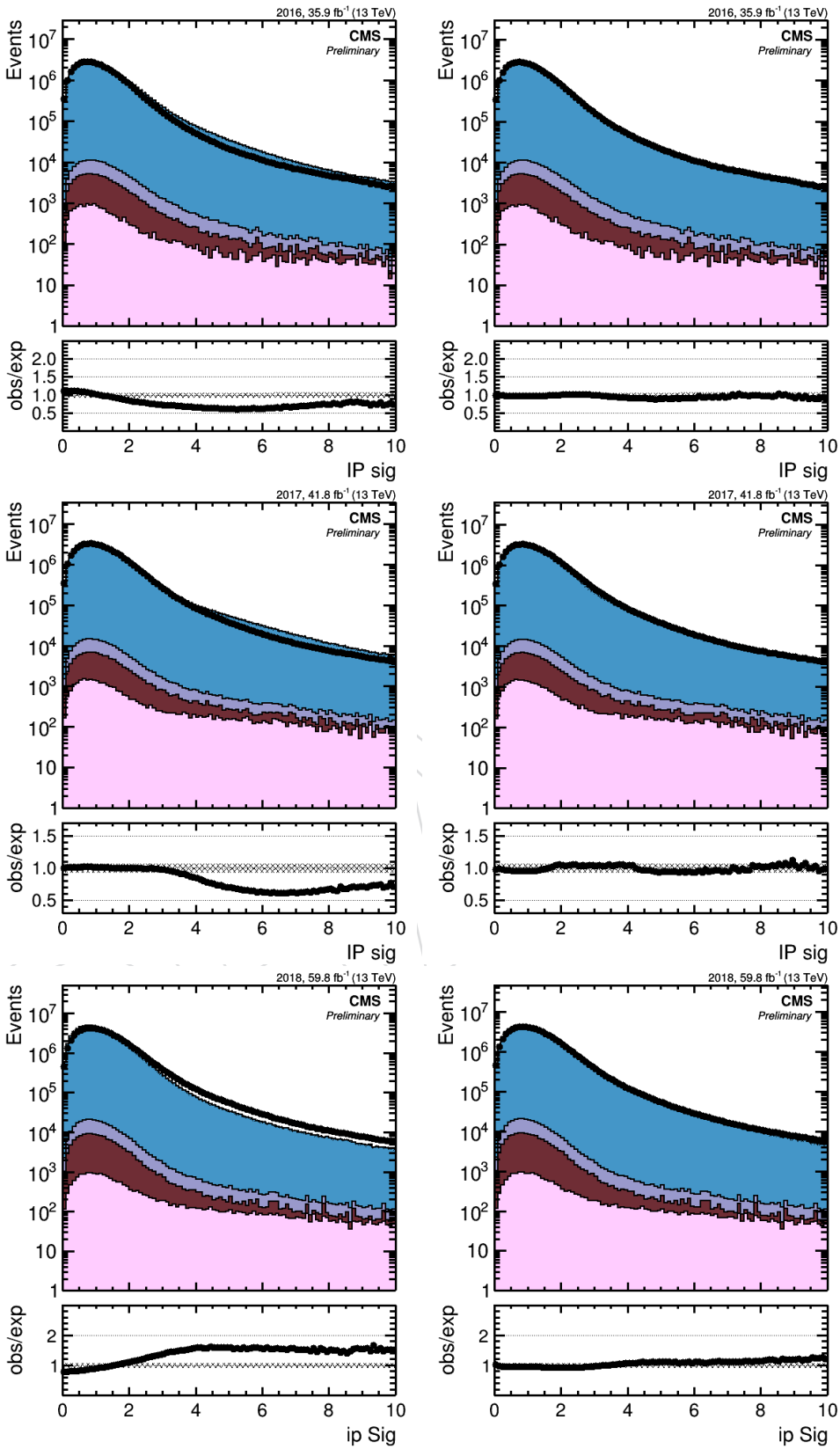

Figure 36: Distribution of the IP significance for MC events in the $Z \to \mu\mu$ sample. Left plot : data are compared to MC simulation before the calibration. Right plot : data are compared to MC simulation after the calibration.

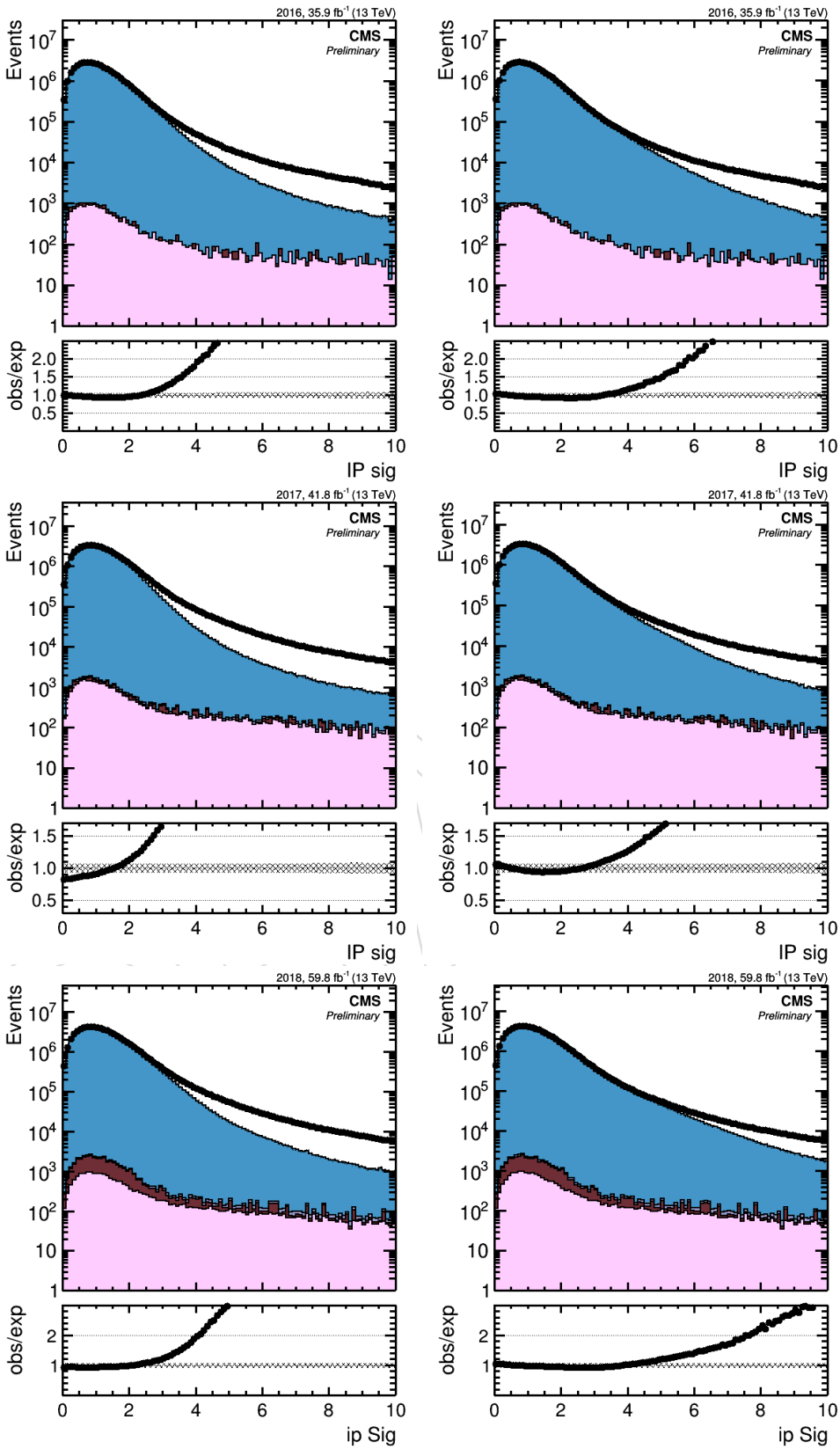

Figure 37: Distribution of the IP significance for embedded events in the $Z \to \mu\mu$ sample. Left plot : data are compared to embedded simulation before the calibration. Right plot : data are compared to embedded simulation after the calibration.

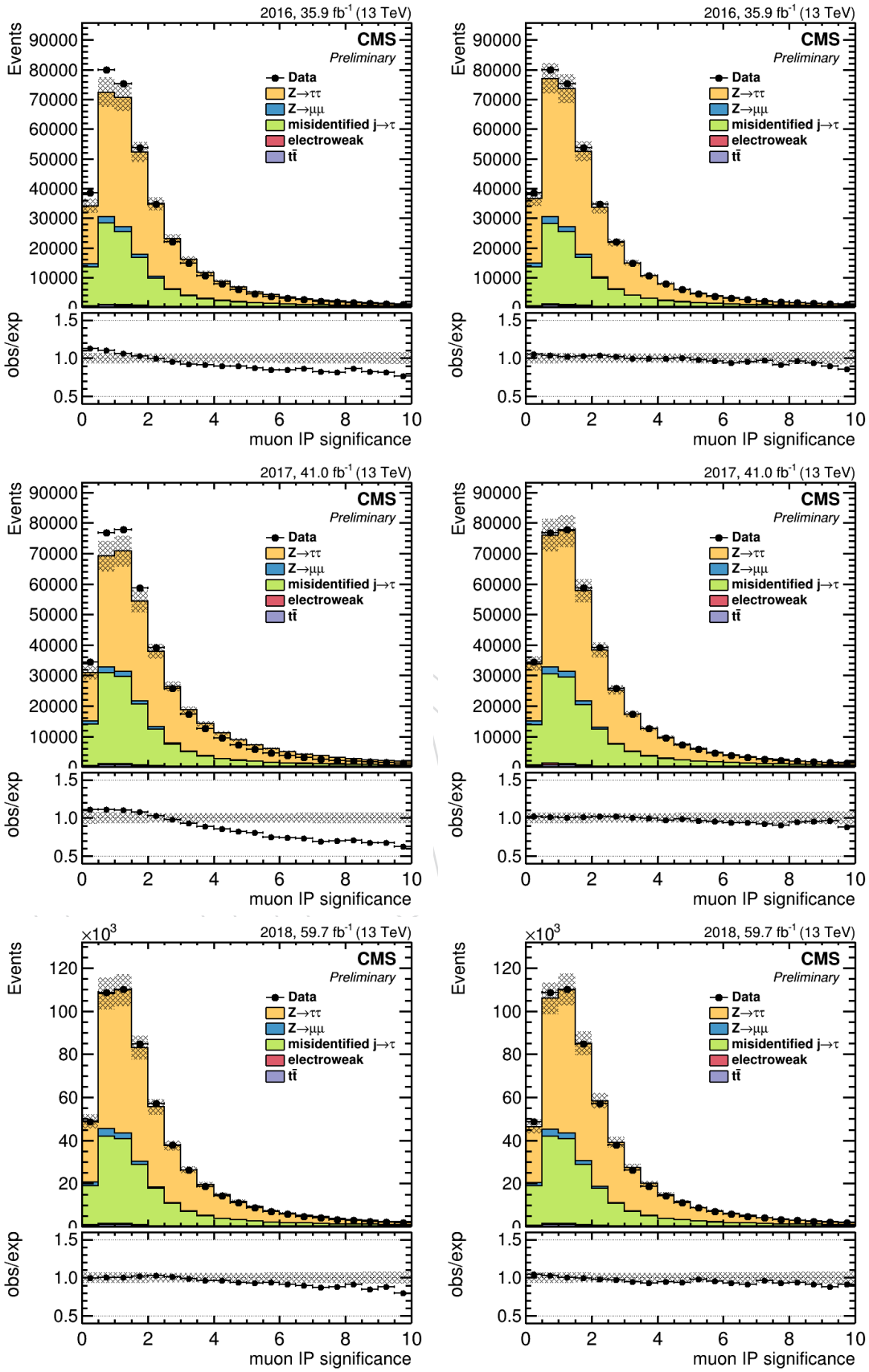

Figure 38: Distribution of the muon IP significance. Left plots : uncorrected IP significance. Right plots : corrected IP significance. The contribution from the $Z \to \tau\tau$ process is estimated with the MC simulation.

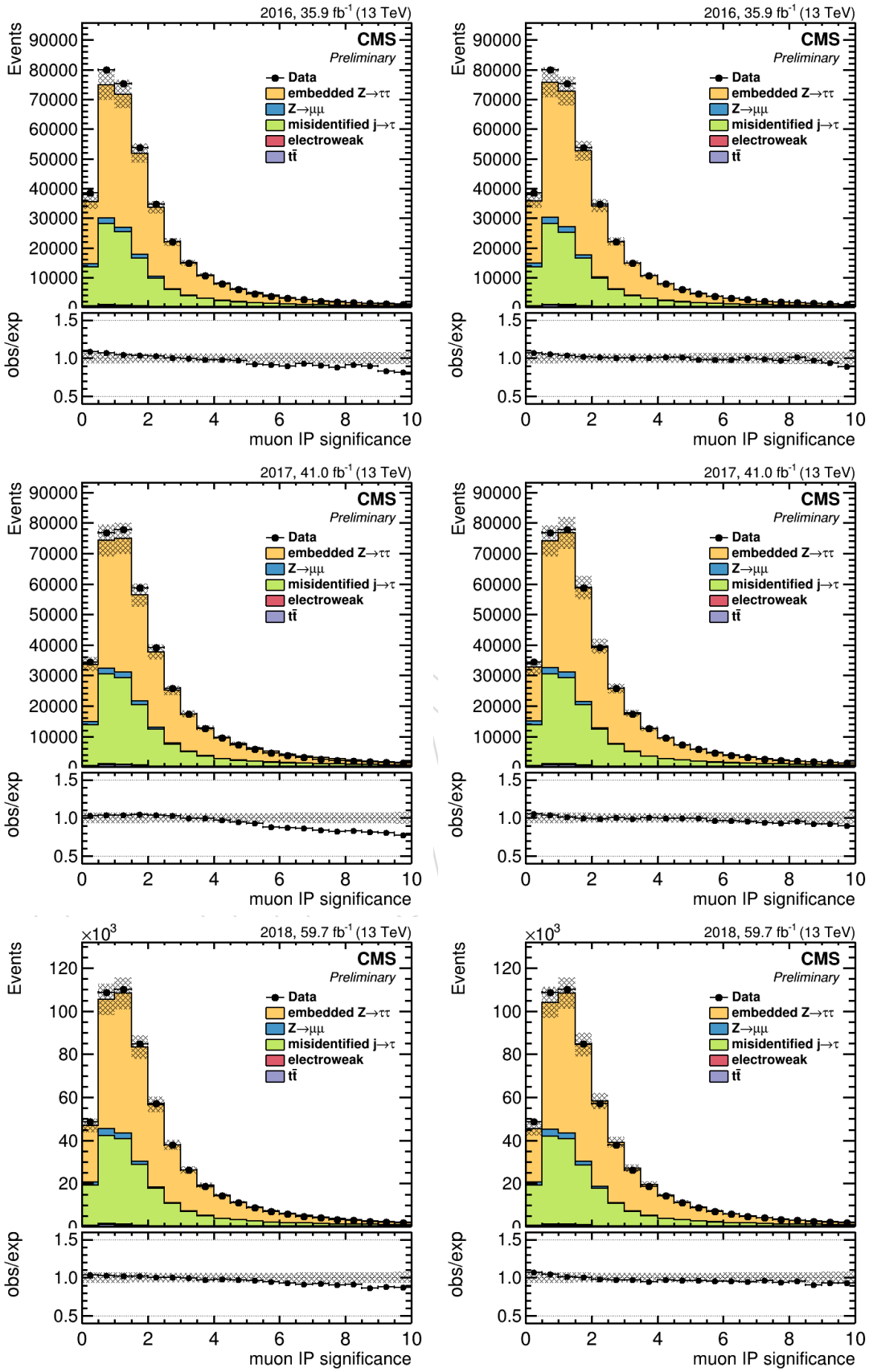

Figure 39: Distribution of the muon IP significance. Left plots : uncorrected IP significance. Right plots : corrected IP significance. The contribution from the $Z \to \tau\tau$ process is estimated with the embedding.

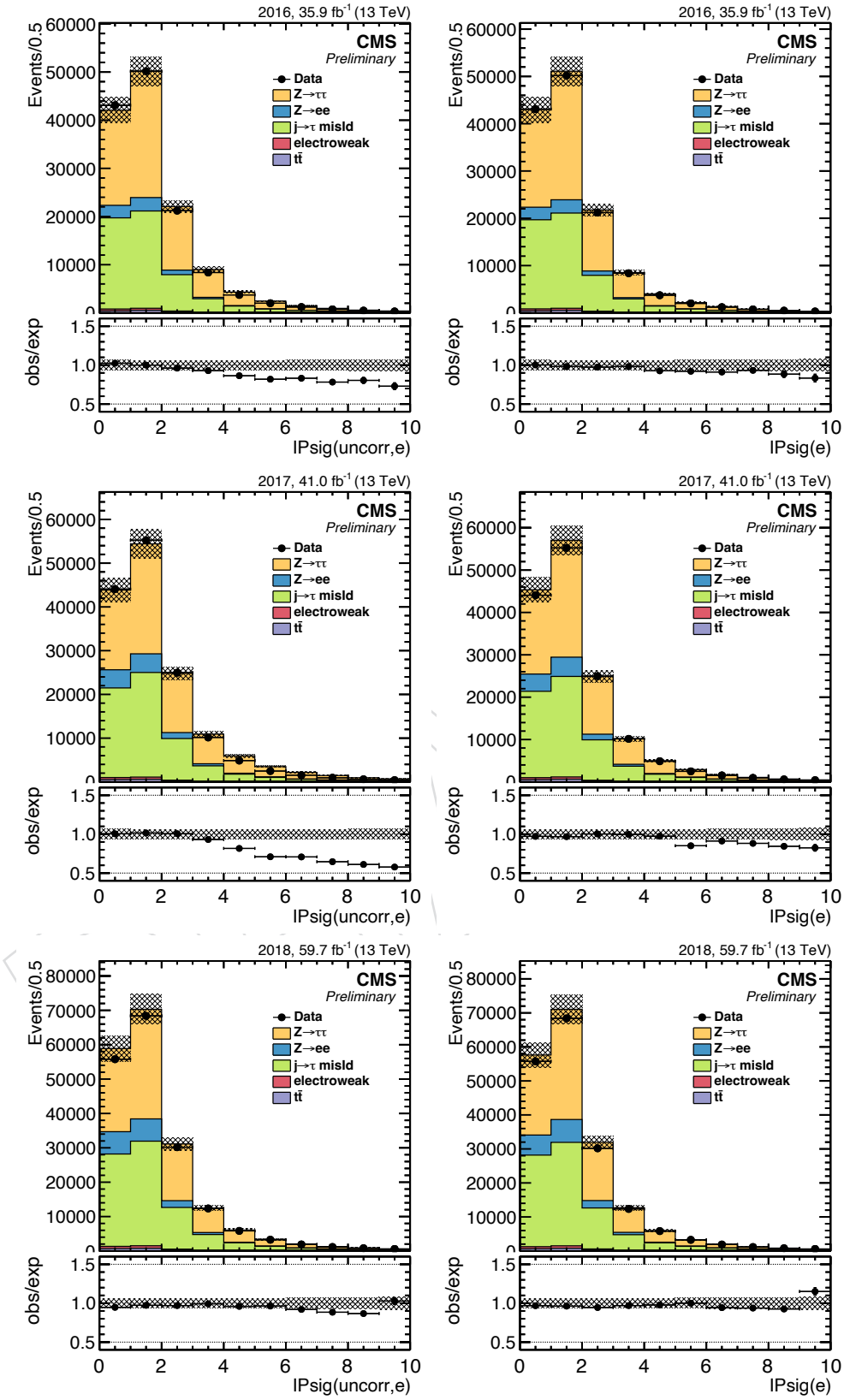

Figure 40: Distribution of the electron IP significance. Left plots : uncorrected IP significance. Right plots : corrected IP significance. The contribution from the $Z \to \tau\tau$ process is estimated with the MC simulation.

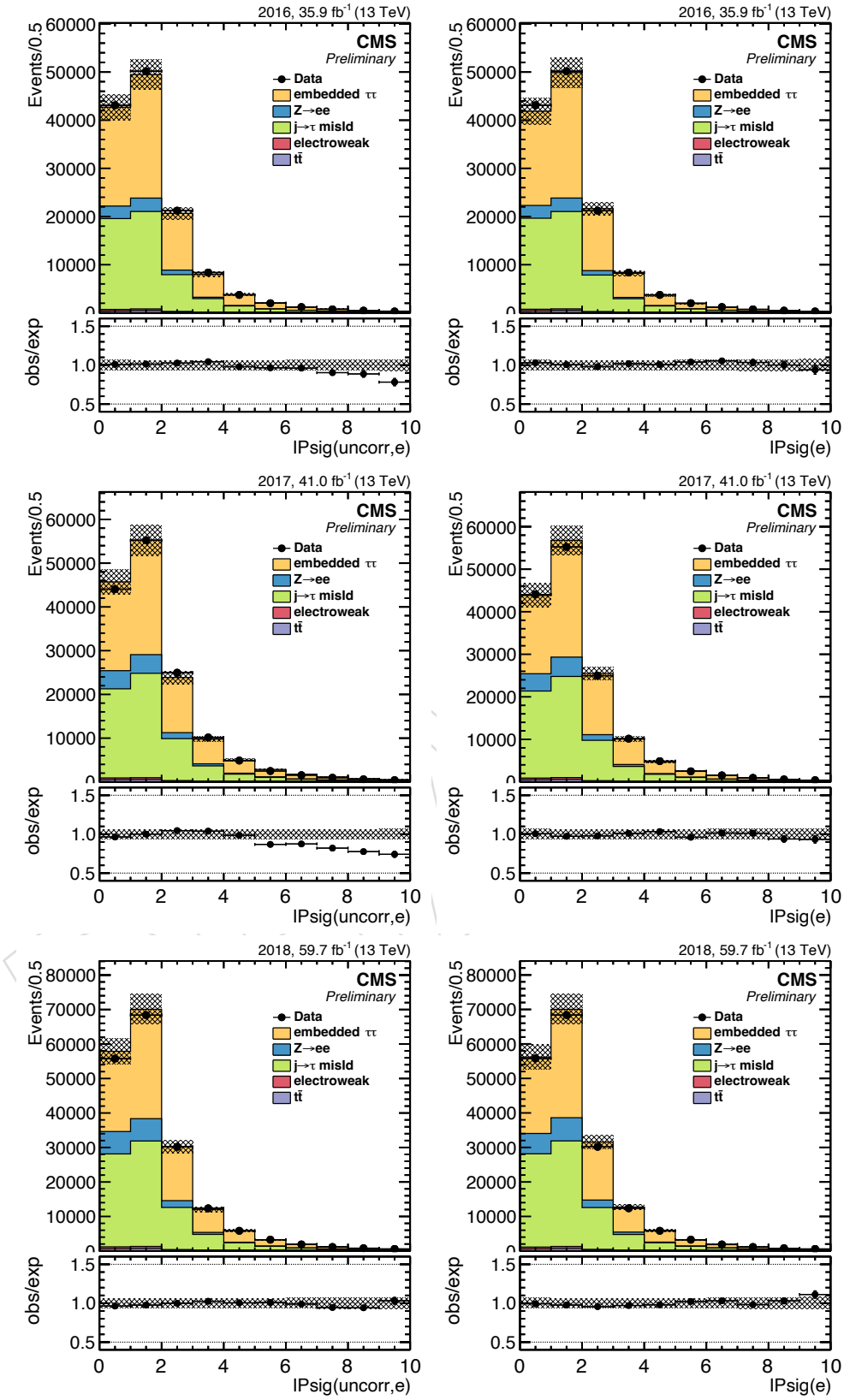

Figure 41: Distribution of the electron IP significance. Left plots : uncorrected IP significance. Right plots : corrected IP significance. The contribution from the $Z \to \tau\tau$ process is estimated with the embedding.

6 Triggers and filters

In this section we state the HLT paths and filters that are used as the first step in the event selection. In chapter 7 we'll outline the offline event selection in more detail.

6.1 Event selection in the $\tau_\mu \tau_h$ channel

For the $\mu\tau_h$ channel we consider exclusively events in data and MC that minimally struck one of the following triggers, listed for 2016, 2017, and 2018 in table in tables 21, 22, and 23, respectively.

$\mu\tau_h$ channel			
HLT Path	L1 seed	Muon filter(s) to match	
HLT_IsoMu22_v HLT_IsoMu22 _eta2p1_v	L1_SingleMu20 L1_SingleMu20er	hltL3crIsoL1sMu20L1f0L2f10QL3f22QL3trkIsoFiltered0p09 hltL3crIsoL1sSingleMu20erL1f0L2f10QL3f22QL3trkIsoFiltered0p09	
HLT_IsoTkMu22_v HLT_IsoTkMu22 _eta2p1_v	L1_SingleMu20 L1_SingleMu20er	hltL3fL1sMu20L1f0Tkf22QL3trkIsoFiltered0p09 hltL3fL1sMu20erL1f0Tkf22QL3trkIsoFiltered0p09	
		Muon filter(s) to match	Tau filter(s) to match
HLT_IsoMu19_eta2p1_LooseIso-PFTau20_v	L1_Mu18er_Tau20er	hltL3crIsoL1sMu18erTauJet20er-L1f0L2f10QL3f19QL3trkIsoFiltered0p09, hltOverlapFilterIsoMu19LooseIsoPFTau20	hltPFTau20TrackLooseIsoAgainstMuon, hltOverlapFilterIsoMu19LooseIsoPFTau20
HLT_IsoMu19_eta2p1_LooseIso-PFTau20_SingleL1_v	L1_SingleMu18er OR L1_SingleMu20er	hltL3crIsoL1sSingleMu18erIorSingleMu20er-L1f0L2f10QL3f19QL3trkIsoFiltered0p09, hltOverlapFilterSingleIsoMu19LooseIso-PFTau20	hltPFTau20TrackLooseIsoAgainstMuon, hltOverlapFilterSingleIsoMu19LooseIso-PFTau20

Table 21: Triggers used to collect the 2016 data samples for the $\tau_\mu \tau_h$ channel.

$\mu\tau_h$ channel			
HLT Path	L1 seed	Muon filter(s) to match	
HLT_IsoMu24_v	L1_SingleMu22	hltL3crIsoL1sSingleMu22L1f0L2f10QL3f24QL3trkIsoFiltered0p07	
HLT_IsoMu27_v	L1_SingleMu22 OR L1_SingleMu25	hltL3crIsoL1sMu22Or25L1f0L2f10QL3f27QL3trkIsoFiltered0p07	
		Muon filter(s) to match	Tau filter(s) to match
HLT_IsoMu20_eta2p1_ LooseChargedIsoPFTau27_ eta2p1_CrossL1_v	L1_Mu18er2p1_Tau24er2p1	hltL3crIsoL1sMu18erTau24erIorMu20er-Tau24erL1f0L2f10QL3f20QL3trkIsoFiltered-0p07, hltOverlapFilterIsoMu20LooseCharged-IsoPFTau27L1Seeded	hltSelectedPFTau27LooseChargedIsolation-AgainstMuonL1HLTMatched, hltOverlapFilterIsoMu20LooseChargedIso-PFTau27L1Seeded

Table 22: Triggers used to collect the 2017 data samples for the $\tau_\mu \tau_h$ channel.

$\mu\tau_h$ channel			
HLT Path	L1 seed	Muon filter(s) to match	
HLT_IsoMu24_v	L1_SingleMu22	hltL3crIsoL1sSingleMu22L1f0L2f10QL3f24QL3trkIsoFiltered0p07	
HLT_IsoMu27_v	L1_SingleMu22 OR L1_SingleMu25	hltL3crIsoL1sMu22Or25L1f0L2f10QL3f27QL3trkIsoFiltered0p07	
		Muon filter(s) to match	Tau filter(s) to match
before run 315974			
HLT_IsoMu20_eta2p1_ LooseChargedIsoPFTau27_ eta2p1_CrossL1_v	L1_Mu18er2p1_Tau24er2p1	hltL3crIsoL1sMu18erTau24erIorMu20er-Tau24erL1f0L2f10QL3f20QL3trkIsoFiltered-0p07, hltOverlapFilterIsoMu20LooseCharged-IsoPFTau27L1Seeded	hltSelectedPFTau27LooseChargedIsolation-AgainstMuonL1HLTMatched, hltOverlapFilterIsoMu20LooseChargedIso-PFTau27L1Seeded
run 315974 to 317509			
HLT_IsoMu20_eta2p1_ LooseChargedIsoPFTau27_ eta2p1_CrossL1_v	L1_Mu18er2p1_Tau24er2p1	hltL3crIsoBigORMu18erTauXXer2p1L1f0-L2f10QL3f20QL3trkIsoFiltered0p07, hltOverlapFilterIsoMu20LooseCharged-IsoPFTau27L1Seeded	hltSelectedPFTau27LooseChargedIsolation-AgainstMuonL1HLTMatched, hltOverlapFilterIsoMu20LooseCharged-IsoPFTau27L1Seeded
after run 317509 and MC			
HLT_IsoMu20_eta2p1_ LooseChargedIsoPFTauHPS27_ eta2p1_TightID_ CrossL1_v	L1_Mu18er2p1_Tau24er2p1	hltL3crIsoBigORMu18erTauXXer2p1L1f0-L2f10QL3f20QL3trkIsoFiltered0p07, hltHpsOverlapFilterIsoMu20LooseCharged-IsoTightOOSCPhotonsPFTau27L1Seeded	hltHpsSelectedPFTau27LooseCharged-IsolationTightOOSCPhotonsAgainst-MuonL1HLTMatched, hltHpsOverlapFilterIsoMu20LooseCharged-IsoTightOOSCPhotonsPFTau27L1Seeded

Table 23: Triggers used to collect the 2018 data samples for the $\mu\tau_h$ channel.

6.2 Event selection in the $\tau_e \tau_h$ channel

For the $\mu\tau_h$ channel we consider exclusively events in data and MC that minimally struck one of the following triggers, listed for 2016, 2017, and 2018 in table in tables 24, 25, and 26, respectively.

DRAFT

$e\tau_h$ channel		
HLT Path	L1 seed	Electron filter to match
HLT_Ele25_eta2p1_WPTight_Gsf_v	L1SingleEGXX OR L1SingleEGXXer2p1 OR L1SingleIsoEGXX OR L1SingleIsoEGXXer2p1	hltEle25erWPTightGsfTrackIsoFilter

Table 24: Triggers used to collect the 2016 data samples for the $e\tau$ channel.

$e\tau_h$ channel			
HLT Path	L1 seed	Electron filter(s) to match	
HLT_Ele27_WPTight_Gsf_v	L1SingleEGXX OR L1SingleEGXXer2p1 OR L1SingleIsoEGXX OR L1SingleIsoEGXXer2p1	hltEle27WPTightGsfTrackIsoFilter	
HLT_Ele32_WPTight_Gsf_v	L1SingleEGXX OR L1SingleEGXXer2p1 OR L1SingleIsoEGXX OR L1SingleIsoEGXXer2p1	hltEle32L1DoubleEGWPTightGsfTrackIsoFilter, hltEGL1SingleEGOrFilter	
		Electron filter(s) to match	Tau filter(s) to match
HLT_Ele24_eta2p1_WPTight_Gsf_LooseChargedIsoPFTau30_eta2p1_CrossL1_v	L1_LooseIsoEG22er2p1_IsoTau-26er2p1_dR_Min0p3 OR L1_LooseIsoEG24er2p1_IsoTau-27er2p1_dR_Min0p3	hltEle24erWPTightGsfTrackIsoFilterForTau, hltOverlapFilterIsoEle24WPTightGsfLoose-IsoPFTau30	hltSelectedPFTau30LooseChargedIsolation-L1HLTMatched, hltOverlapFilterIsoEle24WPTightGsfLoose-IsoPFTau30

Table 25: Triggers used to collect the 2017 data samples for the $e\tau$ channel.

$e\tau_h$ channel			
HLT Path	L1 seed	Electron filter(s) to match	
HLT_Ele32 _WPTight_Gsf_v	L1SingleEGXX OR L1SingleEGXXer2p1 OR L1SingleIsoEGXX OR L1SingleIsoEGXXer2p1	hltEle32WPTightGsfTrackIsoFilter	
HLT_Ele35 _WPTight_Gsf_v	L1SingleEGXX OR L1SingleEGXXer2p1 OR L1SingleIsoEGXX OR L1SingleIsoEGXXer2p1	hltEle35WPTightGsfTrackIsoFilter	
		Electron filter(s) to match	Tau filter(s) to match
before run 317509			
HLT_Ele24_eta2p1_WPTight_Gsf_LooseChargedIsoPFTau30_eta2p1_CrossL1_v	L1_LooseIsoEG22er2p1_IsoTau-26er2p1_dR_Min0p3 OR L1_LooseIsoEG24er2p1_IsoTau-27er2p1_dR_Min0p3	hltEle24erWPTightGsfTrackIsoFilterForTau, hltOverlapFilterIsoEle24WPTightGsfLoose-IsoPFTau30	hltSelectedPFTau30LooseChargedIsolation-L1HLTMatched, hltOverlapFilterIsoEle24WPTightGsfLoose-IsoPFTau30
after run 317509 and MC			
HLT_Ele24_eta2p1_WPTight_Gsf_LooseChargedIsoPFTauHPS30_eta2p1_CrossL1_v	L1_LooseIsoEG22er2p1_IsoTau-26er2p1_dR_Min0p3 OR L1_LooseIsoEG24er2p1_IsoTau-27er2p1_dR_Min0p3	hltEle24erWPTightGsfTrackIsoFilterForTau, hltHpsOverlapFilterIsoMu20LooseCharged-IsoPFTau27L1Seeded	hltHpsSelectedPFTau30LooseChargedIsolation-L1HLTMatched, hltHpsOverlapFilterIsoMu20LooseCharged-IsoPFTau27L1Seeded

Table 26: Triggers used to collect the 2018 data samples for the $e\tau$ channel.

6.3 Event selection in the $\tau_h\tau_h$ channel

The data samples are collected using the triggers listed in table 27, table 28 and table 29.

DRAFT

HLT Path	L1 seed	Tau filter to match
HLT_DoubleMediumIso PFTau35_Trk1_eta2p1_Reg_v	L1_DoubleIsoTau26er OR L1_DoubleIsoTau27er OR L1_DoubleIsoTau28er OR L1_DoubleIsoTau30er OR L1_DoubleIsoTau32er OR L1_DoubleIsoTau39er	hltDoublePFTau35TrackPt1MediumIsolationDz02Reg
HLT_DoubleMediumCombinedIso PFTau35_Trk1_eta2p1_Reg_v	L1_DoubleIsoTau26er OR L1_DoubleIsoTau27er OR L1_DoubleIsoTau28er OR L1_DoubleIsoTau30er OR L1_DoubleIsoTau32er OR L1_DoubleIsoTau39er	hltDoublePFTau35TrackPt1MediumCombinedIsolationDz02Reg

Table 27: Triggers used to collect the 2016 data samples for the $\tau_h\tau_h$ channel.

HLT Path	L1 seed	Tau filter to match
HLT_DoubleTight ChargedIso_PFTau40_Trk1_eta2p1_Reg_v	L1_DoubleIsoTauOR[3]	hltDoublePFTau40TrackPt1 TightChargedIsolationDz02Reg
HLT_DoubleMedium ChargedIso_PFTau40_Trk1_TightID_eta2p1_Reg_v	L1_DoubleIsoTauOR[3]	hltDoublePFTau40TrackPt1 MediumChargedIsolationAnd TightOOSCPhotonsDz02Reg
HLT_DoubleTight ChargedIso_PFTau35_Trk1_TightID_eta2p1_Reg_v	L1_DoubleIsoTauOR[3]	hltDoublePFTau35TrackPt1 TightChargedIsolationAnd TightOOSCPhotonsDz02Reg

3

```
L1_DoubleIsoTau28er2p1 OR L1_DoubleIsoTau30er2p1 OR L1_DoubleIsoTau32er2p1 OR
L1_DoubleIsoTau33er2p1 OR L1_DoubleIsoTau34er2p1 OR L1_DoubleIsoTau35er2p1 OR
   L1_DoubleIsoTau36er2p1 OR L1_DoubleIsoTau38er2p1 OR L1_DoubleTau70er2p1
```

Table 28: Triggers used to collect the 2017 data samples for the $\tau_h\tau_h$ channel.

DRAFT

HLT Path	L1 seed	Tau filter to match
HLT_DoubleTight ChargedIso_PFTau40_Trk1_eta2p1_Reg_v	L1_DoubleIsoTauOR[3]	hltDoublePFTau40TrackPt1 TightChargedIsolationDz02Reg
HLT_DoubleMedium ChargedIso_PFTau40_Trk1_TightID_eta2p1_Reg_v	L1_DoubleIsoTauOR[3]	hltDoublePFTau40TrackPt1 MediumChargedIsolationAnd TightOOSCPhotonsDz02Reg
HLT_DoubleTight ChargedIso_PFTau35_Trk1_TightID_eta2p1_Reg_v	L1_DoubleIsoTauOR[3]	hltDoublePFTau35TrackPt1 TightChargedIsolationAnd TightOOSCPhotonsDz02Reg
(after run 317509 only this) HLT_DoubleMedium ChargedIso_PFTauHPS35_Trk1_eta2p1_Reg_v	L1_DoubleIsoTauOR[3]	hltHpsDoublePFTau35TrackPt1 MediumChargedIsolationAnd Dz02Reg

3

```
L1_DoubleIsoTau28er2p1 OR L1_DoubleIsoTau30er2p1 OR L1_DoubleIsoTau32er2p1 OR
L1_DoubleIsoTau33er2p1 OR L1_DoubleIsoTau34er2p1 OR L1_DoubleIsoTau35er2p1 OR
   L1_DoubleIsoTau36er2p1 OR L1_DoubleIsoTau38er2p1 OR L1_DoubleTau70er2p1
```

Table 29: Triggers used to collect the 2018 data samples for the $\tau_h\tau_h$ channel.

7 Event Selection

7.1 Introduction

$\tau_\mu\tau_h$ In this section we start with describing selections that are general to both the $\tau_\mu\tau_h$ and $\tau_h\tau_h$ channel. Subsequently, we describe by which criteria we select our offline reconstructed objects for the $\tau_\mu\tau_h$ and $\tau_h\tau_h$ channel This is followed by the description of how, in case multiple pairs are available, an optimal $\tau_\mu\tau_h$ or $\tau_h\tau_h$ pair is selected. Finally, we describe how we match the objects from the optimal offline reconstructed pair to the online trigger objects, and how the kinematic cutoffs are adjusted for different trigger matches.

7.2 General event criteria

7.2.1 MET filters

Events are required to pass these $p_{\mathrm{T}}^{\mathrm{miss}}$ filters:

- primary vertex filter (Data and MC);
- beam halo filter super tight (Data and MC);
- HBHE noise filter (Data and MC);
- HBHEiso noise filter (Data and MC);
- eebadSC noise filter (Data);
- ECAL TP filter (Data and MC);
- badMuon filter (Data and MC);
- ECAL bad calibration filter (Data and MC)(2017 and 2018).

7.2.2 Extra lepton veto

The events are rejected if they contain a (very loosely selected) third lepton, separated from the two tau candidates by $\Delta R > 0.5$, that passes the following selection criteria.

Electron:

- $p_{\mathrm{T}} > 10\,\mathrm{GeV}$, and $|\eta|$<2.5.
- $d_Z < 0.2$ cm, and $d_{xy} < 0.045$ cm.
- Pass electron MVA ID 90% efficiency WP without isolation (Fall17-V2 training).
- passConversionVeto().
- gsfTrack()→hitPattern().numberOfHits(reco::HitPattern::MISSING_INNER_HITS))) <= 1.
- I_e(cone size 0.3) $< 0.3 p_{\mathrm{T}}^{e}$.

Muon:

- p_{T}> 10 GeV, and $|\eta| < 2.4$.
- $d_Z < 0.2$ cm, and $d_{xy} < 0.045$ cm.
- Pass Medium ID.
- I_μ(cone size 0.4) $< 0.3 p_{\mathrm{T}}^{\mu}$.

DRAFT

7.2.3 Di-lepton veto

A veto on events containing dileptons pairs is applied. The oppositesign leptons must be separated by $\Delta R > 0.15$, and a loose selection on the leptons is applied. All following conditions must be met:

- Di-muons:
  - $p_{\mathrm{T}} > 15\,\mathrm{GeV}$
  - $|\eta| < 2.4$
  - The muon must be a global muon
  - The muon must be a tracker muon
  - The muon must be a particle flow muon
  - dz<0.2
  - dxy<0.045
  - I_μ(cone size 0.4) $< 0.3 p_{\mathrm{T}}^{\mu}$.
- Di-electrons:
  - $p_{\mathrm{T}} > 15\,\mathrm{GeV}$
  - $|\eta| < 2.5$
  - Fall17V2_cutbased_veto ID
  - dz<0.2
  - dxy<0.045
  - I_e(rho corrected, cone size 0.3) $< 0.3 p_{\mathrm{T}}^{e}$.

7.3 Selection criteria in the $\tau_\mu \tau_h$ final state

The event must pass at least one of the trigger paths listed in Section 6. An event is selected if at least one combination of a muon and a τ_h candidate is found. The pair must have opposite sign and is required to be separated by $\Delta R > 0.5$.

Additionally, all events are required to have a transverse mass between the muon and $p_{\mathrm{T}}^{\mathrm{miss}}$ less than 50 GeV. This selection criterion removes a large fraction of the W+jets background.

Also, events with a b–jet are vetoed; events with one or more jets with $p_{\mathrm{T}} > 20\,\mathrm{GeV}$ and $|\eta| < 2.4$ that passes the medium deepCSV working point are discarded.

The selected muon must meet the following criteria:

- $p_{\mathrm{T}} > 20\,\mathrm{GeV}$ and $|\eta| < 2.4$ (these criteria can be tightened depending on the trigger path that the muon is matched to, see section 7.7);
- $d_{xy} < 0.045$ cm;
- $d_z < 0.2$ cm;
- Muon must meet the medium muon ID;
- Muon relative isolation < 0.15.

In addition the τ_h must meet the following criteria:

- $p_{\mathrm{T}} > 20\,\mathrm{GeV}$ and $|\eta| < 2.3$ (these criteria can be tightened depending on the trigger path, see 7.7);
- Medium deep neural net ID against jets;
- New decay modes excluding 2-prong decays;

DRAFT

- $d_z < 0.2$ cm;
- VVLoose deep neural net ID against electrons;
- Tight deep neural net ID against muons .

Events containing more than one muon candidate are removed by the extra lepton vetos, however it is possible to have more than one candidate pair if two or more τ_h candidates exist. In case the event contains more than one $\mu + \tau_h$ combination after the p_{T}, η, and ID cuts, the pair selection algorithm is applied as in subsection 7.6. The selected pair is additional required to have visible mass > 40 GeV.

7.4 Selection criteria in the $\tau_e \tau_h$ final state

In this section we describe the event selection for the eτ_h channel.

7.4.1 Triggers

We employ the triggers listed in tables 24, 25, and 26. The selected reconstructed leptons, firing the trigger, have to match the HLT objects listed in these tables within $\Delta R < 0.5$. These triggers are applied to the simulated samples, as well.

7.4.2 Event selection

Events in the eτ_h channel are selected by requiring:

- The event to pass the relevant $E_{\mathrm{T}}^{\mathrm{miss}}$ filters listed in Section 7.2.1
- An electron of $p_T^{\mathrm{e}} > 25$ GeV and $|\eta| < 2.1$. Further selection criteria for electron are outlined in Section 4.2.
- A hadronic tau of $p_T^{\tau} > 20$ GeV and $|\eta| < 2.3$, passing decayModeFinding and d_z between leading charged track and first primary vertex $d_z < 0.2$ cm. In addition, it needs to pass the tight working point of the deepTau vs jets discriminator. The tau also needs to pass the loose working point of the deepTau anti-muon discriminator and the tight working point of the deepTau anti-electron discriminator
- The electron and hadronic tau should be separated by $\Delta R > 0.5$

Further kinematic selection depends on the triggers fired. The following criteria are applied:

- 2016 : trg_singleE AND $p_T(\mathrm{e}) > 26$ GeV;
- 2017 : (trg_singleE AND $p_T(\mathrm{e}) > 28$ GeV) OR (trg_etau AND $p_T(\mathrm{e}) > 25$ GeV AND $p_T(\tau) > 35$ GeV AND $|\eta(\tau)| < 2.1$);
- 2018 : (trg_singleE AND $p_T(\mathrm{e}) > 33$ GeV) OR (trg_etau AND $p_T(\mathrm{e}) > 25$ GeV AND $p_T(\tau) > 35$ GeV AND $|\eta(\tau)| < 2.1$);

The boolean variable "trg_singleE" is set to true if one of the single-electron triggers is fired and offline electron matches respective trigger object. The boolean variable "trg_etau" is set to true if the electron-tau cross-trigger is fired and offline electron and tau objects match respective trigger objects.

The following additional selection criteria are applied:

- The electron and hadronic tau must be of opposite charge
- The transverse mass m_{T} of electron and missing transverse energy E_T^{miss} is required to satisfy $m_{\mathrm{T}} < 50$ GeV in order to reject W+jets background.

DRAFT

- Extra muon, electron and di-electron vetos are applied as described in Sections 7.2.2 and 7.2.3.
- Also, events with a b–jet are vetoed; events with one or more jets with $p_T > 20\,\text{GeV}$ and $|\eta| < 2.4$ that passes the medium deepCSV working point are discarded.

7.5 Selection criteria in the $\tau_h\tau_h$ final state

An event is preselected if at least one $\tau_h\tau_h$ pair is found. Each τ_h in the pair is required to have opposite sign (OS) electric charge and separated by $\Delta R > 0.5$. The τ_h candidate is selected if it satisfies the following criteria.

- $p_T > 40\,\text{GeV}$, and $|\eta| < 2.1$.
- New decay mode finding excluding 2-prong decay modes.
- Medium deep neural net ID against jets.
- Particle vertex and beamspot are separated by $d_Z < 0.2\,\text{cm}$ (defined by packedLeadTauCand→dz(), which corresponds to the leading track of the τ_h candidate).
- VVloose deep neural net ID against electrons.
- VLoose deep neural net ID against muons (this is the loosest WP).

In case there are more than one possible candidate pairs, the pair selection algorithm is applied as outlined in subsection 7.6. The selected pair is additional required to have visible mass > 40 GeV.

7.6 Pair selection

After requiring trigger, identification and kinematic cuts there can be more than one possible candidate pair. In this case the pair with the most isolated leptons is chosen as follows:

- Prefer the pair with most isolated candidate 1 (muon for $\tau_\mu\tau_h$ and either of the τ_hs in $\tau_h\tau_h$ for the fully hadronic channel). For muons this means the object with the smallest relative isolation value is preferred, for τ_hs the object with raw deeptau ID output
- If the isolation of candidate 1 is the same in both pairs, prefer the pair with highest candidate 1 p_T
- If the p_T of candidate 1 is the same in both pairs, prefer the pair with most isolated candidate 2 (the other τ_h for the $\tau_h\tau_h$ channel, and the τ_h for $\tau_\mu\tau_h$ channels)
- If the isolation of candidate 2 is the same in both pairs, prefer the pair with highest candidate 2 p_T

7.7 Matching offline reconstructed objects to trigger objects

The following general matching criteria apply. After that the optimal offline pair of objects has been selected, the objects of this pair must be matched to the online trigger objects as indicated in section 6. If this matching is not possible, the event is discarded. The triggered object must be matched to the offline object within $\Delta R < 0.5$.

The reconstructed muon or electron must have minimally a p_T of 1 GeV above the online trigger threshold of the path to which it is matched. The τ_h is required to have p_T of 5 GeV above the online trigger threshold to be less sensitive to the efficiency turn-on, both for the $\tau_h\tau_h$ channel and the cross trigger in the $\tau_\mu\tau_h$ and $\tau_e\tau_h$ channels. For the $\tau_h\tau_h$ channel this never leads to tighter cuts than the offline cuts specified in Section 7.5.

DRAFT

Further, the following more tight constraints may apply, depending on the trigger match:

- Trigger matching in 2016
  Events in the $\mu\tau_h$ channel are required to pass the IsoMu22 OR Mu19Tau20 paths. If matched to IsoMu22, the muon is required to have $|\eta| < 2.1$ and have $p_{\mathrm{T}}^{\mu} > 23\,\mathrm{GeV}$, and the μ must pass the corresponding filter. If matched to the Mu19Tau20 path, it is required to have $20\,\mathrm{GeV} < p_{\mathrm{T}}^{\mu}$.

  In the $\mathrm{e}\tau_h$ channel events are required to pass Ele25 trigger. If matched to the trigger object of the Ele25 trigger, the electron is required to have $p_{\mathrm{T}}^{\mathrm{e}} > 26\,\mathrm{GeV}$, and electron must pass the corresponding filter.

  In the $\tau_h\tau_h$ final state, events are triggered with an OR of two paths, which both require 2 τ_h candidates with $|\eta| < 2.1$ and $p_{\mathrm{T}} > 35\,\mathrm{GeV}$ online.
- Trigger matching in 2017
  Events in the $\mu\tau_h$ channel are required to match to one of three paths, IsoMu24 OR IsoMu27 OR the cross trigger Mu20Tau27. If matched to IsoMu24, the μ is required to have $p_{\mathrm{T}}^{\mu} > 25\,\mathrm{GeV}$ and match the corresponding filter. If matched to IsoMu27, the μ is required to have $p_{\mathrm{T}}^{\mu} > 25\,\mathrm{GeV}$ and match the corresponding filter. The muon p_{T} cut in the case of the IsoMu27 trigger is driven by the fact that we require an OR with the IsoMu24 trigger, and the trigger scale factors are measured for the combination of the two single muon triggers with a common p_{T} cut. If matched to the cross trigger Mu20Tau27, the μ is required to have $21\,\mathrm{GeV} < p_{\mathrm{T}}^{\mu}$ while the τ_h is required to have $p_{\mathrm{T}} > 32\,\mathrm{GeV}$ and $|\eta| < 2.1$.

  In the $\mathrm{e}\tau_h$ channel, events are required to match one of the three paths, Ele27 OR Ele32 OR the cross trigger Ele25Tau30. If event is matched to the Ele27 OR Ele32 HLT paths, the electron is required to have $p_{\mathrm{T}}^{\mathrm{e}} > 28\,\mathrm{GeV}$. If event is matched to the cross trigger Ele24Tau30, the electron is required to have $p_{\mathrm{T}}^{\mathrm{e}} > 25\,\mathrm{GeV}$ while the τ_h is required to have $p_{\mathrm{T}}^{\tau} > 35\,\mathrm{GeV}$ and $|\eta^{\tau}| < 2.1$.

  In the $\tau_h\tau_h$ final state, an OR of 3 trigger paths is considered, with different online p_{T} thresholds and online isolations.
- Trigger matching in 2018
  Events in the $\mu\tau_h$ channel are required to match to one of three paths, IsoMu24, IsoMu27, or the cross trigger Mu20Tau27 (HPS or non-HPS depending on whether it is data, its run number and whether it is MC, see Table 23). If matched to IsoMu24, the μ is required to have $p_{\mathrm{T}}^{\mu} > 25\,\mathrm{GeV}$ and match the corresponding filter. If matched to IsoMu27, the μ is required to have $p_{\mathrm{T}}^{\mu} > 25\,\mathrm{GeV}$ and match the corresponding filter. If matched to the cross trigger Mu20Tau27, the μ is required to have $21\,\mathrm{GeV} < p_{\mathrm{T}}^{\mu}$ while the τ_h is required to have $p_{\mathrm{T}} > 32\,\mathrm{GeV}$ and match the corresponding filter and both particles are required to have $|\eta| < 2.1$.

  In the $\mathrm{e}\tau_h$ channel, events are required to match one of the three paths, Ele32 OR Ele35 OR the cross trigger Ele25Tau30. If event is matched to the Ele32 OR Ele35 HLT paths, the electron is required to have $p_{\mathrm{T}}^{\mathrm{e}} > 33\,\mathrm{GeV}$. If event is matched to the cross trigger Ele24Tau30, the electron is required to have $p_{\mathrm{T}}^{\mathrm{e}} > 25\,\mathrm{GeV}$ while the τ_h is required to have $p_{\mathrm{T}}^{\tau} > 35\,\mathrm{GeV}$ and $|\eta^{\tau}| < 2.1$.

  In the $\tau_h\tau_h$ final state, the trigger paths depend on the run number, as the HPS reconstruction at HLT level was implemented in the middle of the data taking. The trigger data/MC scale factors applied in the analysis take this change of paths into account.

DRAFT

In the $\tau_\mu \tau_h$ channel an event is selected if it passes the single muon trigger OR muon+tau cross trigger. To account for differences in the trigger efficiencies between data and simulated (embedded) events, each event is assigned weight:

$$w_{\text{trig}} = \frac{\epsilon_{\text{trig}}^{\text{data}}}{\epsilon_{\text{trig}}^{\text{MC/emb}}}, \tag{35}$$

where $\epsilon_{\text{trig}}^{\text{data}}$ is the efficiency of event to pass the single muon trigger OR the muon+tau cross trigger as measured for data events, and $\epsilon_{\text{trig}}^{\text{MC/emb}}$ is the efficiency of event to pass the single muon trigger OR the muon+tau cross trigger as determined in the simulated (embedded) events. The HLT filter of the single muon triggers differs from the muon filter of the muon+tau cross trigger only by the online p_{T} threshold. For the muon filter of the muon+tau cross trigger this threshold is lower for all data taking periods. Therefore the efficiency to fire the single muon trigger OR the muon+tau cross trigger can be computed as

$$\epsilon_{\text{trig}} = \epsilon_L + (\epsilon_\ell - \epsilon_L)\epsilon_\tau, \tag{36}$$

where ϵ_L is the efficiency of the single muon trigger, ϵ_ℓ - efficiency of the muon filter of the muon+tau cross trigger, and ϵ_τ - efficiency of the tau filter of the muon+tau trigger. The measurement of the efficiencies ϵ_L and ϵ_ℓ is documented in Ref. [48]. The measurement of the efficiency ϵ_τ is described in Section 5.4.

DRAFT

8 Background estimation

The analysis considers several background which includes: Drell-Yan, $t\bar{t}$, W+jets, QCD, di-boson, single-top, and electroweak W and Z bosons production. The background estimation method used in this analysis follow closely those used in the SM coupling analysis [47]. With the exception of the $j \to \tau_h$ backgrounds all other processes are estimated exactly as described in Ref. [47]. This includes the use of embedded samples to model all processes producing two genuine tau leptons, and MC simulation to model all remaining background except those which include $j \to \tau_h$ candidates. The $j \to \tau_h$ background is estimated using the fake factor method as described in Section 8.1. This procedure is conceptually similar to the method described in Ref. [47] but with some modification which are necessary take into account additional variables dependencies (e.g on the τ_h MVA-DM).

8.1 The fake factor method

Backgrounds in which a jet fakes a τ_h can be difficult to model using MC due to the poor description of the jet $\to \tau_h$ fake rate in simulation. In addition, the small probability of a jet being misidentified as a τ_h necessitates the production of high-statistics MC samples at a significant computational expense. These shortcomings motivate the use of data-driven estimates for these processes. One such procedure is the fake factor (FF) method.

The FF method models jet $\to \tau_h$ backgrounds from side-band regions in data, in which a τ_h candidate fails the nominal `Medium` DeepTau ID requirement applied in the signal region (SR) but passes the `VVVLoose` working point. These side-band regions will be referred to here as application regions (AR). The basic idea of the method is to scale events in the AR by ratios, $\mathrm{FF_i}$, defined as

$$\mathrm{FF_i} = \frac{N(\texttt{Medium})}{N(\texttt{VVVLoose \&\& !Medium})}, \tag{37}$$

where $N(X)$ is the number of events meeting the identification requirement X. These $\mathrm{FF_i}$ ratios are measured in control-regions enriched in jet $\to \tau_h$ events referred to here as determination regions (DR). The $\mathrm{FF_i}$ are measured in bins of N_{jets}, the MVA-DM, and the dependence on p_T is accounted for using fitted functions. In the $\tau_\mu \tau_h$ channel separate $\mathrm{FF_i}$ are measured for events that pass the single muon and muon+tau cross triggers. The $\mathrm{FF_i}$ are measured separately for the dominant jet $\to \tau_h$ processes, which for the $\tau_\mu \tau_h$ channel includes QCD, W+jets and $t\bar{t}$, and for the $\tau_h \tau_h$ channel includes only QCD. For the $\tau_\mu \tau_h$ channels the $\mathrm{FF_i}$ measured for the W+jets process are also used to model sub-dominant processes such as Z+jets, whereas for the $\tau_h \tau_h$ channel the $\mathrm{FF_i}$ measured for QCD events are used to model all processes. The $\mathrm{FF_i}$ are also corrected to account for extrapolations from the DR to the SR, and for missing variable dependencies (via non-closure corrections).

The FF_i measured for the different processes are combined into an overall factor, $\overline{\mathrm{FF}}$, using

$$\overline{\mathrm{FF}} = \sum_i f_i \cdot \mathrm{FF}_i, \tag{38}$$

where the factor f_i is defined as

$$f_i = \frac{n_i}{\sum_j n_j}, \tag{39}$$

which is the fraction of events with a jet $\to \tau_h$ originating from process i over the total number of jet $\to \tau_h$ events for all processes in the AR.

8.1.1 Fake factors in the $\tau_h\tau_h$ channel

The FF_i in the $\tau_h\tau_h$ are measured only for the dominant QCD process. The DR in this case is defined by inverting the requirement of the τ_h pair to have opposite-sign (OS) charges such that a same-sign (SS) pair are selected. All other selections are kept the same as for the SR. The FF_{QCD} are measured for the leading τ_h candidate only. The FF_{QCD} are measured for three N_{jets} bins (0, 1, $\geq$ 2) and 5 MVA-DM bins (0, 1, 2, 10, 11). The MVA-DM = 0 bins are further split into two bins depending on the τ_h impact parameter significance ($S_{IP} < 1.5$, $S_{IP} \geq 1.5$). In each bin the dependence on the τ_h p_T is fitted using the superposition of a Landau and a zeroth order polynomial. In some cases where the statistical population of a bin is insufficient the Landau+pol0 fit can fail to converge properly or give unreasonable trends that are overly influenced by statistical fluctuations. In such cases the p_T dependence is instead fitted using a first order polynomial. The fits are performed separately for each era (2016, 2017, and 2018). Examples of the resulting fits performed for 2018 are shown in Figures 42–50, which are chosen to illustrate the MVA-DM, N_{jets}, and S_{IP} dependencies respectively.

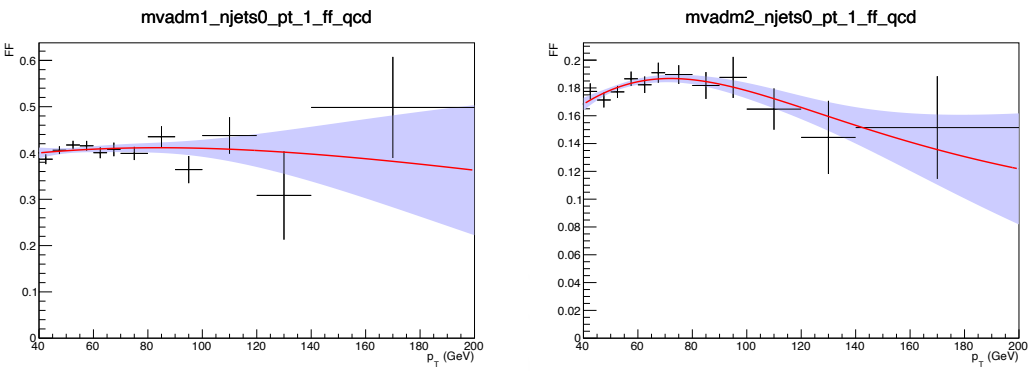

(a) MVA-DM = 1

(b) MVA-DM = 2

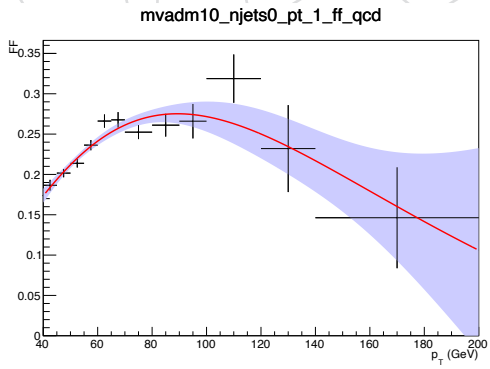

(c) MVA-DM = 10

Figure 42: Examples of the 2018 fake factor fits in the $\tau_h\tau_h$ channel illustrating the dependence on MVA-DM. The fitted fake factors measured for τ_h candidates with MVA-DM = 1, 2, and 10 are shown.

The measured FF_{QCD} are then corrected to account for non-closures and DR vs SR differences. The non-closure correction is derived by applying the derived FF_{QCD} to the DR events, and taking the residual data/prediction differences as the correction. The only significance non-closures are observed for E_T^{miss} related variables and are largest for events with $N_{jets} = 0$. Non-closures are observed for both the magnitude of the E_T^{miss} and the $\Delta\phi$ between the tau and the $\vec{E}_T^{miss}$ vector. The origin of this non-closure is understood to arise from events where the the

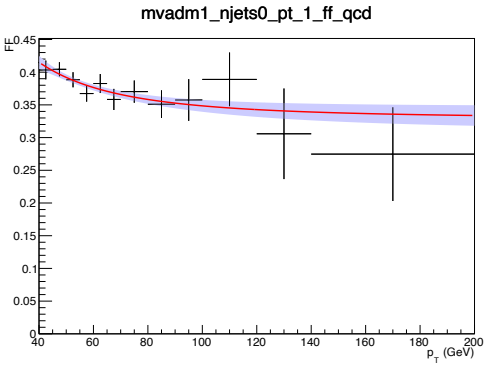

(a) MVA-DM = 1

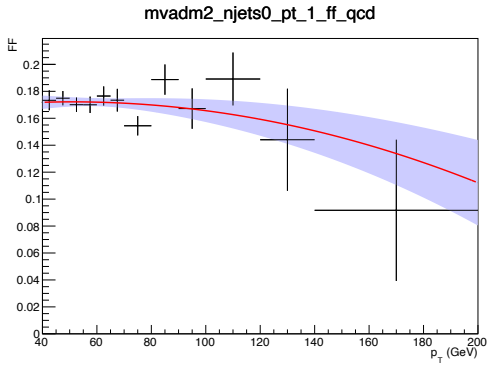

(b) MVA-DM = 2

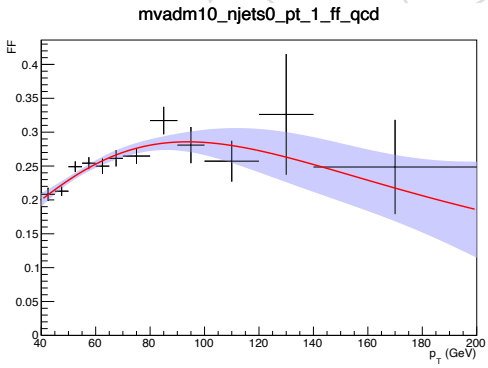

(c) MVA-DM = 10

Figure 43: Examples of the 2017 fake factor fits in the $\tau_h\tau_h$ channel illustrating the dependence on MVA-DM. The fitted fake factors measured for τ_h candidates with MVA-DM = 1, 2, and 10 are shown.

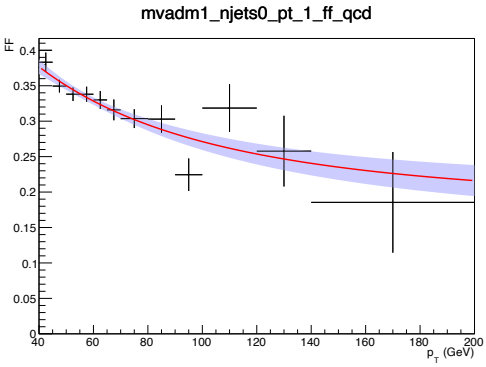

(a) MVA-DM = 1

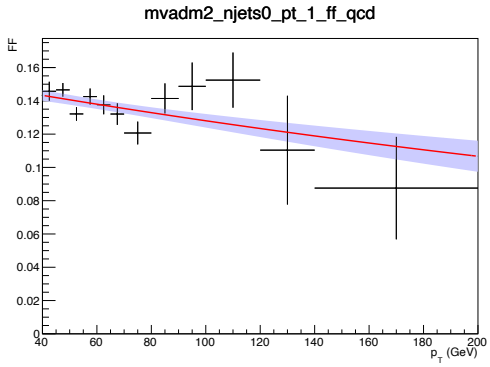

(b) MVA-DM = 2

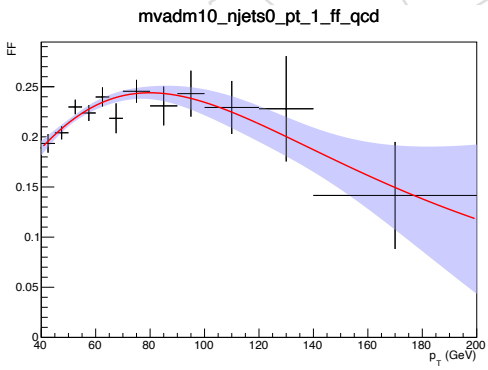

(c) MVA-DM = 10

Figure 44: Examples of the 2016 fake factor fits in the $\tau_h\tau_h$ channel illustrating the dependence on MVA-DM. The fitted fake factors measured for τ_h candidates with MVA-DM = 1, 2, and 10 are shown.

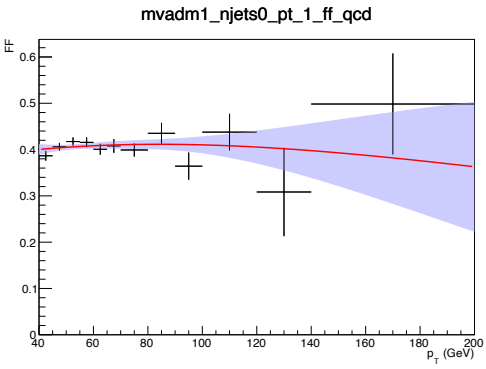

(a) $N_{\text{jets}} = 0$

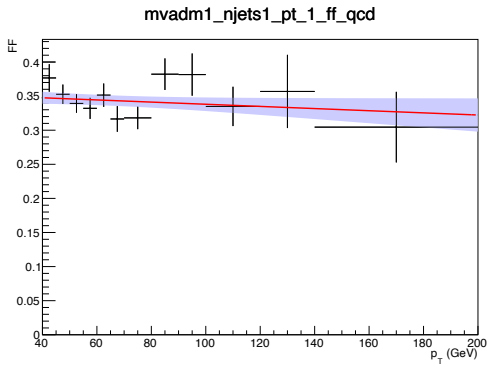

(b) $N_{\text{jets}} = 1$

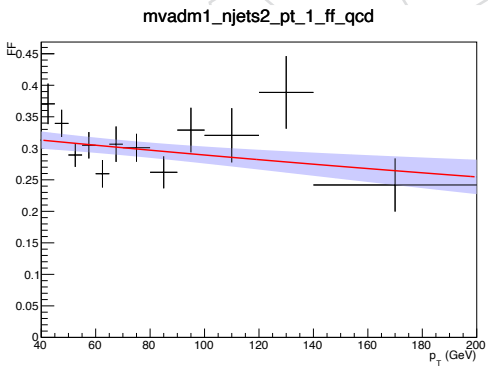

(c) $N_{\text{jets}} \geq 2$

Figure 45: Examples of the 2018 fake factor fits in the $\tau_{\text{h}}\tau_{\text{h}}$ channel illustrating the dependence on N_{jets}. The fitted fake factors measured events with $N_{\text{jets}} = 0$, $N_{\text{jets}} = 1$, and $N_{\text{jets}} \geq 2$ are shown.

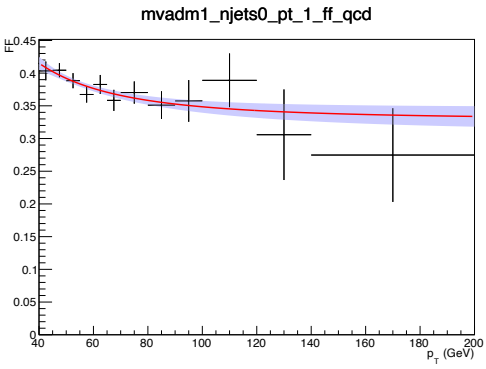

(a) $N_{\text{jets}} = 0$

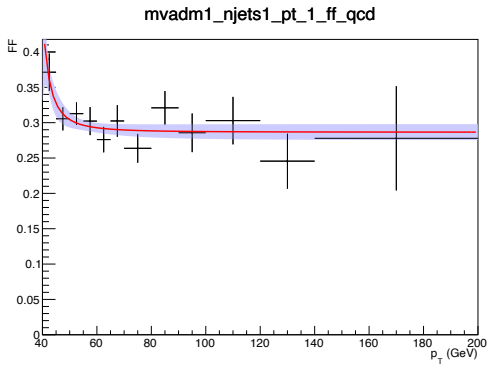

(b) $N_{\text{jets}} = 1$

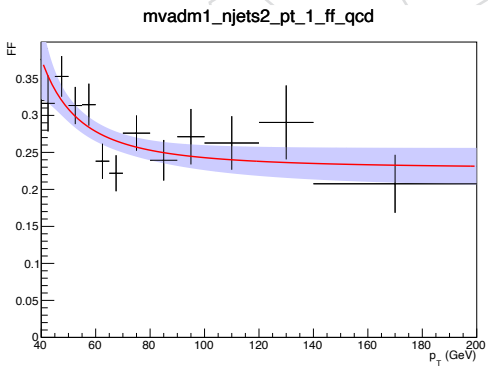

(c) $N_{\text{jets}} \geq 2$

Figure 46: Examples of the 2017 fake factor fits in the $\tau_{\text{h}}\tau_{\text{h}}$ channel illustrating the dependence on N_{jets}. The fitted fake factors measured events with $N_{\text{jets}} = 0$, $N_{\text{jets}} = 1$, and $N_{\text{jets}} \geq 2$ are shown.

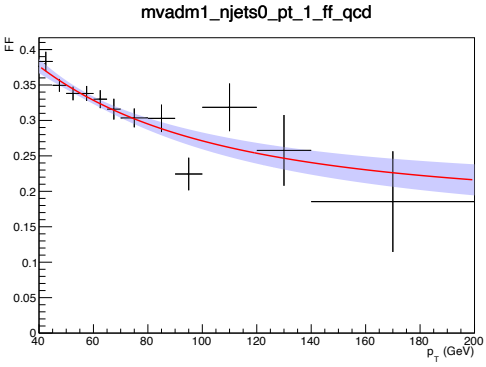

(a) $N_{\text{jets}} = 0$

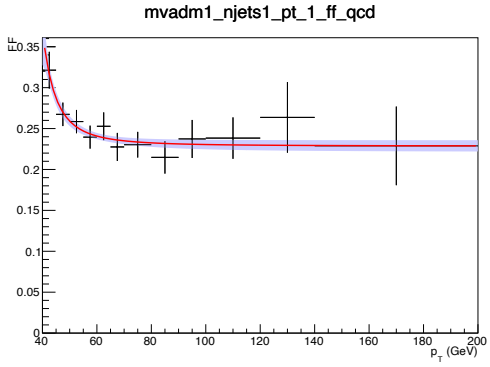

(b) $N_{\text{jets}} = 1$

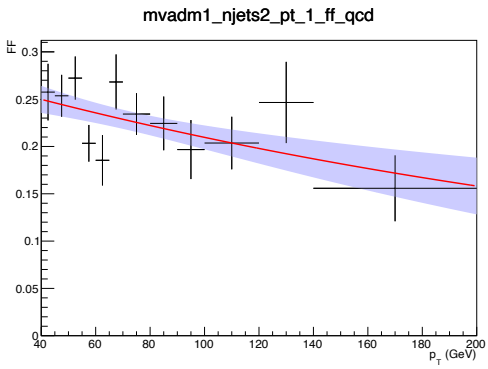

(c) $N_{\text{jets}} \geq 2$

Figure 47: Examples of the 2016 fake factor fits in the $\tau_h\tau_h$ channel illustrating the dependence on N_{jets}. The fitted fake factors measured events with $N_{\text{jets}} = 0$, $N_{\text{jets}} = 1$, and $N_{\text{jets}} \geq 2$ are shown.

DRAFT

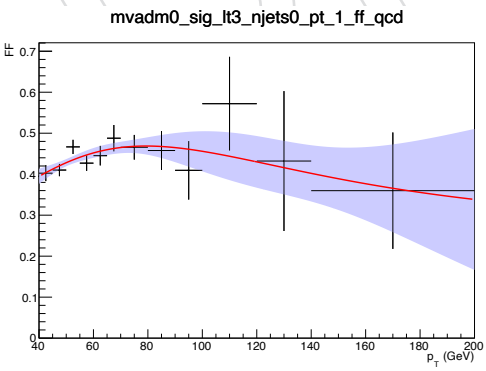

(a) $S_{\text{IP}} < 1.5$

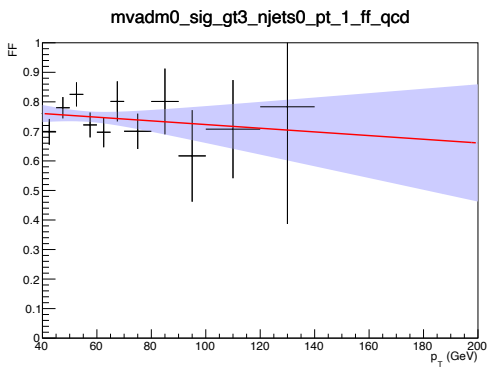

(b) $S_{\text{IP}} \geq 1.5$

Figure 48: Examples of the 2018 fake factor fits in the $\tau_h\tau_h$ channel illustrating the dependence on the S_{IP}. The left and right insets shows the fake factors measured for τ_h candidates with $S_{\text{IP}} < 1.5$ and $S_{\text{IP}} \geq 1.5$ respectively.

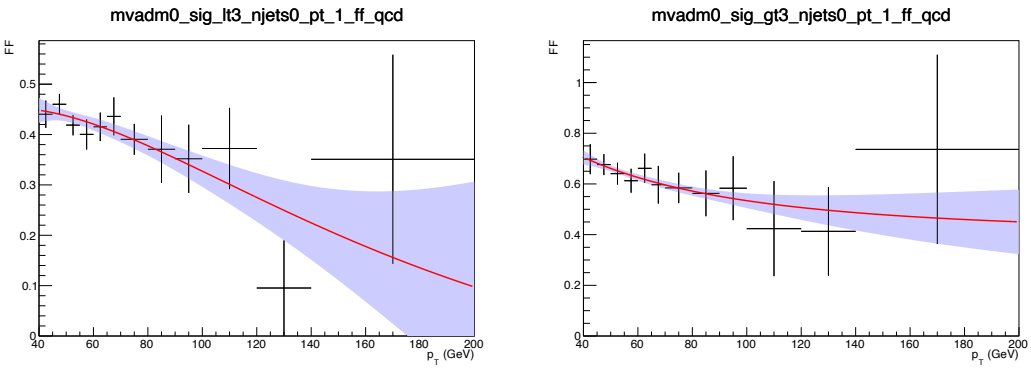

(a) $S_{\mathrm{IP}} < 1.5$ (b) $S_{\mathrm{IP}} \geq 1.5$

Figure 49: Examples of the 2017 fake factor fits in the $\tau_{\mathrm{h}}\tau_{\mathrm{h}}$ channel illustrating the dependence on the S_{IP}. The left and right insets shows the fake factors measured for τ_{h} candidates with $S_{\mathrm{IP}} < 1.5$ and $S_{\mathrm{IP}} \geq 1.5$ respectively.

DRAFT

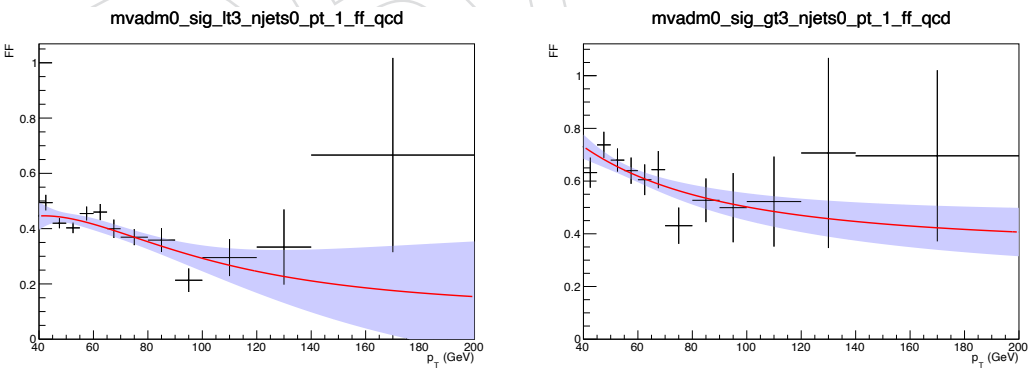

(a) $S_{\mathrm{IP}} < 1.5$ (b) $S_{\mathrm{IP}} \geq 1.5$

Figure 50: Examples of the 2016 fake factor fits in the $\tau_{\mathrm{h}}\tau_{\mathrm{h}}$ channel illustrating the dependence on the S_{IP}. The left and right insets shows the fake factors measured for τ_{h} candidates with $S_{\mathrm{IP}} < 1.5$ and $S_{\mathrm{IP}} \geq 1.5$ respectively.

Schematic for tau-tau channel regions

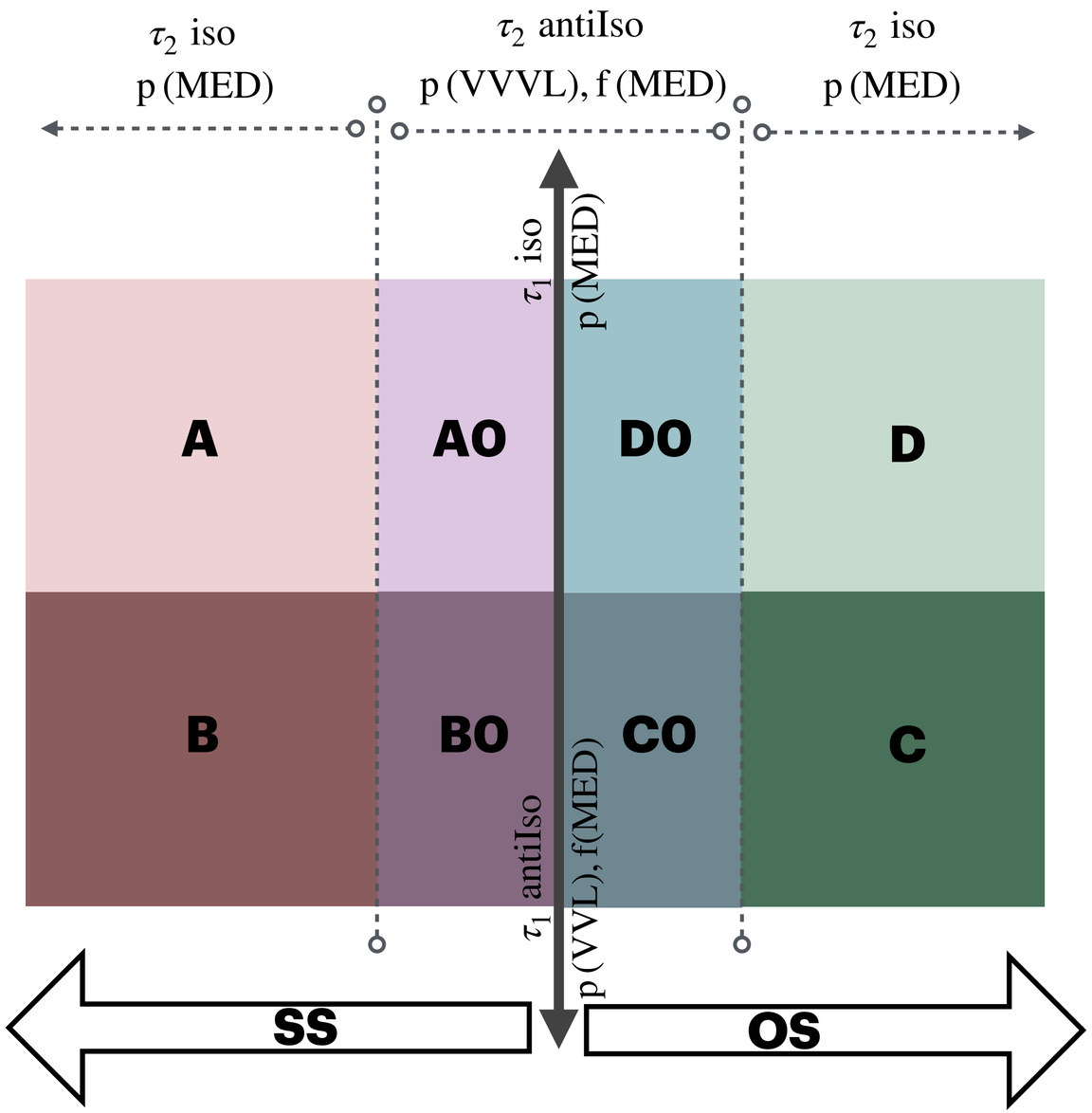

A & B	Derivation regions [+ for Closure]
AO & BO	Derivation regions
CO	Application region
DO	Extrapolation Correction region
C	Application region
D	Signal region

jet energy is poorly measured (for the jet that contain the τ_h candidate), which simultaneously gives rise to fake E_T^{miss} and changes the isolation of the τ_h candidate. A variable C_{QCD} is defined in order to parametrise the non-closure correction, which is defined as

$$C_{QCD} = \frac{E_T^{miss}}{p_T^{\tau_h}} \cos \Delta\phi(\vec{E_T^{miss}}, \vec{\tau_h}). \tag{40}$$

where $\Delta\phi(\vec{E_T^{miss}}, \vec{\tau_h})$ is the separation in the azimuthal angle between the τ_h and the E_T^{miss}. This variable basically represents the amount of fake E_T^{miss} aligned with the τ_h, relative to the τ_h p_T (making it analogous to a relative isolation -type variable). The correction is measured separately for the N_{jets} = 0, 1, $\geq$ 2 bins which are fitted using polynomials. The non-closure corrections derived for 2018 are shown in Figure 51.

An additional correction is applied to account for differences in the DR and AR/SR which, can arise if there are slightly different fake rates for OS and SS pairs. The origin of these differences are due to different jet flavour compositions in OS and SS events, as the fake rates are known to depend on the flavour of the initial parton producing the jet. Events with different jet flavour compositions can have different kinematics and therefore the OS/SS correction can vary differentially. The correction is derived by selecting a second region orthogonal to the SR by inverting the isolation requirement for the sub-leading τ_h candidate, which is required to pass the `VVVLoose` but fail the `VVLoose` working points. A set of FF_{QCD} and non-closure corrections are derived for SS events using exactly the same procedure described above. These FF_{QCD} are then applied to the anti-isolated OS events and compared to the isolated OS events to derived the correction. The correction is derived in bins of N_{jets} and is parametrised as a function of the ΔR between the two τ_h candidates and fitted using a first order polynomial. This choice is motivated as the jet flavour composition is found to vary most strongly as a function of these variables, and most significantly for $N_{jets} = 0$ events (for the higher jet multiplicity bins the corrections are close to unity). In principle other variables could be considered for this parametrisation, however we choose this parametrisation as it accounts for the largest differential dependencies, and is found to give good closure for all important variables.

Since the FF_i measured for QCD are applied also for the other processes in this channel no fractions are requires and $\overline{FF} = FF_{QCD}$. The AR in this channel is defined by requiring the lead τ_h candidate to pass the `VVVLoose` but fail the `Medium` DeepTau ID discriminant with all other selections kept identical to the SR definition. The jet $\rightarrow$ τ_h background in the SR is then estimated by applying the measured $\overline{FF}$ to the events in the AR. The contribution of processes producing genuine τ_h or $l \rightarrow \tau_h$ candidates is subtracted using simulated events. This procedure alone would lead to an underestimate of sub-dominant processes with only one jet $\rightarrow$ τ_h fake, where the sub-leading τ_h is faked by a jet (such as W+jet events). These events are therefore added back using MC.

The measured fake factors are applied to the DR events to check that the method closes. Comparisons of the data with the predictions for these checks are shown in Figures 54–55 for several important variables. Data/background comparisons for inclusive SR events will be shown in Section 9.

8.1.2 Fake factors in the $\tau_\mu \tau_h$ channels

In the $\tau_\mu \tau_h$ channel there are several processes that yield a significant contribution to the jet $\rightarrow$ τ_h background. This includes QCD, W+jets, and $t\bar{t}$. The former two are in generally the most significant and contribute with approximately equal weights. The $t\bar{t}$ is typically small but can become more significant in regions of parameter space with multiple jets. The W+jets DR is

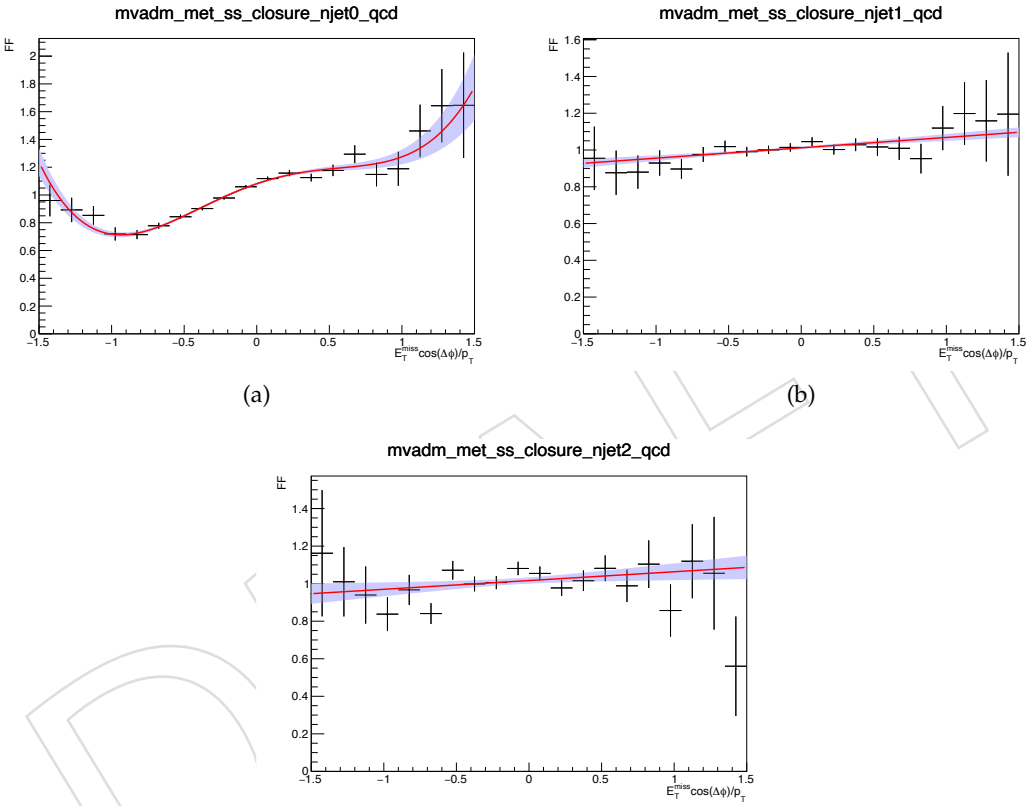

(a) (b) (c)

Figure 51: The non-closure corrections derived for the 2018 fake factors as a function of C_{QCD} for $\tau_h\tau_h$ events. The correction derived for events 0, 1, and ≥ 2 jets are shown in the upper left, upper right and lower insets respectively.

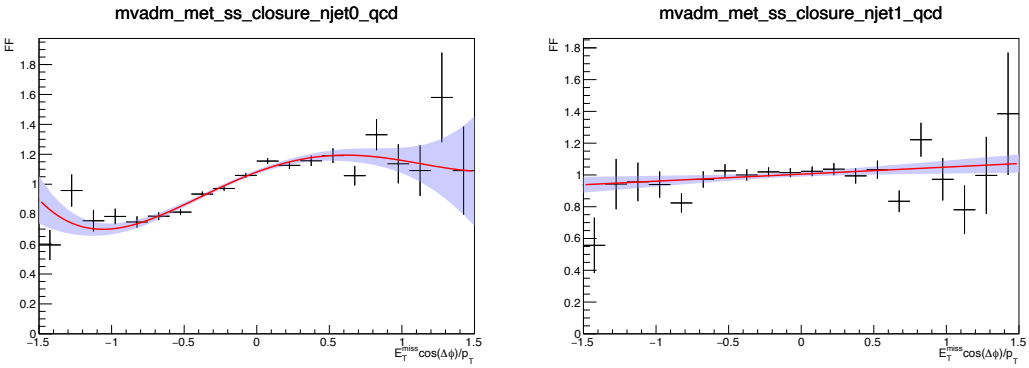

(a)

(b)

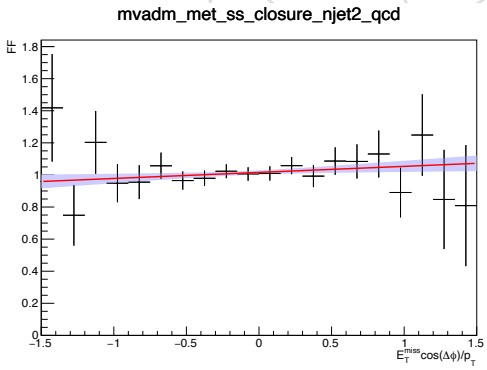

(c)

Figure 52: The non-closure corrections derived for the 2017 fake factors as a function of C_{QCD} for $\tau_h\tau_h$ events. The correction derived for events 0, 1, and ≥ 2 jets are shown in the upper left, upper right and lower insets respectively.

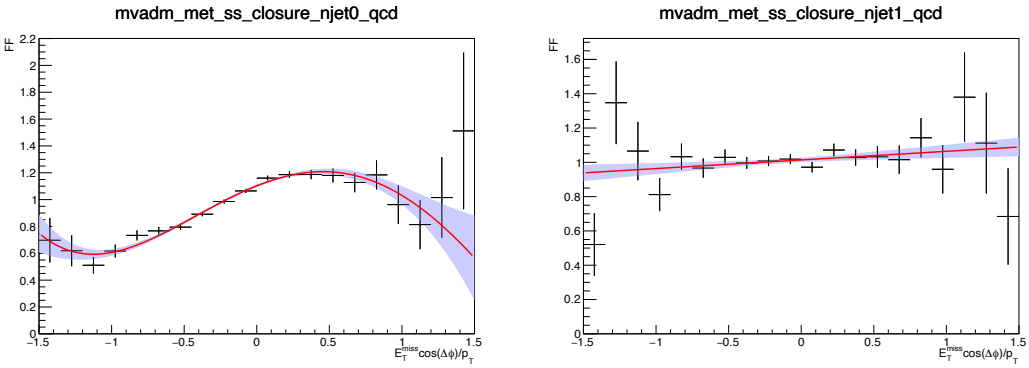

(a)

(b)

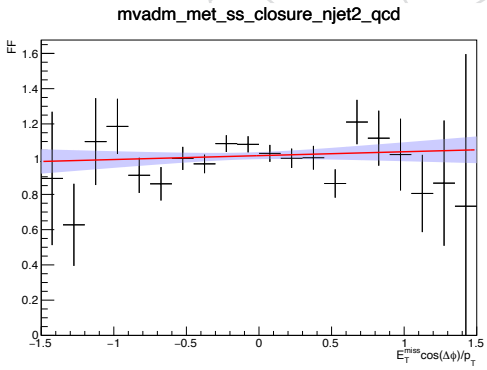

(c)

Figure 53: The non-closure corrections derived for the 2016 fake factors as a function of C_{QCD} for $\tau_h\tau_h$ events. The correction derived for events 0, 1, and ≥ 2 jets are shown in the upper left, upper right and lower insets respectively.

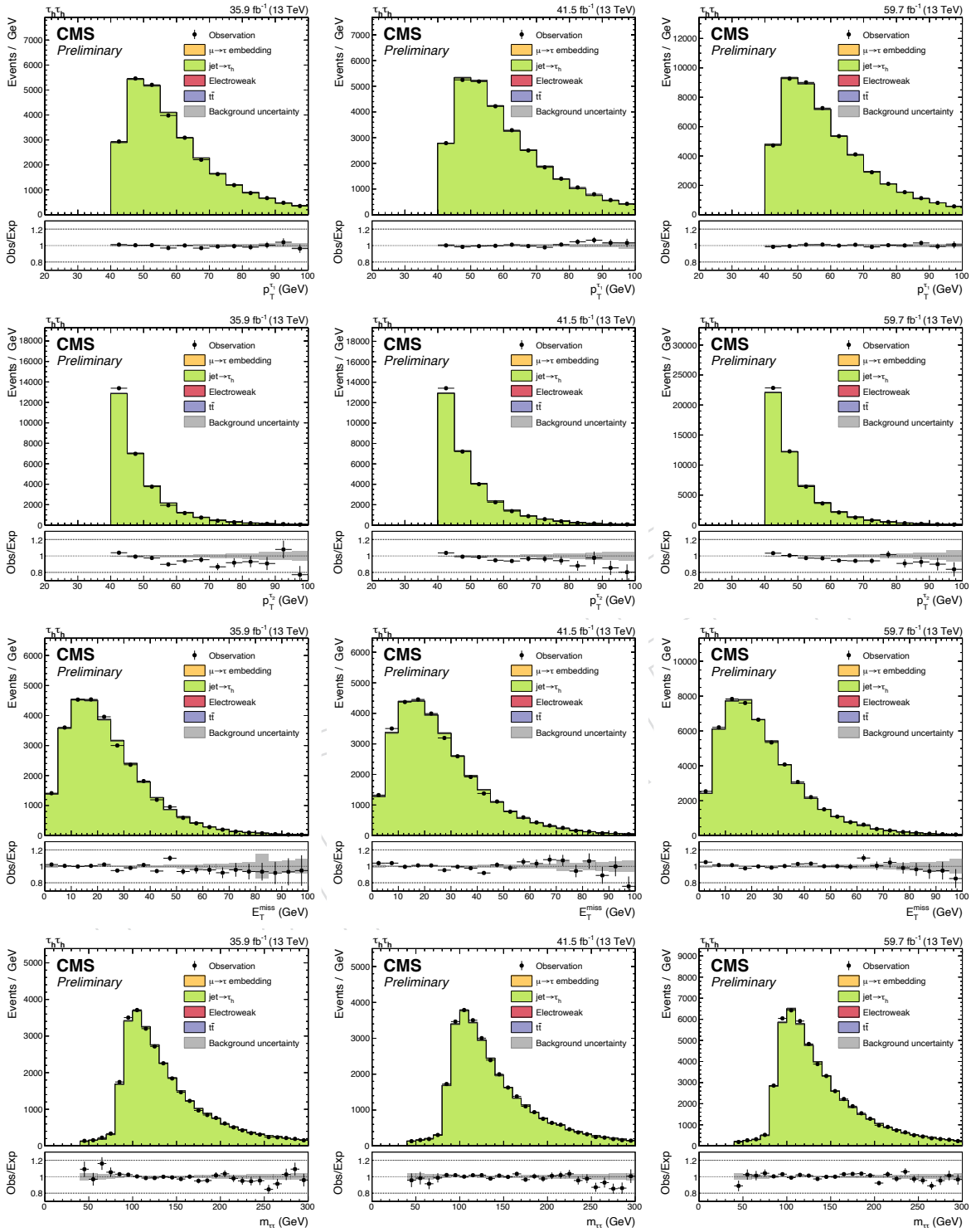

Figure 54: Closure comparisons of data with the FF prediction in the $\tau_h\tau_h$ channel when applying the measured fake factors for the DR events. The plots are shown for 2016, 2017, and 2018 in the left, center, and right columns. From top to bottom the comparisons are shown for the following variables: leading τ_h p_T, sub-leading τ_h p_T, E_T^{miss}, visible mass of the $\tau_h\tau_h$ pair.

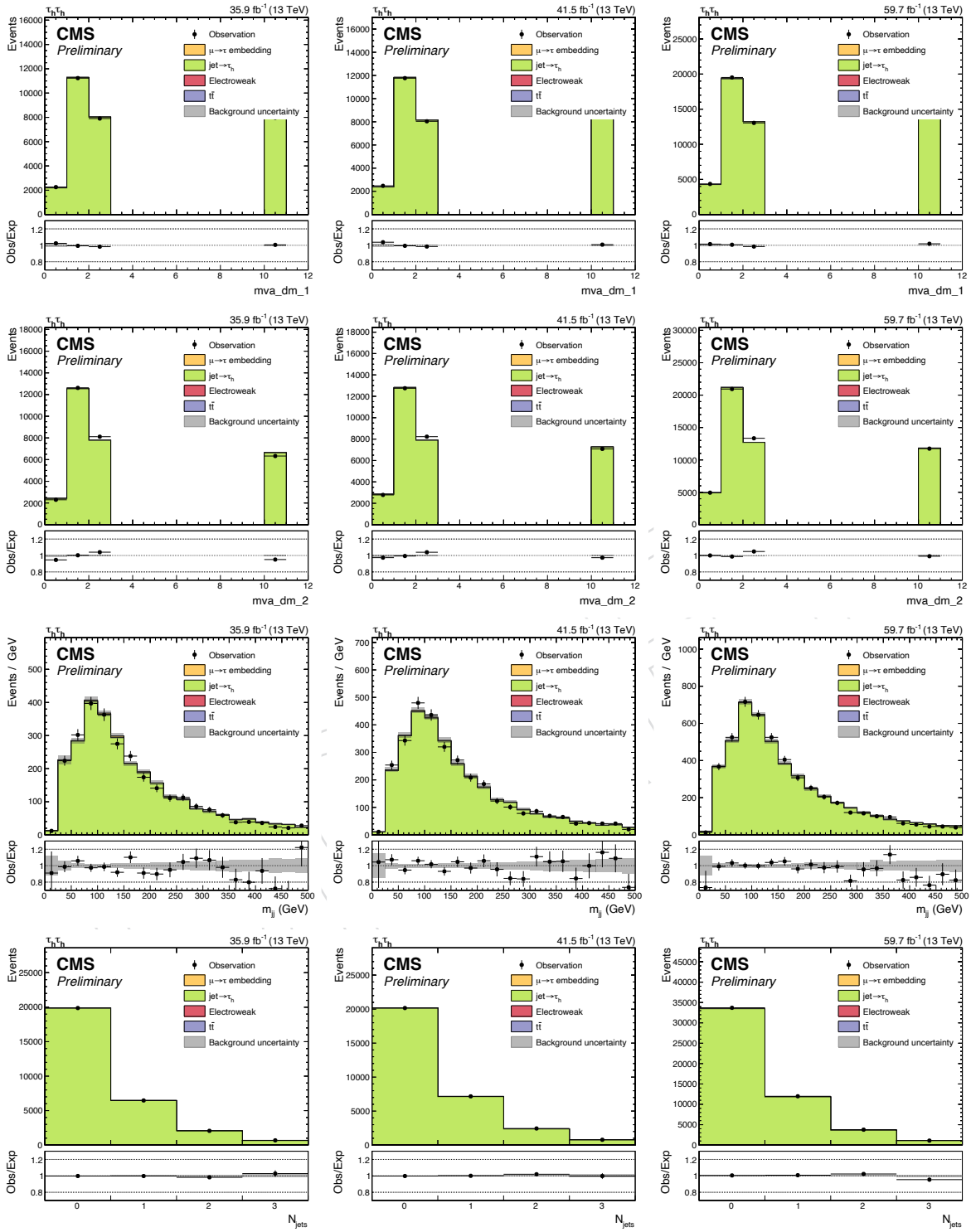

Figure 55: Closure comparisons of data with the FF prediction in the $\tau_h\tau_h$ channel when applying the measured fake factors for the DR events. The plots are shown for 2016, 2017, and 2018 in the left, center, and right columns. From top to bottom the comparisons are shown for the following variables: leading τ_h MVA-DM, sub-leading τ_h MVA-DM, m_{jj}, and N_{jets}.

defined by applying a cut of $m_{\mathrm{T}} > 70$ GeV, with all other selections kept the same as the SR. The contribution of other processes to the DR (except QCD) is subtracted using MC. The QCD DR is defined by requiring the τ_μ and τ_{h} pair to have SS charges. An additional $I^{\mathrm{l}}_{rel} > 0.05$ requirement is used to reduce processes producing genuine leptons. The contribution of other processes to the DR is again subtracted using MC. It is not possible to define a DR that is sufficiently pure in $\mathrm{t\bar{t}}$ events to make a reasonable measurement of $\mathrm{FF_{t\bar{t}}}$. The $\mathrm{FF_{t\bar{t}}}$ are therefore derived from MC. A comparison of the $\mathrm{FF_W}$ measured in data and MC shows only an $\sim$ 10–20% differences in the fake rates in data and MC. This observation coupled with the fact that the $\mathrm{t\bar{t}}$ contribution is small compared to the other processes means that any bias introduced by using $\mathrm{FF_{t\bar{t}}}$ measured in MC is negligible compared to the uncertainties on the fake factors.

In the case of QCD and W+jets the $\mathrm{FF_i}$ are measured for three N_{jets} bins (0, 1, $\geq$ 2) and 5 MVA-DM bins (0, 1, 2, 10, 11). The MVA-DM = 0 bins are further split into two bins depending on the τ_{h} impact parameter significance ($S_{\mathrm{IP}} < 1.5$, $S_{\mathrm{IP}} \geq 1.5$). The $\mathrm{FF_i}$ are also measured separately for events passing the single muon and muon+tau cross triggers, where the latter is defined as all events that fail the muon lepton trigger. This is necessary as the ID and isolation selections used in the trigger result in different $\mathrm{FF_i}$ values. The $\mathrm{FF_{t\bar{t}}}$ are measured only in bins of MVA-DM and S_{IP}. Further binning is not necessary in this case as the $\mathrm{t\bar{t}}$ fractions are small and such events are usually accompanied by several jets. For the bins passing the single lepton triggers the dependence on the τ_{h} p_{T} is fitted using the superposition of a Landau and a zeroth order polynomial. In some cases where the statistical population of a bin is insufficient the Landau+pol0 fit can fail to converge properly or give unrealisable trends that are overly influenced by statistical fluctuations. In such cases the p_{T} dependence is instead fitted using either a zeroth or first order polynomial depending on the available statistics. The bins that pass the muon+tau cross triggers are less populated compared to the single muon bins and therefore first order polynomials are used as the fitting functions. In this case bins suffering from low statistics are alternatively fitted using zeroth order polynomials. Examples of the resulting fits are shown in Figures 56–58, which are chosen to illustrate the dependence of the fake factors on the considered process.

After applying the $\mathrm{FF_{QCD}}$ ($\mathrm{FF_W}$) fake factors to the events in the corresponding DR non-closures are observed in the $E_{\mathrm{T}}^{\mathrm{miss}}$ variables and $p_{\mathrm{T}}^{\tau_\mu}$ distributions affecting mainly the events with $N_{\mathrm{jets}} = 0$. As for the $\tau_{\mathrm{h}}\tau_{\mathrm{h}}$ channel the non-closure in the $E_{\mathrm{T}}^{\mathrm{miss}}$ variables for the QCD fake factors are again corrected as a function of C_{QCD}. The situation for the W+jets (and $\mathrm{t\bar{t}}$) corrections is slightly different due to the presence of genuine missing energy from neutrinos. In this case the correction variable is suitable modified to approximately subtract the genuine $E_{\mathrm{T}}^{\mathrm{miss}}$ from the total. This approximation assumes the neutrino is back-to-back and balanced with the muon (which is exactly true for W bosons produce at rest in the transverse direction), the transverse components of the 3-vector of the muon are then added to $\vec{E_{\mathrm{T}}^{\mathrm{miss}}}$ defining the resulting vector $\vec{E_{\mathrm{T}}^{\mathrm{miss}\prime}} + \mu$. The variable used to parametrise the W+jets correction, C_{W}, is then defined in the same way as C_{QCD} except using $\vec{E_{\mathrm{T}}^{\mathrm{miss}\prime}} + \mu$ instead of $\vec{E_{\mathrm{T}}^{\mathrm{miss}}}$:

$$C_{\mathrm{W}} = \frac{E_{\mathrm{T}}^{\mathrm{miss}+\mu}}{p_{\mathrm{T}}^{\tau_{\mathrm{h}}}} \cos\Delta\phi(\vec{E_{\mathrm{T}}^{\mathrm{miss}+\mu}}, \vec{\tau_{\mathrm{h}}}). \tag{41}$$

For the QCD and W+jets these corrections are derived separately for each N_{jets} bin, for $\mathrm{t\bar{t}}$ the correction is derived inclusively in N_{jets}. Example of the corrections derived for QCD, W+jets, and $\mathrm{t\bar{t}}$ are shown in Figures 59–61. The QCD corrections are fitted using a first order polynomial and the W+jet and $\mathrm{t\bar{t}}$ are fitted using error functions. After applying this derived correction to the fake factors the muon p_{T} distribution is also corrected for the W+jets and QCD fake factors.

DRAFT

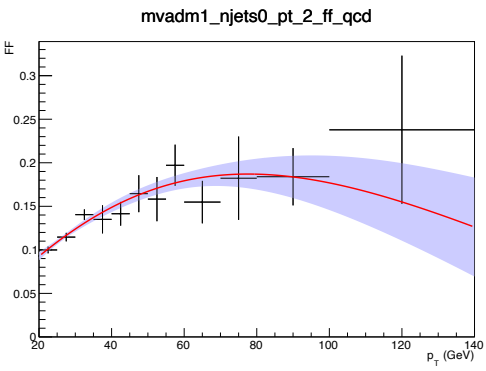

(a) QCD

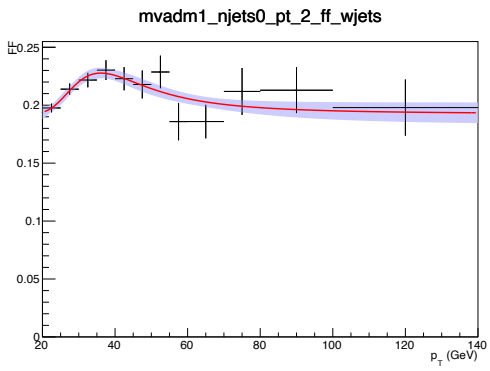

(b) W+jets

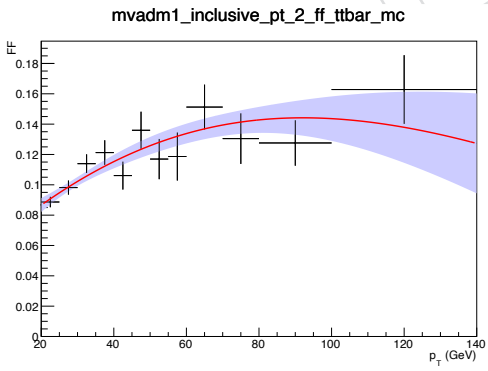

(c) $t\bar{t}$

Figure 56: Examples of the 2018 fake factor fits in the $\tau_\mu \tau_h$ channel illustrating the dependence the considered process. The fitted fake factors measured for τ_h candidates with MVA-DM = 1 are shown for QCD, W+jets and $t\bar{t}$ events. The QCD and W+jets measurements were performed for events with no jets in the final state, whereas for $t\bar{t}$ the fake-factors are measured inclusively in N_{jets}.

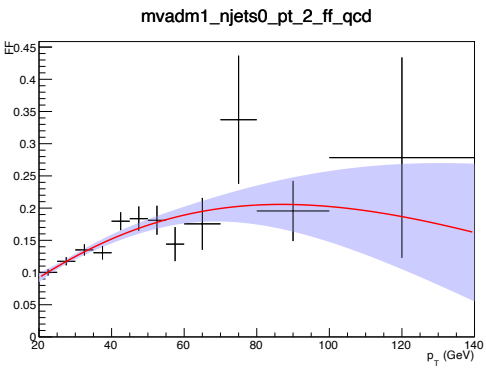

(a) QCD

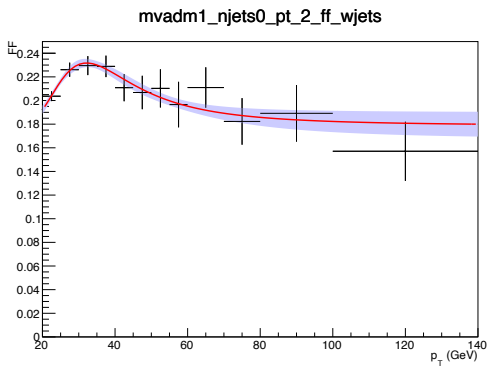

(b) W+jets

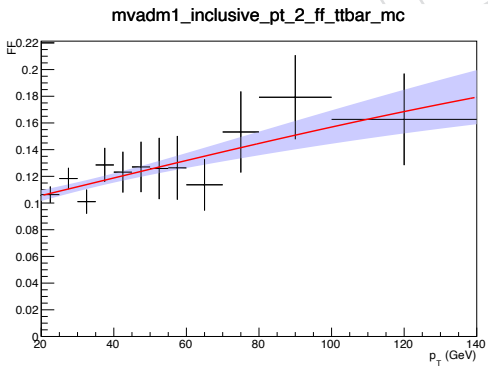

(c) $t\bar{t}$

Figure 57: Examples of the 2017 fake factor fits in the $\tau_\mu \tau_h$ channel illustrating the dependence the considered process. The fitted fake factors measured for τ_h candidates with MVA-DM = 1 are shown for QCD, W+jets and $t\bar{t}$ events. The QCD and W+jets measurements were performed for events with no jets in the final state, whereas for $t\bar{t}$ the fake-factors are measured inclusively in N_{jets}.

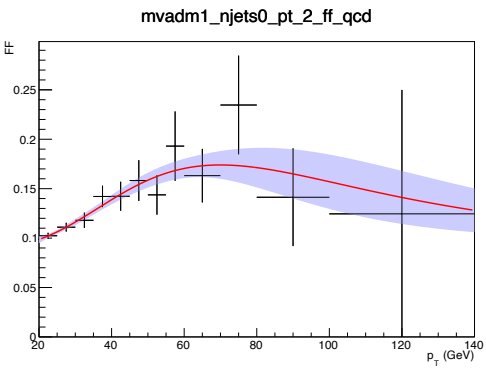

(a) QCD

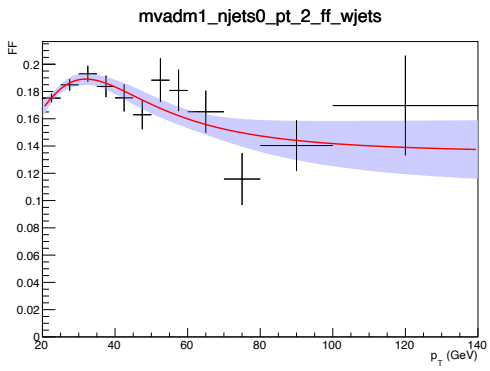

(b) W+jets

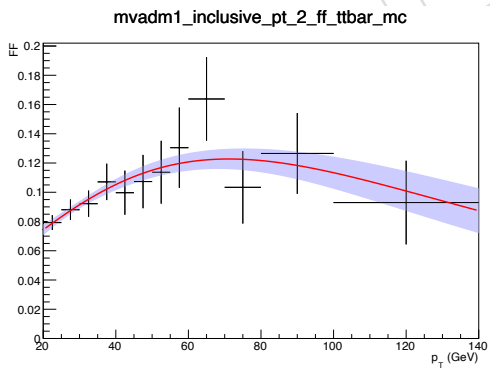

(c) $t\bar{t}$

Figure 58: Examples of the 2016 fake factor fits in the $\tau_\mu \tau_h$ channel illustrating the dependence the considered process. The fitted fake factors measured for τ_h candidates with MVA-DM = 1 are shown for QCD, W+jets and $t\bar{t}$ events. The QCD and W+jets measurements were performed for events with no jets in the final state, whereas for $t\bar{t}$ the fake-factors are measured inclusively in N_{jets}.

No significance disagreement is observed for $t\bar{t}$ and therefore this correction is not needed. Examples of the the p_T correction for QCD and W+jets events are shown in Figures 62–64. As verified using W+jets MC, the p_T non-closure is a result of variation in the different flavour compositions of the jets as a function of the muon p_T.

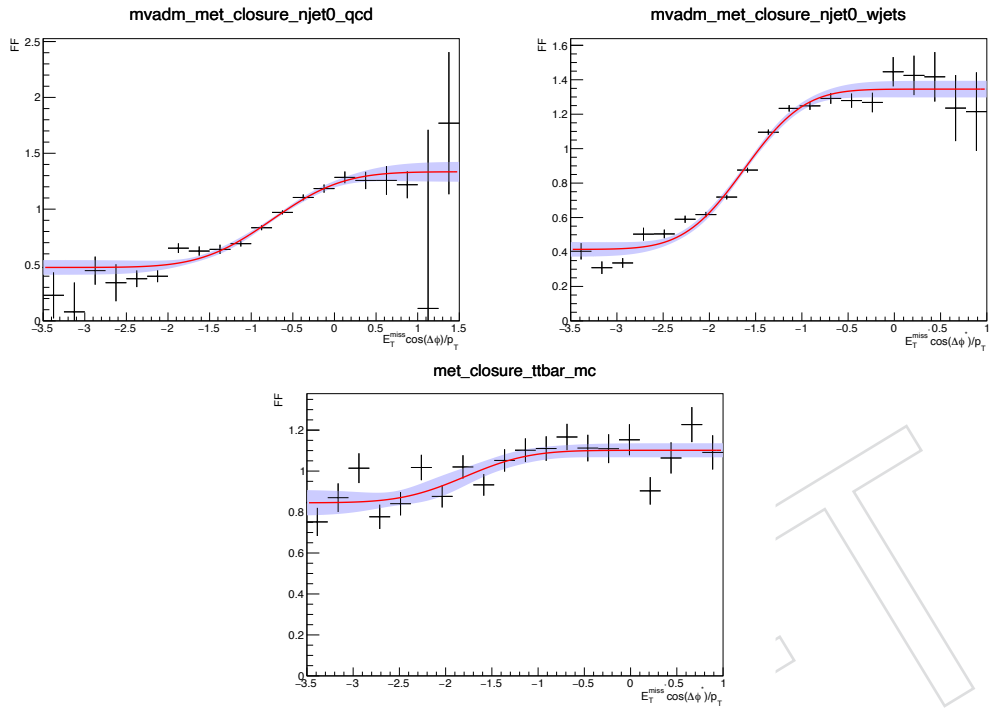

Figure 59: The 2018 E_T^{miss} non-closure corrections for the QCD (upper left), W+jets (upper right), and $t\bar{t}$ (lower).

Additional corrections are applied to account for differences in the determination regions and signal regions. For the QCD fake factors such differences can arise if there are slight differences in the fake rates for events where the lepton is anti-isolated or for events with SS $\tau_l\tau_h$ pairs. The correction for the lepton isolation is derived by applying the measured fake factors including non-closure corrections to SS events. The differences between the data and the prediction as a function of I^l_{rel} is then taken as the correction. This is fitted using a third order polynomial. The corrections are shown in the left insets of Figure 65–67. To corrected for differences in the fake factors in OS vs SS events fake factors are measured as described above for events with $0.25 < I^l_{rel} < 0.5$. These fake factors are also corrected to account for non-closures in the E_T^{miss} and p_T^l distributions as describe previously. These fake factors are then applied to OS events in the AR defined with the same I^l_{rel} requirement as the DR. This prediction is then compared to the data and the difference is taken as the OS/SS correction which is fitted using a third order polynomial. The corrections are shown in the right insets of Figure 65–67.

For the W+jets fake factors a correction is derived to account for differences in the measured fake factors in the high m_T DR and the low m_T SR. This correction is derived from MC. Fake factors are measured for simulated W+jets events and corrected using exactly the same procedures outlined above. These fake factors are then applied to the simulated events in the AR and the difference between the resulting prediction and the simulation in the SR is taken as the correction. Such non closures are a result of variation in the jet flavour compositions in the high and low m_T regions. The correction is measured separately for each N_{jet} bin and parametrised as a function of the W boson p_T (reconstructed from the E_T^{miss} and muon system). The corrections derived for the $N_{jet} = 0$ and $N_{jet} = 1$ bins are shown in Figures 68–70. This choice is found

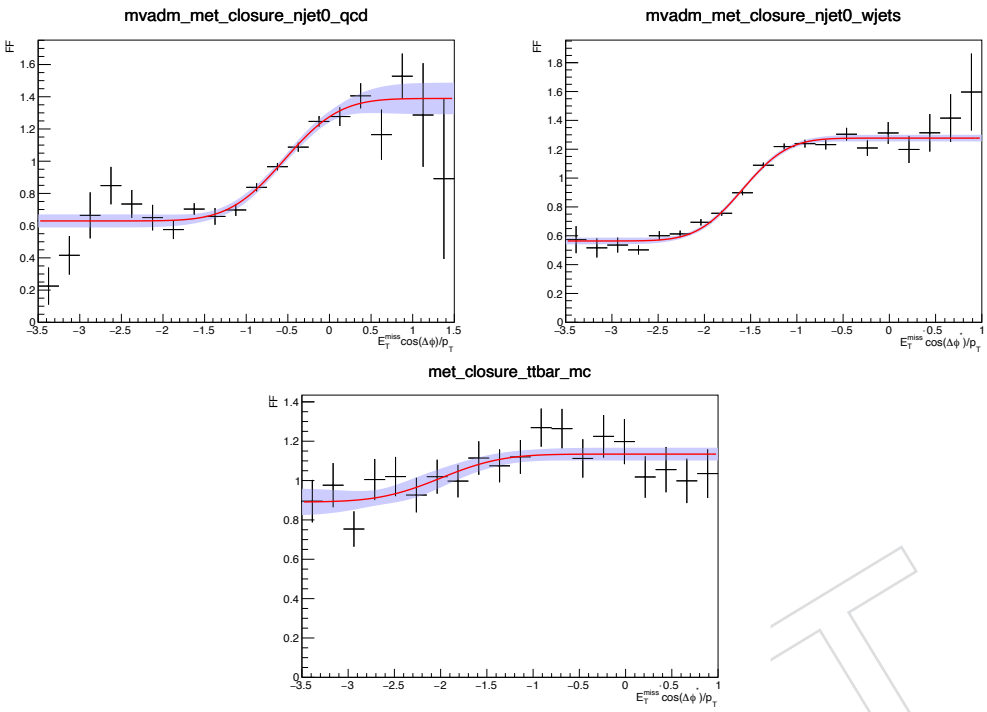

Figure 60: The 2017 E_T^{miss} non-closure corrections for the QCD (upper left), W+jets (upper right), and $t\bar{t}$ (lower).

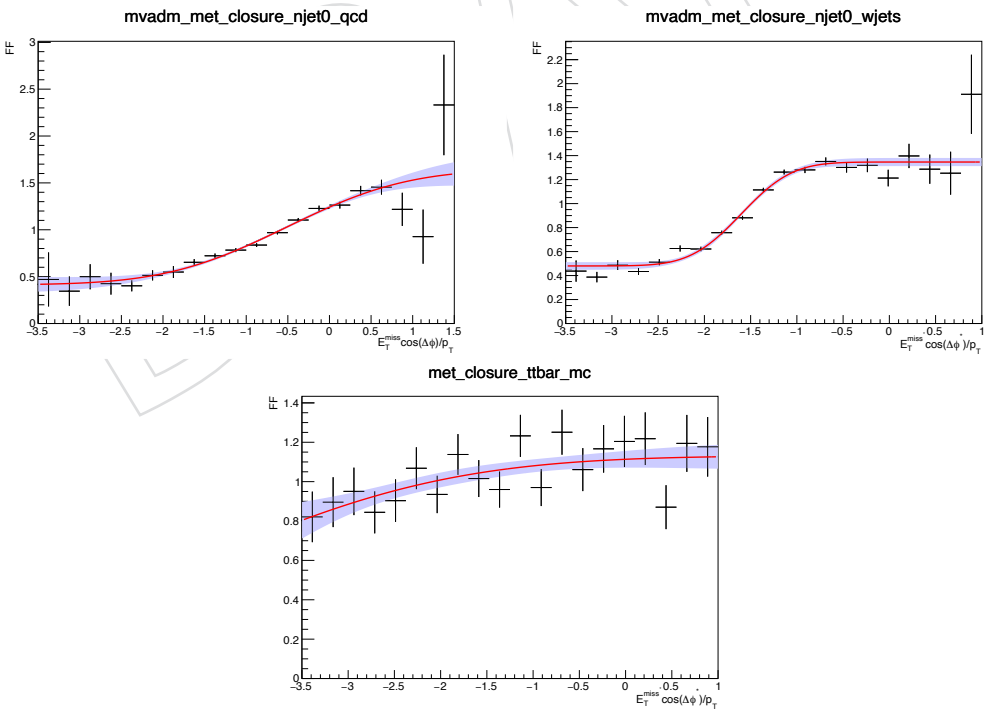

Figure 61: The 2016 E_T^{miss} non-closure corrections for the QCD (upper left), W+jets (upper right), and $t\bar{t}$ (lower).

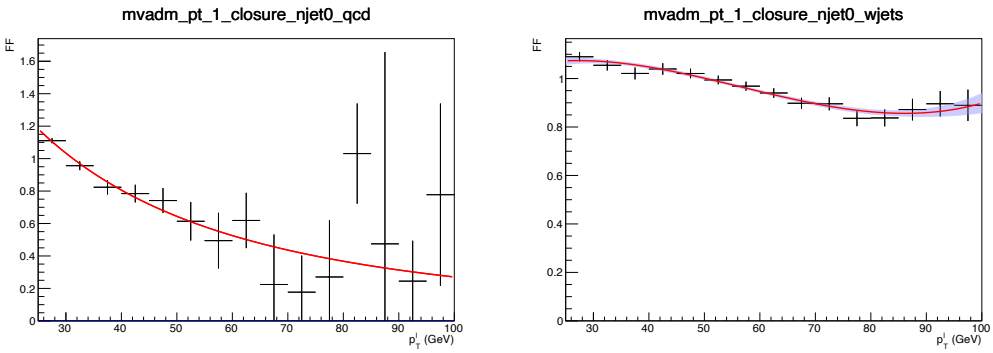

Figure 62: The 2018 muon p_T non-closure corrections for the QCD (left) and W+jets (right).

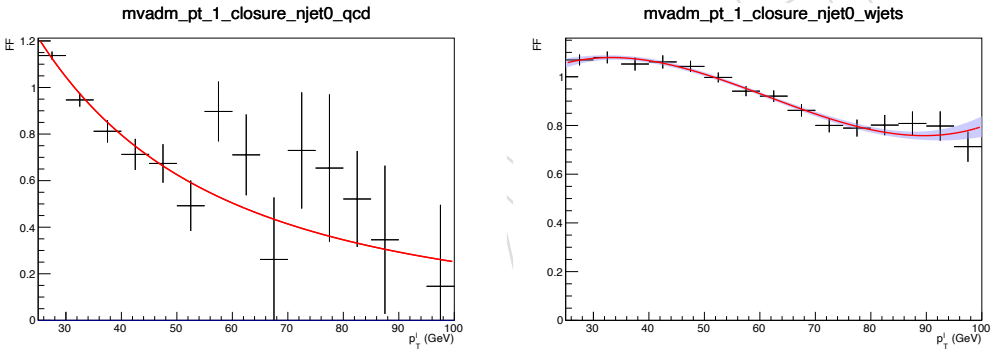

Figure 63: The 2017 muon p_T non-closure corrections for the QCD (left) and W+jets (right).

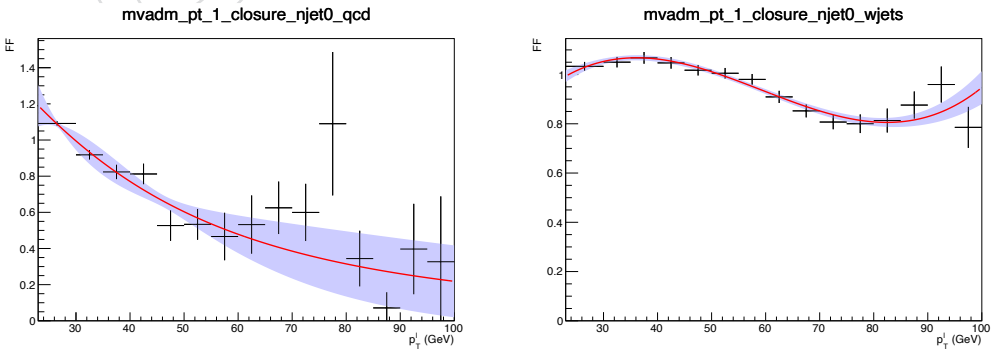

Figure 64: The 2018 muon p_T non-closure corrections for the QCD (left) and W+jets (right).

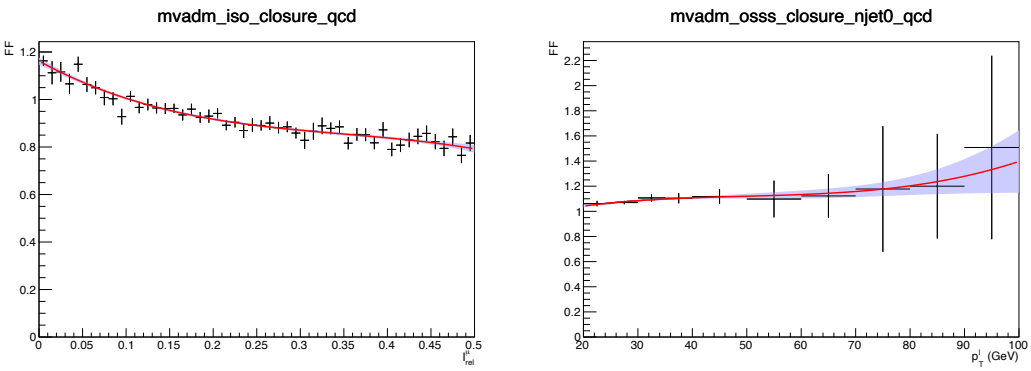

(a) (b)

Figure 65: The corrections derived for the 2018 fake factors to account for differences in the QCD fake factors due to the inverted cut on I^{l}_{rel} (left) and due OS vs SS selections (right).

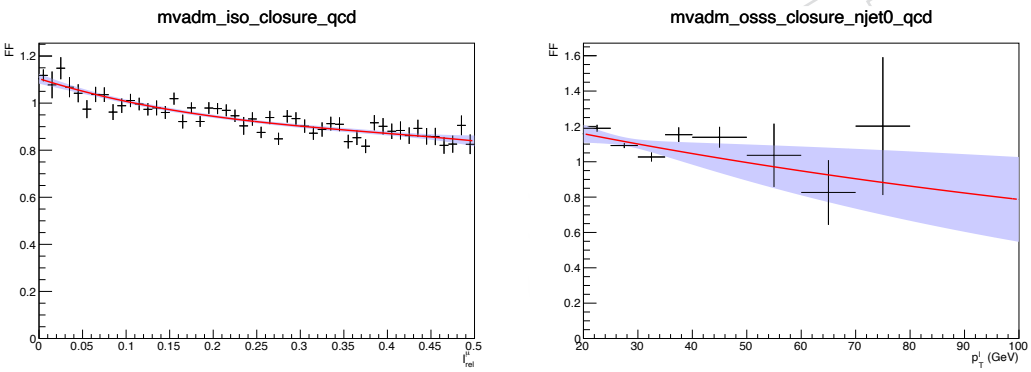

(a) (b)

Figure 66: The corrections derived for the 2017 fake factors to account for differences in the QCD fake factors due to the inverted cut on I^{l}_{rel} (left) and due OS vs SS selections (right).

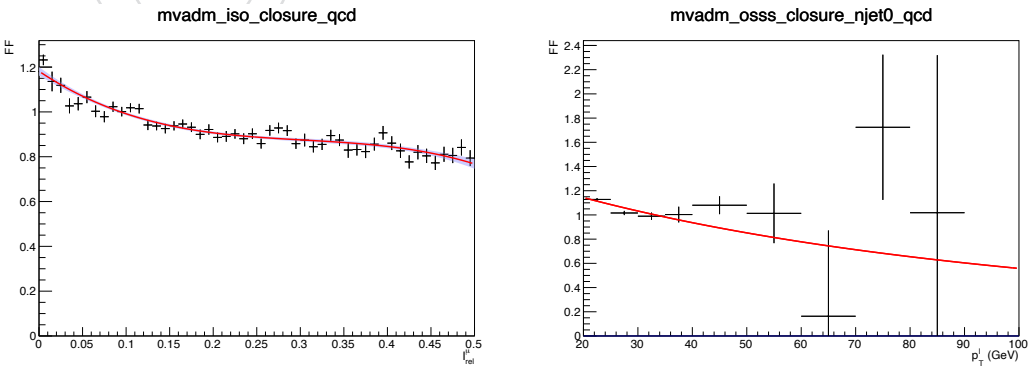

(a) (b)

Figure 67: The corrections derived for the 2016 fake factors to account for differences in the QCD fake factors due to the inverted cut on I^{l}_{rel} (left) and due OS vs SS selections (right).

to give good closure for all important variables.

For the $t\bar{t}$ since the fake factors are derived from MC a correction is derived by comparing the W+jets fake factors in data and simulation. The differences between the two as a function of MVA-DM, and $p_{\mathrm{T}}^{\tau_{\mathrm{h}}}$ are used as the correction. The size of the corrections are shown in Figure 71. In the p_{T} regions most relevant to the analysis the size of the corrections are O(10%). The choice of W+jets events to measure this correction is driven by the need to select a region pure in fake τ_{h} candidates with sufficient statistics to make a meaningful measurement. It was considered to use control regions pure in $t\bar{t}$ events to measure these corrections which can be defined, for example, by requiring the presence of b-jets, but such regions are plagued by large fractions of events with genuine τ_{h} candidates which must be subtracted using MC. In such cases it is not clear if the derived correction is meaningful and not driven by data/MC differences in the subtracted component. Given the small fraction of $t\bar{t}$ events to to overall jet$\rightarrow \tau_{\mathrm{h}}$ yield any bias introduced by the procedure used to measure and correct the $t\bar{t}$ fake factors is expected to be negligible compared to the other fake factor uncertainties on the QCD and W+jets processes. Nevertheless, as an extra precaution a conservative uncertainty defined by applying $\pm$ 100% of the corrections is included to cover any differences in the corrections derived using W+jets and $t\bar{t}$.

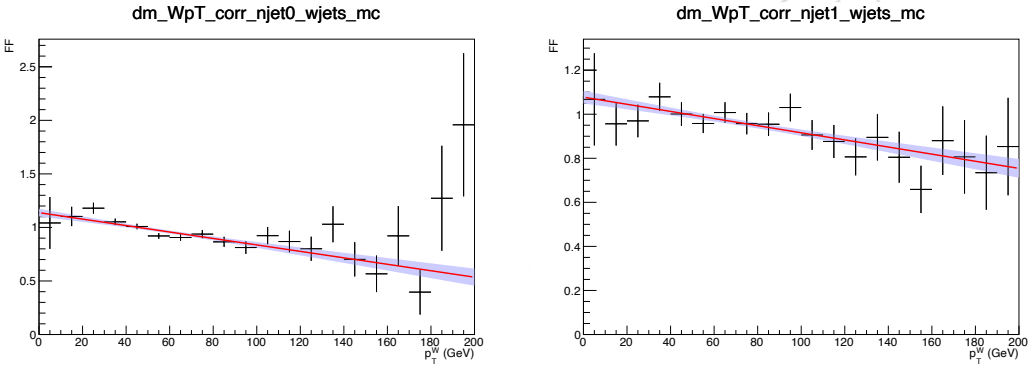

(a) $\tau_\mu\tau_{\mathrm{h}}$ (b) $\tau_e\tau_{\mathrm{h}}$

Figure 68: The corrections derived for the 2018 fake factors to account for differences in the W+jets fake factors due the inverted m_{T} selection used to define the DR. The corrections are parametrised as a function of the W boson p_{T} and are shown for events with zero jets (left) and one jet (right).

The $\mathrm{FF_i}$'s measured for the three processes and then combined into an overall $\overline{\mathrm{FF}}$ using the fractions which encode the probability of an AR event originating from each process. It is beneficial to parametrises the fractions using variables that have good differentiation between the different processes. However, there are several variables that give comparable separation between the processes, and some of these may be more or less important in different regions of the phase space making the optimal choice of parametrisation unclear. A multiclass BDT is therefore trained to improve the separation between the three main processes. The BDT has three classes for QCD, W+jets and $t\bar{t}$. The following variables are included in the BDT: $p_{\mathrm{T}}^{\tau_{\mathrm{h}}}$, p_{T}^{μ}, $E_{\mathrm{T}}^{\mathrm{miss}}$, N_{jets}, m_{jj}, m_T, $p_{\mathrm{T}}^{\tau\tau}$, m_{vis}, and the tau MVA-DM. The output of the BDT is three scores for each process which sum to unity analogous to probabilities. Therefore fractions binned in any two of these scores is sufficient to optimally parametrises the fractions over the whole phase space. We choose to bin the fraction in the QCD and W+jets BDT scores - but the choice is arbitrary. The fractions are estimated as follows:

1. Events are selected in data and simulation where the τ_{h} candidate passes the `VVVLoose`

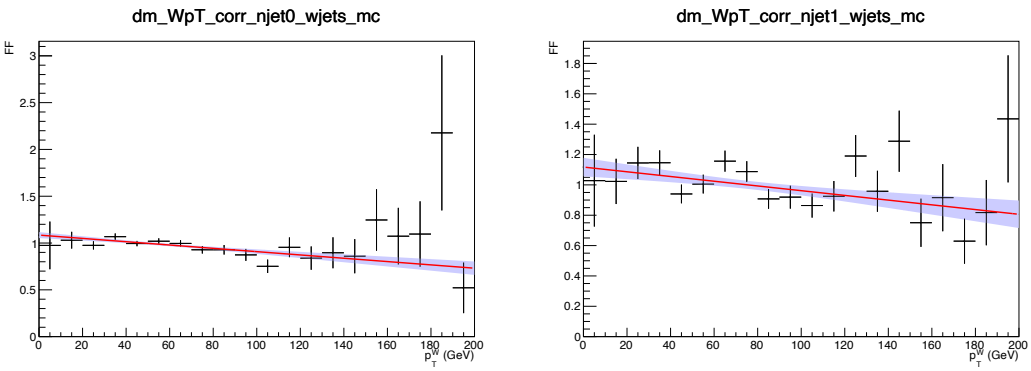

(a) $\tau_\mu \tau_h$ (b) $\tau_e \tau_h$

Figure 69: The corrections derived for the 2017 fake factors to account for differences in the W+jets fake factors due the inverted m_T selection used to define the DR. The corrections are parametrised as a function of the W boson p_T and are shown for events with zero jets (left) and one jet (right).

DRAFT

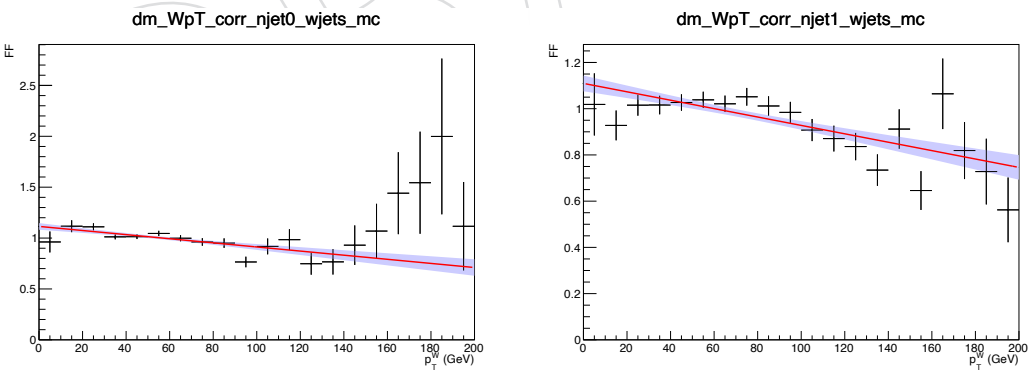

(a) $\tau_\mu \tau_h$ (b) $\tau_e \tau_h$

Figure 70: The corrections derived for the 2016 fake factors to account for differences in the W+jets fake factors due the inverted m_T selection used to define the DR. The corrections are parametrised as a function of the W boson p_T and are shown for events with zero jets (left) and one jet (right).

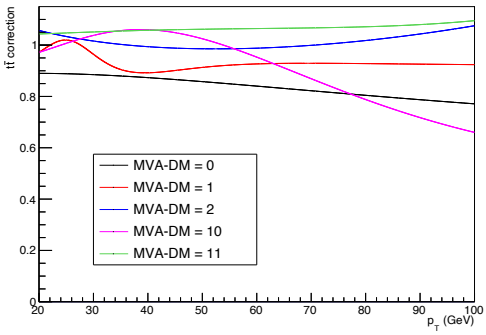

(a) 2016

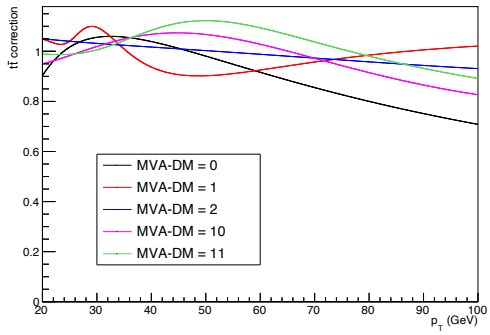

(b) 2017

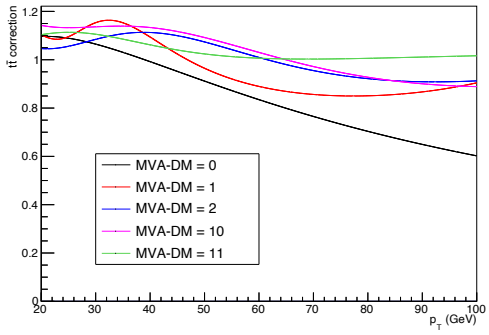

(c) 2018

Figure 71: The corrections applied to the $t\bar{t}$ fake factors to account for differences in fake rates in data and MC.

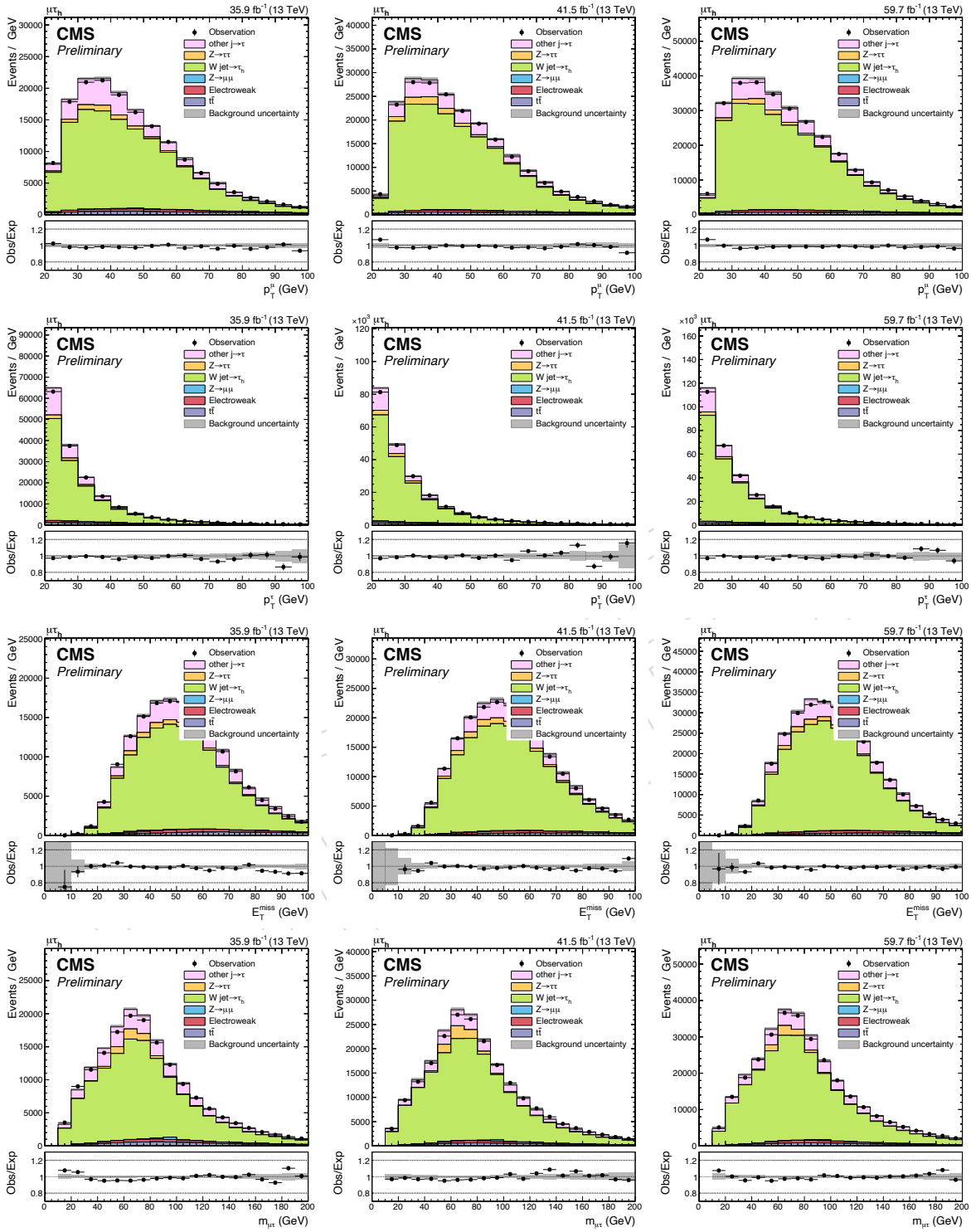

Figure 72: Closure comparisons of data with the FF prediction in the $\tau_\mu \tau_\mathrm{h}$ channel when applying the measured W+jets fake factors for the W+jets DR events. The plots are shown for 2016, 2017, and 2018 in the left, center, and right columns. From top to bottom the comparisons are shown for the following variables: τ_μ p_T, τ_h p_T, $E_\mathrm{T}^\mathrm{miss}$, visible mass of the $\tau_\mu \tau_\mathrm{h}$ pair.

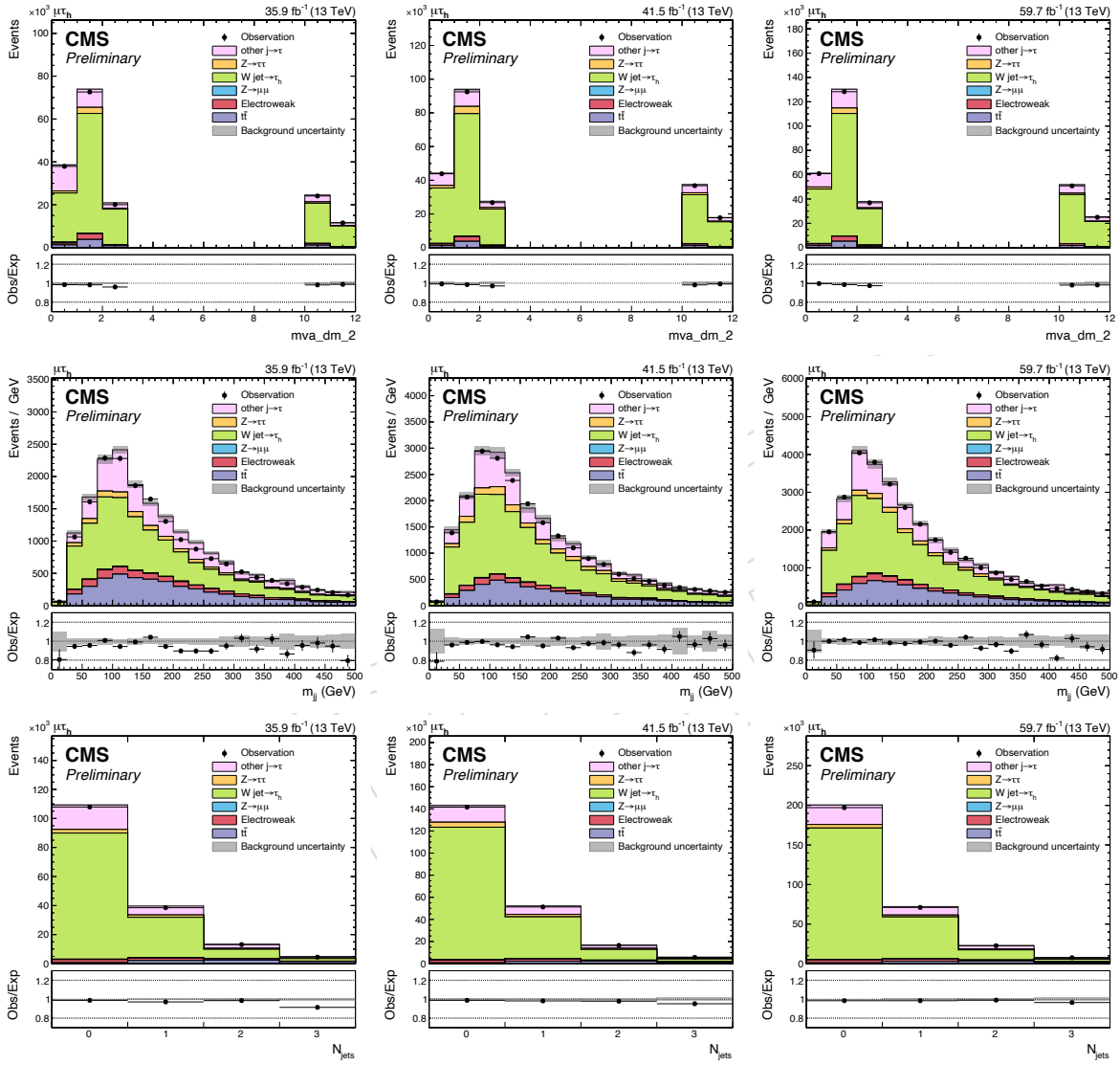

Figure 73: Closure comparisons of data with the FF prediction in the $\tau_\mu \tau_\mathrm{h}$ channel when applying the measured W+jets fake factors for the W+jets DR events. The plots are shown for 2016, 2017, and 2018 in the left, center, and right columns. From top to bottom the comparisons are shown for the following variables: τ_h MVA-DM, m_{jj}, and N_jets.

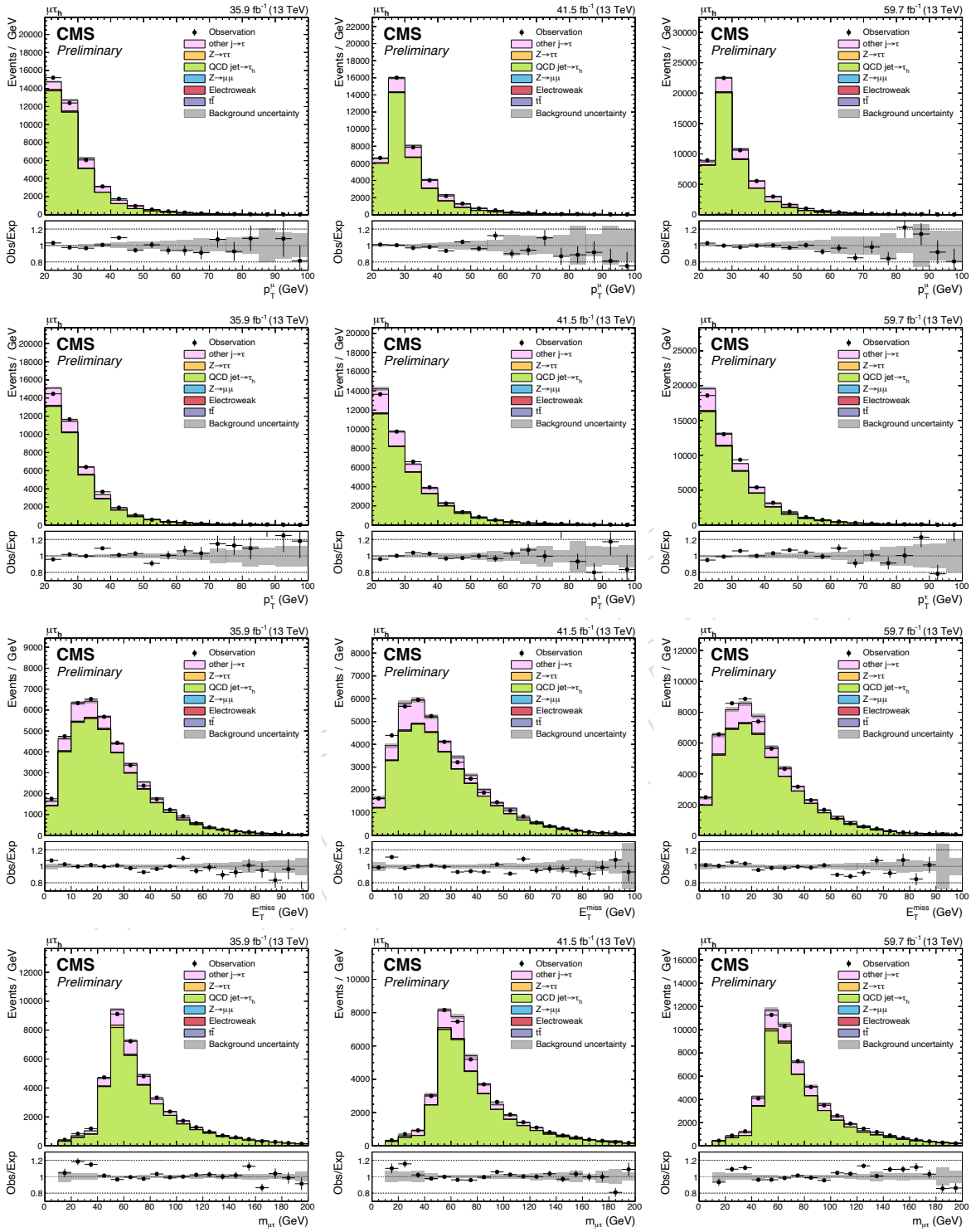

Figure 74: Closure comparisons of data with the FF prediction in the $\tau_\mu\tau_\mathrm{h}$ channel when applying the measured QCD fake factors for the QCD DR events. The plots are shown for 2016, 2017, and 2018 in the left, center, and right columns. From top to bottom the comparisons are shown for the following variables: τ_μ p_T, τ_h p_T, $E_\mathrm{T}^\mathrm{miss}$, visible mass of the $\tau_\mu\tau_\mathrm{h}$ pair.

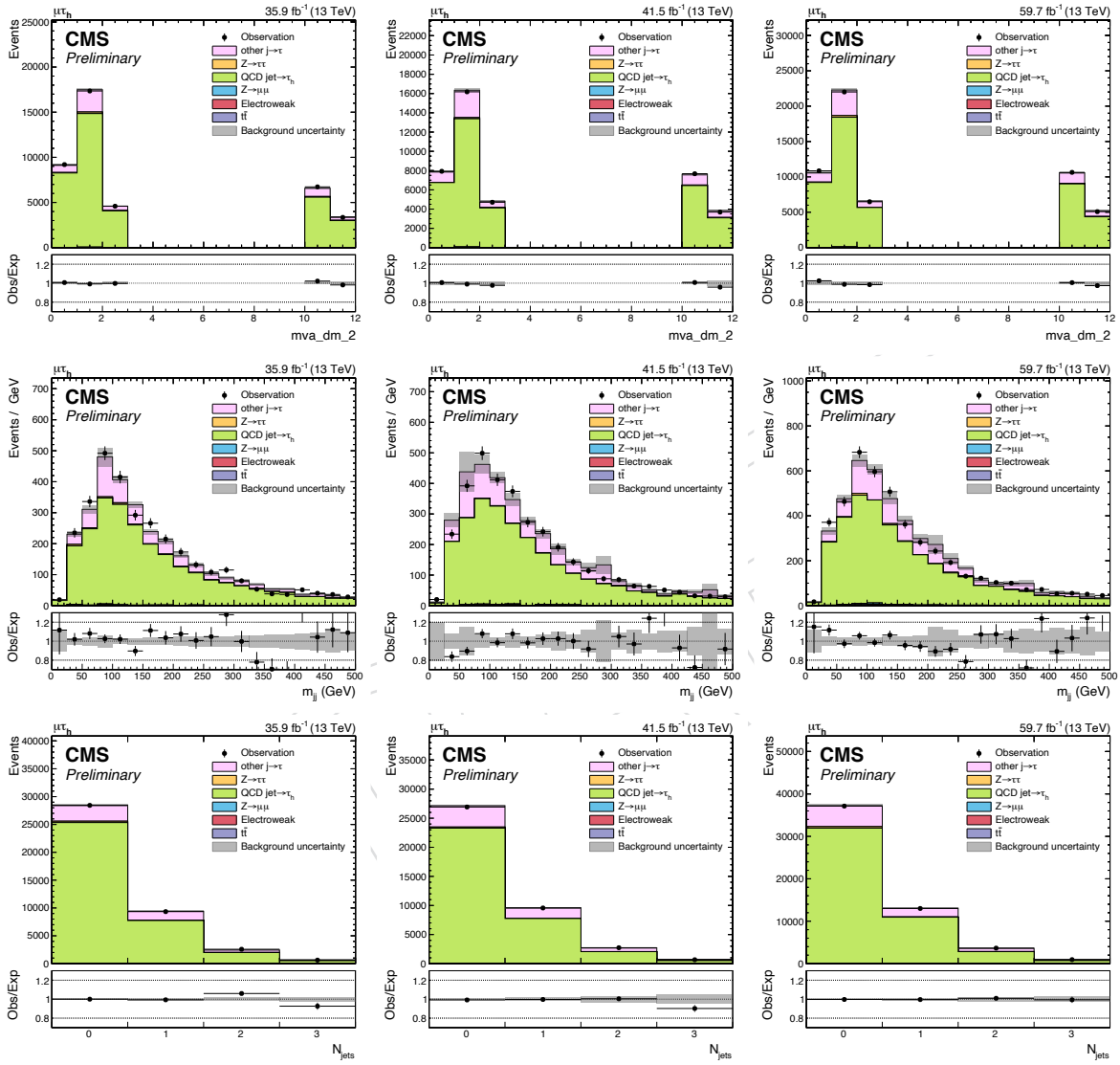

Figure 75: Closure comparisons of data with the FF prediction in the $\tau_\mu \tau_\mathrm{h}$ channel when applying the measured QCD fake factors for the QCD DR events. The plots are shown for 2016, 2017, and 2018 in the left, center, and right columns. From top to bottom the comparisons are shown for the following variables: τ_h MVA-DM, m_{jj}, and N_jets.

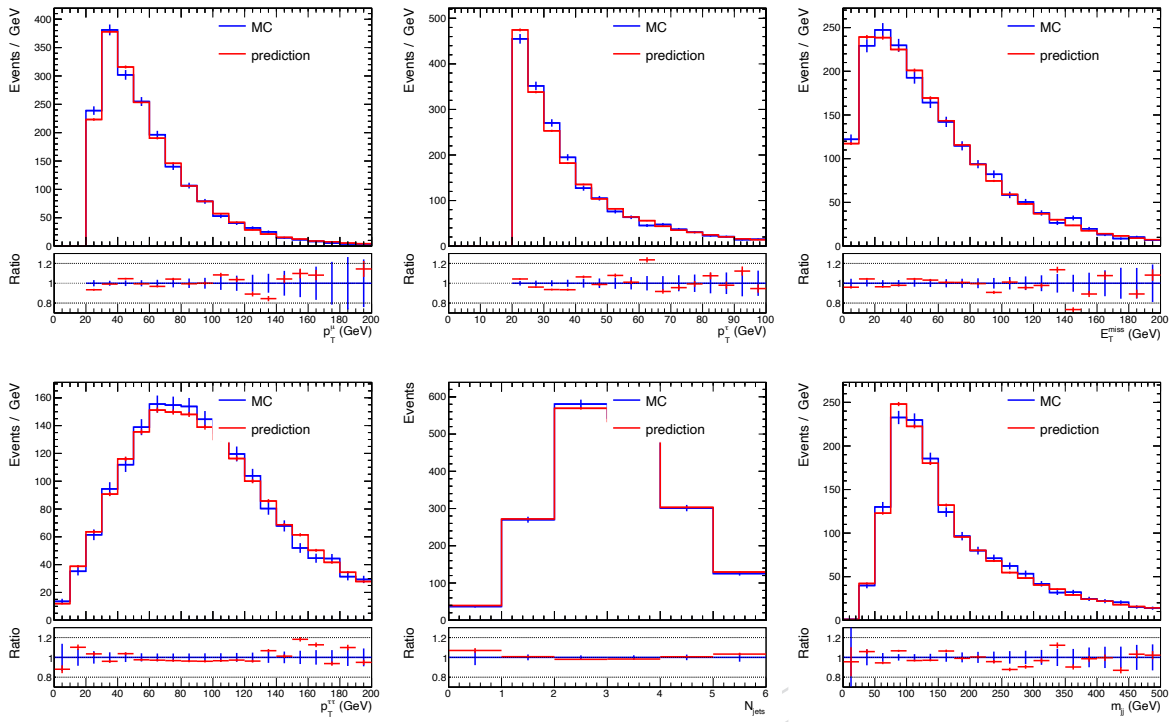

Figure 76: Closure comparisons of MC with the FF prediction in the $\tau_\mu\tau_h$ channel in 2018 when applying the measured $t\bar{t}$ fake factors for the $t\bar{t}$ DR events. The plots are shown for τ_μ p_T, τ_h p_T, E_T^{miss}, p_T of the $\tau_\mu\tau_h$+E_T^{miss} system , N_{jets}, and m_{jj}.

but fail the `Medium` DeepTau ID discriminant.

2. The number of W+jets and $t\bar{t}$ events contribution to this region is estimated from the MC. The contribution of smaller processes such as DY+jets and diboson are included also in the W+jets total.

3. The contribution of QCD events is estimated by subtracting all other processes from the data using MC.

4. The fractions are then determined by dividing each individual contribution by the sum of the $j \to \tau_h$ fake events.

n FigureThe resulting fractions binned in the W+jets and QCD scores are shown for the three processes in Figure 77.

The AR in these channels is defined by requiring the τ_h candidate to pass the `VVVLoose` but fail the `Medium` DeepTau ID discriminant with all other selections kept identical to the SR definition. The jet $\to$ τ_h background in the SR is then estimated by applying the measured $\overline{FF}$ to the events in the AR. The contribution of processes producing genuine τ_h or l $\to$ τ_h candidates is subtracted using simulated events.

The measured fake factors are applied to the DR events to check that the method closes. This is done separately for the W+jets and QCD fake factors in the corresponding control regions. Comparisons of the data with the predictions for these checks are shown for several important variables in Figures 72–73 for W+jets, Figures 74–75 for QCD, and Figure 76 for $t\bar{t}$. Data/background comparisons for inclusive SR events will be shown in Section 9.

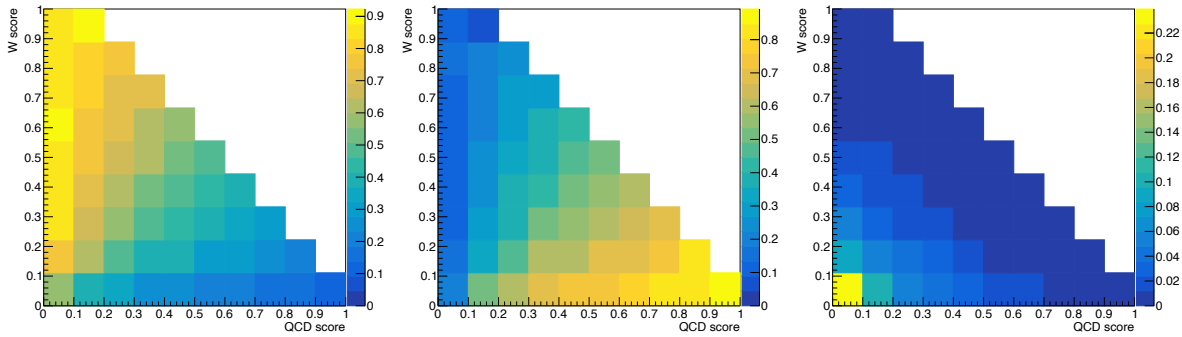

Figure 77: The fractions measured for the dominant processes W+jets (left), QCD (middle), and $t\bar{t}$ (right).

8.1.3 Fake factors in the $\tau_e\tau_h$ channels

In the $\tau_e\tau_h$ channel there are several processes that yield a significant contribution to the jet $\rightarrow$ τ_h background. This includes QCD, W+jets, and $t\bar{t}$. The former two are in generally the most significant and contribute with approximately equal weights. The $t\bar{t}$ is typically small but can become more significant in regions of parameter space with multiple jets. The W+jets DR is defined by applying a cut of $m_T > 70$ GeV, with all other selections kept the same as the SR. The contribution of other processes to the DR (except QCD) is subtracted using MC. The QCD DR is defined by requiring the τ_e and τ_h pair to have SS charges. An additional $I^l_{rel} > 0.05$ requirement is used to reduce processes producing genuine leptons. The contribution of other processes to the DR is again subtracted using MC. It is not possible to define a DR that is sufficiently pure in $t\bar{t}$ events to make a reasonable measurement of $FF_{t\bar{t}}$. The $FF_{t\bar{t}}$ are therefore derived from MC. A comparison of the FF_W measured in data and MC shows only an $\sim$ 10–20% differences in the fake rates in data and MC. This observation coupled with the fact that the $t\bar{t}$ contribution is small compared to the other processes means that any bias introduced by using $FF_{t\bar{t}}$ measured in MC is negligible compared to the uncertainties on the fake factors.

In the case of QCD and W+jets the FF_i are measured for three N_{jets} bins (0, 1, $\geq$ 2) and 5 MVA-DM bins (0, 1, 2, 10, 11). The MVA-DM = 0 bins are further split into two bins depending on the τ_h impact parameter significance ($S_{IP} < 1.5$, $S_{IP} \geq 1.5$). The FF_i are also measured separately for events passing the single electron and electron+tau cross triggers, where the latter is defined as all events that fail the single electron trigger. This is necessary as the ID and isolation selections used in the trigger result in different FF_i values. The $FF_{t\bar{t}}$ are measured only in bins of MVA-DM and S_{IP}. Further binning is not necessary in this case as the $t\bar{t}$ fractions are small and such events are usually accompanied by several jets. For the bins passing the single lepton triggers the dependence on the τ_h p_T is fitted using a first order polynomial. In some cases where the statistical population of a bin is insufficient the first order polynomial fit can fail to converge properly or give unrealisable trends that are overly influenced by statistical fluctuations. In such cases the p_T dependence is instead fitted using either a zeroth order polynomial. Examples of the resulting fits are shown in Figures 78–80, which are chosen to illustrate the dependence of the fake factors on the considered process.

After applying the FF_{QCD} (FF_W) fake factors to the events in the corresponding DR non-closures are observed in the E_T^{miss} variables and $p_T^{\tau_e}$ distributions affecting mainly the events with $N_{jets} = 0$. As for the $\tau_e\tau_h$ channel the non-closure in the E_T^{miss} variables for the QCD fake factors are again corrected as a function of C_{QCD}. The situation for the W+jets (and $t\bar{t}$) corrections is slightly different due to the presence of genuine missing energy from neutrinos. In this case the

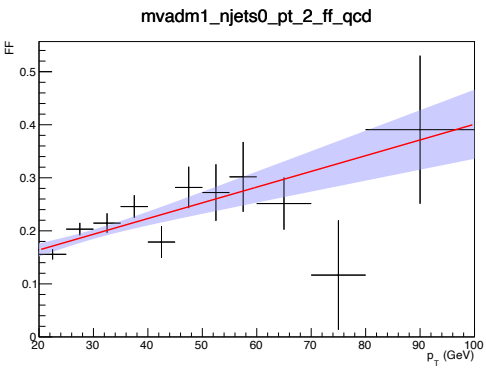

(a) QCD

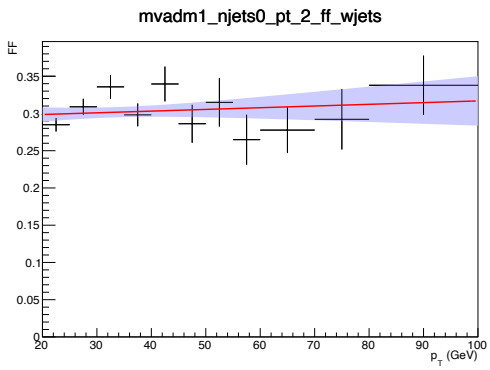

(b) W+jets

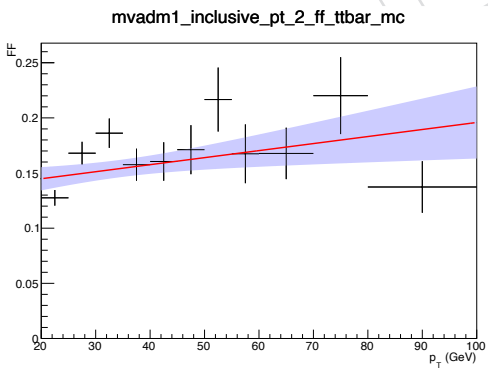

(c) $t\bar{t}$

Figure 78: Examples of the 2018 fake factor fits in the $\tau_e\tau_h$ channel illustrating the dependence the considered process. The fitted fake factors measured for τ_h candidates with MVA-DM = 1 are shown for QCD, W+jets and $t\bar{t}$ events. The QCD and W+jets measurements were performed for events with no jets in the final state, whereas for $t\bar{t}$ the fake-factors are measured inclusively in N_{jets}.

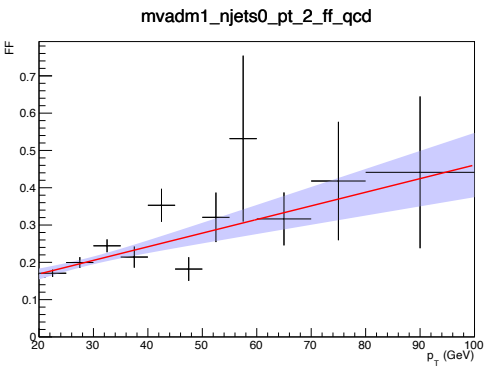

(a) QCD

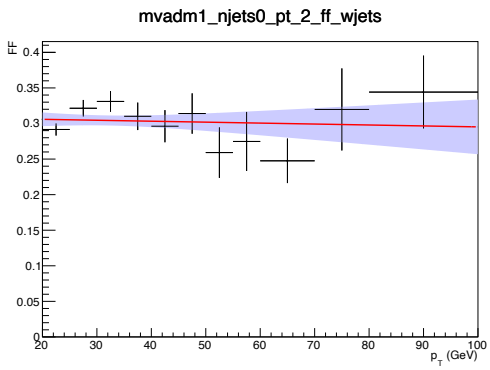

(b) W+jets

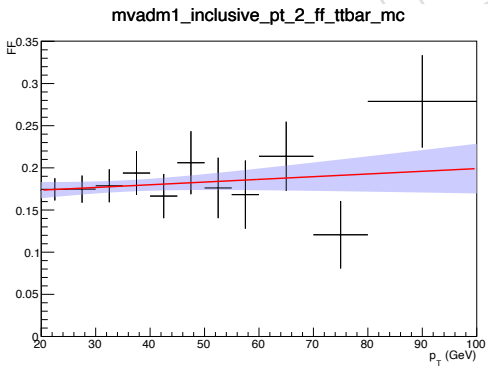

(c) $t\bar{t}$

Figure 79: Examples of the 2017 fake factor fits in the $\tau_e\tau_h$ channel illustrating the dependence the considered process. The fitted fake factors measured for τ_h candidates with MVA-DM = 1 are shown for QCD, W+jets and $t\bar{t}$ events. The QCD and W+jets measurements were performed for events with no jets in the final state, whereas for $t\bar{t}$ the fake-factors are measured inclusively in N_{jets}.

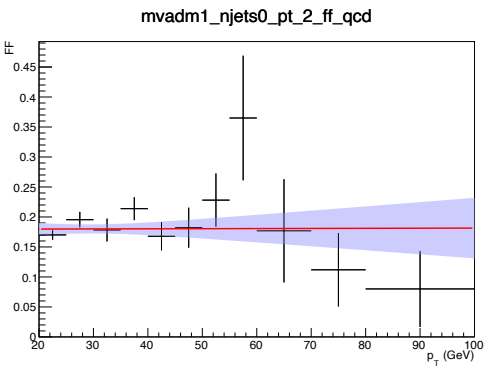

(a) QCD

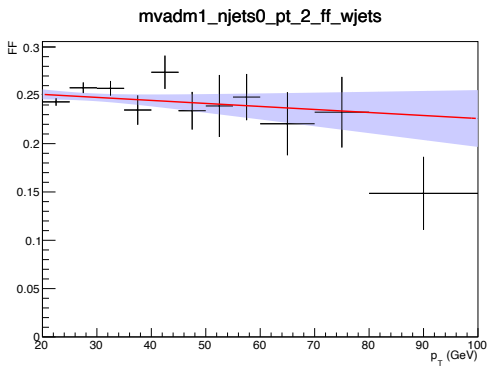

(b) W+jets

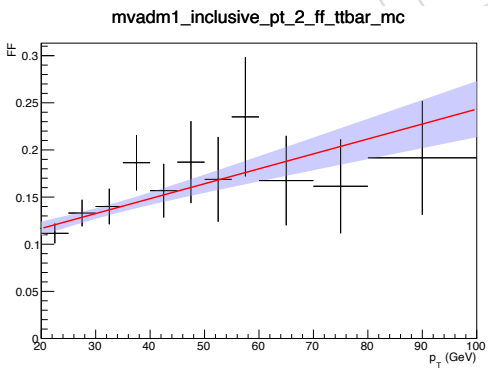

(c) $t\bar{t}$

Figure 80: Examples of the 2016 fake factor fits in the $\tau_e\tau_h$ channel illustrating the dependence the considered process. The fitted fake factors measured for τ_h candidates with MVA-DM = 1 are shown for QCD, W+jets and $t\bar{t}$ events. The QCD and W+jets measurements were performed for events with no jets in the final state, whereas for $t\bar{t}$ the fake-factors are measured inclusively in N_{jets}.

correction variable is suitable modified to approximately subtract the genuine $E_{\mathrm{T}}^{\mathrm{miss}}$ from the total. This approximation assumes the neutrino is back-to-back and balanced with the electron (which is exactly true for W bosons produce at rest in the transverse direction), the transverse components of the 3-vector of the electron are then added to $\vec{E_{\mathrm{T}}^{\mathrm{miss}}}$ defining the resulting vector $\vec{E_{\mathrm{T}}^{\mathrm{miss}\prime}} + e$. The variable used to parametrise the W+jets correction, C_{W}, is then defined in the same way as C_{QCD} except using $\vec{E_{\mathrm{T}}^{\mathrm{miss}\prime}} + e$ instead of $\vec{E_{\mathrm{T}}^{\mathrm{miss}}}$:

$$C_{\mathrm{W}} = \frac{E_{\mathrm{T}}^{\mathrm{miss}+e}}{p_{\mathrm{T}}^{\tau_{\mathrm{h}}}} \cos\Delta\phi(\vec{E_{\mathrm{T}}^{\mathrm{miss}+e}}, \vec{\tau_{\mathrm{h}}}). \tag{42}$$

For the QCD and W+jets these corrections are derived separately for each N_{jets} bin, for $\mathrm{t\bar{t}}$ the correction is derived inclusively in N_{jets}. Example of the corrections derived for QCD, W+jets, and $\mathrm{t\bar{t}}$ are shown in Figures 81–83. The QCD corrections are fitted using a first order polynomial and the W+jet and $\mathrm{t\bar{t}}$ are fitted using error functions. After applying this derived correction to the fake factors the electron p_{T} distribution is also corrected for the W+jets and QCD fake factors. No significance disagreement is observed for $\mathrm{t\bar{t}}$ and therefore this correction is not needed. The QCD correction is found to depend softly on the τ_{h} p_{T} therefore the correction is derived in 3 $p_{\mathrm{T}}^{\tau_{\mathrm{h}}}$ regions: $p_{\mathrm{T}}^{\tau_{\mathrm{h}}} < 30$ GeV, $30 < p_{\mathrm{T}}^{\tau_{\mathrm{h}}} < 40$ GeV, and $p_{\mathrm{T}}^{\tau_{\mathrm{h}}} > 40$ GeV. Examples of the the p_{T} correction for QCD and W+jets events are shown in Figures 84–86. As verified using W+jets MC, the p_{T} non-closure is a result of variation in the different flavour compositions of the jets as a function of the electron p_{T}.

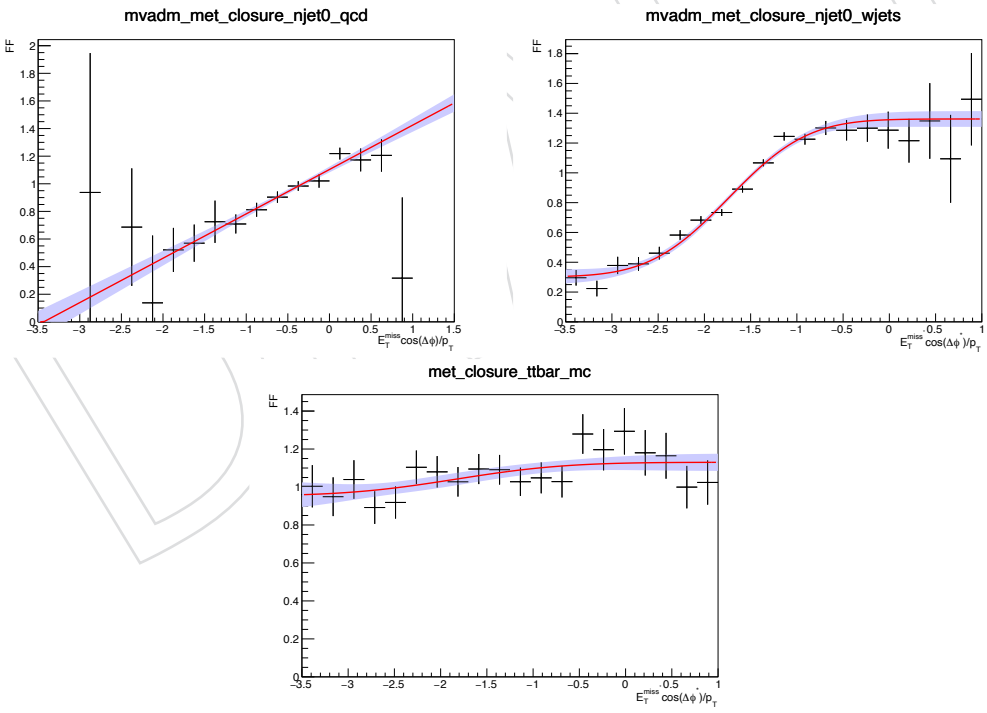

Figure 81: The 2018 $E_{\mathrm{T}}^{\mathrm{miss}}$ non-closure corrections for the QCD (upper left), W+jets (upper right), and $\mathrm{t\bar{t}}$ (lower).

Additional corrections are applied to account for differences in the determination regions and signal regions. For the QCD fake factors such differences can arise if there are slight differences in the fake rates for events where the lepton is anti-isolated or for events with SS $\tau_l\tau_{\mathrm{h}}$ pairs. The correction for the lepton isolation is derived by applying the measured fake factors including non-closure corrections to SS events. The differences between the data and the prediction as

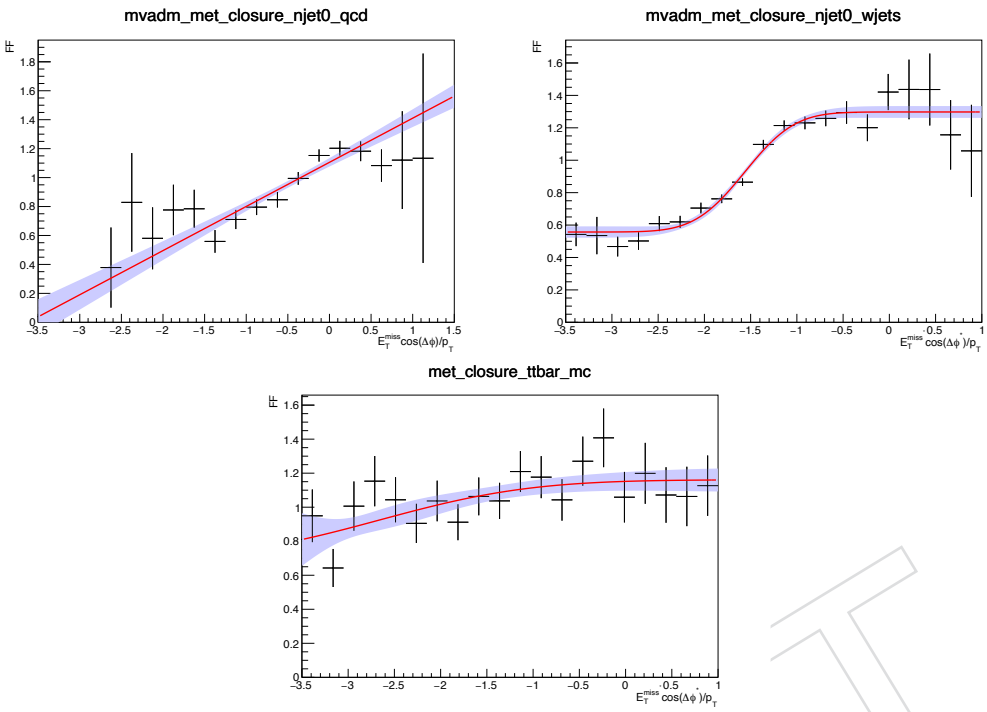

Figure 82: The 2017 E_T^{miss} non-closure corrections for the QCD (upper left), W+jets (upper right), and $t\bar{t}$ (lower).

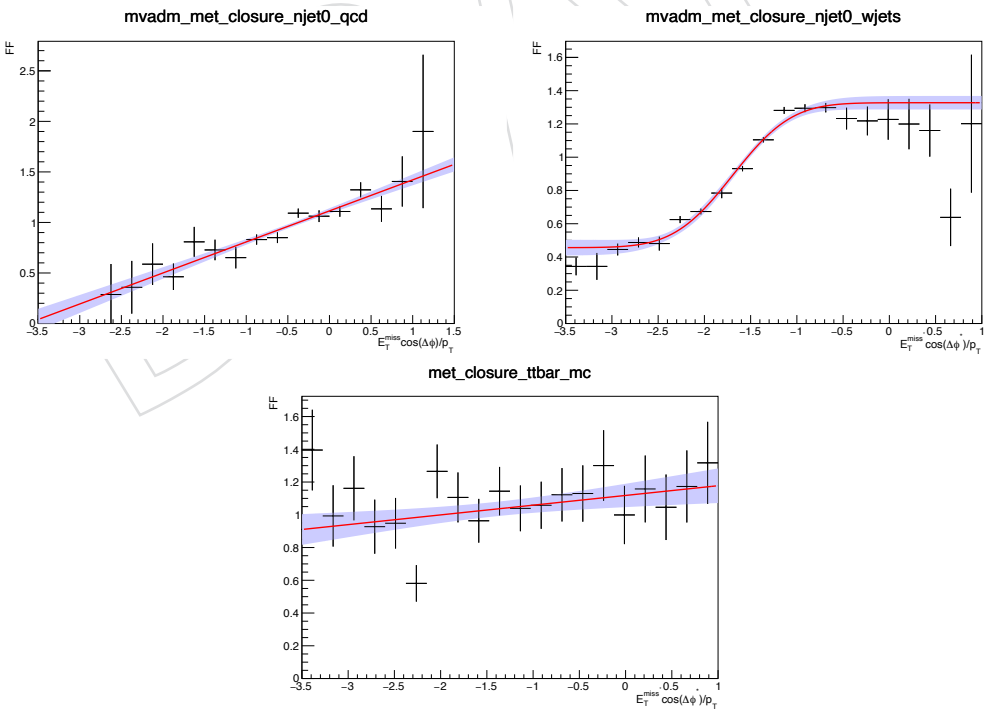

Figure 83: The 2016 E_T^{miss} non-closure corrections for the QCD (upper left), W+jets (upper right), and $t\bar{t}$ (lower).

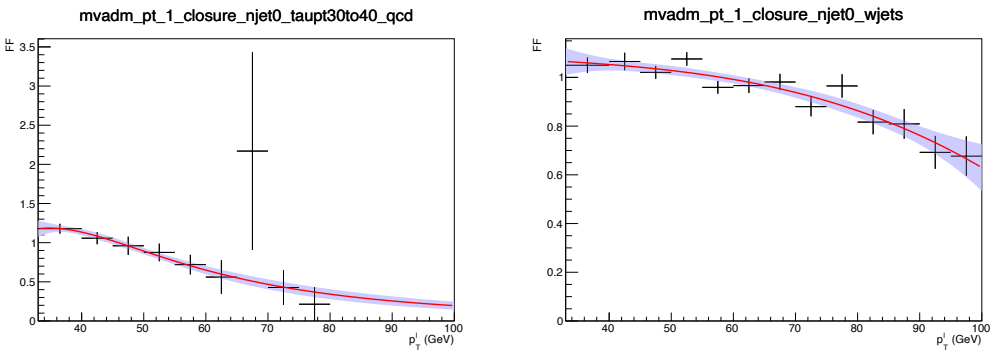

Figure 84: The 2018 electron p_T non-closure corrections for the QCD (left) and W+jets (right). For the QCD the correction is shown for the $30 < p_T^{\tau_h} < 40$ GeV region.

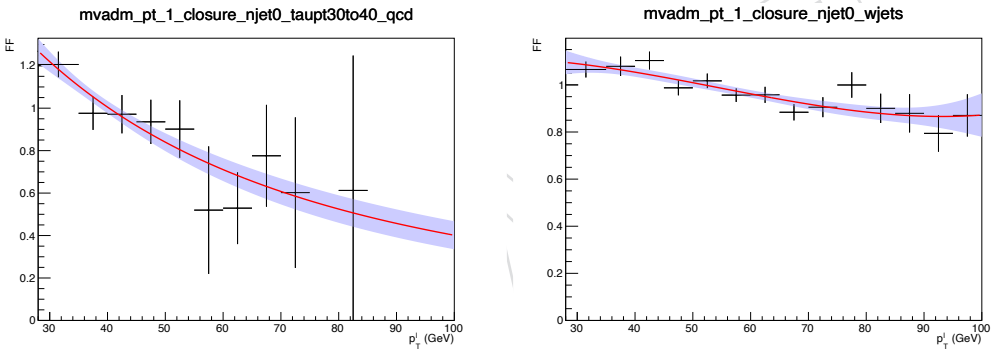

Figure 85: The 2017 electron p_T non-closure corrections for the QCD (left) and W+jets (right). For the QCD the correction is shown for the $30 < p_T^{\tau_h} < 40$ GeV region.

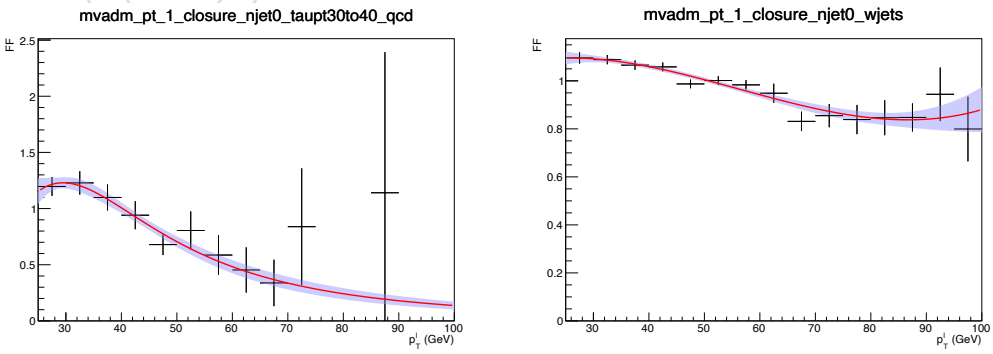

Figure 86: The 2018 electron p_T non-closure corrections for the QCD (left) and W+jets (right). For the QCD the correction is shown for the $30 < p_T^{\tau_h} < 40$ GeV region.

a function of I^{l}_{rel} is then taken as the correction. This is fitted using a third order polynomial. The corrections are shown in the left insets of Figure 87–89. To corrected for differences in the fake factors in OS vs SS events fake factors are measured as described above for events with $0.25 < I^{l}_{rel} < 0.5$. These fake factors are also corrected to account for non-closures in the $E_{\mathrm{T}}^{\mathrm{miss}}$ and p^{l}_{T} distributions as describe previously. These fake factors are then applied to OS events in the AR defined with the same I^{l}_{rel} requirement as the DR. This prediction is then compared to the data and the difference is taken as the OS/SS correction which is fitted using a first order polynomial. The corrections are shown in the right insets of Figure 87–89.

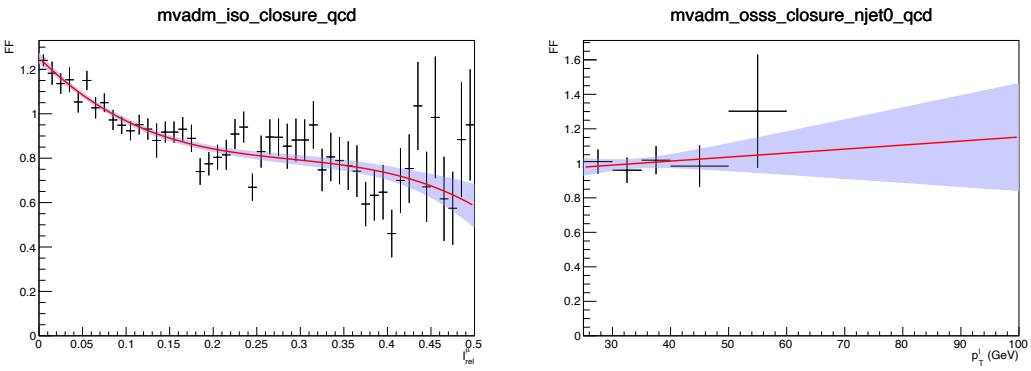

(a) (b)

Figure 87: The corrections derived for the 2018 fake factors to account for differences in the QCD fake factors due to the inverted cut on I^{l}_{rel} (left) and due OS vs SS selections (right).

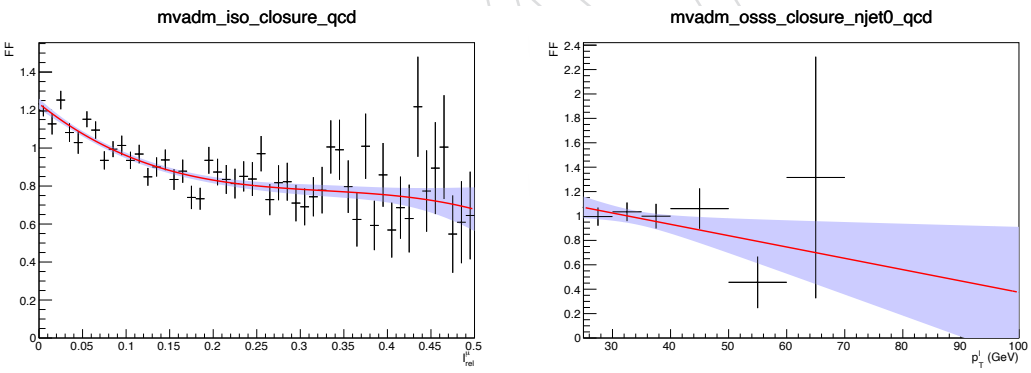

(a) (b)

Figure 88: The corrections derived for the 2017 fake factors to account for differences in the QCD fake factors due to the inverted cut on I^{l}_{rel} (left) and due OS vs SS selections (right).

For the W+jets fake factors a correction is derived to account for differences in the measured fake factors in the high m_{T} DR and the low m_{T} SR. This correction is derived from MC. Fake factors are measured for simulated W+jets events and corrected using exactly the same procedures outlined above. These fake factors are then applied to the simulated events in the AR and the difference between the resulting prediction and the simulation in the SR is taken as the correction. Such non closures are a result of variation in the jet flavour compositions in the high and low m_{T} regions. The correction is measured separately for each N_{jet} bin and parametrised as a function of the W boson p_{T} (reconstructed from the $E_{\mathrm{T}}^{\mathrm{miss}}$ and electron system). The corrections derived for the $N_{\mathrm{jet}} = 0$ and $N_{\mathrm{jet}} = 1$ bins are shown in Figures 90–92. This choice is found to give good closure for all important variables.

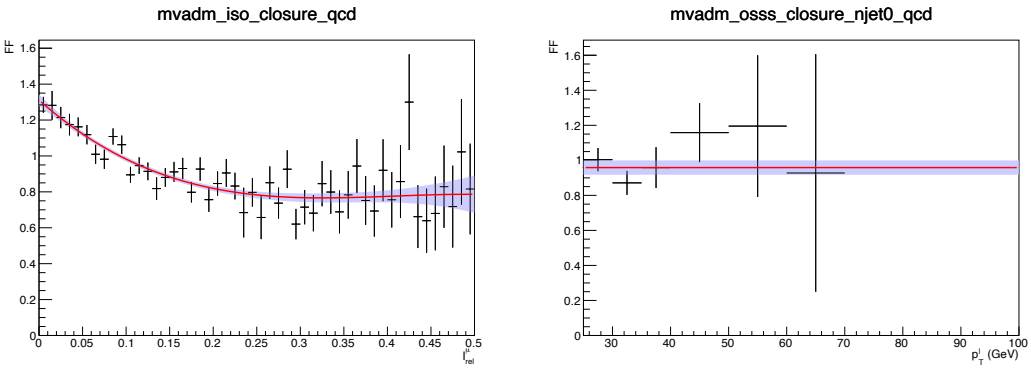

(a) (b)

Figure 89: The corrections derived for the 2016 fake factors to account for differences in the QCD fake factors due to the inverted cut on I^{l}_{rel} (left) and due OS vs SS selections (right).

For the $t\bar{t}$ since the fake factors are derived from MC a correction is derived by comparing the W+jets fake factors in data and simulation. The differences between the two as a function of MVA-DM, and $p_T^{\tau_h}$ are used as the correction. In the p_T regions most relevant to the analysis the size of the corrections are O(10%). The choice of W+jets events to measure this correction is driven by the need to select a region pure in fake τ_h candidates with sufficient statistics to make a meaningful measurement. It was considered to use control regions pure in $t\bar{t}$ events to measure these corrections which can be defined, for example, by requiring the presence of b-jets, but such regions are plagued by large fractions of events with genuine τ_h candidates which must be subtracted using MC. In such cases it is not clear if the derived correction is meaningful and not driven by data/MC differences in the subtracted component. Given the small fraction of $t\bar{t}$ events to to overall jet$\rightarrow \tau_h$ yield any bias introduced by the procedure used to measure and correct the $t\bar{t}$ fake factors is expected to be negligible compared to the other fake factor uncertainties on the QCD and W+jets processes. Nevertheless, as an extra precaution a conservative uncertainty defined by applying $\pm$ 100% of the corrections is included to cover any differences in the corrections derived using W+jets and $t\bar{t}$.

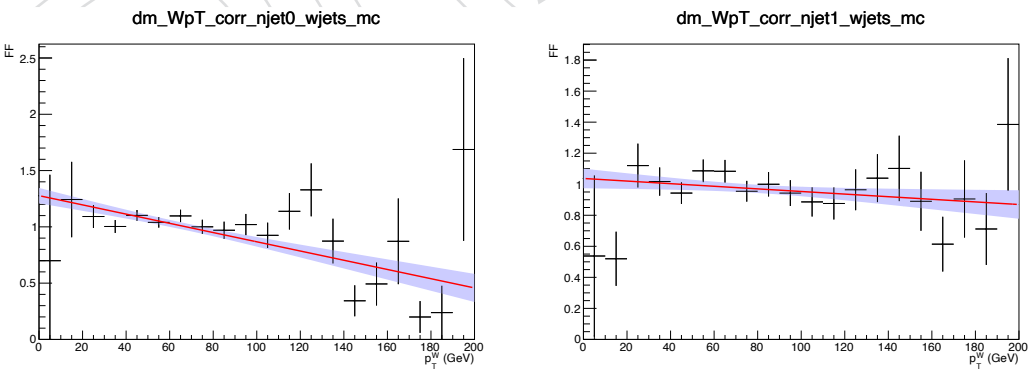

(a) $N_{jets} = 0$ (b) $N_{jets} = 1$

Figure 90: The corrections derived for the 2018 fake factors to account for differences in the W+jets fake factors due the inverted m_T selection used to define the DR. The corrections are parametrised as a function of the W boson p_T and are shown for events with zero jets (left) and one jet (right).

The FF_i's measured for the three processes and then combined into an overall $\overline{FF}$ using the fractions which encode the probability of an AR event originating from each process. The

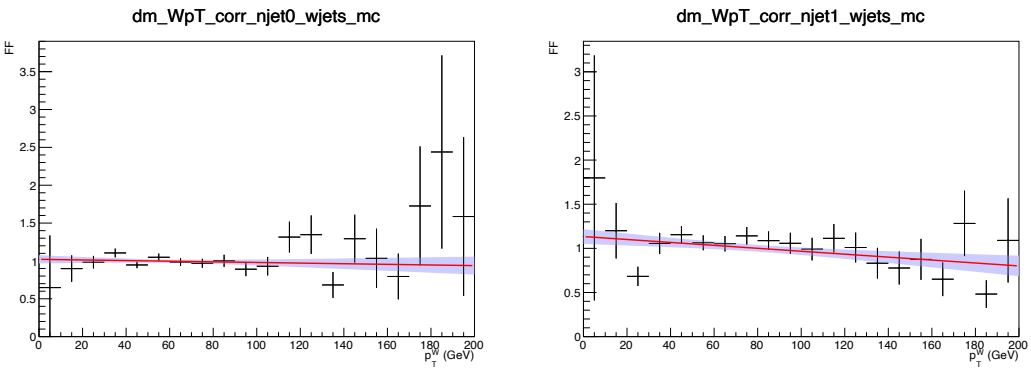

(a) $N_{jets} = 0$ (b) $N_{jets} = 1$

Figure 91: The corrections derived for the 2017 fake factors to account for differences in the W+jets fake factors due the inverted m_T selection used to define the DR. The corrections are parametrised as a function of the W boson p_T and are shown for events with zero jets (left) and one jet (right).

DRAFT

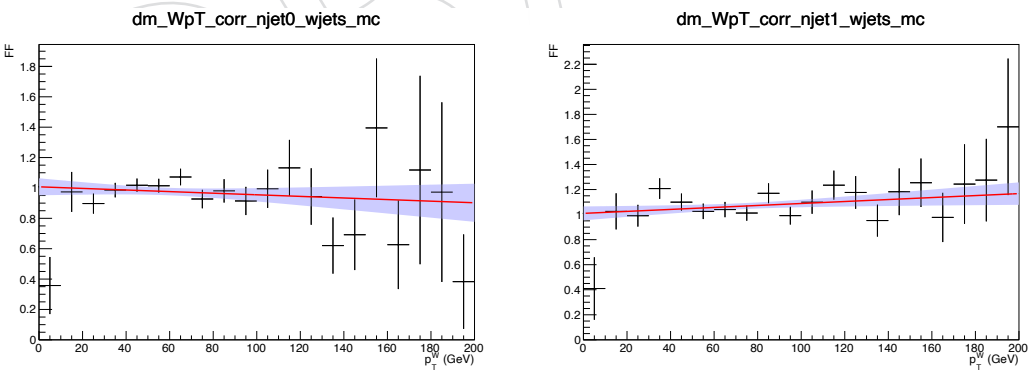

(a) $N_{jets} = 0$ (b) $N_{jets} = 1$

Figure 92: The corrections derived for the 2016 fake factors to account for differences in the W+jets fake factors due the inverted m_T selection used to define the DR. The corrections are parametrised as a function of the W boson p_T and are shown for events with zero jets (left) and one jet (right).

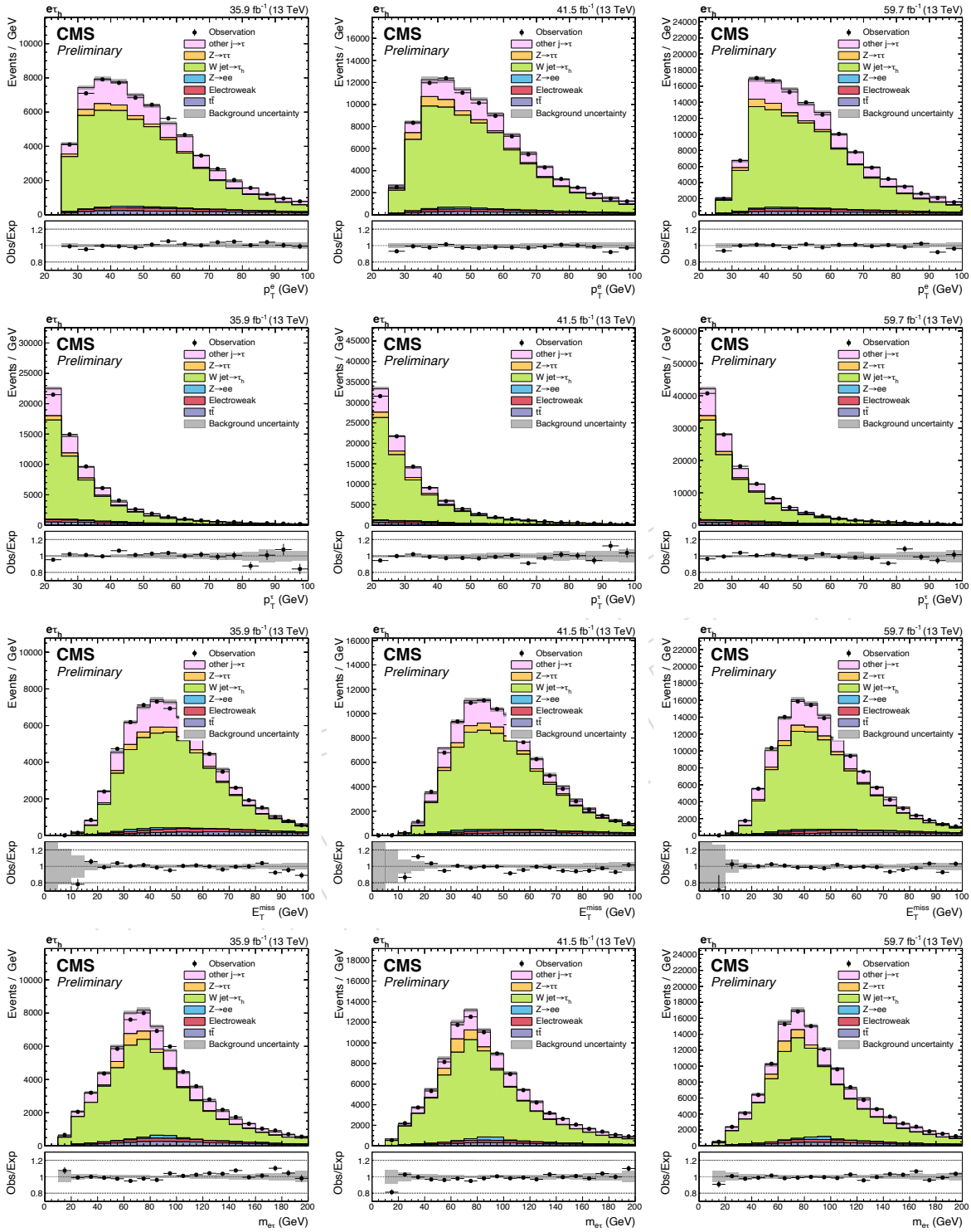

Figure 93: Closure comparisons of data with the FF prediction in the $\tau_e\tau_\mathrm{h}$ channel when applying the measured W+jets fake factors for the W+jets DR events. The plots are shown for 2016, 2017, and 2018 in the left, center, and right columns. From top to bottom the comparisons are shown for the following variables: τ_e p_T, τ_h p_T, $E_\mathrm{T}^\mathrm{miss}$, visible mass of the $\tau_e\tau_\mathrm{h}$ pair.

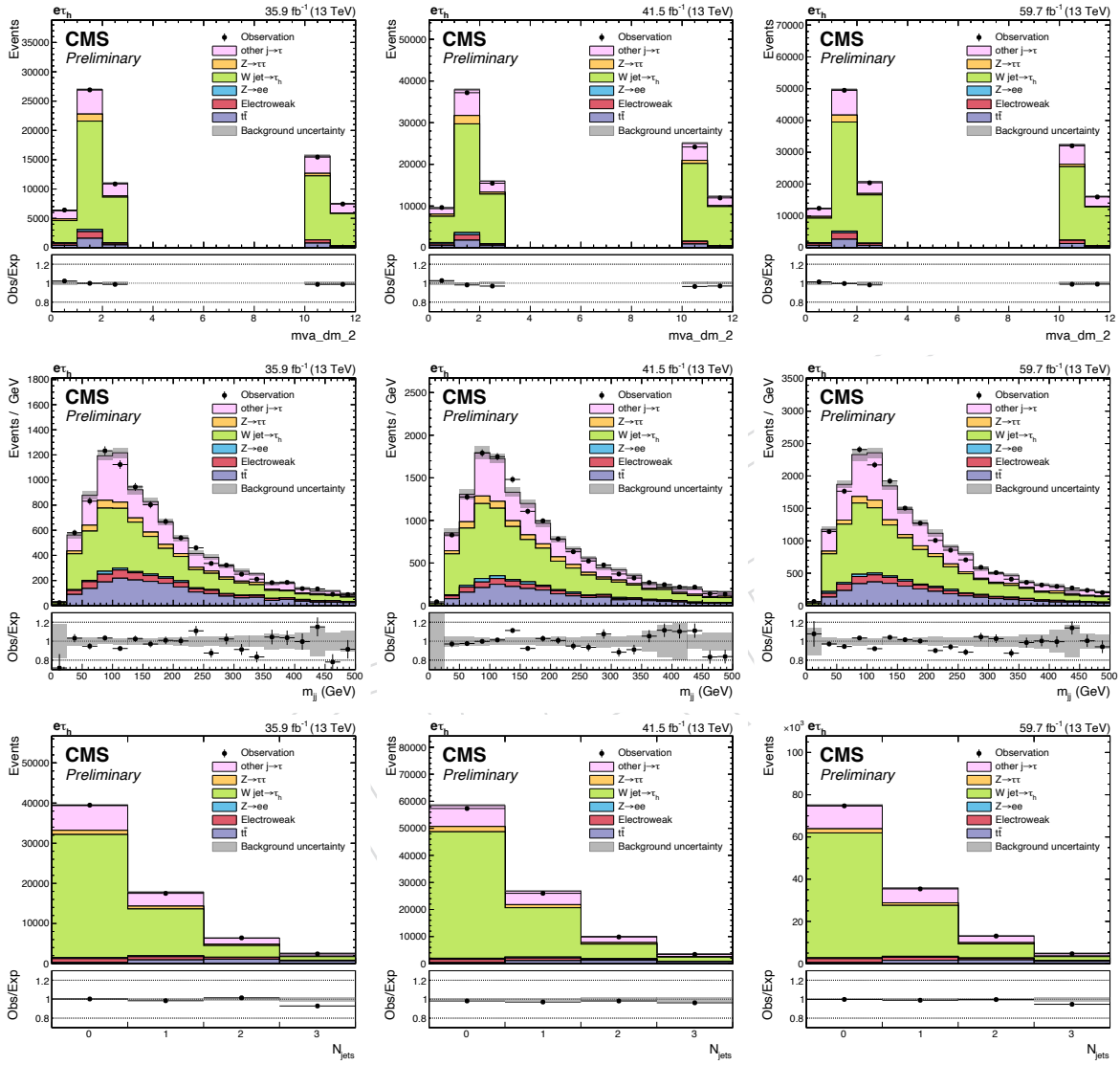

Figure 94: Closure comparisons of data with the FF prediction in the $\tau_e\tau_\mathrm{h}$ channel when applying the measured W+jets fake factors for the W+jets DR events. The plots are shown for 2016, 2017, and 2018 in the left, center, and right columns. From top to bottom the comparisons are shown for the following variables: τ_h MVA-DM, m_{jj}, and N_jets.

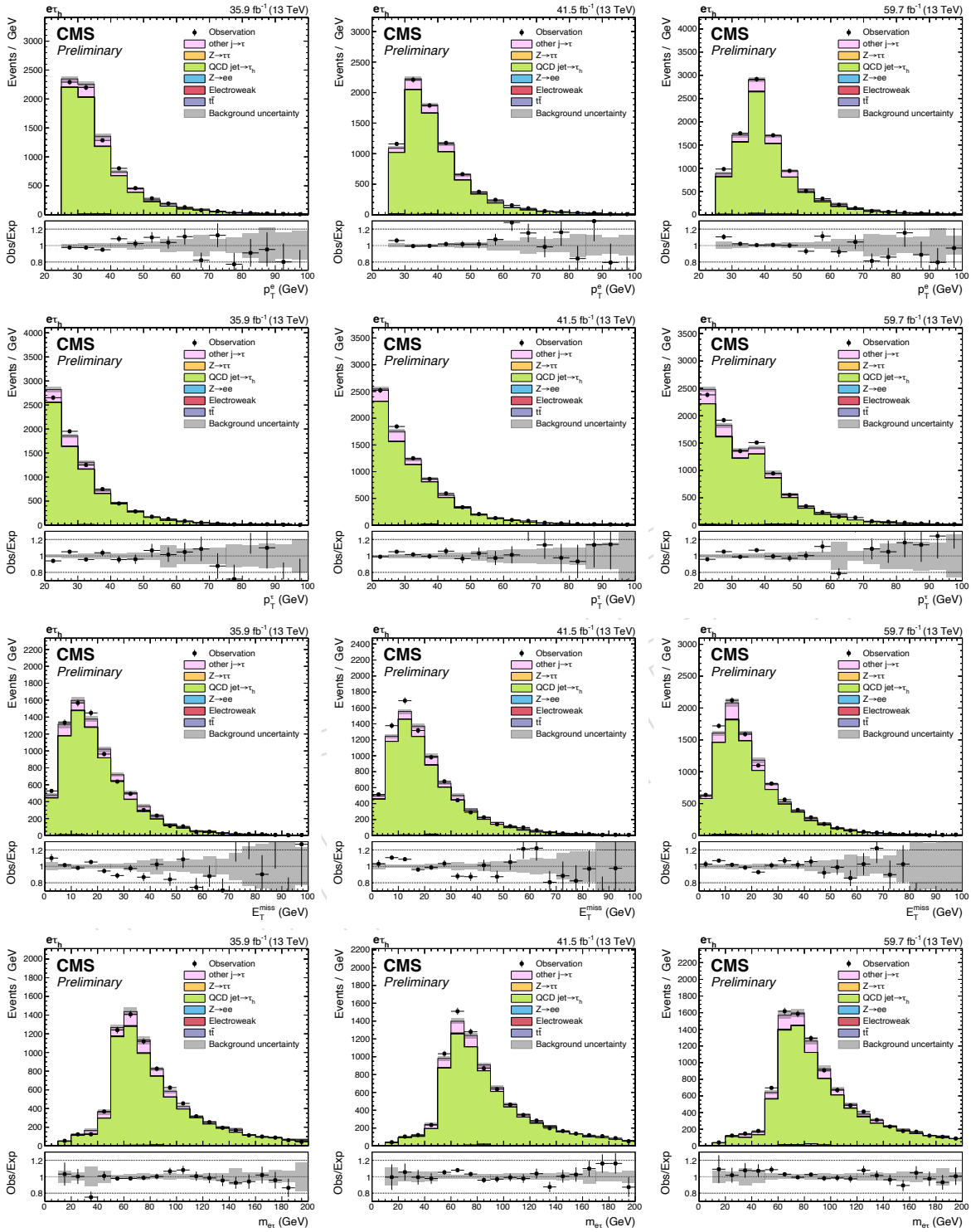

Figure 95: Closure comparisons of data with the FF prediction in the $\tau_e\tau_\mathrm{h}$ channel when applying the measured QCD fake factors for the QCD DR events. The plots are shown for 2016, 2017, and 2018 in the left, center, and right columns. From top to bottom the comparisons are shown for the following variables: τ_e p_T, τ_h p_T, $E_\mathrm{T}^\mathrm{miss}$, visible mass of the $\tau_e\tau_\mathrm{h}$ pair.

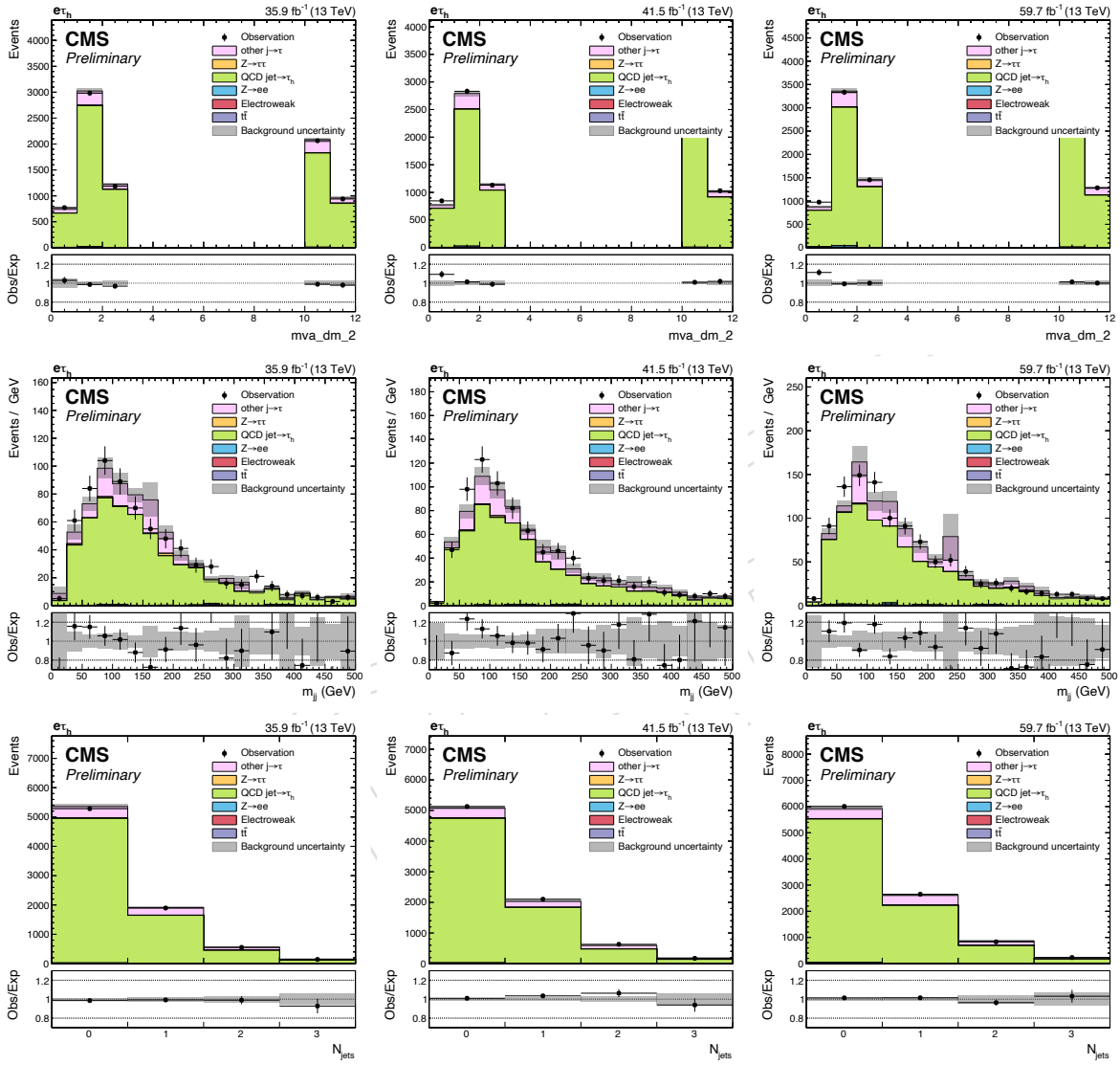

Figure 96: Closure comparisons of data with the FF prediction in the $\tau_e\tau_h$ channel when applying the measured QCD fake factors for the QCD DR events. The plots are shown for 2016, 2017, and 2018 in the left, center, and right columns. From top to bottom the comparisons are shown for the following variables: τ_h MVA-DM, m_{jj}, and N_{jets}.

fractions are derived in the same way as for the $\tau_e\tau_h$ channel.

The AR in these channels is defined by requiring the τ_h candidate to pass the `VVVLoose` but fail the `Medium` DeepTau ID discriminant with all other selections kept identical to the SR definition. The jet $\rightarrow \tau_h$ background in the SR is then estimated by applying the measured $\overline{\text{FF}}$ to the events in the AR. The contribution of processes producing genuine τ_h or $l \rightarrow \tau_h$ candidates is subtracted using simulated events.

The measured fake factors are applied to the DR events to check that the method closes. This is done separately for the W+jets and QCD fake factors in the corresponding control regions. Comparisons of the data with the predictions for these checks are shown for several important variables in Figures 93–94 for W+jets, and Figures 95–96 for QCD. Data/background comparisons for inclusive SR events will be shown in Section 9.

8.1.4 Treatment of statistical uncertainties

The uncertainty bands on the fitted functions for the uncorrected fake factors are used to estimate the statistical uncertainties on the measured fake factors. Simply taking the upper and lower values of the bands as the $\pm\, 1\sigma$ variations would only allow the fake factors in all p_T regions to be simultaneously increased or decreased during the fit to data, whereas in reality we expect the fitted functions to have at least one point in which the uncertainty flips sign and fake factors below this point will be decreased while simultaneously being increased above the point (and vice versa). In principle an uncertainty per degree of freedom of the fitted function could be included to mitigate this effect. However the functional form of the fake factors typically has 4 degrees of freedom so this would require a very large set of nuisance parameters to be included (4 per N_{jets}/MVA-DM/S_{IP} bin per channel per process per year).

To reduce the number of nuisance parameters by $\approx$ a factor of 2 the statistical uncertainties are decomposed into two contributions. The first contribution affects purely the normalisation of a N_{jets}/MVA-DM/S_{IP} bin (i.e the relative uncertainty is constant as a function of p_T). The second contribution changes sign at a particular value of p_T, where below this value the fake factor is decreased (increased) and above this value the fake factor is increased (decreased) by the upwards (downwards) pull on the nuisance parameter. The two contributions are additionally required to sum in quadrature to the total uncertainty. Uncertainties split in shape and normalization uncertainties capture the main variations induced by the uncertainties. This describes the two leading degrees of freedom of the fake factor p_T fits, similar procedures were applied and validated in the MSSM Higgs boson search [52] and the Z$\rightarrow \tau\tau$ cross section measurement [53].

The p_T value at which the shape uncertainty changes sign, p_T^0, is determined by the point at which the size of the total relative uncertainty is minimal. The size of the relative uncertainty at this point also determines the size of the normalisation uncertainty (since the second uncertainty is 0 at this point by construction). The magnitude of the second uncertainty is then determined as a function of p_T by subtracting in quadrature the normalisation uncertainty (σ_1) from the total uncertainty (σ_{tot}). Thus, the shape uncertainty (σ_2) is given by the formula:

$$\sigma_2(p_T) = \begin{cases} -\sqrt{\sigma_{\text{tot}}^2 - \sigma_1^2}, & \text{if } p_T < p_T^0. \\ +\sqrt{\sigma_{\text{tot}}^2 - \sigma_1^2} & \text{otherwise.} \end{cases} \tag{43}$$

Examples of the decomposed uncertainties can be seen in Figure 97, which illustrate the decomposition for the "standard" Landau+pol0 functional form (left inset) and for a simpler first order polynomial fit (right inset).

DRAFT

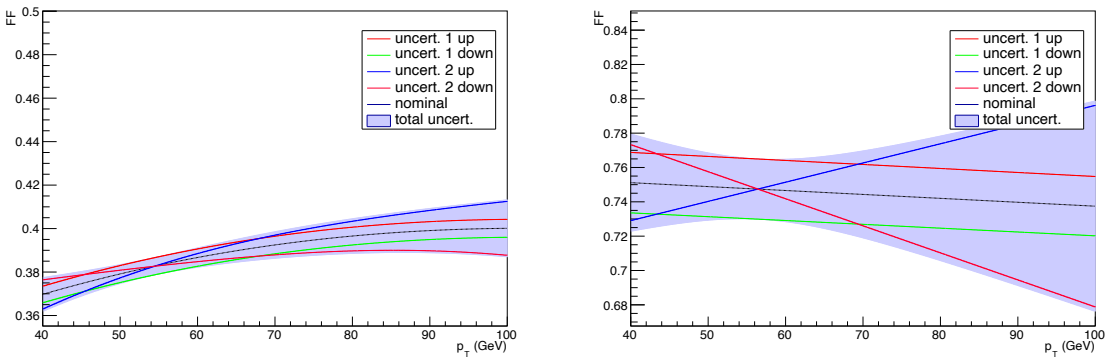

Figure 97: Examples of how the statistical uncertainty bands are decomposed into two contributions. One contribution affects only the normalisation which is denoted "uncert. 1" in the legend, and the second contribution which affects also the shape which is denoted "uncert 2." in the legends. Examples are shown for the "standard" functional form of the fitted fake factors (Landau+pol0) in the left inset, and a pol1 fit in the right inset.

8.1.5 Fake factor fits and corrections summary

The full set of the raw fake factor fits and corrections are included in Appendix E for reference.

DRAFT

9 Control plots

9.1 $\tau_\mu \tau_h$ channel

In Fig. 98-100(2016), Fig. 102-104(2017), and Fig. 106 108(2018) we display prefit control distributions for observables that are used in the multivariate discriminant (DNN) to distinguish the signal from background events. In Fig. 261(2016), Fig. 265(2017) and Fig. 269(2018) we display a few auxiliary control distributions of observables not used in the multivariate discriminant.

The plots are obtained after inclusive selection of $\tau_\mu \tau_h$ events as described in Section 7. Several additional cuts are applied:

- number of b-tagged jets = 0 (to reject top-pair and single-top backgrounds),
- visible mass of muon and tau lepton, $m_{\text{vis}} > 40\,\text{GeV}$.

The contribution from background processes is estimated as discussed in Section 8. The signal estimate is obtained from the simulated signal samples, described in Section 3.

In Appendix D.1 we display the distribution of the same distributions but without using the embedding technique, to review the normalisation using the Drell-Yan Monte-Carlo simulations is correct. The purpose of this is to gain confidence that the signal normalisation is also correct.

9.2 $\tau_e \tau_h$ channel

In Fig. 110–112(2016), Fig. 114–116(2017), and Fig. 118–120(2018) we display prefit control distributions for observables that are used in the multivariate discriminant (DNN) to distinguish the signal from background events. In Fig. 113(2016), Fig. 117(2017) and Fig. 121(2018) we display a few auxiliary control distributions of observables not used in the multivariate discriminant.

The plots are obtained after inclusive selection of $\tau_\text{e} \tau_h$ events as described in Section 7.

The contribution from background processes is estimated as discussed in Section 8. The signal estimate is obtained from the simulated signal samples, described in Section 3.

In Appendix D.2 we display the distribution of the same distributions but without using the embedding technique, to review the normalisation using the Drell-Yan Monte-Carlo simulations is correct. The purpose of this is to gain confidence that the signal normalisation is also correct.

9.3 $\tau_h \tau_h$ channel

Control plots for all variables used in the training of the BDT are shown in Fig. 282– 285. The MVA-DM which is not used in the BDT but is used to split into categories are shown in Fig. 286, and the subleading τ_h p_T, as well as the subleading jet p_T distributions are shown in 127. Additionally, plots of the visible and SVFit mass distributions, as well as the leading and subleading tau lepton p_T, with the full set of shape systematics is included in Fig. 128 and 129. In Appendix D.3 we display the distribution of the same distributions but without using the embedding technique, to review the normalisation using the Drell-Yan Monte-Carlo simulations is correct. The purpose of this is to gain confidence that the signal normalisation is also correct.

DRAFT

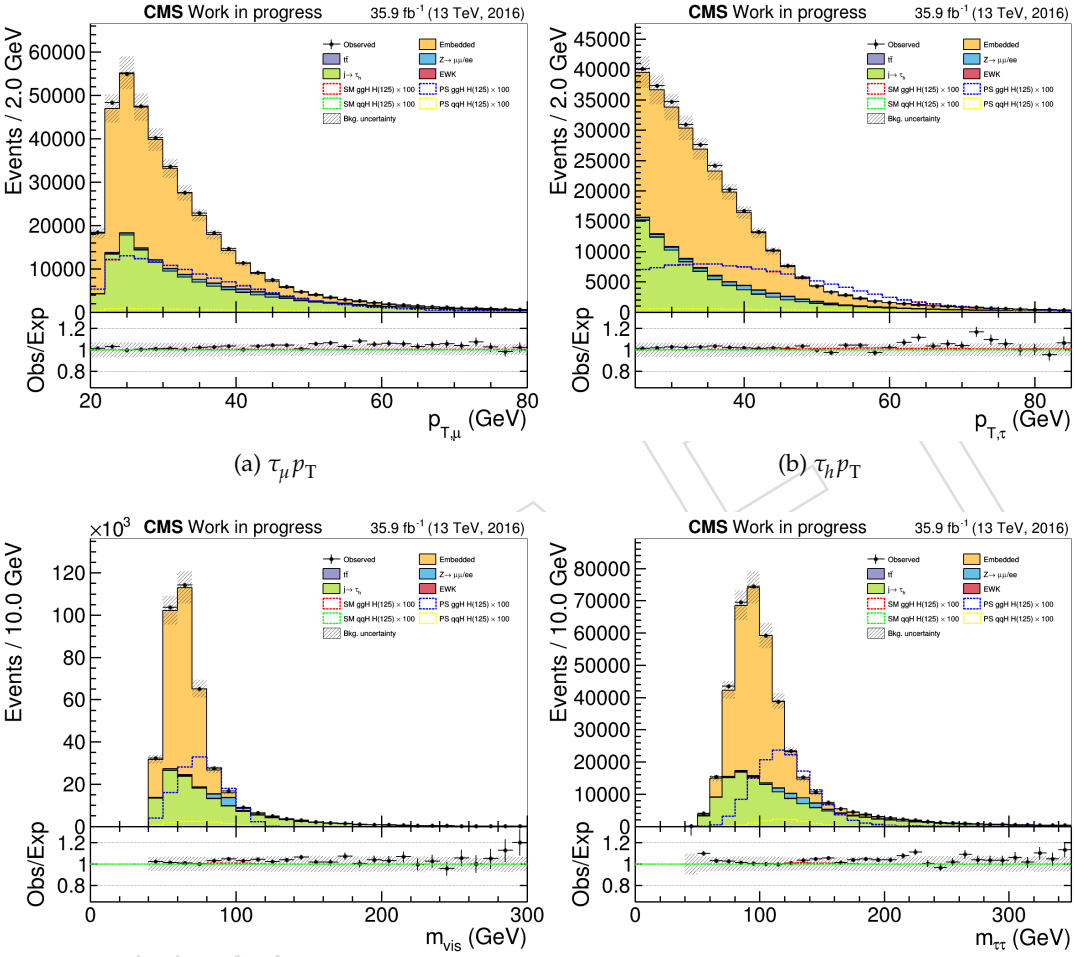

(a) $\tau_\mu p_T$

(b) $\tau_h p_T$

(c) m_{vis}

(d) $m_{\tau\tau}$

Figure 98: Pre-fit 2016 data/background comparisons for $\mu\tau_h$ events are shown for variables used in the multivariate discriminant. In all distributions the background uncertainty shown by the shaped-grey band includes the normalization altering uncertainties

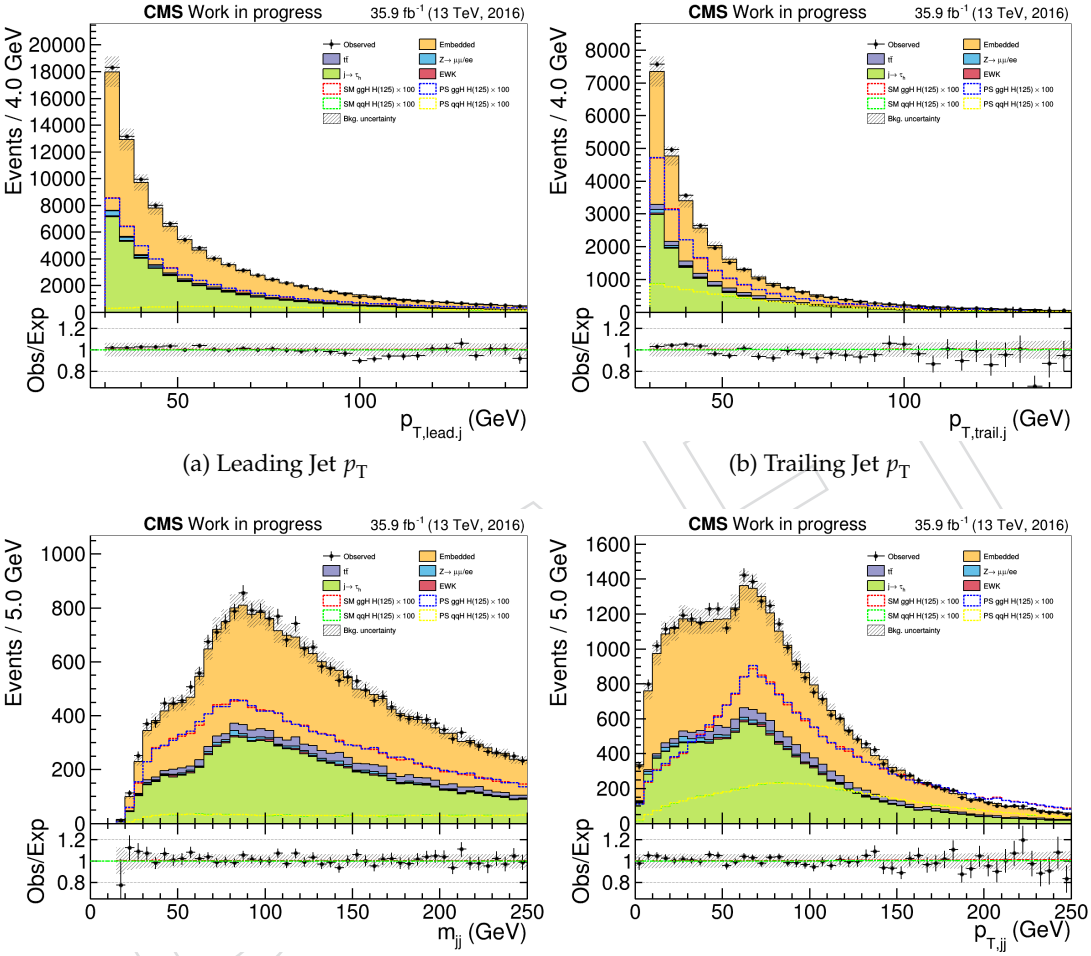

(a) Leading Jet p_{T}

(b) Trailing Jet p_{T}

(c) m_{jj}

(d) p_{Tjj}

Figure 99: Pre-fit 2016 data/background comparisons for $\mu\tau_h$ events are shown for variables used in the multivariate discriminant. In all distributions the background uncertainty shown by the shaped-grey band includes the normalization altering uncertainties

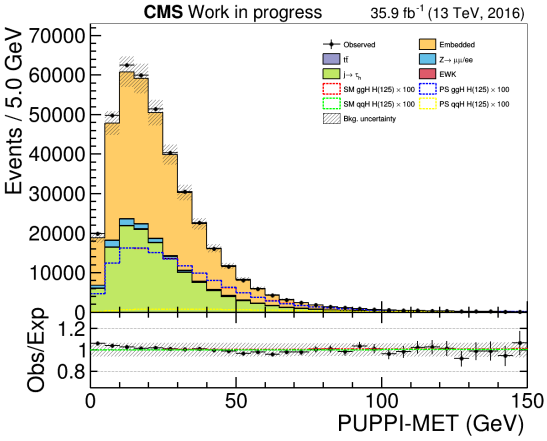

(a) puppi MET

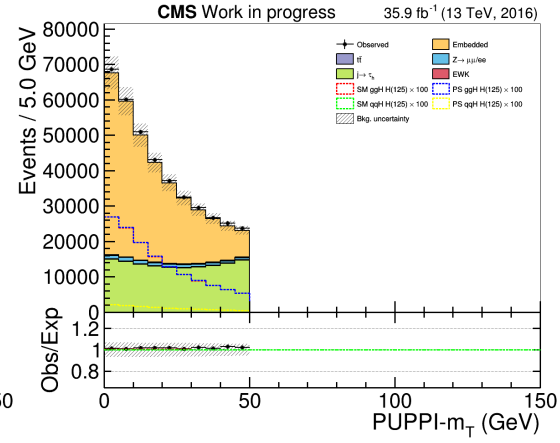

(b) puppi m_{T}

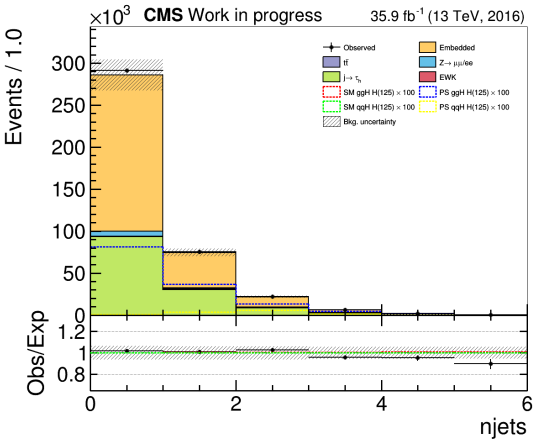

(c) number of jets

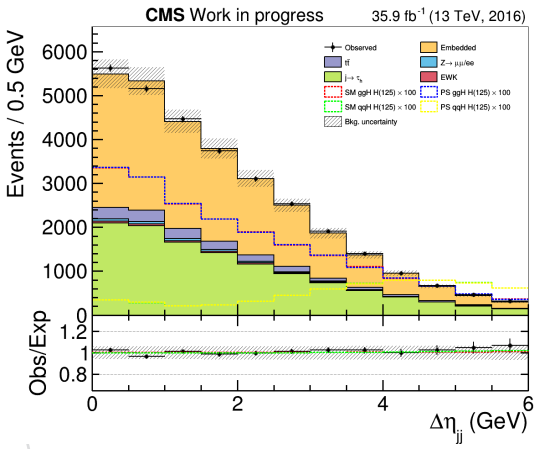

(d) Jet $\Delta\eta$

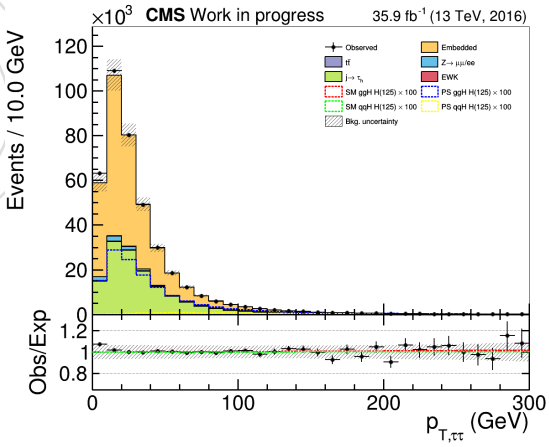

(e) $p_{\tau\tau}$

Figure 100: Pre-fit 2016 data/background comparisons for $\mu\tau_h$ events are shown for variables used in the multivariate discriminant. In all distributions the background uncertainty shown by the shaped-grey band includes the normalization altering uncertainties

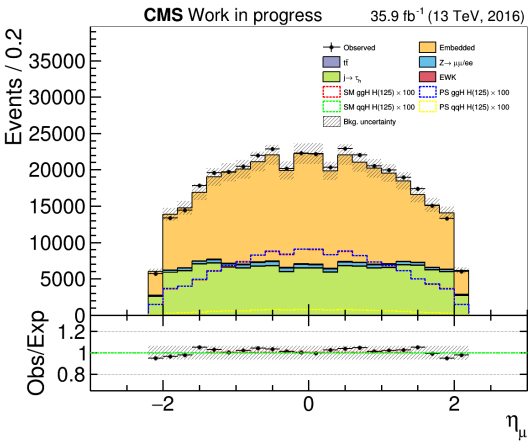

(a) $\tau_\mu \eta$

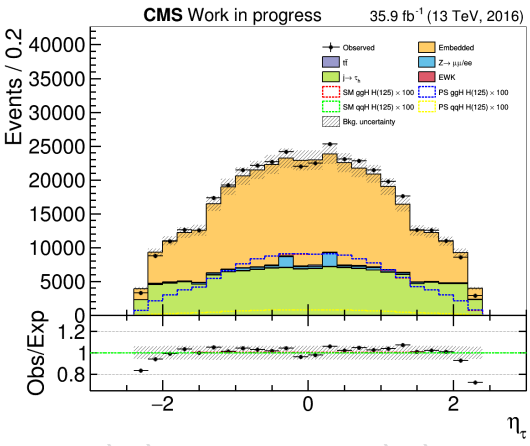

(b) $\tau_h \eta$

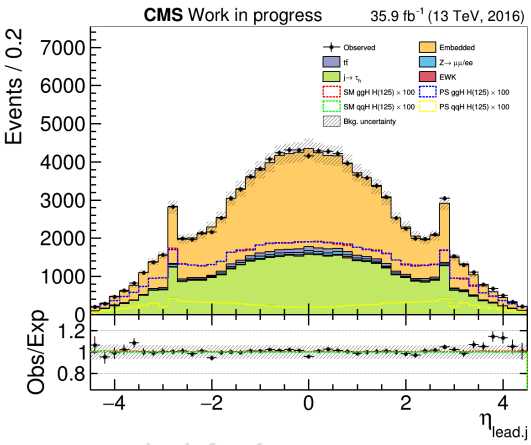

(c) Leading jet η

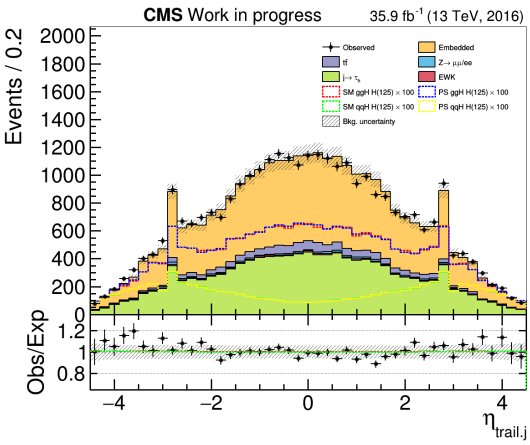

(d) Trailing jet η

Figure 101: Pre-fit 2016 data/background comparisons for $\mu\tau_h$ events are shown for auxilary variables (i.e. not used in the multivariate discriminant). In all distributions the background uncertainty shown by the shaped-grey band includes the full uncertainty model

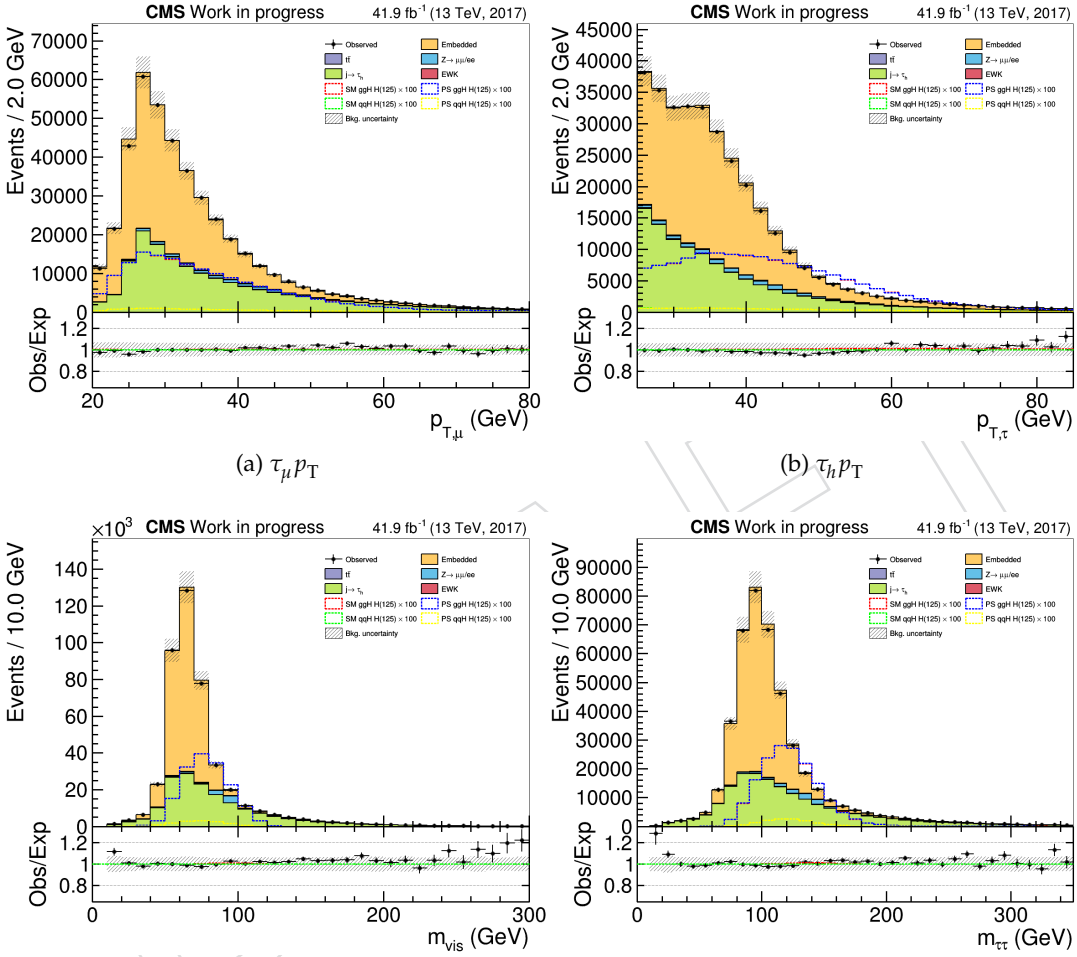

(a) $\tau_\mu p_T$

(b) $\tau_h p_T$

(c) m_{vis}

(d) $m_{\tau\tau}$

Figure 102: Pre-fit 2017 data/background comparisons for $\mu\tau_h$ events are shown for variables used in the multivariate discriminant. In all distributions the background uncertainty shown by the shaped-grey band includes the normalization altering uncertainties

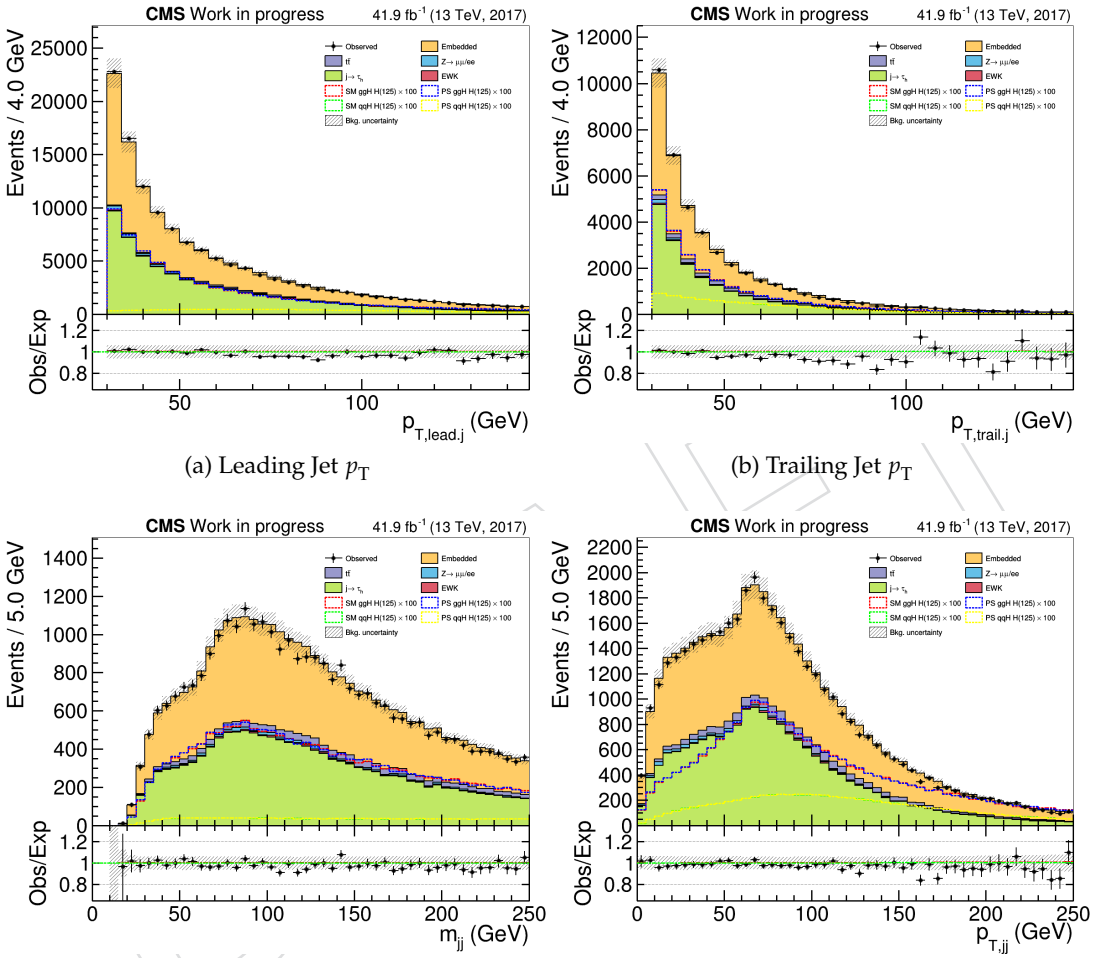

(a) Leading Jet p_{T}

(b) Trailing Jet p_{T}

(c) m_{jj}

(d) p_{Tjj}

Figure 103: Pre-fit 2017 data/background comparisons for $\mu\tau_h$ events are shown for variables used in the multivariate discriminant. In all distributions the background uncertainty shown by the shaped-grey band includes the normalization altering uncertainties

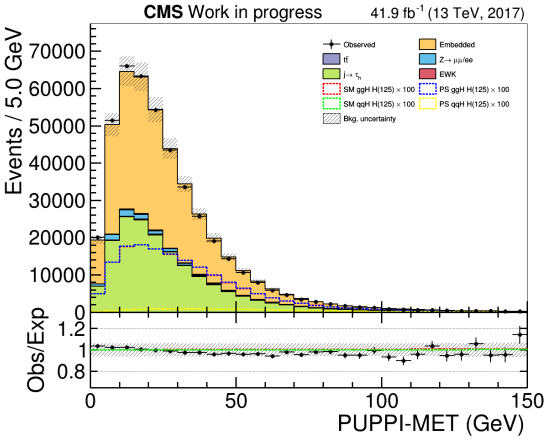

(a) puppi MET

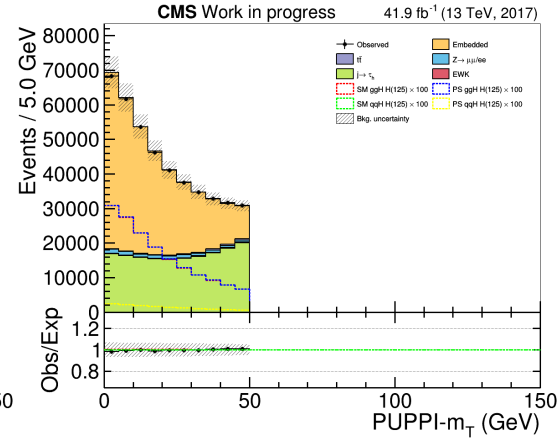

(b) puppi m_{T}

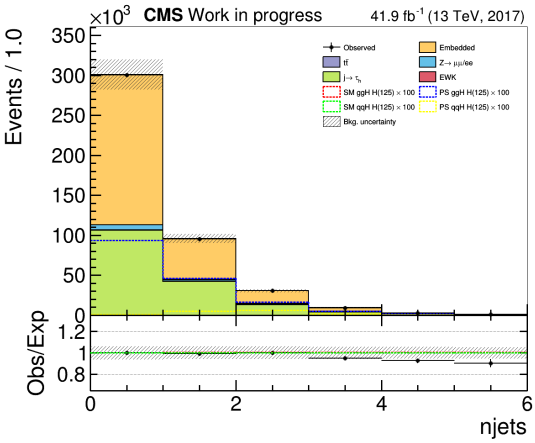

(c) number of jets

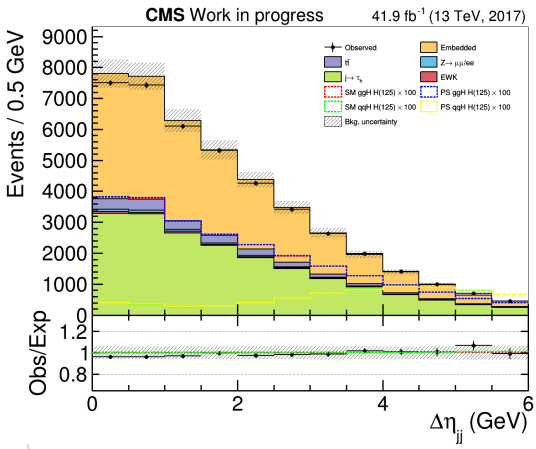

(d) Jet $\Delta\eta$

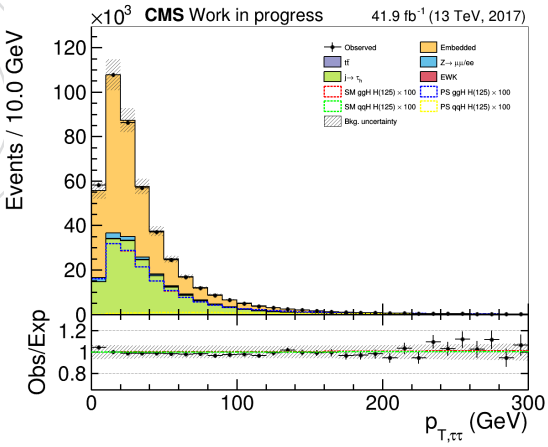

(e) $p_{\tau\tau}$

Figure 104: Pre-fit 2017 data/background comparisons for $\mu\tau_h$ events are shown for variables used in the multivariate discriminant. In all distributions the background uncertainty shown by the shaped-grey band includes the normalization altering uncertainties

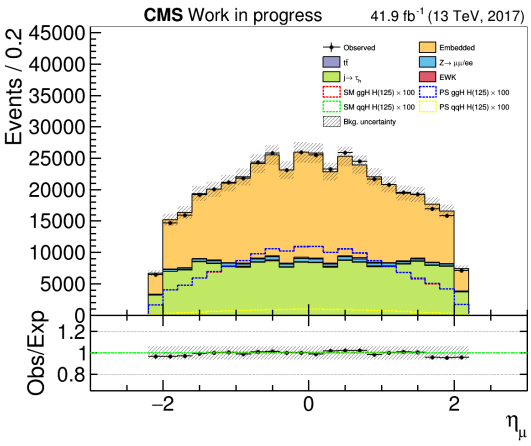

(a) $\tau_\mu \eta$

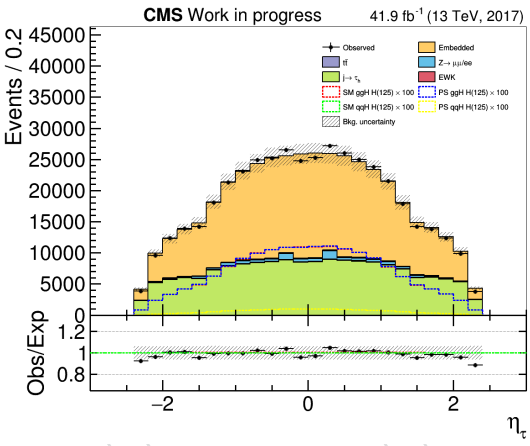

(b) $\tau_h \eta$

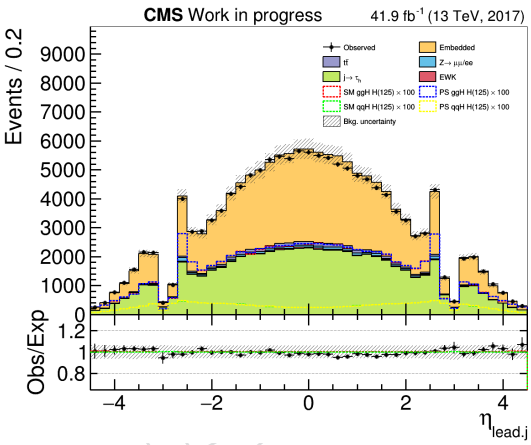

(c) Leading jet η

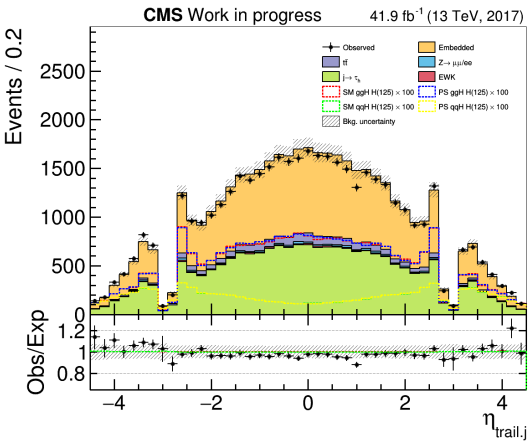

(d) Trailing jet η

Figure 105: Pre-fit 2017 data/background comparisons for $\mu\tau_h$ events are shown for auxilary variables (i.e. not used in the multivariate discriminant). In all distributions the background uncertainty shown by the shaped-grey band includes the full uncertainty model

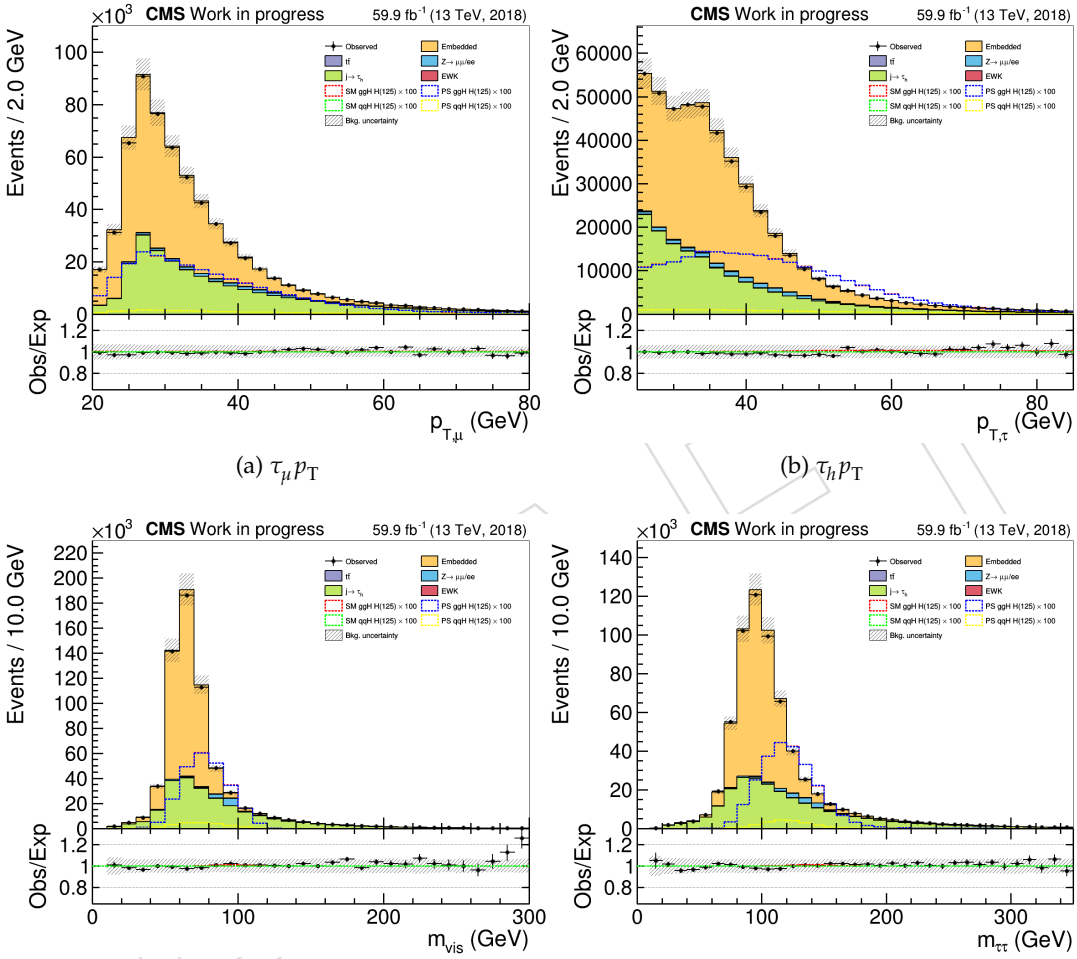

(a) $\tau_\mu p_T$ (b) $\tau_h p_T$

(c) m_{vis} (d) $m_{\tau\tau}$

Figure 106: Pre-fit 2018 data/background comparisons for $\mu\tau_h$ events are shown for variables used in the multivariate discriminant. In all distributions the background uncertainty shown by the shaped-grey band includes the normalization altering uncertainties

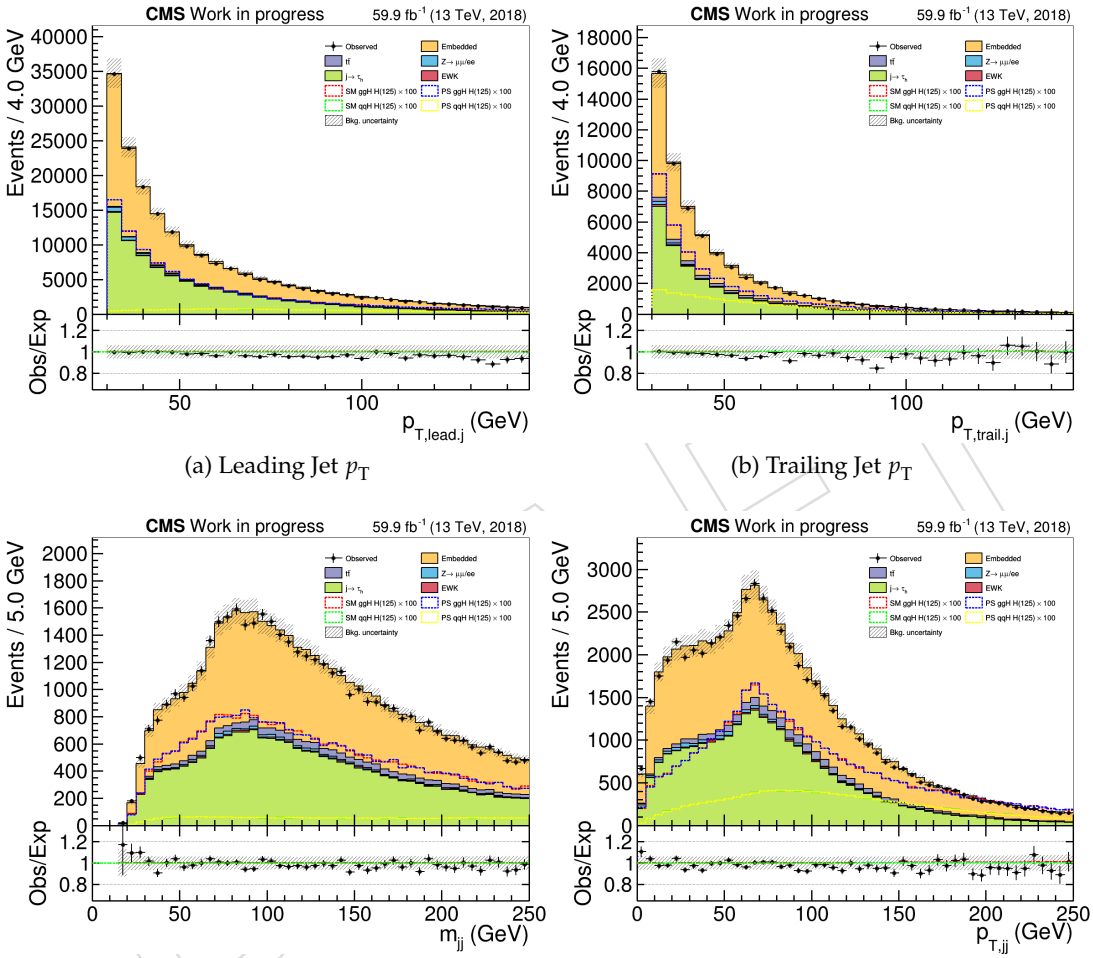

(a) Leading Jet p_T

(b) Trailing Jet p_T

(c) m_{jj}

(d) p_{Tjj}

Figure 107: Pre-fit 2018 data/background comparisons for $\mu\tau_h$ events are shown for variables used in the multivariate discriminant. In all distributions the background uncertainty shown by the shaped-grey band includes the normalization altering uncertainties

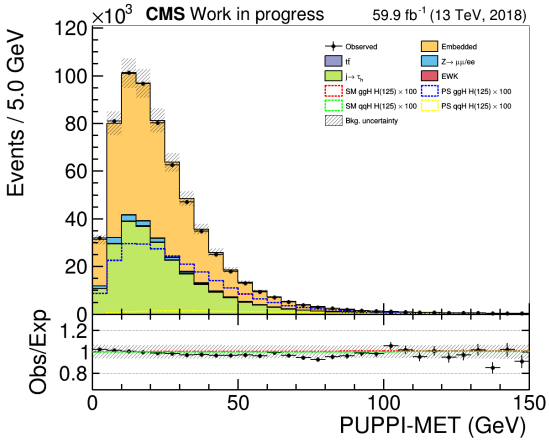

(a) puppi MET

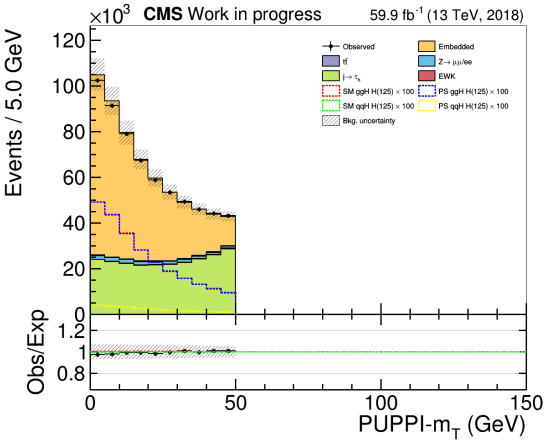

(b) puppi m_{T}

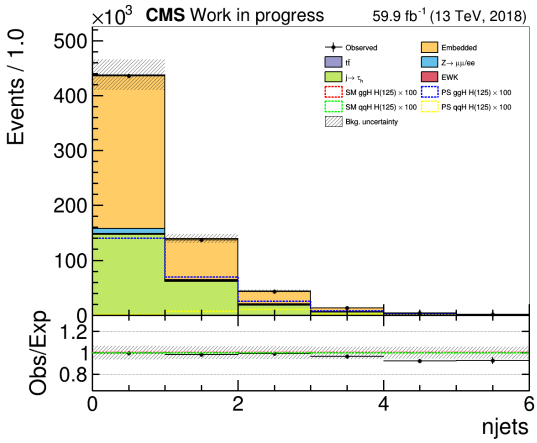

(c) number of jets

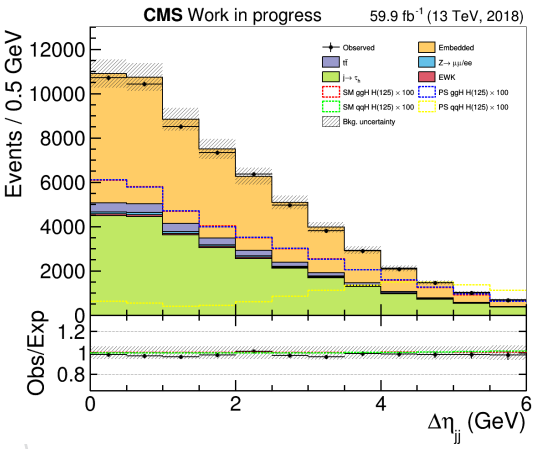

(d) Jet $\Delta\eta$

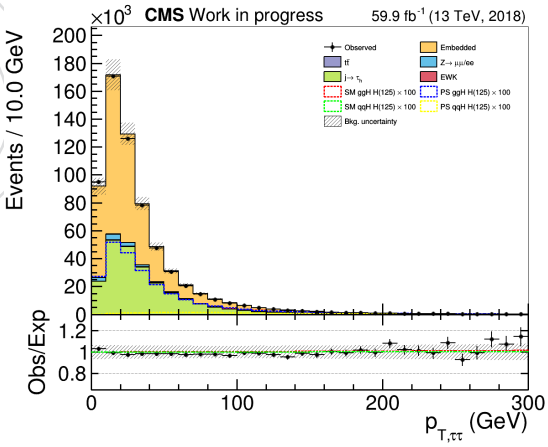

(e) $p_{\tau\tau}$

Figure 108: Pre-fit 2018 data/background comparisons for $\mu\tau_h$ events are shown for variables used in the multivariate discriminant. In all distributions the background uncertainty shown by the shaped-grey band includes the normalization altering uncertainties

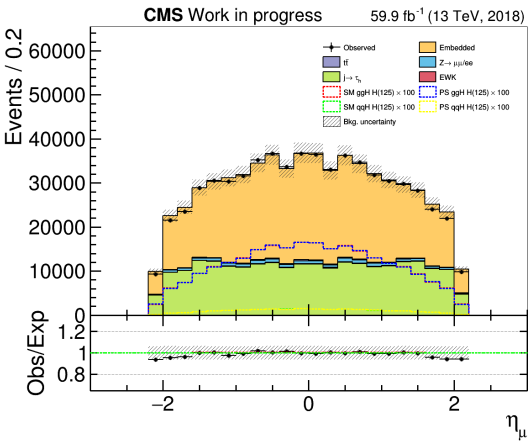

(a) $\tau_\mu \eta$

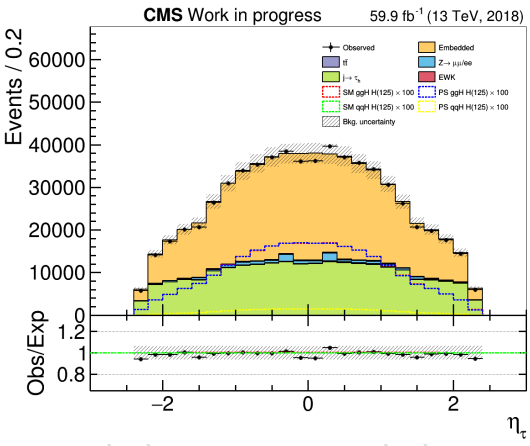

(b) $\tau_h \eta$

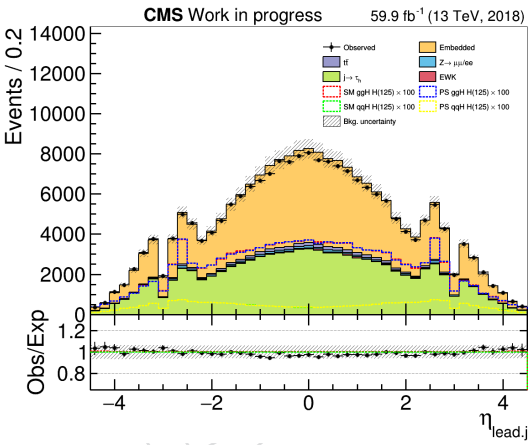

(c) Leading jet η

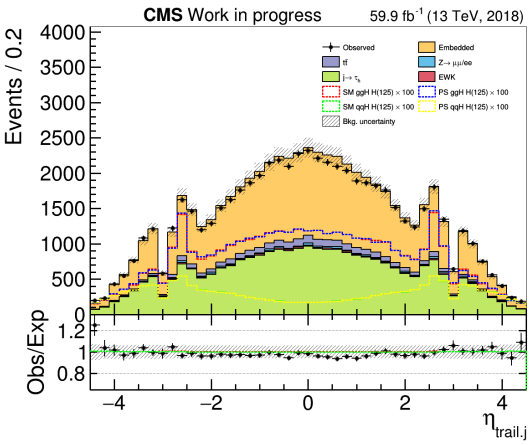

(d) Trailing jet η

Figure 109: Pre-fit 2018 data/background comparisons for $\mu\tau_h$ events are shown for auxilary variables (i.e. not used in the multivariate discriminant). In all distributions the background uncertainty shown by the shaped-grey band includes the full uncertainty model

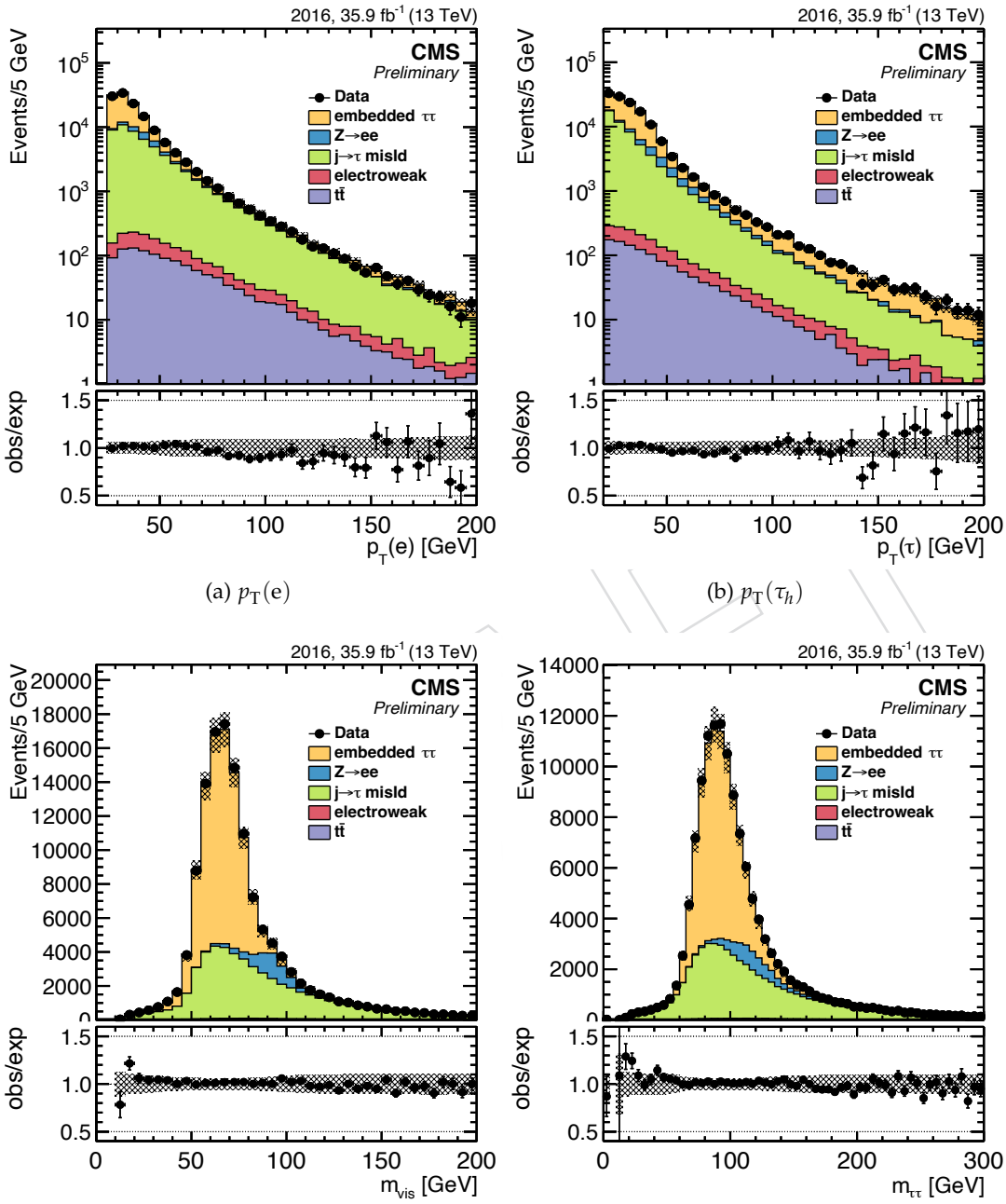

(a) $p_{\mathrm{T}}(\mathrm{e})$

(b) $p_{\mathrm{T}}(\tau_h)$

(c) m_{vis}

(d) $m_{\tau\tau}$

Figure 110: Pre-fit 2016 data/background comparisons for eτ_h events are shown for variables used in the multivariate discriminant. In all distributions the background uncertainty shown by the shaped-grey band includes the normalization altering uncertainties

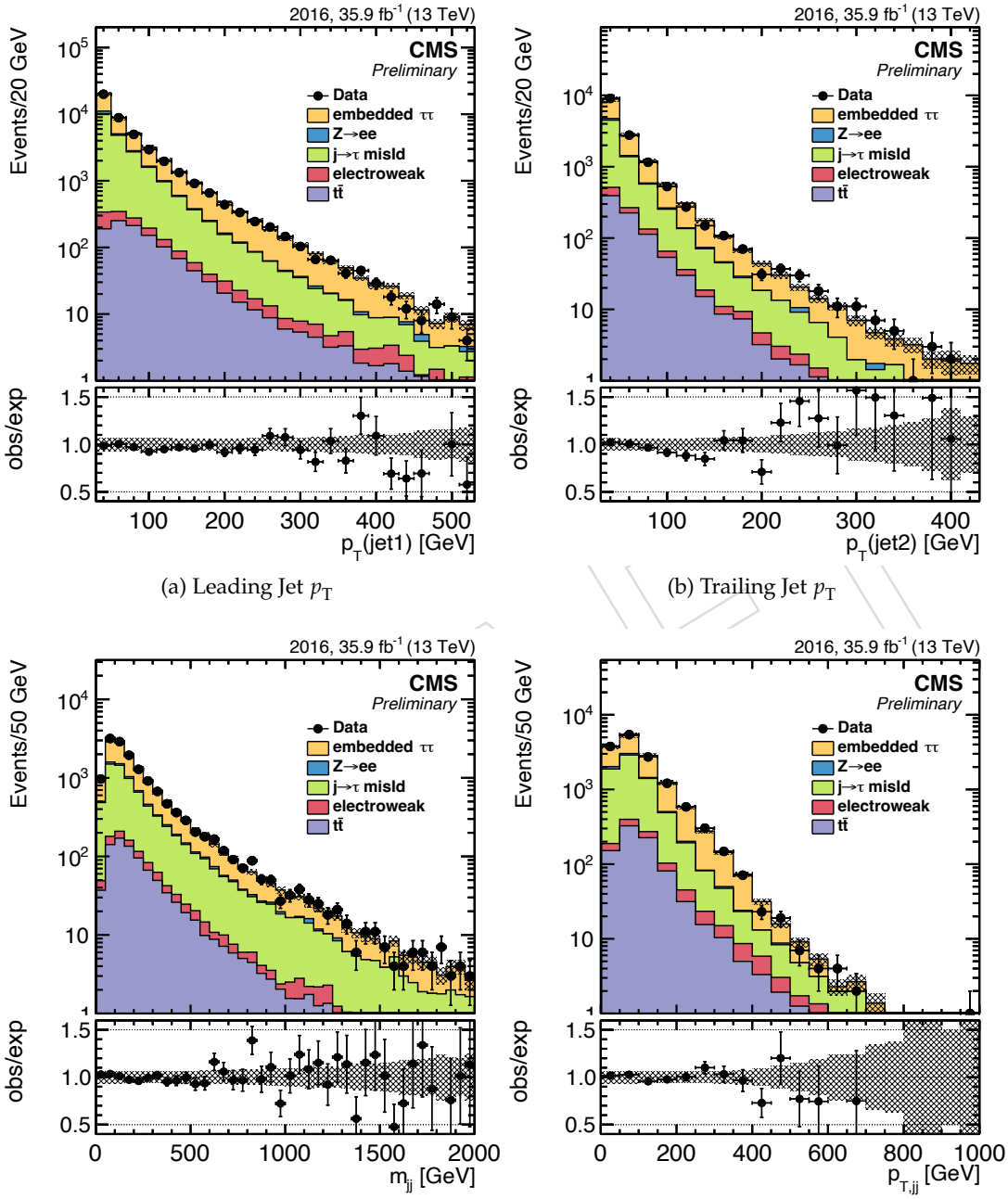

(a) Leading Jet p_T

(b) Trailing Jet p_T

(c) m_{jj}

(d) p_{Tjj}

Figure 111: Pre-fit 2016 data/background comparisons for eτ_h events are shown for variables used in the multivariate discriminant. In all distributions the background uncertainty shown by the shaped-grey band includes the normalization altering uncertainties

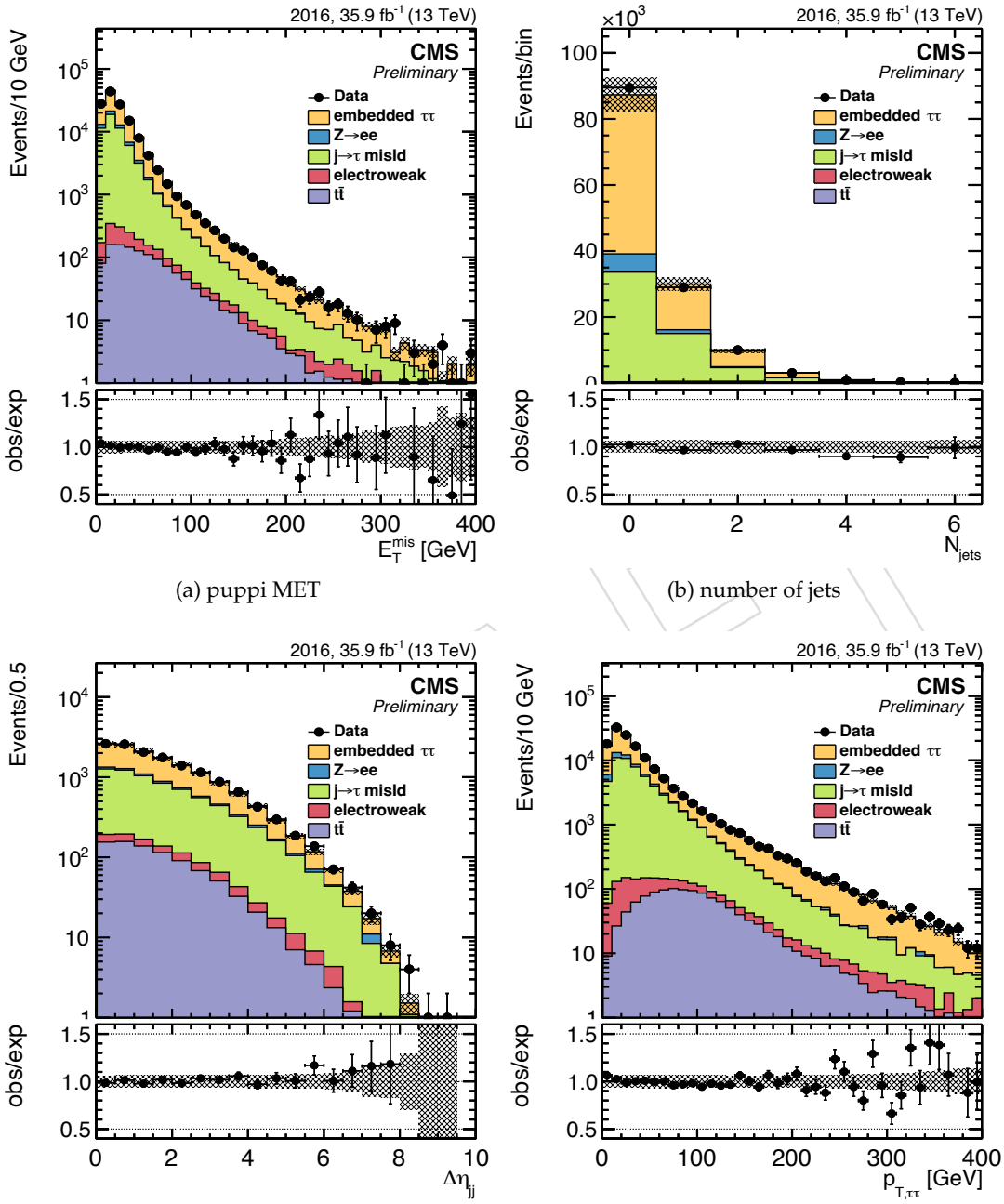

(a) puppi MET

(b) number of jets

(c) Jet $\Delta\eta$

(d) $p_{\tau\tau}$

Figure 112: Pre-fit 2016 data/background comparisons for eτ_h events are shown for variables used in the multivariate discriminant. In all distributions the background uncertainty shown by the shaped-grey band includes the normalization altering uncertainties

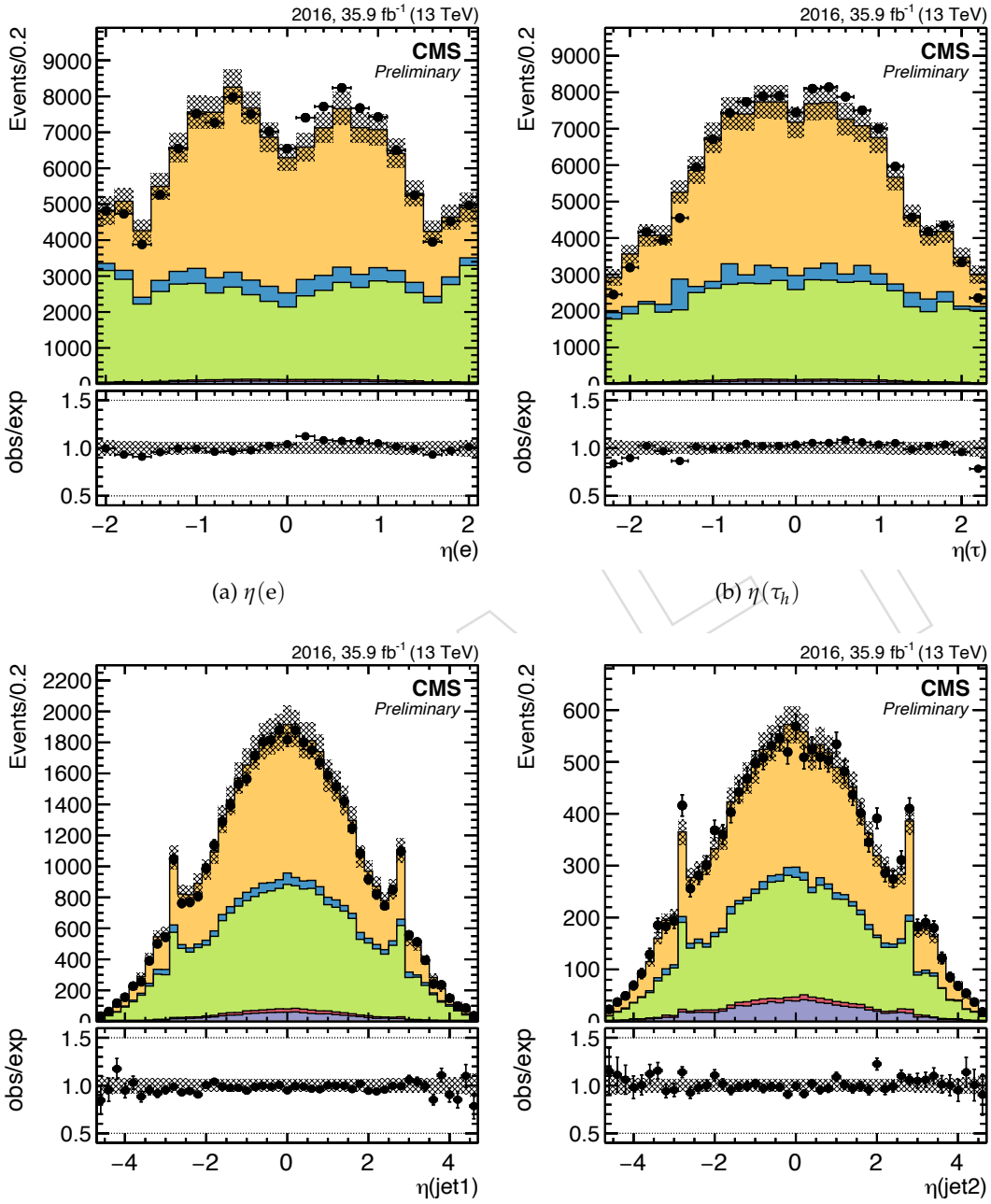

(a) $\eta(\mathrm{e})$

(b) $\eta(\tau_h)$

(c) Leading jet η

(d) Trailing jet η

Figure 113: Pre-fit 2016 data/background comparisons for eτ_h events are shown for auxilary variables (i.e. not used in the multivariate discriminant). In all distributions the background uncertainty shown by the shaped-grey band includes the full uncertainty model

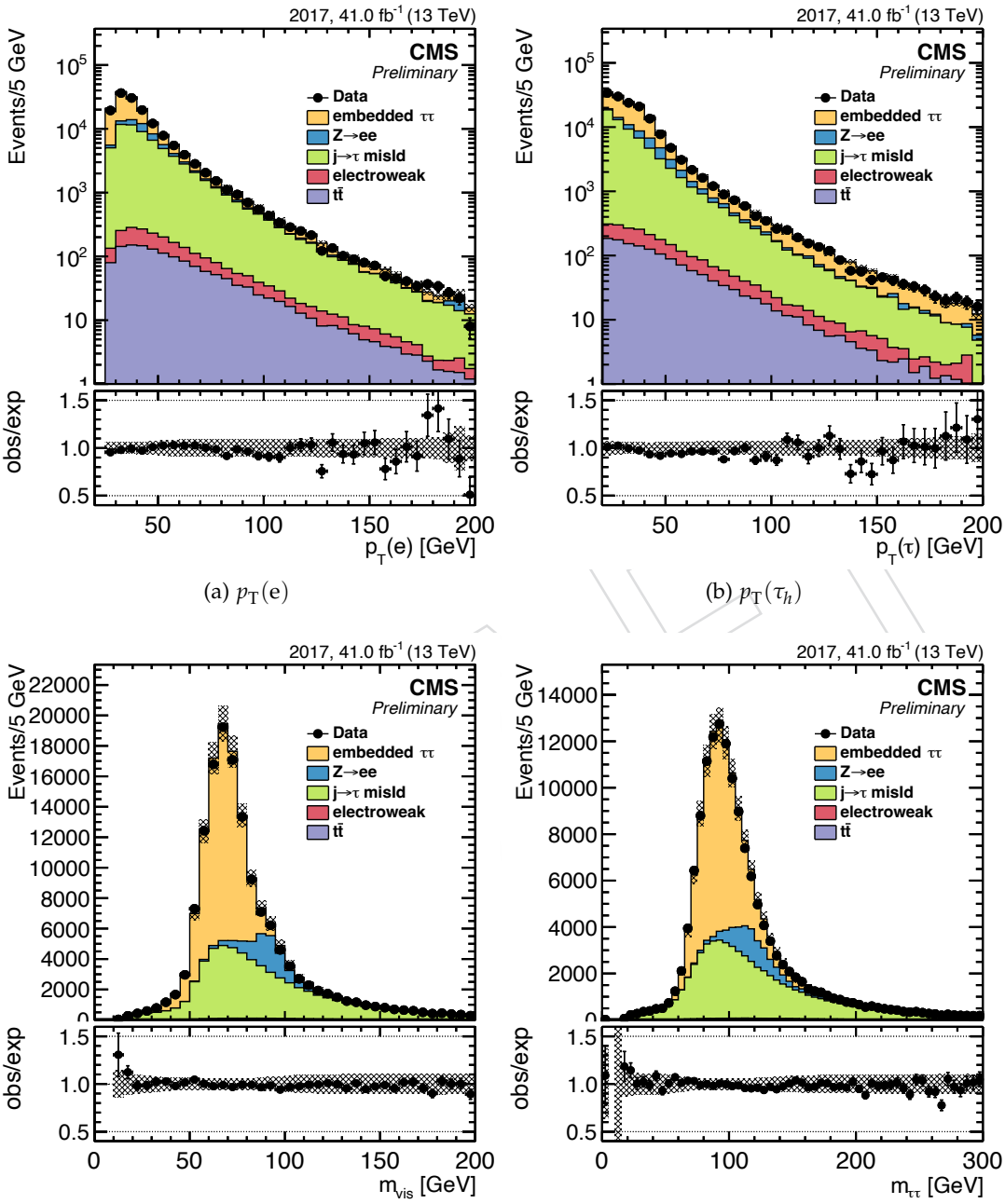

(a) $p_{\mathrm{T}}(\mathrm{e})$

(b) $p_{\mathrm{T}}(\tau_h)$

(c) m_{vis}

(d) $m_{\tau\tau}$

Figure 114: Pre-fit 2017 data/background comparisons for eτ_h events are shown for variables used in the multivariate discriminant. In all distributions the background uncertainty shown by the shaped-grey band includes the normalization altering uncertainties

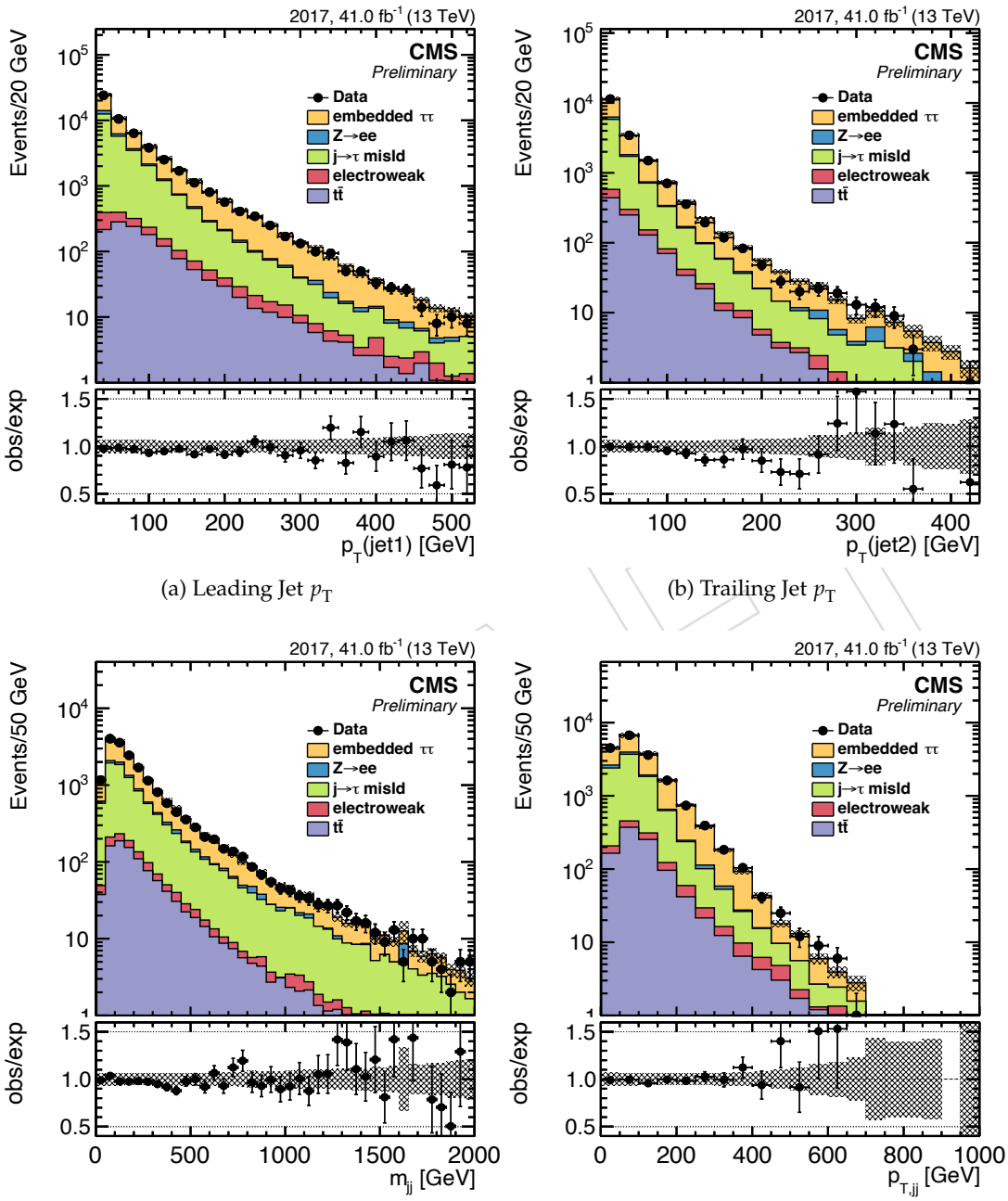

(a) Leading Jet p_T

(b) Trailing Jet p_T

(c) m_{jj}

(d) p_{Tjj}

Figure 115: Pre-fit 2017 data/background comparisons for eτ_h events are shown for variables used in the multivariate discriminant. In all distributions the background uncertainty shown by the shaped-grey band includes the normalization altering uncertainties

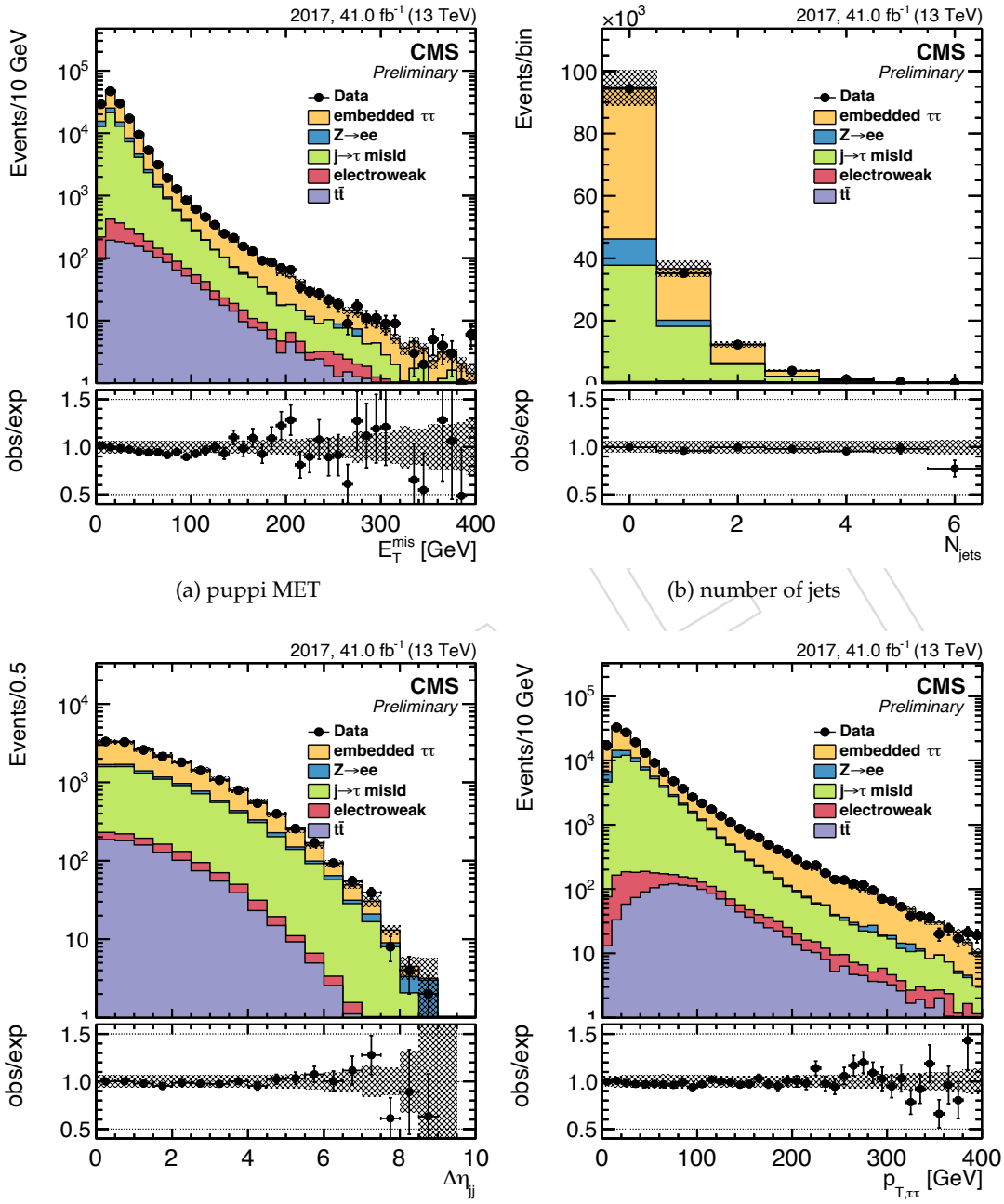

(a) puppi MET

(b) number of jets

(c) Jet $\Delta\eta$

(d) $p_{\tau\tau}$

Figure 116: Pre-fit 2017 data/background comparisons for eτ_h events are shown for variables used in the multivariate discriminant. In all distributions the background uncertainty shown by the shaped-grey band includes the normalization altering uncertainties

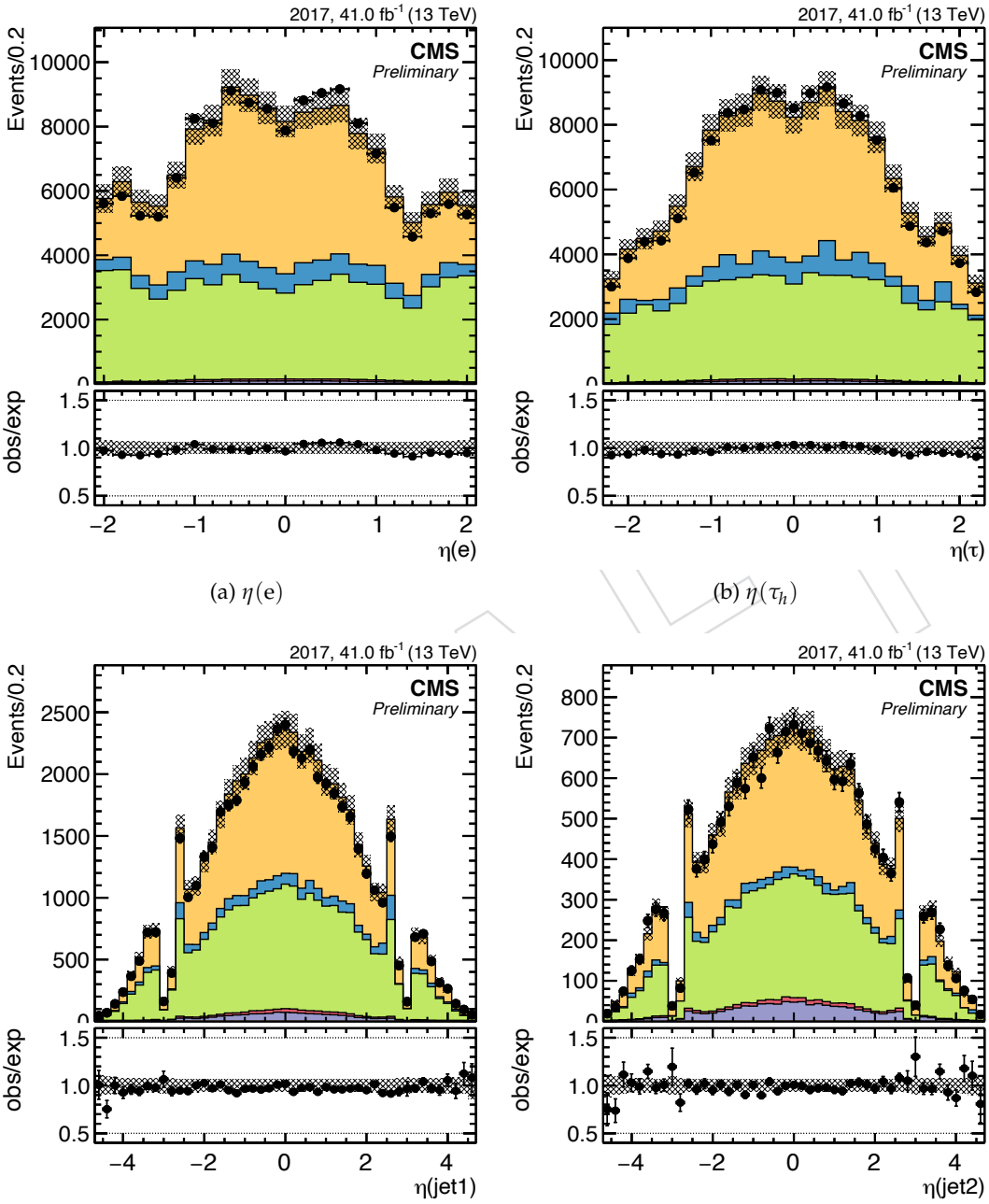

(a) $\eta(\mathrm{e})$

(b) $\eta(\tau_h)$

(c) Leading jet η

(d) Trailing jet η

Figure 117: Pre-fit 2017 data/background comparisons for $\mathrm{e}\tau_h$ events are shown for auxilary variables (i.e. not used in the multivariate discriminant). In all distributions the background uncertainty shown by the shaped-grey band includes the full uncertainty model

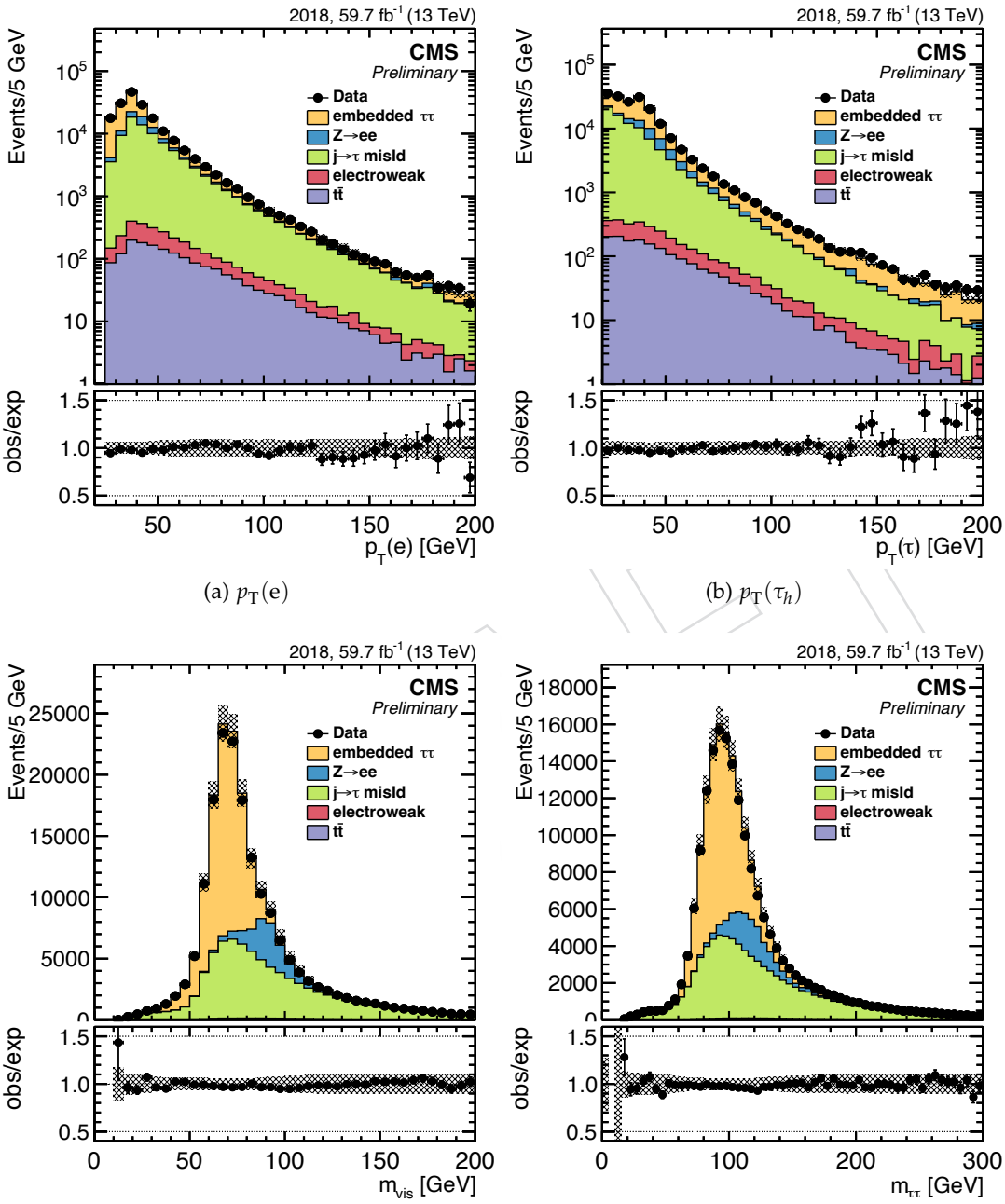

(a) $p_{\mathrm{T}}(\mathrm{e})$

(b) $p_{\mathrm{T}}(\tau_h)$

(c) m_{vis}

(d) $m_{\tau\tau}$

Figure 118: Pre-fit 2018 data/background comparisons for eτ_h events are shown for variables used in the multivariate discriminant. In all distributions the background uncertainty shown by the shaped-grey band includes the normalization altering uncertainties

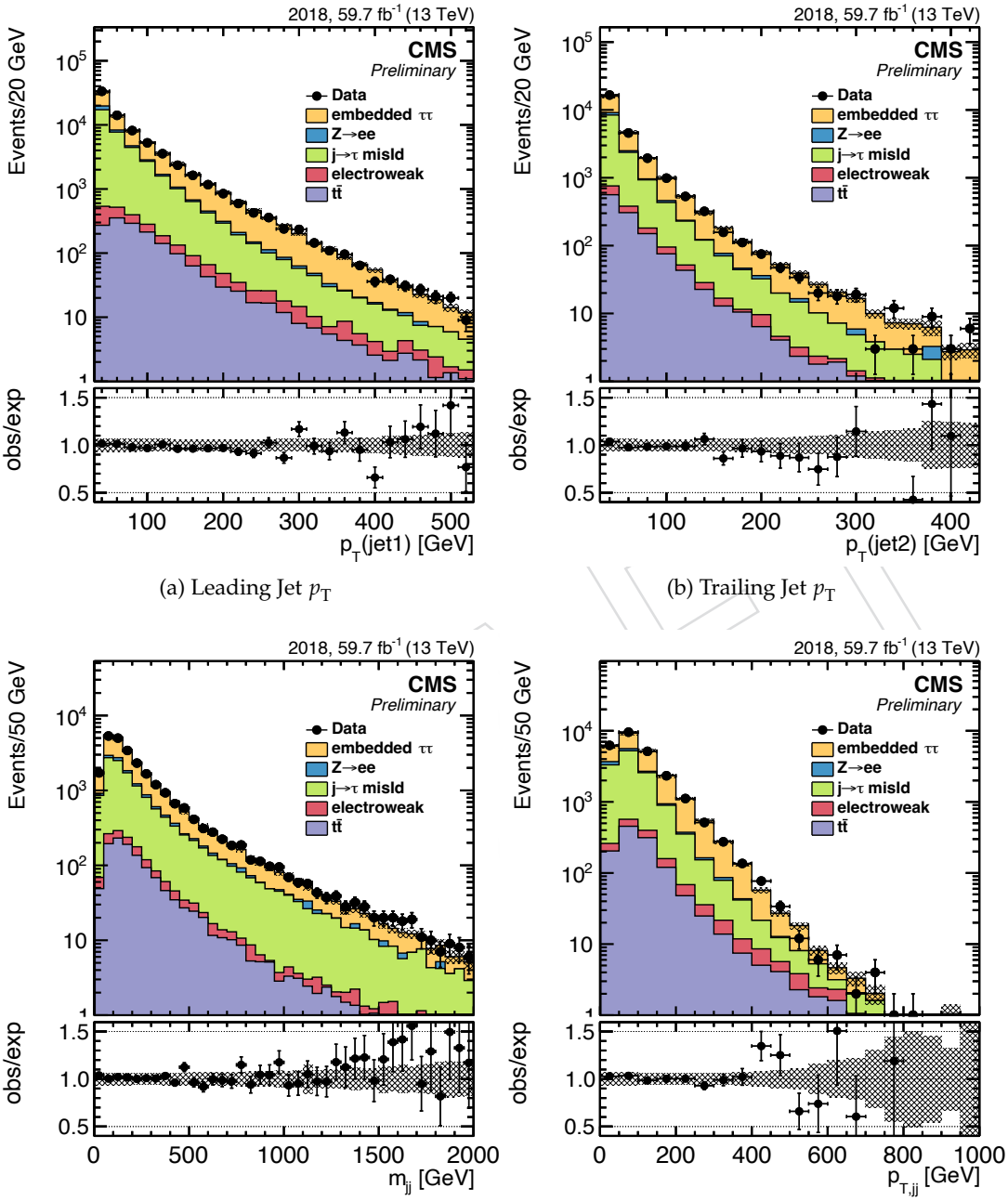

(a) Leading Jet p_T

(b) Trailing Jet p_T

(c) m_{jj}

(d) p_{Tjj}

Figure 119: Pre-fit 2018 data/background comparisons for eτ_h events are shown for variables used in the multivariate discriminant. In all distributions the background uncertainty shown by the shaped-grey band includes the normalization altering uncertainties

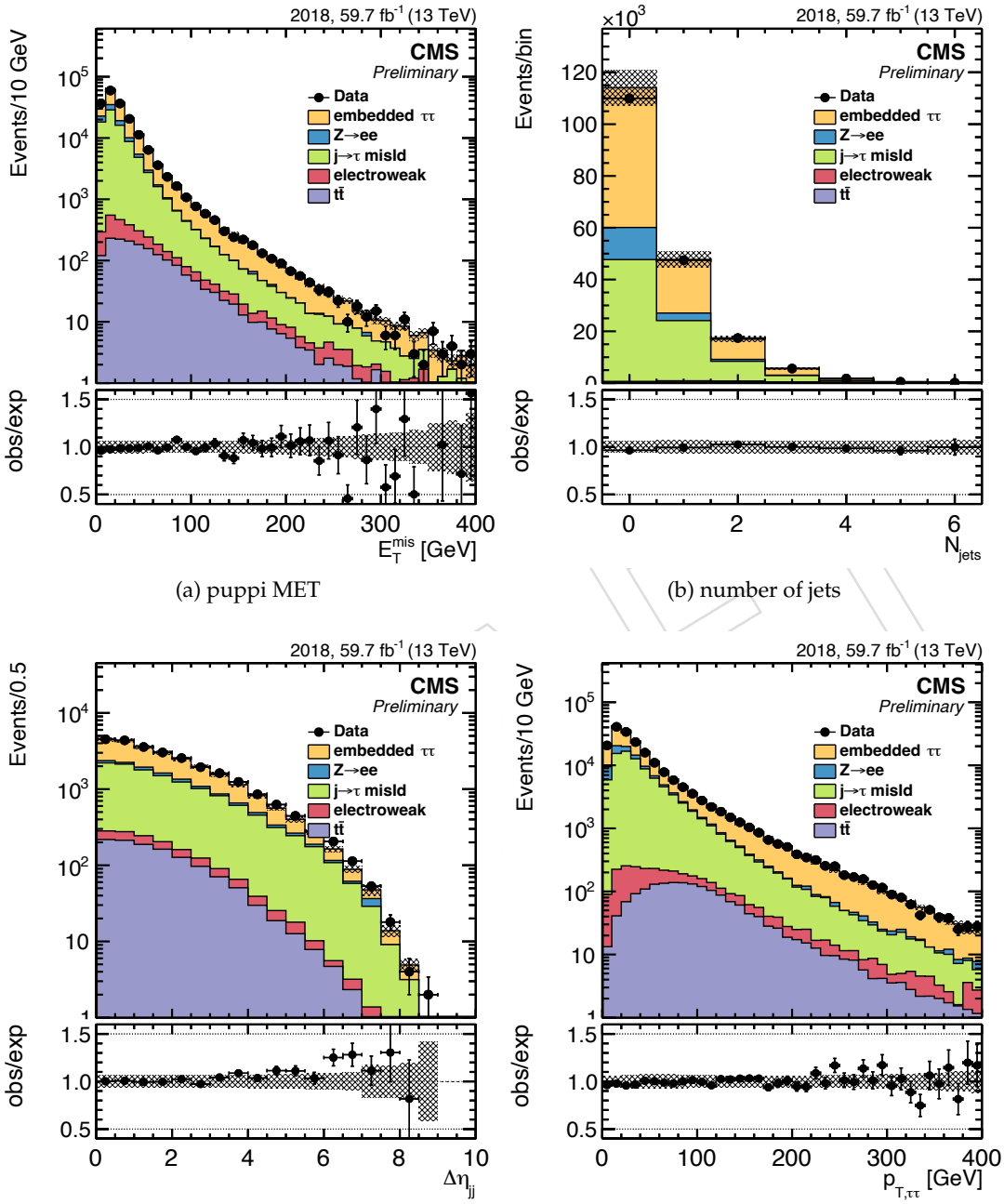

(a) puppi MET

(b) number of jets

(c) Jet $\Delta\eta$

(d) $p_{\tau\tau}$

Figure 120: Pre-fit 2018 data/background comparisons for eτ_h events are shown for variables used in the multivariate discriminant. In all distributions the background uncertainty shown by the shaped-grey band includes the normalization altering uncertainties

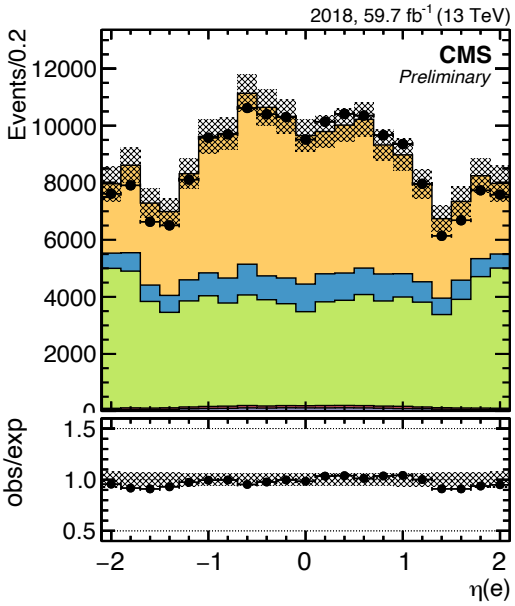

(a) $\eta(\mathrm{e})$

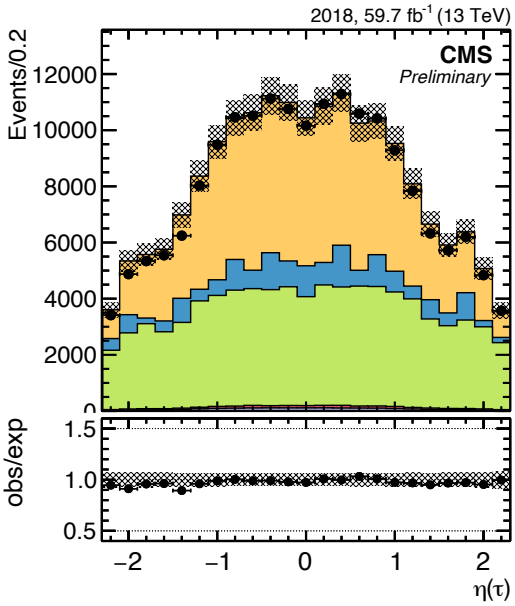

(b) $\eta(\tau_h)$

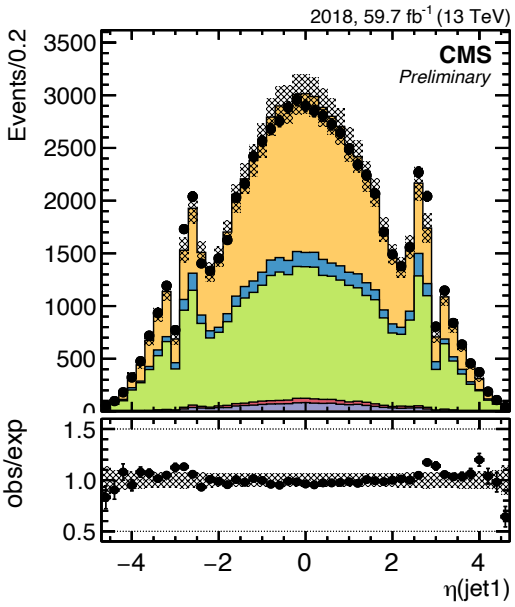

(c) Leading jet η

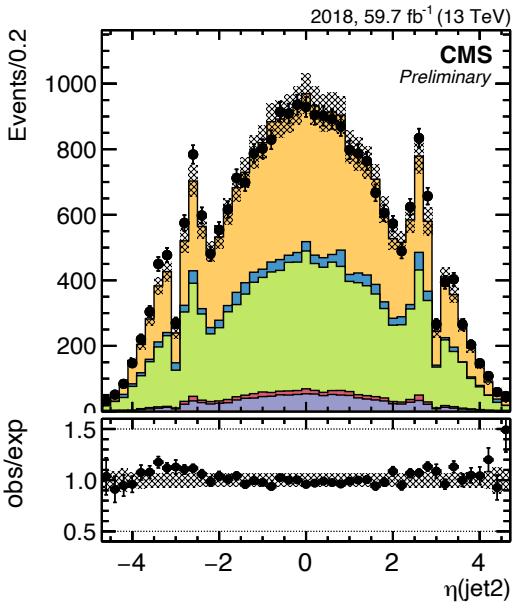

(d) Trailing jet η

Figure 121: Pre-fit 2018 data/background comparisons for eτ_h events are shown for auxilary variables (i.e. not used in the multivariate discriminant). In all distributions the background uncertainty shown by the shaped-grey band includes the full uncertainty model

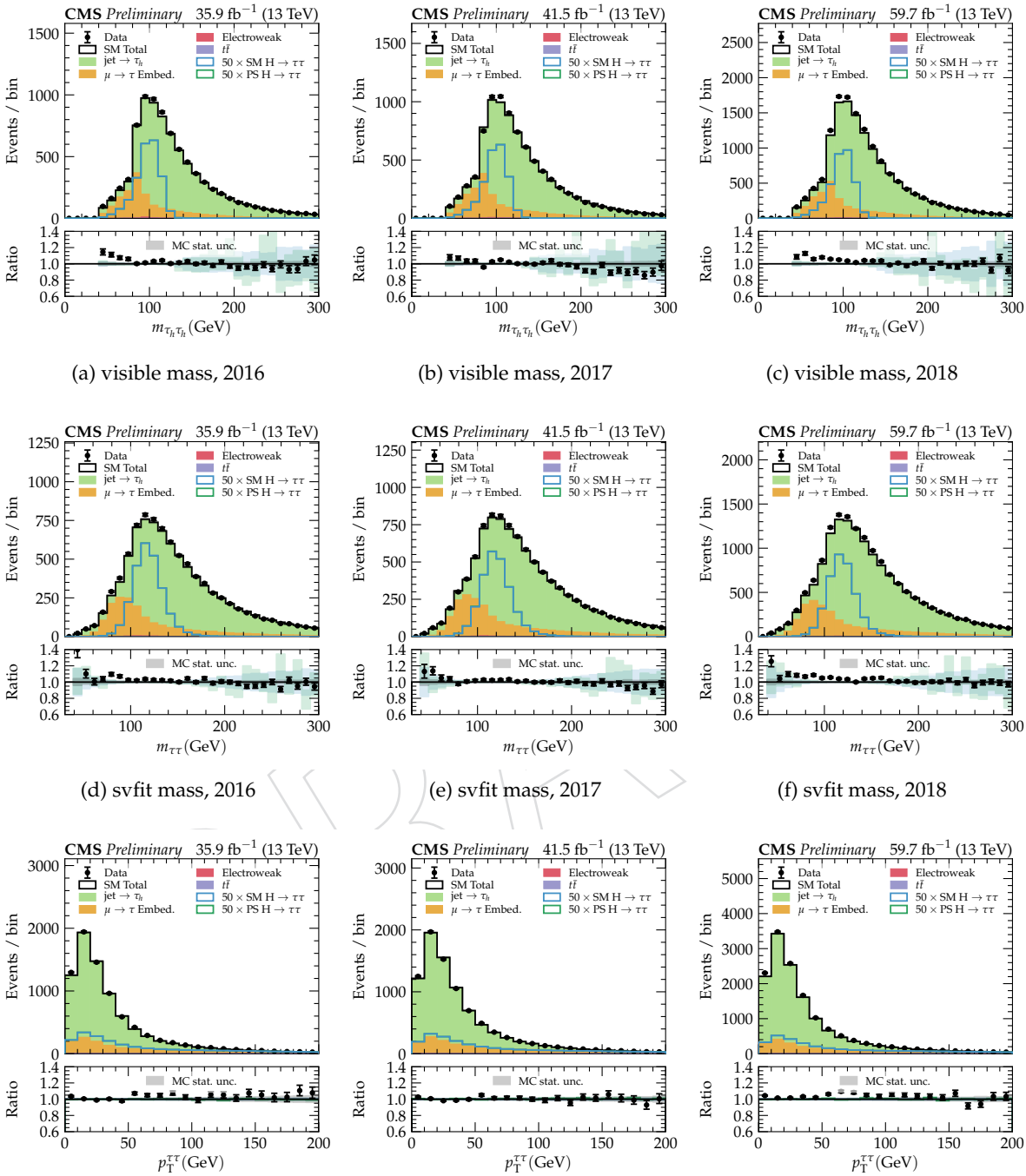

(a) visible mass, 2016 (b) visible mass, 2017 (c) visible mass, 2018

(d) svfit mass, 2016 (e) svfit mass, 2017 (f) svfit mass, 2018

(g) higgs p_T, 2016 (h) higgs p_T, 2017 (i) higgs p_T, 2018

Figure 122: Inclusive, prefit plots for 2016, 2017 and 2018 of the input features to the BDT. The signals are scaled by a factor of 50 and the uncertainty band considers only statistical uncertainty. Additionally, the ratio of signals with respect to the SM signal is shown including the uncertainty band on this showing statistical uncertainty.

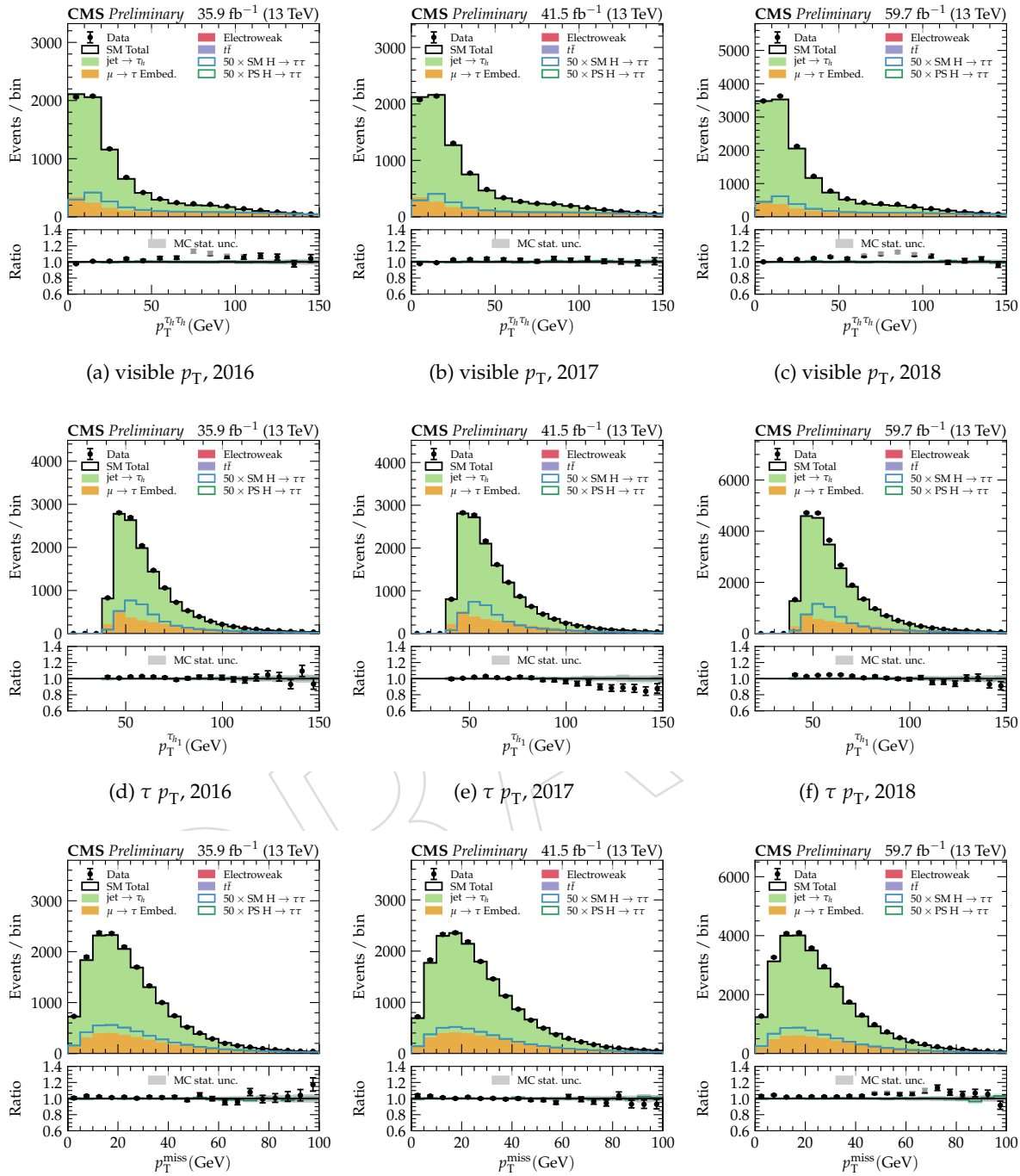

(a) visible p_T, 2016 (b) visible p_T, 2017 (c) visible p_T, 2018

(d) τ p_T, 2016 (e) τ p_T, 2017 (f) τ p_T, 2018

(g) p_T^{miss}, 2016 (h) p_T^{miss}, 2017 (i) p_T^{miss}, 2018

Figure 123: Inclusive, prefit plots for 2016, 2017 and 2018 of the input features to the BDT. The signals are scaled by a factor of 50 and the uncertainty band considers only statistical uncertainty. Additionally, the ratio of signals with respect to the SM signal is shown including the uncertainty band on this showing statistical uncertainty.

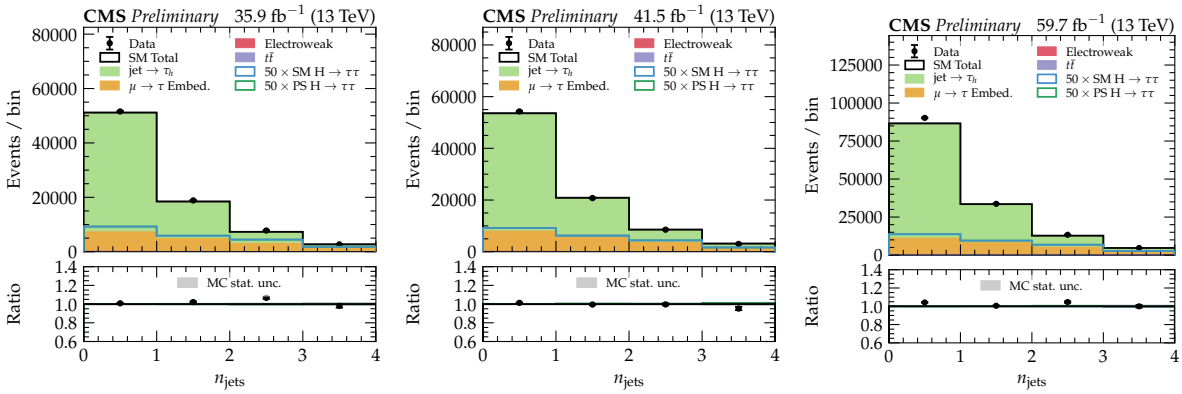

(a) number of jets, 2016 (b) number of jets, 2017 (c) number of jets, 2018

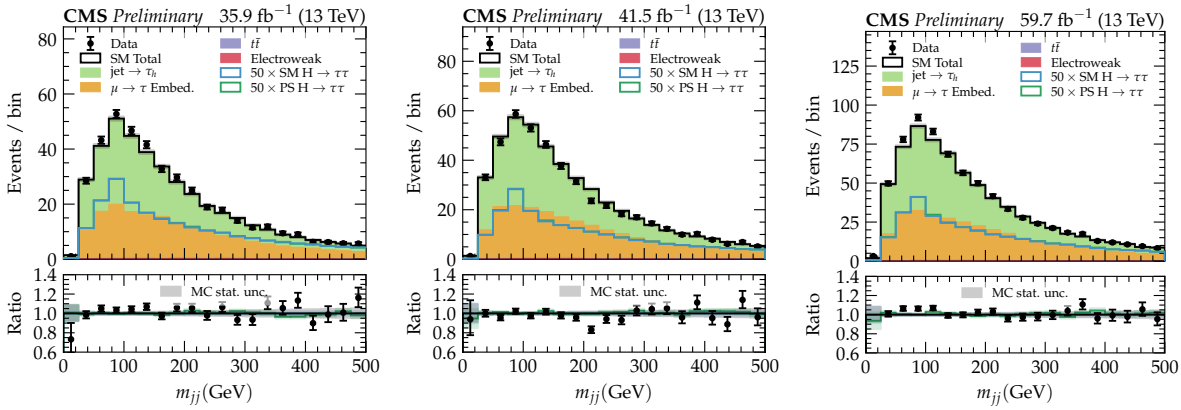

(d) dijet mass, 2016 (e) dijet mass, 2017 (f) dijet mass, 2018

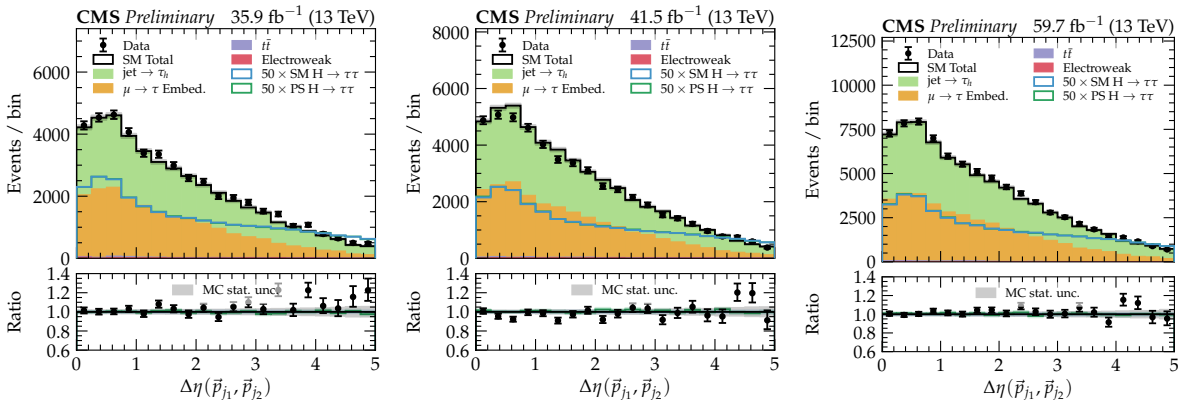

(g) $|\Delta\eta|$ of jets, 2016 (h) $|\Delta\eta|$ of jets, 2017 (i) $|\Delta\eta|$ of jets, 2018

Figure 124: Inclusive, prefit plots for 2016, 2017 and 2018 of the input features to the BDT. The signals are scaled by a factor of 50 and the uncertainty band considers only statistical uncertainty. Additionally, the ratio of signals with respect to the SM signal is shown including the uncertainty band on this showing statistical uncertainty.

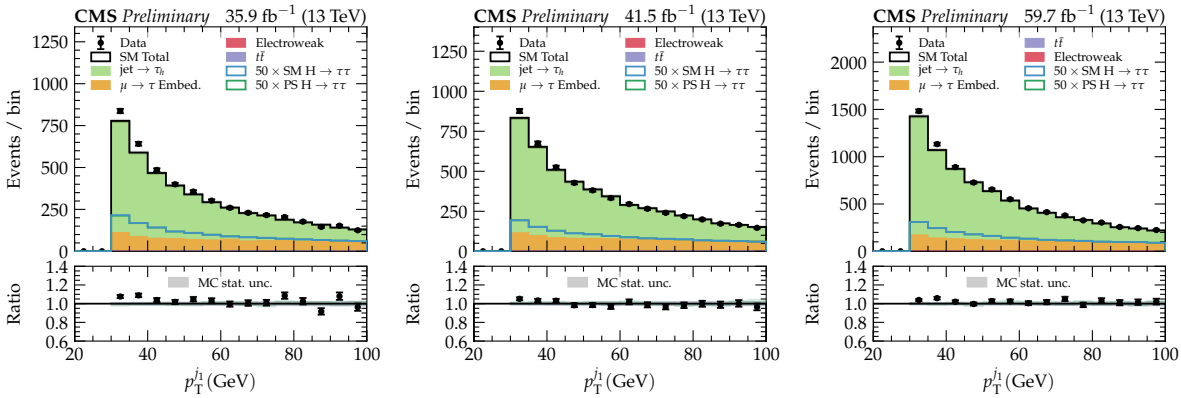

(a) leading jet p_T, 2016 (b) leading jet p_T, 2017 (c) leading jet p_T, 2018

Figure 125: Inclusive, prefit plots for 2016, 2017 and 2018 of the input features to the BDT. The signals are scaled by a factor of 50 and the uncertainty band considers only statistical uncertainty. Additionally, the ratio of signals with respect to the SM signal is shown including the uncertainty band on this showing statistical uncertainty.

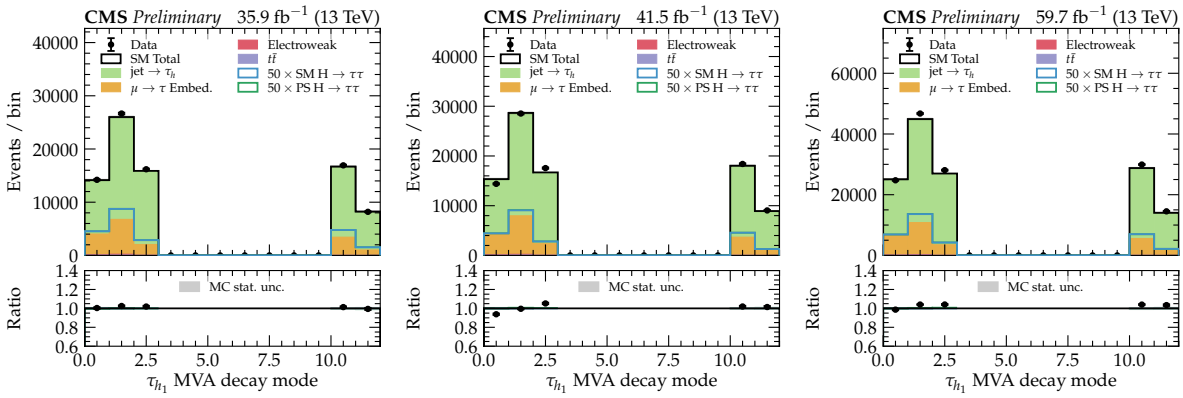

(a) leading τ_h MVA DM, 2016

(b) leading τ_h MVA DM, 2017

(c) leading τ_h MVA DM, 2018

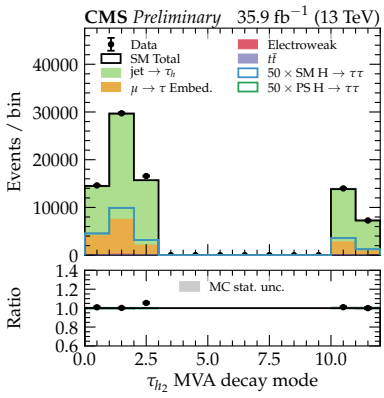

(d) sub-leading τ_h MVA DM, 2016

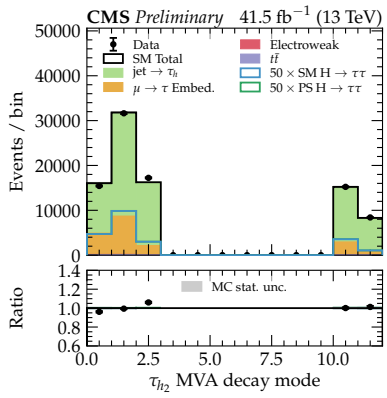

(e) sub-leading τ_h MVA DM, 2017

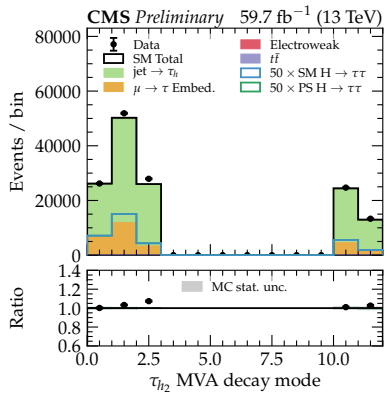

(f) sub-leading τ_h MVA DM, 2018

Figure 126: Inclusive, prefit plots for 2016, 2017 and 2018 of the τ_h MVA decay mode. The signals are scaled by a factor of 50 and the uncertainty band considers only statistical uncertainty. Additionally, the ratio of signals with respect to the SM signal is shown including the uncertainty band on this showing statistical uncertainty.

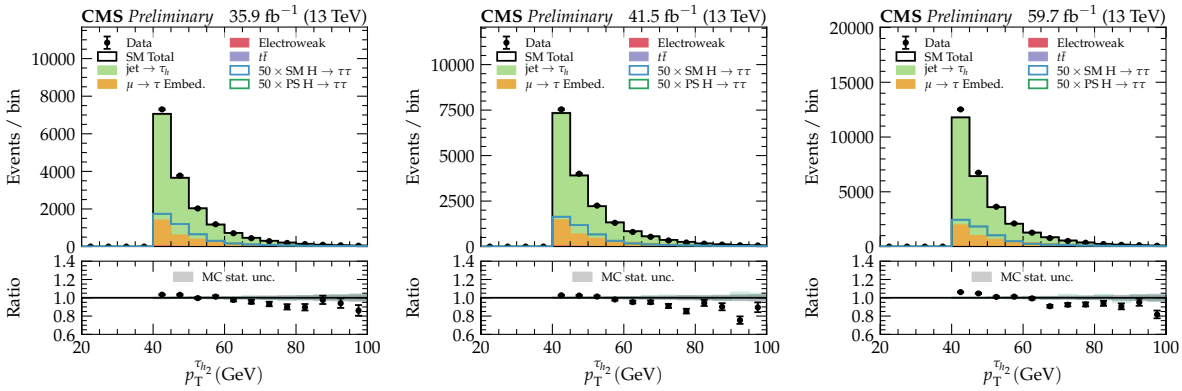

(a) subleading τ_h p_T, 2016

(b) subleading τ_h p_T, 2017

(c) subleading τ_h p_T, 2018

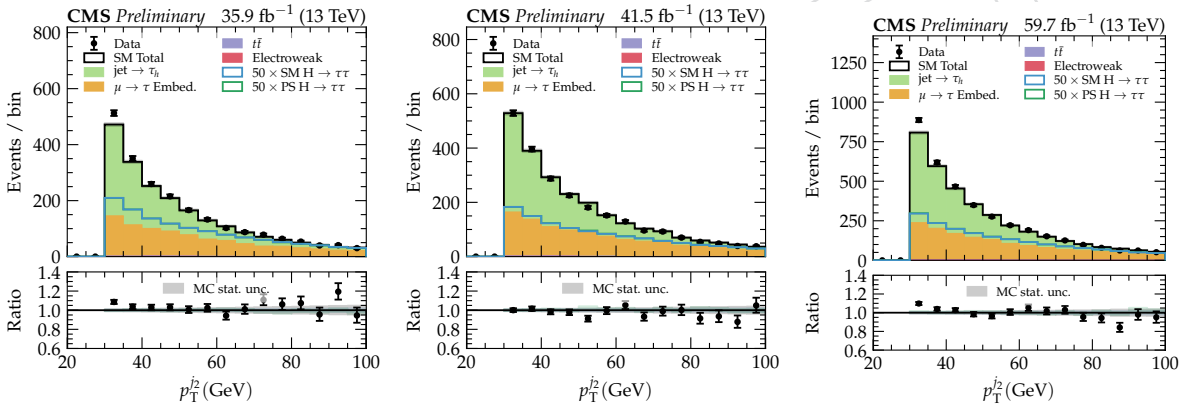

(d) subleading jet p_T, 2016

(e) subleading jet p_T, 2017

(f) subleading jet p_T, 2018

Figure 127: Inclusive, prefit plots for 2016, 2017 and 2018 of the subleading τ_h and jet p_T. The signals are scaled by a factor of 50 and the uncertainty band considers only statistical uncertainty. Additionally, the ratio of signals with respect to the SM signal is shown including the uncertainty band on this showing statistical uncertainty.

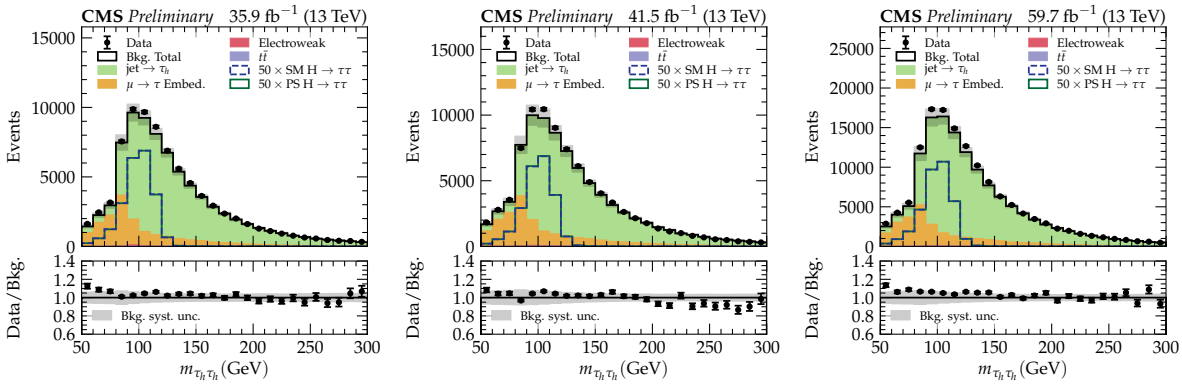

(a) visible mass, 2016 (b) visible mass, 2017 (c) visible mass, 2018

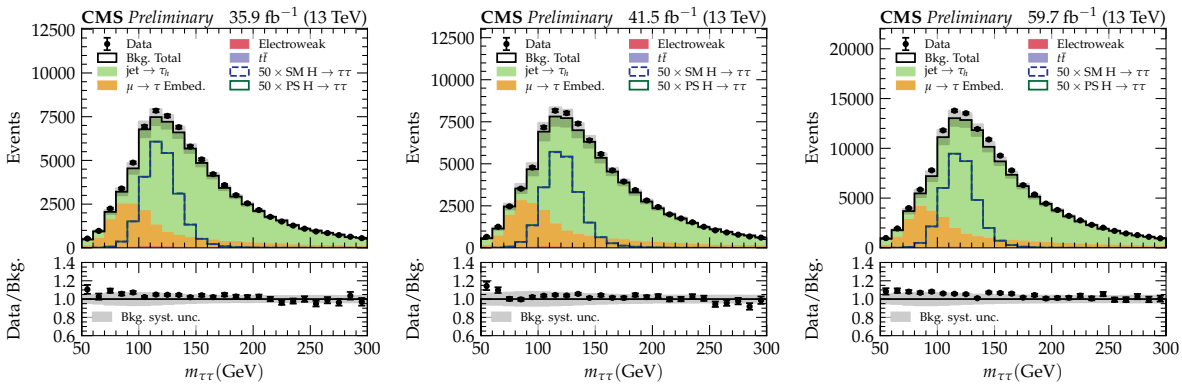

(d) svfit mass, 2016 (e) svfit mass, 2017 (f) svfit mass, 2018

Figure 128: Additional, inclusive, prefit plots for 2016, 2017 and 2018 of the mass variables with the full uncertainty. The signals are scaled by a factor of 50.

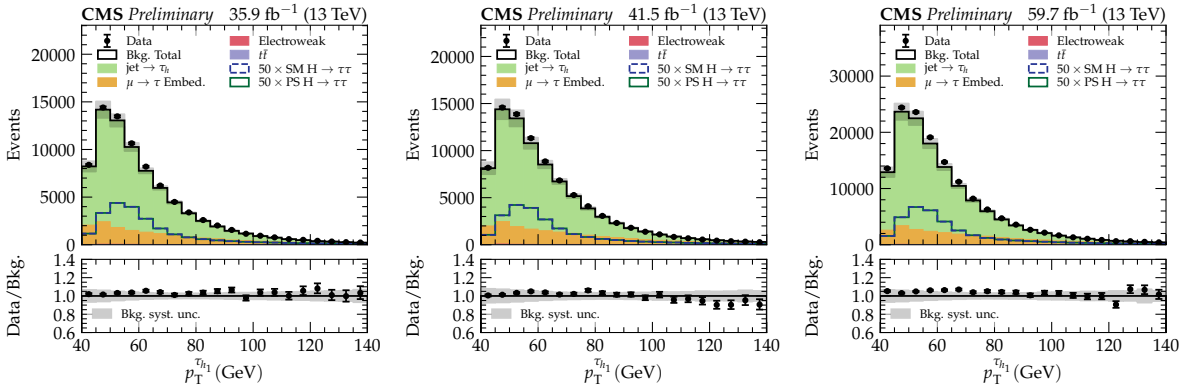

(a) leading τ_h p_T, 2016 (b) leading τ_h p_T, 2017 (c) leading τ_h p_T, 2018

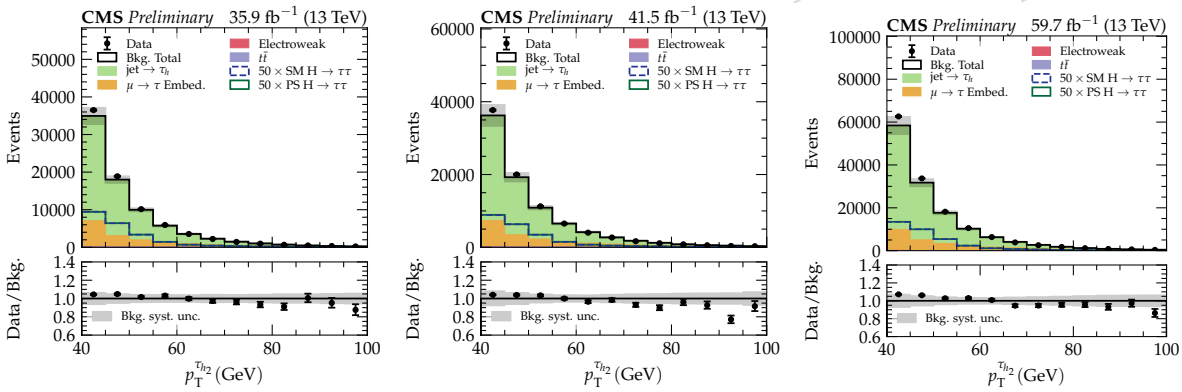

(d) subleading τ_h p_T, 2016 (e) subleading τ_h p_T, 2017 (f) subleading τ_h p_T, 2018

Figure 129: Additional, inclusive, prefit plots for 2016, 2017 and 2018 of the τ_h p_T variables with the full uncertainty.. The signals are scaled by a factor of 50.

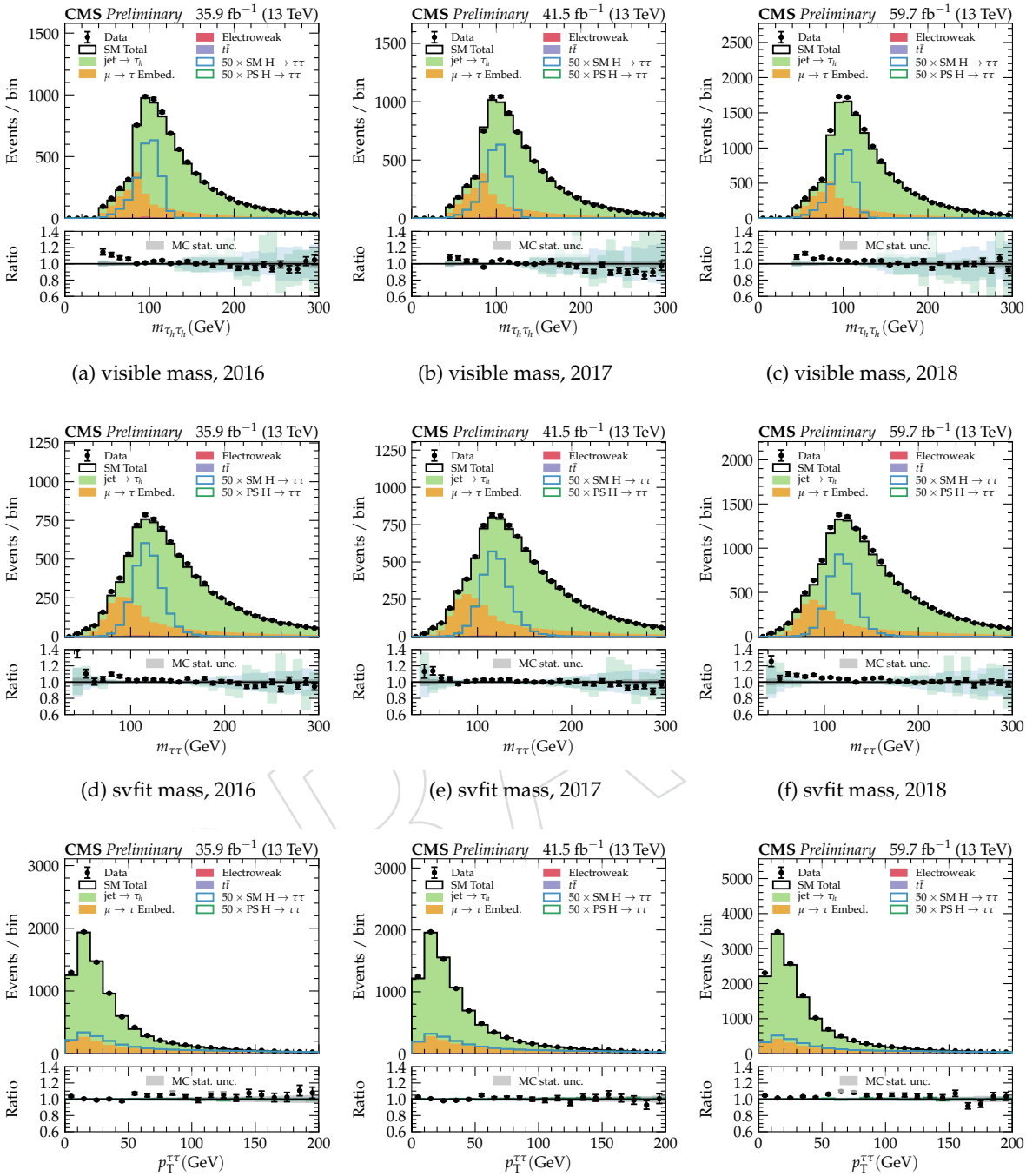

(a) visible mass, 2016 (b) visible mass, 2017 (c) visible mass, 2018

(d) svfit mass, 2016 (e) svfit mass, 2017 (f) svfit mass, 2018

(g) higgs p_T, 2016 (h) higgs p_T, 2017 (i) higgs p_T, 2018

Figure 130: Inclusive, prefit plots for 2016, 2017 and 2018 of the input features to the BDT. The signals are scaled by a factor of 50 and the uncertainty band considers only statistical uncertainty. Additionally, the ratio of signals with respect to the SM signal is shown including the uncertainty band on this showing statistical uncertainty.

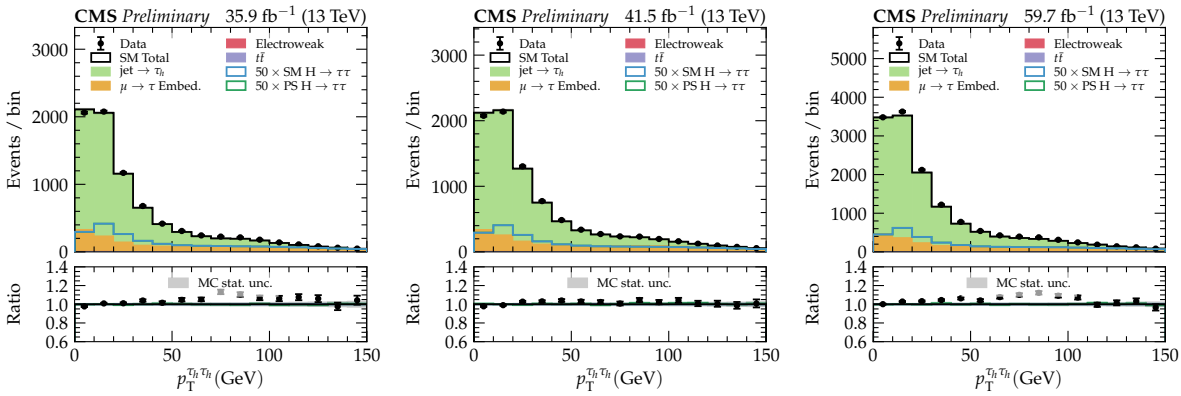

(a) visible p_T, 2016 (b) visible p_T, 2017 (c) visible p_T, 2018

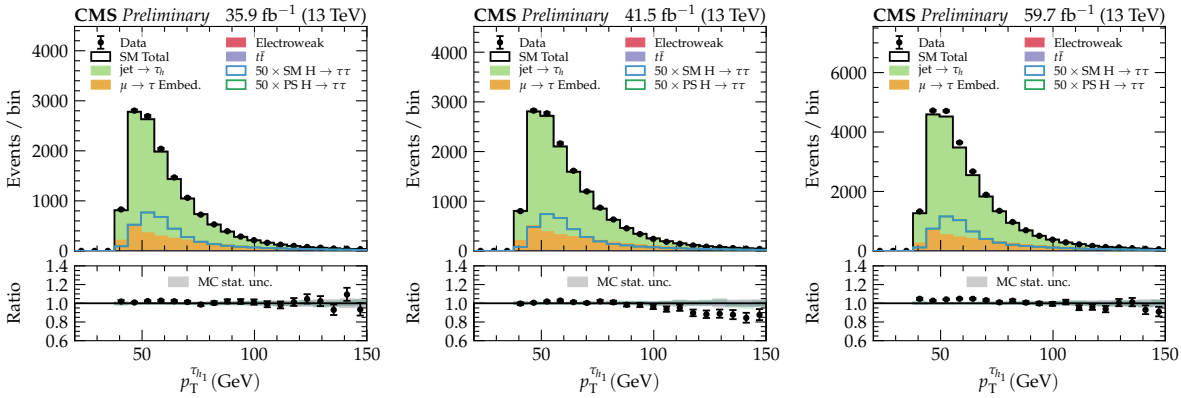

(d) τ p_T, 2016 (e) τ p_T, 2017 (f) τ p_T, 2018

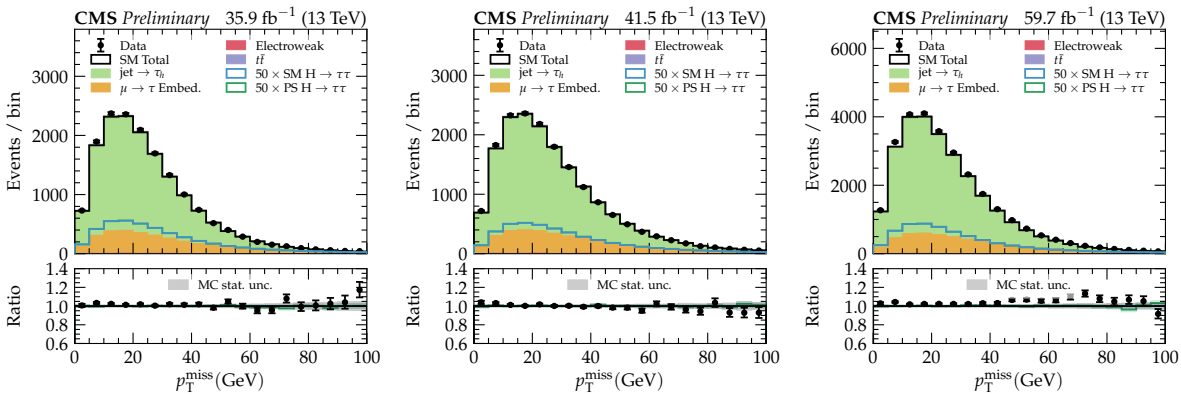

(g) p_T^{miss}, 2016 (h) p_T^{miss}, 2017 (i) p_T^{miss}, 2018

Figure 131: Inclusive, prefit plots for 2016, 2017 and 2018 of the input features to the BDT. The signals are scaled by a factor of 50 and the uncertainty band considers only statistical uncertainty. Additionally, the ratio of signals with respect to the SM signal is shown including the uncertainty band on this showing statistical uncertainty.

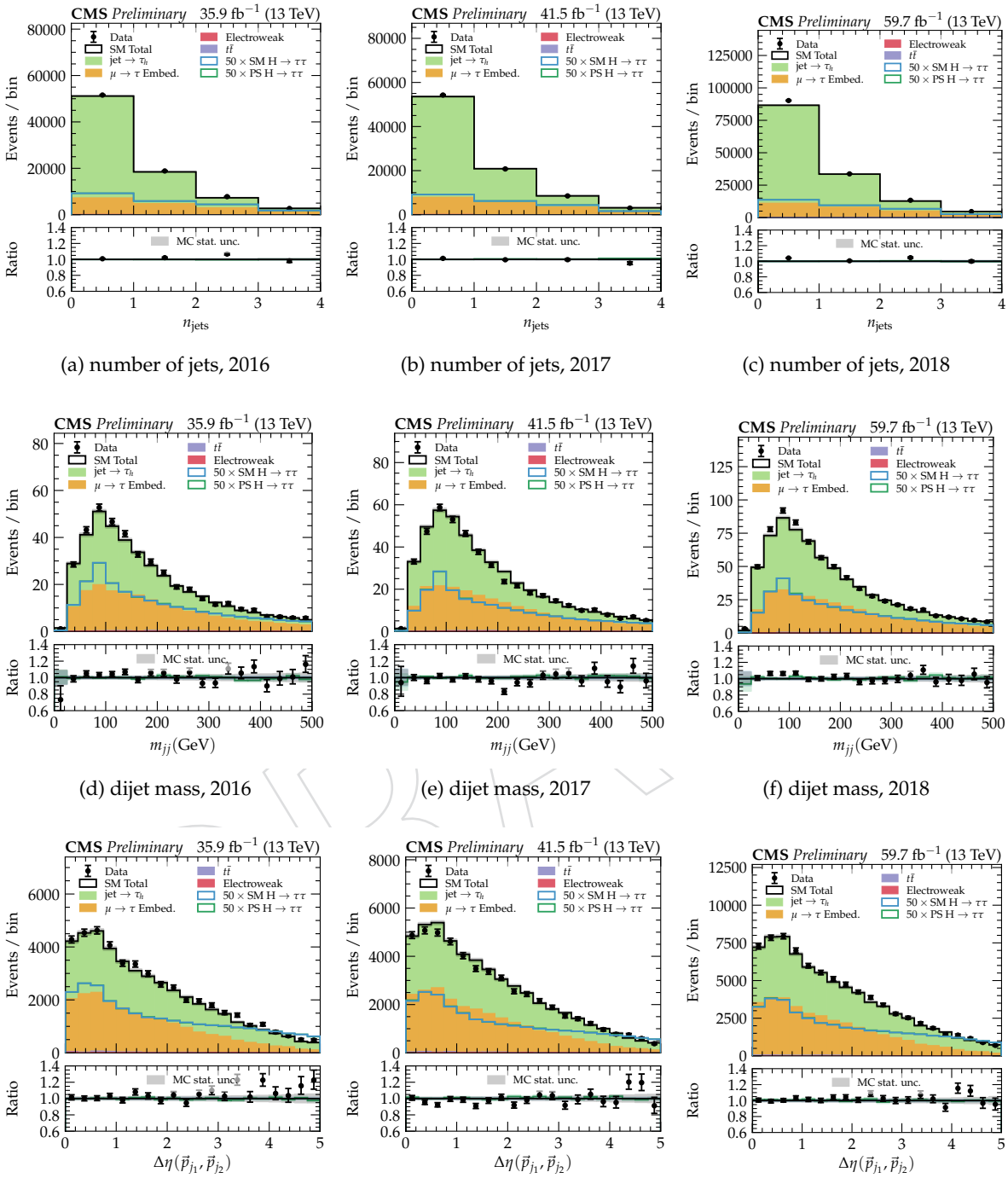

(a) number of jets, 2016

(b) number of jets, 2017

(c) number of jets, 2018

(d) dijet mass, 2016

(e) dijet mass, 2017

(f) dijet mass, 2018

(g) $|\Delta\eta|$ of jets, 2016

(h) $|\Delta\eta|$ of jets, 2017

(i) $|\Delta\eta|$ of jets, 2018

Figure 132: Inclusive, prefit plots for 2016, 2017 and 2018 of the input features to the BDT. The signals are scaled by a factor of 50 and the uncertainty band considers only statistical uncertainty. Additionally, the ratio of signals with respect to the SM signal is shown including the uncertainty band on this showing statistical uncertainty.

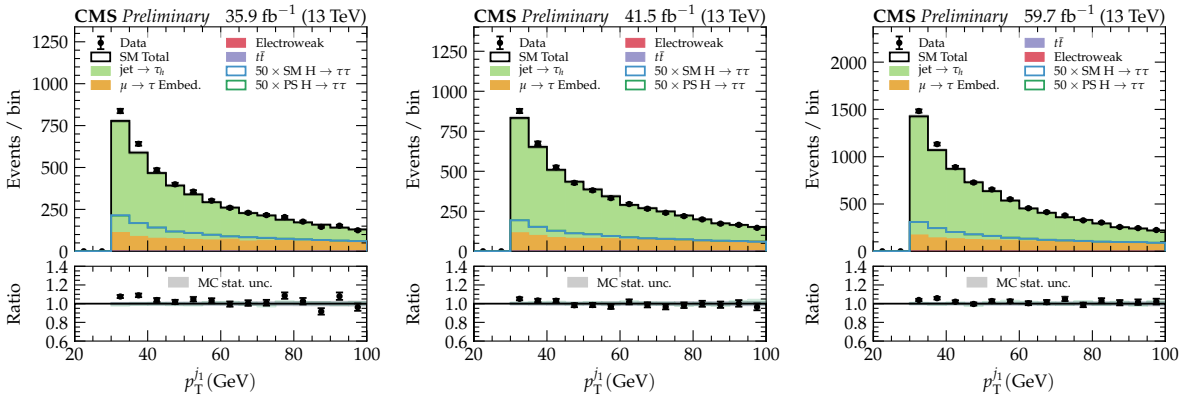

(a) leading jet p_T, 2016 (b) leading jet p_T, 2017 (c) leading jet p_T, 2018

Figure 133: Inclusive, prefit plots for 2016, 2017 and 2018 of the input features to the BDT. The signals are scaled by a factor of 50 and the uncertainty band considers only statistical uncertainty. Additionally, the ratio of signals with respect to the SM signal is shown including the uncertainty band on this showing statistical uncertainty.

10 Categorisation

10.1 $\tau_h\tau_h$ channel

The event categorisation is performed using a BDT with the the XGBoost package. The ML method is formulated as a multi-class problem. In this subsection the training and performance of the BDT will be outlined. This follows very closely to what is employed in [54].

Since the $\tau_h\tau_h$ channel is dominated by backgrounds containing contributions from real and fake τ processes, mainly ZTT and QCD, the training is performed using three categories:

- higgs: combines the H $\rightarrow$ $\tau\tau$ samples, reweighted to the SM scenario, so this includes ggH, VBF and VH samples
- embedded data: processes involving real τ leptons
- jetFakes: processes involving fake τ leptons

The ggH, VBF and VH samples are reweighted by their cross-section before merging into one training class and then the three training classes (higgs, embedded, fakes) are normalised to account for unbalanced datasets. They are normalised using a class weight that scales each training category to the same scale such that they are treated (overall) equally important in the training. This is done using

$$c_n = \frac{\sum_{i \in \text{events inclusively}} w_i}{\sum_{j \in \text{events} \in \text{category } n} w_j}, \tag{44}$$

where i runs over the full training dataset and j runs over the events associated to a specific class the weight is being derived for.

Tests have been performed to show that there is negligible difference between the expected sensitivities obtained by training on the PS-reweighted sample. This gives confidence that the training is independent of which CP state is trained on, and that the input variables do not bias our (expected) results. For the final result, the training will be performed on the official samples outlined in table

For training, the dataset is split into even and odd event numbers, which in turn are split into training and validation datasets. This type of cross-validation allows separate BDTs to be trained on the even and odd fold's training subset and can then be tested by applying the BDT trained on the even fold onto the odd event numbers and vice versa. This ensures that the full available statistics is used for training, while no bias is introduced. Finally, the same selection is applied to the training set as described in 7.

The following variables were used as inputs for the BDT training:

- leading τ_h p_T
- visible di-τ_h p_T
- full di-τ_h + MET p_T
- visible di-τ_h mass
- SVFit mass
- leading jet p_T
- MET
- number of jets
- invariant mass of di-jet system

DRAFT

- absolute difference in jet η

The distributions for the input features are shown in Fig. 282 – 285. These show the ratio of the signal distributions with respect to the SM signal expectation each bin in addition to the standard data vs. background MC ratio. Additionally, the τ_h MVA decay mode plots are shown in Fig. 286 with the same features, which will be used at later stage to make datacards for the specific τ_h decay modes. The distributions show compatible results for two signals of different CP states.

For each year a separate training has been performed. A sophisticated choice of hyperparameters has not been performed in order to not overtune the current set-up. On application of a trained model each event is assigned to a category depending on the class that received the highest score. Thus each event is categorised into one of the three classes: higgs, zttEmbed or jetFakes. Plots of the categories can be found in Fig 134 – 136.

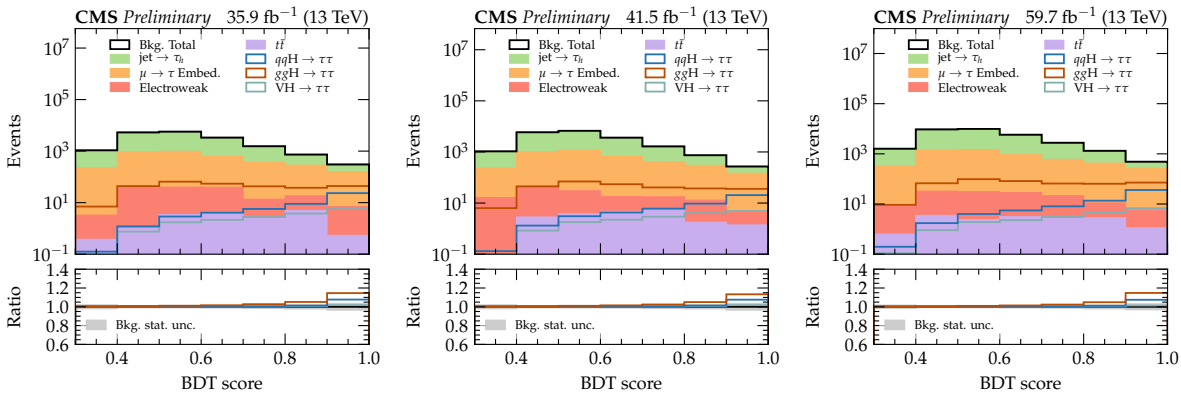

(a) 2016 (b) 2017 (c) 2018

Figure 134: The higgs category for 2016, 2017 and 2018. Both plots are prefit and are inclusive in decay mode, and data is blinded. The uncertainty band considers only statistical uncertainty. The background processes sorted by the sum of their contributions across all bins, such that the largest background appears on the top and vice versa. The lower panels show the ratio of the signal+background yield to the background yield in each bin.

In order to measure $\phi_{\tau\bar{\tau}}$ it is necessary to further split the higgs category by the reconstructed τ_h decay modes as different combinations of decay modes use different definitions of ϕ_{CP} and even in cases where the same definitions are used the amplitude of the resulting sinusoidal/cosinusoidal distributions are different and so the sensitivity is improved by splitting them.

The splitting of the categories is based mainly on the MVA-DM of the τ_h candidates, targeting different combinations of hadronic tau decays. In the case of τ_h decays to a single $\pi^{\pm}$ an additional cut requiring the S_{IP} to be $> 1.5\sigma$ is used to reject poorly reconstructed impact parameters which dilute the sensitivity to $\phi_{\tau\bar{\tau}}$. In cases where the decay plane method employed it is also necessary to ensure that all charged and neutral pions are reconstructed. The former is guaranteed by the HPS algorithm which always requires either one or three charged prongs corresponding to the charged pions. The reconstruction of a π^0 is however not guaranteed by the HPS algorithm, and 1-prong taus with no such π^0 candidate are allocated HPS-DM=0. For this reason in cases where the τ_h is reconstructed as MVA-DM=1,2 the HPS-DM is also required to be >0 to reject such events. In summary the considered tau decays and corresponding re-

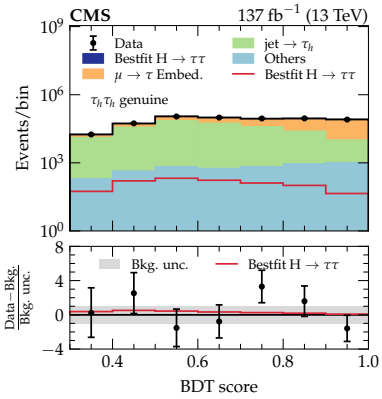

Figure 135: The zttEmbed category for the three years combined. The plot is postfit and are inclusive in decay mode. The uncertainty band considers only statistical uncertainty. The background processes sorted by the sum of their contributions across all bins, such that the largest background appears on the top and vice versa. The lower panel shows the ratio of data minus background divided by the background uncertainty.

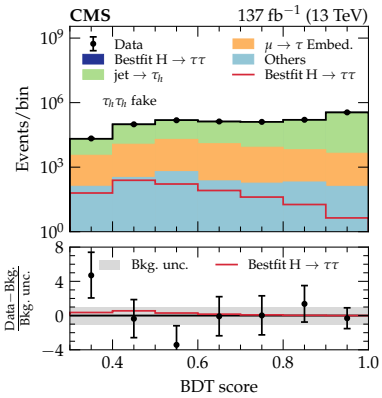

Figure 136: The jetfakes category for the three years combined. The plot is postfit and are inclusive in decay mode. The background processes sorted by the sum of their contributions across all bins, such that the largest background appears on the top and vice versa. The lower panel shows the ratio of data minus background divided by the background uncertainty.

construction level cuts are:

- $\tau^\pm \to \pi^\pm\nu$: MVA-DM=0 and $S_{\mathrm{IP}} > 1.5\sigma$
- $\tau^\pm \to \rho^\pm\nu$: MVA-DM=1 and HPS-DM>0
- $\tau^\pm \to \mathrm{a}_1{}^\pm(\to \pi^0\pi^0\pi^\pm)\nu$: MVA-DM=2 and HPS-DM>0
- $\tau^\pm \to \mathrm{a}_1(\to \pi^\pm\pi^\pm\pi^\mp)^\pm\nu$: MVA-DM=10

For the $\tau_\mathrm{h}\tau_\mathrm{h}$ channel we can consider categories for each possible pairing of these τ_h decay modes which would give 10 categories in total: $\rho^\pm + \rho^\mp$, $\rho^\pm + \pi^\mp$, $\rho^\pm + \mathrm{a}_1{}^\mp(\to \pi^\mp\pi^\mp\pi^\pm)$, $\pi^\pm + \pi^\mp$, $\pi^\pm + \mathrm{a}_1{}^\mp(\to \pi^\mp\pi^\mp\pi^\pm)$, $\rho^\pm + \mathrm{a}_1{}^\mp(\to \pi^0\pi^0\pi^\mp)$, $\mathrm{a}_1{}^\pm(\to \pi^0\pi^0\pi^\pm)$+$\mathrm{a}_1{}^\mp(\to \pi^0\pi^0\pi^\mp)$, $\pi^\pm + \mathrm{a}_1{}^\mp(\to \pi^0\pi^0\pi^\mp)$, $\mathrm{a}_1{}^\pm(\to \pi^\pm\pi^\mp\pi^\mp)$+$\mathrm{a}_1{}^\mp(\to \pi^\mp\pi^\mp\pi^\pm)$, $\mathrm{a}_1{}^\pm(\to \pi^\pm\pi^\mp\pi^\mp)$+$\mathrm{a}_1{}^\mp(\to \pi^0\pi^0\pi^\mp)$. However, the $\mathrm{a}_1{}^\pm(\to \pi^0\pi^0\pi^\pm)$+$\mathrm{a}_1{}^0(\to \pi^0\pi^0\pi^\mp)$ and $\rho^\pm + \mathrm{a}_1{}^\mp(\to \pi^0\pi^0\pi^\mp)$ categories are difficult to disentangle because of the limited ability of the decay mode MVA to

separate MVA-DM 1 and 2 and therefore these two categories are merged giving a total of 9 signal categories.

The postfit two-dimensional distributions of the NN score and $\phi_{\tau\bar{\tau}}$ observable in the *higgs* category for the 10 decay modes defined above are shown in Appendix B.

DRAFT

10.2 $\tau_\mu \tau_h$ channel

In the $\tau_\mu \tau_h$ channel the separation between the signals and the main background processes is operated with a multi-class Deep Neural Network (DNN). The architecture of the DNN is similar to the one previously used in the study of Higgs decays in tau leptons with machine learning techniques [54]. The DNN is trained on Monte Carlo simulations for the signals and main background processes, with the exception of the QCD multijet process which is estimated from collected data. Three output classes are defined:

- *higgs*: signal category, trained with ggH and VBF samples;
- *ztt*: background category for processes with genuine tau lepton pairs, it is trained with simulated $Z \to \tau\tau$ sample, $t\bar{t}$ events with genuine tau pairs;
- *fakes*: background category, trained with all other processes, most noticibly $Z \to \mu\mu$, $W + Jets$, $t\bar{t}$ with jet faking hadronic tau leptons and an estimation for the QCD multijet process obtained by selecting data events with a muon and an identified tau with the same sign.

The use of one category for both ggH and VBF categories is based on the fact that in this analysis the distinction between different production modes for the Higgs boson is less relevant compared to the separation between the Higgs signal in its entirety and the background processes. Using two different categories furthermore may result in ggH events with two jets to be assigned either to the ggH category or the VBF one leading to an overall lower predicted score for both categories. It should also be noted that both for the DY process and the $t\bar{t}$ one, events are divided in the two background categories based on whether two genuine tau leptons were present in the final state.

The input variables for the DNN training are the following:

- muon p_T;
- tau lepton p_T;
- combined p_T of muon, tau lepton and missing transverse momentum ($p_{T,\tau\tau}$);
- number of jets;
- p_T of the leading jet (in events with one or more jets);
- p_T of the trailing jet (in events with two or more jets);
- combined p_T for the two leading jets ($p_{T,jj}$);
- invariant mass of the two leading jets (m_{jj});
- separation in pseudorapidity between the two leading jets ($\Delta\eta_{jj}$);
- visible mass (m_{vis});
- invariant di-tau mass ($m_{\tau\tau}$), obtained with the FastMTT algorithm;
- missing transverse energy, (PUPPI-met);
- tranverse mass of the muon and MET system (m_T).

The distribution for these variables for the all years can be found in Fig. 98-100(2016), Fig. 102-104(2017), and Fig. 106-108(2018). In terms of architecture the DNN comprises 3 hidden layers with 100 nodes each. The training is performed to increase the model accuracy until the loss function has not improved at the percent level in 20 consecutive epochs, or upon reaching 150 epochs.

In Fig. 137, 138, and 139 we display the NN score disrtibutions for the signal, Ztt, and jetfake

DRAFT

respectively, for 2016, 2017, and 2018.

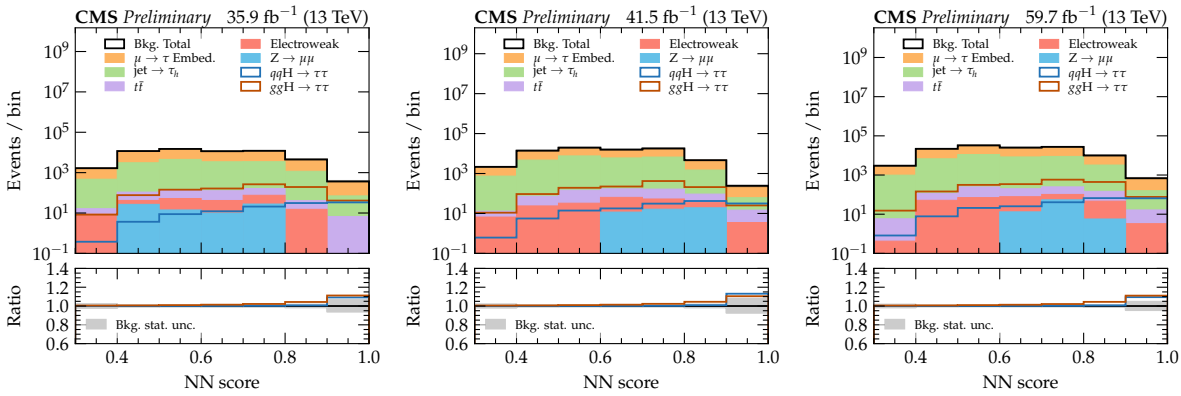

(a) 2016 (b) 2017 (c) 2018

Figure 137: The Higgs category for 2016, 2017 and 2018. The plots are prefit and are inclusive in decay mode. The uncertainty band consists of statistical uncertainties in the background templates. The background processes sorted by the sum of their contributions across all bins, such that the largest background appears on the top and vice versa. The lower panels show the ratio of the signal+background yield to the background yield in each bin.

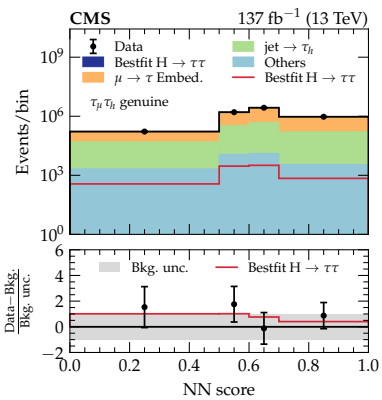

Figure 138: The zttEmbed category for the three years combined. The plot is postfit and are inclusive in decay mode. The uncertainty band considers only statistical uncertainty. The background processes sorted by the sum of their contributions across all bins, such that the largest background appears on the top and vice versa. The lower panel shows the ratio of data minus background divided by the background uncertainty.

As was the case for the $\tau_h\tau_h$ channel in order to measure $\phi_{\tau\bar{\tau}}$ it is necessary to further split the higgs category by the reconstructed τ_h decay modes. The same selections as described in Section 10.1 are used to identify the four considered τ_h decay modes. In the case the muon is also require to have $S_{IP} > 1.5\sigma$ to reject poorly reconstructed impact parameters which dilute the sensitivity to $\phi_{\tau\bar{\tau}}$. The muon and τ_h candidates are then combined to to form four categories: $\mu^\pm + \rho^\mp$, $\mu^\pm + \pi^\mp$, $\mu^\pm + a_1{}^\mp(\to \pi^\mp\pi^\mp\pi^\pm)$, $\mu^\pm + a_1{}^\mp(\to \pi^0\pi^0\pi^\mp)$.

The postfit two-dimensional distributions of the NN score and $\phi_{\tau\bar{\tau}}$ observable in the *higgs* category for the four decay modes defined above are shown in Appendix B.

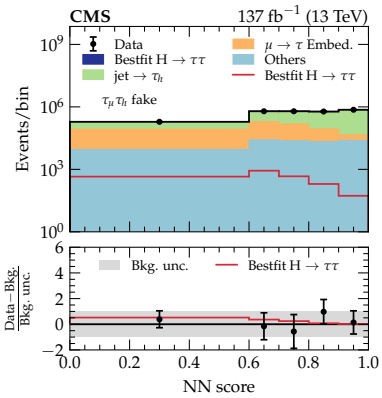

Figure 139: The jetfakes category for the three years combined. The plot is postfit and are inclusive in decay mode. The background processes sorted by the sum of their contributions across all bins, such that the largest background appears on the top and vice versa. The lower panel shows the ratio of data minus background divided by the background uncertainty.

DRAFT

10.3 $\tau_e\tau_h$ channel

In the $\tau_e\tau_h$ channel the separation between the signals and the main background processes is performed in the same way as in the $\tau_\mu\tau_h$ channel. The multi-class DNN is used to discriminate the signal (the gluon-gluon fusion and Vector Boson fusion production of the Higgs boson) against background with genuine di-tau pairs and events where the hadronic tau lepton decay is mimicked by hadronic jets. The list of input variables passed to the DNN, is identical to that used in the $\tau_\mu\tau_h$ channel with the exception that muon kinematic variables are replaced by the electron kinematic variables. The list of variables passed to the DNN includes

- electron p_T;
- tau lepton p_T;
- combined p_T of electron, tau lepton and missing transverse momentum ($p_{T,\tau\tau}$);
- number of jets;
- p_T of the leading jet (in events with one or more jets);
- p_T of the trailing jet (in events with two or more jets);
- combined p_T for the two leading jets ($p_{T,jj}$);
- invariant mass of the two leading jets (m_{jj});
- separation in pseudorapidity between the two leading jets ($\Delta\eta_{jj}$);
- visible mass (m_{vis}) of the electron and detectable decay products of the hadronically decaying tau lepton;
- invariant di-tau mass ($m_{\tau\tau}$), obtained with the SV fit algorithm;
- missing transverse energy, obtained with the PUPPI algorithm (PUPPI-met);
- tranverse mass of the electron and MET system (m_T).

The distribution for these variables for the all years can be found in Fig. 110-112(2016), Fig. 114-116(2017), and Fig. 118-120(2018). In terms of architecture the DNN comprises 3 hidden layers with 100 nodes each. The training is performed to increase the model accuracy until the loss function has not improved at the percent level in 20 consecutive epochs, or upon reaching 150 epochs.

Events are classified into three categories:

- *higgs*: signal category, trained with ggH and VBF samples;
- *ztt*: background category for processes with genuine tau lepton pairs, it is trained with simulated $Z \to \tau\tau$ sample, $t\bar{t}$ events with genuine tau pairs;
- *fakes*: background category, trained with all other processes, most noticibly $Z \to$ ee, $W + Jets$, $t\bar{t}$ with jet faking hadronic tau leptons.

In Fig. 140, and 141 we display the NN score disrtibutions for the *ztt*, and *fakes* categories, respectively, for 2016, 2017, and 2018.

In order to measure $\phi_{\tau\bar{\tau}}$ the higgs category is further splitted by the reconstructed τ_h decay modes. The same selections as described in Sections 10.2 and 10.1 are used to identify the four considered τ_h decay modes. The electron is also required to have $S_\mathrm{IP} > 1.5\sigma$ to reject poorly reconstructed impact parameters which dilute the sensitivity to $\phi_{\tau\bar{\tau}}$. The electron and τ_h candidates are then combined to form four categories: $\mathrm{e}^\pm + \rho^\mp$, $\mathrm{e}^\pm + \pi^\mp$, $\mathrm{e}^\pm + \mathrm{a}_1{}^\mp(\to \pi^\mp\pi^\mp\pi^\pm)$, $\mathrm{e}^\pm + \mathrm{a}_1{}^\mp(\to \pi^0\pi^0\pi^\mp)$.

The postfit two-dimensional distributions of the NN score and $\phi_{\tau\bar{\tau}}$ observable in the *higgs* cat-

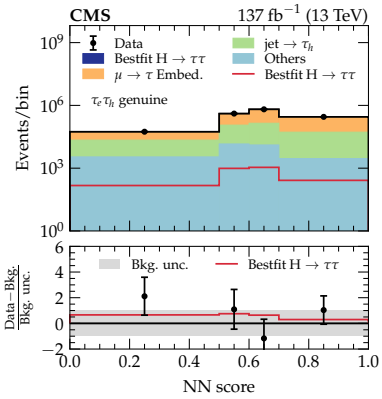

Figure 140: The zttEmbed category for the three years combined. The plot is postfit and are inclusive in decay mode. The uncertainty band considers only statistical uncertainty. The background processes sorted by the sum of their contributions across all bins, such that the largest background appears on the top and vice versa. The lower panel shows the ratio of data minus background divided by the background uncertainty.

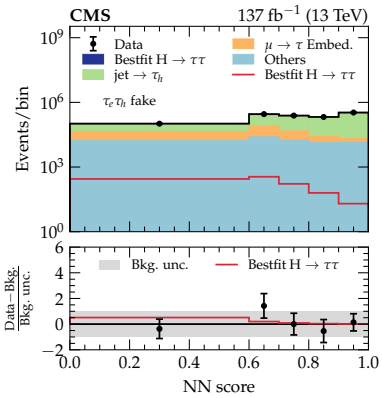

Figure 141: The jetfakes category for the three years combined. The plot is postfit and are inclusive in decay mode. The background processes sorted by the sum of their contributions across all bins, such that the largest background appears on the top and vice versa. The lower panel shows the ratio of data minus background divided by the background uncertainty.

egory for the four decay modes defined above are shown in Appendix B.

DRAFT

11 Smoothing of background templates

The signal and background templates uses in the analysis can suffer from limited statistical populations especially in the high NN/BDT score bins which by design reject a large fraction of the background. It is beneficial to use smoother background templates if possible as this minimises the impact of bin-by-bin uncertainties on the result. Additionally this also minimises the possibility of the result being biased due to statistical fluctuations in the background predictions.

To reduce the impact of statistical fluctuations the templates are smoothed exploiting known symmetries in the background distributions. The two symmetries that are exploited are related to templates which are known to flat as a function of ϕ_{CP}, and templates that are known to be (anti)symmetric about $\phi_{\mathrm{CP}} = \pi$. These two types of smoothing will be referred to here as "flattening" and "symmetrising" respectively.

In the absence of reconstruction level effects all backgrounds with genuine tau leptons are known to be flat as a function of ϕ_{CP}. Additionally, independent smearing of the input 4-vectors would not result in a bias towards particular ϕ_{CP} values. Bias towards specific ϕ_{CP} values originate from sources of smearing which smear the input 4-vectors in a correlated way. The most notable example of such is the smearing of the PV which shifts the two impact parameters in the $\pi + \pi$ and $\mu + \pi$ channels. This effect results in ϕ_{CP} to be peaked at $\phi_{\mathrm{CP}} = 0$ and 2π. This effect is illustrated in Figure 142 a) which shows the gen-level ϕ_{CP} with and without smearing of the PV. Other effects that can generate such biases include detector misalignments but such effects are expected to be small and thus the analysis is not sensitive to them.

In cases where the background distributions are not flat there is still a symmetry about $\phi_{\mathrm{CP}} = \pi$ which can be exploited to smooth the templates. This symmetry is not expected to be destroyed by any reconstruction effects. The sign of the O^* variables (defined in equation 3) determines whether an event is allocated to the $\phi_{\mathrm{CP}} < \pi$ or the $\phi_{\mathrm{CP}} > \pi$ bins. The effect of smearing the PV in this case however doesn't not affect differently the $O^* < 0$ and $O^* > 0$ regions, as illustrated in Figure 142 b), and therefore does not destroy the symmetry about $\phi_{\mathrm{CP}} = \pi$.

For the reasons outlined above backgrounds with two genuine tau leptons are flattened with the exception of the templates in the $\pi + \pi$ and $\mu + \pi$ channels which are instead symmetrised. Backgrounds with $j \to \tau_{\mathrm{h}}$ fakes are found to have symmetric but non-flat shapes in general due to kinematic effects. For example in the $\mu + \rho$ channel in some regions of space the muon and $j \to \tau_{\mathrm{h}}$ candidate are preferentially back-to-back as they may originate from a leptonically decaying W boson recoiling against a jet with fakes a τ_{h}. For a high p_{T} muon with a approximately straight track the impact parameter is perpendicular to the muon track by definition and therefore must also be approximately perpendicular to the recoiling "π^0" from the $j \to \tau_{\mathrm{h}}$ candidate. This creates a preference for $\phi_{\mathrm{CP}} = \frac{\pi}{2}$ values. All $j \to \tau_{\mathrm{h}}$ templates in all categories are therefore symmetrised rather than flattened.

For the remaining smaller background processes which tend to include at least one genuine τ_{h} (the largest being $\mathrm{t\bar{t}}$) the background templates are found to follow the same trends as the background with two genuine taus. Namely, the distributions are flat in all categories except the $\pi + \pi$ and $\mu + \pi$ channels where they are not flat but symmetric. Therefore, the same procedures as also applied to these processes.

The CP-odd and CP-even signal processes also have a symmetry about $\phi_{\mathrm{CP}} = \pi$ that can be exploited. The mixed CP scenario ($\phi_{\tau\bar{\tau}} = 45^o$) is not symmetric about $\phi_{\mathrm{CP}} = \pi$ but the interference contribution to the template is anti-symmetric, this means that after subtracting the CP-odd and CP-even contributions to the template the magnitudes of the bin contents are equal

but their sign is opposite. The anti-symmetry is exploited by reweighting the signal process to the scenario with $\phi_{\tau\bar{\tau}} = -45^o$ (which has opposite sign of the interference) and then pairing bins in $\phi_{\mathrm{CP}} < \pi$ region of the $\phi_{\tau\bar{\tau}} = 45^o$ template with bins in the $\phi_{\mathrm{CP}} > \pi$ region of the $\phi_{\tau\bar{\tau}} = -45^o$ template.

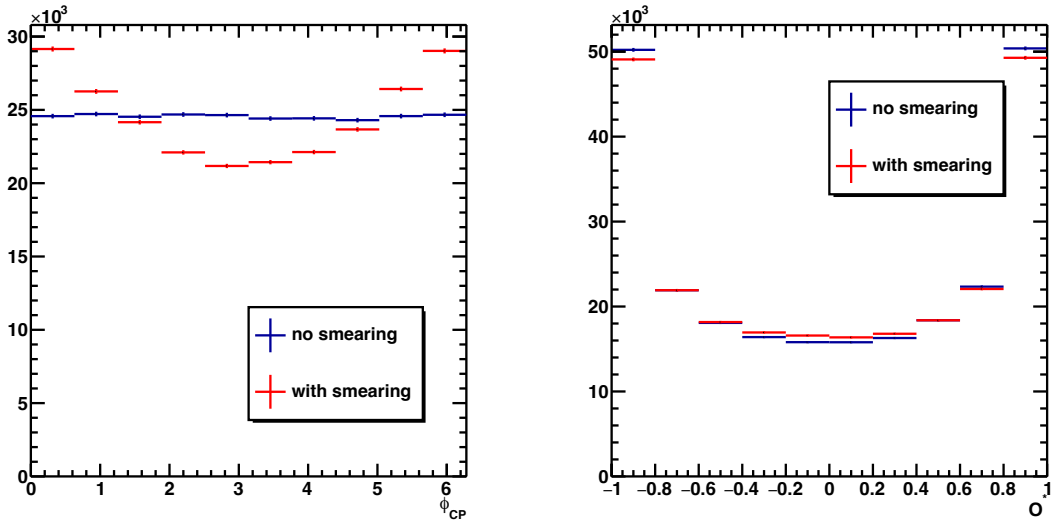

(a) (b)

Figure 142: Left: the generator-level distribution of ϕ_{CP} for $\pi + \pi$ events without any smearing of the PV (blue) and after smearing of the PV (red). Right: the generator-level distribution of O^* for $\pi + \pi$ events without any smearing of the PV (blue) and after smearing of the PV (red)

The symmetrisation procedure involves setting the bin content, c, of two symmetric bins (i and j) equal to their average bin content:

$$c'_i = c'_j = \frac{1}{2}(c_i + c_j), \tag{45}$$

where the prime (′) denotes the bin contents after symmetrisation. The statistical uncertainties, u, of the bins are set to

$$u'_i = u'_j = \frac{1}{2}\sqrt{u_i^2 + u_j^2}. \tag{46}$$

For the anti-symmetrisation the same procedure is use except bin i comes from the $\phi_{\tau\bar{\tau}} = 45^o$ template whereas bin j comes from the $\phi_{\tau\bar{\tau}} = -45^o$ template.

The flattening procedure involves setting the bin content of N ϕ_{CP} bins equal to their average:

$$c'_j = \frac{1}{N}\sum_{i=1}^{N} c_i \text{ for } 1 \leq j \leq N. \tag{47}$$

The statistical uncertainties in this case are set to

$$u'_j = \frac{1}{N}\sqrt{\sum_{i=1}^{N} u_i^2} \text{ for } 1 \leq j \leq N. \tag{48}$$

In both cases the statistical bin-by-bin uncertainties are correctly correlated when performing the fit to data, such that the number of independent bin-by-bin uncertainties is reduced by a factor of $\frac{1}{2}$ for symmetrised templates and by a factor of $\frac{1}{N}$ for flattened templates.

DRAFT

The choices made for the background smoothing are validated in two ways. Firstly, χ^2 tests are performed to check the smoothed and un-smoothed templates are statistically compatible. These tests demonstrate that the smoothed distributions are compatible with the un-smoothed distributions within statistical variations.

Secondly, a toy study is performed to check if the result is biased by the smoothing procedure. This toy study is performed as follows:

- A set of toy datasets are generated according to the un-smoothed templates allowing for only statistical fluctuations in the bin contents (i.e no systematic uncertainty variations).
- A set of toy datasets are generated according to the smoothed templates again allowing for only statistical fluctuations.
- Both sets of toy experiments are fit using the smoothed background model model and comparisons are made of the distributions of the best fit values of ϕ_{CP} and the profile likelihood ratios $-2\Delta \ln L = -2(\ln L(\phi_{\tau\bar{\tau}} = X) - \ln(\hat{\phi_{\mathrm{CP}}}))$, where X corresponds the the $\phi_{\tau\bar{\tau}}$ mixing angle scenario assumed for the signal when generating the toys.

The above procedure is performed for mixing angle scenarios X = 0°, 45°, and 90°. The idea behind these tests is to assume that the data is distributed according to the un-smoothed templates and then check that if choice of smoothed templates for the signal+background model biases the results assuming the data is not distributed according to the smoothed model.

The distributions of $\phi_{\tau\bar{\tau}}$ and $-2\Delta \ln L$ for O(200) toys are shown in Figures **??** and **??** respectively, for each mixing angle scenario. The distributions for the smoothed toys and un-smoothed toys are observed to be very similar, as too are the mean values of the distributions indicated by the arrows. This demonstrates that the choice of the smoothed background model does not bias the results.

DRAFT

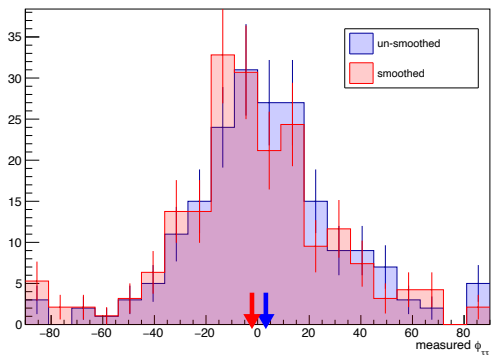

(a) $\phi_{\tau\bar{\tau}} = 0^o$

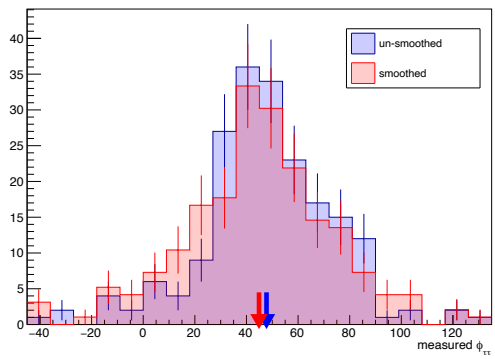

(b) $\phi_{\tau\bar{\tau}} = 45^o$

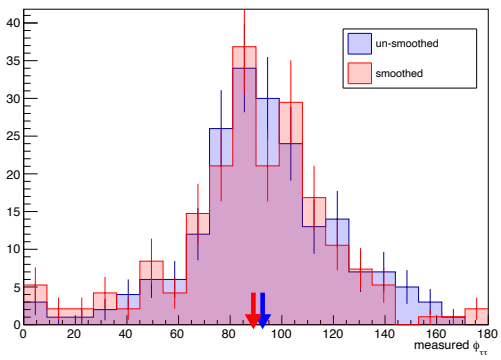

(c) $\phi_{\tau\bar{\tau}} = 90^o$

Figure 143: The measured best-fit values of $\phi_{\tau\bar{\tau}}$ for toy experiments generated according to the smoothed background templates (red labelled "merged" in the legend) and the un-smoothed background templates (blue labelled "merged" in the legend). The arrows indicate the mean values of the distributions. The distributions are shown for three different scenarios of signal mixing angle $\phi_{\tau\bar{\tau}} = 0^o$, 45°, *and* 90° in insets a, b, and c respectively.

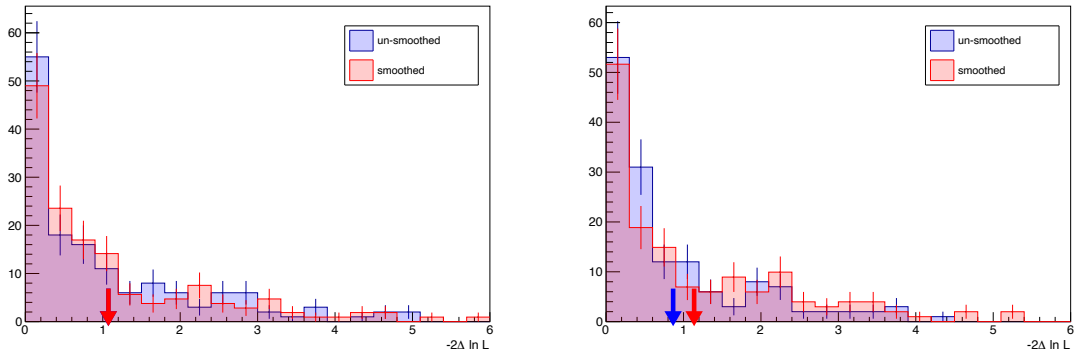

(a) $\phi_{\tau\bar{\tau}} = 0^{o}$

(b) $\phi_{\tau\bar{\tau}} = 45^{o}$

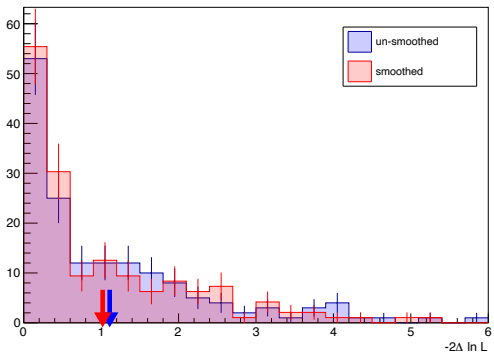

(c) $\phi_{\tau\bar{\tau}} = 90^{o}$

Figure 144: The values obtained for the profile likelihood ratios, $-2\Delta \ln L = -2(\ln L(\phi_{\tau\bar{\tau}} = X) - \ln(\hat{\phi_{\mathrm{CP}}}))$, for toy experiments generated according to the smoothed background templates (red labelled "merged" in the legend) and the un-smoothed background templates (blue labelled "merged" in the legend). The arrows indicate the mean values of the distributions. The distributions are shown for three different scenarios of signal mixing angle $X = \phi_{\tau\bar{\tau}} = 0^{o}$, 45°, and 90° in insets a, b, and c respectively.

12 Systematic uncertainties

12.1 Normalization Uncertainties

This section describes all uncertainties that affect only the normalization of the background/signal processes.

- **Luminosity**
  The luminosity uncertainty amounts to 2.5%, 2.3%, and 2.5% on the data collected during the 2016, 2017, and 2018 respectively. The luminosity uncertainty is applied to all backgrounds and signal processes where the yield is estimated from MC. The luminosity uncertainty partially correlated between years as recommended in Ref. [55].
- **Muon reconstruction/identification efficiency**
  The uncertainty on the muon reconstruction efficiency including tracking, identification, and isolation is 1%. It is treated as correlated between years and channels with electrons.
- **Muon trigger efficiency**
  The uncertainty in the trigger efficiency is 2% per muon leg. It is treated as being uncorrelated between years and channels.
- **B-tag scale-factors**
  For the $\tau_\mu \tau_h$ channel, which contains a veto on events containing b-jets, an uncertainty on the $t\bar{t}$ and VV processes event yields is applied. This is derived by propagating the uncertainties on the b-tag scale-factors provided by the BTV POG [**?**] and determining the variation in the event yields. The magnitude of this uncertainty ranges from 1%-9%. The uncertainties on the event yields for other MC processes is found to be negligible ($\approx$ 0.1%). These uncertainties are treated as being uncorrelated between years (we are checking with the experts if this is the correct treatment).
- **Background normalization uncertainty**
  For the embedded samples a 4% systematic uncertainty on the event yield is applied. This comes from the uncertainty on the measurement of the muon identification/trigger efficiencies used to scale the embedded samples (2% per muon = 4%). The uncertainties are treated as being uncorrelated between years.

  A 4.2% uncertainty is applied to the $t\bar{t}$ process to account for the uncertainty on the cross-section fully correlated between years.

  A 2% uncertainty is applied to the $Z \to ll$ process to account for the uncertainty on the Drell-Yan cross-section fully correlated between years.

  A 5% uncertainty is applied to the di-boson and single-top processes to account for the uncertainties on the production cross-sections fully correlated between years.

  A 4% uncertainty is applied to the EWKZ process to account for the uncertainty on the production cross-section fully correlated between years.

  The uncertainties on the ggH production cross-section recommended in YR4 [56] are applied. The uncertainties on the cross-section include a 3.9% uncertainty due to variations of the QCD scales and a 3.2% uncertainty from PDF+α_s variations.

DRAFT

Table 30: Uncertainty in the muon energy scale

$\|\eta\|$ bin	[0,1.2]	[1.2,2.1]	[2.1,2.4]
Uncertainty	0.4%	0.9%	2.7%

The uncertainties on the VBF Higgs production cross-section recommended in YR4 [56] are applied which include a 0.4% uncertainty from variations of QCD scales and a 2.1% uncertainty from PDF+α_s variations. The uncertainties are fully correlated between years.

The uncertainties on the W(Z)H associated production cross-sections recommended in YR4 [56] are applied which include a 1.9%(1.6%) uncertainty from the QCD scale variations and a 1.9%(1.6%) uncertainty from PDF+α_s variations. The uncertainties are fully correlated between years.

The recommended uncertainties on the $H \to \tau\tau$ branching fraction provided in YR4 [56] are applied to all Higgs signal samples (ggH, VBF, and VH). These uncertainties include a 1.7% uncertainty due to missing higher order corrections, a 0.99% parametric uncertainty on the quark masses, and a 0.62% parametric uncertainty on α_s.

- **$l \to \tau_h$ fake-rate**

  For τ_h candidates matched to electrons at the generated level in the $\tau_\mathrm{h}\tau_\mathrm{h}$ final state (the vast majority of light lepton to τ_h fakes in this channel), the uncertainty related to the identification of the fake τ_h is 5% in 2016, and 1% in 2017 and 2018.

  For τ_h candidates matched to muons at generated level in the $\mu\tau_\mathrm{h}$ final state, the uncertainty related to the identification of the identification of the fake τ_h (including the anti-muon discriminator) is split into four independent uncertainties depending on the MVA-DM of the $\mu \to \tau_\mathrm{h}$ candidate. The size of the uncertainties are 20%, 30%, and 40% for MVA-DM = 0, 1 and 2, and 10 and 11 respectively.

  In all cases the $l \to \tau_h$ fake-rate uncertainty is included only for the dominant Z→ee process and is treated as being uncorrelated between years because the source of the uncertainty is mostly statistical.

- **S_IP correction uncertainty** For categories containing MVA-DM=0 taus which use the additional cut on the S_IP to reject poorly reconstructed impact parameters a normalization uncertainty included to account for the uncertainty on the S_IP correction. This uncertainty is estimated by varying the size of the S_IP corrections by $\pm$ 25% (such shifts are found to cover any residual non-closures after applying the derived correction).

12.2 Shape uncertainties

This section describes all uncertainties that effect the shapes of the background/signal processes. Some of these may effect the shapes only for the specific event categories and are therefore included as a mixture of shape/normalization uncertainties. Cases such as these will be indicated in the descriptions.

- **Tau reconstruction/identification efficiency**
  For τ_h candidates matched to τ_h at generated level, the ID scale factors are com-

DRAFT

Table 31: Groups of sources of jet energy scale uncertainties used in the analysis. The last column indicates the correlation between years per uncertainty.

Group	Members of the group	Correlation
Absolute	AbsoluteMPFBias, AbsoluteScale, Fragmentation, PileUpDataMC, PileUpPtRef, RelativeFSR, SinglePionECAL, SinglePionHCAL	yes
Absolute_year	AbsoluteStat, RelativeStatFSR, TimePtEta	no
BBEC1	PileUpPtBB, PileUpPtEC1, RelativePtBB	yes
BBEC1_year	RelativeJEREC1, RelativePtEC1, RelativeStatEC	no
EC2	PileUpPtEC2	yes
EC2_year	RelativeJEREC2, RelativePtEC2	no
FlavorQCD	FlavorQCD	yes
HF	PileUpPtHF, RelativeJERHF, RelativePtHF	yes
HF_year	RelativeStatHF	no
RelativeBal	RelativeBal	yes
RelativeSample	RelativeSample	no

puted in 2 p_T bins (20–40 and 40+ GeV), and in 5 MVA-DM bins (MVA-DM = 0, 1, 2, 10, 11). The uncertainty also depends on the p_T and MVA-DM bin and comes from the uncertainties for the ID scale factor fits described in Section 5.1; it is typically of the order of 3% and statistically dominated. An uncorrelated shape uncertainty is considered for each of the bins. The uncertainties are uncorrelated between years because the origin of the uncertainty is statistical mostly. The uncertainties are fully correlated between the $\tau_h\tau_h$, $\tau_e\tau_h$, and $\tau_\mu\tau_h$ channels since the same vs jets ID working point is used. These uncertainties cover any potential differences in yields in each of the MVA-DM bins with can be due to mismodelling of the initial HPS tau reconstruction, the deepTau discriminants, or the MVA-DM discriminant. However, since the separating power of the ϕ_{CP} discriminant depends on the genuine tau decay mode types selected in each MVA-DM bin, an additional uncertainty could be considered to account for the migrations of different tau decay mode types between MVA-DM bins. We checked the effect of including such migration uncertainties on the ϕ_{CP} discriminant shapes (using exaggerated values for the migration uncertainties) but found the effect on the shapes to be negligible compared to the statistical uncertainties on the signal templates, hence they are neglected. Additionally, a yield uncertainty of 3% is taken into account for real τ_h related to the discriminators against electrons and muons. This uncertainty is uncorrelated between final states since different working points are used.

- **Tau trigger efficiency**
  For triggers with τ_h legs, the uncertainty is p_T and MVA-DM dependent, and comes from the fits of the turn-ons described in Section 5.4. The τ_h trigger uncertainties are treated as being uncorrelated between MVA-DM bins. The uncertainties are predominantly statistical in nature and are therefore uncorrelated between years and channels.

- **Hadronic tau energy scale**
  The energy scale of real τ_h is corrected by decay mode. The uncertainty in the correction depends on the decay mode and on the year. For MC events it ranges between 0.8 and 1.1%. For embedded events it ranges between 0.2 and 0.5%. The uncertain-

DRAFT

ties are uncorrelated between years and between decay modes. The shifts of the τ_{h} energy scale are propagated to the $E_{\mathrm{T}}^{\mathrm{miss}}$.

- **Muon energy scale**
  The energy scale of muons is not corrected with Rochester corrections because the analysis does not need to describe precisely the mass of any narrow dimuon resonance. The uncertainty in the muon energy scale corresponds to the Muon POG recommendation in the case where no such correction is applied. The uncertainty depends on the muon pseudorapidity, and varies between 0.4-2.7%.
- **$\mu \to \tau_h$ energy scale**
  Two uncorrelated uncertainties that effect the 1-prong and 1-prong+1-π^0 tau decay modes is applied to the $Z \to ll$ process in the $\tau_\mu \tau_h$ channel. The uncertainties vary the energy-scale correction by 1% for both the 1-prong and 1-prong+1-π^0 decay modes. Shifts in the energy scales are also propagated to the $E_{\mathrm{T}}^{\mathrm{miss}}$. The uncertainties are uncorrelated between years.
- **JES uncertainty**
  The jet energy scale is corrected event-by-event with the jet energy corrections derived by the JetMET POG. There are 27 sources of uncertainties, which are merged into different groups based on the correlations between uncertainties, mostly related to the detector regions. The groups of uncertainties follow exactly the recommendations from jetMET and are detailed in Table 31, which also indicates how the uncertainties are correlated between years. For MC samples without recoil corrections applied the uncertainties are also propagated to the $E_{\mathrm{T}}^{\mathrm{miss}}$.
- **Jet energy resolution**
  Jets in simulation are smeared to match the jet energy resolution in data. Uncertainties in the smearing are taken into account as an additional shape uncertainty, uncorrelated between years.
- **MET unclustered energy uncertainty**
  The MET unclustered energy uncertainty is applied to all MC processes that do not have recoil correction applied, namely the $\mathrm{t\bar{t}}$ and VV processes, as recommended by the JetMET POG [57]. In the $\tau_h \tau_h$ channel the effect on the shapes for the VV and $\mathrm{t\bar{t}}$ processes in the di-jet category is found to be negligible and therefore is included only as a normalization uncertainty with a magnitude in the range 4-16%. The uncertainty is treated as uncorrelated between years.
- **MET recoil correction uncertainties**.
  For all MC processes that have recoil correction the hadronic response and its resolution are varied within the uncertainties determined during the computation of the recoil corrections. The uncertainty is treated as uncorrelated between years.
- **Non-$Z \to \tau\tau$ contribution to embedded samples**
  The embedded samples provide an estimate for all processes producing a pair of genuine tau leptons and therefore contain a small amount of $\mathrm{t\bar{t}}$ and VV events. The recommendation by the embedding group [58, 59] is to apply a shape uncertainty defined by adding/subtracting 10% of the VV and $\mathrm{t\bar{t}}$ contribution estimated using MC to the embedded templates to cover any bias by introduced the embedding procedure in modelling these events. The uncertainty is treated as fully correlated between years.
- **Top p_T re-weighting**
  Uncertainty between no and twice the correction on the re-weighting applied to $\mathrm{t\bar{t}}$

DRAFT

events in all channels. Fully correlated between years.

- **DY p_T re-weighting**
  Uncertainty between $\pm$ 10% of the correction on the re-weighting applied to $Z \to ll$ events in all channels. The uncertainty is correlated between 2017 and 2018 and uncorrelated for 2016 (due to different generator level p_{T} spectra in 2016).
- **Fake-factor uncertainties**
  The backgrounds with jets misidentified as τ_{h} are estimated from data with the fake factor method. There are different sources of uncertainty related to this method.

  In the $\tau_{\mathrm{h}}\tau_{\mathrm{h}}$ channel the following uncertainties are applied:
  - Statistical uncertainties on the measured fake factors - these uncertainties are taken from the uncertainty bands on the fitted functions, split into two independent uncertainties using the procedure outlined in Section 8.1.4. Due to the statistical nature of these uncertainties there are separate uncertainties for each N_{jets}/MVA-DM/S_{IP} bin and the uncertainties are treated as uncorrelated across years.
  - A systematic uncertainty due to the $E_{\mathrm{T}}^{\mathrm{miss}}$ non-closure correction - this uncertainty is defined by applying the correction twice for the upwards variation and not applying the correction for the downwards variations. The uncertainty is treated as being uncorrected between the jet multiplicity bins in which it is measured. This uncertainty is treated as uncorrelated across years.
  - A systematic uncertainty due to the OS/SS extrapolation corrections - this uncertainty is defined by taking the difference between the correction as a function of ΔR and N_{jets} to a flat correction. An additional normalization uncertainty in also included which is equal to the size of the flat OS/SS correction. These uncertainty is treated as being uncorrected between the jet multiplicity bins in which it is measured. These uncertainty is treated as fully uncorrelated across years.
  - A small non-closure is observed in the subleading tau MVA-DM distribution for sub-leading τ_{h} candidates with MVA-DM=2 (see Figures 55). An additional 5% uncertainty per selected MVA-DM=2 subleading τ_{h} is applied to account for this non-closure.

  In the $\tau_{\mu}\tau_{\mathrm{h}}$ and $\tau_{e}\tau_{\mathrm{h}}$ channels the following uncertainties are applied:
  - Statistical uncertainties on the measured W+jets and QCD fake factors - these uncertainties are taken from the uncertainty bands on the fitted functions. Due to the statistical nature of these uncertainties there are separate uncertainties for each N_{jets}/MVA-DM/S_{IP} bin and the uncertainties are treated as uncorrelated across years. Note the statistical uncertainties are neglected for the $t\bar{t}$ process as the overall effect on the templates is very small due to the small $\mathrm{t\bar{t}}$ fractions. The uncertainty is also small compared to the $\mathrm{t\bar{t}}$ systematic uncertainties described below.
  - For the QCD fake factors a systematic uncertainty due to the $E_{\mathrm{T}}^{\mathrm{miss}}$ non-closure correction - this uncertainty is defined by applying the correction twice for the upwards variation and not applying the correction for the downwards variations. The uncertainty is treated as being uncorrected between the jet multiplicity bins in which it is measured. This uncertainty is treated as uncorrelated across years.

DRAFT

- For the QCD fake factors a systematic uncertainty due to the light lepton p_T non-closure correction - this uncertainty is defined by applying the correction twice for the upwards variation and not applying the correction for the downwards variations. This uncertainty is treated as fully correlated across years.
- For the QCD fake factors a systematic uncertainty due to the OS/SS and anti-iso $\rightarrow$ iso extrapolation corrections - this uncertainty is defined by applying the corrections twice for the upwards variation and not applying the correction for the downwards variations. The uncertainty is treated as being uncorrected between the jet multiplicity bins in which it is measured. This uncertainty is treated as uncorrelated across years.
- For the W+jets fake factors a systematic uncertainty due to the E_T^{miss} non-closure correction - this uncertainty is defined by applying the correction twice for the upwards variation and not applying the correction for the downwards variations. This uncertainty is treated as fully correlated across years.
- For the W+jets fake factors a systematic uncertainty due to the light lepton p_T non-closure correction - this uncertainty is defined by applying the correction twice for the upwards variation and not applying the correction for the downwards variations. The uncertainty is treated as being uncorrected between the jet multiplicity bins in which it is measured. This uncertainty is treated as uncorrelated across years.
- For the W+jets fake factors a systematic uncertainty due to the high-m_T $\rightarrow$ low-m_T extrapolation correction - this uncertainty is defined by applying the corrections twice for the upwards variation and not applying the correction for the downwards variations. This uncertainty is treated as fully correlated across years.
- For the $t\bar{t}$ fake factors a systematic uncertainty due to the E_T^{miss} non-closure correction - this uncertainty is defined by applying the correction twice for the upwards variation and not applying the correction for the downwards variations. The uncertainty is treated as being uncorrected between the jet multiplicity bins in which it is measured. This uncertainty is treated as uncorrelated across years.
- For the $t\bar{t}$ fake factors a systematic uncertainty to account for possible differences between the fake factors in MC and data (as the $t\bar{t}$ fake factors are measured from MC) - this uncertainty is determined by comparing the fake factors derived for W+jets in data and MC. The uncertainty is treated as being uncorrected between the jet multiplicity bins in which it is measured. This uncertainty is treated as uncorrelated across years.

- **Theoretical uncertainties on the signal shapes**
  The dominant theoretical uncertainties on the signal acceptance and distribution shapes are considered. These dominant sources of uncertainties include QCD μ_R and μ_F scale variations and partons shower μ_R scale variations. The other sources of theoretical uncertainties, namely the PDF, α_s, and underlying event tune uncertainties are found to have negligible affects in comparison and are consequently neglected.

  For the QCD scale uncertainty the recommendation is to vary the μ_R and μ_F scales independently by factors of 2 and $\frac{1}{2}$ $\times$ the nominal values under the constraint that

DRAFT

$\frac{1}{4} < \frac{\mu_R}{\mu_F} < 4$ and take the envelope of the variation as the uncertainty. However, the outside of the envelope of scale variations is found to be given by the scale choices of $\mu_R = \mu_F = 2$ and $\mu_R = \mu_F = \frac{1}{2}$ and hence these scales are used to define the up and down uncertainty variations. This choice also allows the correlations between different bins and event categories to be determined. Event weights are included in the MC samples which correspond to the different scale variations and are used to re-weight the MC samples to estimate the uncertainties. For each scale choice the inclusive event yield is normalized to the nominal yield such that the uncertainty on the cross-section described in the previous section is not counted twice.

For the parton shower uncertainties the μ_R scale used in the parton shower generation is varied by factors of of 2 and $\frac{1}{2}$. This variation is performed separately for both ISR and FSR contributions leading to two independent nuisance parameters. The variation in μ_R as performed using the event weights computed by PYTHIA 8 as described in Ref. [60].

- **Prefiring uncertainty**
  In 2016/2017 the uncertainties on the prefiring probability is taken as the maximum of the statistical uncertainties on the prefire map bins and 20%. The uncertainty is treated as being correlated between years.
- **Finite statistics in background templates**
  Limitations in the event statistic of the signal/background templates are accounted for using the "Barlow-Beeston" method, which assigns a single nuisance parameter per bin per process [49, 50]. For background templates which have been smoothed as described in Section 11 the bin-by-bin uncertainties have been properly correlated such that there is only one independent nuisance parameter per N ϕ_{CP} bins for the flattened backgrounds, and one parameter per each pair of symmetrised bins.

12.3 Correlations between MC and embedded uncertainties

For uncertainties that are common to MC and embedded samples the recommendations are the treat the lepton and τ_{h} identification uncertainties and the τ_{h} energy scale uncertainties as being 50% correlated. All other common uncertainties are treated as being uncorrelated.

DRAFT

13 Results

In order to extract the CP mixing angle, $\phi_{\tau\bar{\tau}}$, a simultaneous fit to the data is performed using the likelihood function, $L(\vec{\sigma}, \mathcal{B}^{\tau\bar{\tau}}, \phi_{\tau\bar{\tau}}, \vec{\theta})$ that depends on the Higgs boson production cross section $\vec{\sigma}$=$(\sigma_{\text{ggh}}, \sigma_{\text{VBF}}, \sigma_{\text{hW}}, \sigma_{\text{hZ}})$, branching fraction of $\text{h} \to \tau\bar{\tau}$ decay, CP mixing angle $\phi_{\tau\bar{\tau}}$ and the nuisance parameters $\vec{\theta}$ accounting for the systematic uncertainties. The likelihood function is defined as a product of conditional probabilities P over binned distributions of the discriminating observables in each event category j,

$$L(\vec{\sigma}, \mathcal{B}^{\tau\bar{\tau}}, \phi_{\tau\bar{\tau}}, \vec{\theta}) = \prod_{j}^{N_{\text{categories}}} \prod_{i}^{N_{\text{bin}}} P(n_{i,j} \mid \mathcal{L} \cdot \vec{\sigma} \cdot \mathcal{B}^{\tau\bar{\tau}} \cdot \vec{A}_{i,j}(\vec{\theta}, \phi_{\tau\bar{\tau}}) + B_{i,j}(\vec{\theta})) \times \prod_{m}^{N_{\text{nuisance}}} C_m(\vec{\theta}) \tag{49}$$

with Poisson distributions P corresponding to the observation of $n_{i,j}$ events in each bin i of the discriminating observable given the expectation for the background, $B_{i,j}(\vec{\theta})$, and for the signal, $S_{i,j}(\vec{\theta}) = \mathcal{L} \cdot \vec{\sigma} \cdot \mathcal{B}^{\tau\bar{\tau}} \cdot \vec{A}_{i,j}(\vec{\theta}, \phi_{\tau\bar{\tau}})$, where L is the integrated luminosity and $\vec{A}_{i,j}(\vec{\theta}, \phi_{\tau\bar{\tau}})$ is the signal acceptance in each production bin. Constraints on the nuisance parameters corresponding to systematic uncertainties described in section 12.3 are represented by the functions $C_m(\vec{\theta})$. The fit is performed using the Combine framework [61].

During the extraction of $\phi_{\tau\bar{\tau}}$, two rate parameters are required, one to scale the ggH cross-section (times $\mathcal{B}^{\tau\bar{\tau}}$) and equivalently one for qqH. Both are left freely floating in the fit as nuisance parameters.

Using the negative log-likelihood, which is defined as

$$-2\Delta \ln L = -2 \cdot \left(\ln(L\phi_{\tau\bar{\tau}}) - \ln(L\phi_{\tau\bar{\tau}}^{\text{best fit}}) \right), \tag{50}$$

we can find the 68% and 95% confidence intervals when $-2\Delta \ln L = 0.99$ and $-2\Delta \ln L = 3.84$.

The input to the likelihood fits are the ϕ_{CP} distributions for the signal category, split in windows of NN/BDT score, as well as the NN/BDT score distributions for the background distributions. This allows backgrounds and systematics to be further constrained and helps to improve the fit.

13.1 Results in the $\tau_\mu \tau_h$ channel

The input to the likelihood fits are ϕ_{CP} distributions, in windows of increasing neural net score. We exemplarily display the postfit unrolled distribution for the most sensitive decay mode in the $\tau_\mu \tau_h$ channel, which is the $\mu^\pm + \rho^\mp$ mode, in Fig. 145. Further plots used in the fit can be found in Appendix B.

DRAFT

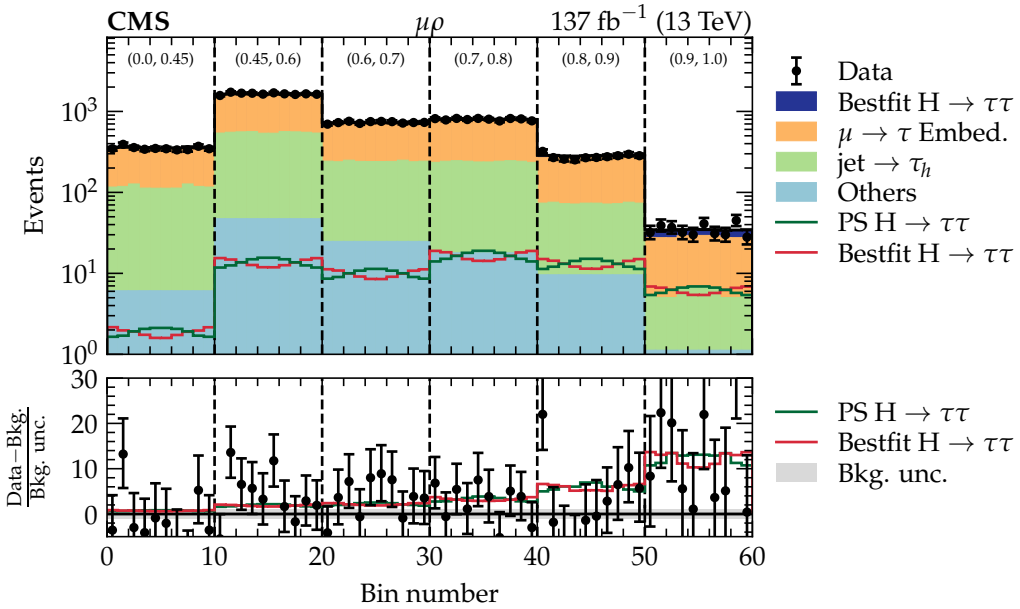

Figure 145: Distribution (postfit) of ϕ_{CP} of the $\mu^\pm + \rho^\mp$ channel, in windows of increasing NN score. The x-axis represents the cyclic bins in ϕ_{CP} in the range of $(0, 2\pi)$. The uncertainty band represents the full uncertainty. In the bottom plot the data minus the background template divided by the uncertainty in the background template is displayed, as well as the signal samples divided by the uncertainty in the background template. The uncertainty band consists of the sum of the postfit uncertainties in the background templates.

13.2 Results in the $\tau_e\tau_h$ channel

The input to the likelihood fits are ϕ_{CP} distributions, in windows of increasing neural net score. We exemplarily display the postfit unrolled distribution for one of the most sensitive decay mode in the $\tau_e\tau_h$ channel, which is the $e^{\pm} + \rho^{\mp}$ mode for the 2018 dataset, in Fig. 146. Further plots used in the fit can be found in Appendix B.

In fig. 147–150 the leading 120 impacts in the $\tau_e\tau_h$ channel are displayed.

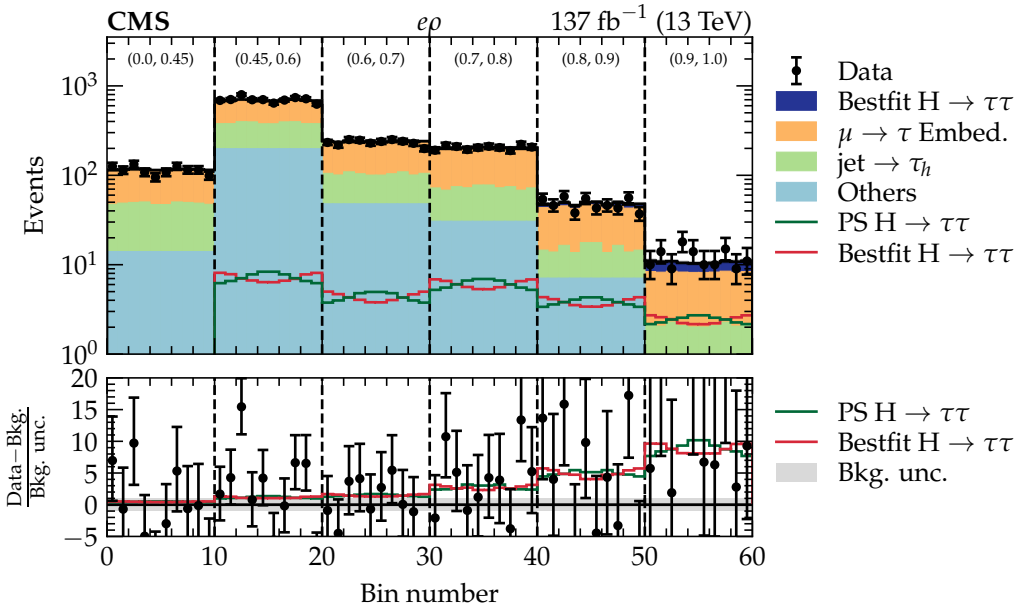

Figure 146: Distribution (postfit) of ϕ_{CP} of the $e^{\pm} + \rho^{\mp}$ channel, in windows of increasing NN score. The x-axis represents the cyclic bins in ϕ_{CP} in the range of $(0, 2\pi)$. The uncertainty band represents the full uncertainty. In the bottom plot the data minus the background template divided by the uncertainty in the background template is displayed, as well as the signal samples divided by the uncertainty in the background template. The uncertainty band consists of the sum of the postfit uncertainties in the background templates.

DRAFT

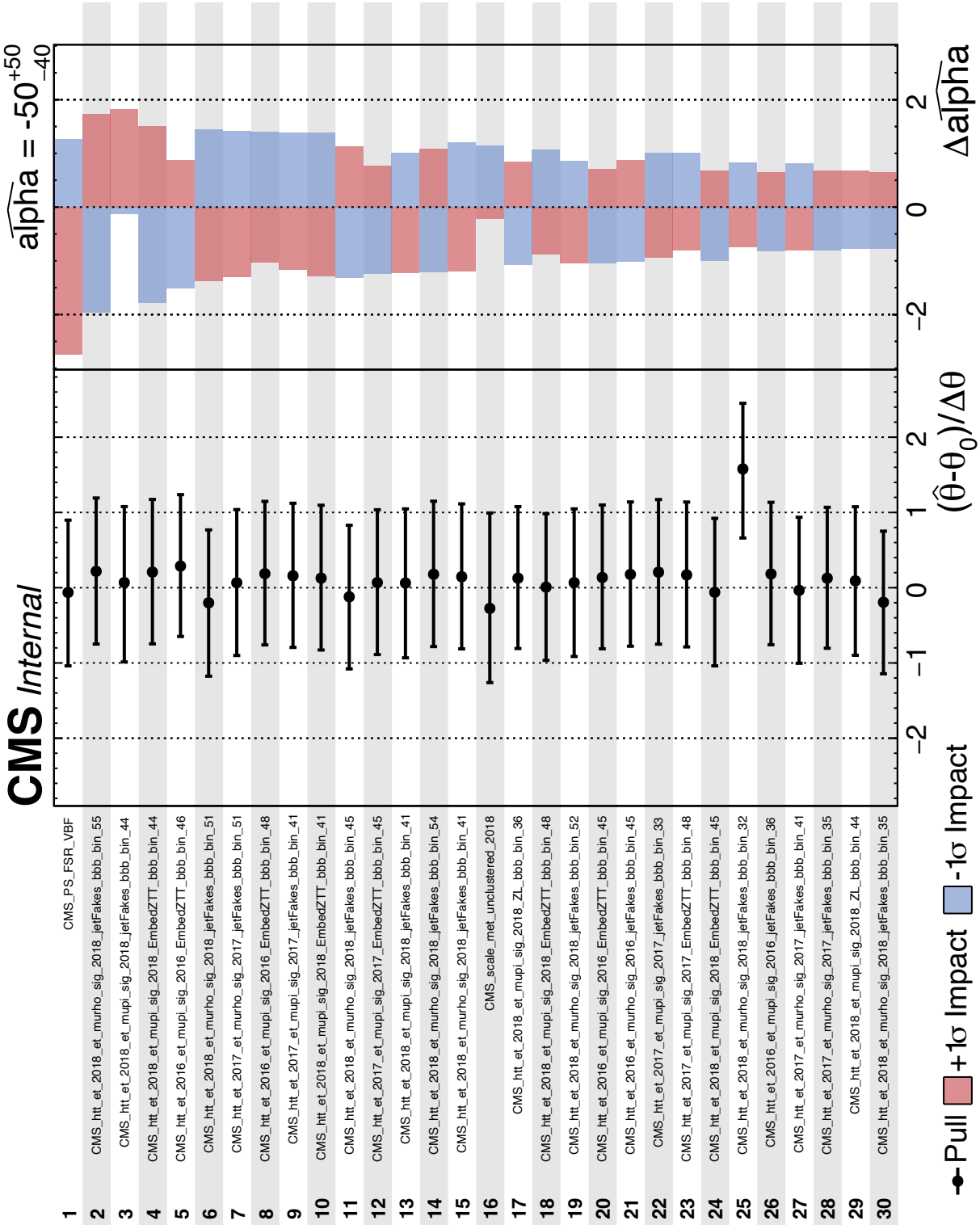

Figure 147: Expected impacts and constraints of the 1-30 ranked nuisance parameters in the $\tau_e\tau_h$ channel.

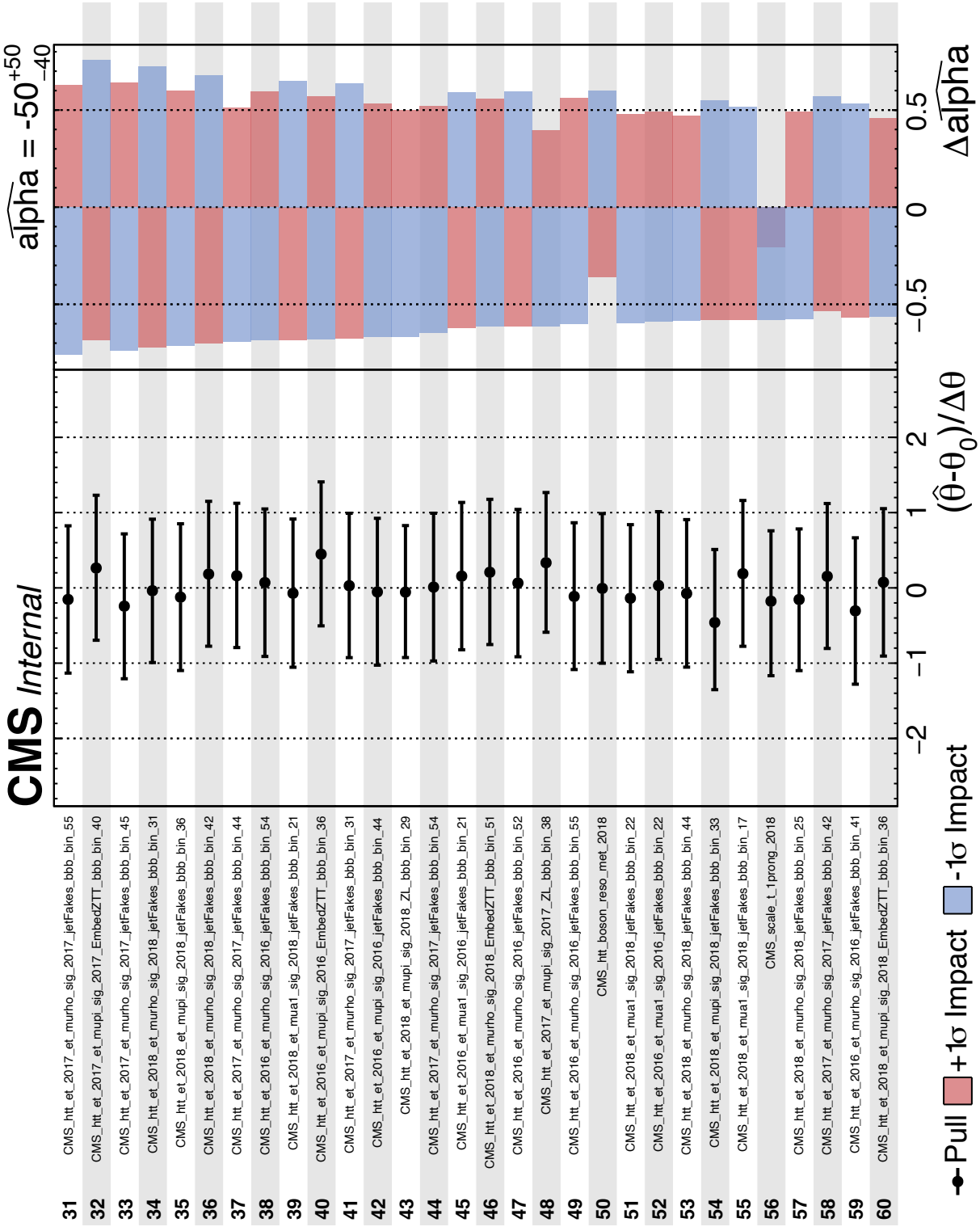

Figure 148: Expected impacts and constraints of the 30-60 ranked nuisance parameters in the $\tau_e\tau_h$ channel.

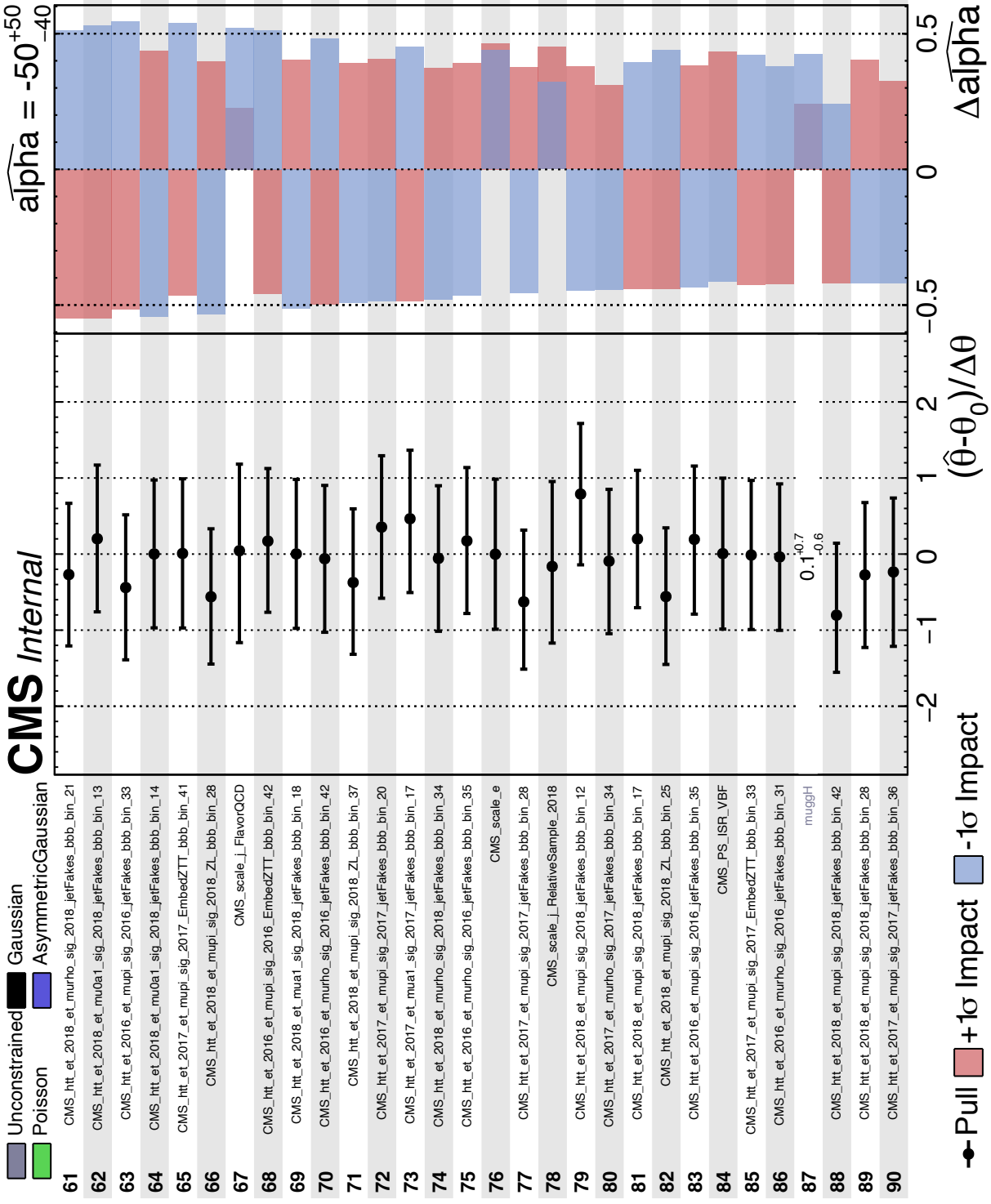

Figure 149: Expected impacts and constraints of the 60-90 ranked nuissance parameters in the $\tau_e\tau_h$ channel.

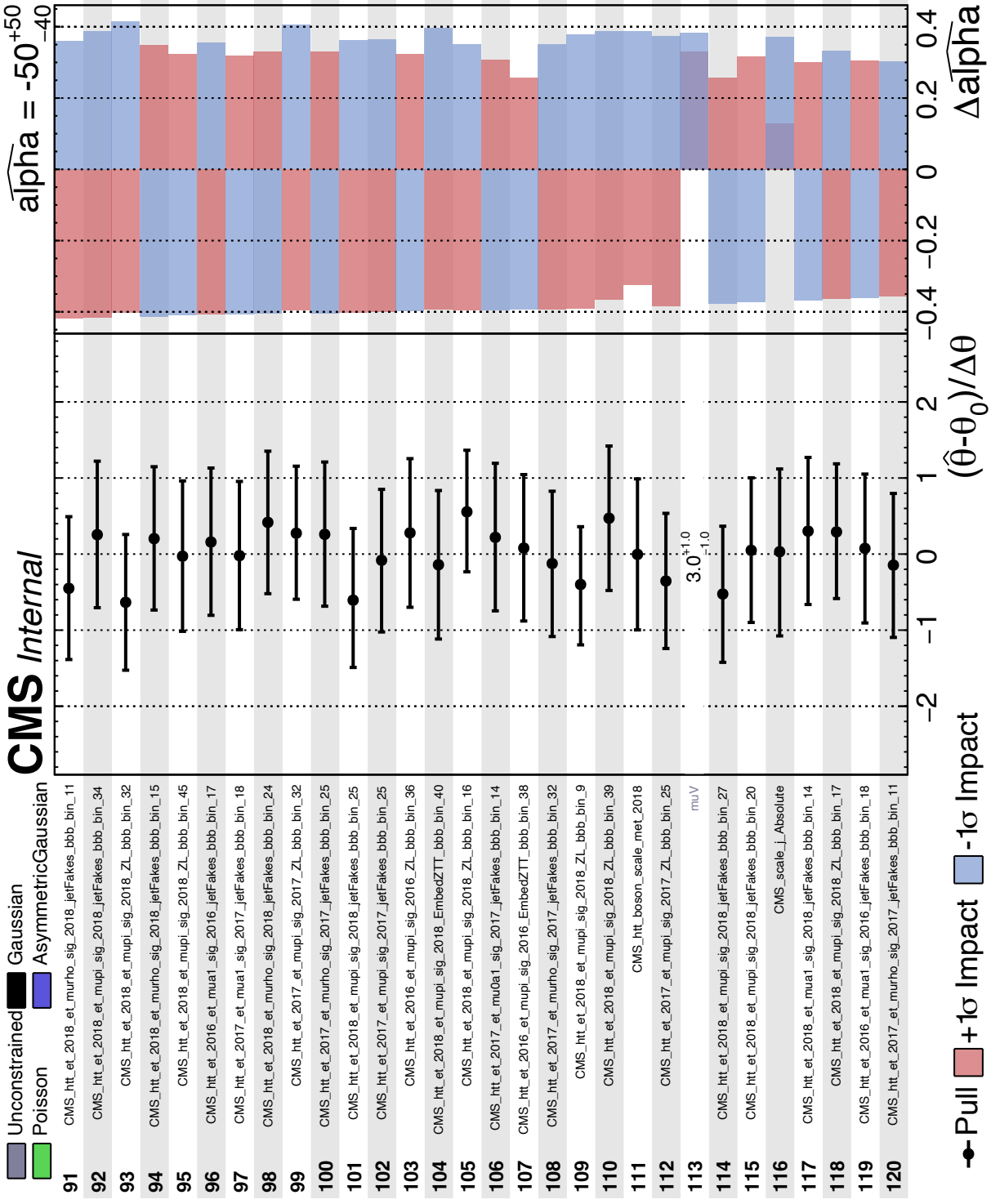

Figure 150: Expected impacts and constraints of the 90-120 ranked nuissance parameters in the $\tau_e\tau_h$ channel.

13.3 Results in the $\tau_h\tau_h$ channel

The input to the likelihood fits are ϕ_{CP} distributions, in windows of increasing neural net score. We exemplarily display the post-fit unrolled distribution for one of the most sensitive decay mode in the $\tau_h\tau_h$ channel, which is the $\pi^{\pm} + \rho^{\mp}$ mode, in Fig. 151. Further plots used in the fit can be found in Appendix B.

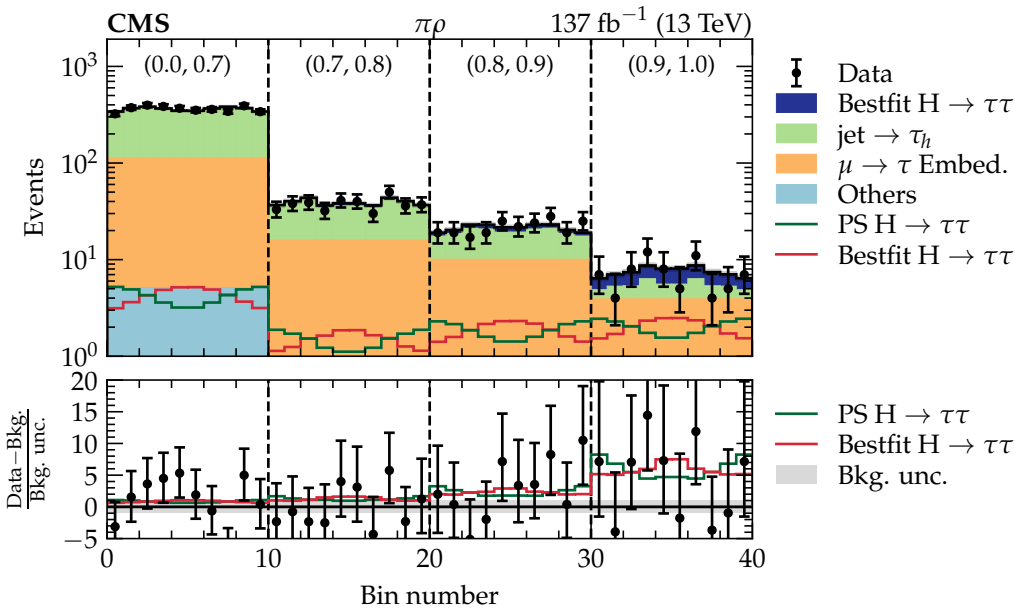

Figure 151: Distribution (postfit) of ϕ_{CP} of the $\pi^{\pm} + \rho^{\mp}$ channel, in windows of increasing NN score. The x-axis represents the cyclic bins in ϕ_{CP} in the range of $(0, 2\pi)$. The uncertainty band represents the full uncertainty. In the bottom plot the data minus the background template divided by the uncertainty in the background template is displayed, as well as the signal samples divided by the uncertainty in the background template. The uncertainty band consists of the sum of the postfit uncertainties in the background templates.

DRAFT

13.4 Observed impacts in the $\tau_\mu \tau_h$ and $\tau_h \tau_h$ channel

The observed impacts and constraints for the first 200 nuissance parameters are shown in Figures 152–155.

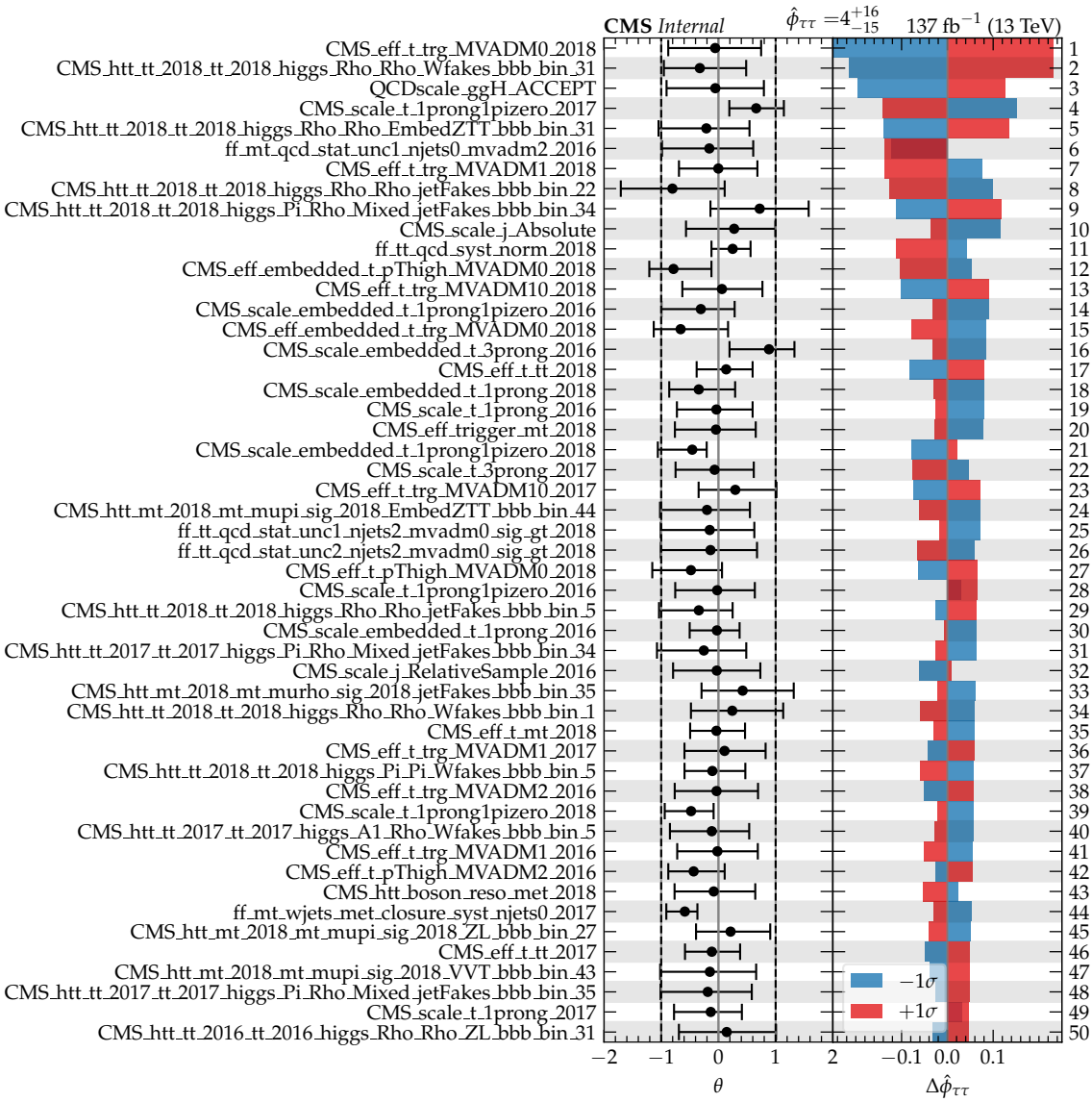

Figure 152: Impacts and constraints the 1-50 ranked for nuissance parameters.

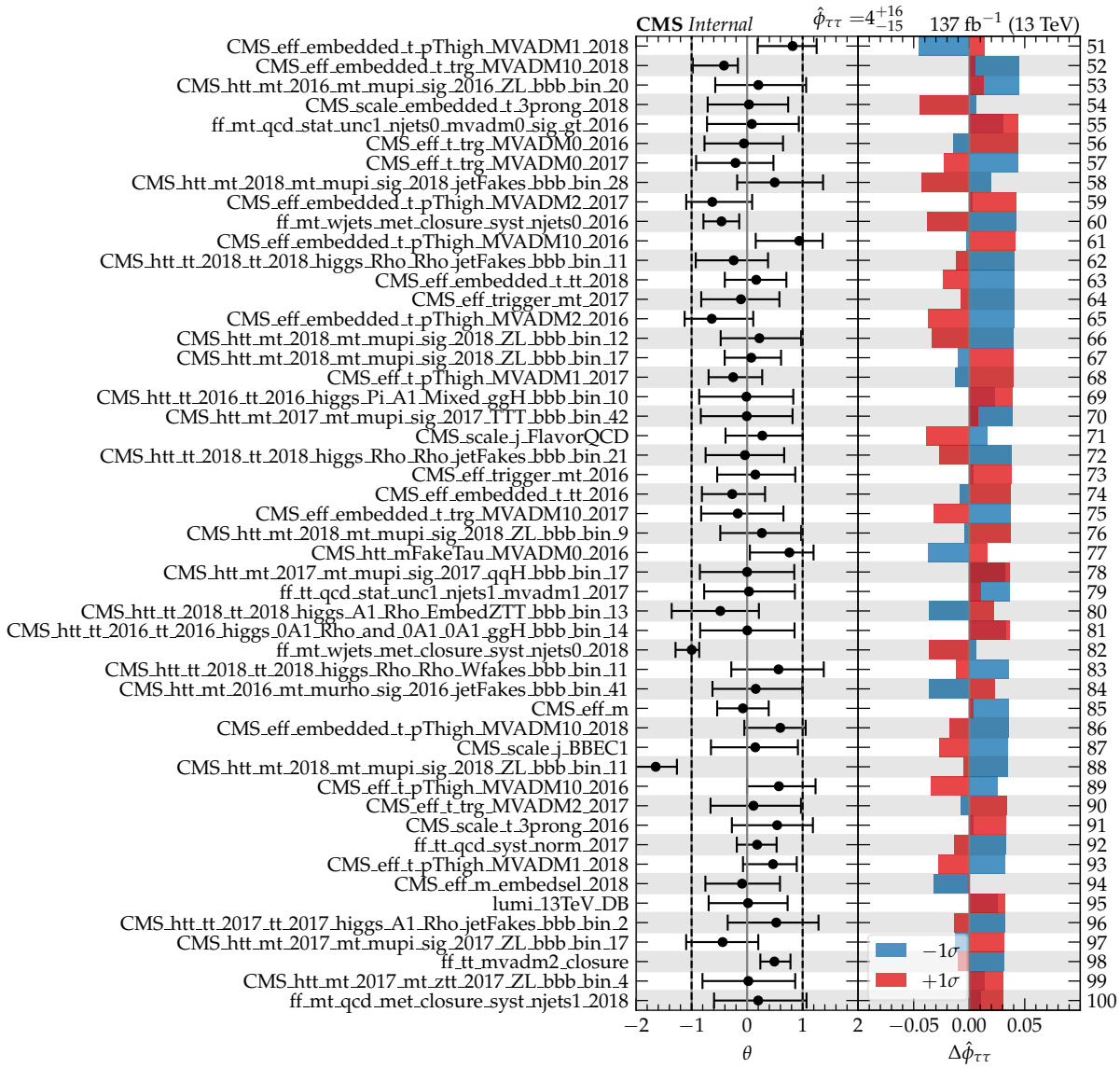

Figure 153: Impacts and constraints the 50-100 ranked for nuissance parameters.

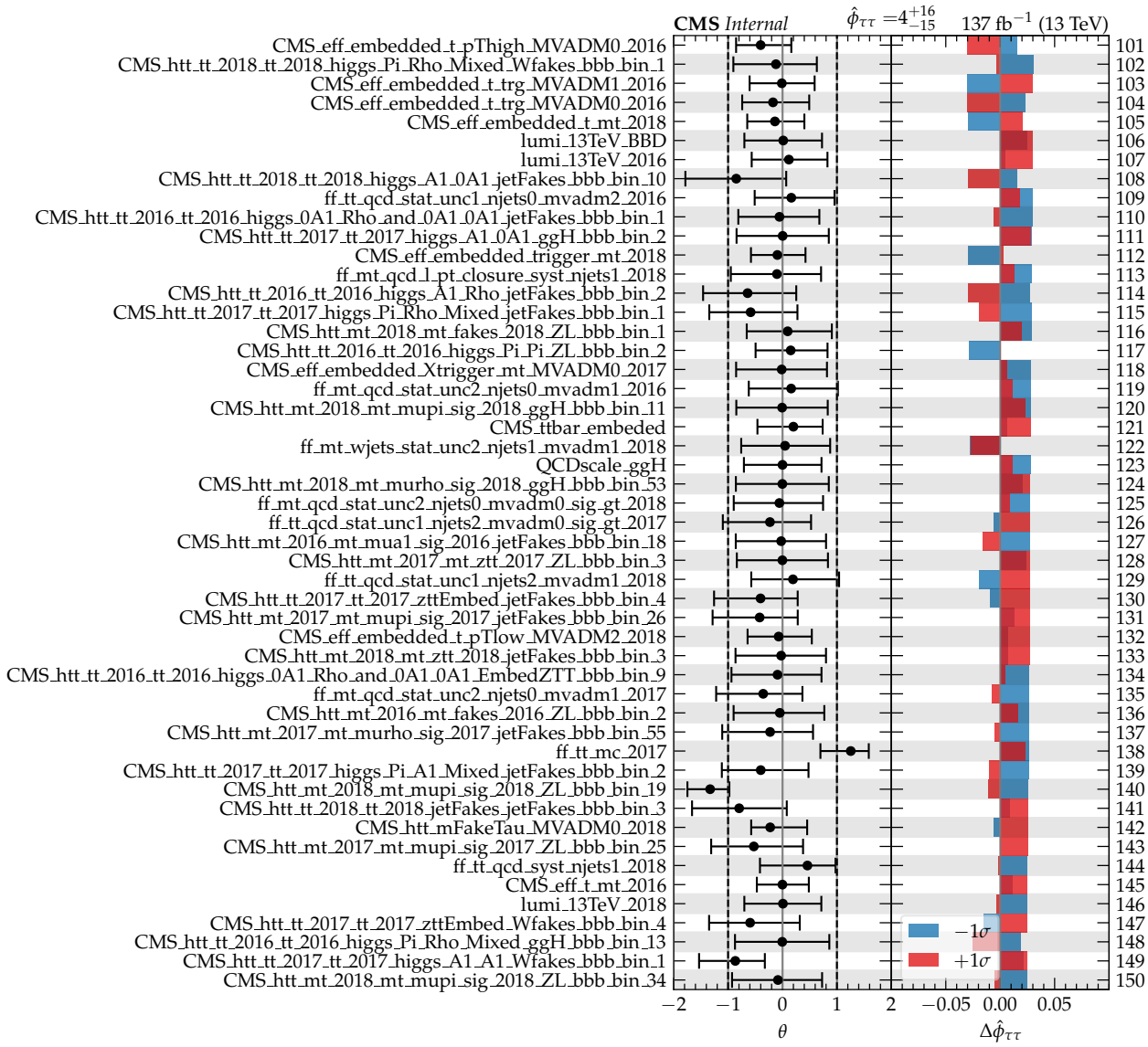

Figure 154: Impacts and constraints the 100-150 ranked for nuissance parameters.

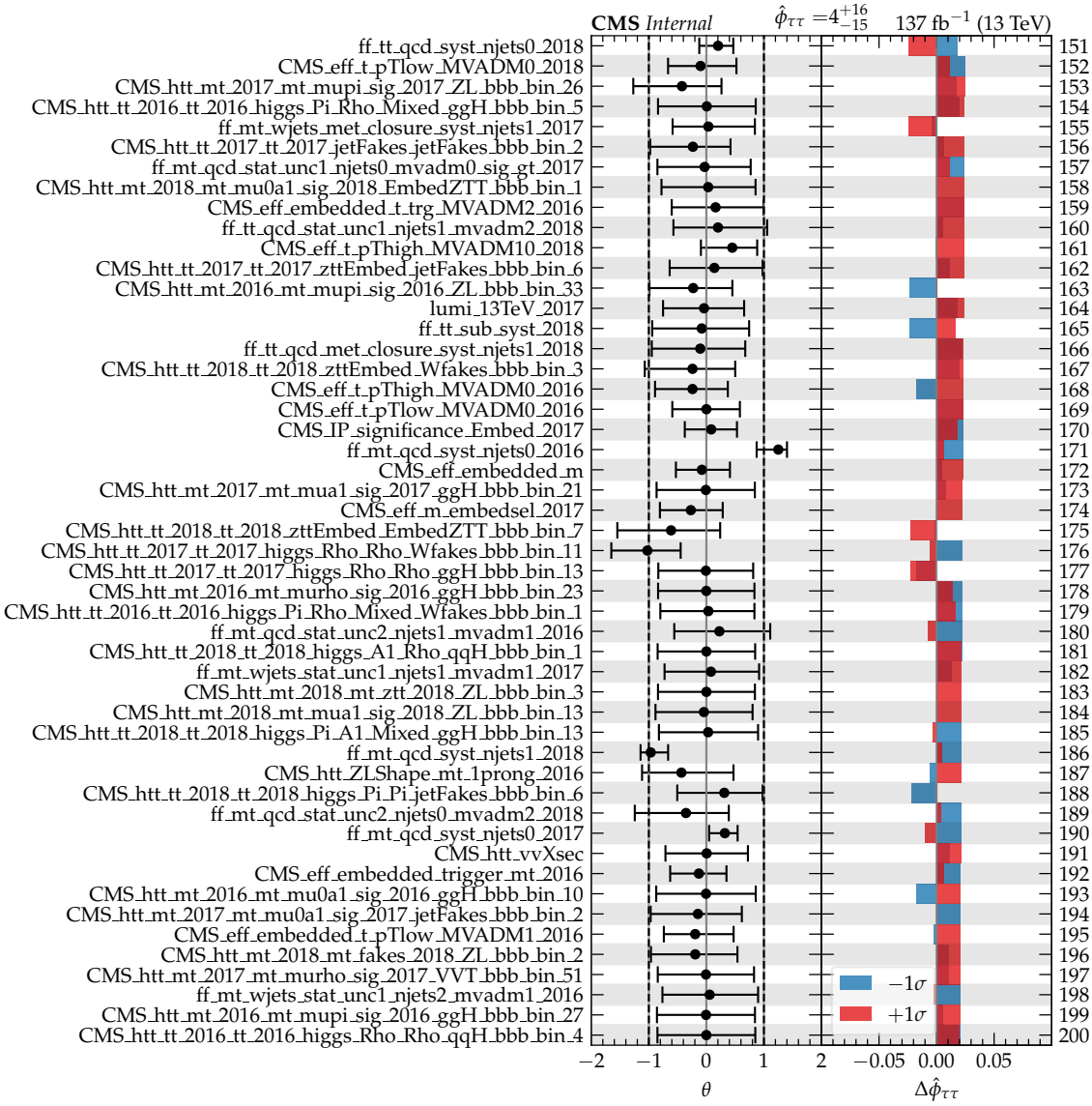

Figure 155: Impacts and constraints the 150-200 ranked for nuissance parameters.

13.5 Combined results

In Fig. 156 we present the combined log-likelihood scan, from which we obtain a 3.0σ (2.6σ) observed (expected) sensitivity to distinguish between the scalar and pseudoscalar hypotheses. From the combination we extract $\phi_{\tau\bar{\tau}} = -1 \pm 18\ (0 \pm 21)\ ^\circ$ at the 68% CL, and $\phi_{\tau\bar{\tau}} = -1 \pm 39\ (0 \pm 47)\ ^\circ$ at the 95% CL. This result is compatible with the standard model predictions within the uncertainties.

The uncertainty can be decomposed into the following components: statistical, bin-by-bin fluctuations in the background samples, experimental systematical uncertainties, and theoretical uncertainties. In this decomposition we obtain $\phi_{\tau\bar{\tau}} = (-1 \pm 18\,(\text{stat}) \pm 2(\text{bin-by-bin}) \pm 1\,(\text{syst}) \pm 1(\text{theory}))^\circ$.

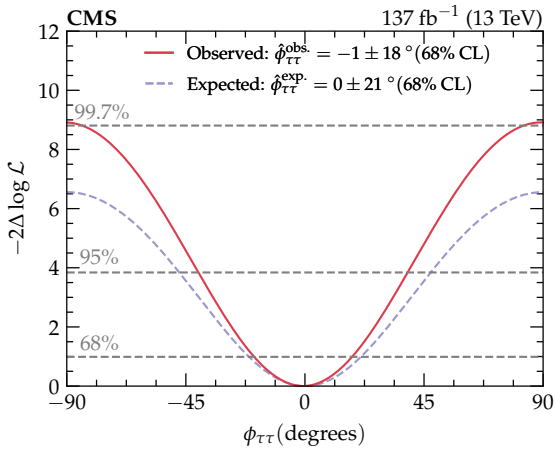

Figure 156: Negative log–likelihood scans for the combination of the $\tau_e\tau_h$, $\tau_\mu\tau_h$ and $\tau_h\tau_h$ channel. The expected sensitivity between the scalar and pseudo-scalar scenarios defined at $\phi_{\tau\bar{\tau}} = 0$ and $\phi_{\tau\bar{\tau}} = \pm 90$, respectively, is about 2.6σ. The expected value for $\phi_{\tau\bar{\tau}}$ is $0 \pm 21(47)^\circ$ at 68 (95)% CL, whilst the observed value for $\phi_{\tau\bar{\tau}}$ is $-1 \pm 18(39)^\circ$ at 68 (95)% CL. The pseudo-scalar hypothesis is rejected at 3.0σ.

In Table 32 we depict the expected sensitivities per decay mode as well as the combined sensitivities.
It can be seen that in the $\tau_\mu\tau_h$ channel the $\mu^\pm\rho^\mp$ mode is the most sensitive decay mode, followed by the $\mu^\pm\pi^\mp$ and $\mu^\pm a_1{}^\mp$ modes, respectively. For both the $\tau_\mu\tau_h$ and $\tau_h\tau_h$ channel it holds that the $a_1{}^\pm(\rightarrow \pi^0\pi^0\pi^\pm)$ mode is the least sensitive.
For the $\tau_h\tau_h$ channel, the ρ decay has the optimal sensitivity, although the π mode performs comparable in the most significant decay combination, despite the fact that the ρ is statistically enhanced w.r.t. π. The π is the second most sensitive mode, followed by the a_1 mode. In the $\tau_e\tau_h$ mode no individual mode has sensitivity above 1 σ, and the most sensitive channel is the eρ channel.

The statistical uncertainties in data are vastly leading in this analysis. From the systematical uncertainties, the statistical uncertainties in the background templates are one of the driving sources . Since the dominant contributions to the backgrounds are determined themselves in a data-driven manner, the amount of data itself is the limiting factor in this uncertainty. This other significant sources of systematic uncertainties are those related to: the hadronic trigger efficiency, theory, the tau energy scale, and the fake factor method.

DRAFT

Table 32: The obtained expected sensitivities in standard deviations to distinguish between a CP-even and odd coupling. Results are displayed for the individual decay modes (combined with their background categories), the combined $\tau_e\tau_h$, $\tau_\mu\tau_h$ and $\tau_h\tau_h$ channels with their background categories, and the overall combination.

Decay mode	Expected sensitivity
$\tau_e\tau_h$	0.99
$e\rho$	0.57
$e\pi$	0.54
ea_1^{3p}	0.38
ea_1^{1p}	0.17
$\tau_\mu\tau_h$	1.47
$\mu\rho$	1.16
$\mu\pi$	0.71
μa_1^{3p}	0.51
μa_1^{1p}	0.24
$\tau_h\tau_h$	1.85
$\rho\rho$	1.10
$\rho\pi$	1.08
ρa_1^{3p}	0.65
$\pi\pi$	0.39
πa_1^{3p}	0.48
$a_1^{1p}\rho$ and $a_1^{1p}a_1^{1p}$	0.30
πa_1^{1p}	0.23
$a_1^{3p}a_1^{3p}$	0.28
$a_1^{3p}a_1^{1p}$	0.13
Combined	2.6

DRAFT

The fit allows to extract the values of the signal normalisation w.r.t. the predictions of the standard model (using a common rate parameter μ to simultaneously scale both ggH and VBF yields). The observed (expected) value is 0.82 ± 0.15 (1.0 ± 0.16). The value is compatible with what was obtained by dedicated coupling analyses [62]. The uncertainty is larger than the value obtained by these analyses, which is attributed to the additional $\tau_e\tau_\mu$ channels that are included in the coupling analyses [62], and the fact that the CP measurement is optimised for sensitivity to $\phi_{\tau\bar{\tau}}$ rather than the signal rates.

The data collected in 2018 provides the largest contribution to the total sensitivity by way of the larger integrated luminosity for this era. 2016 and 2017 have similar sensitivities owing to the similar integrated luminosities for these two datasets.

The observed scans of the rate parameters are shown in Figure 157– 159.

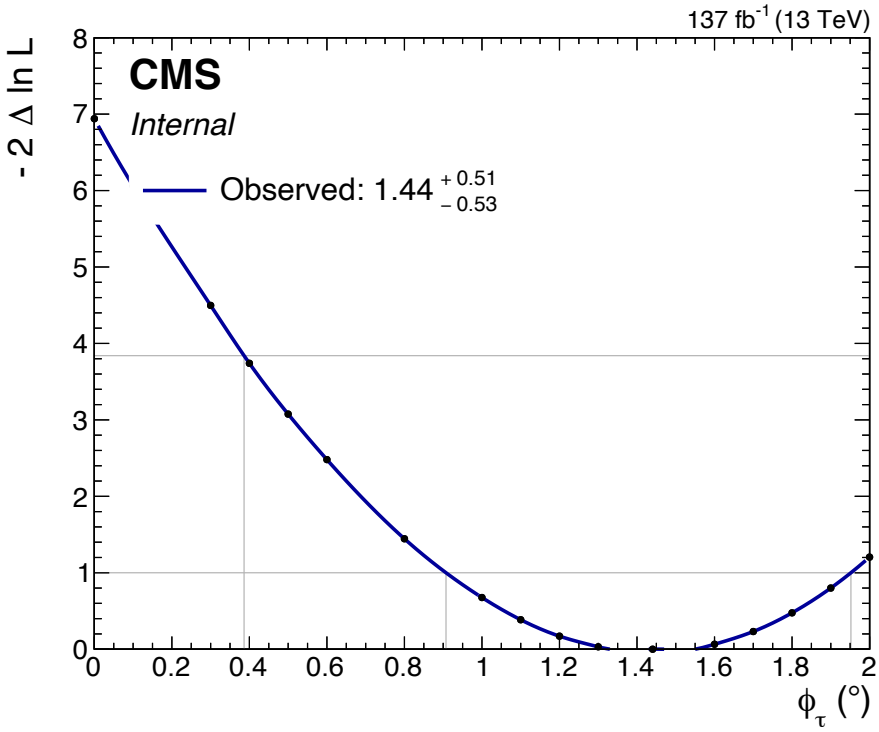

Figure 157: Negative log–likelihood scan for the μ_V rate parameter.

In addition we may reparametrise the likelihood from Equation 13 in terms of κ_τ and $\tilde{\kappa}_\tau$. They are related to the CP-mixing angle $\phi_{\tau\bar{\tau}}$ through the following relationship:

$$\tan\phi_{\tau\bar{\tau}} = \frac{\tilde{\kappa}_\tau}{\kappa_\tau}, \tag{51}$$

where the individual rate parameters μ_{ggH} and μ_V have been set to a value of 1. This assumption is well motivated and allows the two-dimensional scans of the κ_τ and $\tilde{\kappa}_\tau$ to be performed. In the case of a two-dimensional negative log–likelihood the 68% and 95% confidence intervals are found when $-2\Delta\ln L_{2D} = 2.28$ and 5.99, which is defined analogously as in Equation 50, where the likelihood is now a function of both κ_τ and $\tilde{\kappa}_\tau$. The result of the scan is shown in Figure 160.

In order to make a two-dimensional scan of κ_τ and $\tilde{\kappa}_\tau$, as defined in Eq. 51, we parameterise the likelihood from Eq. 13 in terms of κ_τ and $\tilde{\kappa}_\tau$. All other Higgs couplings are fixed to the SM expectation values.

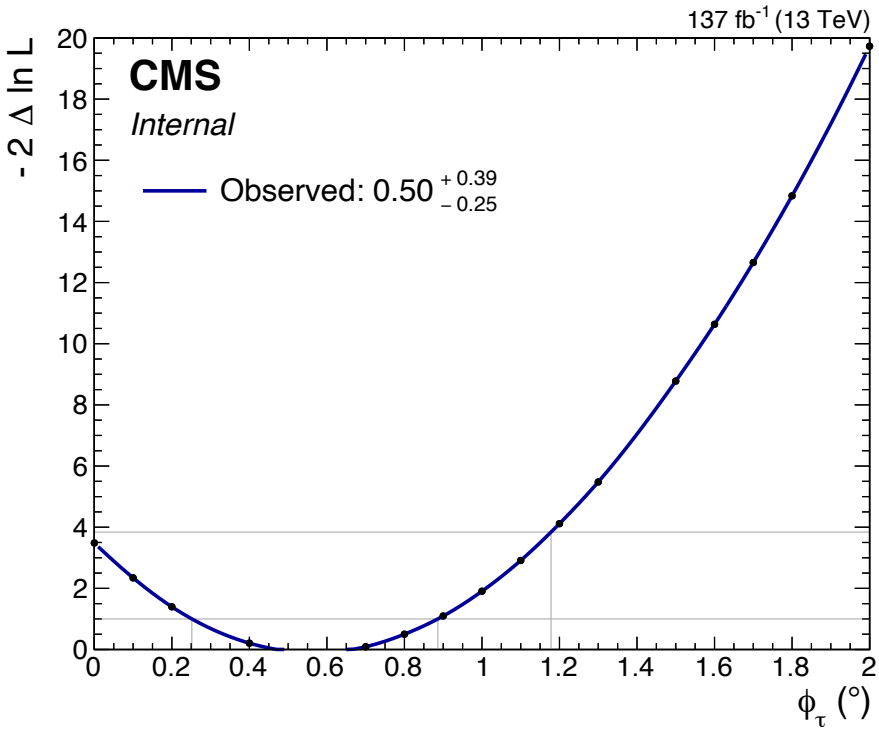

Figure 158: Negative log–likelihood scan for the $\mu_{gg\mathrm{H}}$ rate parameter.

In the case of a two-dimensional negative log-likelihood the 68, 95, and 99.7% confidence intervals are found when $-2\Delta \ln L_{2\mathrm{D}} = 2.30$, 5.99, and 11.62 [**?**], which is defined analogously as in Eq. 50, where the likelihood is now a function of both κ_τ and $\tilde{\kappa}_\tau$. The observed result of the scan is shown in Fig. 160.It should be noted that the fit is only sensitive to the relative sign between κ_τ and $\tilde{\kappa}_\tau$.

In Fig. 161 we display a scan of the branching fraction modifier with respect to the SM value $\mu^{\tau\tau}$ versus $\phi_{\tau\tau}$. We observe that there is no strong correlation between these. In this fit the signal strength modifiers $\vec{\mu}$ were fixed to their SM expectation values.

DRAFT

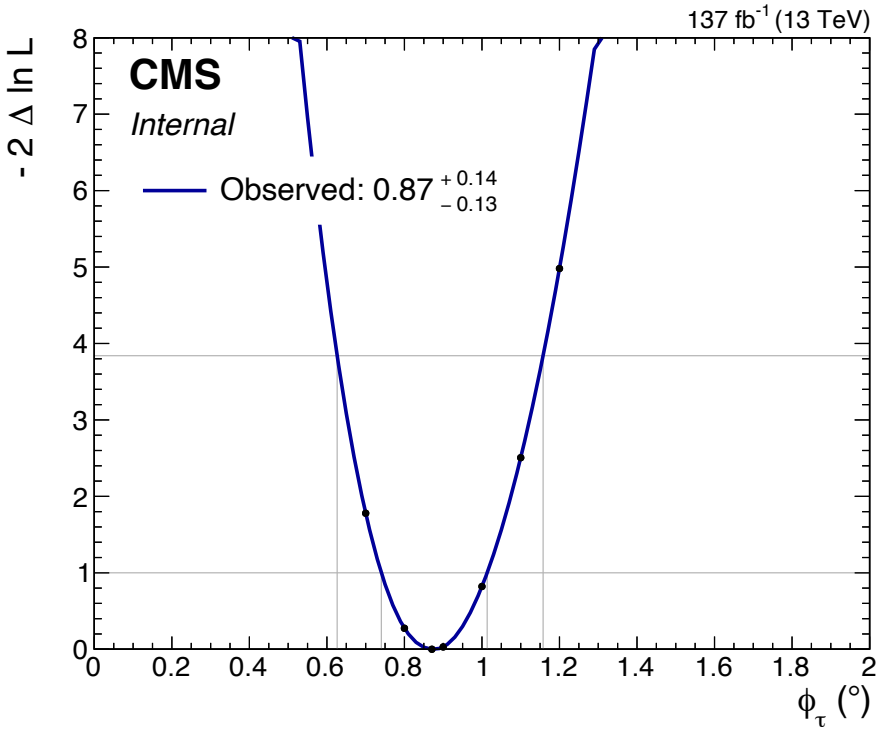

Figure 159: Negative log–likelihood scan for the inclusive rate parameter.

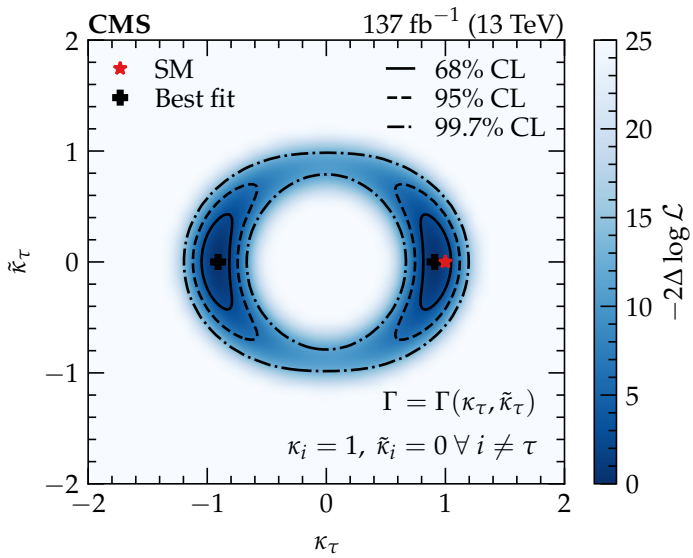

Figure 160: Two-dimensional scan of the (reduced) Yukawa couplings.

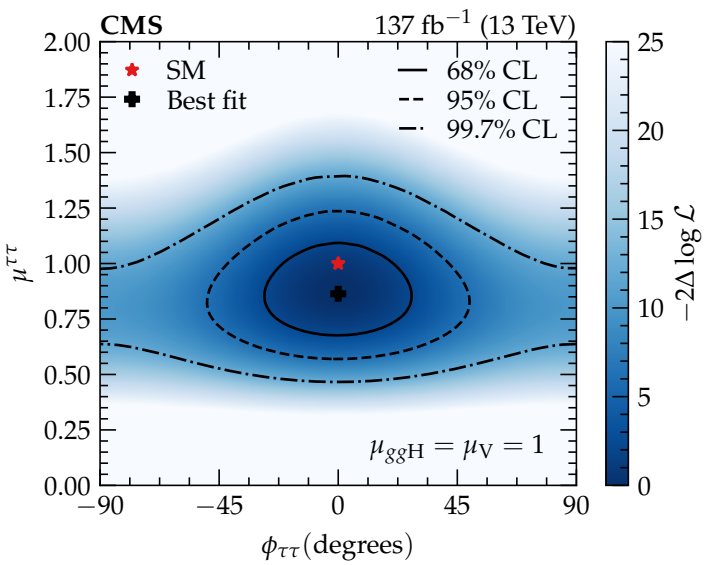

Figure 161: 2-dimensional scan of $\phi_{\tau\bar{\tau}}$ vs $\mu^{\tau_h\tau_h}$

14 Summary

A measurement of the CP properties of the Higgs coupling to tau leptons is presented. The observed (expected) full Run-2 significance to separate between CP-even and CP-odd states is 3.0σ (2.6σ). The observed (expected) mixing angle $\phi_{\tau\bar{\tau}}$ was was found to be -1 ± 18 $(0 \pm 21)^{\circ}$ at 68% CL, and -1 ± 39 $(0 \pm 47^{\circ})$ at 95% CL. The results are compatible with predictions for the standard model Higgs boson.

DRAFT

A Jacobi Matrices for Impact Parameter Significance

The Jacobian matrix used in Eq. 20 is defined as

$$J_{\vec{x}} = \frac{\partial \vec{x}}{\partial \left(\frac{q}{p}, \lambda, \phi, d_{xy}, d_{sz}\right)}. \tag{52}$$

The entries of the matrix are then calculated to be:

$$\frac{\partial x_1}{\partial \frac{q}{p}} = -\frac{\operatorname{sgn}\frac{q}{p} \cdot \cos\lambda}{B \cdot \left(\frac{q}{p}\right)^2} \cdot \left[\sin\phi \cdot \left(1 - \cos t'_{\min}\right) + \cos\phi \cdot \sin t'_{\min}\right], \tag{53}$$

$$\frac{\partial x_1}{\partial \lambda} = -\frac{\operatorname{sgn}\frac{q}{p} \cdot \sin\lambda}{\left(B \cdot \frac{q}{p}\right)} \cdot \left[\sin\phi \cdot \left(1 - \cos t'_{\min}\right) + \cos\phi \cdot \sin t'_{\min}\right], \tag{54}$$

$$\frac{\partial x_1}{\partial \phi} = -d_{xy} \cdot \cos\phi + \frac{\operatorname{sgn}\frac{q}{p} \cdot \cos\lambda}{\left(B \cdot \frac{q}{p}\right)} \cdot \left[\cos\phi \cdot \left(1 - \cos t'_{\min}\right) - \sin\phi \cdot \sin t'_{\min}\right], \tag{55}$$

$$\frac{\partial x_1}{\partial d_{xy}} = -\sin\phi, \tag{56}$$

$$\frac{\partial x_1}{\partial d_{sz}} = 0, \tag{57}$$

$$\frac{\partial x_2}{\partial \frac{q}{p}} = \frac{\operatorname{sgn}\frac{q}{p} \cdot \cos\lambda}{B \cdot \left(\frac{q}{p}\right)^2} \cdot \left[\cos\phi \cdot \left(1 - \cos t'_{\min}\right) - \sin\phi \cdot \sin t'_{\min}\right], \tag{58}$$

$$\frac{\partial x_2}{\partial \lambda} = \frac{\operatorname{sgn}\frac{q}{p} \cdot \sin\lambda}{\left(B \cdot \frac{q}{p}\right)} \cdot \left[\cos\phi \cdot \left(1 - \cos t'_{\min}\right) - \sin\phi \cdot \sin t'_{\min}\right], \tag{59}$$

$$\frac{\partial x_2}{\partial \phi} = -d_{xy} \cdot \sin\phi + \frac{\operatorname{sgn}\frac{q}{p} \cdot \cos\lambda}{\left(B \cdot \frac{q}{p}\right)} \cdot \left[\sin\phi \cdot \left(1 + \cos t'_{\min}\right) + \cos\phi \cdot \sin t'_{\min}\right], \tag{60}$$

$$\frac{\partial x_2}{\partial d_{xy}} = \cos\phi, \tag{61}$$

$$\frac{\partial x_2}{\partial d_{sz}} = 0, \tag{62}$$

$$\frac{\partial x_3}{\partial \frac{q}{p}} = -\frac{\operatorname{sgn}\frac{q}{p} \cdot \sin\lambda}{B \cdot \left(\frac{q}{p}\right)^2} \cdot t'_{\min}, \tag{63}$$

DRAFT

$$\frac{\partial x_3}{\partial \lambda} = \frac{\operatorname{sgn} \frac{q}{p} \cdot \cos \lambda}{B \cdot \frac{q}{p}} \cdot t'_{\min} + \frac{d_{sz}}{\cos \lambda} \cdot \tan \lambda, \tag{64}$$

$$\frac{\partial x_3}{\partial \phi} = 0, \tag{65}$$

$$\frac{\partial x_3}{\partial d_{xy}} = 0, \tag{66}$$

$$\frac{\partial x_3}{\partial d_{sz}} = \frac{1}{\cos \lambda}. \tag{67}$$

The Jacobian matrix used in Eq. 21 is defined as and calculated to be:

$$J_{\vec{n}} = \frac{\partial \vec{n}}{\partial \left(n_x, n_y, n_z, V_x, V_y, V_z \right)} = \begin{pmatrix} 1 & 0 & 0 & -1 & 0 & 0 \\ 0 & 1 & 0 & 0 & -1 & 0 \\ 0 & 0 & 1 & 0 & 0 & -1 \end{pmatrix}. \tag{68}$$

DRAFT

B Plots of all categories used in the final fit

The set of postfit plots showing all $\tau_\mu\tau_h$ unrolled postfit distributions are shown in Fig. 162 – 191. The set of postfit plots showing all $\tau_h\tau_h$ unrolled postfit distributions are shown in Fig. 166 – 257. The set of postfit plots in the $a_1^{3pr}a_1^{3pr}$ signal category, where the polarimetric vector method is used, are shown in Fig. 175. The set of unrolled postfit distributions of the $\tau_e\tau_h$ channel are shown in Fig. 176 – 179.

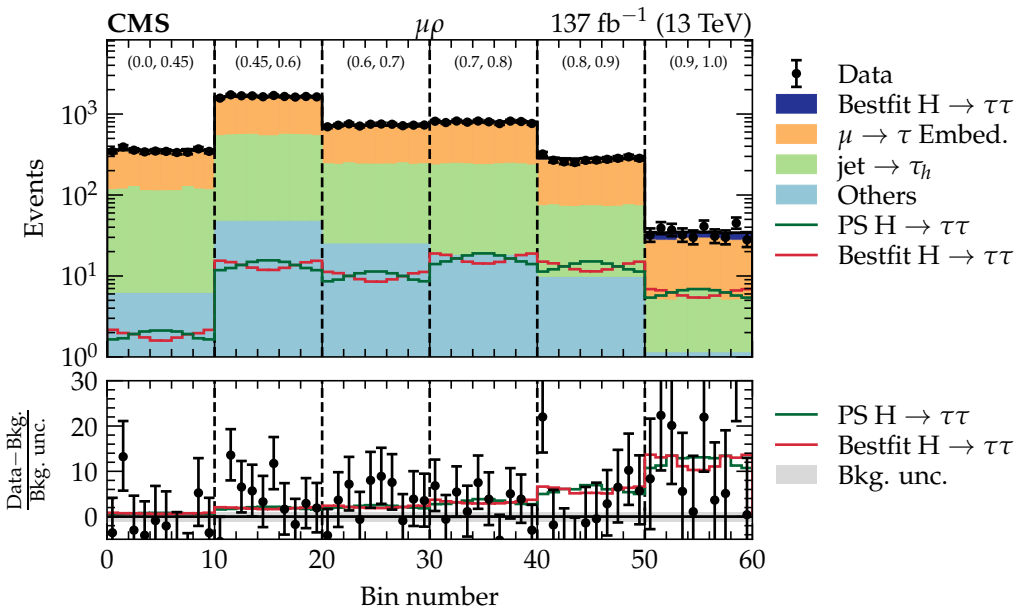

Figure 162: Postfit distribution of ϕ_{CP} of the $\mu^\pm + \rho^\mp$ channel for all years combined, in windows of increasing NN score ranging between $(0, 1)$. The x-axis represents the cyclic bins in ϕ_{CP} in the range of $(0, 2\pi)$. The uncertainty band represents the full uncertainty. In the bottom plot the data minus the background template divided by the uncertainty in the background template is displayed, as well as the signal samples divided by the uncertainty in the background template. The uncertainty band consists of the sum of the postfit uncertainties in the background templates.

DRAFT

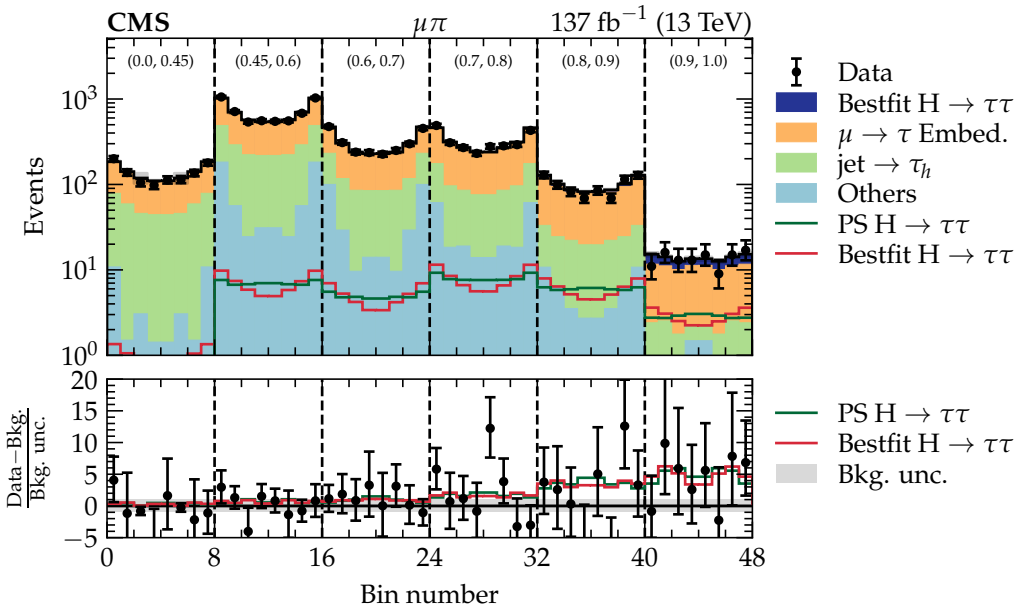

Figure 163: Postfit distribution of ϕ_{CP} of the $\mu^{\pm} + \pi^{\mp}$ channel for all years, in windows of increasing NN score ranging between $(0, 1)$. The x-axis represents the cyclic bins in ϕ_{CP} in the range of $(0, 2\pi)$. The uncertainty band represents the full uncertainty. In the bottom plot the data minus the background template divided by the uncertainty in the background template is displayed, as well as the signal samples divided by the uncertainty in the background template. The uncertainty band consists of the sum of the postfit uncertainties in the background templates.

DRAFT

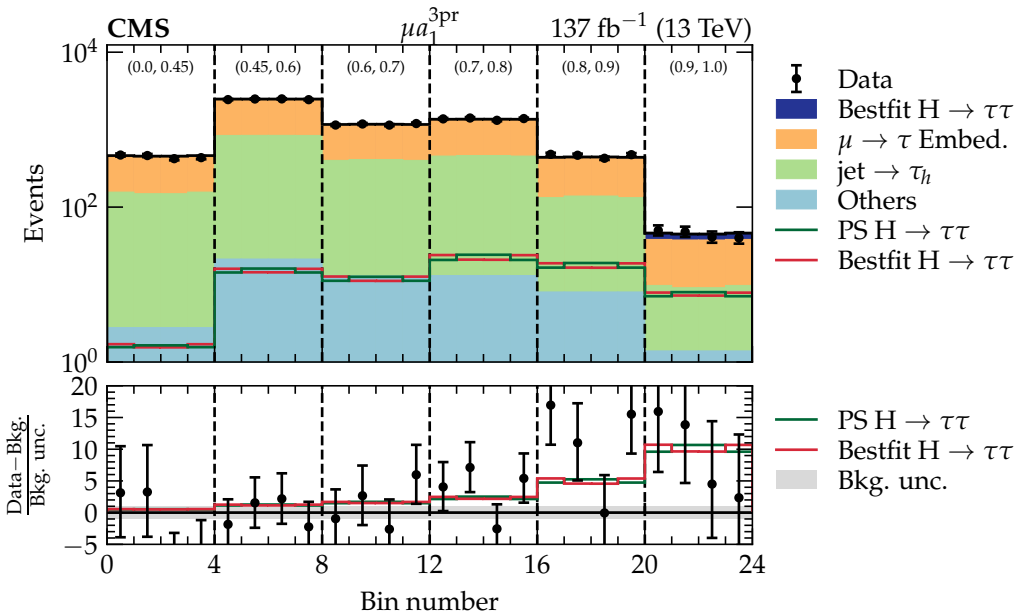

Figure 164: Postfit distribution of ϕ_{CP} of the $\mu^{\pm} + a_1^{1p}$ channel for all years, in windows of increasing NN score ranging between $(0, 1)$. The x-axis represents the cyclic bins in ϕ_{CP} in the range of $(0, 2\pi)$. The uncertainty band represents the full uncertainty. In the bottom plot the data minus the background template divided by the uncertainty in the background template is displayed, as well as the signal samples divided by the uncertainty in the background template. The uncertainty band consists of the sum of the postfit uncertainties in the background templates.

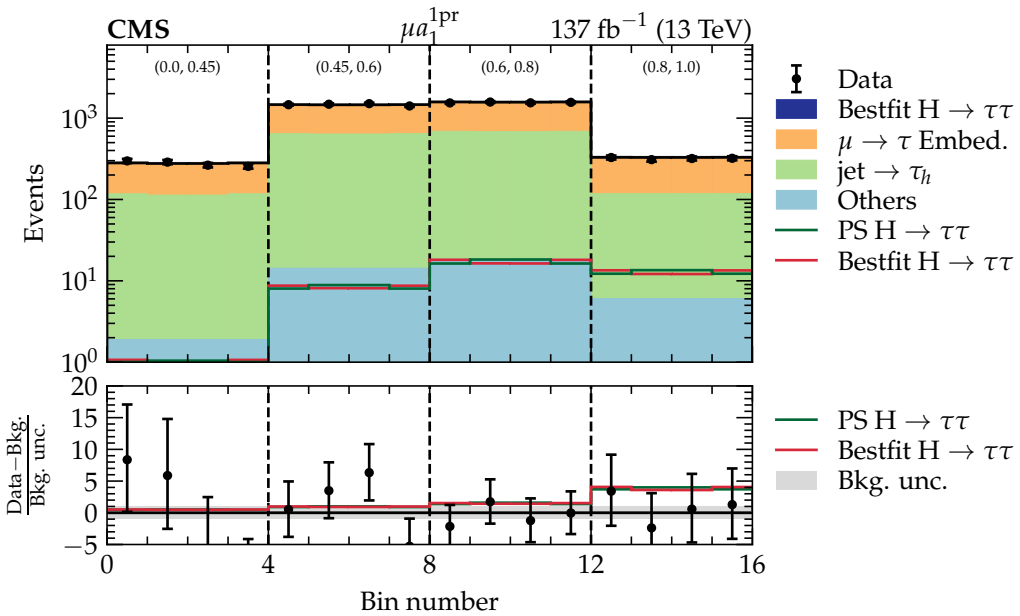

Figure 165: Postfit distribution of ϕ_{CP} of the $\mu^{\pm} + a_1^{3p}$ channel for all years, in windows of increasing NN score ranging between $(0, 1)$. The x-axis represents the cyclic bins in ϕ_{CP} in the range of $(0, 2\pi)$. The uncertainty band represents the full uncertainty. In the bottom plot the data minus the background template divided by the uncertainty in the background template is displayed, as well as the signal samples divided by the uncertainty in the background template. The uncertainty band consists of the sum of the postfit uncertainties in the background templates.

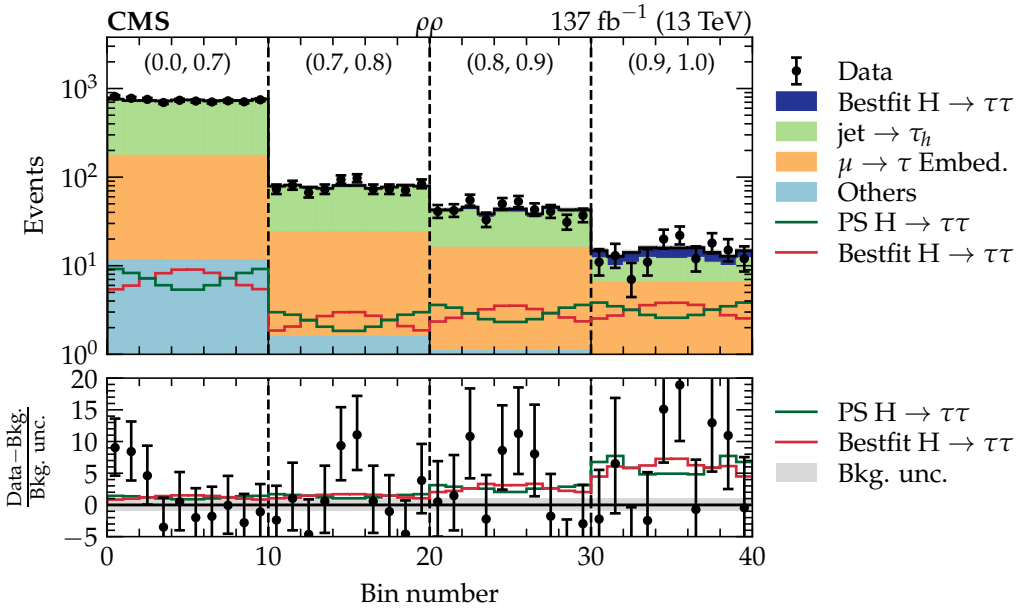

Figure 166: Postfit distribution of ϕ_{CP} of the $\rho^{\pm} + \rho^{\mp}$ channel for all years, in windows of increasing BDT score. The x-axis represents the cyclic bins in ϕ_{CP} in the range of $(0, 2\pi)$. The uncertainty band represents the full uncertainty. In the bottom plot the data minus the background template divided by the uncertainty in the background template is displayed, as well as the signal samples divided by the uncertainty in the background template. The uncertainty band consists of the sum of the postfit uncertainties in the background templates.

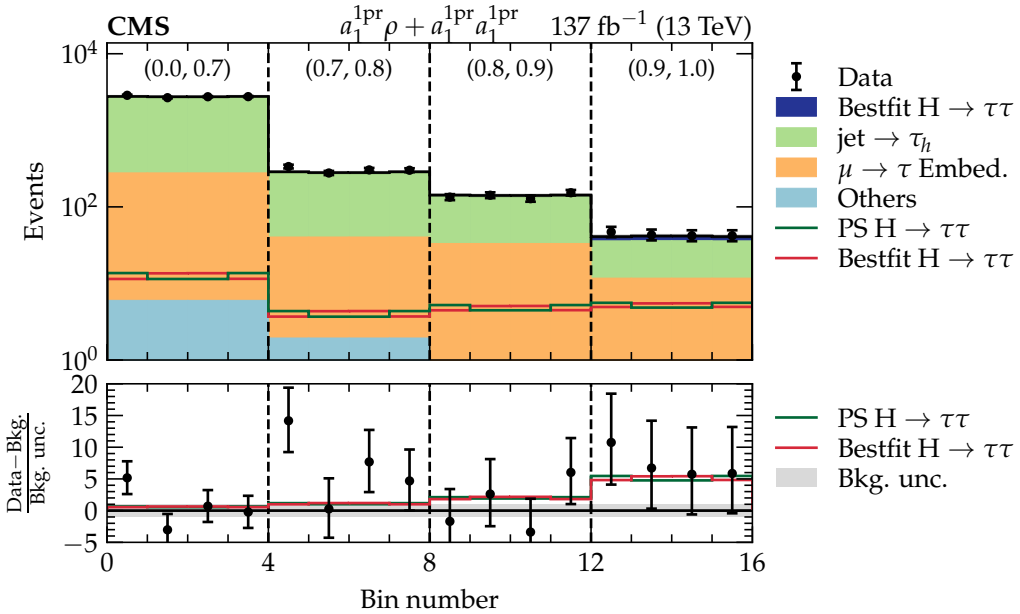

Figure 167: Postfit distribution of ϕ_{CP} of the $a_1^{\pm,1pr} + \rho^{\mp}$ and $a_1^{1p} + a_1^{1p}$ channel for all years, in windows of increasing BDT score ranging between $(0, 1)$. The x-axis represents the cyclic bins in ϕ_{CP} in the range of $(0, 2\pi)$. The uncertainty band represents the full uncertainty. In the bottom plot the data minus the background template divided by the uncertainty in the background template is displayed, as well as the signal samples divided by the uncertainty in the background template. The uncertainty band consists of the sum of the postfit uncertainties in the background templates.

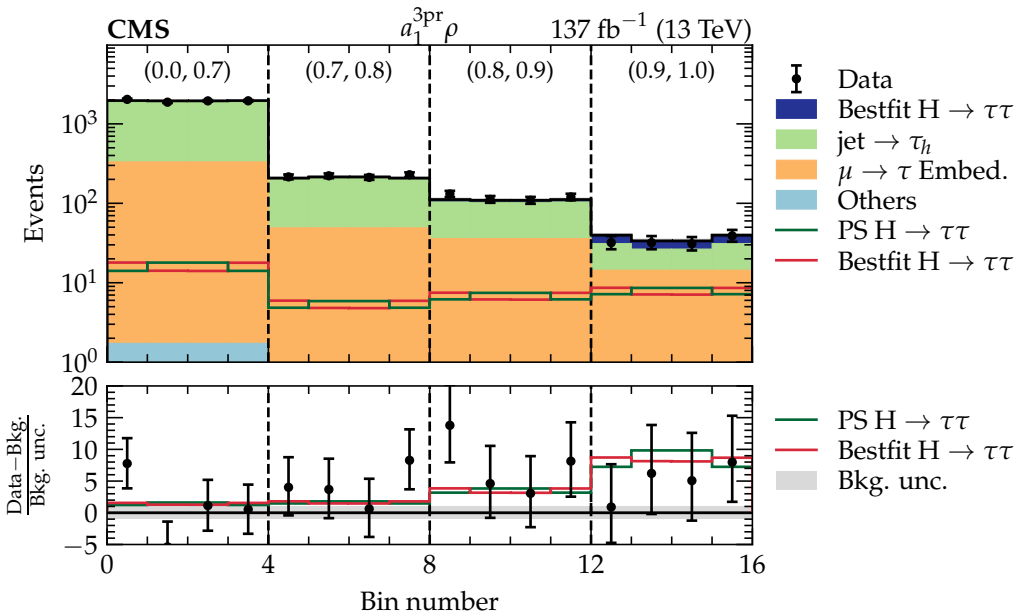

Figure 168: Postfit distribution of ϕ_{CP} of the $a_1^{3p} + \rho^{\mp}$ channel for all years, in windows of increasing BDT score ranging between $(0, 1)$. The x-axis represents the cyclic bins in ϕ_{CP} in the range of $(0, 2\pi)$. The uncertainty band represents the full uncertainty. In the bottom plot the data minus the background template divided by the uncertainty in the background template is displayed, as well as the signal samples divided by the uncertainty in the background template. The uncertainty band consists of the sum of the postfit uncertainties in the background templates.

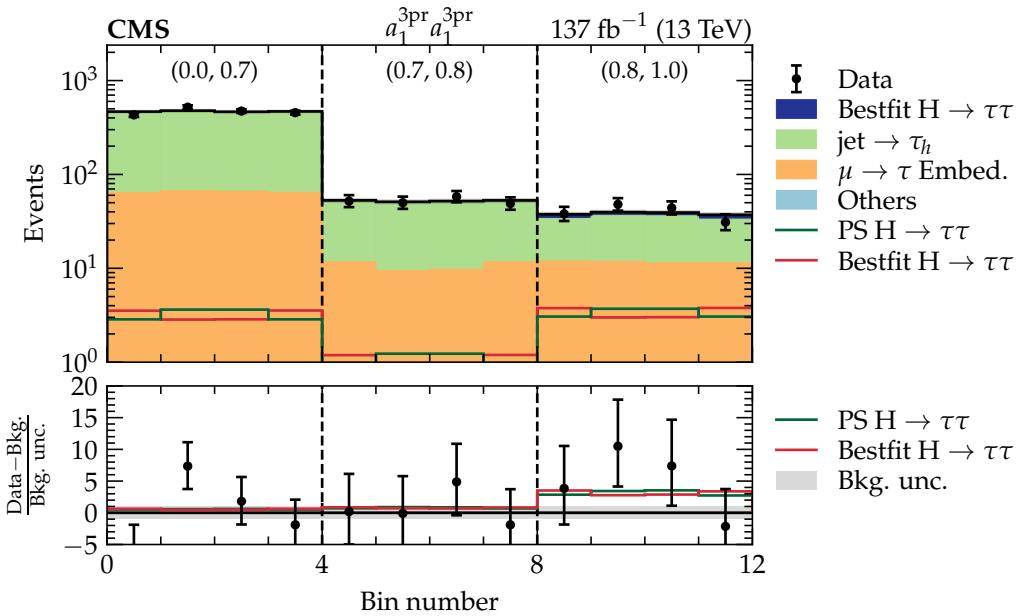

Figure 169: Postfit distribution of ϕ_{CP} of the $a_1^{3p} + a_1^{\mp,3pr}$ channel for all years, in windows of increasing BDT score ranging between $(0, 1)$. The x-axis represents the cyclic bins in ϕ_{CP} in the range of $(0, 2\pi)$. The uncertainty band represents the full uncertainty. In the bottom plot the data minus the background template divided by the uncertainty in the background template is displayed, as well as the signal samples divided by the uncertainty in the background template. The uncertainty band consists of the sum of the postfit uncertainties in the background templates.

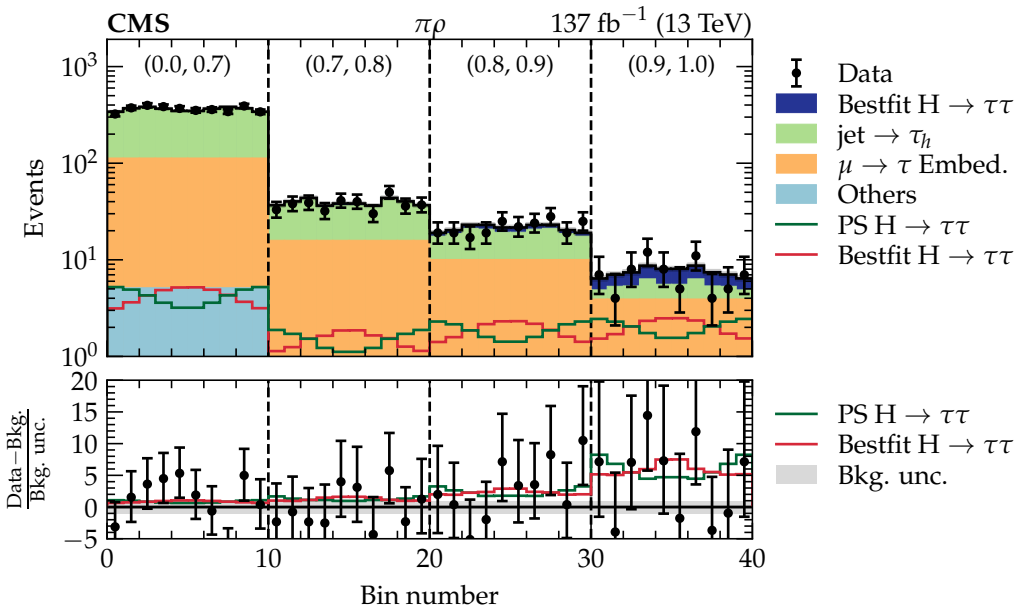

Figure 170: Postfit distribution of ϕ_{CP} of the $\pi^{\pm} + \rho^{\mp}$ channel for all years, in windows of increasing BDT score ranging between $(0, 1)$. The x-axis represents the cyclic bins in ϕ_{CP} in the range of $(0, 2\pi)$. The uncertainty band represents the full uncertainty. In the bottom plot the data minus the background template divided by the uncertainty in the background template is displayed, as well as the signal samples divided by the uncertainty in the background template. The uncertainty band consists of the sum of the postfit uncertainties in the background templates.

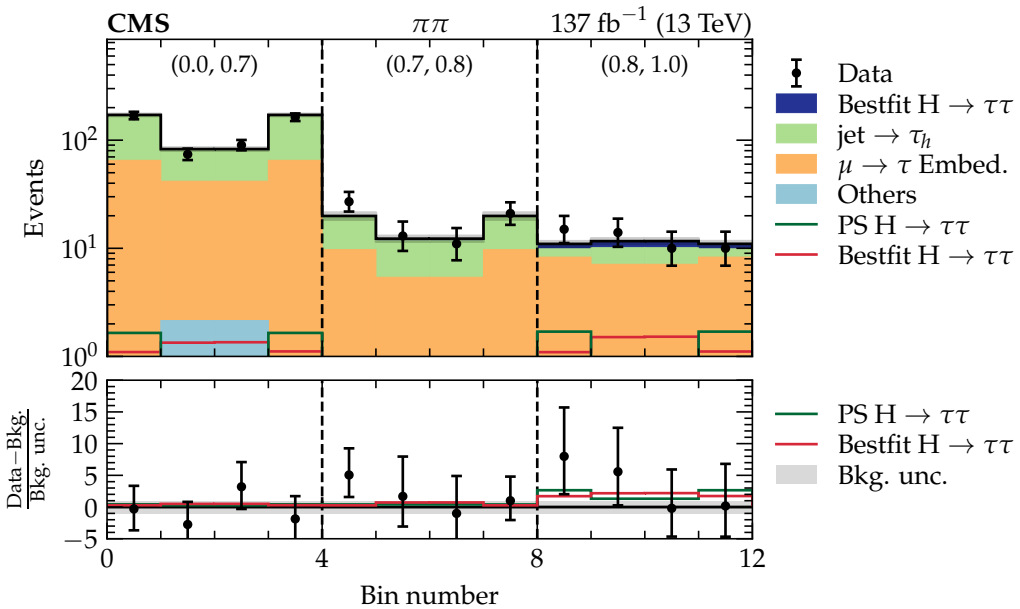

Figure 171: Postfit distribution of ϕ_{CP} of the $\pi^{\pm} + \pi^{\mp}$ channel for all years, in windows of increasing BDT score ranging between $(0, 1)$. The x-axis represents the cyclic bins in ϕ_{CP} in the range of $(0, 2\pi)$. The uncertainty band represents the full uncertainty. In the bottom plot the data minus the background template divided by the uncertainty in the background template is displayed, as well as the signal samples divided by the uncertainty in the background template. The uncertainty band consists of the sum of the postfit uncertainties in the background templates.

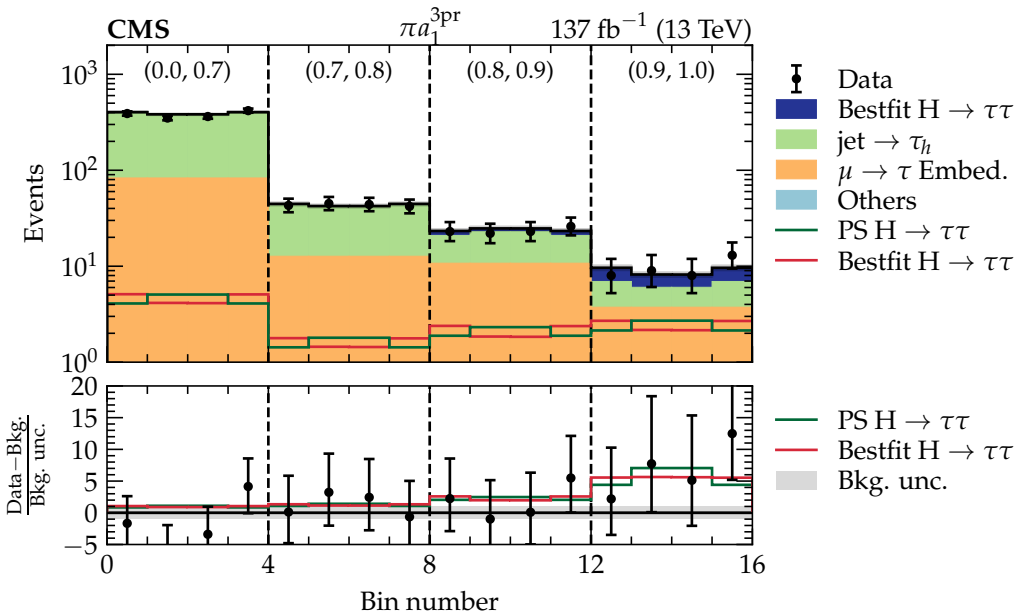

Figure 172: Postfit distribution of ϕ_{CP} of the $\pi^{\pm} + a_1^{3p}$ channel for all years, in windows of increasing BDT score ranging between $(0, 1)$. The x-axis represents the cyclic bins in ϕ_{CP} in the range of $(0, 2\pi)$. The uncertainty band represents the full uncertainty. In the bottom plot the data minus the background template divided by the uncertainty in the background template is displayed, as well as the signal samples divided by the uncertainty in the background template. The uncertainty band consists of the sum of the postfit uncertainties in the background templates.

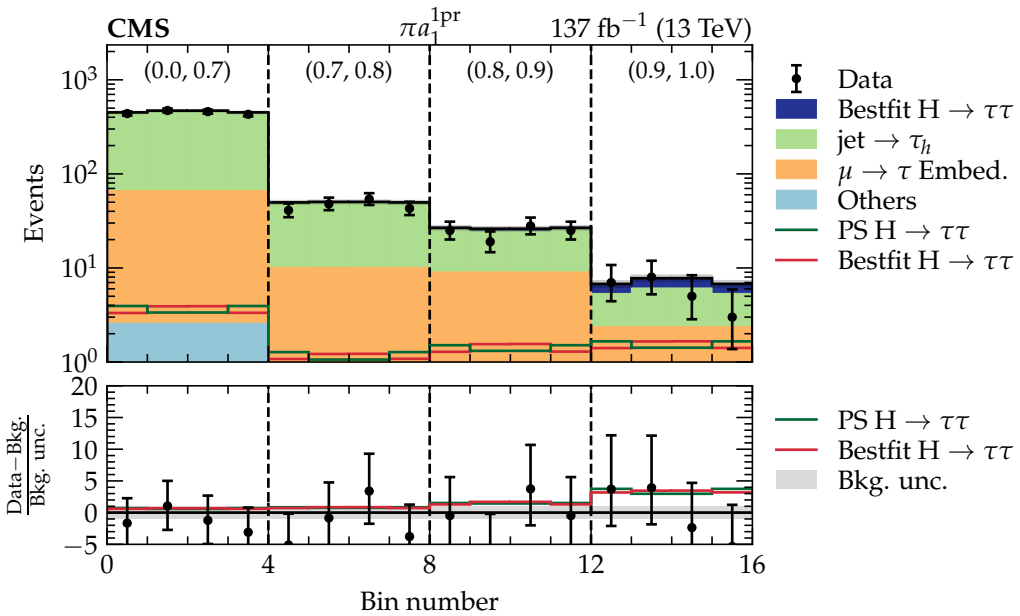

Figure 173: Postfit distribution of ϕ_{CP} of the $\pi^{\pm} + a_1^{1p}$ channel for all years, in windows of increasing BDT score ranging between $(0, 1)$. The x-axis represents the cyclic bins in ϕ_{CP} in the range of $(0, 2\pi)$. The uncertainty band represents the full uncertainty. In the bottom plot the data minus the background template divided by the uncertainty in the background template is displayed, as well as the signal samples divided by the uncertainty in the background template. The uncertainty band consists of the sum of the postfit uncertainties in the background templates.

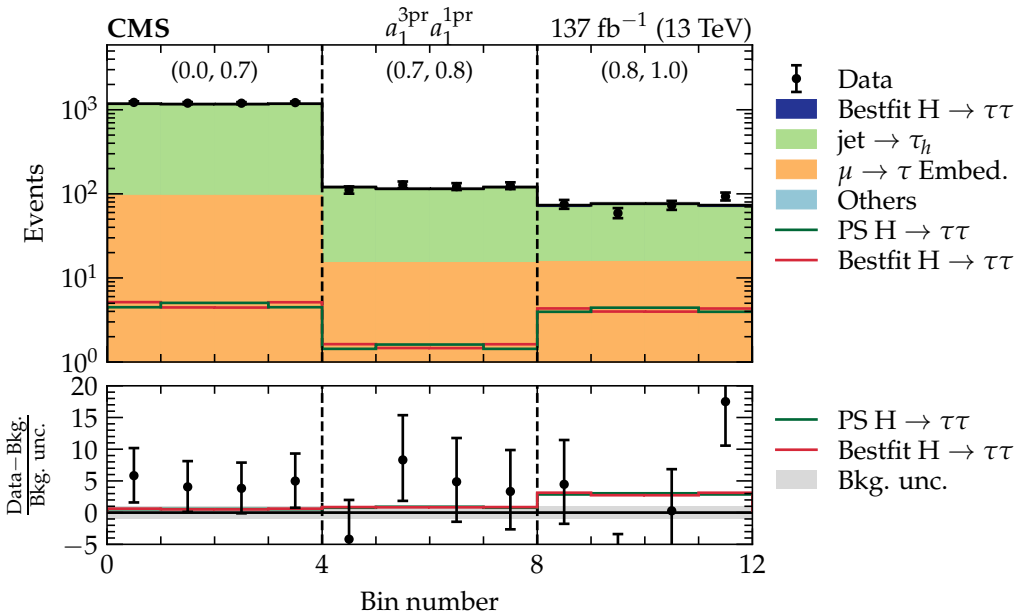

Figure 174: Postfit distribution of ϕ_{CP} of the $a_1^{3p} + a_1^{1p}$ channel for all years, in windows of increasing BDT score ranging between $(0, 1)$. The x-axis represents the cyclic bins in ϕ_{CP} in the range of $(0, 2\pi)$. The uncertainty band represents the full uncertainty. In the bottom plot the data minus the background template divided by the uncertainty in the background template is displayed, as well as the signal samples divided by the uncertainty in the background template. The uncertainty band consists of the sum of the postfit uncertainties in the background templates.

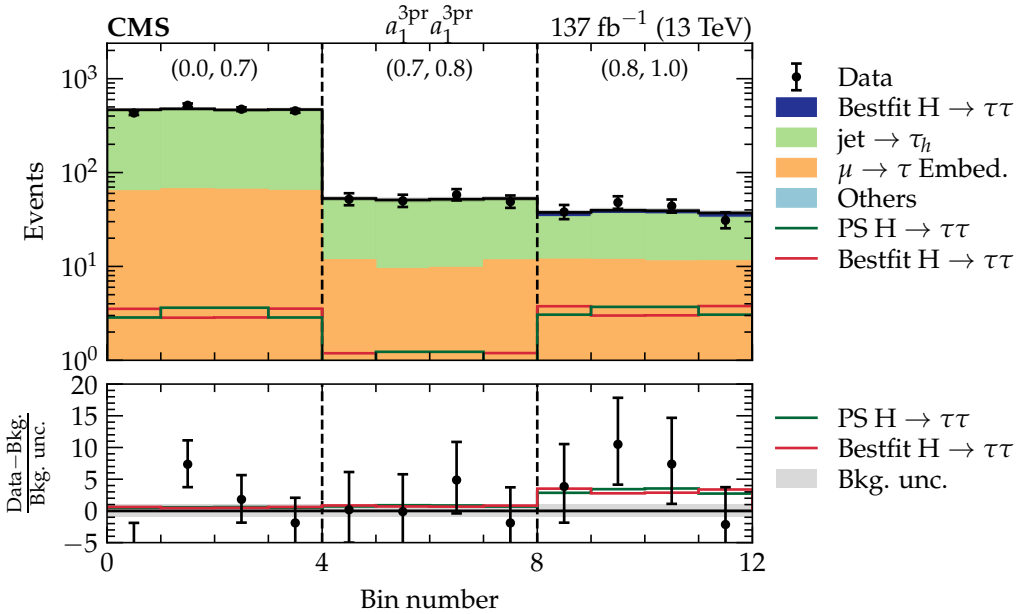

Figure 175: Postfit distribution of ϕ_{CP} of the $a_1^{3p} + a_1^{3p}$ channel for all years using the polarimetric vector method, in windows of increasing BDT score ranging between $(0, 1)$. The x-axis represents the cyclic bins in ϕ_{CP} in the range of $(0, 2\pi)$. The uncertainty band represents the full uncertainty.

DRAFT

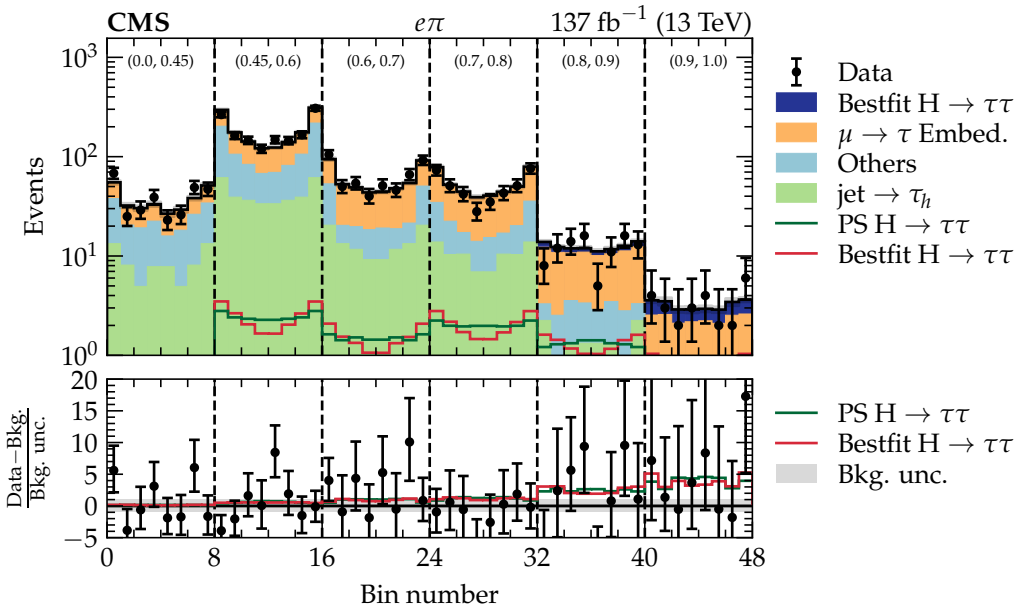

Figure 176: Postfit distribution of ϕ_{CP} of the $\mathrm{e}^{\pm} + \pi^{\mp}$ channel for all years, in windows of increasing NN score ranging between $(0, 1)$. The x-axis represents the cyclic bins in ϕ_{CP} in the range of $(0, 2\pi)$. The uncertainty band represents the full uncertainty. In the bottom plot the data minus the background template divided by the uncertainty in the background template is displayed, as well as the signal samples divided by the uncertainty in the background template. The uncertainty band consists of the sum of the postfit uncertainties in the background templates.

DRAFT

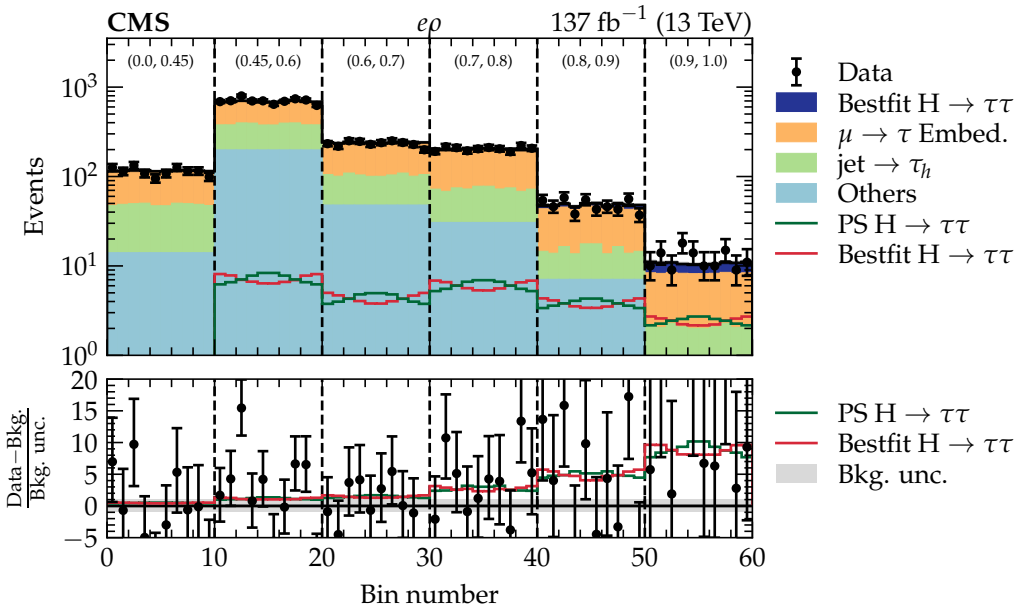

Figure 177: Postfit distribution of ϕ_{CP} of the $e^{\pm} + \rho^{\mp}$ channel for all years, in windows of increasing NN score ranging between $(0, 1)$. The x-axis represents the cyclic bins in ϕ_{CP} in the range of $(0, 2\pi)$. The uncertainty band represents the full uncertainty. In the bottom plot the data minus the background template divided by the uncertainty in the background template is displayed, as well as the signal samples divided by the uncertainty in the background template. The uncertainty band consists of the sum of the postfit uncertainties in the background templates.

DRAFT

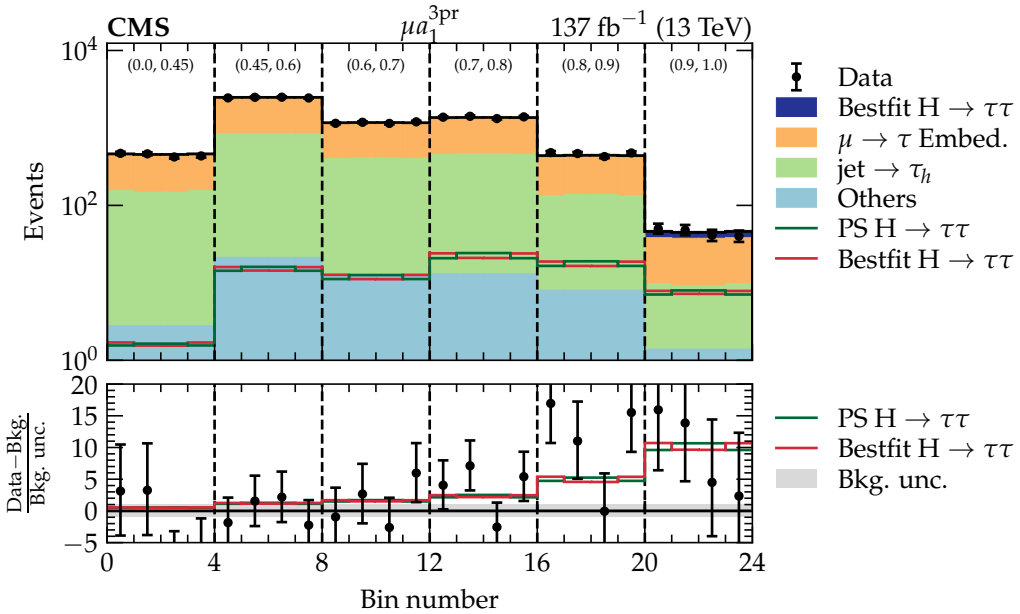

Figure 178: Postfit distribution of ϕ_{CP} of the $e^{\pm} + a_1^{3p}$ channel for all years, in windows of increasing NN score ranging between $(0, 1)$. The x-axis represents the cyclic bins in ϕ_{CP} in the range of $(0, 2\pi)$. The uncertainty band represents the full uncertainty. In the bottom plot the data minus the background template divided by the uncertainty in the background template is displayed, as well as the signal samples divided by the uncertainty in the background template. The uncertainty band consists of the sum of the postfit uncertainties in the background templates.

DRAFT

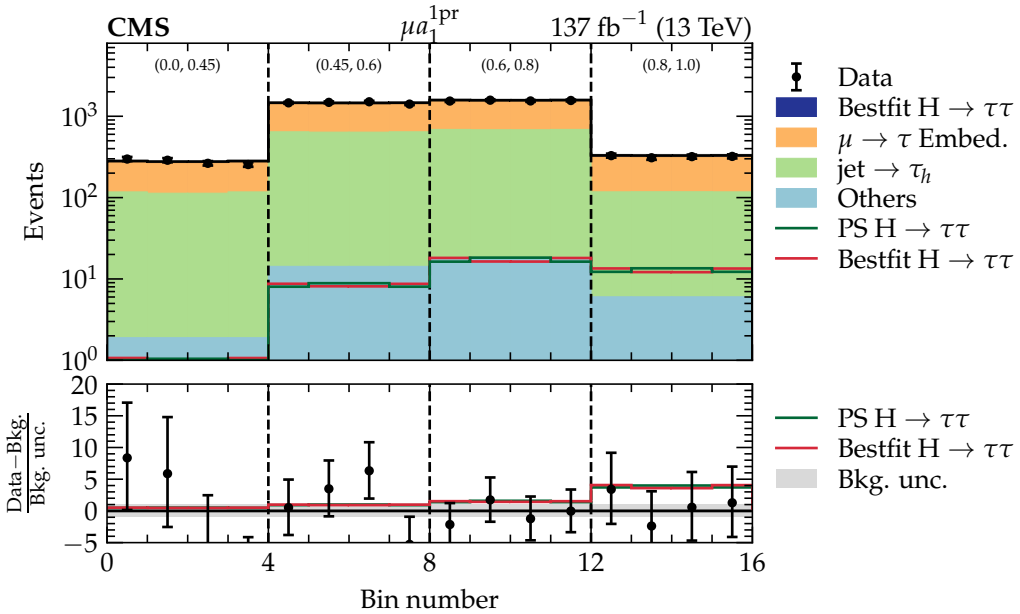

Figure 179: Postfit distribution of ϕ_{CP} of the $e^{\pm} + a_1^{1p}$ channel for all years, in windows of increasing NN score ranging between $(0, 1)$. The x-axis represents the cyclic bins in ϕ_{CP} in the range of $(0, 2\pi)$. The uncertainty band represents the full uncertainty. In the bottom plot the data minus the background template divided by the uncertainty in the background template is displayed, as well as the signal samples divided by the uncertainty in the background template. The uncertainty band consists of the sum of the postfit uncertainties in the background templates.

DRAFT

C Plots of background categories split by MVA-DM

This section shows prefit plots for the *ZTT* and *fakes* background categories which have additionally been split into MVA-DM bins and unrolled as a function of ϕ_{CP} to match the corresponding signal categories. These distributions are not included in the final fit to data but are used to check the modelling of the backgrounds.

C.1 Unrolled plots in the *ZTT* category

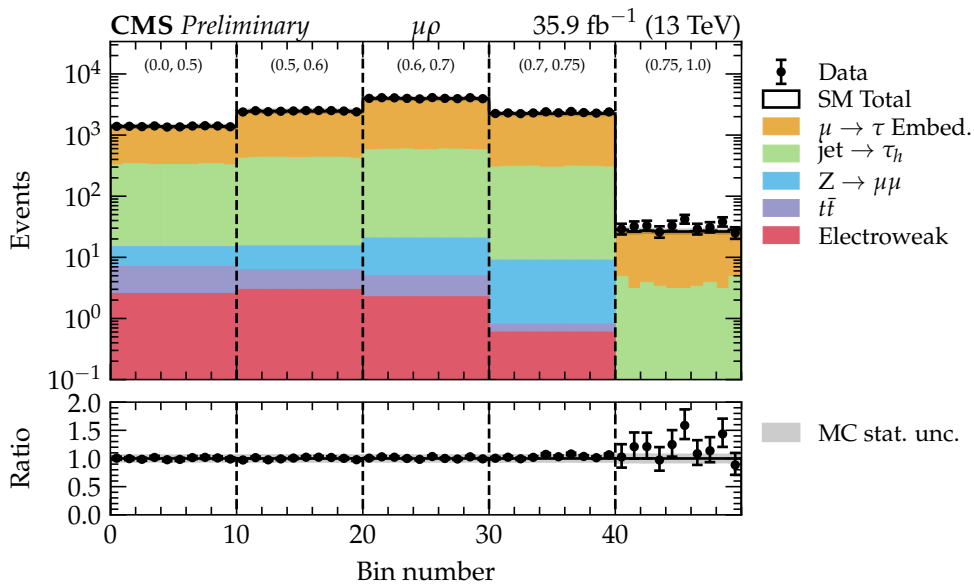

Figure 180: Distribution of ϕ_{CP} of the $\mu^{\pm} + \rho^{\mp}$ channel in the *ZTT* background category for 2016, in windows of increasing NN score ranging between $(0, 1)$. The x-axis represents the cyclic bins in ϕ_{CP} in the range of $(0, 2\pi)$. The uncertainty band represents the full uncertainty.

DRAFT

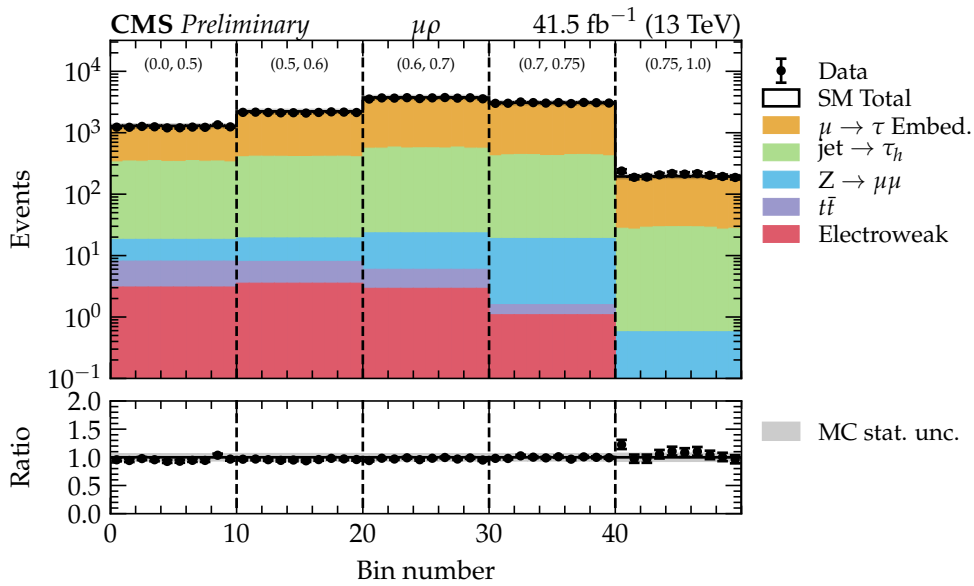

Figure 181: Distribution of ϕ_{CP} of the $\mu^{\pm} + \rho^{\mp}$ channel in the *ZTT* background category for 2017, in windows of increasing NN score ranging between $(0, 1)$. The x-axis represents the cyclic bins in ϕ_{CP} in the range of $(0, 2\pi)$. The uncertainty band represents the full uncertainty.

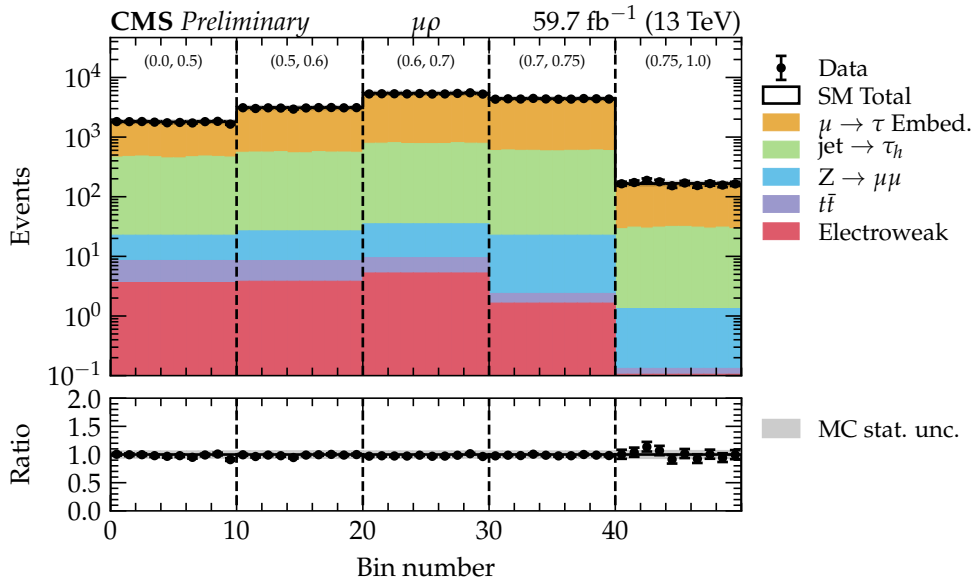

Figure 182: Distribution of ϕ_{CP} of the $\mu^{\pm} + \rho^{\mp}$ channel in the *ZTT* background category for 2018, in windows of increasing NN score ranging between $(0, 1)$. The x-axis represents the cyclic bins in ϕ_{CP} in the range of $(0, 2\pi)$. The uncertainty band represents the full uncertainty.

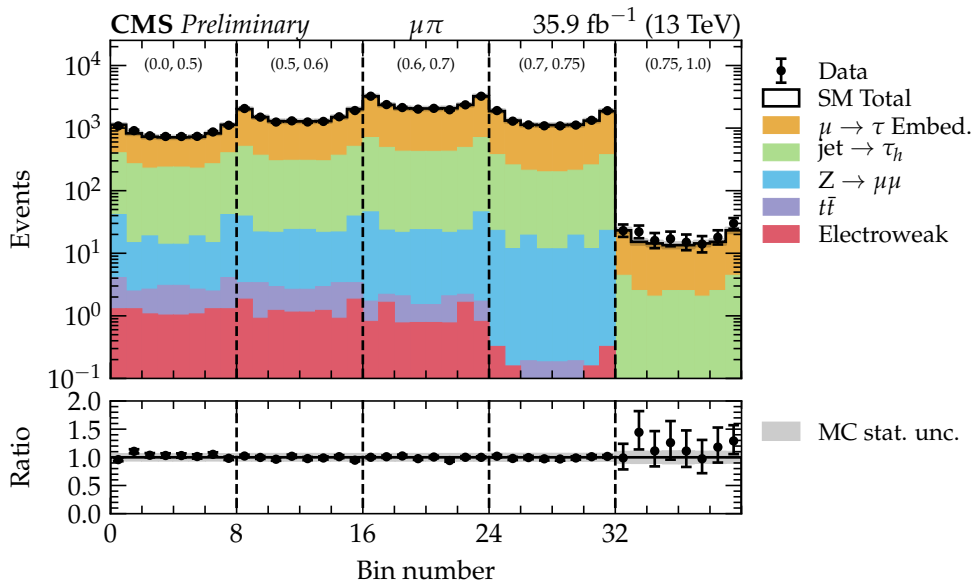

Figure 183: Distribution of ϕ_{CP} of the $\mu^{\pm} + \pi^{\mp}$ channel in the *ZTT* background category for 2016, in windows of increasing NN score ranging between $(0, 1)$. The x-axis represents the cyclic bins in ϕ_{CP} in the range of $(0, 2\pi)$. The uncertainty band represents the full uncertainty.

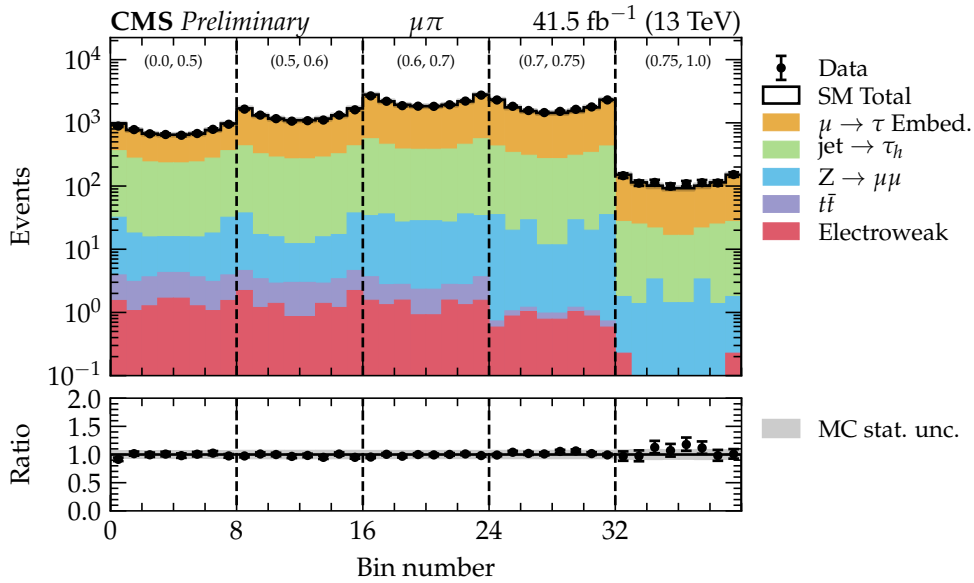

Figure 184: Distribution of ϕ_{CP} of the $\mu^{\pm} + \pi^{\mp}$ channel in the *ZTT* background category for 2017, in windows of increasing NN score ranging between $(0, 1)$. The x-axis represents the cyclic bins in ϕ_{CP} in the range of $(0, 2\pi)$. The uncertainty band represents the full uncertainty.

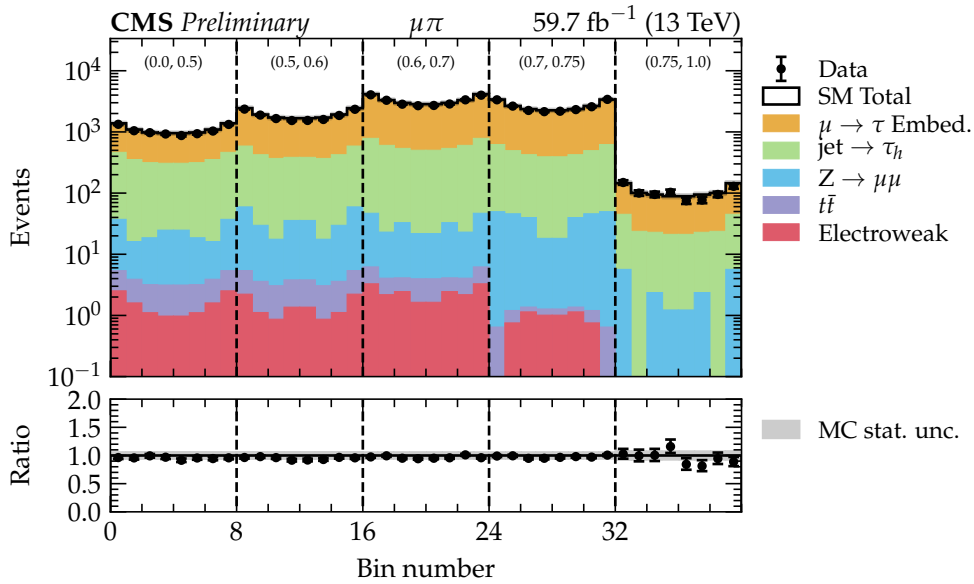

Figure 185: Distribution of ϕ_{CP} of the $\mu^{\pm} + \pi^{\mp}$ channel in the *ZTT* background category for 2018, in windows of increasing NN score ranging between $(0, 1)$. The x-axis represents the cyclic bins in ϕ_{CP} in the range of $(0, 2\pi)$. The uncertainty band represents the full uncertainty.

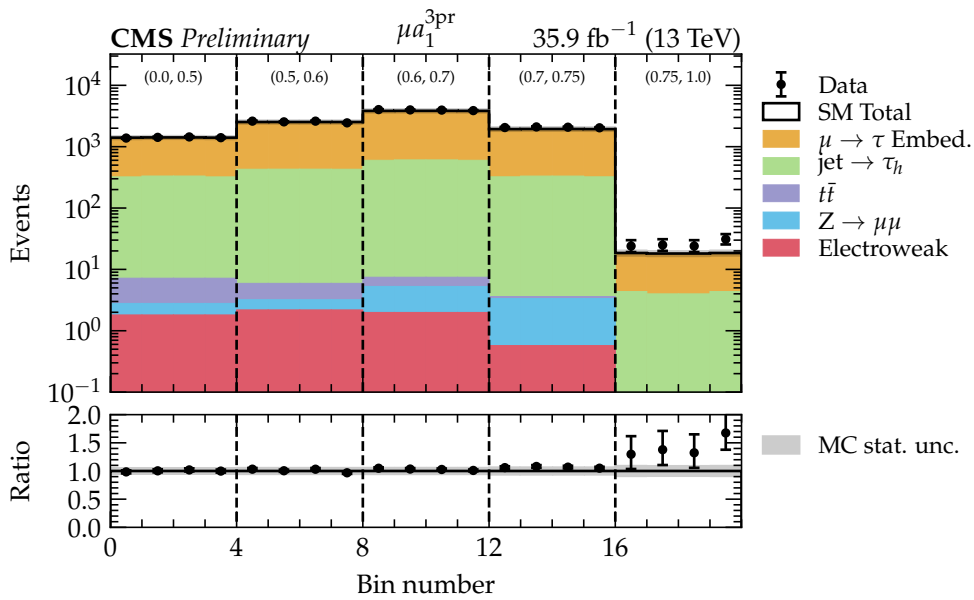

Figure 186: Distribution of ϕ_{CP} of the $\mu^{\pm} + a_1{}^{\mp,1pr}$ channel in the *ZTT* background category for 2016, in windows of increasing NN score ranging between $(0, 1)$. The x-axis represents the cyclic bins in ϕ_{CP} in the range of $(0, 2\pi)$. The uncertainty band represents the full uncertainty.

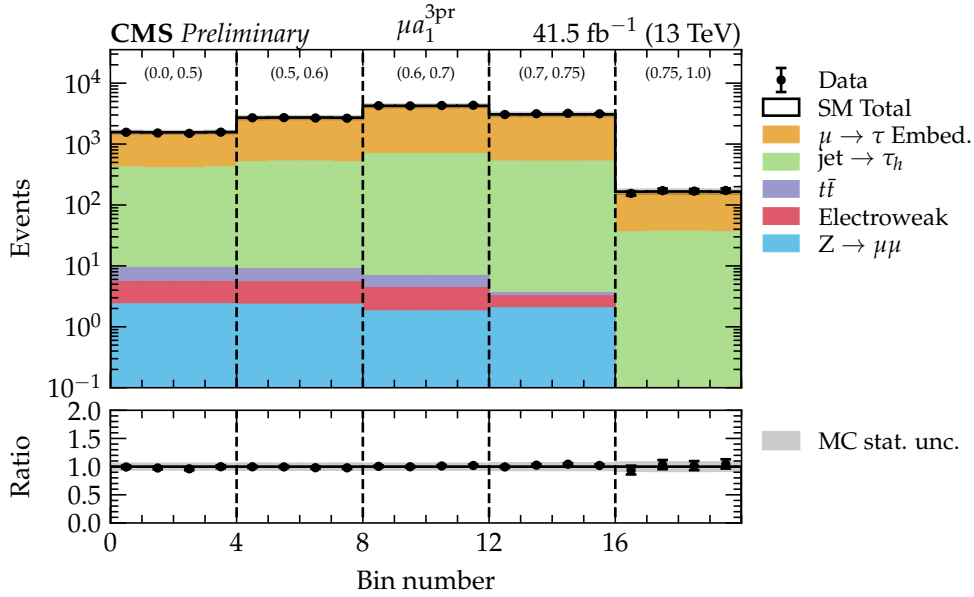

Figure 187: Distribution of ϕ_{CP} of the $\mu^{\pm} + a_1{}^{\mp,1pr}$ channel in the *ZTT* background category for 2017, in windows of increasing NN score ranging between $(0, 1)$. The x-axis represents the cyclic bins in ϕ_{CP} in the range of $(0, 2\pi)$. The uncertainty band represents the full uncertainty.

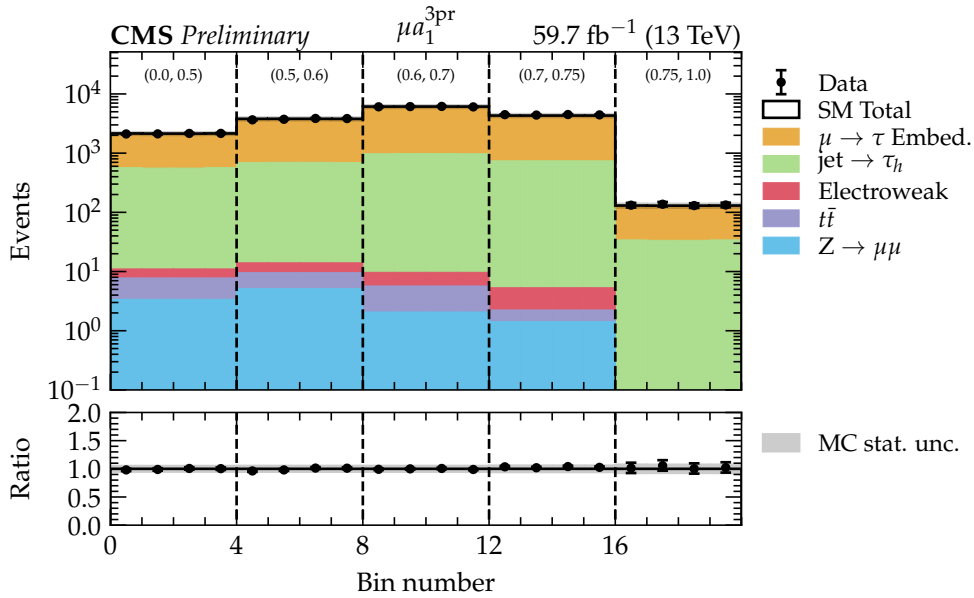

Figure 188: Distribution of ϕ_{CP} of the $\mu^{\pm} + a_1{}^{\mp,1pr}$ channel in the *ZTT* background category for 2018, in windows of increasing NN score ranging between $(0, 1)$. The x-axis represents the cyclic bins in ϕ_{CP} in the range of $(0, 2\pi)$. The uncertainty band represents the full uncertainty.

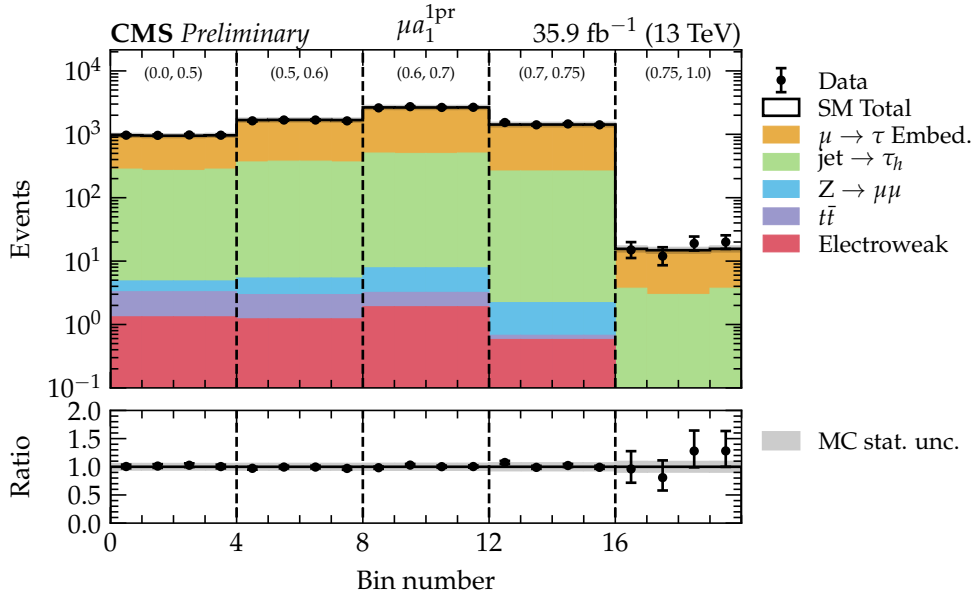

Figure 189: Distribution of ϕ_{CP} of the $\mu^{\pm} + a_1{}^{\mp,3pr}$ channel in the *ZTT* background category for 2016, in windows of increasing NN score ranging between $(0, 1)$. The x-axis represents the cyclic bins in ϕ_{CP} in the range of $(0, 2\pi)$. The uncertainty band represents the full uncertainty.

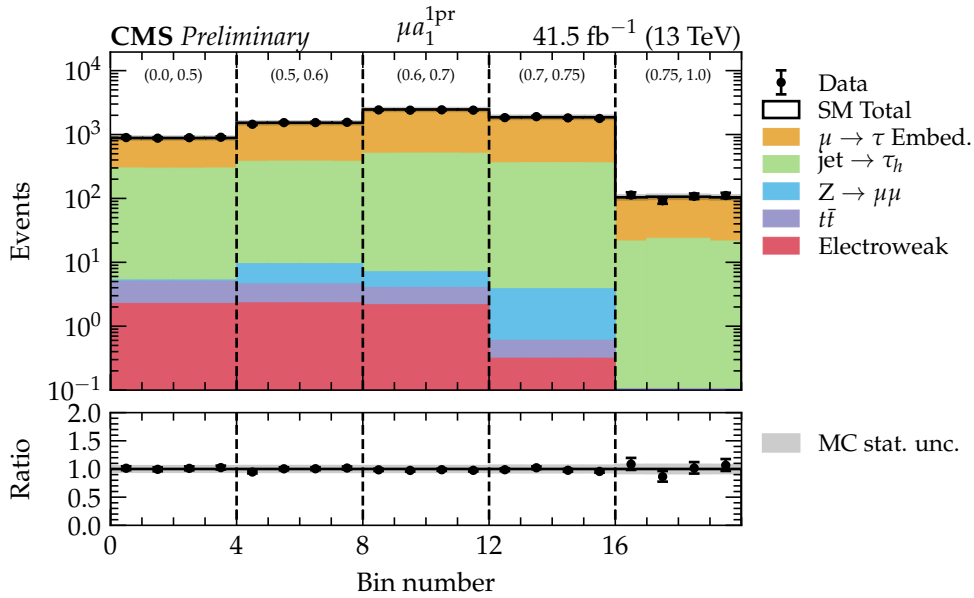

Figure 190: Distribution of ϕ_{CP} of the $\mu^{\pm} + a_1{}^{\mp,3pr}$ channel in the *ZTT* background category for 2017, in windows of increasing NN score ranging between $(0, 1)$. The x-axis represents the cyclic bins in ϕ_{CP} in the range of $(0, 2\pi)$. The uncertainty band represents the full uncertainty.

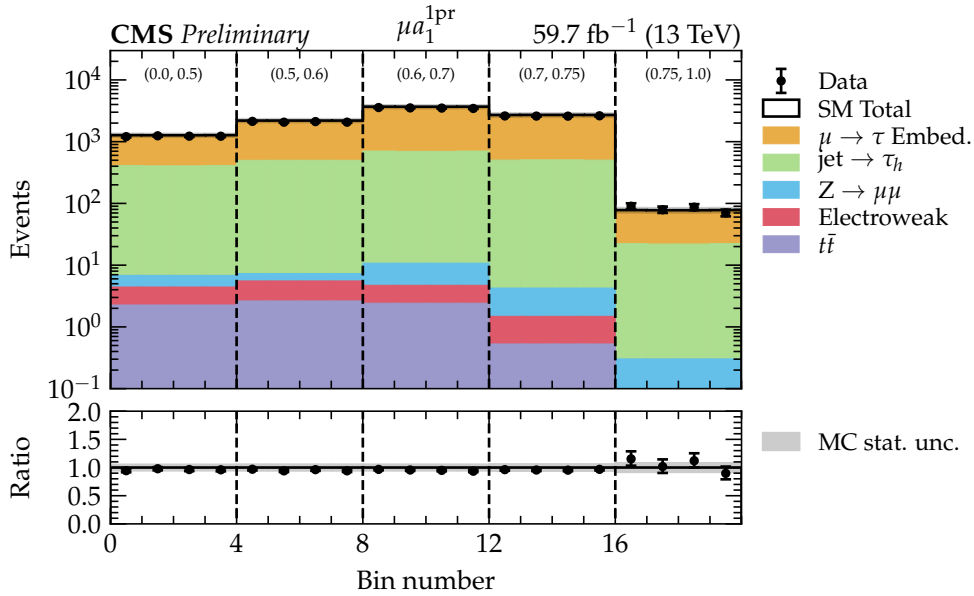

Figure 191: Distribution of ϕ_{CP} of the $\mu^{\pm} + a_1{}^{\mp,3pr}$ channel in the *ZTT* background category for 2018, in windows of increasing NN score ranging between $(0, 1)$. The x-axis represents the cyclic bins in ϕ_{CP} in the range of $(0, 2\pi)$. The uncertainty band represents the full uncertainty.

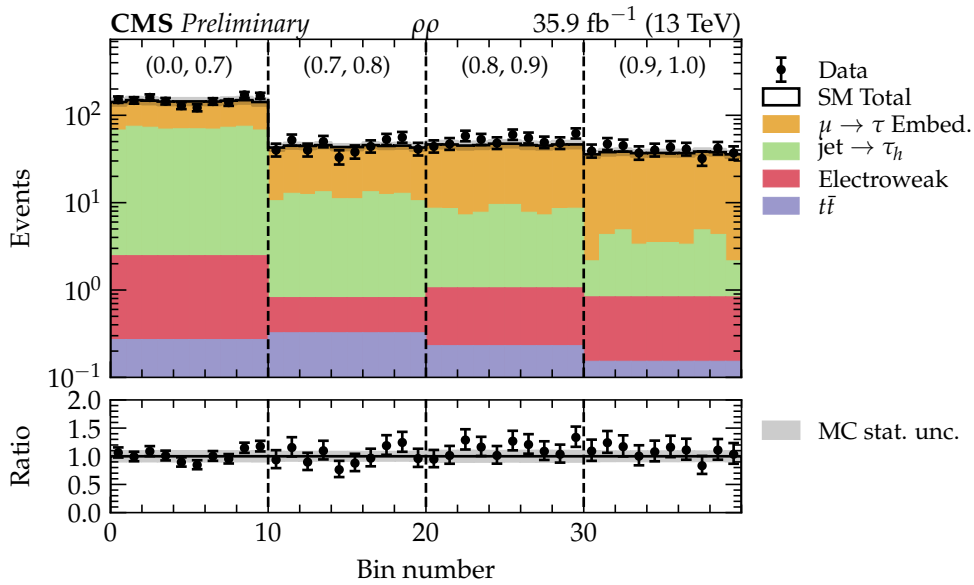

Figure 192: Distribution of ϕ_{CP} of the $\rho^{\pm} + \rho^{\mp}$ channel in the *ZTT* background category for 2016, in windows of increasing BDT score ranging between $(0, 1)$. The x-axis represents the cyclic bins in ϕ_{CP} in the range of $(0, 2\pi)$. The uncertainty band represents the full uncertainty.

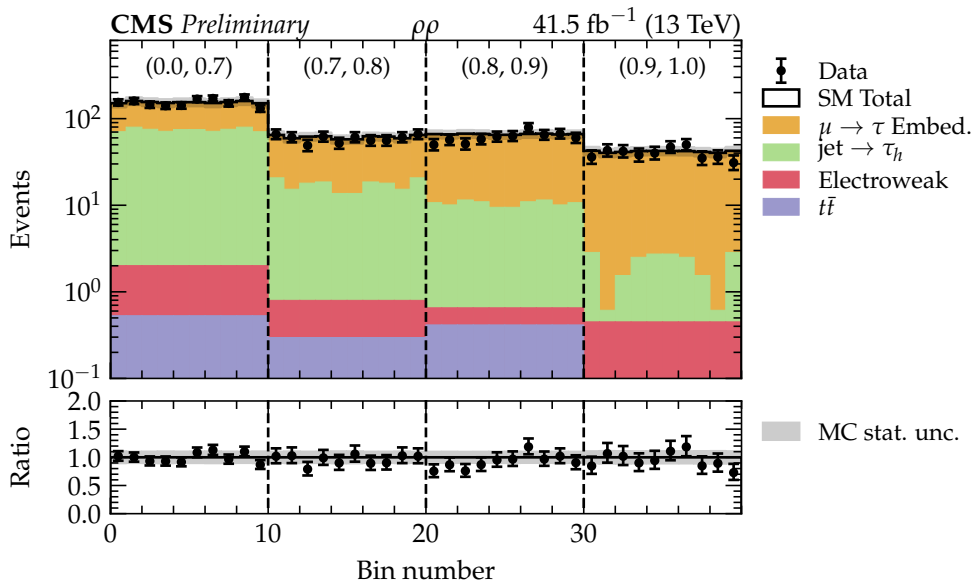

Figure 193: Distribution of ϕ_{CP} of the $\rho^{\pm} + \rho^{\mp}$ channel in the *ZTT* background category for 2017, in windows of increasing BDT score ranging between $(0, 1)$. The x-axis represents the cyclic bins in ϕ_{CP} in the range of $(0, 2\pi)$. The uncertainty band represents the full uncertainty.

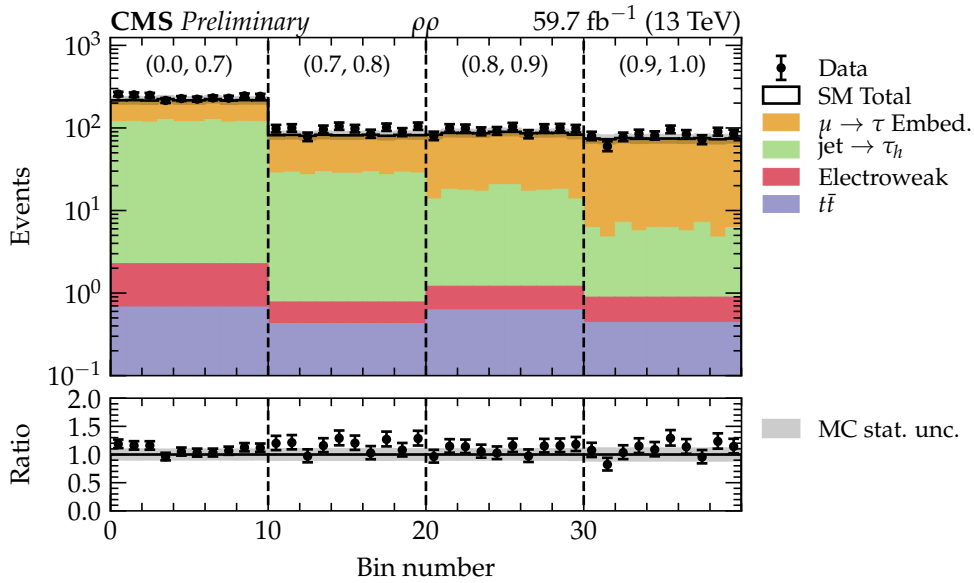

Figure 194: Distribution of ϕ_{CP} of the $\rho^{\pm} + \rho^{\mp}$ channel in the *ZTT* background category for 2018, in windows of increasing BDT score. The x-axis represents the cyclic bins in ϕ_{CP} in the range of $(0, 2\pi)$. The uncertainty band represents the full uncertainty.

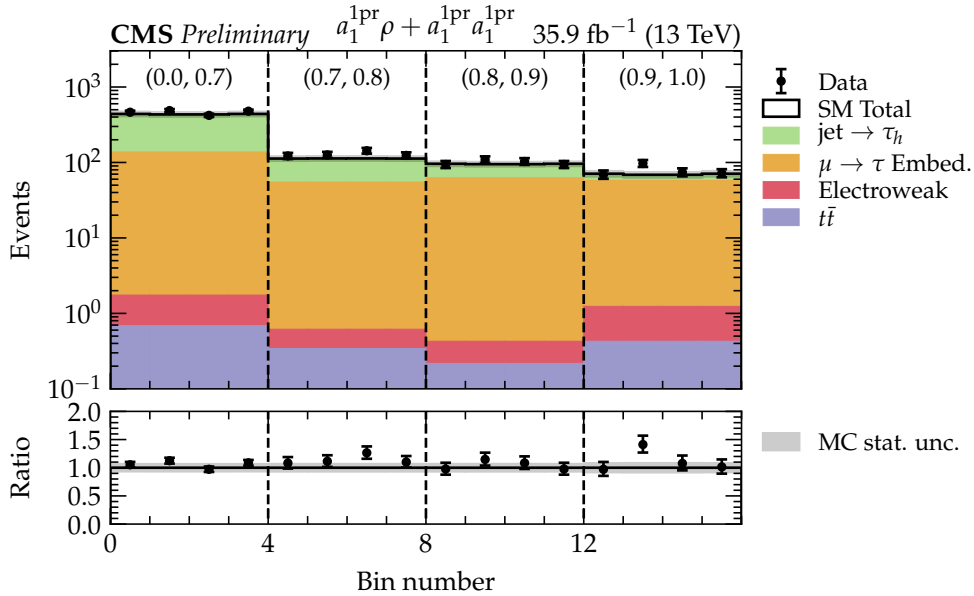

Figure 195: Distribution of ϕ_{CP} of the $a_1^{\pm,1pr} + \rho^{\mp}$ and $a_1^{\pm,1pr} + a_1^{\pm,1pr}$ channel in the *ZTT* background category for 2016, in windows of increasing BDT score ranging between $(0, 1)$. The x-axis represents the cyclic bins in ϕ_{CP} in the range of $(0, 2\pi)$. The uncertainty band represents the full uncertainty.

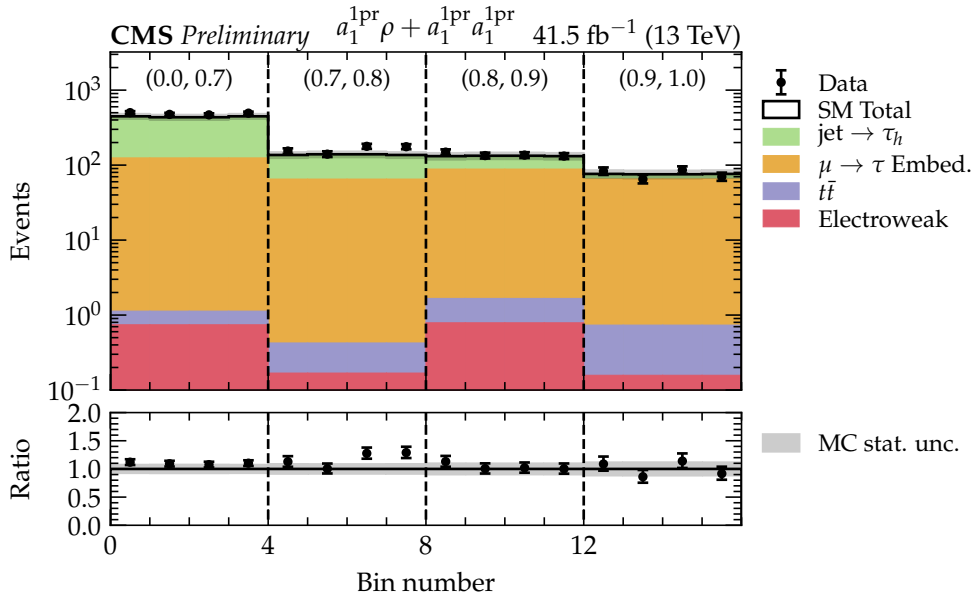

Figure 196: Distribution of ϕ_{CP} of the $a_1^{\pm,1pr} + \rho^{\mp}$ and $a_1^{\pm,1pr} + a_1^{\pm,1pr}$ channel in the *ZTT* background category for 2017, in windows of increasing BDT score ranging between $(0, 1)$. The x-axis represents the cyclic bins in ϕ_{CP} in the range of $(0, 2\pi)$. The uncertainty band represents the full uncertainty.

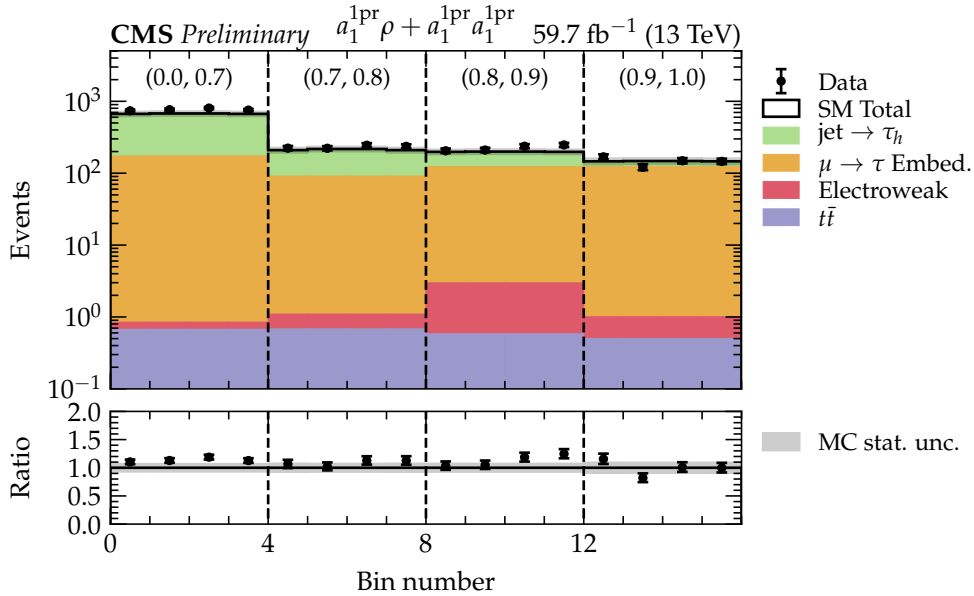

Figure 197: Distribution of ϕ_{CP} of the $a_1^{\pm,1pr} + \rho^{\mp}$ and $a_1^{\pm,1pr} + a_1^{\pm,1pr}$ channel in the *ZTT* background category for 2018, in windows of increasing BDT score ranging between $(0, 1)$. The x-axis represents the cyclic bins in ϕ_{CP} in the range of $(0, 2\pi)$. The uncertainty band represents the full uncertainty.

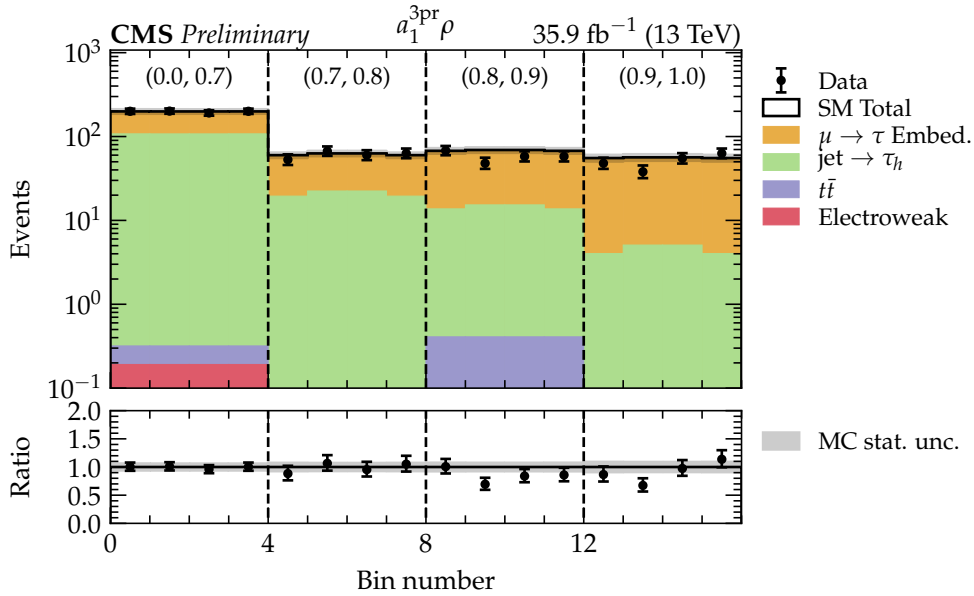

Figure 198: Distribution of ϕ_{CP} of the $a_1^{\pm,3pr} + \rho^{\mp}$ channel in the *ZTT* background category for 2016, in windows of increasing BDT score ranging between $(0, 1)$. The x-axis represents the cyclic bins in ϕ_{CP} in the range of $(0, 2\pi)$. The uncertainty band represents the full uncertainty.

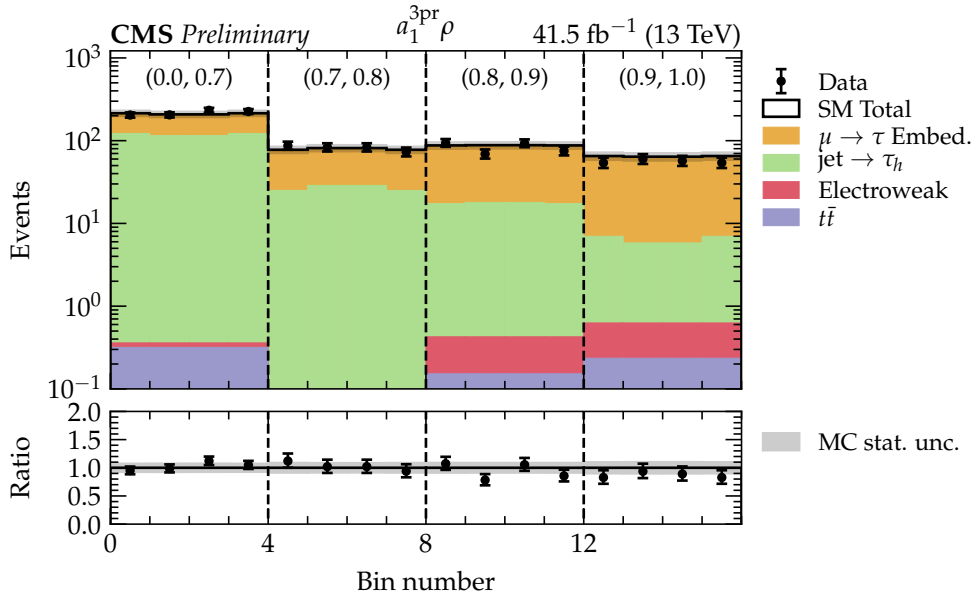

Figure 199: Distribution of ϕ_{CP} of the $a_1^{\pm,3pr} + \rho^{\mp}$ channel in the *ZTT* background category for 2017, in windows of increasing BDT score ranging between $(0, 1)$. The x-axis represents the cyclic bins in ϕ_{CP} in the range of $(0, 2\pi)$. The uncertainty band represents the full uncertainty.

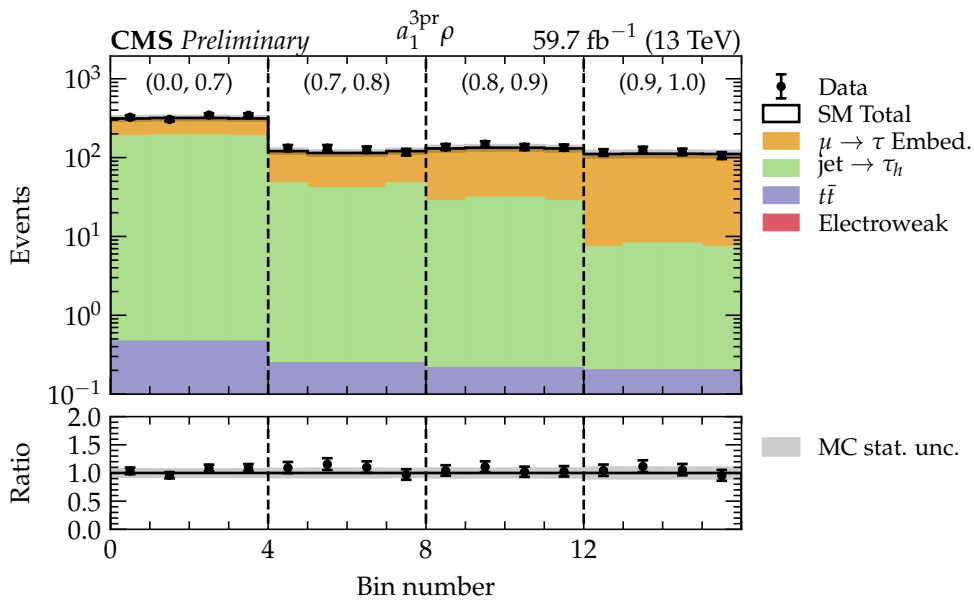

Figure 200: Distribution of ϕ_{CP} of the $a_1^{\pm,3pr} + \rho^{\mp}$ channel in the *ZTT* background category for 2018, in windows of increasing BDT score ranging between $(0, 1)$. The x-axis represents the cyclic bins in ϕ_{CP} in the range of $(0, 2\pi)$. The uncertainty band represents the full uncertainty.

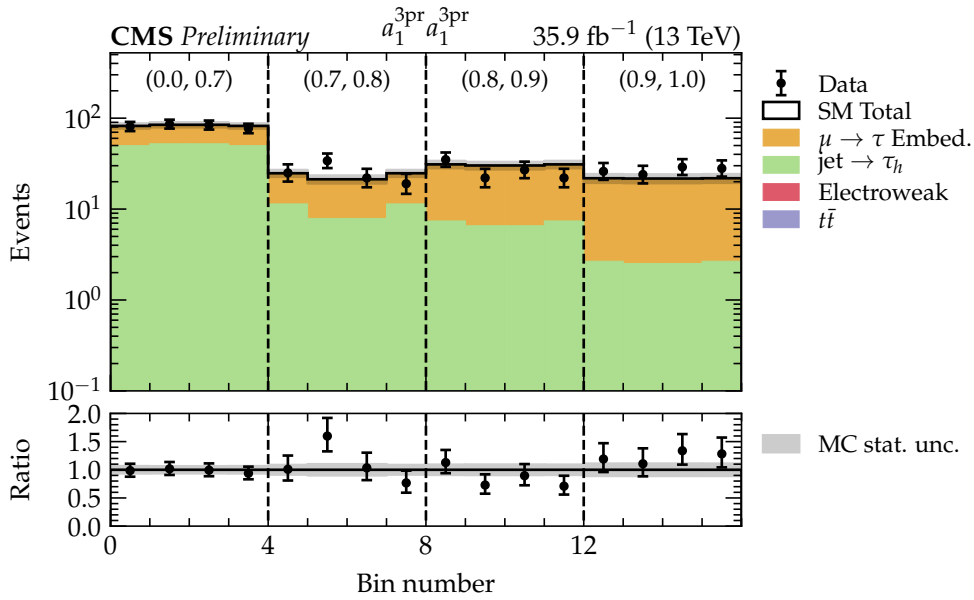

Figure 201: Distribution of ϕ_{CP} of the $a_1^{\pm,3pr} + a_1^{\mp,3pr}$ channel in the *ZTT* background category for 2016, in windows of increasing BDT score ranging between $(0, 1)$. The x-axis represents the cyclic bins in ϕ_{CP} in the range of $(0, 2\pi)$. The uncertainty band represents the full uncertainty.

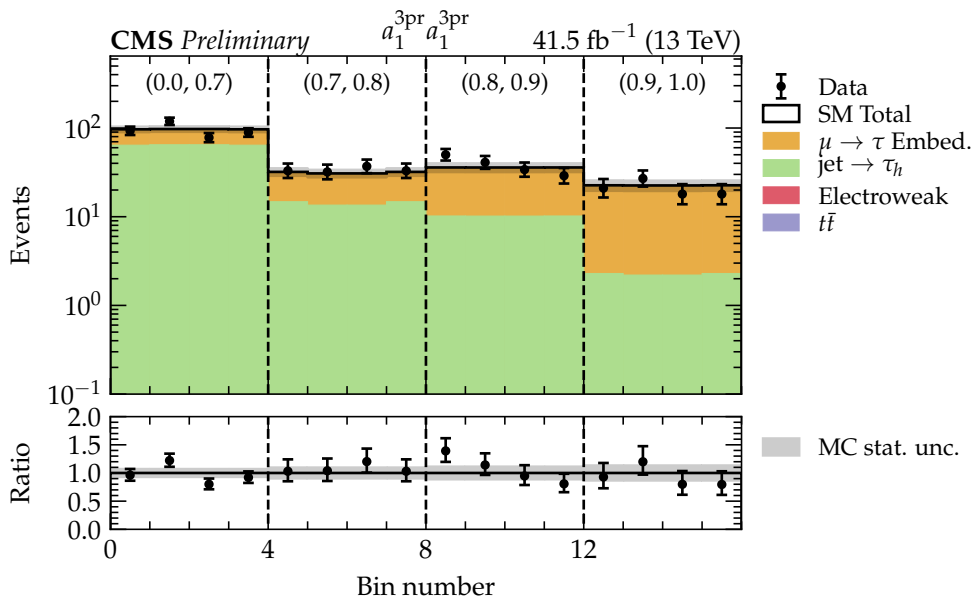

Figure 202: Distribution of ϕ_{CP} of the $a_1^{\pm,3pr} + a_1^{\mp,3pr}$ channel in the *ZTT* background category for 2017, in windows of increasing BDT score ranging between $(0, 1)$. The x-axis represents the cyclic bins in ϕ_{CP} in the range of $(0, 2\pi)$. The uncertainty band represents the full uncertainty.

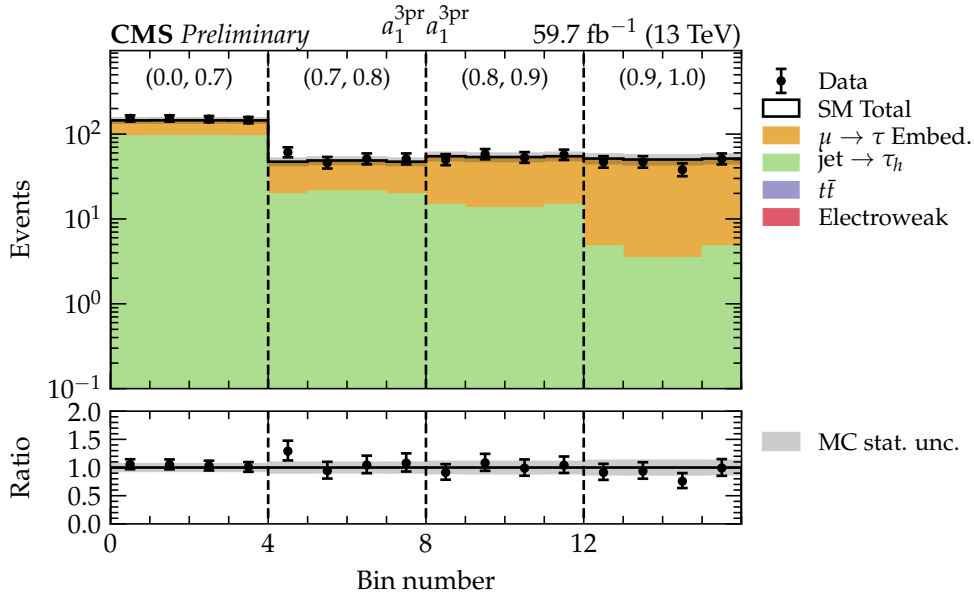

Figure 203: Distribution of ϕ_{CP} of the $a_1^{\pm,3pr} + a_1^{\mp,3pr}$ channel in the *ZTT* background category for 2018, in windows of increasing BDT score ranging between $(0, 1)$. The x-axis represents the cyclic bins in ϕ_{CP} in the range of $(0, 2\pi)$. The uncertainty band represents the full uncertainty.

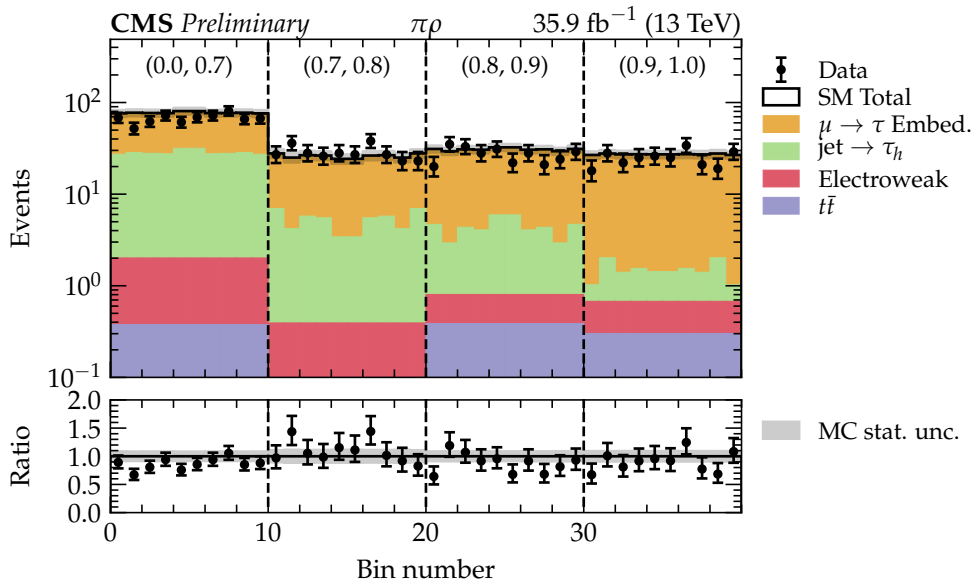

Figure 204: Distribution of ϕ_{CP} of the $\pi^{\pm} + \rho^{\mp}$ channel in the *ZTT* background category for 2016, in windows of increasing BDT score ranging between $(0, 1)$. The x-axis represents the cyclic bins in ϕ_{CP} in the range of $(0, 2\pi)$. The uncertainty band represents the full uncertainty.

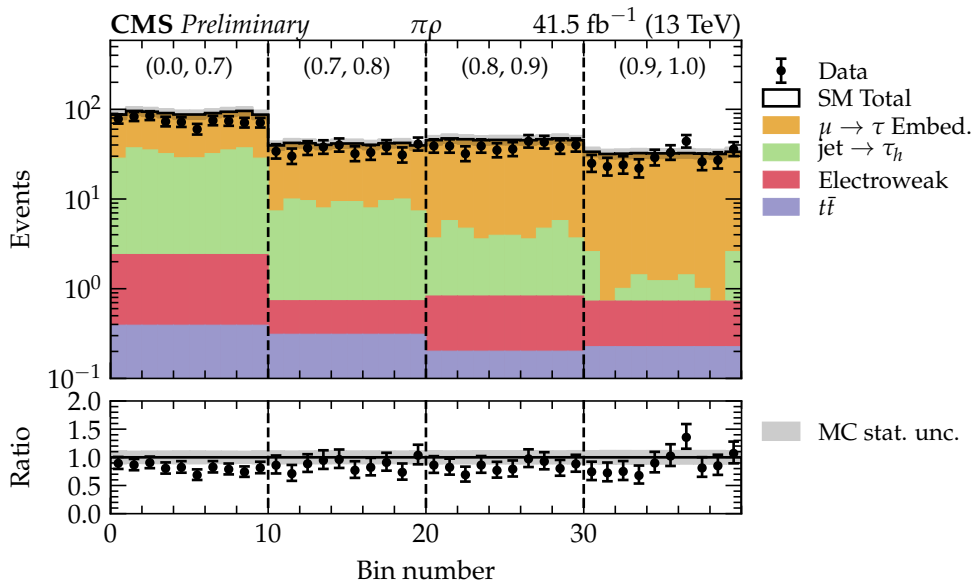

Figure 205: Distribution of ϕ_{CP} of the $\pi^{\pm} + \rho^{\mp}$ channel in the *ZTT* background category for 2017, in windows of increasing BDT score ranging between $(0, 1)$. The x-axis represents the cyclic bins in ϕ_{CP} in the range of $(0, 2\pi)$. The uncertainty band represents the full uncertainty.

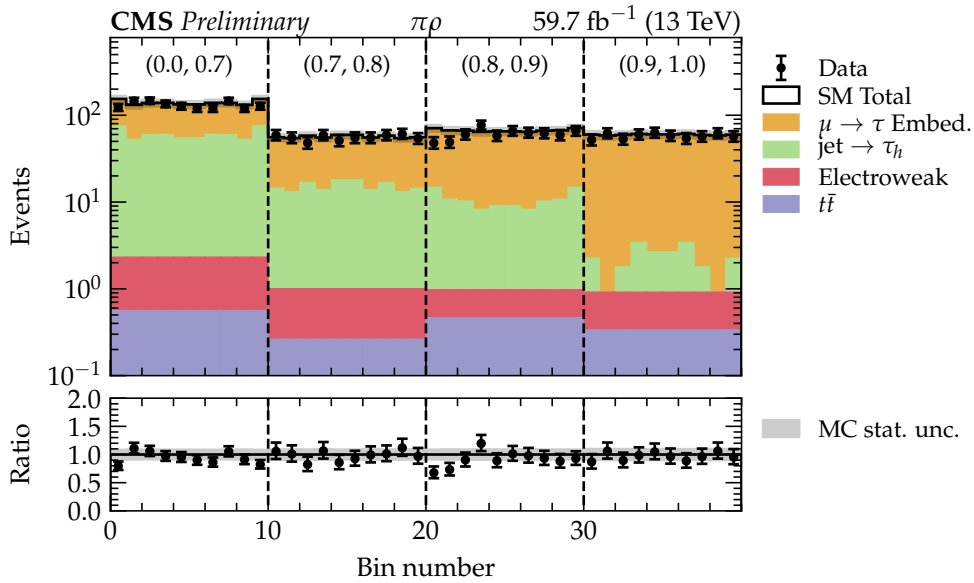

Figure 206: Distribution of ϕ_{CP} of the $\pi^{\pm} + \rho^{\mp}$ channel in the *ZTT* background category for 2018, in windows of increasing BDT score ranging between $(0, 1)$. The x-axis represents the cyclic bins in ϕ_{CP} in the range of $(0, 2\pi)$. The uncertainty band represents the full uncertainty.

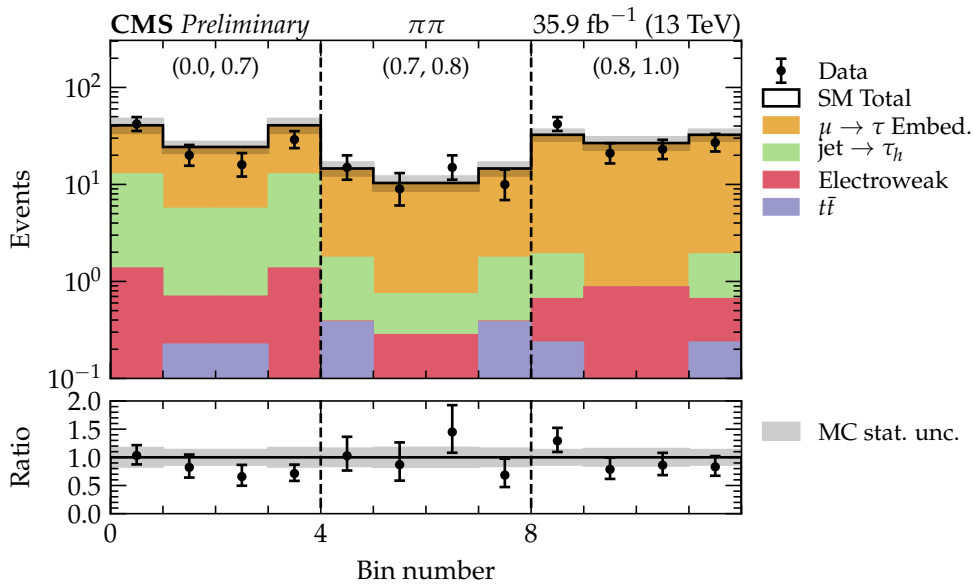

Figure 207: Distribution of ϕ_{CP} of the $\pi^{\pm} + \pi^{\mp}$ channel in the *ZTT* background category for 2016, in windows of increasing BDT score ranging between $(0, 1)$. The x-axis represents the cyclic bins in ϕ_{CP} in the range of $(0, 2\pi)$. The uncertainty band represents the full uncertainty.

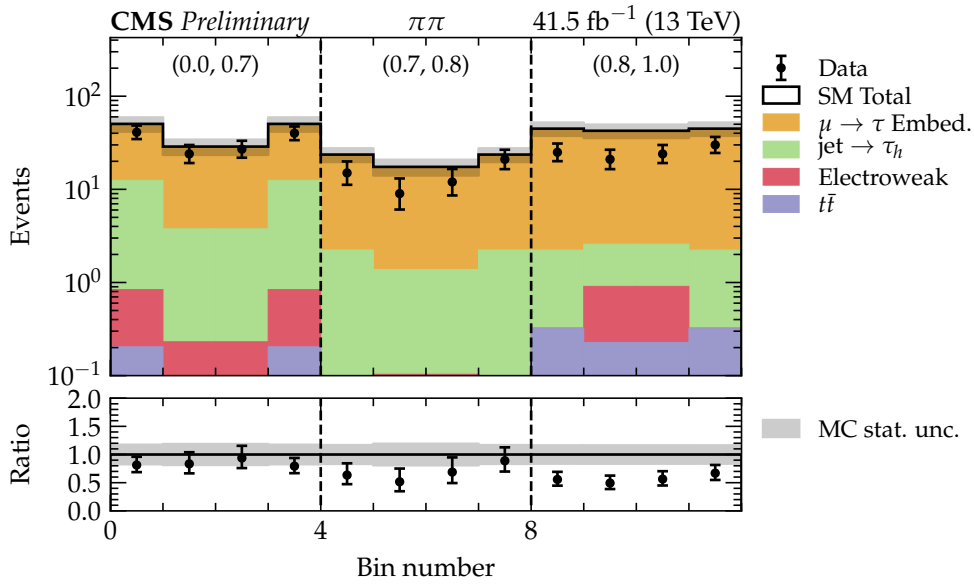

Figure 208: Distribution of ϕ_{CP} of the $\pi^{\pm} + \pi^{\mp}$ channel in the *ZTT* background category for 2017, in windows of increasing BDT score ranging between $(0, 1)$. The x-axis represents the cyclic bins in ϕ_{CP} in the range of $(0, 2\pi)$. The uncertainty band represents the full uncertainty.

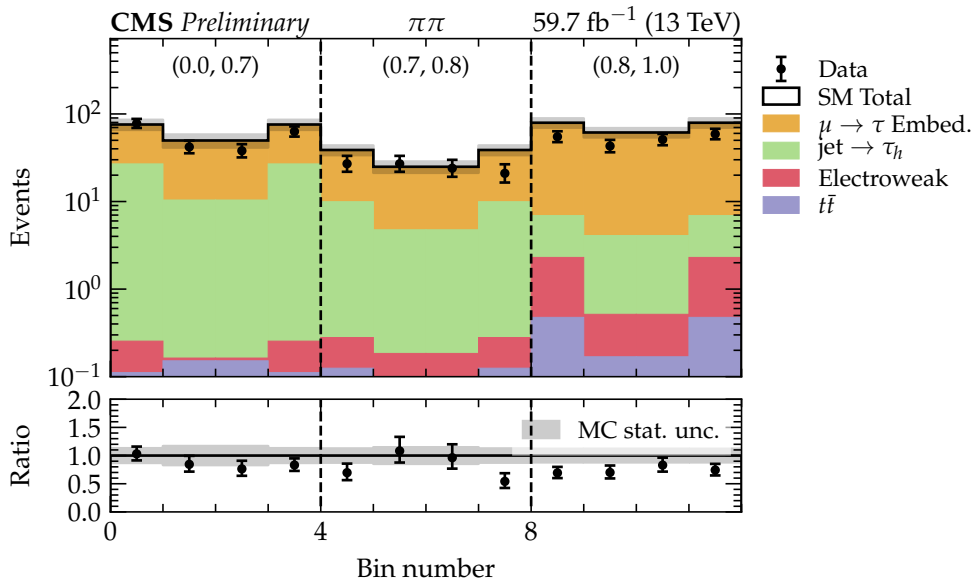

Figure 209: Distribution of ϕ_{CP} of the $\pi^{\pm} + \pi^{\mp}$ channel in the *ZTT* background category for 2018, in windows of increasing BDT score ranging between $(0, 1)$. The x-axis represents the cyclic bins in ϕ_{CP} in the range of $(0, 2\pi)$. The uncertainty band represents the full uncertainty.

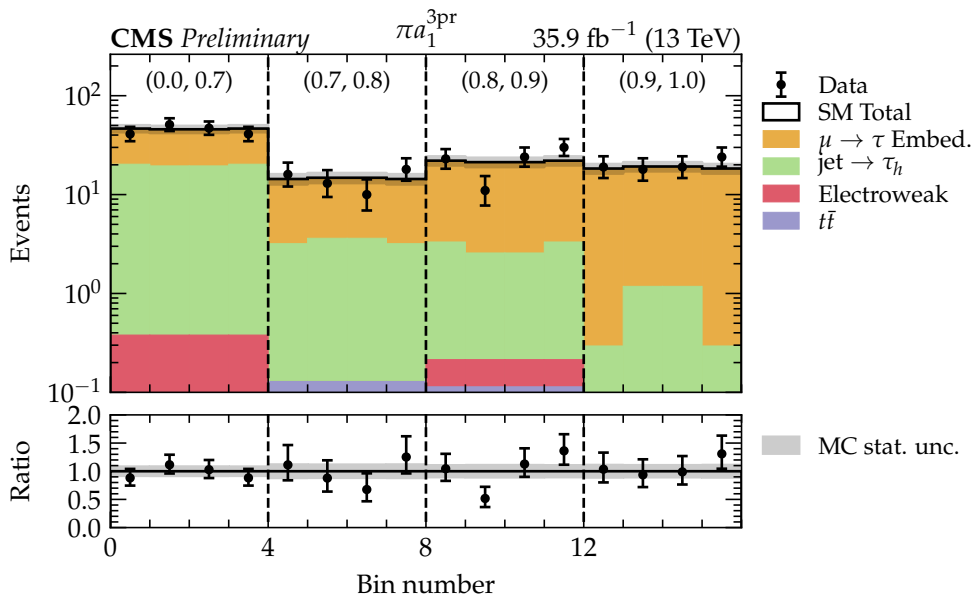

Figure 210: Distribution of ϕ_{CP} of the $\pi^{\pm} + a_1{}^{\mp,3pr}$ channel in the *ZTT* background category for 2016, in windows of increasing BDT score ranging between $(0, 1)$. The x-axis represents the cyclic bins in ϕ_{CP} in the range of $(0, 2\pi)$. The uncertainty band represents the full uncertainty.

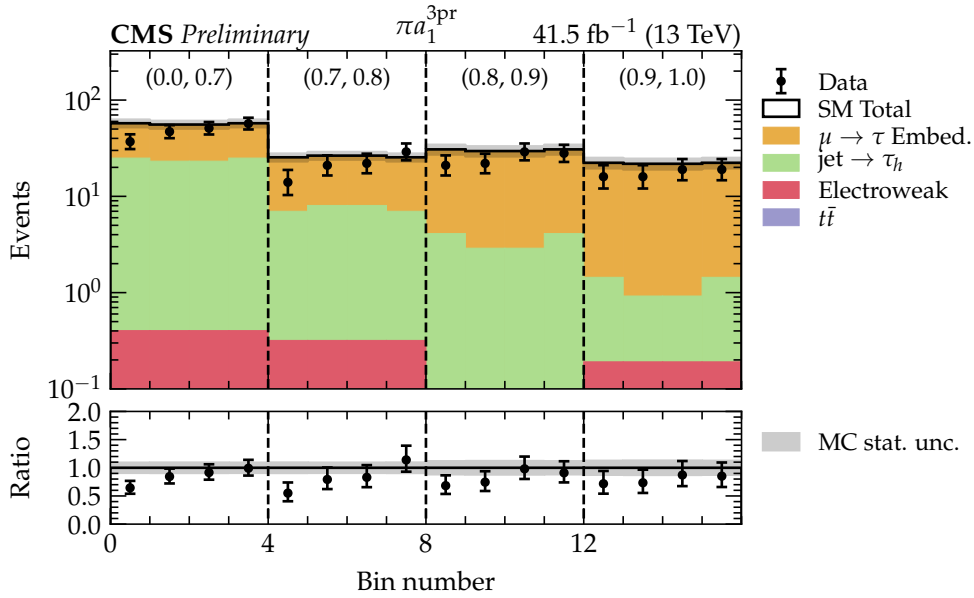

Figure 211: Distribution of ϕ_{CP} of the $\pi^{\pm} + a_1{}^{\mp,3pr}$ channel in the *ZTT* background category for 2017, in windows of increasing BDT score ranging between $(0, 1)$. The x-axis represents the cyclic bins in ϕ_{CP} in the range of $(0, 2\pi)$. The uncertainty band represents the full uncertainty.

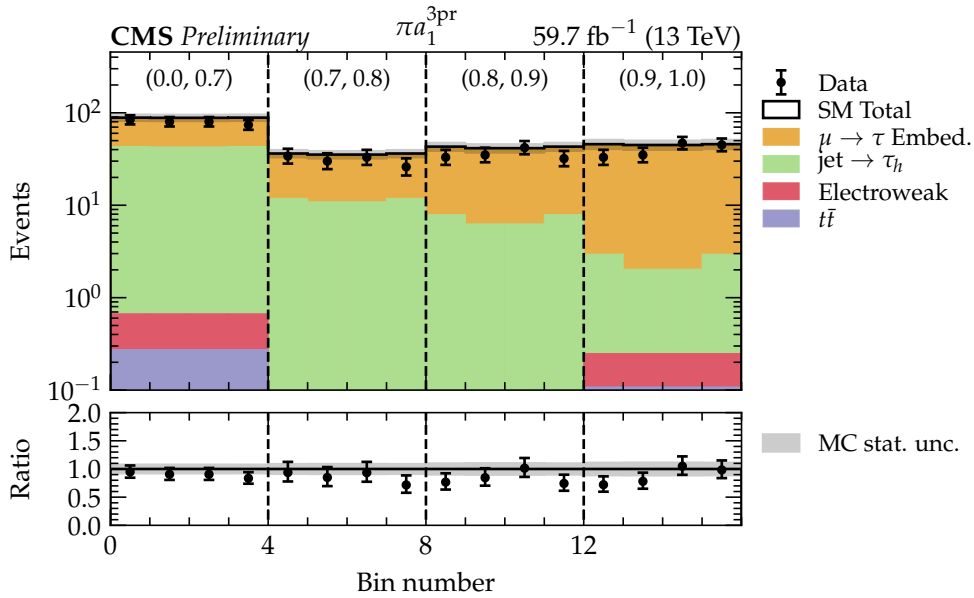

Figure 212: Distribution of ϕ_{CP} of the $\pi^{\pm} + a_1{}^{\mp,3pr}$ channel in the *ZTT* background category for 2018, in windows of increasing BDT score ranging between $(0, 1)$. The x-axis represents the cyclic bins in ϕ_{CP} in the range of $(0, 2\pi)$. The uncertainty band represents the full uncertainty.

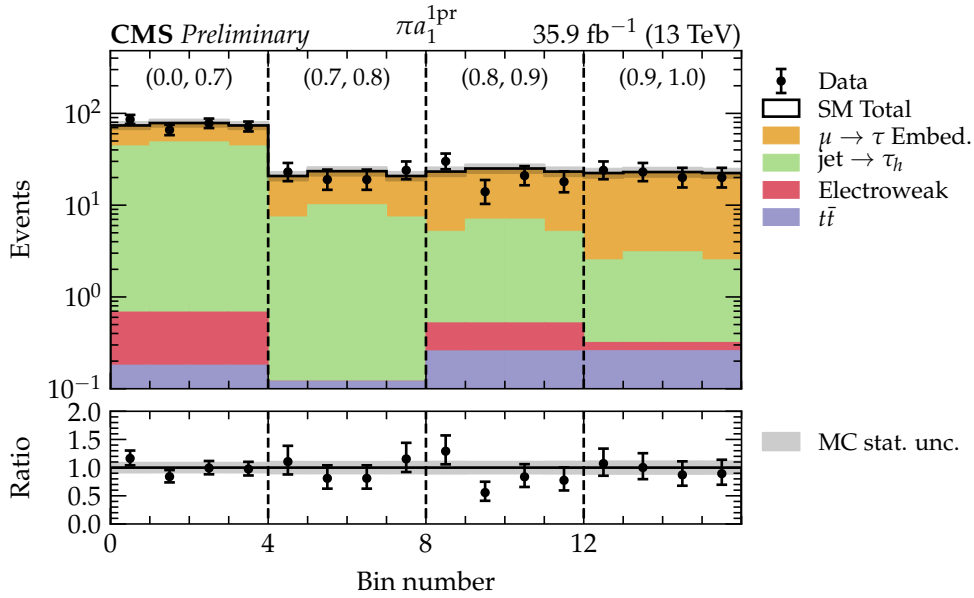

Figure 213: Distribution of ϕ_{CP} of the $\pi^{\pm} + a_1{}^{\mp,1pr}$ channel in the *ZTT* background category for 2016, in windows of increasing BDT score ranging between $(0, 1)$. The x-axis represents the cyclic bins in ϕ_{CP} in the range of $(0, 2\pi)$. The uncertainty band represents the full uncertainty.

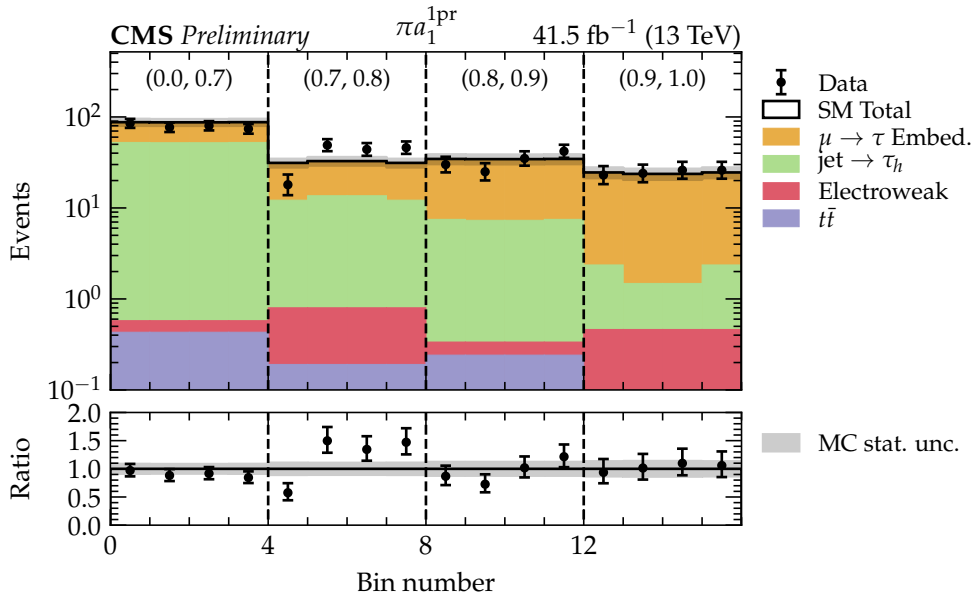

Figure 214: Distribution of ϕ_{CP} of the $\pi^{\pm} + a_1{}^{\mp,1pr}$ channel in the *ZTT* background category for 2017, in windows of increasing BDT score ranging between $(0, 1)$. The x-axis represents the cyclic bins in ϕ_{CP} in the range of $(0, 2\pi)$. The uncertainty band represents the full uncertainty.

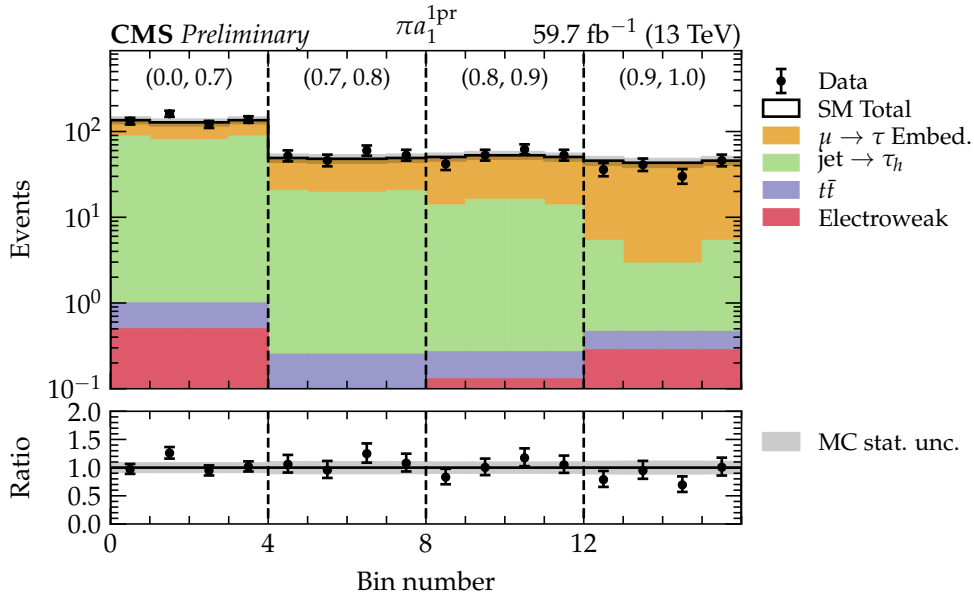

Figure 215: Distribution of ϕ_{CP} of the $\pi^{\pm} + a_1{}^{\mp,1pr}$ channel in the *ZTT* background category for 2018, in windows of increasing BDT score ranging between $(0, 1)$. The x-axis represents the cyclic bins in ϕ_{CP} in the range of $(0, 2\pi)$. The uncertainty band represents the full uncertainty.

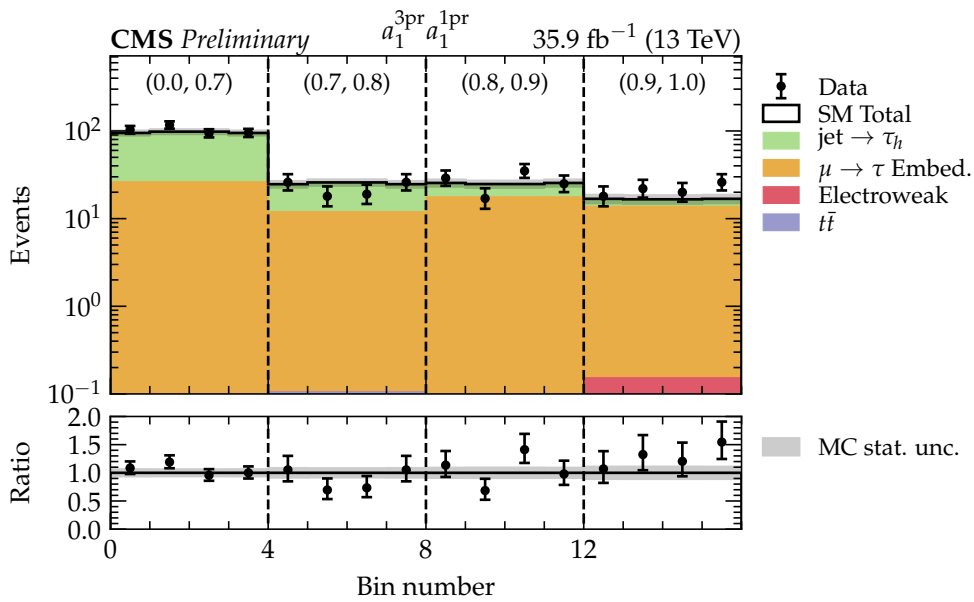

Figure 216: Distribution of ϕ_{CP} of the $a_1{}^{\pm,3pr} + a_1{}^{\mp,1pr}$ channel in the *ZTT* background category for 2016, in windows of increasing BDT score ranging between $(0, 1)$. The x-axis represents the cyclic bins in ϕ_{CP} in the range of $(0, 2\pi)$. The uncertainty band represents the full uncertainty.

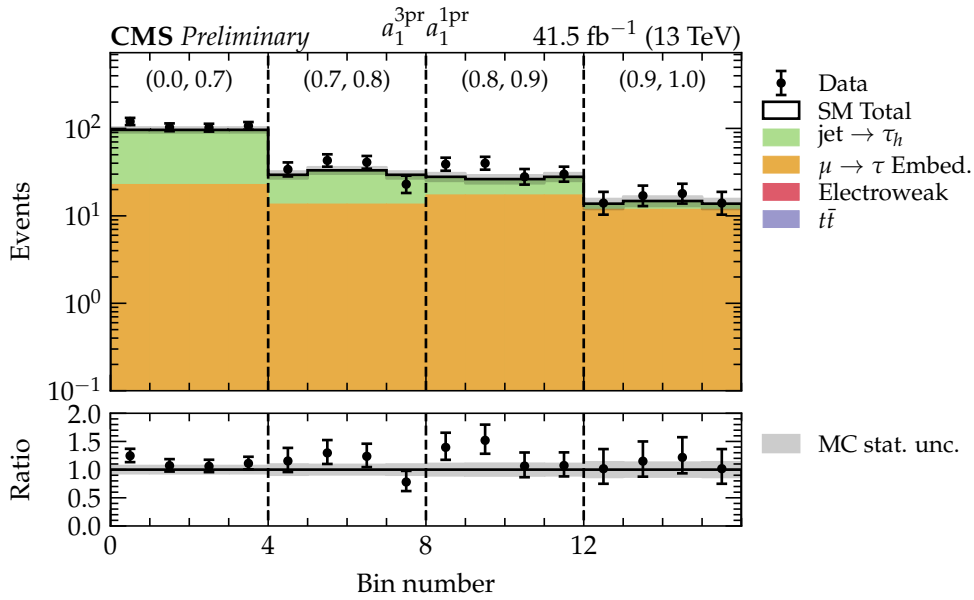

Figure 217: Distribution of ϕ_{CP} of the $a_1^{\pm,3pr} + a_1^{\mp,1pr}$ channel in the *ZTT* background category for 2017, in windows of increasing BDT score ranging between $(0, 1)$. The x-axis represents the cyclic bins in ϕ_{CP} in the range of $(0, 2\pi)$. The uncertainty band represents the full uncertainty.

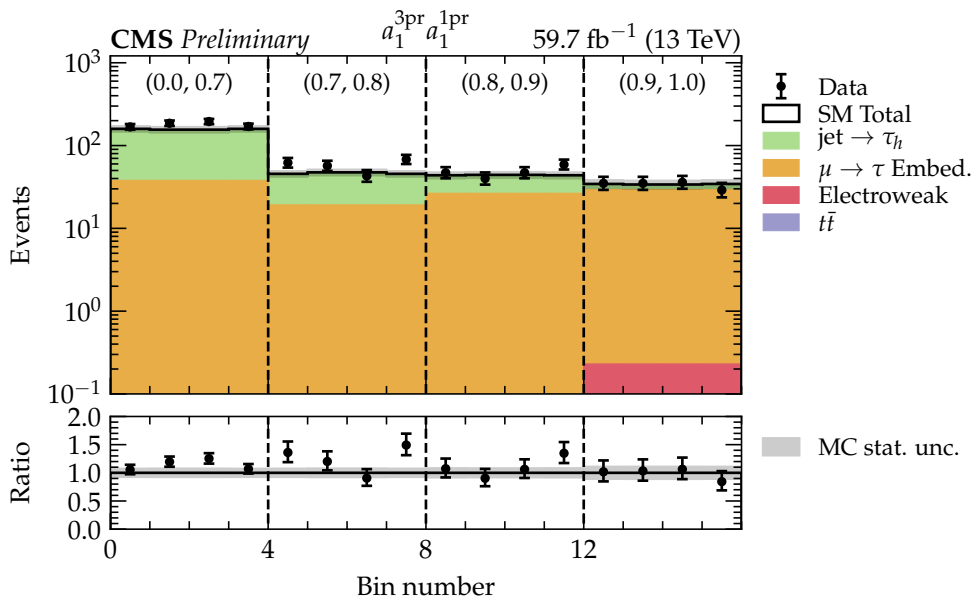

Figure 218: Distribution of ϕ_{CP} of the $a_1^{\pm,3pr} + a_1^{\mp,1pr}$ channel in the *ZTT* background category for 2018, in windows of increasing BDT score ranging between $(0, 1)$. The x-axis represents the cyclic bins in ϕ_{CP} in the range of $(0, 2\pi)$. The uncertainty band represents the full uncertainty.

C.2 Unrolled plots in the *fakes* category

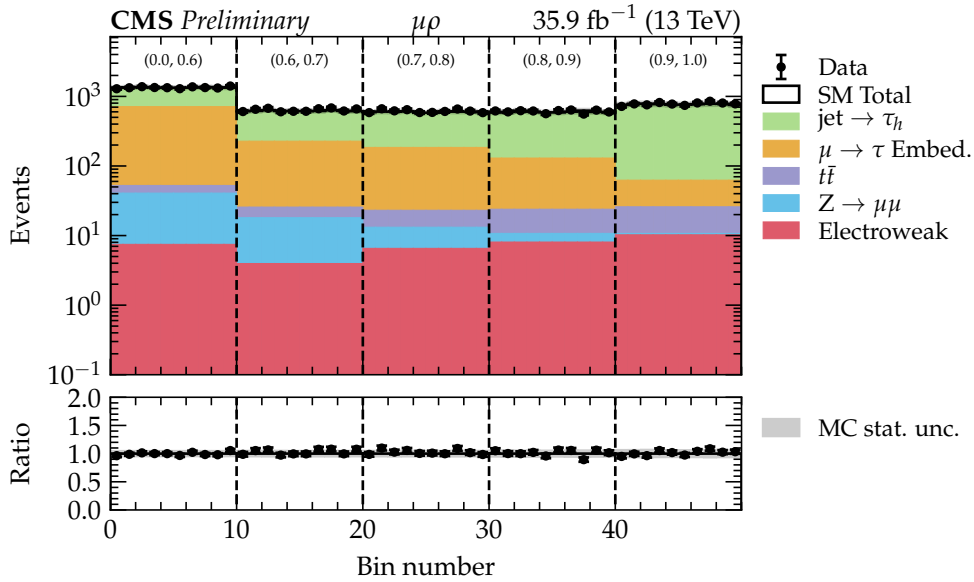

Figure 219: Distribution of ϕ_{CP} of the $\mu^{\pm} + \rho^{\mp}$ channel in the *fakes* background category for 2016, in windows of increasing NN score ranging between $(0, 1)$. The x-axis represents the cyclic bins in ϕ_{CP} in the range of $(0, 2\pi)$. The uncertainty band represents the full uncertainty.

DRAFT

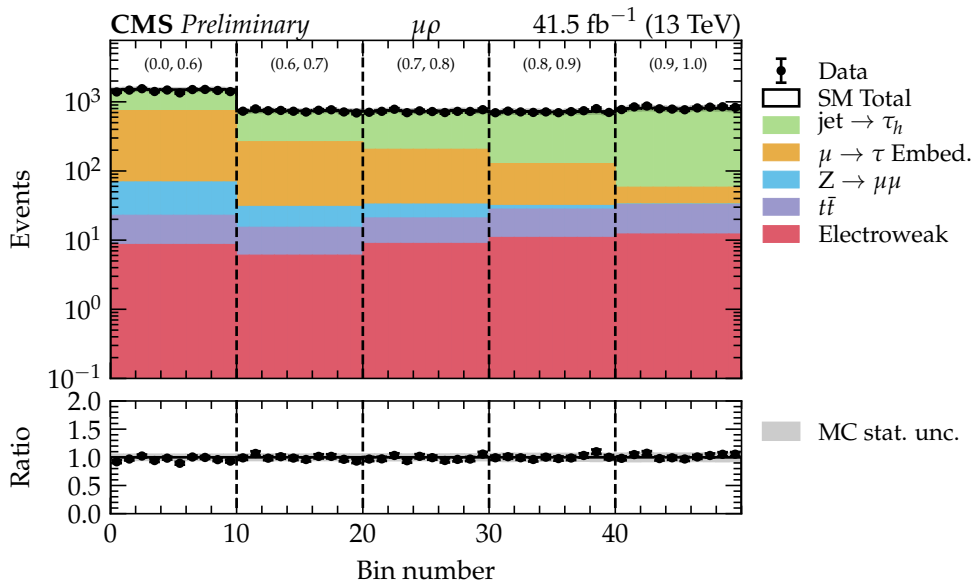

Figure 220: Distribution of ϕ_{CP} of the $\mu^{\pm} + \rho^{\mp}$ channel in the *fakes* background category for 2017, in windows of increasing NN score ranging between $(0, 1)$. The x-axis represents the cyclic bins in ϕ_{CP} in the range of $(0, 2\pi)$. The uncertainty band represents the full uncertainty.

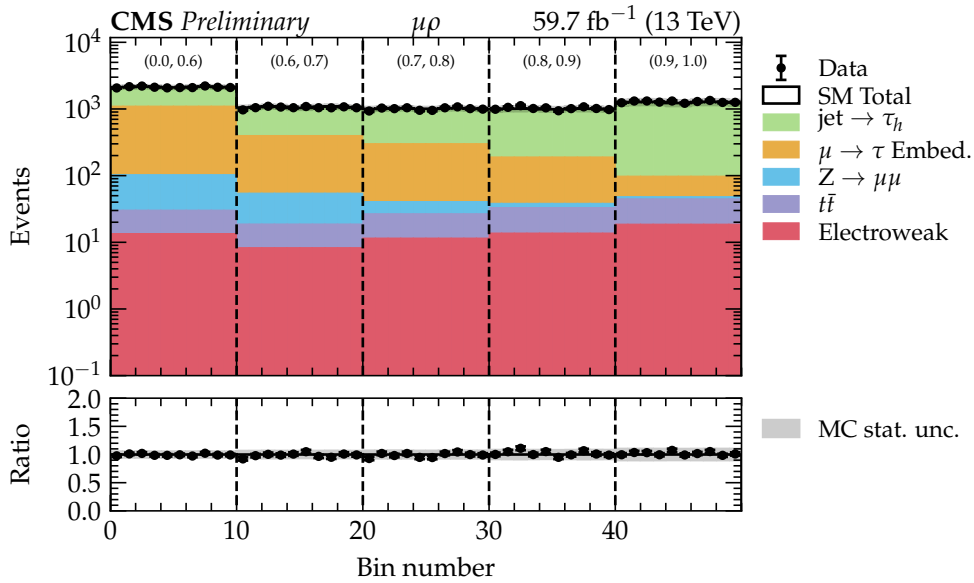

Figure 221: Distribution of ϕ_{CP} of the $\mu^{\pm} + \rho^{\mp}$ channel in the *fakes* background category for 2018, in windows of increasing NN score ranging between $(0, 1)$. The x-axis represents the cyclic bins in ϕ_{CP} in the range of $(0, 2\pi)$. The uncertainty band represents the full uncertainty.

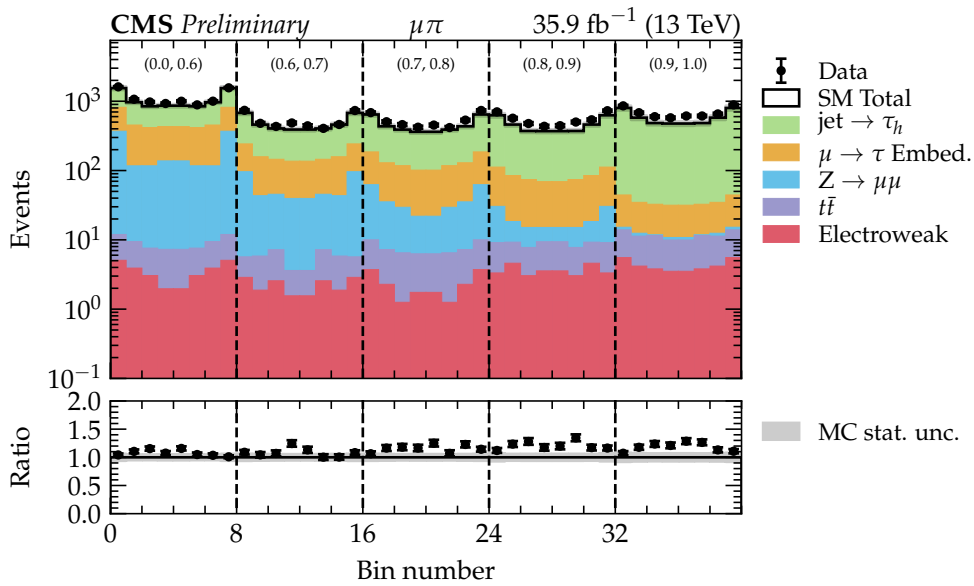

Figure 222: Distribution of ϕ_{CP} of the $\mu^{\pm} + \pi^{\mp}$ channel in the *fakes* background category for 2016, in windows of increasing NN score ranging between $(0, 1)$. The x-axis represents the cyclic bins in ϕ_{CP} in the range of $(0, 2\pi)$. The uncertainty band represents the full uncertainty.

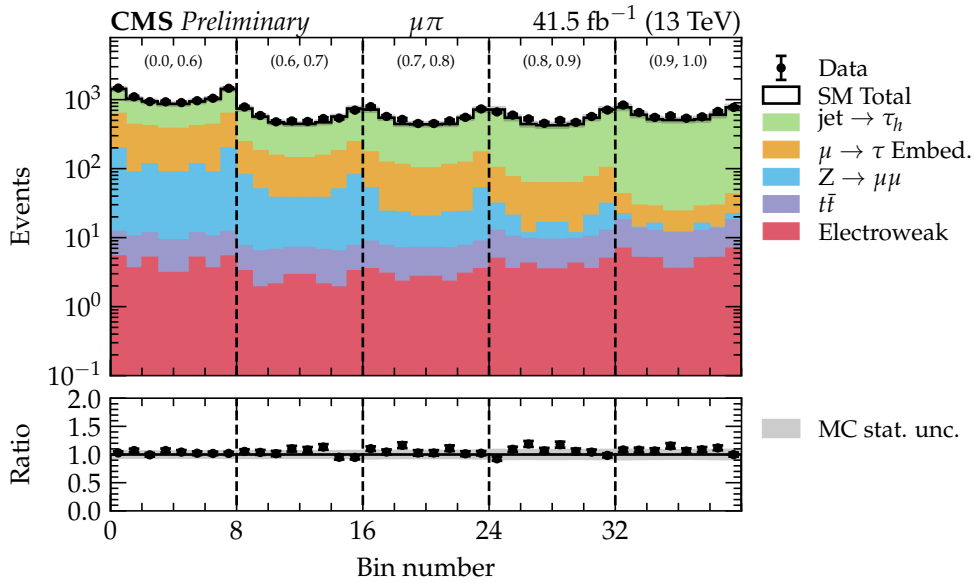

Figure 223: Distribution of ϕ_{CP} of the $\mu^{\pm} + \pi^{\mp}$ channel in the *fakes* background category for 2017, in windows of increasing NN score ranging between $(0, 1)$. The x-axis represents the cyclic bins in ϕ_{CP} in the range of $(0, 2\pi)$. The uncertainty band represents the full uncertainty.

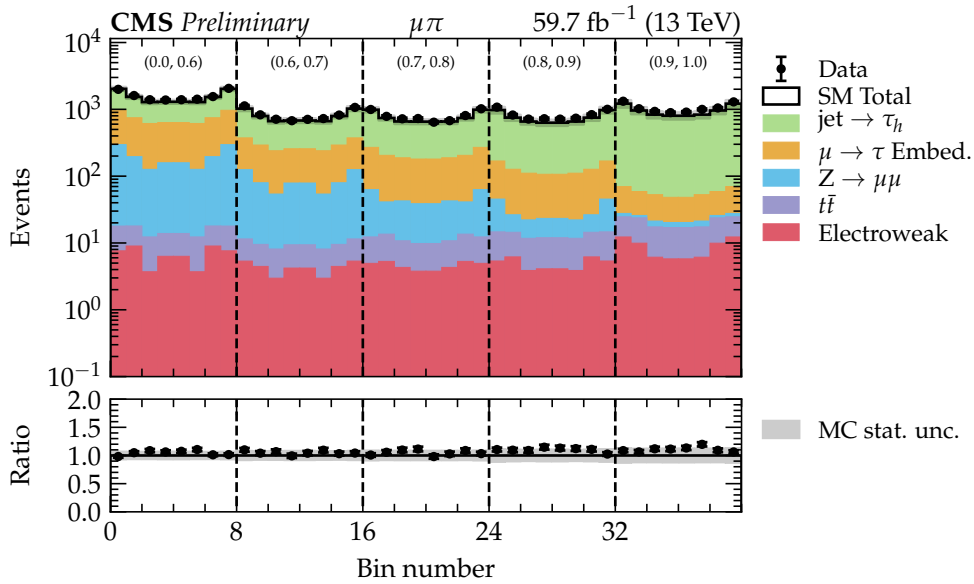

Figure 224: Distribution of ϕ_{CP} of the $\mu^{\pm} + \pi^{\mp}$ channel in the *fakes* background category for 2018, in windows of increasing NN score ranging between $(0, 1)$. The x-axis represents the cyclic bins in ϕ_{CP} in the range of $(0, 2\pi)$. The uncertainty band represents the full uncertainty.

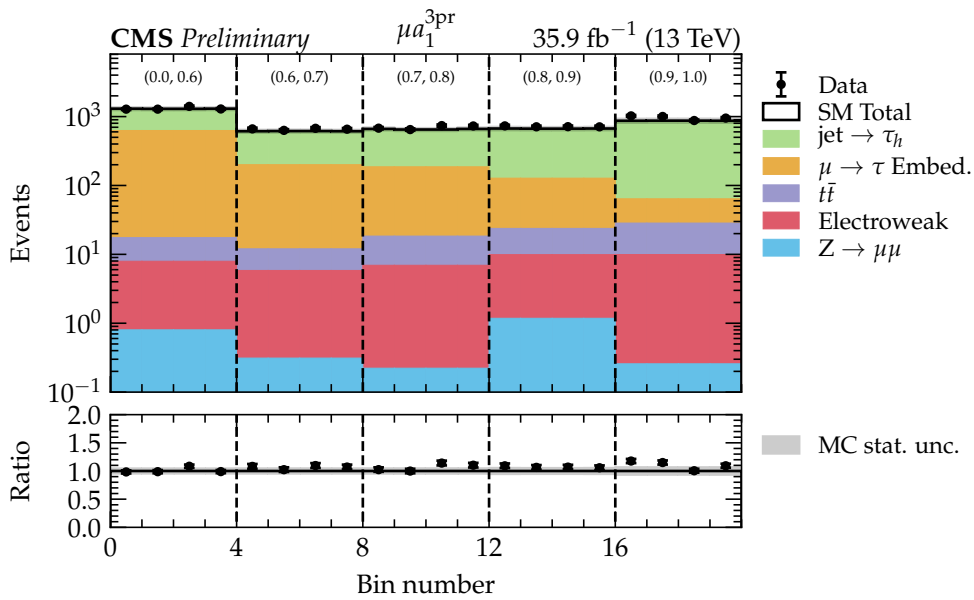

Figure 225: Distribution of ϕ_{CP} of the $\mu^{\pm} + a_1{}^{\mp,1pr}$ channel in the *fakes* background category for 2016, in windows of increasing NN score ranging between $(0, 1)$. The x-axis represents the cyclic bins in ϕ_{CP} in the range of $(0, 2\pi)$. The uncertainty band represents the full uncertainty.

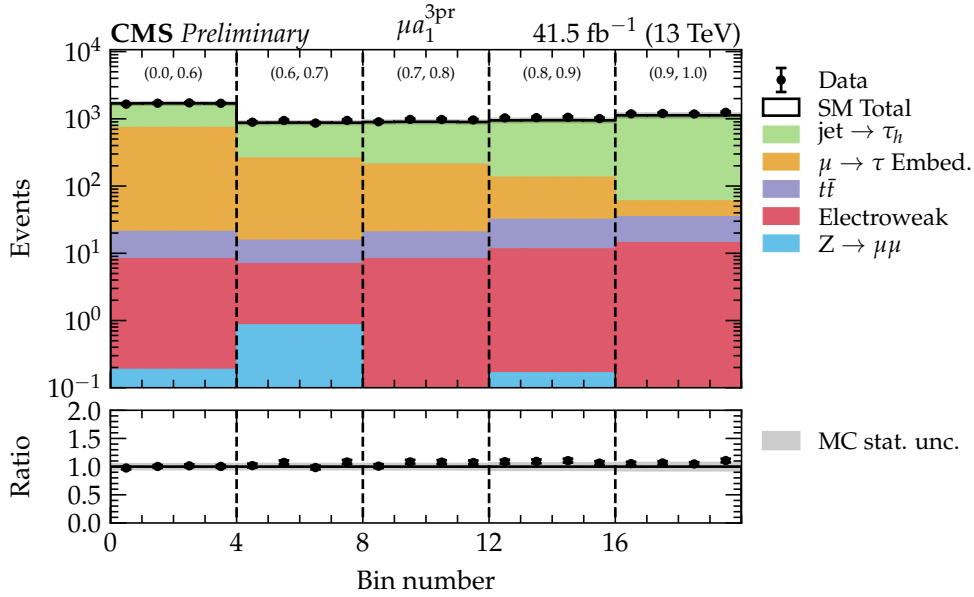

Figure 226: Distribution of ϕ_{CP} of the $\mu^{\pm} + a_1{}^{\mp,1pr}$ channel in the *fakes* background category for 2017, in windows of increasing NN score ranging between $(0, 1)$. The x-axis represents the cyclic bins in ϕ_{CP} in the range of $(0, 2\pi)$. The uncertainty band represents the full uncertainty.

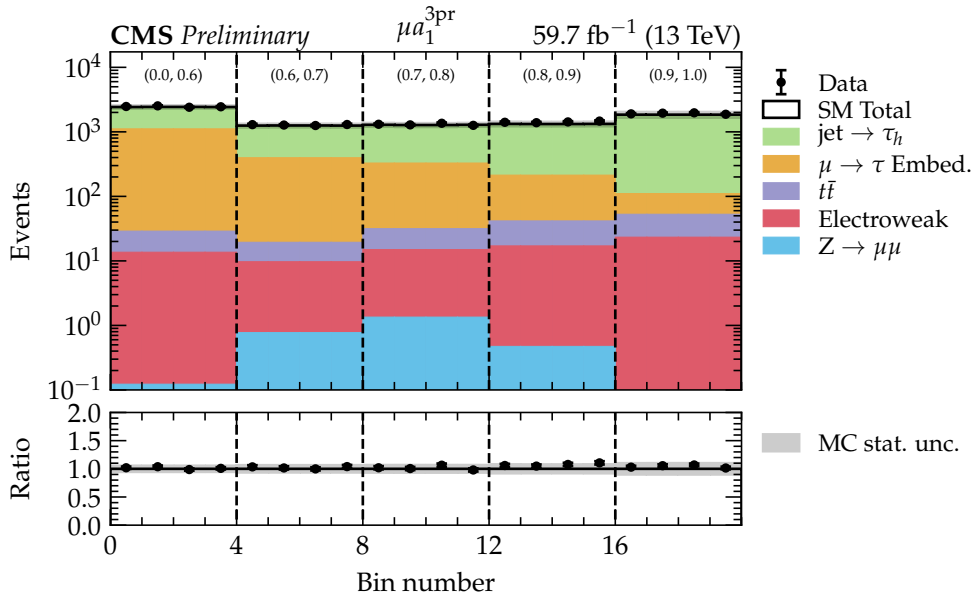

Figure 227: Distribution of ϕ_{CP} of the $\mu^{\pm} + a_1{}^{\mp,1pr}$ channel in the *fakes* background category for 2018, in windows of increasing NN score ranging between $(0, 1)$. The x-axis represents the cyclic bins in ϕ_{CP} in the range of $(0, 2\pi)$. The uncertainty band represents the full uncertainty.

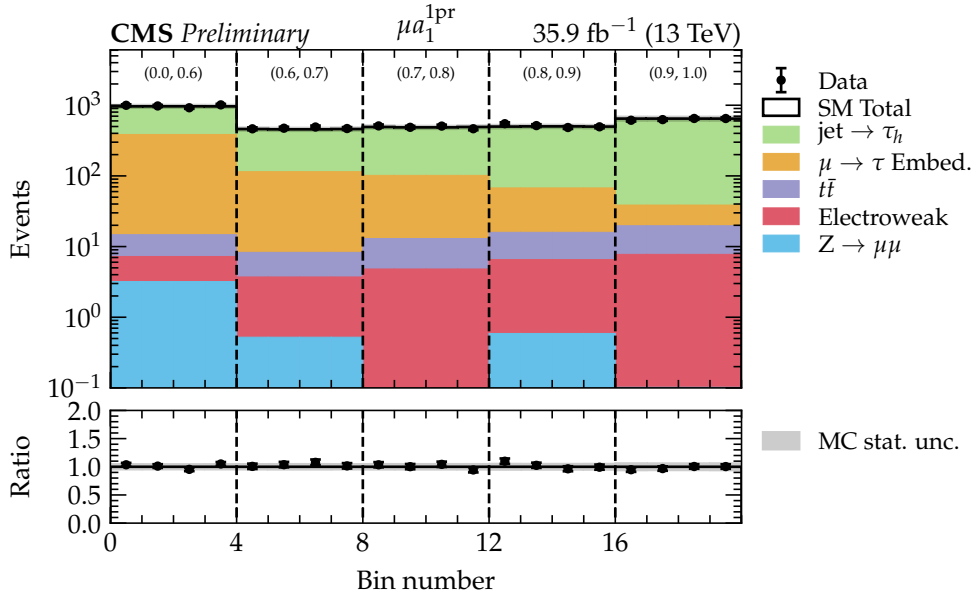

Figure 228: Distribution of ϕ_{CP} of the $\mu^{\pm} + a_1{}^{\mp,3pr}$ channel in the *fakes* background category for 2016, in windows of increasing NN score ranging between $(0, 1)$. The x-axis represents the cyclic bins in ϕ_{CP} in the range of $(0, 2\pi)$. The uncertainty band represents the full uncertainty.

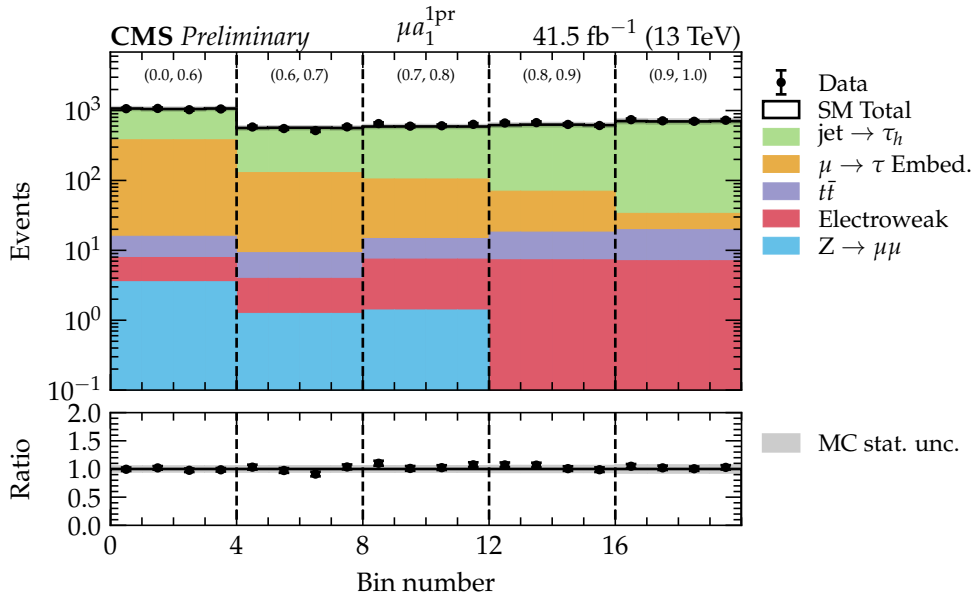

Figure 229: Distribution of ϕ_{CP} of the $\mu^{\pm} + a_1{}^{\mp,3pr}$ channel in the *fakes* background category for 2017, in windows of increasing NN score ranging between $(0, 1)$. The x-axis represents the cyclic bins in ϕ_{CP} in the range of $(0, 2\pi)$. The uncertainty band represents the full uncertainty.

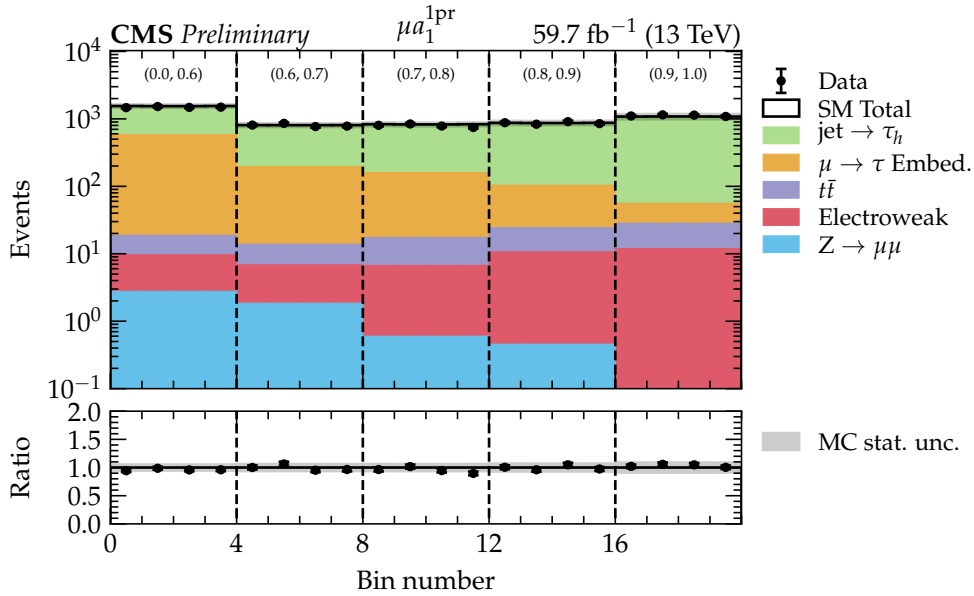

Figure 230: Distribution of ϕ_{CP} of the $\mu^{\pm} + a_1{}^{\mp,3pr}$ channel in the *fakes* background category for 2018, in windows of increasing NN score ranging between $(0, 1)$. The x-axis represents the cyclic bins in ϕ_{CP} in the range of $(0, 2\pi)$. The uncertainty band represents the full uncertainty.

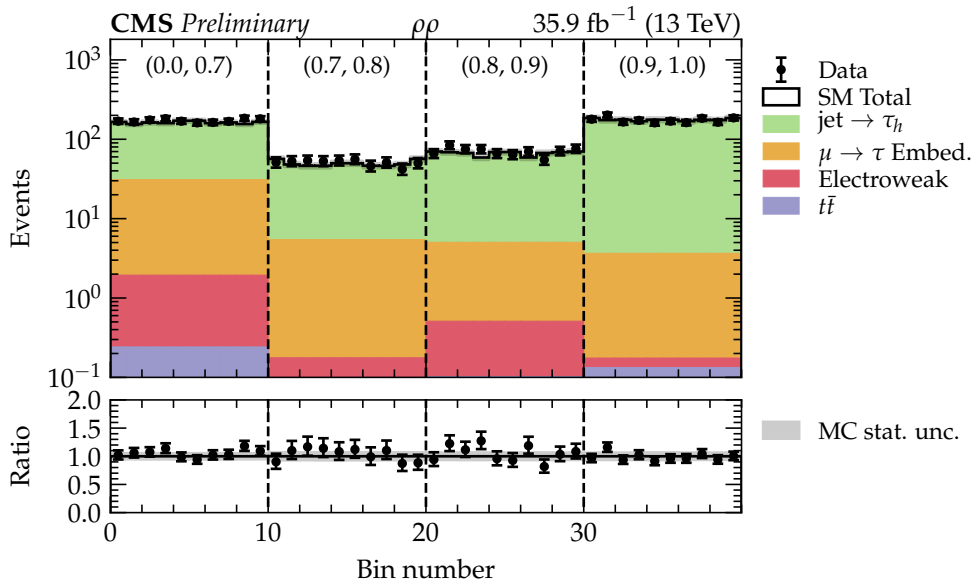

Figure 231: Distribution of ϕ_{CP} of the $\rho^{\pm} + \rho^{\mp}$ channel in the *fakes* background category for 2016, in windows of increasing BDT score ranging between $(0, 1)$. The x-axis represents the cyclic bins in ϕ_{CP} in the range of $(0, 2\pi)$. The uncertainty band represents the full uncertainty.

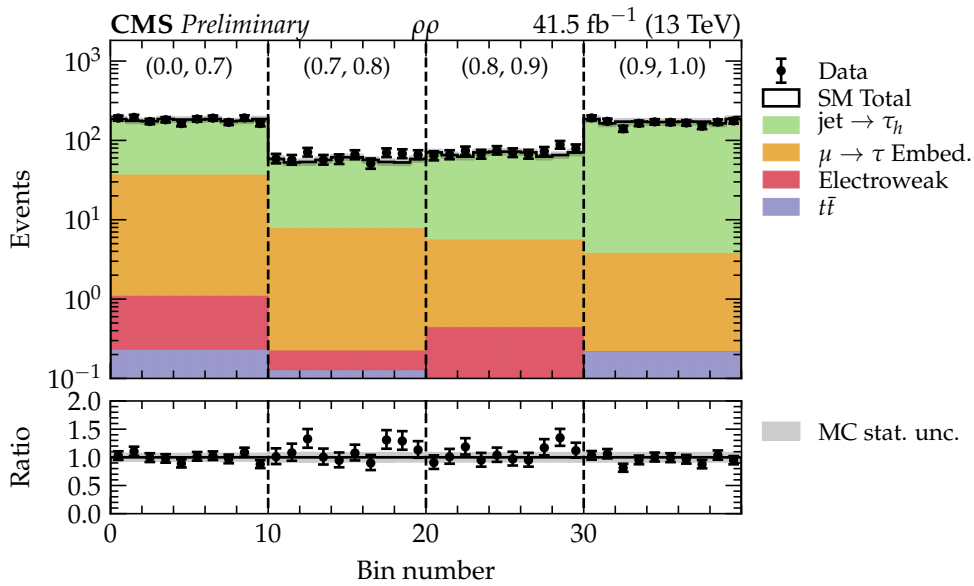

Figure 232: Distribution of ϕ_{CP} of the $\rho^{\pm} + \rho^{\mp}$ channel in the *fakes* background category for 2017, in windows of increasing BDT score ranging between $(0, 1)$. The x-axis represents the cyclic bins in ϕ_{CP} in the range of $(0, 2\pi)$. The uncertainty band represents the full uncertainty.

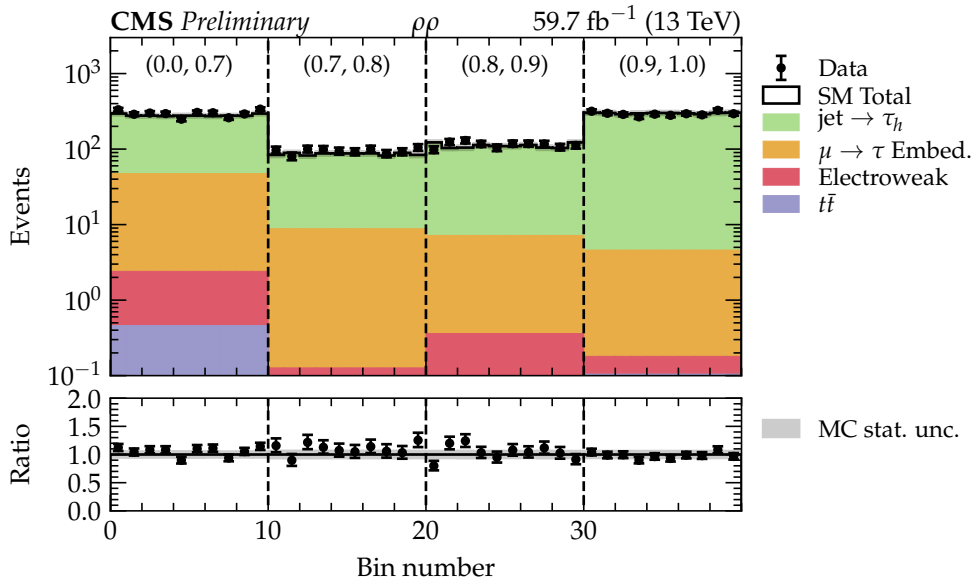

Figure 233: Distribution of ϕ_{CP} of the $\rho^{\pm} + \rho^{\mp}$ channel in the *fakes* background category for 2018, in windows of increasing BDT score. The x-axis represents the cyclic bins in ϕ_{CP} in the range of $(0, 2\pi)$. The uncertainty band represents the full uncertainty.

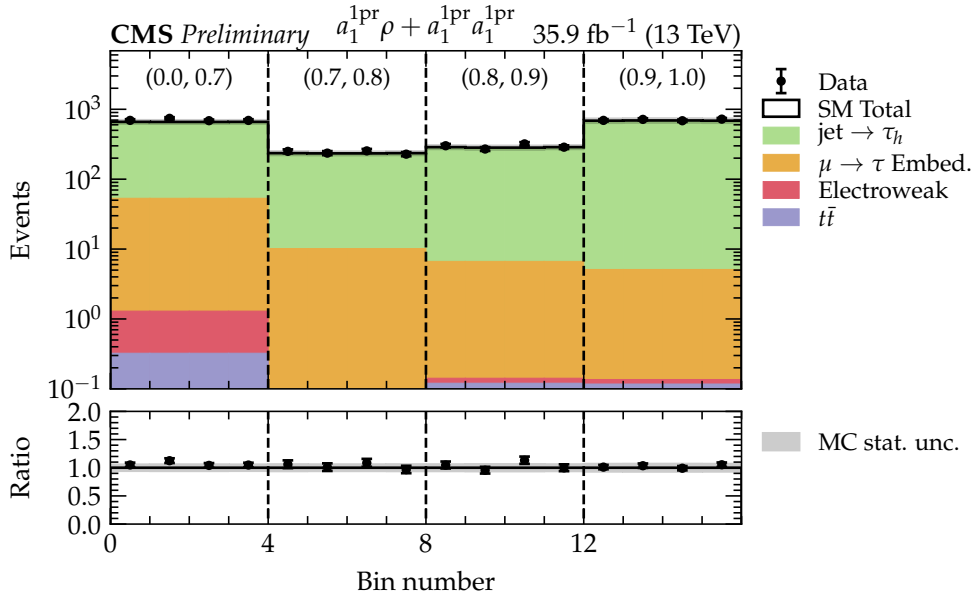

Figure 234: Distribution of ϕ_{CP} of the $a_1^{\pm,1pr} + \rho^{\mp}$ and $a_1^{\pm,1pr} + a_1^{\pm,1pr}$ channel in the *fakes* background category for 2016, in windows of increasing BDT score ranging between $(0, 1)$. The x-axis represents the cyclic bins in ϕ_{CP} in the range of $(0, 2\pi)$. The uncertainty band represents the full uncertainty.

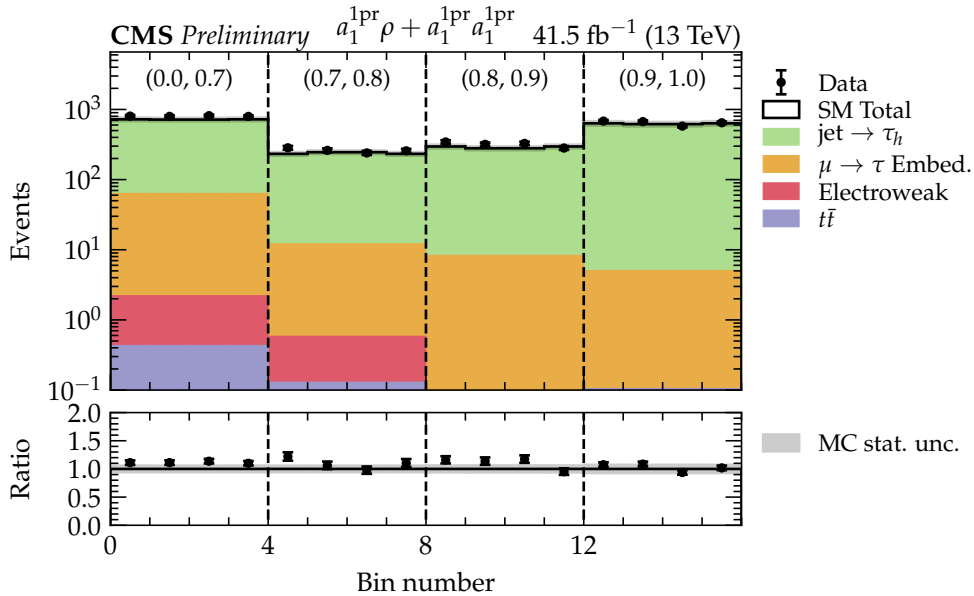

Figure 235: Distribution of ϕ_{CP} of the $a_1^{\pm,1pr} + \rho^{\mp}$ and $a_1^{\pm,1pr} + a_1^{\pm,1pr}$ channel in the *fakes* background category for 2017, in windows of increasing BDT score ranging between $(0, 1)$. The x-axis represents the cyclic bins in ϕ_{CP} in the range of $(0, 2\pi)$. The uncertainty band represents the full uncertainty.

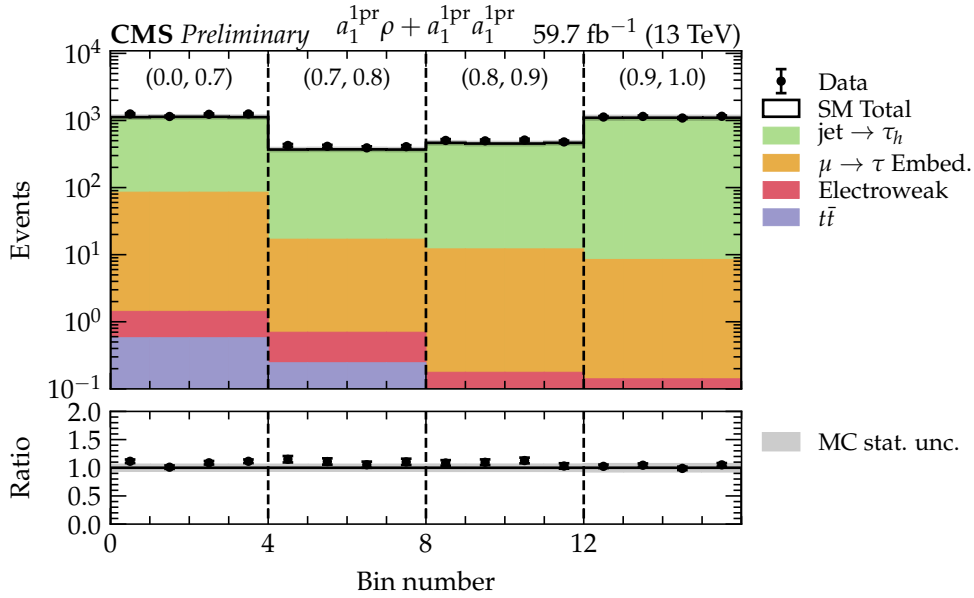

Figure 236: Distribution of ϕ_{CP} of the $a_1^{\pm,1pr} + \rho^{\mp}$ and $a_1^{\pm,1pr} + a_1^{\pm,1pr}$ channel in the *fakes* background category for 2018, in windows of increasing BDT score ranging between $(0, 1)$. The x-axis represents the cyclic bins in ϕ_{CP} in the range of $(0, 2\pi)$. The uncertainty band represents the full uncertainty.

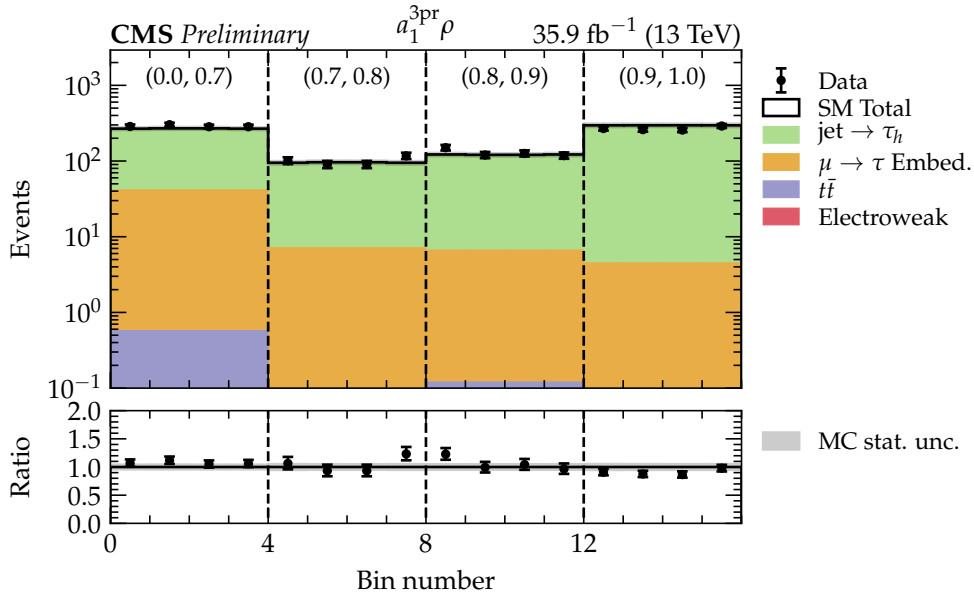

Figure 237: Distribution of ϕ_{CP} of the $a_1^{\pm,3pr} + \rho^{\mp}$ channel in the *fakes* background category for 2016, in windows of increasing BDT score ranging between $(0, 1)$. The x-axis represents the cyclic bins in ϕ_{CP} in the range of $(0, 2\pi)$. The uncertainty band represents the full uncertainty.

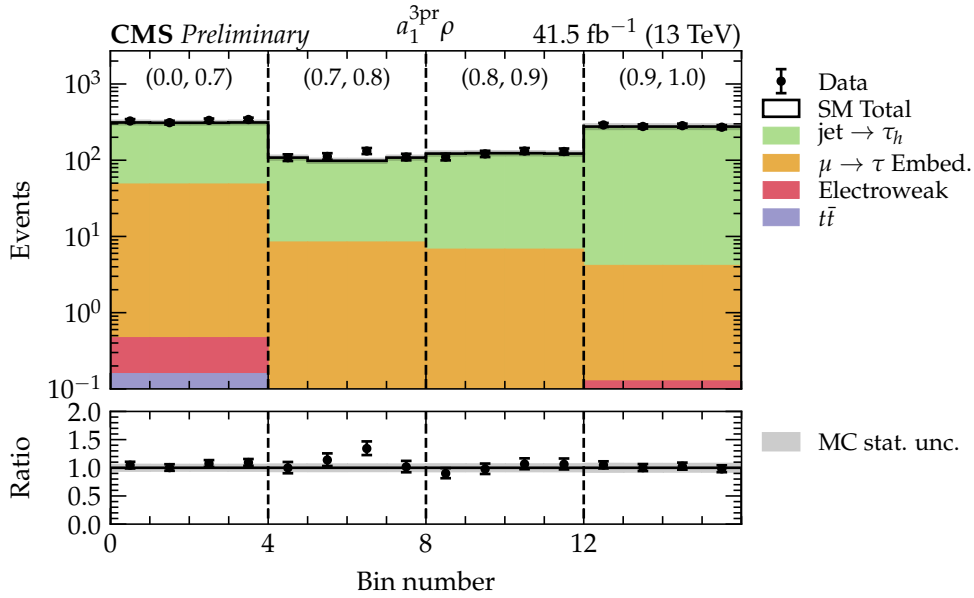

Figure 238: Distribution of ϕ_{CP} of the $a_1^{\pm,3pr} + \rho^{\mp}$ channel in the *fakes* background category for 2017, in windows of increasing BDT score ranging between $(0, 1)$. The x-axis represents the cyclic bins in ϕ_{CP} in the range of $(0, 2\pi)$. The uncertainty band represents the full uncertainty.

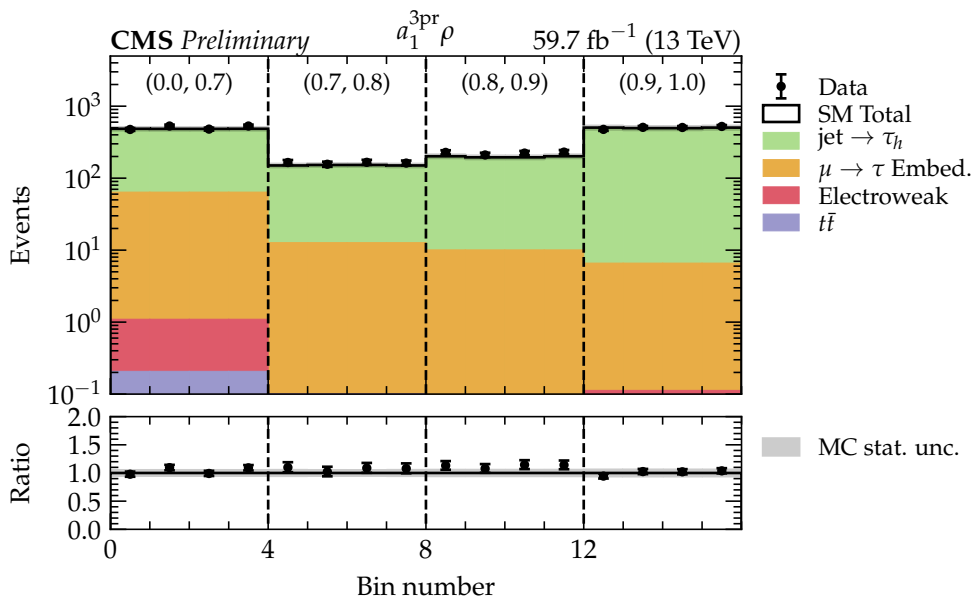

Figure 239: Distribution of ϕ_{CP} of the $a_1^{\pm,3pr} + \rho^{\mp}$ channel in the *fakes* background category for 2018, in windows of increasing BDT score ranging between $(0, 1)$. The x-axis represents the cyclic bins in ϕ_{CP} in the range of $(0, 2\pi)$. The uncertainty band represents the full uncertainty.

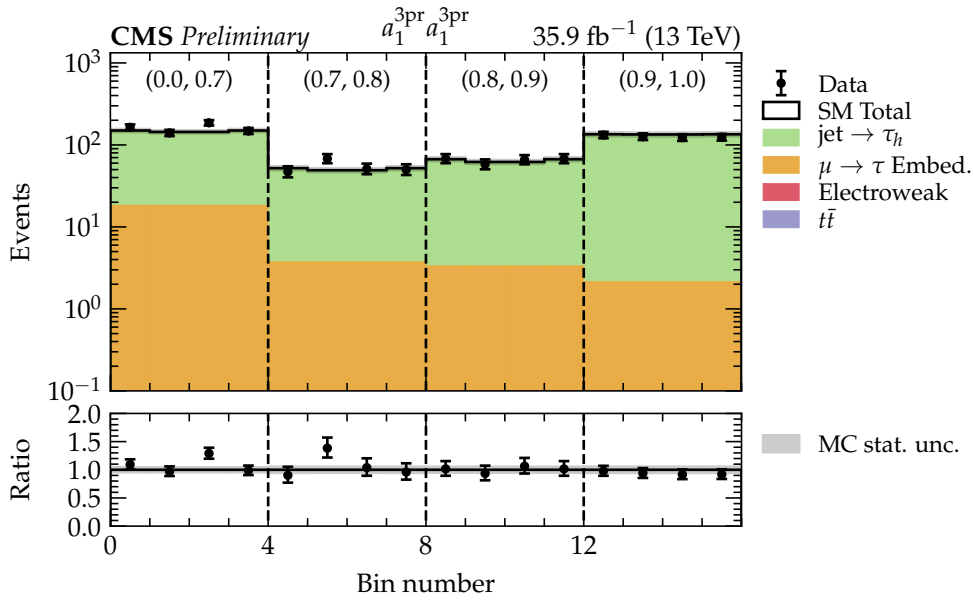

Figure 240: Distribution of ϕ_{CP} of the $a_1^{\pm,3pr} + a_1^{\mp,3pr}$ channel in the *fakes* background category for 2016, in windows of increasing BDT score ranging between $(0, 1)$. The x-axis represents the cyclic bins in ϕ_{CP} in the range of $(0, 2\pi)$. The uncertainty band represents the full uncertainty.

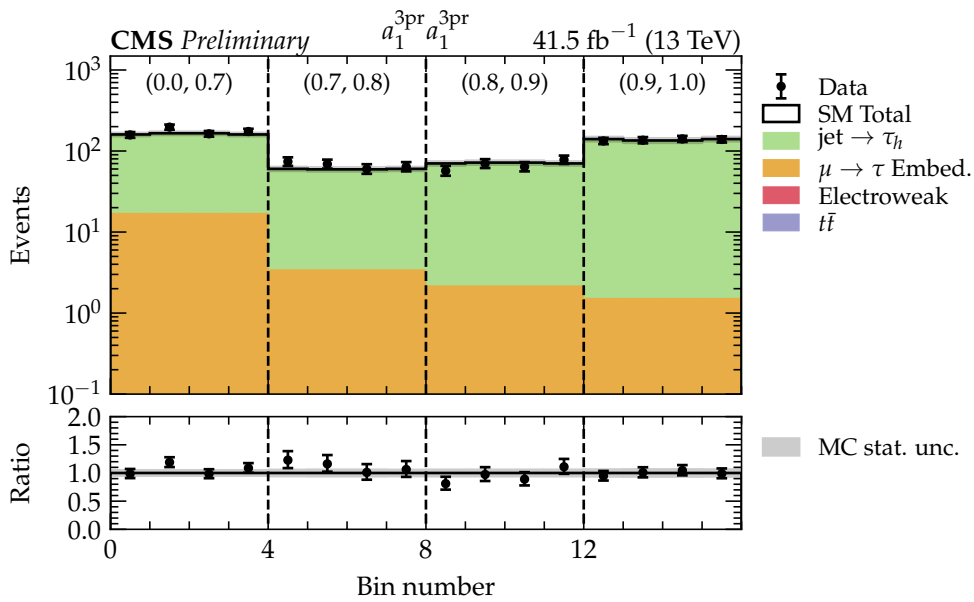

Figure 241: Distribution of ϕ_{CP} of the $a_1^{\pm,3pr} + a_1^{\mp,3pr}$ channel in the *fakes* background category for 2017, in windows of increasing BDT score ranging between $(0, 1)$. The x-axis represents the cyclic bins in ϕ_{CP} in the range of $(0, 2\pi)$. The uncertainty band represents the full uncertainty.

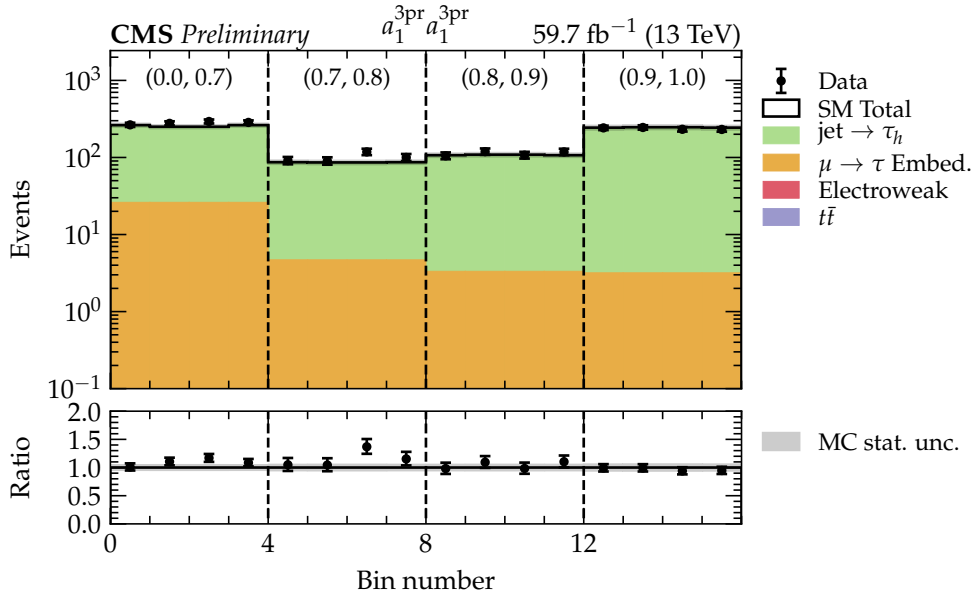

Figure 242: Distribution of ϕ_{CP} of the $a_1^{\pm,3pr} + a_1^{\mp,3pr}$ channel in the *fakes* background category for 2018, in windows of increasing BDT score ranging between $(0, 1)$. The x-axis represents the cyclic bins in ϕ_{CP} in the range of $(0, 2\pi)$. The uncertainty band represents the full uncertainty.

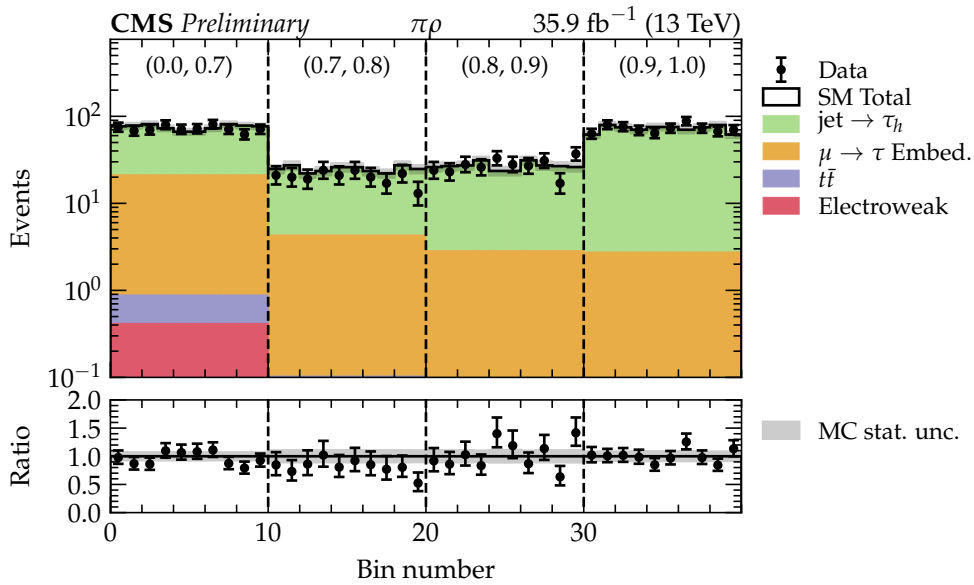

Figure 243: Distribution of ϕ_{CP} of the $\pi^{\pm} + \rho^{\mp}$ channel in the *fakes* background category for 2016, in windows of increasing BDT score ranging between $(0, 1)$. The x-axis represents the cyclic bins in ϕ_{CP} in the range of $(0, 2\pi)$. The uncertainty band represents the full uncertainty.

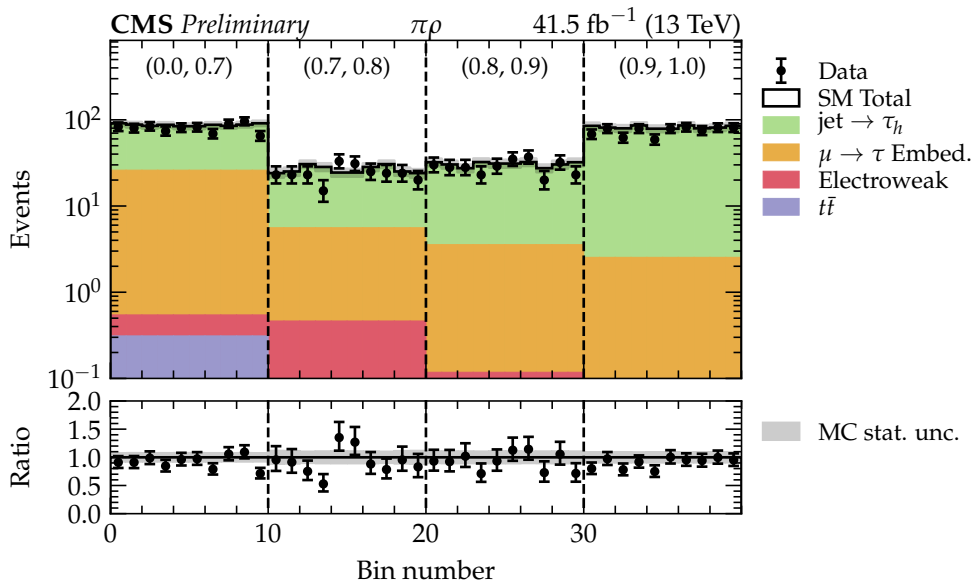

Figure 244: Distribution of ϕ_{CP} of the $\pi^{\pm} + \rho^{\mp}$ channel in the *fakes* background category for 2017, in windows of increasing BDT score ranging between $(0, 1)$. The x-axis represents the cyclic bins in ϕ_{CP} in the range of $(0, 2\pi)$. The uncertainty band represents the full uncertainty.

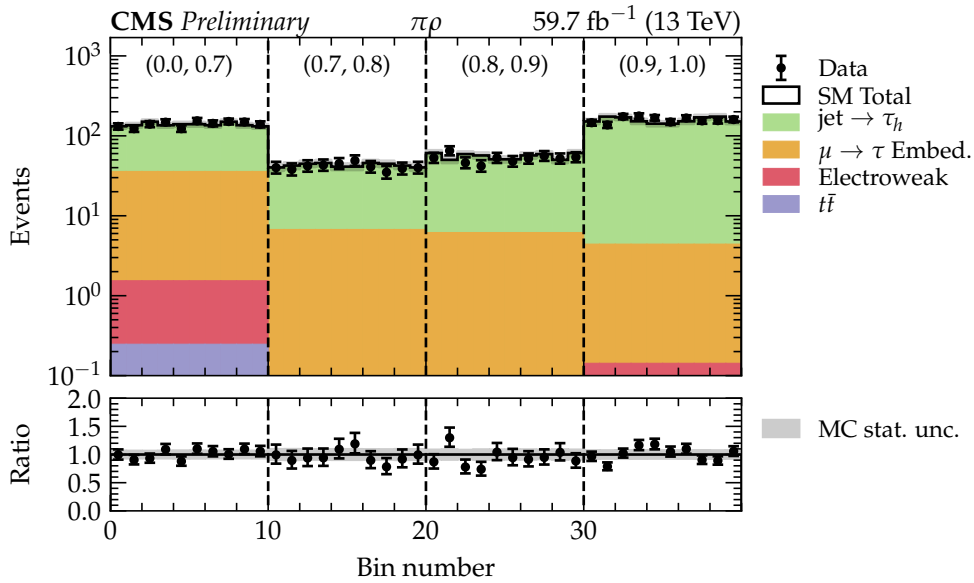

Figure 245: Distribution of ϕ_{CP} of the $\pi^{\pm} + \rho^{\mp}$ channel in the *fakes* background category for 2018, in windows of increasing BDT score ranging between $(0, 1)$. The x-axis represents the cyclic bins in ϕ_{CP} in the range of $(0, 2\pi)$. The uncertainty band represents the full uncertainty.

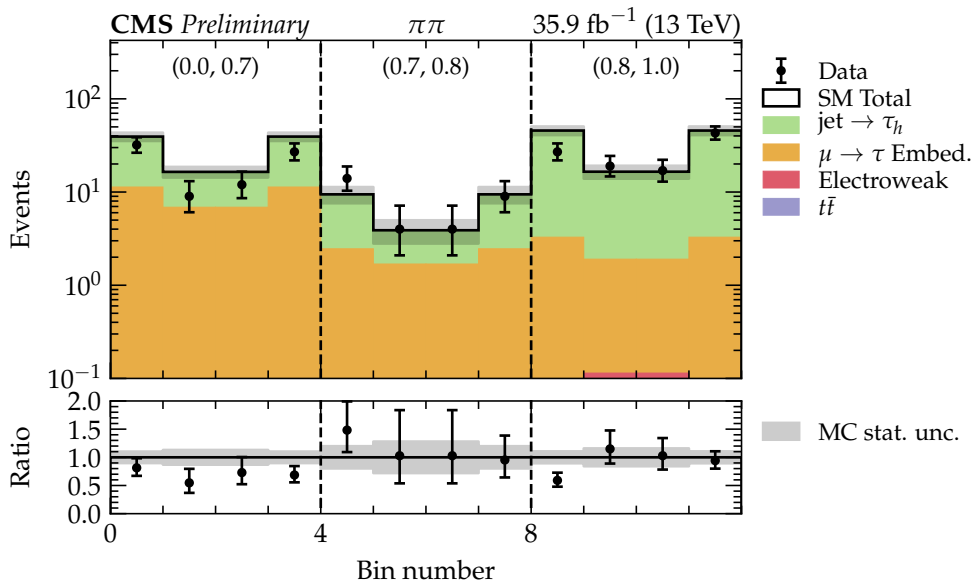

Figure 246: Distribution of ϕ_{CP} of the $\pi^{\pm} + \pi^{\mp}$ channel in the *fakes* background category for 2016, in windows of increasing BDT score ranging between $(0, 1)$. The x-axis represents the cyclic bins in ϕ_{CP} in the range of $(0, 2\pi)$. The uncertainty band represents the full uncertainty.

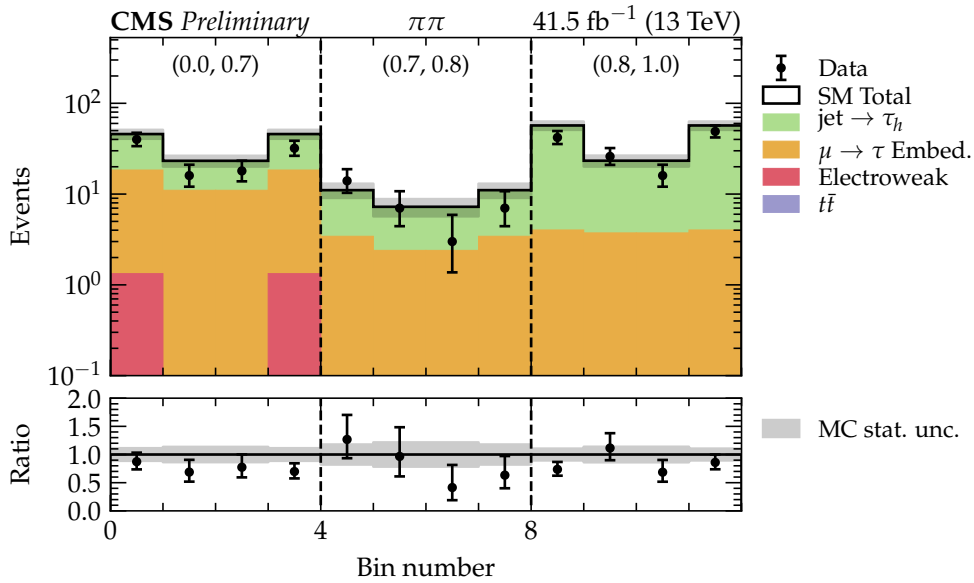

Figure 247: Distribution of ϕ_{CP} of the $\pi^{\pm} + \pi^{\mp}$ channel in the *fakes* background category for 2017, in windows of increasing BDT score ranging between $(0, 1)$. The x-axis represents the cyclic bins in ϕ_{CP} in the range of $(0, 2\pi)$. The uncertainty band represents the full uncertainty.

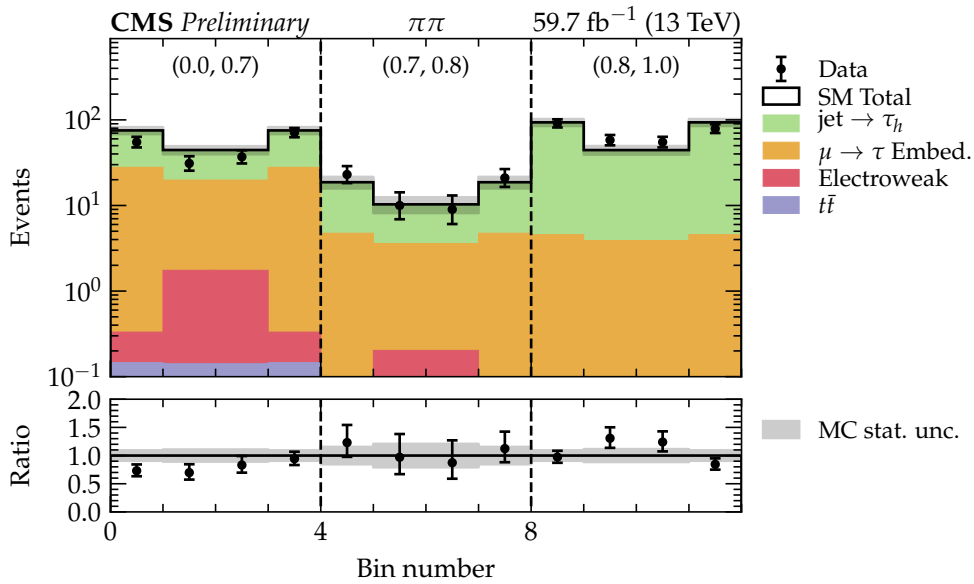

Figure 248: Distribution of ϕ_{CP} of the $\pi^{\pm} + \pi^{\mp}$ channel in the *fakes* background category for 2018, in windows of increasing BDT score ranging between $(0, 1)$. The x-axis represents the cyclic bins in ϕ_{CP} in the range of $(0, 2\pi)$. The uncertainty band represents the full uncertainty.

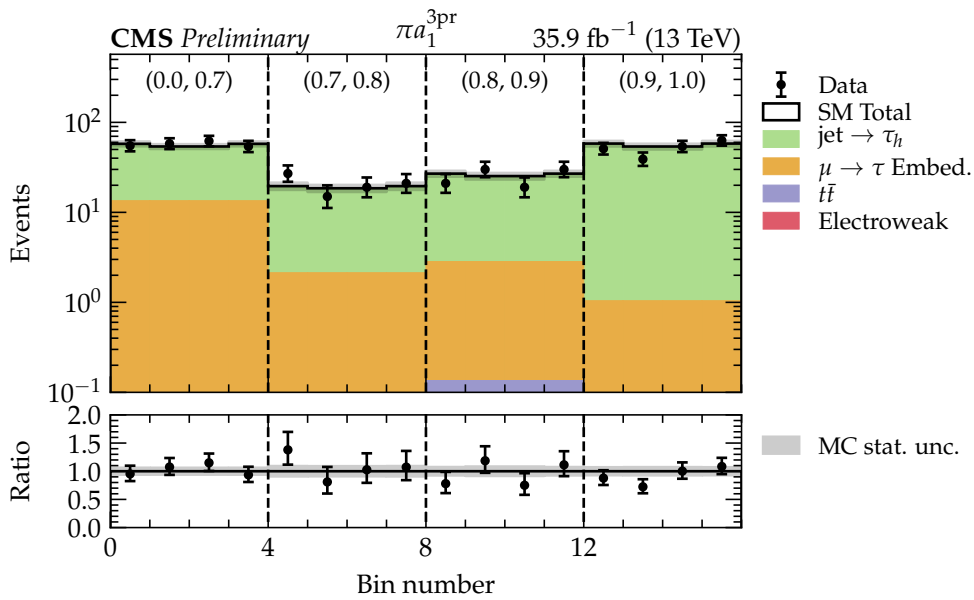

Figure 249: Distribution of ϕ_{CP} of the $\pi^{\pm} + a_1{}^{\mp,3pr}$ channel in the *fakes* background category for 2016, in windows of increasing BDT score ranging between $(0, 1)$. The x-axis represents the cyclic bins in ϕ_{CP} in the range of $(0, 2\pi)$. The uncertainty band represents the full uncertainty.

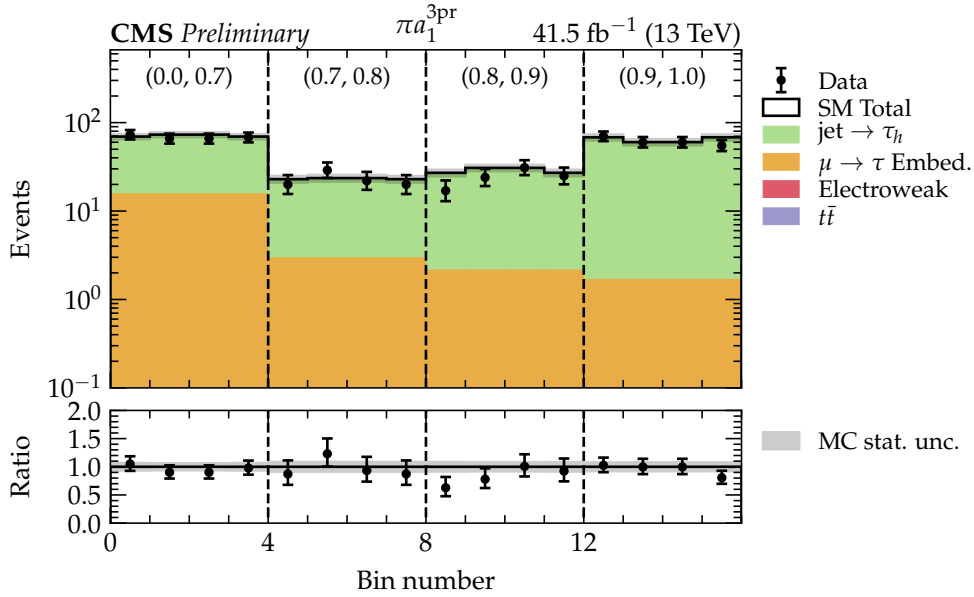

Figure 250: Distribution of ϕ_{CP} of the $\pi^{\pm} + a_1{}^{\mp,3pr}$ channel in the *fakes* background category for 2017, in windows of increasing BDT score ranging between $(0, 1)$. The x-axis represents the cyclic bins in ϕ_{CP} in the range of $(0, 2\pi)$. The uncertainty band represents the full uncertainty.

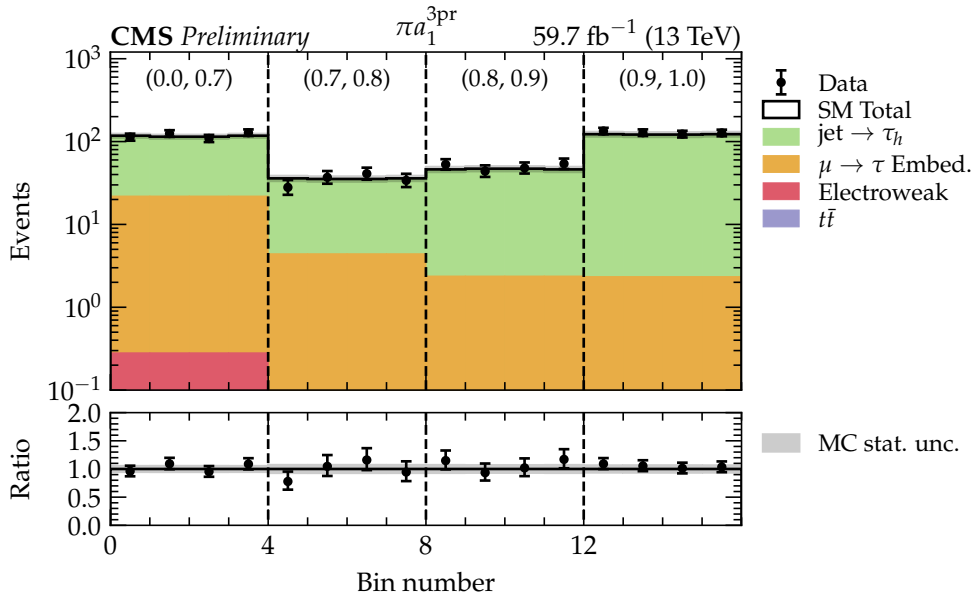

Figure 251: Distribution of ϕ_{CP} of the $\pi^{\pm} + a_1{}^{\mp,3pr}$ channel in the *fakes* background category for 2018, in windows of increasing BDT score ranging between $(0, 1)$. The x-axis represents the cyclic bins in ϕ_{CP} in the range of $(0, 2\pi)$. The uncertainty band represents the full uncertainty.

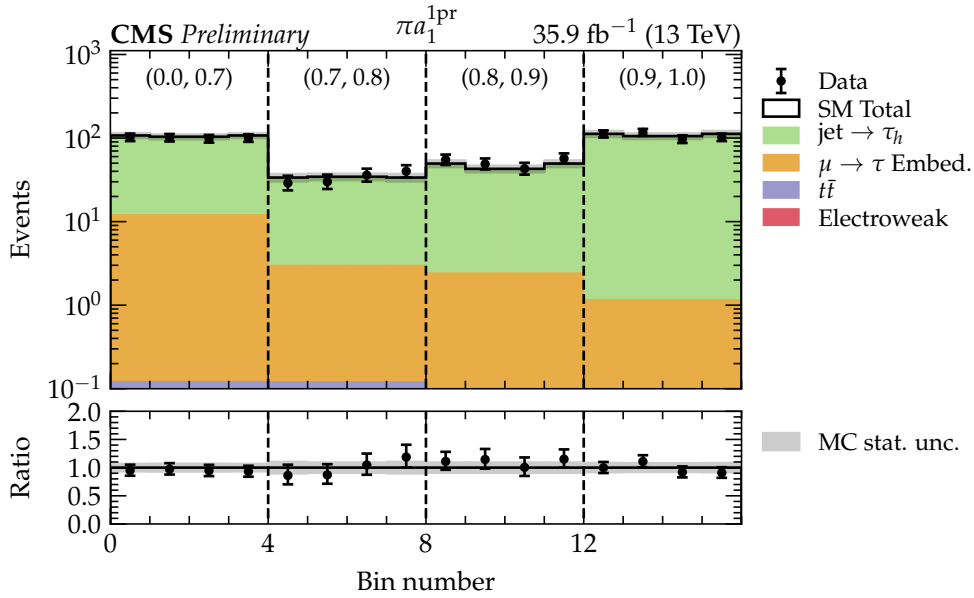

Figure 252: Distribution of ϕ_{CP} of the $\pi^{\pm} + a_1{}^{\mp,1pr}$ channel in the *fakes* background category for 2016, in windows of increasing BDT score ranging between $(0, 1)$. The x-axis represents the cyclic bins in ϕ_{CP} in the range of $(0, 2\pi)$. The uncertainty band represents the full uncertainty.

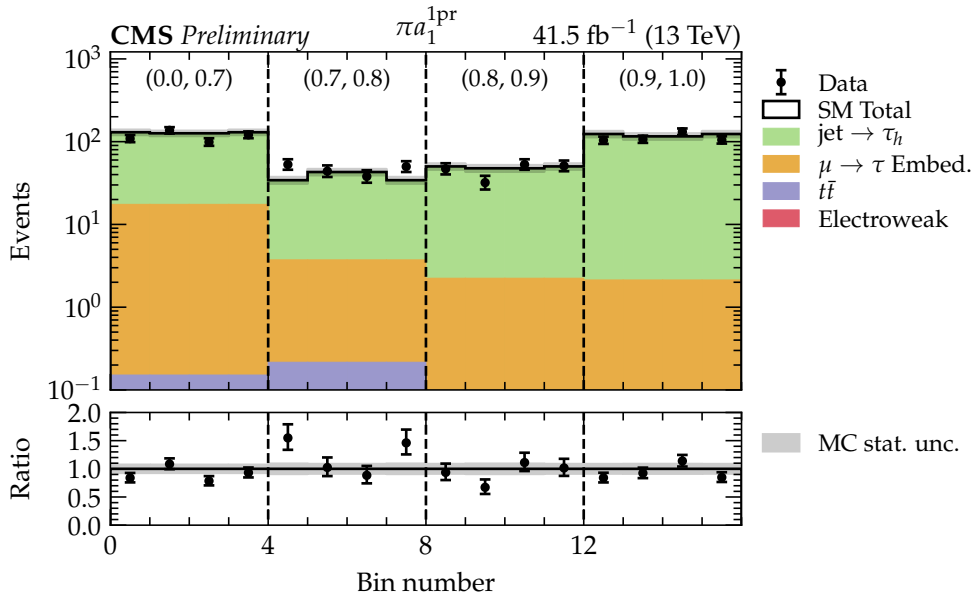

Figure 253: Distribution of ϕ_{CP} of the $\pi^{\pm} + a_1{}^{\mp,1pr}$ channel in the *fakes* background category for 2017, in windows of increasing BDT score ranging between $(0, 1)$. The x-axis represents the cyclic bins in ϕ_{CP} in the range of $(0, 2\pi)$. The uncertainty band represents the full uncertainty.

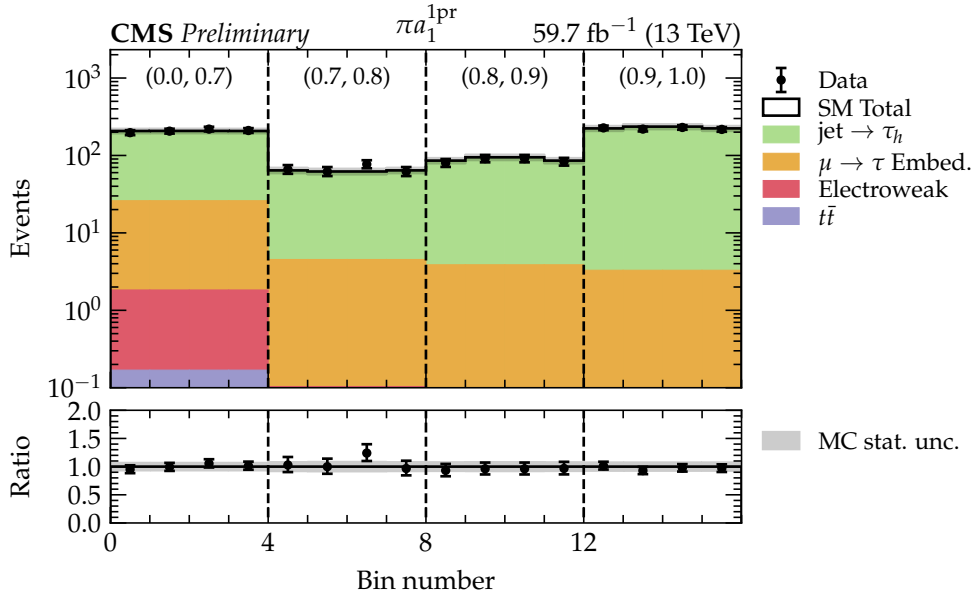

Figure 254: Distribution of ϕ_{CP} of the $\pi^{\pm} + a_1{}^{\mp,1pr}$ channel in the *fakes* background category for 2018, in windows of increasing BDT score ranging between $(0, 1)$. The x-axis represents the cyclic bins in ϕ_{CP} in the range of $(0, 2\pi)$. The uncertainty band represents the full uncertainty.

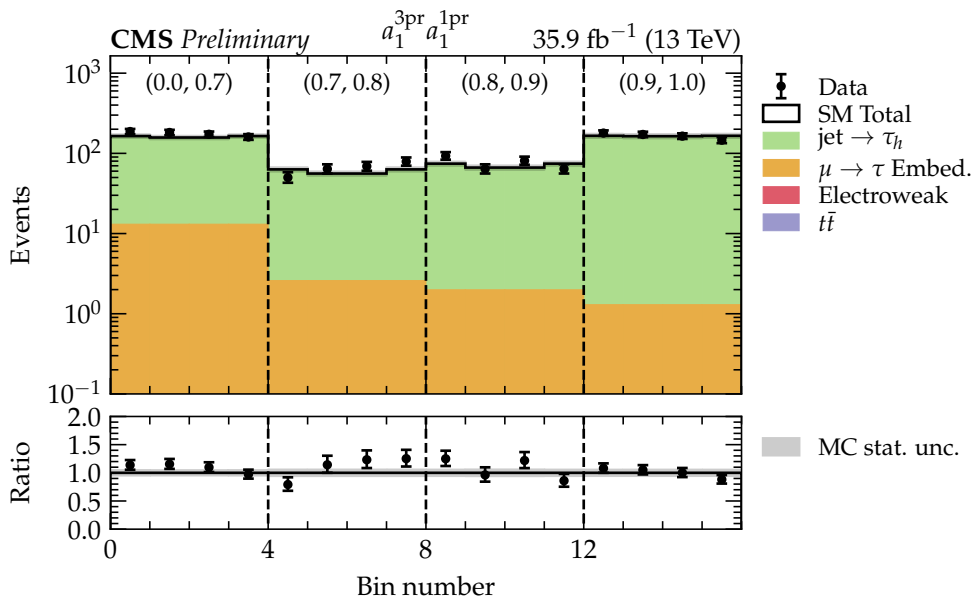

Figure 255: Distribution of ϕ_{CP} of the $a_1{}^{\pm,3pr} + a_1{}^{\mp,1pr}$ channel in the *fakes* background category for 2016, in windows of increasing BDT score ranging between $(0, 1)$. The x-axis represents the cyclic bins in ϕ_{CP} in the range of $(0, 2\pi)$. The uncertainty band represents the full uncertainty.

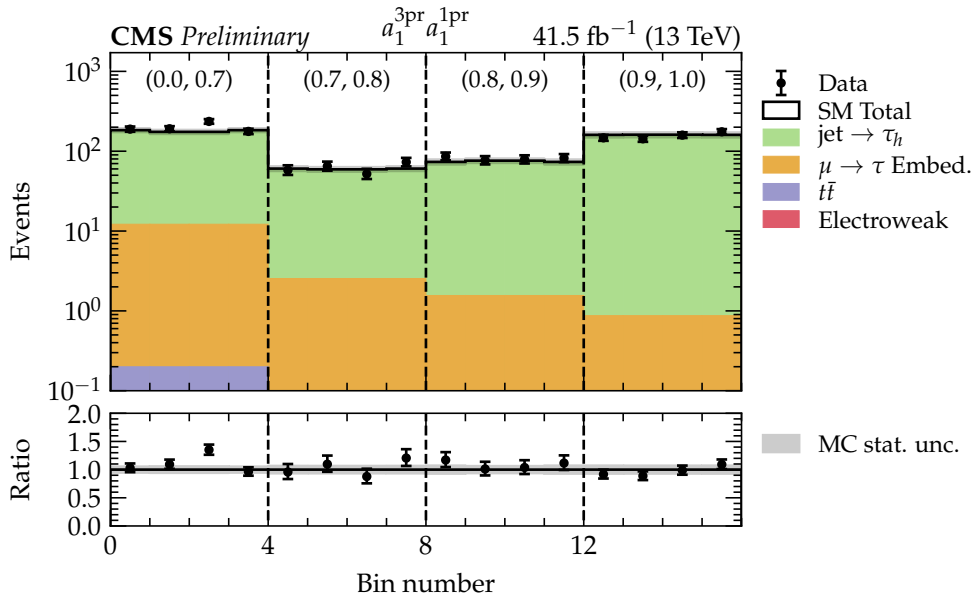

Figure 256: Distribution of ϕ_{CP} of the $a_1^{\pm,3pr} + a_1^{\mp,1pr}$ channel in the *fakes* background category for 2017, in windows of increasing BDT score ranging between $(0, 1)$. The x-axis represents the cyclic bins in ϕ_{CP} in the range of $(0, 2\pi)$. The uncertainty band represents the full uncertainty.

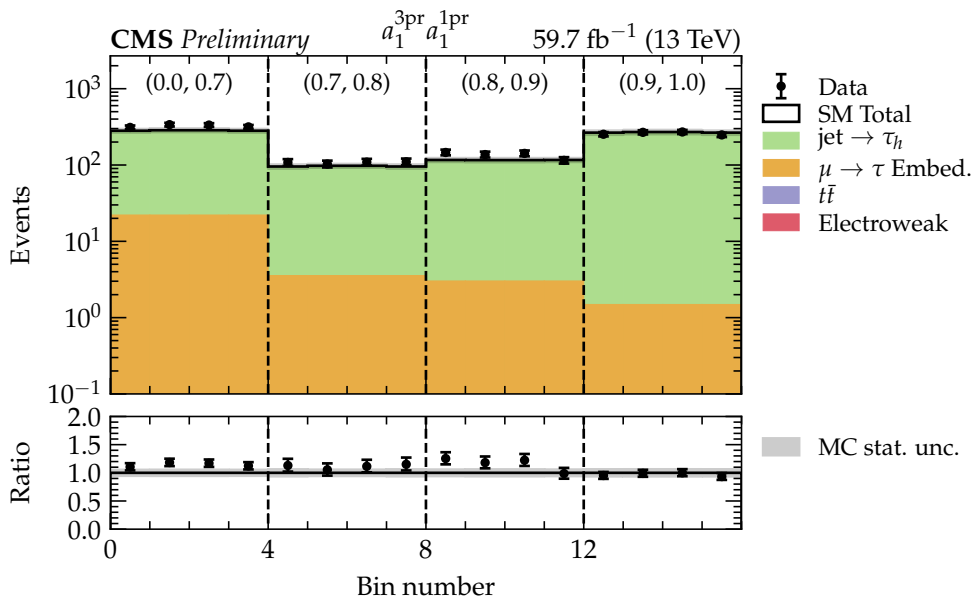

Figure 257: Distribution of ϕ_{CP} of the $a_1^{\pm,3pr} + a_1^{\mp,1pr}$ channel in the *fakes* background category for 2018, in windows of increasing BDT score ranging between $(0, 1)$. The x-axis represents the cyclic bins in ϕ_{CP} in the range of $(0, 2\pi)$. The uncertainty band represents the full uncertainty.

D Control plots using MC to model $Z \to \tau\tau$

This section contains versions of the control plots using MC to model the Z$\to \tau\tau_{\mathrm{h}}$ background instead of the embedded samples. The purpose of such plot is to demonstrate that we model the data correctly using MC, which is relevant as we use MC to model our signal processes.

D.1 Results in the $\tau_\mu\tau_h$ hannel

In Fig. 258-260(2016), Fig. 262-264(2017), and Fig. 266 268(2018) we display prefit control distributions for observables that are used in the multivariate discriminant (DNN) to distinguish the signal from background events.

The plots are obtained after inclusive selection of $\tau_\mu\tau_h$ events as described in Section 7. Several additional cuts are applied:

- number of b-tagged jets = 0 (to reject top-pair and single-top backgrounds),
- visible mass of muon and tau lepton, $m_{\mathrm{vis}} > 40\,\mathrm{GeV}$

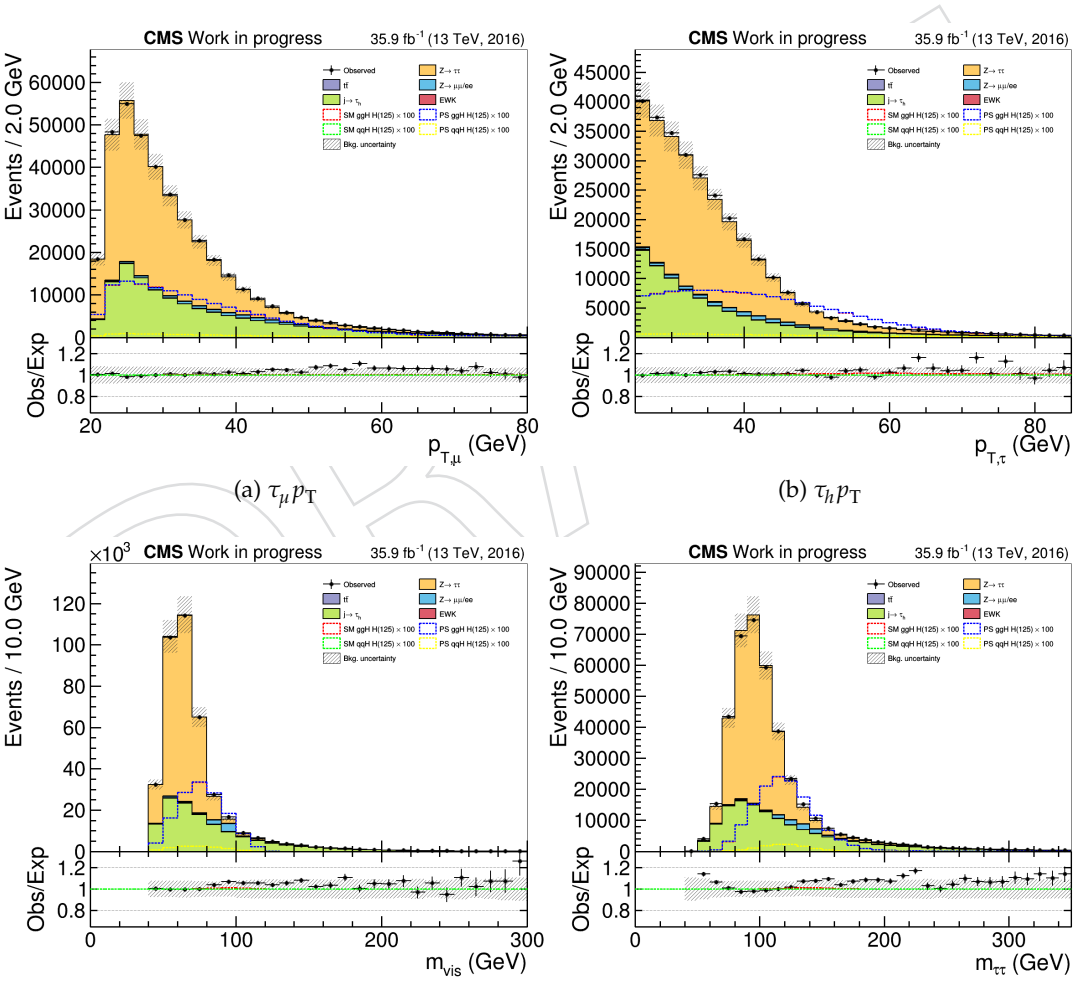

(a) $\tau_\mu p_{\mathrm{T}}$ (b) $\tau_h p_{\mathrm{T}}$

(c) m_{vis} (d) $m_{\tau\tau}$

Figure 258: Pre-fit 2016 data/background comparisons for $\mu\tau_h$ events are shown for variables used in the multivariate discriminant. In all distributions the background uncertainty shown by the shaped-grey band includes the normalisation altering uncertainties

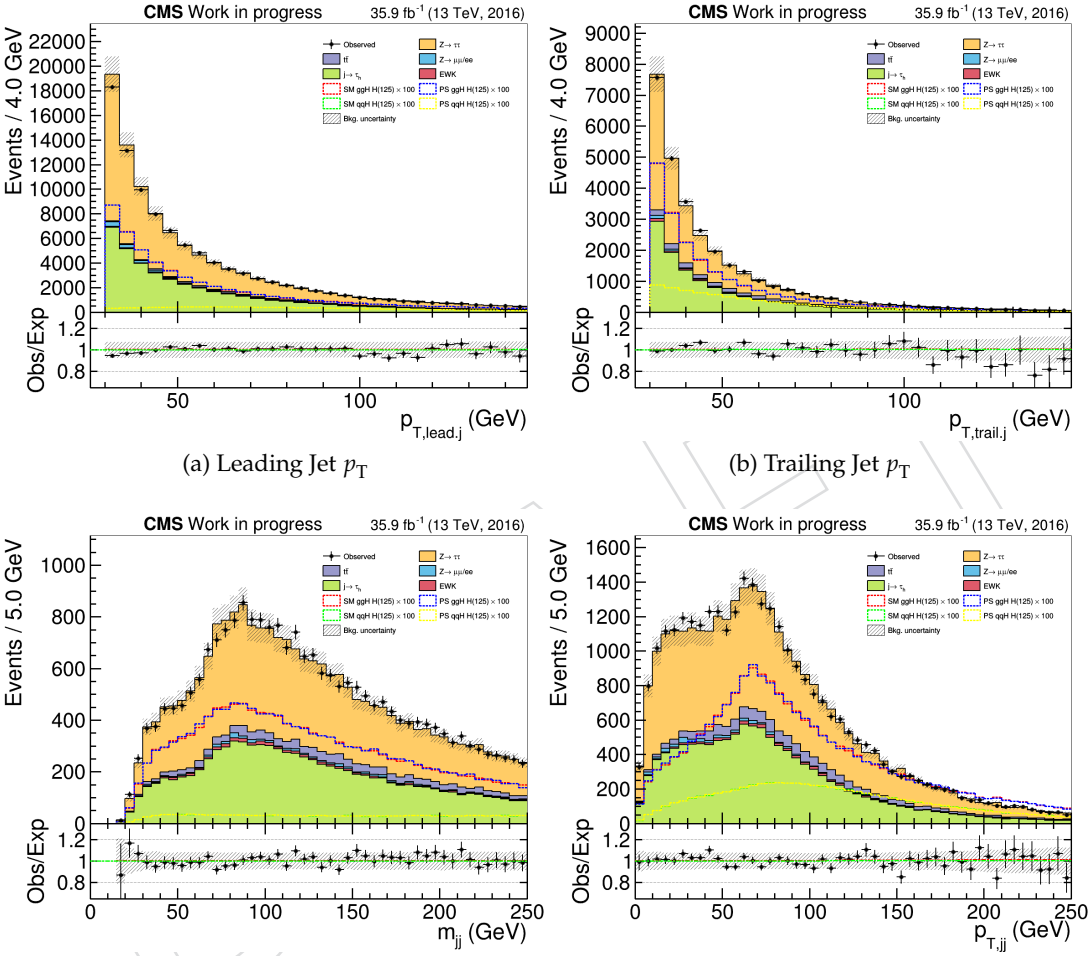

(a) Leading Jet p_{T}

(b) Trailing Jet p_{T}

(c) m_{jj}

(d) p_{Tjj}

Figure 259: Pre-fit 2016 data/background comparisons for $\mu\tau_h$ events are shown for variables used in the multivariate discriminant. In all distributions the background uncertainty shown by the shaped-grey band includes the normalisation altering uncertainties

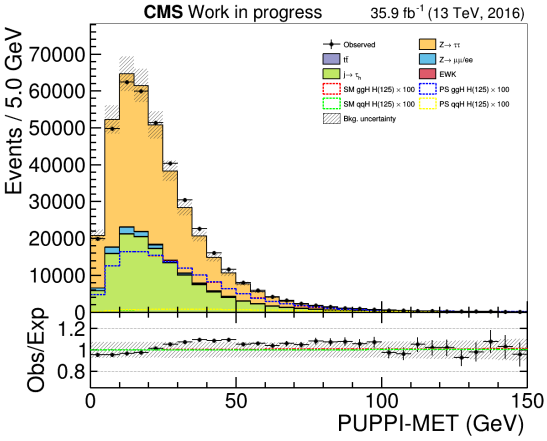

(a) puppi MET

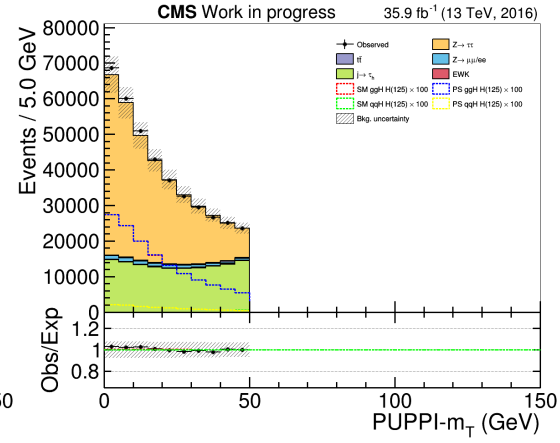

(b) puppi m_{T}

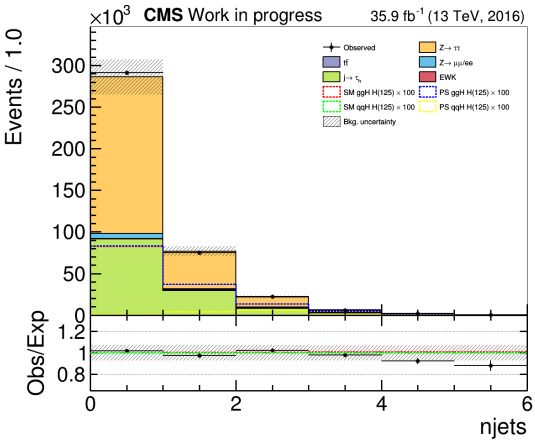

(c) number of jets

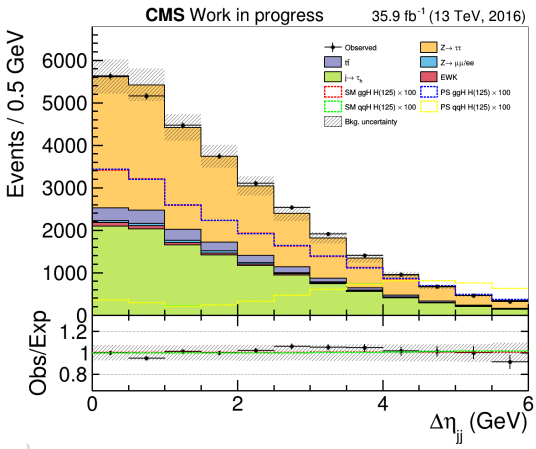

(d) Jet $\Delta\eta$

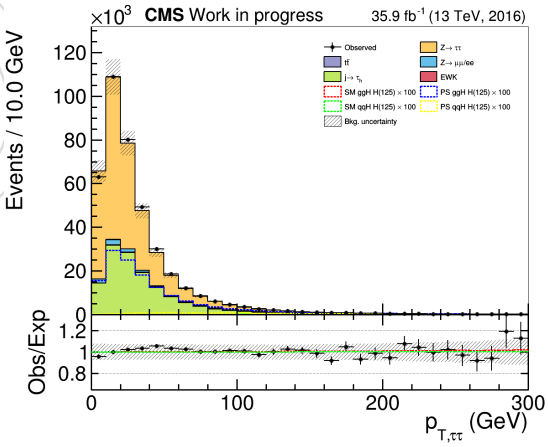

(e) $p_{\tau\tau}$

Figure 260: Pre-fit 2016 data/background comparisons for $\mu\tau_h$ events are shown for variables used in the multivariate discriminant. In all distributions the background uncertainty shown by the shaped-grey band includes the normalisation altering uncertainties

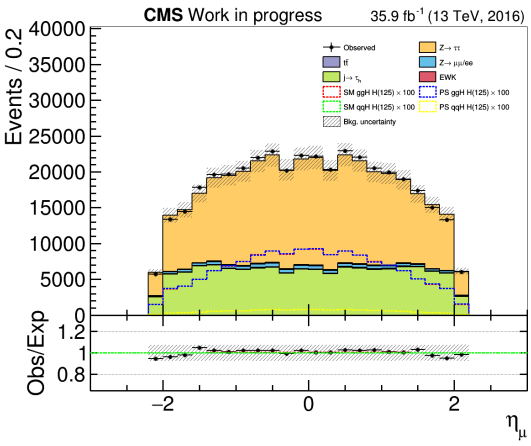

(a) $\tau_\mu \eta$

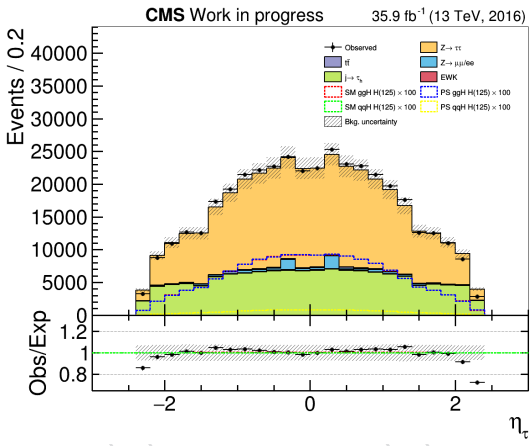

(b) $\tau_h \eta$

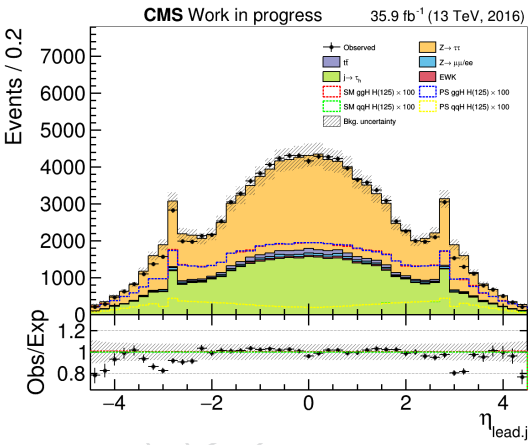

(c) Leading jet η

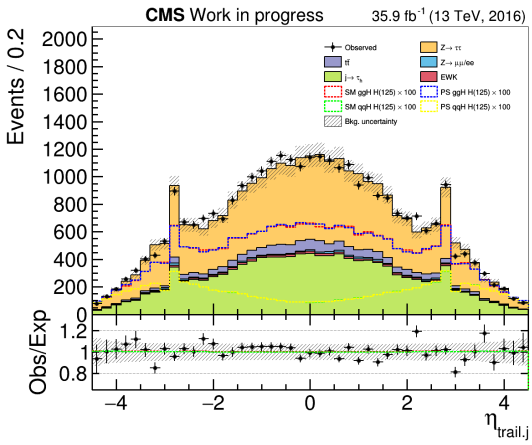

(d) Trailing jet η

Figure 261: Pre-fit 2016 data/background comparisons for $\mu\tau_h$ events are shown for auxilary variables (i.e. not used in the multivariate discriminant). In all distributions the background uncertainty shown by the shaped-grey band includes the full uncertainty model

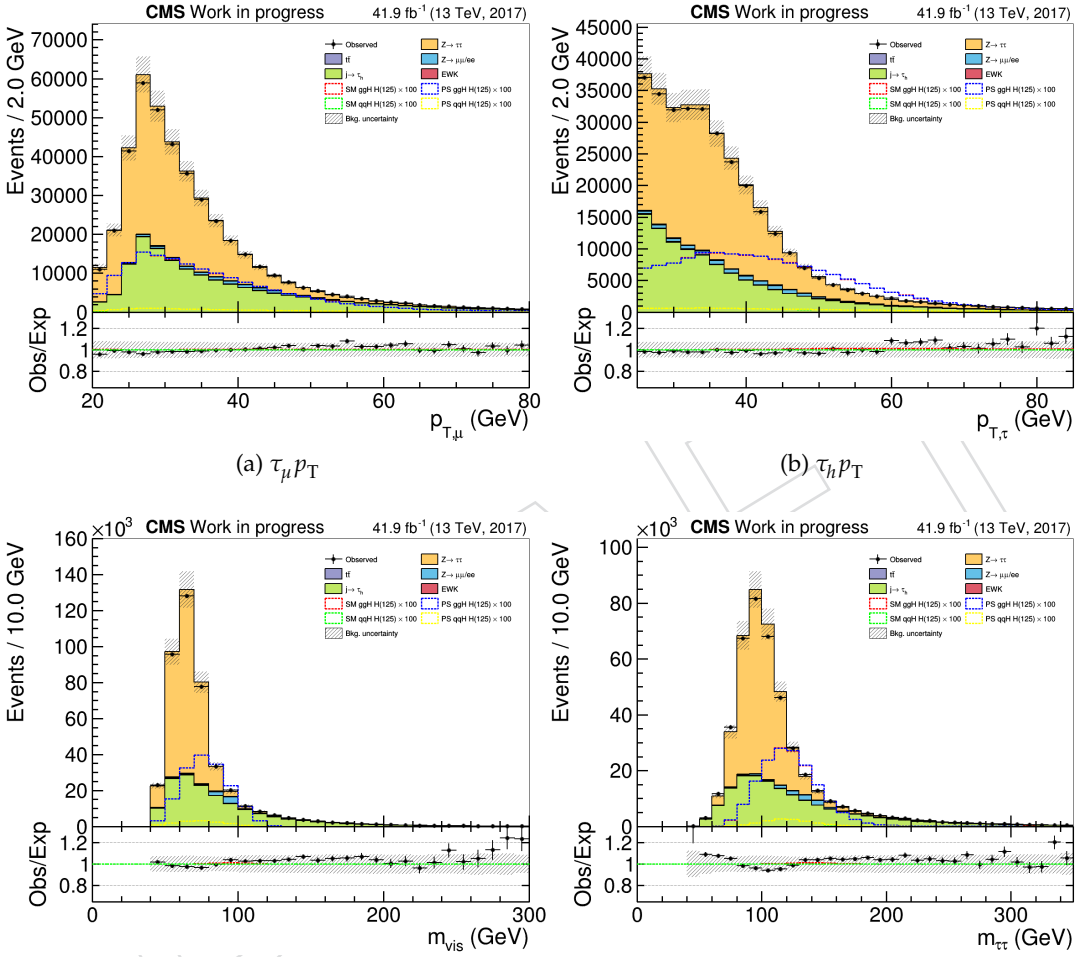

(a) $\tau_\mu p_T$ (b) $\tau_h p_T$

(c) m_{vis} (d) $m_{\tau\tau}$

Figure 262: Pre-fit 2017 data/background comparisons for $\mu\tau_h$ events are shown for variables used in the multivariate discriminant. In all distributions the background uncertainty shown by the shaped-grey band includes the normalisation altering uncertainties

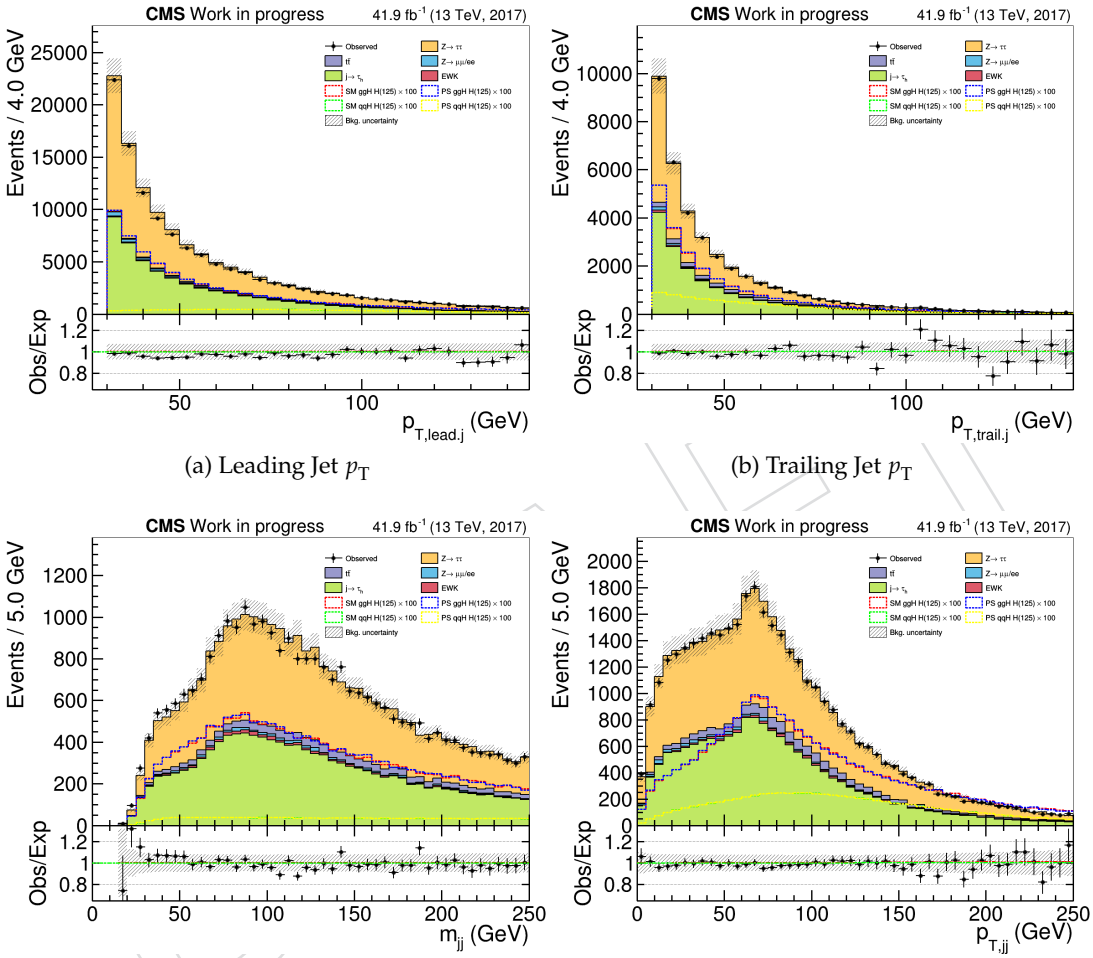

(a) Leading Jet p_{T}

(b) Trailing Jet p_{T}

(c) m_{jj}

(d) p_{Tjj}

Figure 263: Pre-fit 2017 data/background comparisons for $\mu\tau_h$ events are shown for variables used in the multivariate discriminant. In all distributions the background uncertainty shown by the shaped-grey band includes the normalisation altering uncertainties

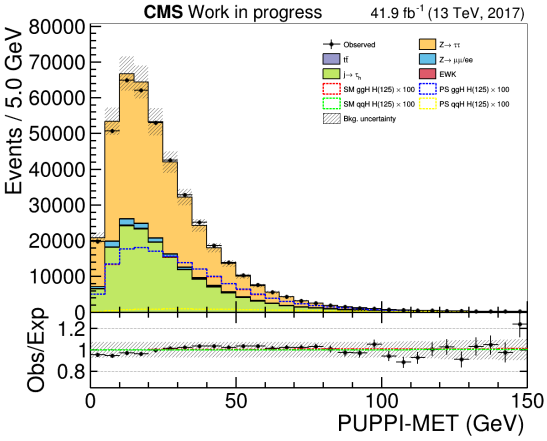

(a) puppi MET

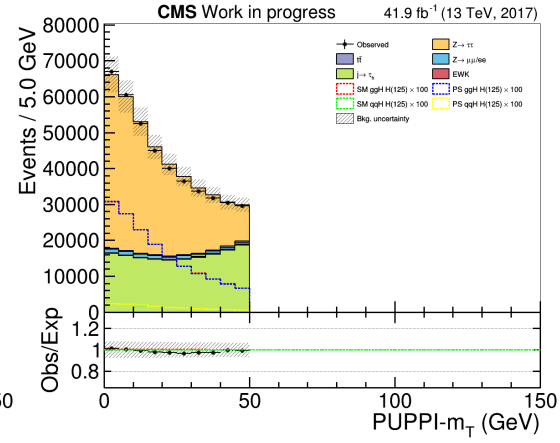

(b) puppi m_{T}

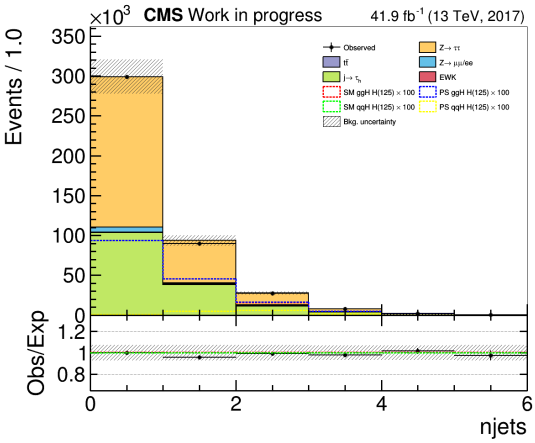

(c) number of jets

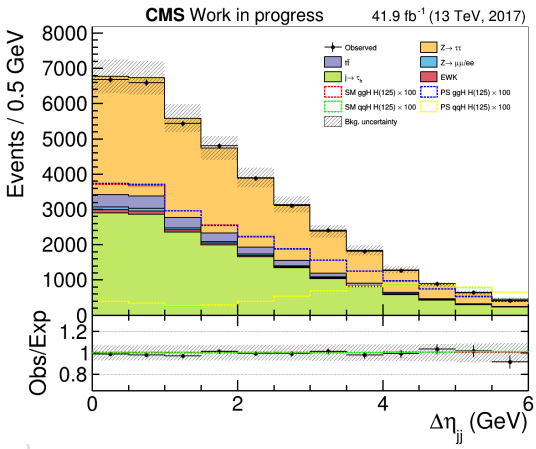

(d) Jet $\Delta\eta$

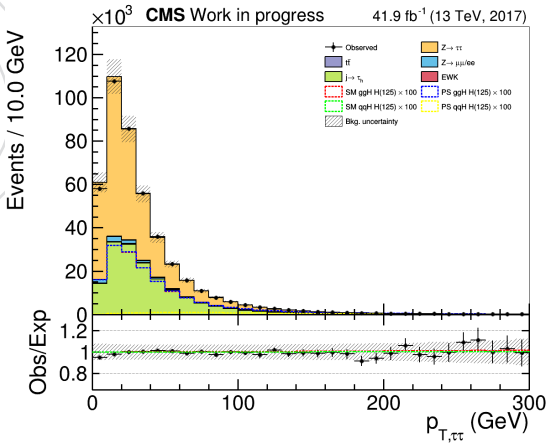

(e) $p_{\tau\tau}$

Figure 264: Pre-fit 2017 data/background comparisons for $\mu\tau_h$ events are shown for variables used in the multivariate discriminant. In all distributions the background uncertainty shown by the shaped-grey band includes the normalisation altering uncertainties

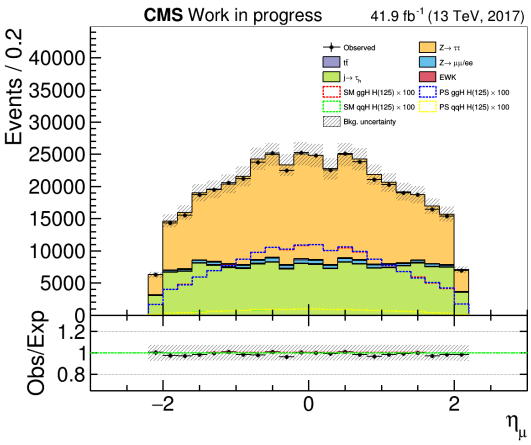

(a) $\tau_\mu \eta$

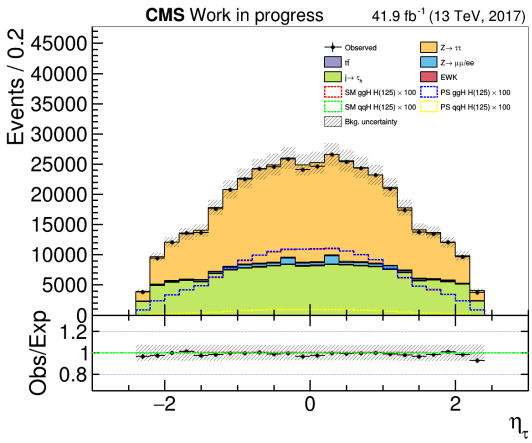

(b) $\tau_h \eta$

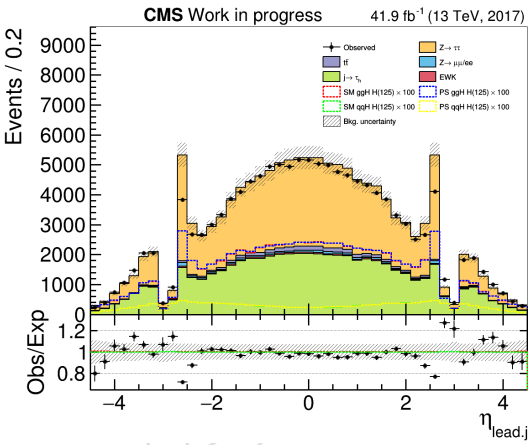

(c) Leading jet η

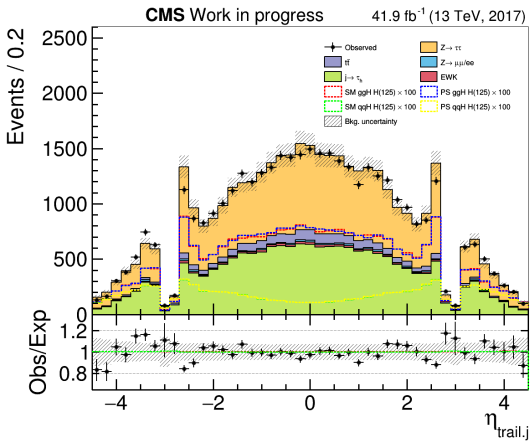

(d) Trailing jet η

Figure 265: Pre-fit 2017 data/background comparisons for $\mu\tau_h$ events are shown for auxilary variables (i.e. not used in the multivariate discriminant). In all distributions the background uncertainty shown by the shaped-grey band includes the full uncertainty model

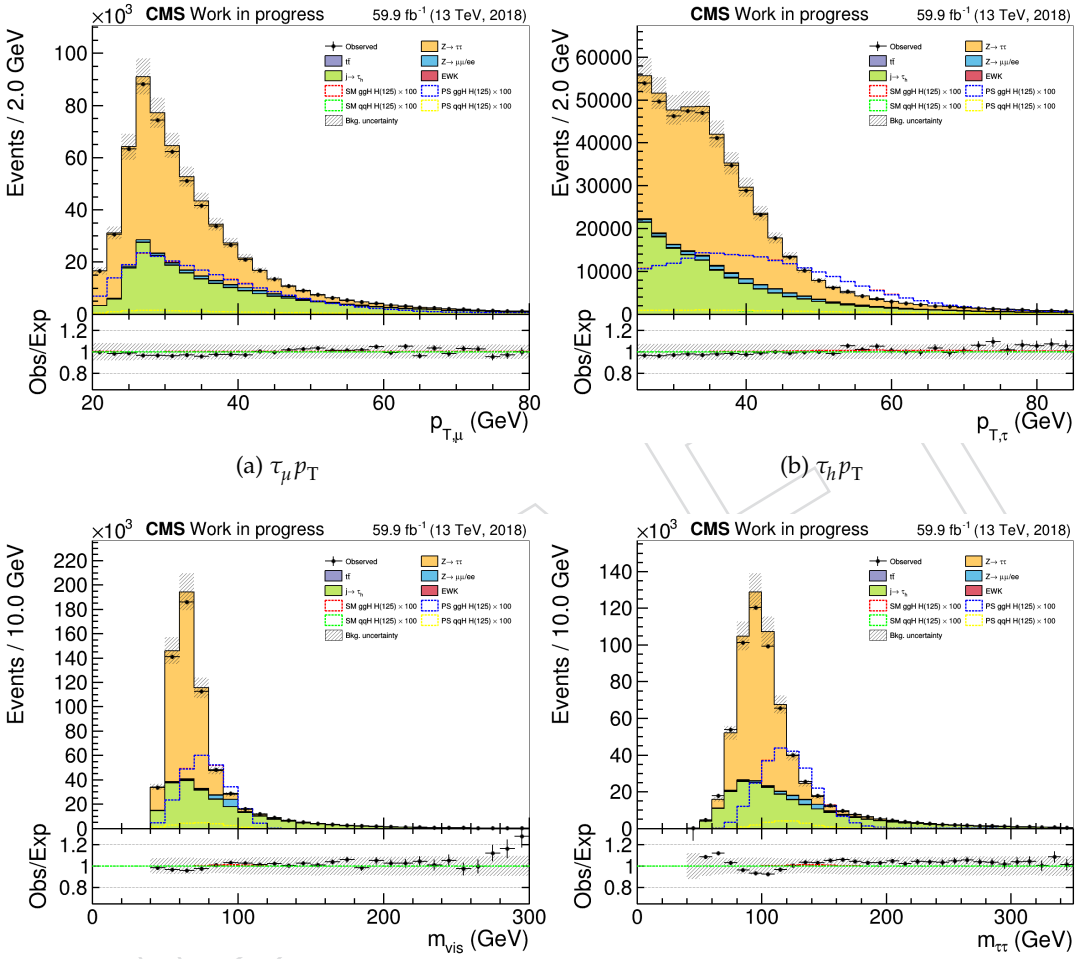

(a) $\tau_\mu p_{\mathrm{T}}$ (b) $\tau_h p_{\mathrm{T}}$

(c) m_{vis} (d) $m_{\tau\tau}$

Figure 266: Pre-fit 2018 data/background comparisons for $\mu\tau_h$ events are shown for variables used in the multivariate discriminant. In all distributions the background uncertainty shown by the shaped-grey band includes the normalisation altering uncertainties

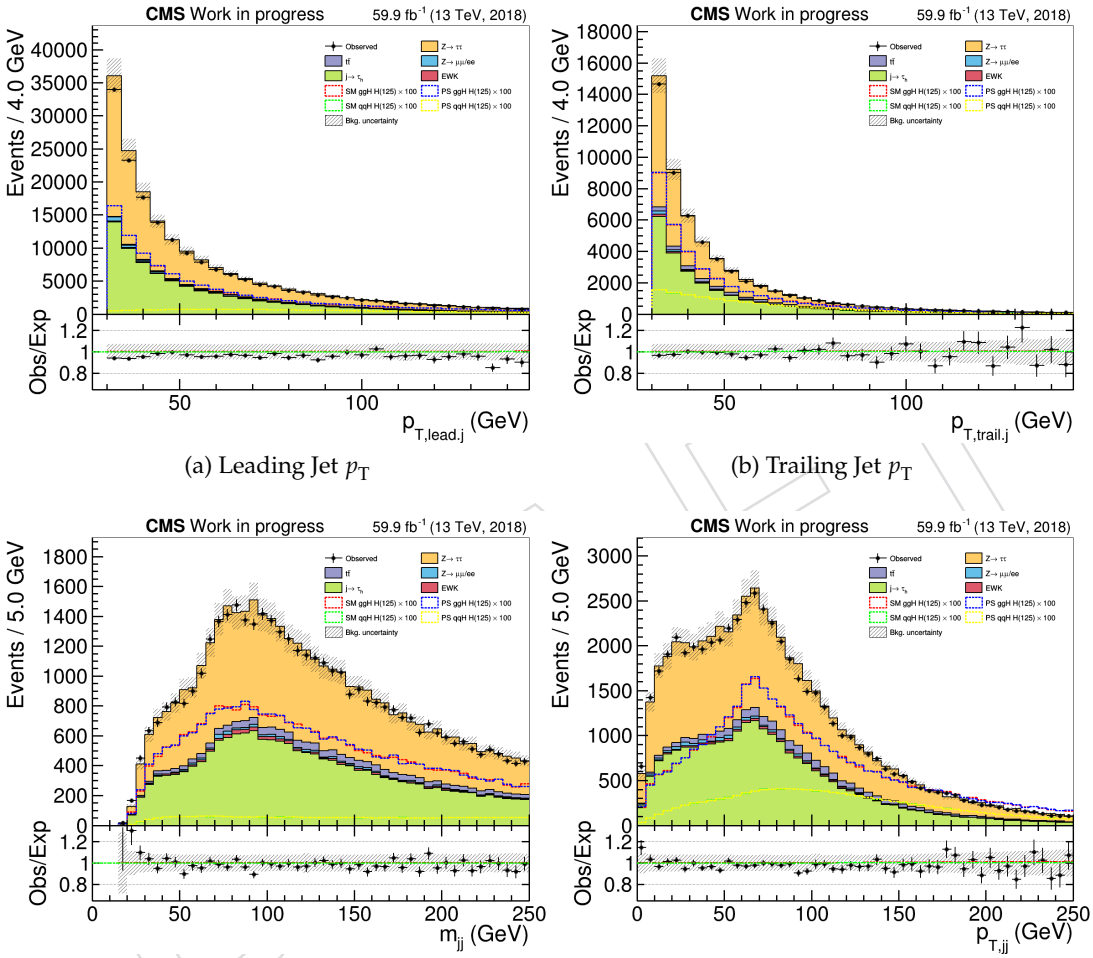

(a) Leading Jet p_{T}

(b) Trailing Jet p_{T}

(c) m_{jj}

(d) p_{Tjj}

Figure 267: Pre-fit 2018 data/background comparisons for $\mu\tau_h$ events are shown for variables used in the multivariate discriminant. In all distributions the background uncertainty shown by the shaped-grey band includes the normalisation altering uncertainties

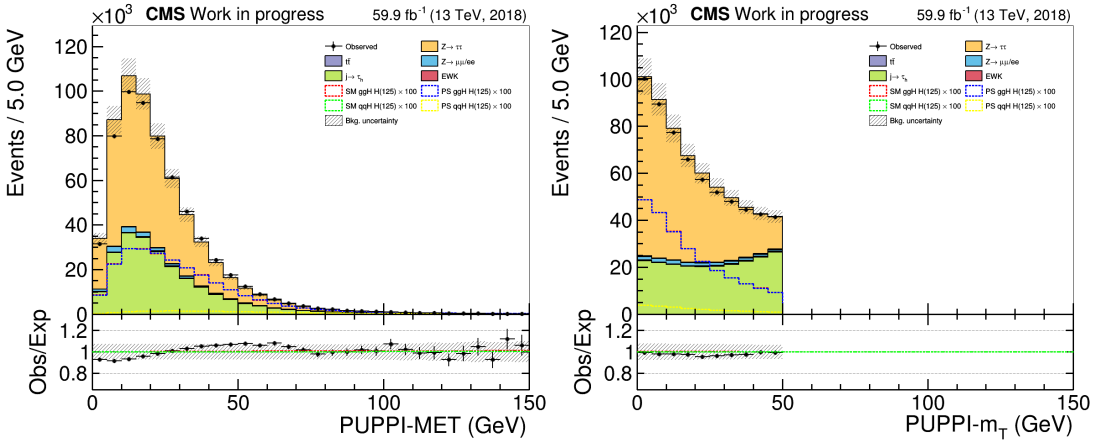

(a) puppi MET

(b) puppi m_{T}

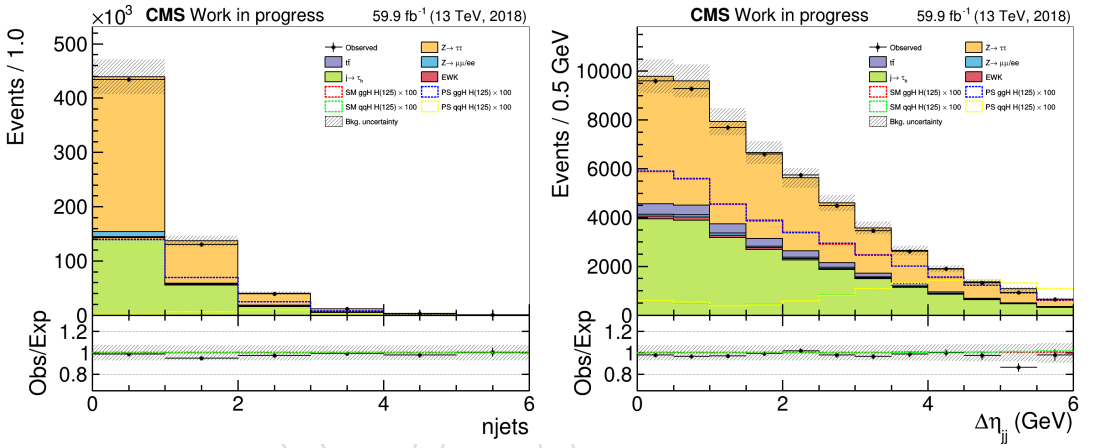

(c) number of jets

(d) Jet $\Delta\eta$

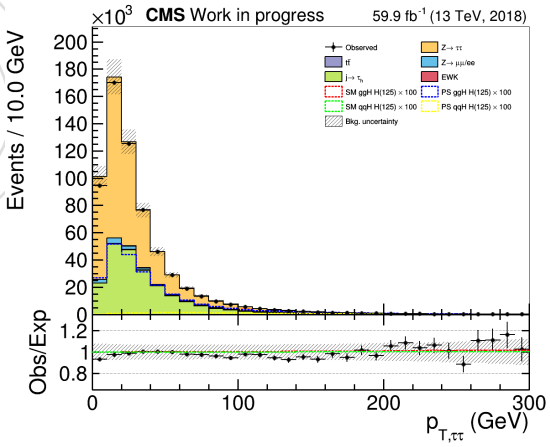

(e) $p_{\tau\tau}$

Figure 268: Pre-fit 2018 data/background comparisons for $\mu\tau_h$ events are shown for variables used in the multivariate discriminant. In all distributions the background uncertainty shown by the shaped-grey band includes the normalisation altering uncertainties

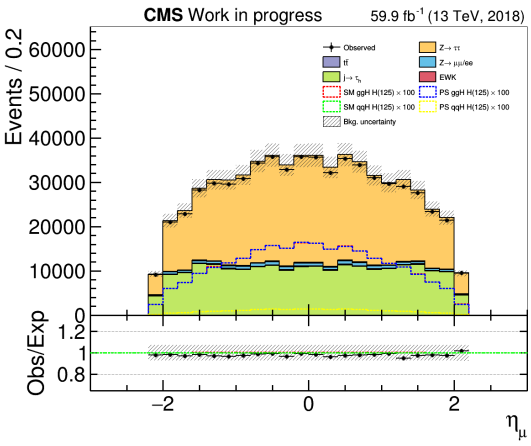

(a) $\tau_\mu \eta$

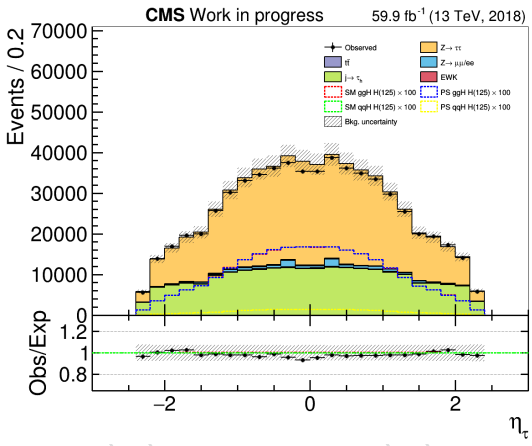

(b) $\tau_h \eta$

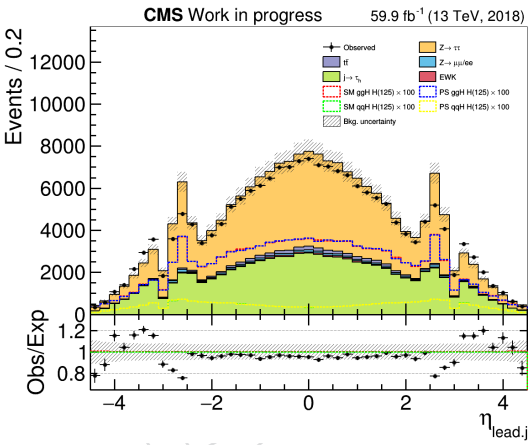

(c) Leading jet η

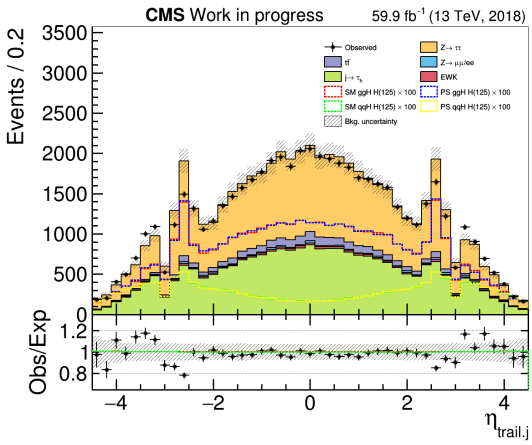

(d) Trailing jet η

Figure 269: Pre-fit 2018 data/background comparisons for $\mu\tau_h$ events are shown for auxilary variables (i.e. not used in the multivariate discriminant). In all distributions the background uncertainty shown by the shaped-grey band includes the full uncertainty model

D.2 Results in the $\tau_e\tau_h$ hannel

In Fig. 270-272(2016), Fig. 274-276(2017), and Fig. 278 280(2018) we display prefit control distributions for observables that are used in the multivariate discriminant (DNN) to distinguish the signal from background events. In Fig. 273(2016), Fig. 277(2017) and Fig. 281(2018) we display a few auxiliary control distributions of observables not used in the multivariate discriminant.

The plots are obtained after inclusive selection of $\tau_e\tau_h$ events as described in Section 7. Several additional cuts are applied:

- puppi $m_T < 50\,\text{GeV}$ (to reject W+Jets background),
- number of b-tagged jets = 0 (to reject top-pair and single-top backgrounds),

DRAFT

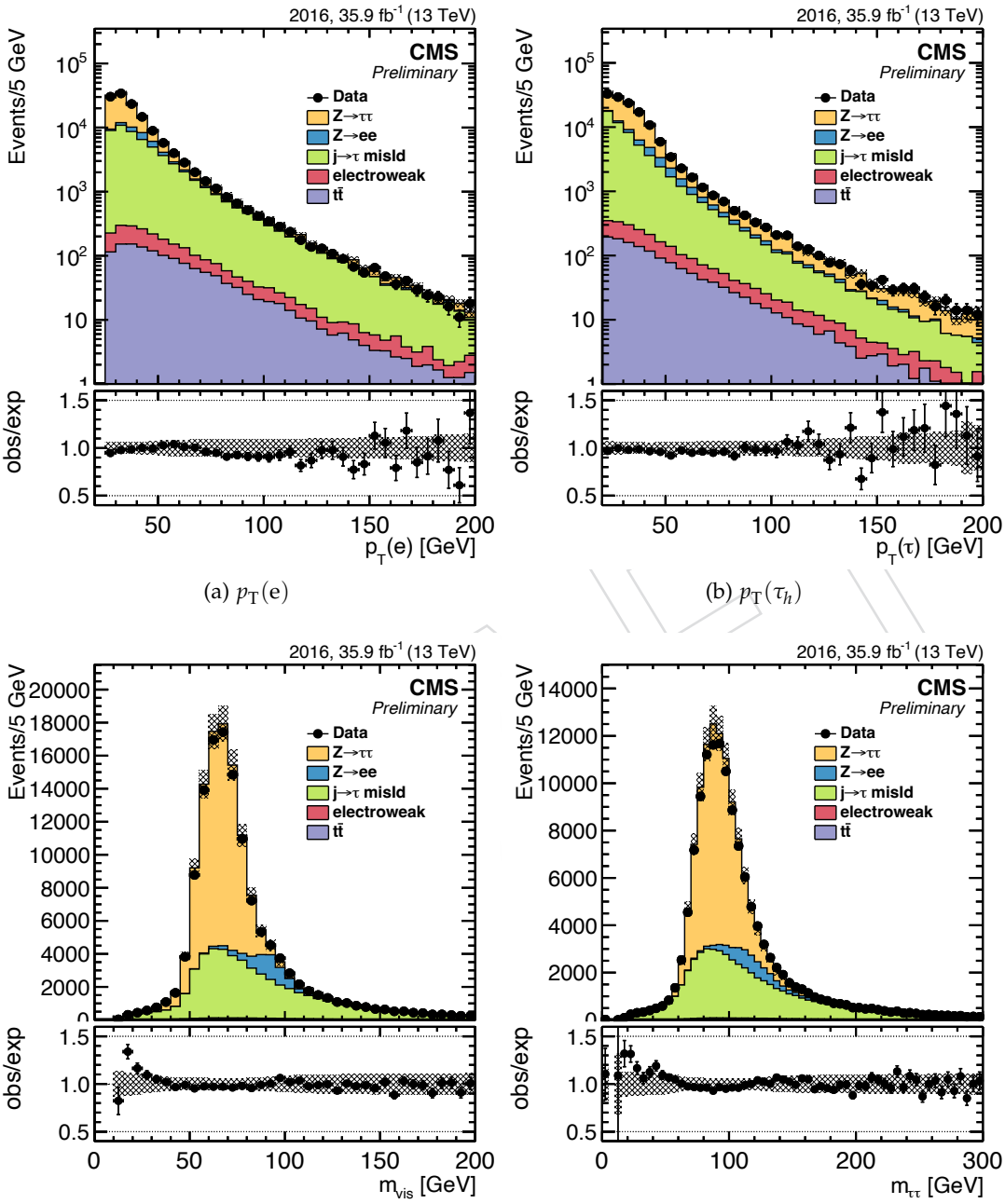

(a) $p_{\mathrm{T}}(\mathrm{e})$ (b) $p_{\mathrm{T}}(\tau_h)$

(c) m_{vis} (d) $m_{\tau\tau}$

Figure 270: Pre-fit 2016 data/background comparisons for eτ_h events are shown for variables used in the multivariate discriminant. In all distributions the background uncertainty shown by the shaped-grey band includes the normalisation altering uncertainties

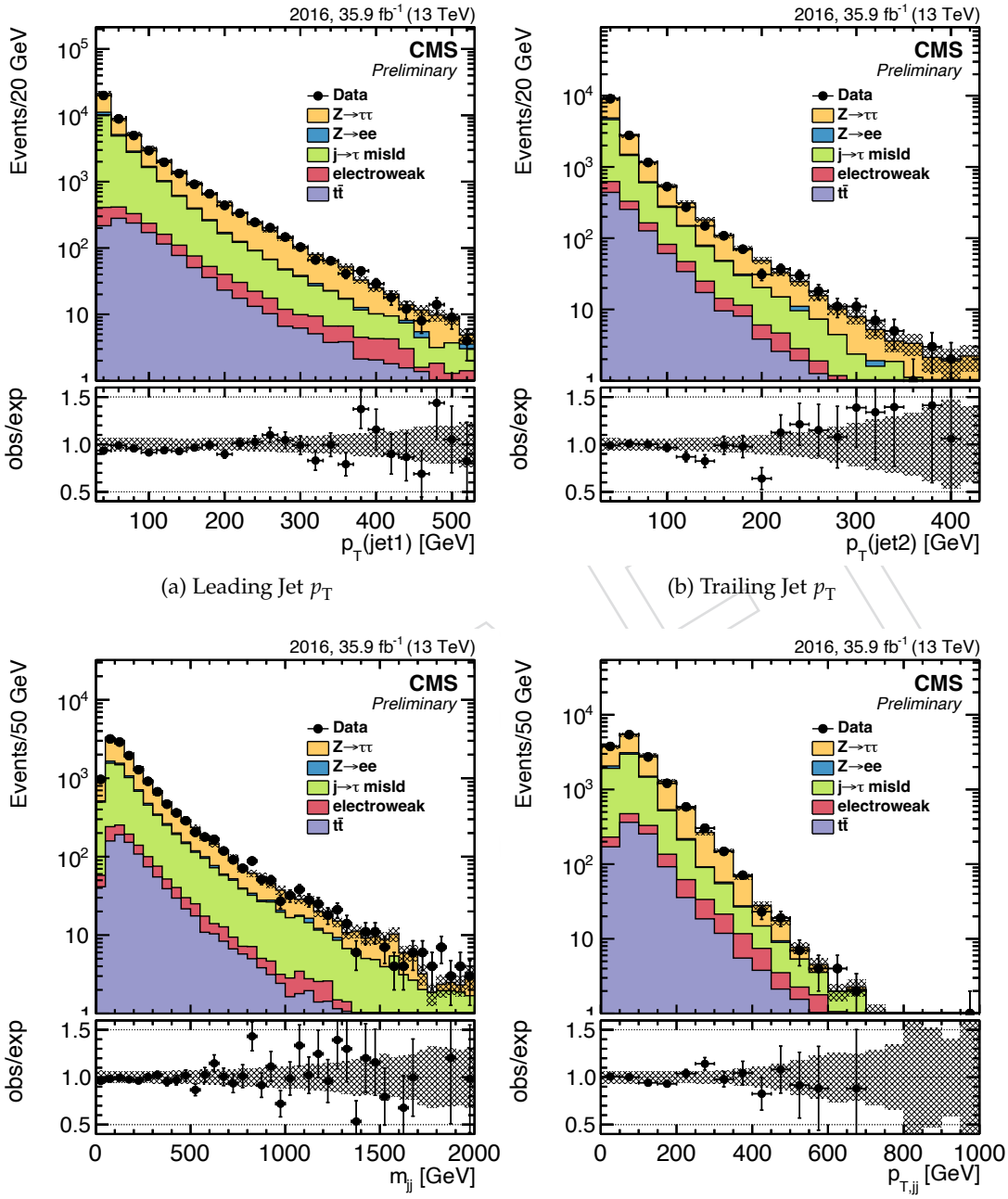

(a) Leading Jet p_T

(b) Trailing Jet p_T

(c) m_{jj}

(d) p_{Tjj}

Figure 271: Pre-fit 2016 data/background comparisons for eτ_h events are shown for variables used in the multivariate discriminant. In all distributions the background uncertainty shown by the shaped-grey band includes the normalisation altering uncertainties

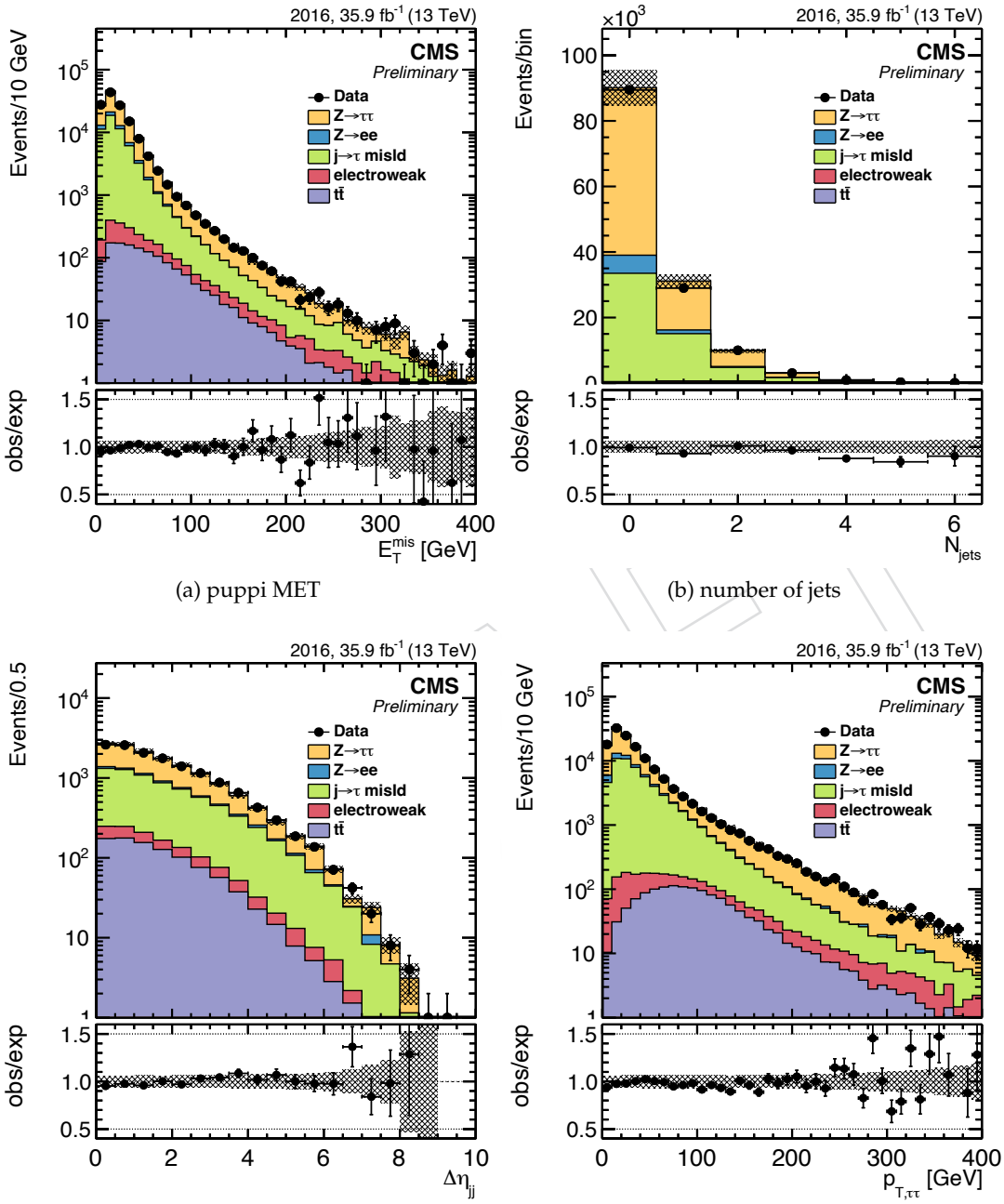

(a) puppi MET

(b) number of jets

(c) Jet $\Delta\eta$

(d) $p_{\tau\tau}$

Figure 272: Pre-fit 2016 data/background comparisons for eτ_h events are shown for variables used in the multivariate discriminant. In all distributions the background uncertainty shown by the shaped-grey band includes the normalisation altering uncertainties

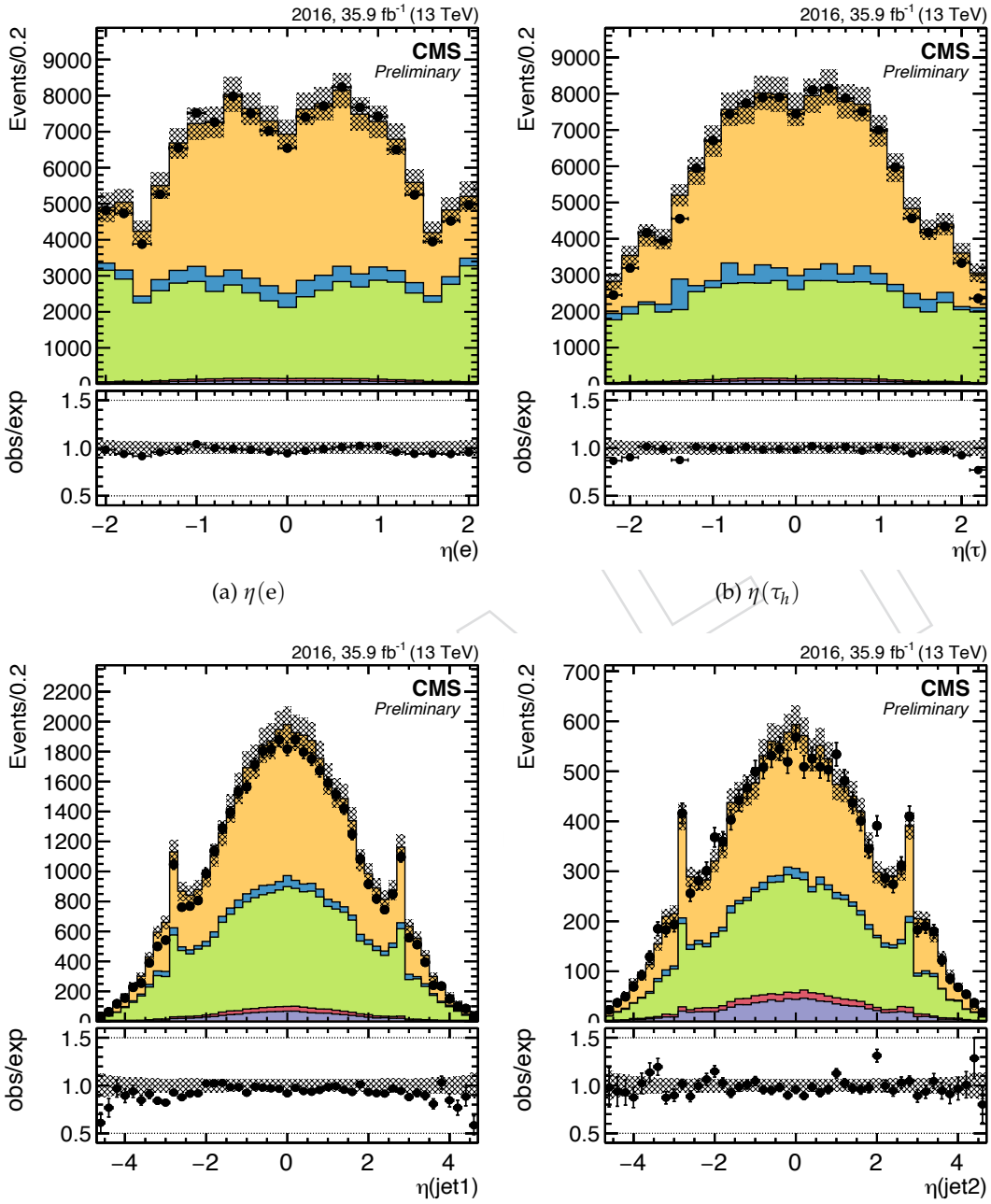

(a) $\eta(\mathrm{e})$

(b) $\eta(\tau_h)$

(c) Leading jet η

(d) Trailing jet η

Figure 273: Pre-fit 2016 data/background comparisons for eτ_h events are shown for auxilary variables (i.e. not used in the multivariate discriminant). In all distributions the background uncertainty shown by the shaped-grey band includes the full uncertainty model

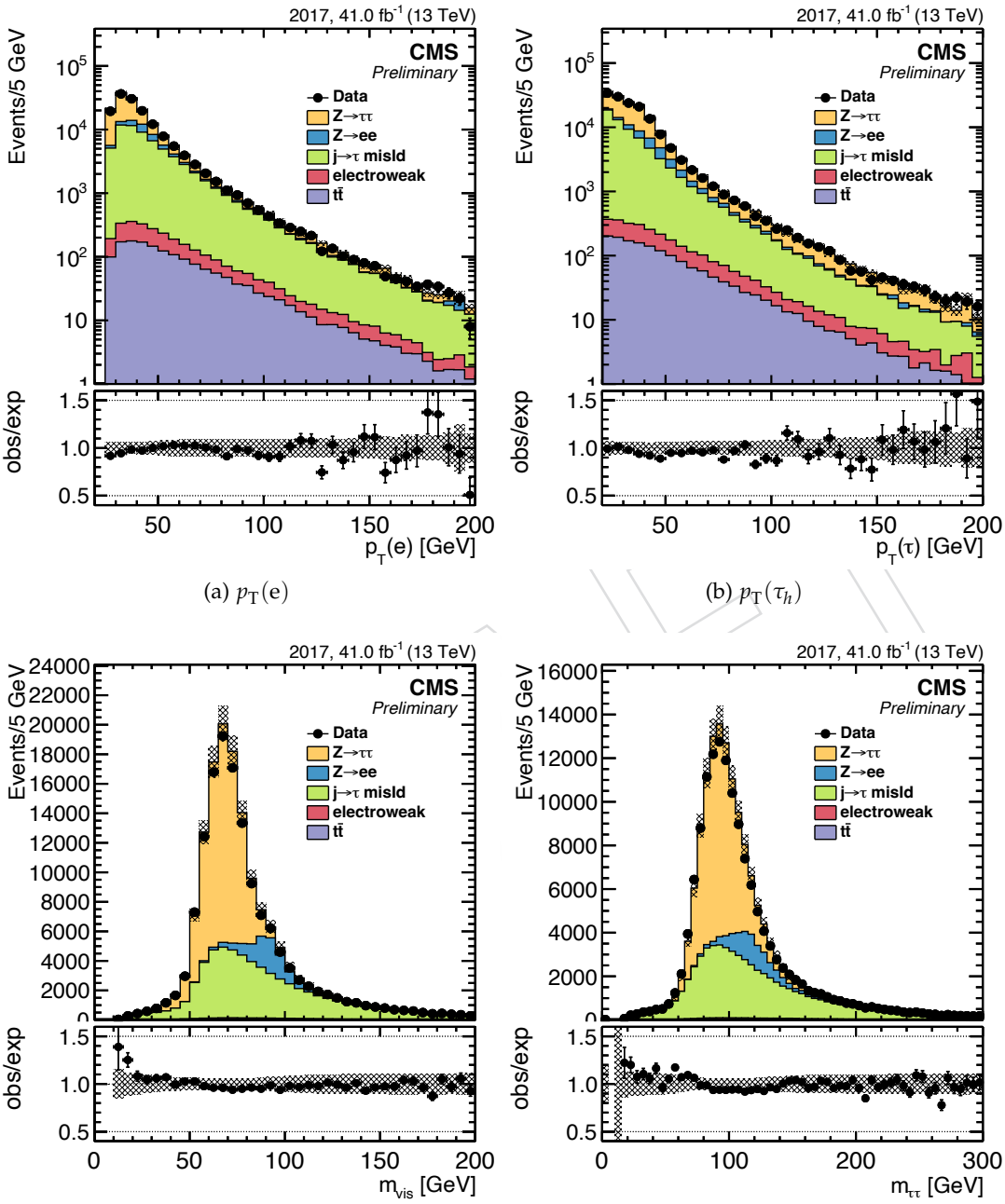

(a) $p_{\mathrm{T}}(\mathrm{e})$

(b) $p_{\mathrm{T}}(\tau_h)$

(c) m_{vis}

(d) $m_{\tau\tau}$

Figure 274: Pre-fit 2017 data/background comparisons for eτ_h events are shown for variables used in the multivariate discriminant. In all distributions the background uncertainty shown by the shaped-grey band includes the normalisation altering uncertainties

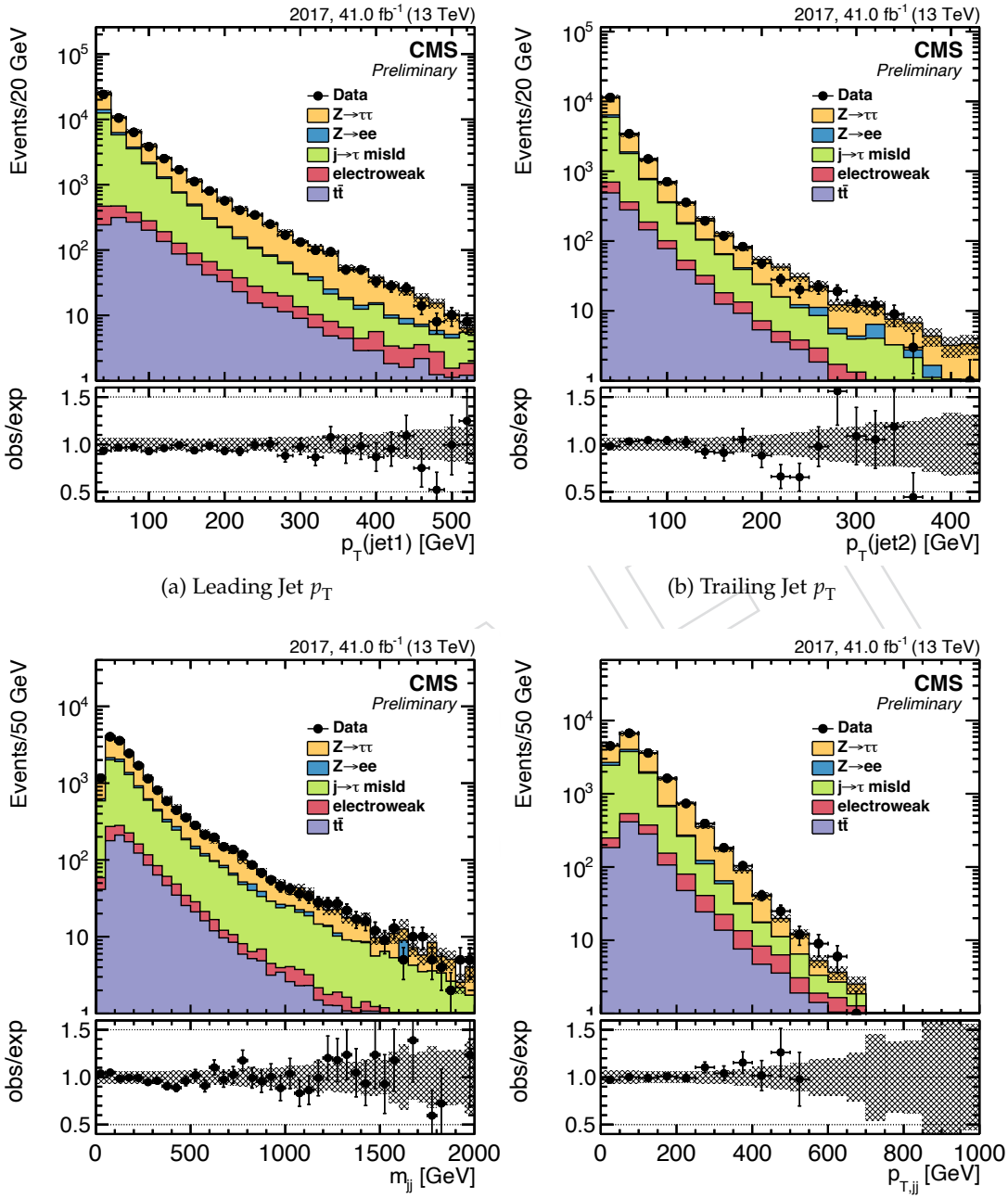

(a) Leading Jet p_T

(b) Trailing Jet p_T

(c) m_{jj}

(d) p_{Tjj}

Figure 275: Pre-fit 2017 data/background comparisons for eτ_h events are shown for variables used in the multivariate discriminant. In all distributions the background uncertainty shown by the shaped-grey band includes the normalisation altering uncertainties

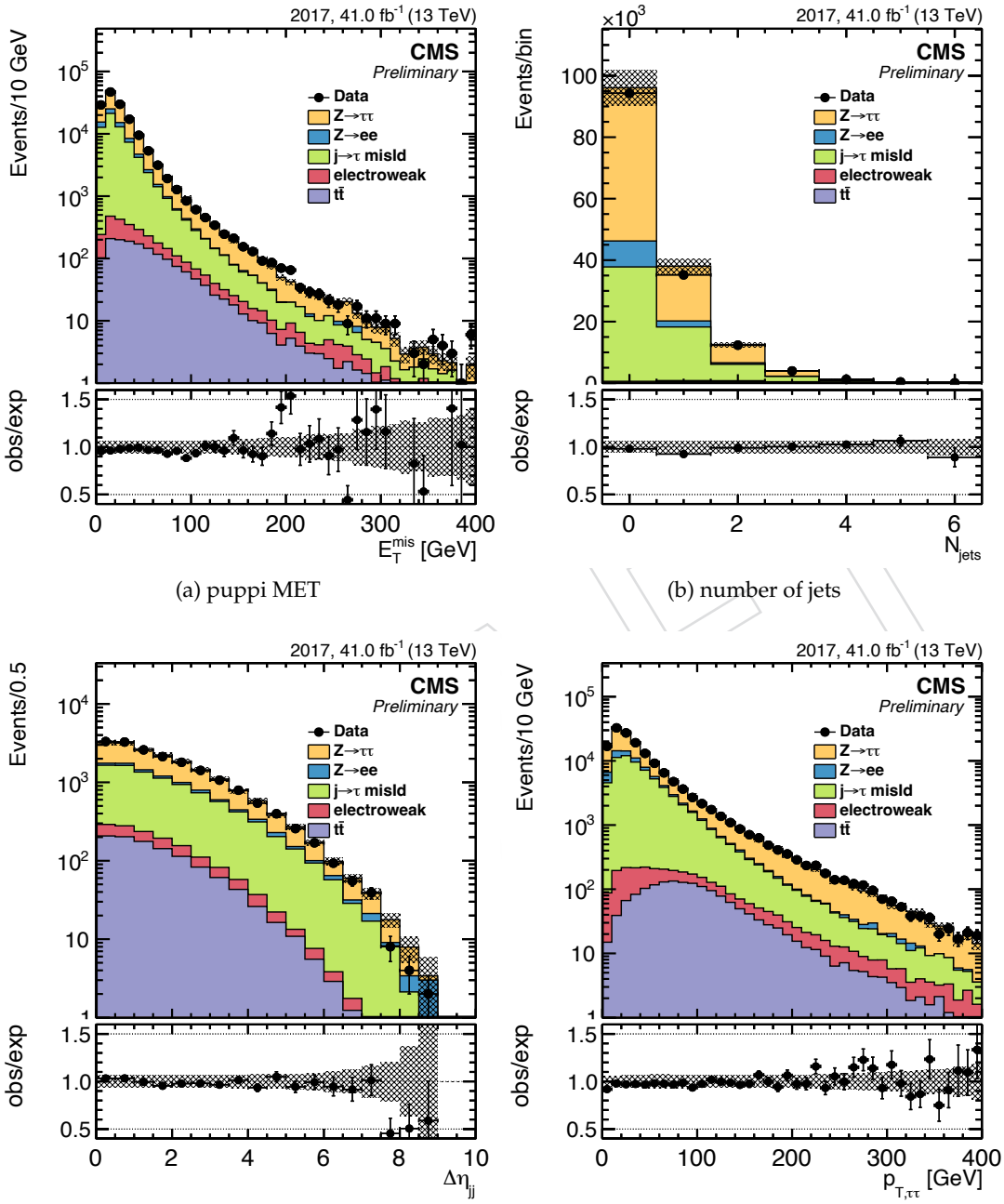

(a) puppi MET

(b) number of jets

(c) Jet $\Delta\eta$

(d) $p_{\tau\tau}$

Figure 276: Pre-fit 2017 data/background comparisons for eτ_h events are shown for variables used in the multivariate discriminant. In all distributions the background uncertainty shown by the shaped-grey band includes the normalisation altering uncertainties

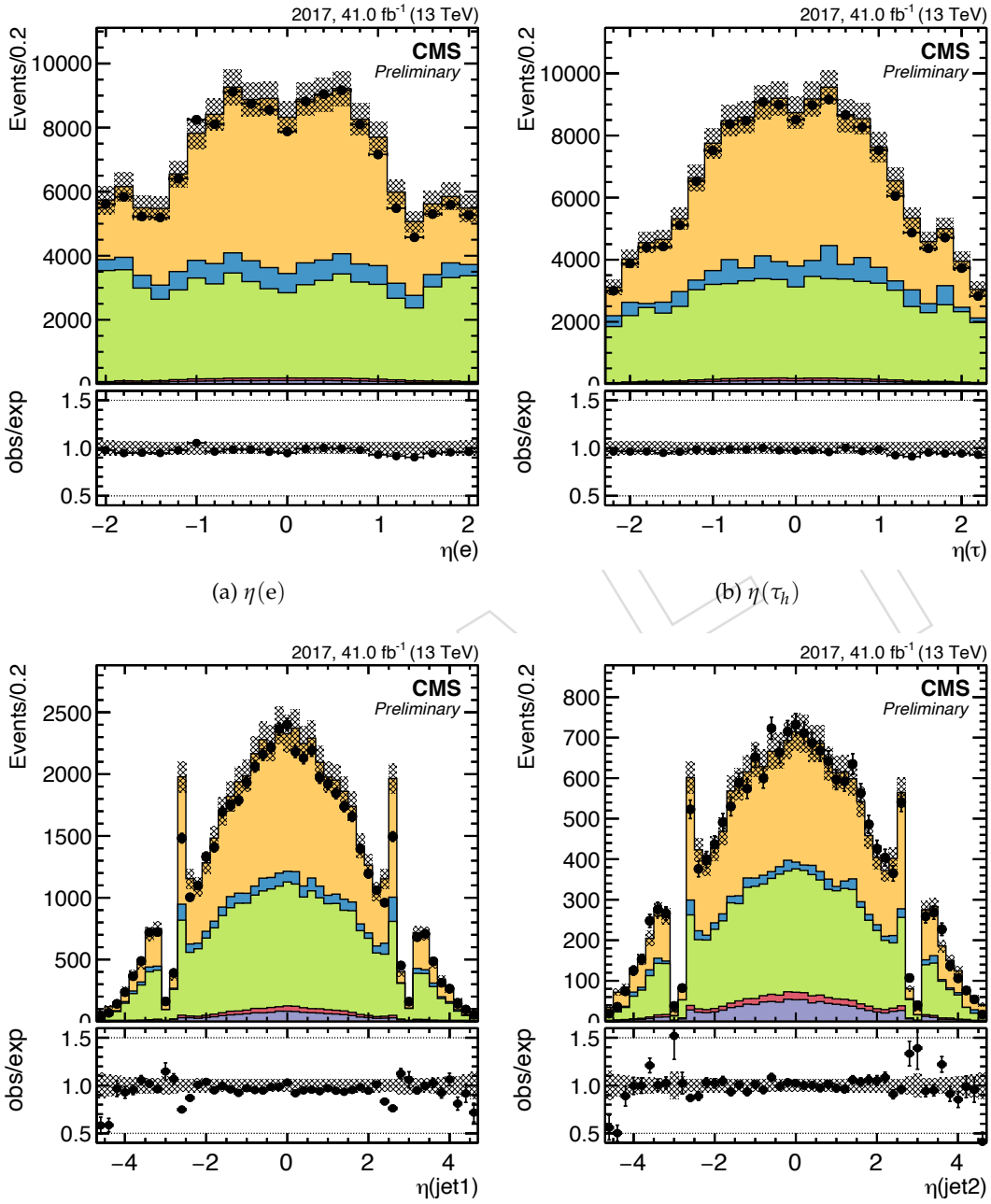

(a) $\eta(\mathrm{e})$

(b) $\eta(\tau_h)$

(c) Leading jet η

(d) Trailing jet η

Figure 277: Pre-fit 2017 data/background comparisons for eτ_h events are shown for auxilary variables (i.e. not used in the multivariate discriminant). In all distributions the background uncertainty shown by the shaped-grey band includes the full uncertainty model

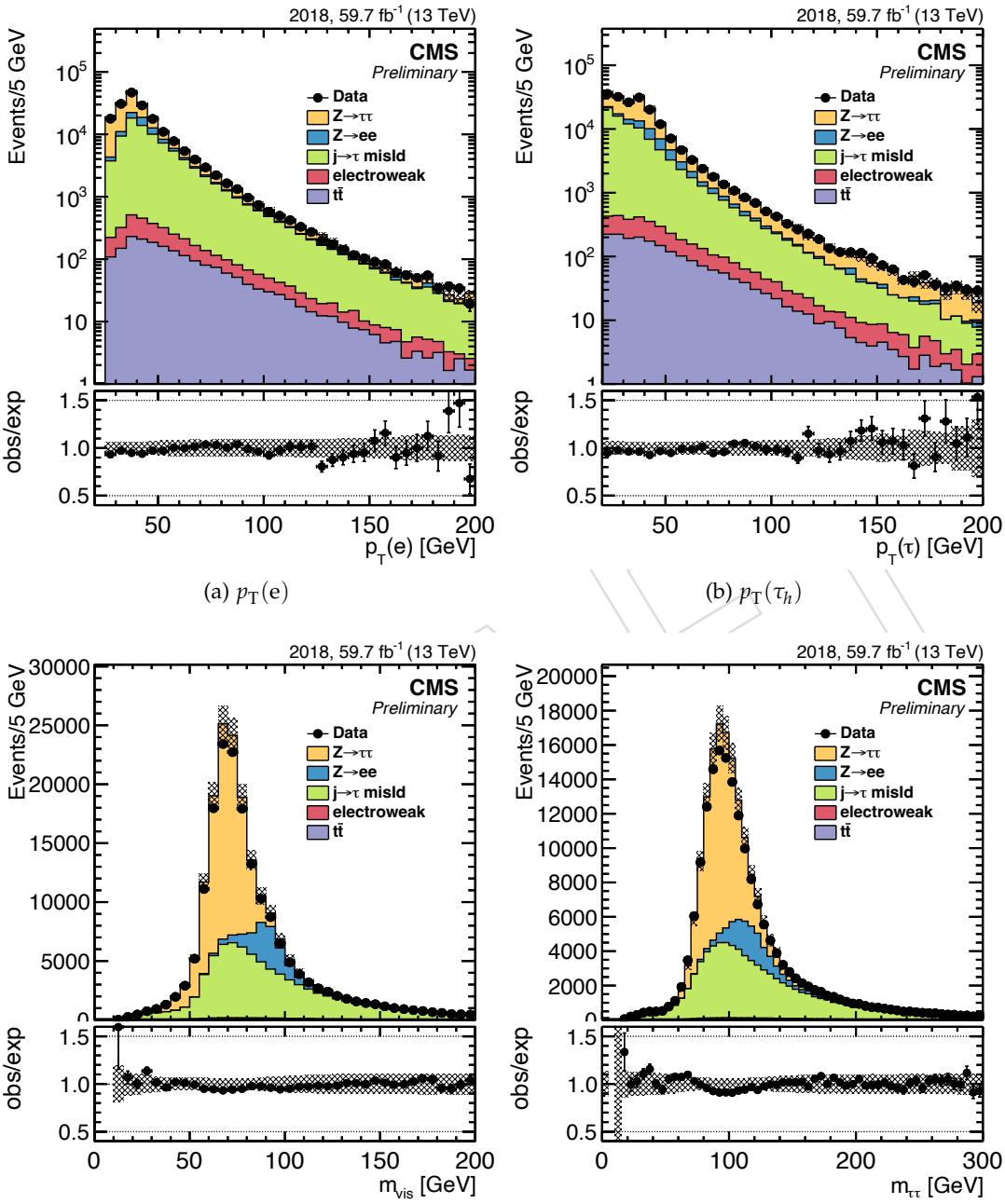

(a) $p_{\mathrm{T}}(\mathrm{e})$

(b) $p_{\mathrm{T}}(\tau_h)$

(c) m_{vis}

(d) $m_{\tau\tau}$

Figure 278: Pre-fit 2018 data/background comparisons for eτ_h events are shown for variables used in the multivariate discriminant. In all distributions the background uncertainty shown by the shaped-grey band includes the normalisation altering uncertainties

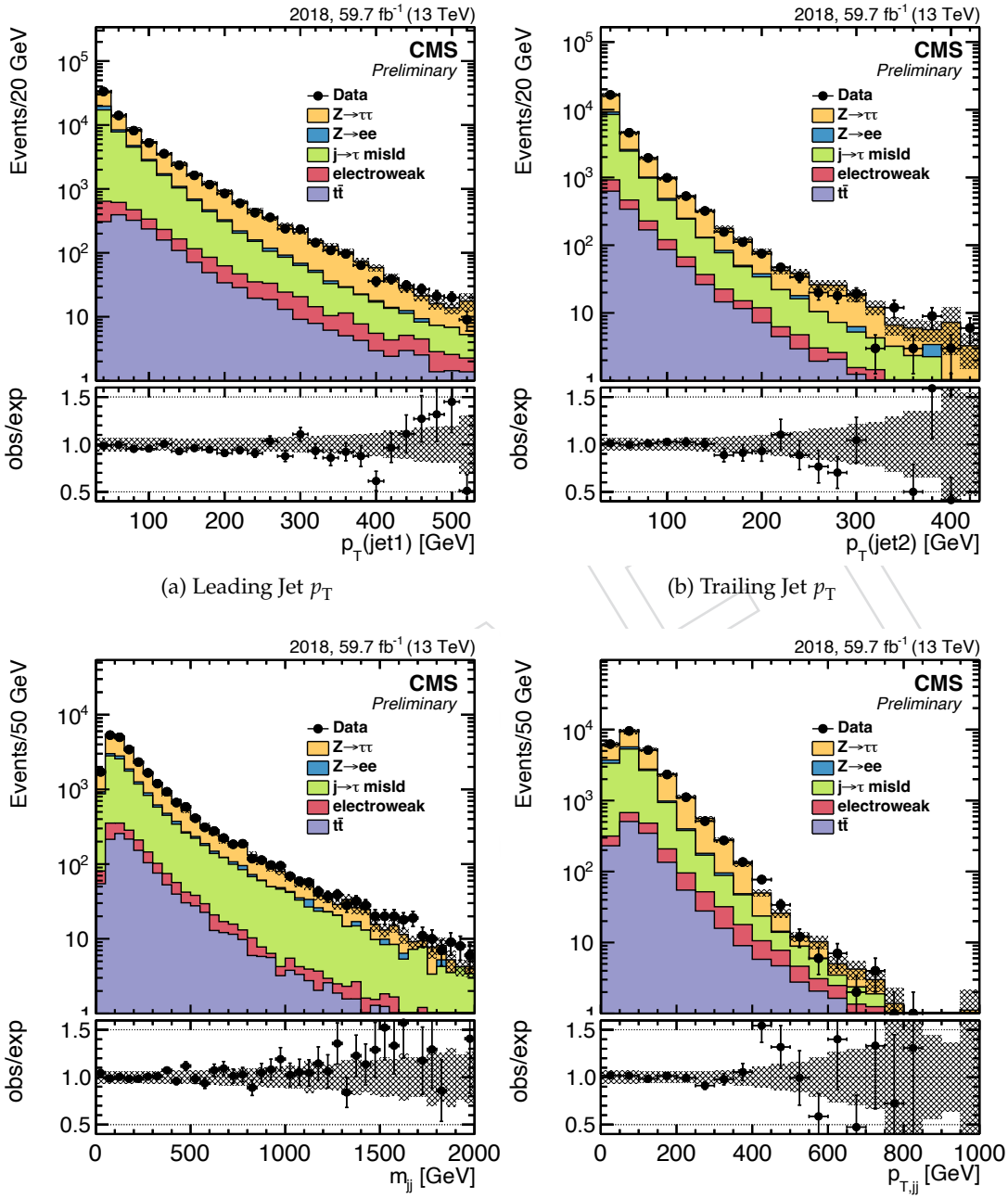

(a) Leading Jet p_T

(b) Trailing Jet p_T

(c) m_{jj}

(d) p_{Tjj}

Figure 279: Pre-fit 2018 data/background comparisons for eτ_h events are shown for variables used in the multivariate discriminant. In all distributions the background uncertainty shown by the shaped-grey band includes the normalisation altering uncertainties

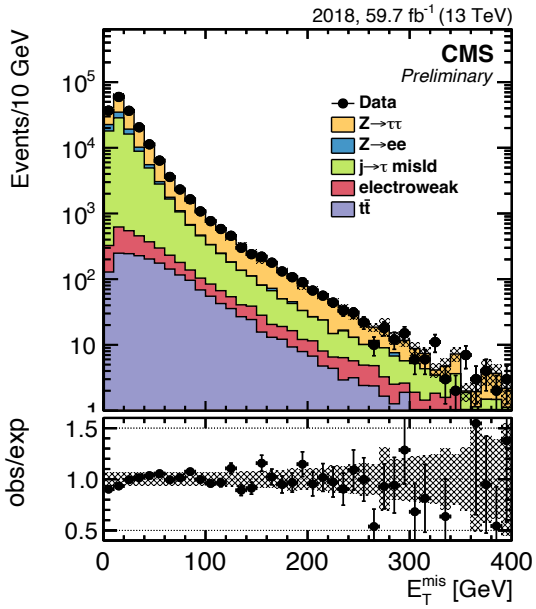

(a) puppi MET

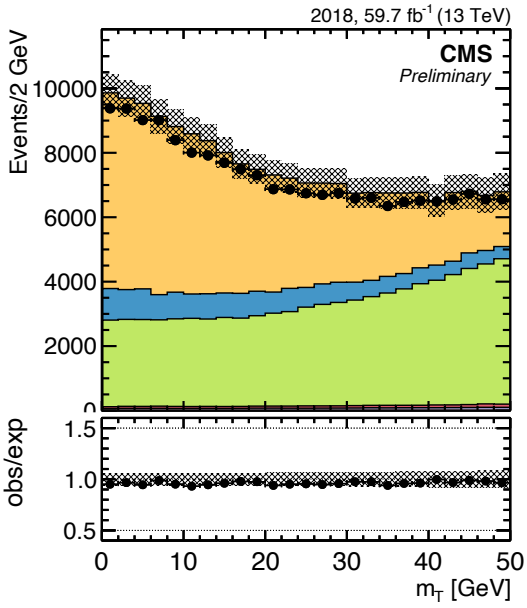

(b) puppi m_T

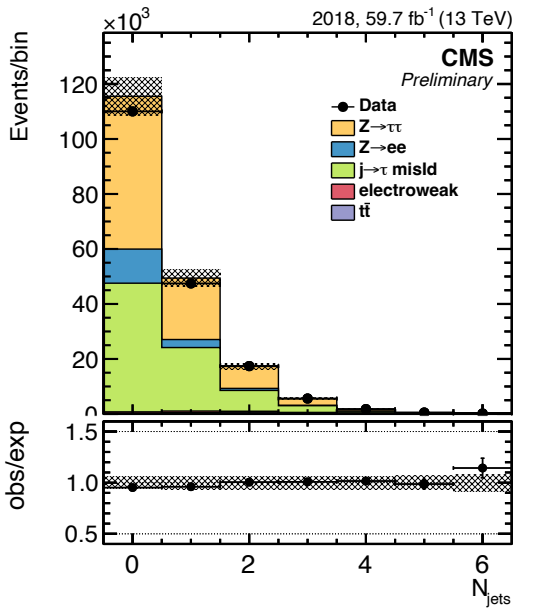

(c) number of jets

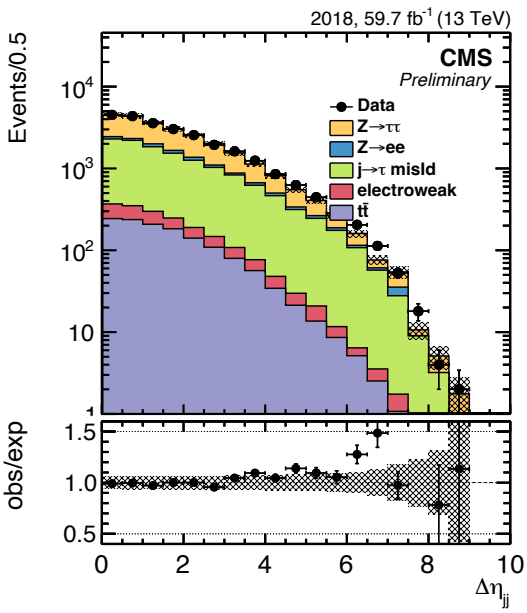

(d) Jet $\Delta\eta$

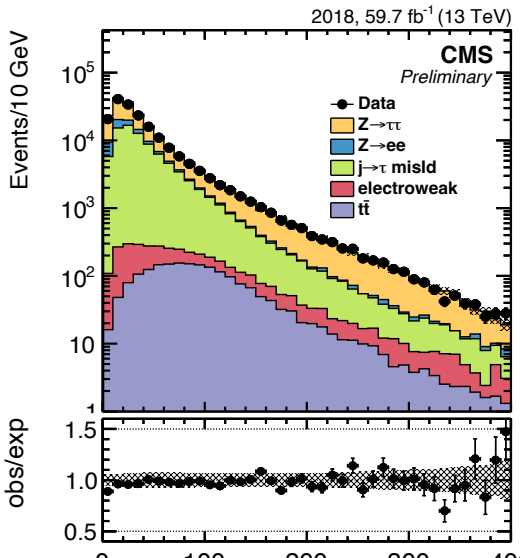

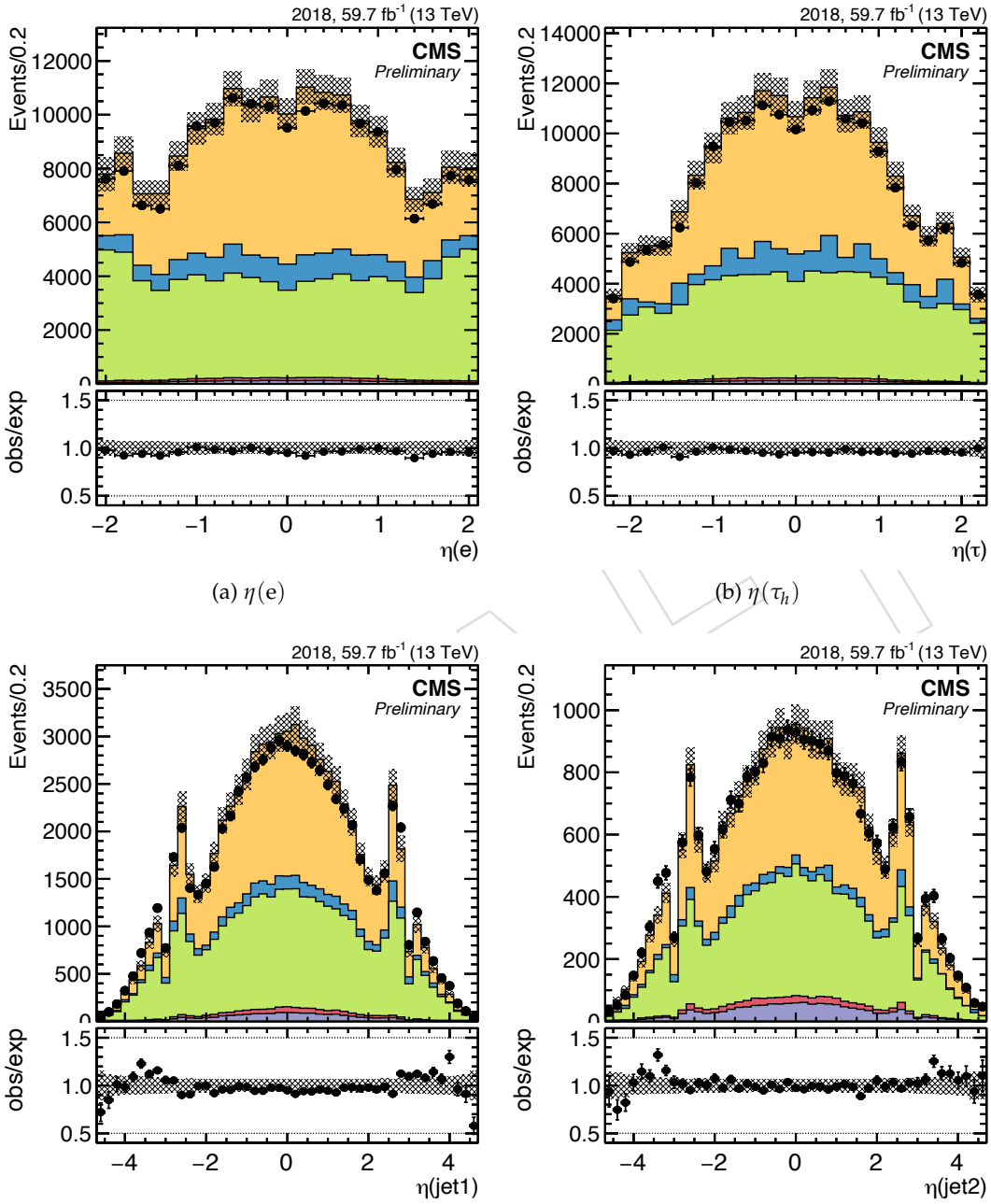

(a) $\eta(\mathrm{e})$

(b) $\eta(\tau_h)$

(c) Leading jet η

(d) Trailing jet η

Figure 281: Pre-fit 2018 data/background comparisons for eτ_h events are shown for auxilary variables (i.e. not used in the multivariate discriminant). In all distributions the background uncertainty shown by the shaped-grey band includes the full uncertainty model

D.3 Results in the $\tau_h\tau_h$ hannel

Control plots for all variables used in the training of the BDT are shown in Fig. 282 – 285. The MVA-DM, subleading τ_{h} and jet p_{T}, which are not used in the BDT are also compared in Fig. 286 – 287.

DRAFT

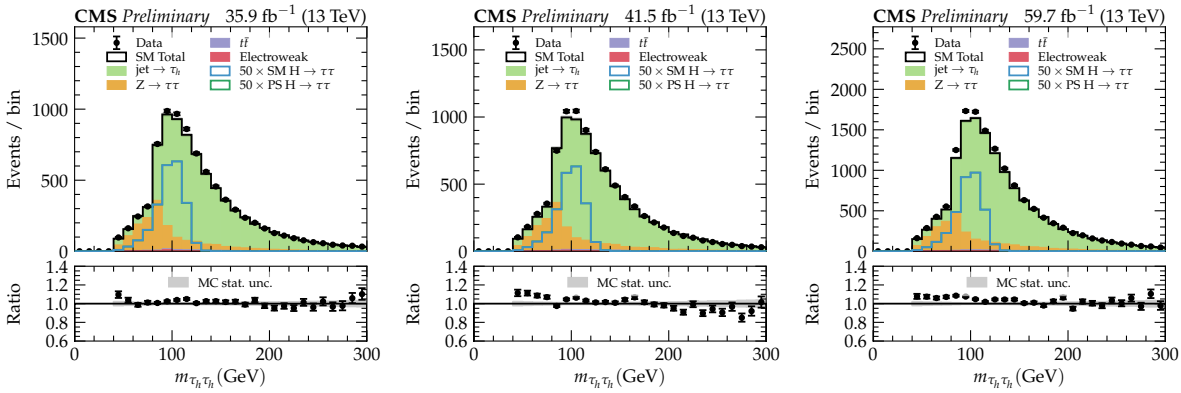

(a) visible mass, 2016 (b) visible mass, 2017 (c) visible mass, 2018

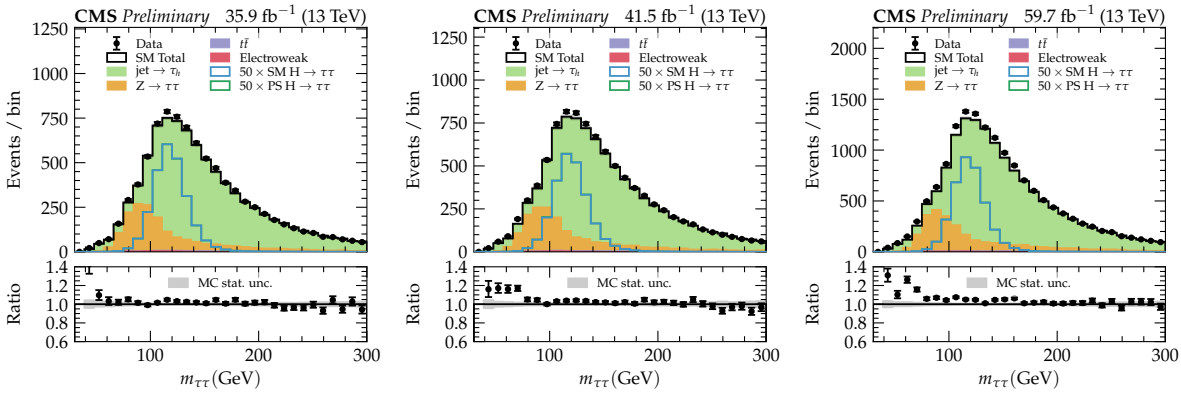

(d) svfit mass, 2016 (e) svfit mass, 2017 (f) svfit mass, 2018

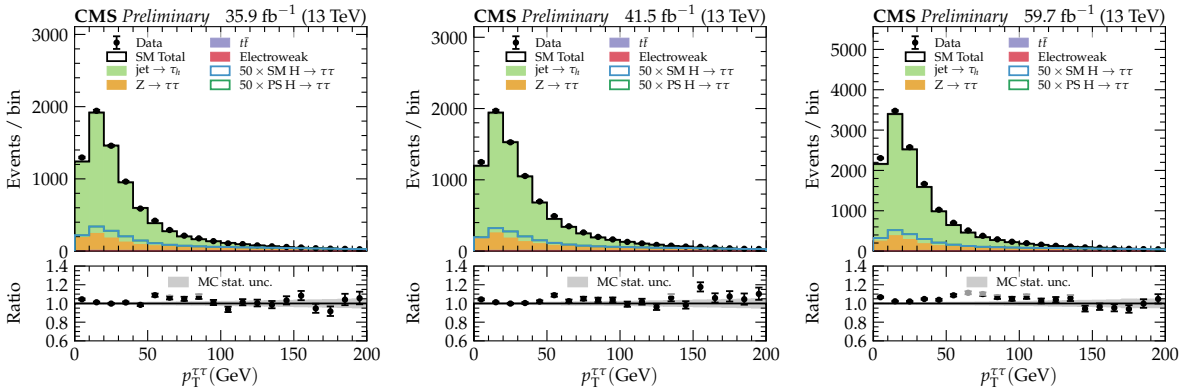

(g) higgs p_T, 2016 (h) higgs p_T, 2017 (i) higgs p_T, 2018

Figure 282: Inclusive, prefit plots for 2016, 2017 and 2018 of the input features to the BDT. The signals are scaled by a factor of 50 and the uncertainty band considers only statistical uncertainty.

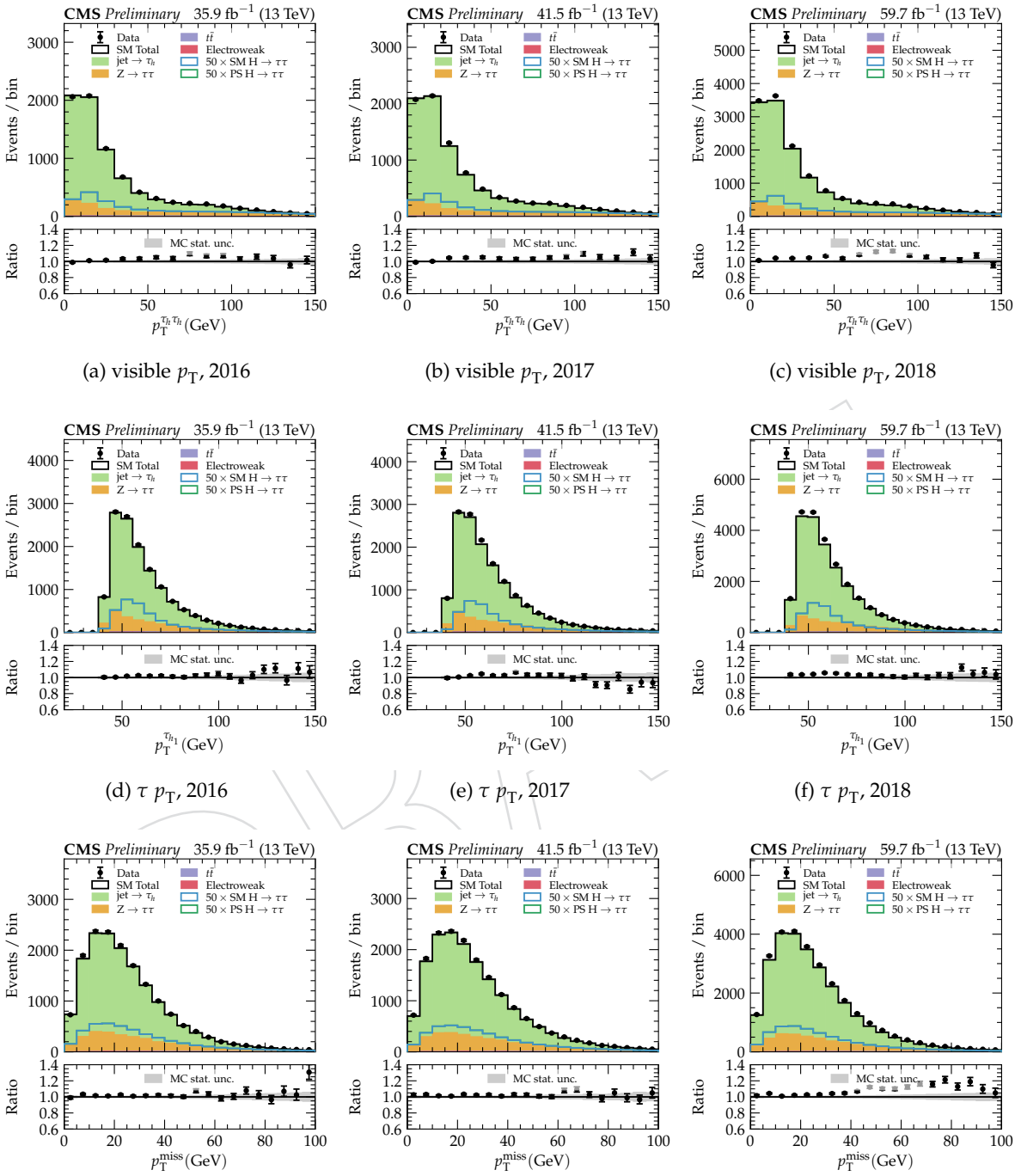

(a) visible p_T, 2016 (b) visible p_T, 2017 (c) visible p_T, 2018

(d) τ p_T, 2016 (e) τ p_T, 2017 (f) τ p_T, 2018

(g) p_T^{miss}, 2016 (h) p_T^{miss}, 2017 (i) p_T^{miss}, 2018

Figure 283: Inclusive, prefit plots for 2016, 2017 and 2018 of the input features to the BDT. The signals are scaled by a factor of 50 and the uncertainty band considers only statistical uncertainty.

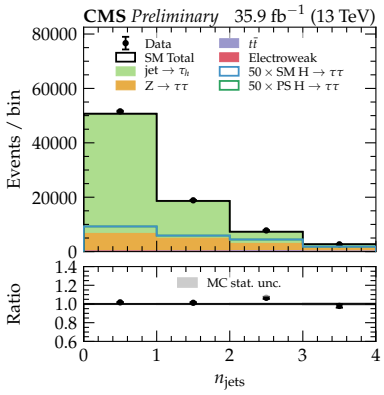

(a) number of jets, 2016

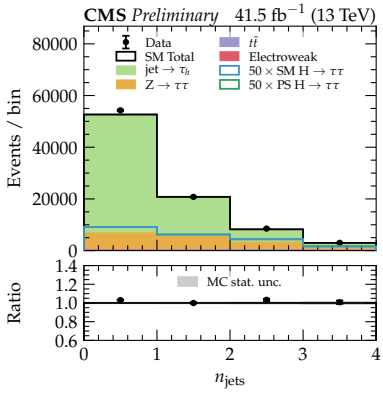

(b) number of jets, 2017

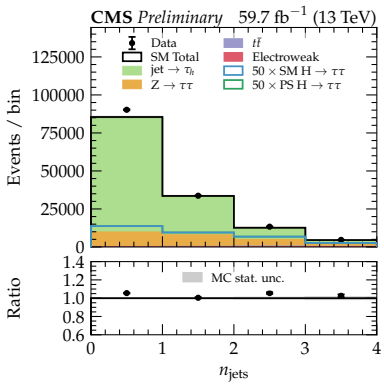

(c) number of jets, 2018

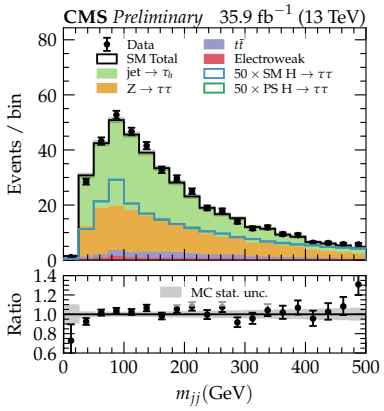

(d) dijet mass, 2016

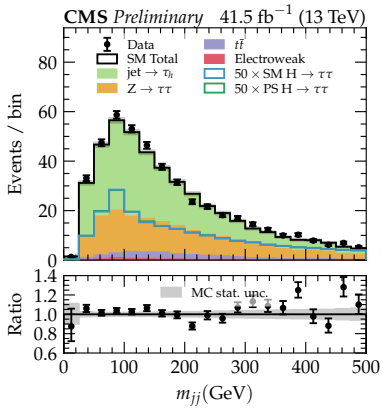

(e) dijet mass, 2017

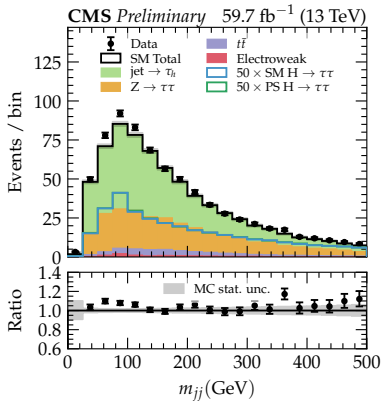

(f) dijet mass, 2018

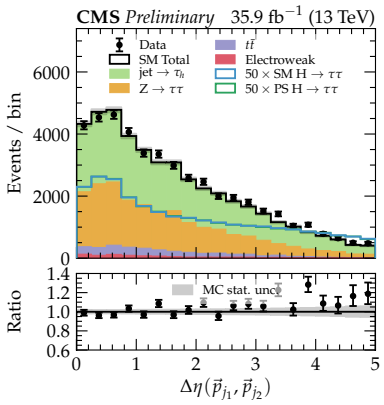

(g) $|\Delta\eta|$ of jets, 2016

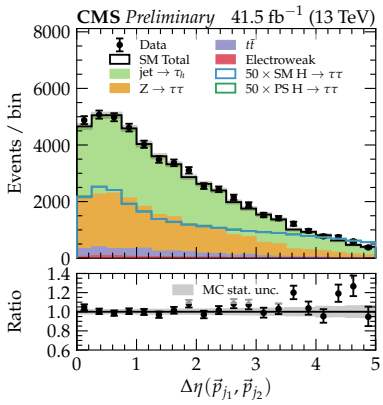

(h) $|\Delta\eta|$ of jets, 2017

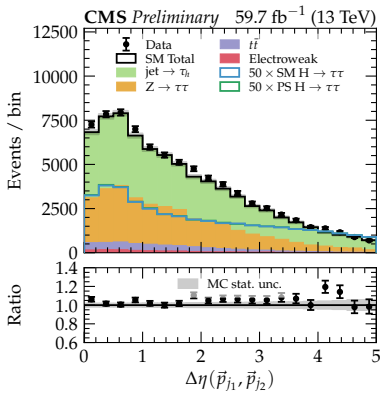

(i) $|\Delta\eta|$ of jets, 2018

Figure 284: Inclusive, prefit plots for 2016, 2017 and 2018 of the input features to the BDT. The signals are scaled by a factor of 50 and the uncertainty band considers only statistical uncertainty.

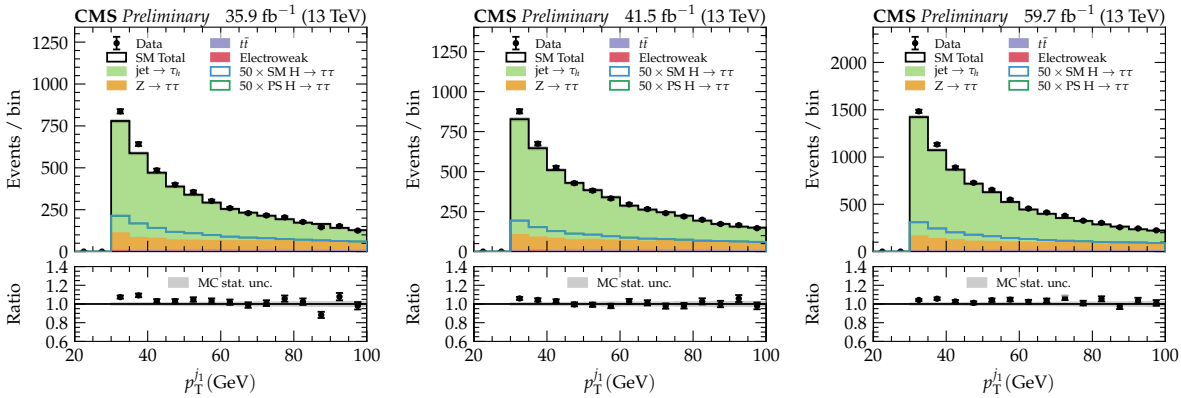

(a) leading jet p_T, 2016 (b) leading jet p_T, 2017 (c) leading jet p_T, 2018

Figure 285: Inclusive, prefit plots for 2016, 2017 and 2018 of the input features to the BDT. The signals are scaled by a factor of 50 and the uncertainty band considers only statistical uncertainty.

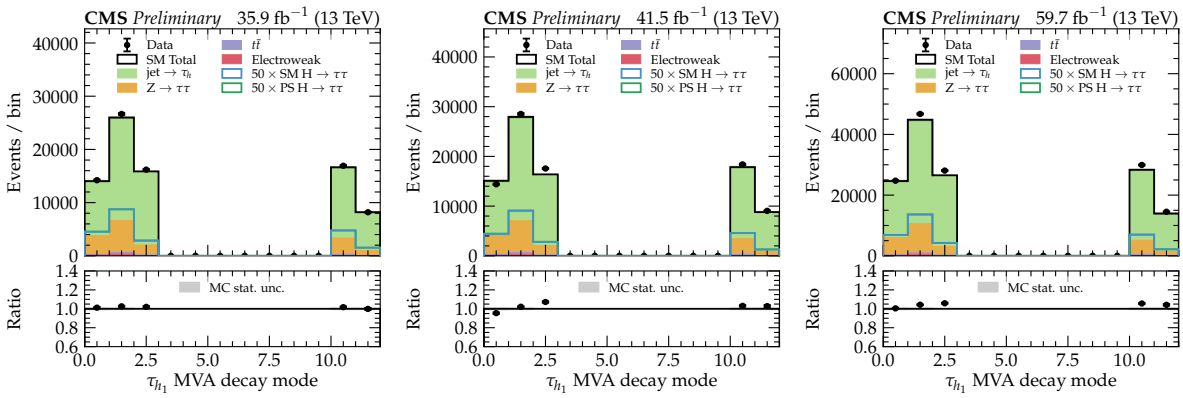

(a) leading τ_h MVA DM, 2016 (b) leading τ_h MVA DM, 2017 (c) leading τ_h MVA DM, 2018

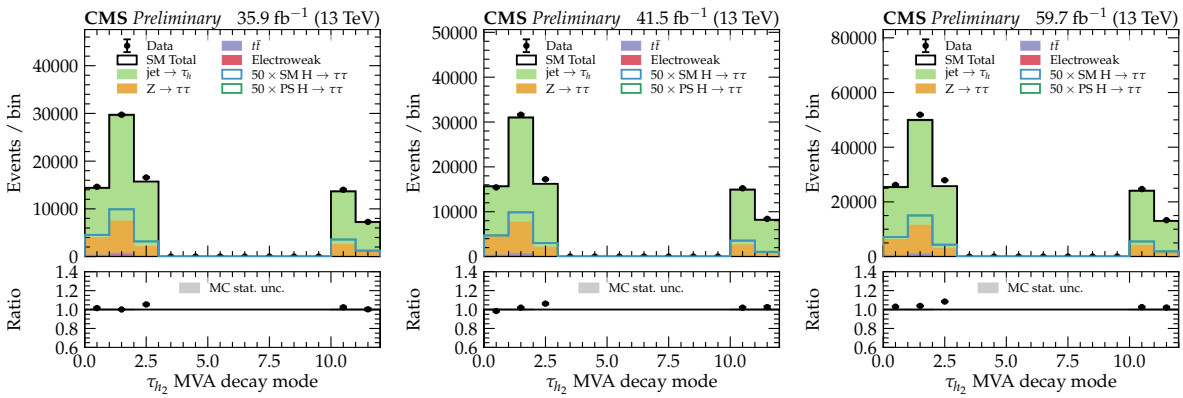

(d) sub-leading τ_h MVA DM, 2016 (e) sub-leading τ_h MVA DM, 2017 (f) sub-leading τ_h MVA DM, 2018

Figure 286: Inclusive, prefit plots for 2016, 2017 and 2018 of the τ_h MVA decay mode. The signals are scaled by a factor of 50 and the uncertainty band considers only statistical uncertainty.

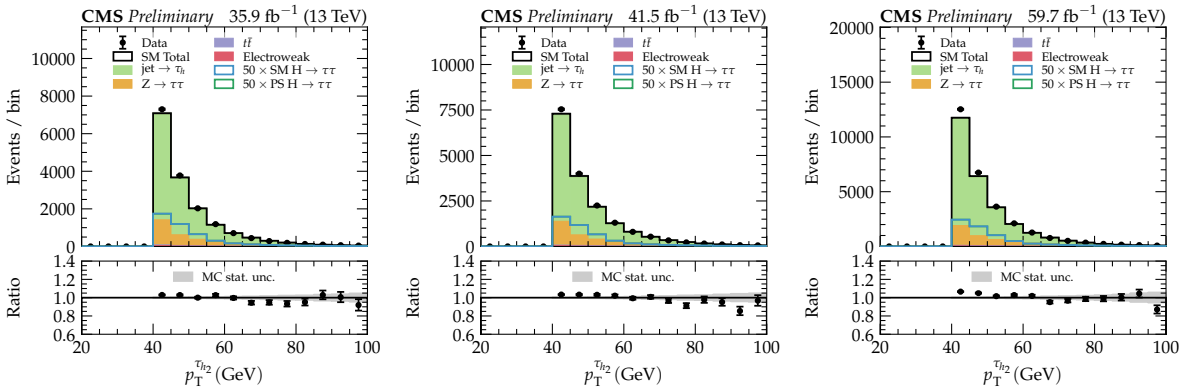

(a) subleading τ_h p_T, 2016 (b) subleading τ_h p_T, 2017 (c) subleading τ_h p_T, 2018

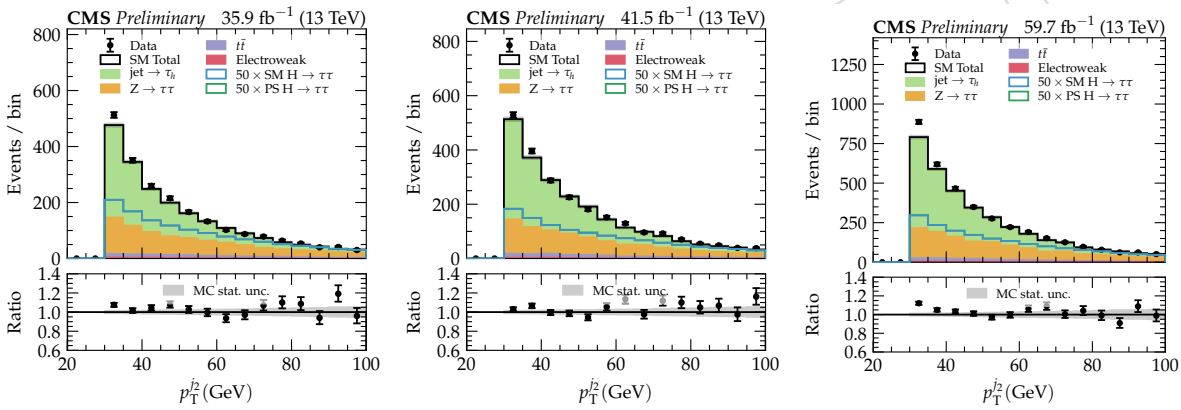

(d) subleading jet p_T, 2016 (e) subleading jet p_T, 2017 (f) subleading jet p_T, 2018

Figure 287: Inclusive, prefit plots for 2016, 2017 and 2018 of the subleading τ_h and jet p_T. The signals are scaled by a factor of 50 and the uncertainty band considers only statistical uncertainty.

E Fake factor fits

This section shows the fitted functions for all raw fake factors and corrections that are used in the analysis. Only the nominal values of the fitted functions are shown without the corresponding uncertainty bands. In the case of the W+jets raw fake factors the fake factors measured using MC events are also shown for comparison.

E.1 Raw fake factor fits in the $\tau_h\tau_h$ channel

The fits of the raw (un-corrected) QCD fake factors in the $\tau_\mathrm{h}\tau_\mathrm{h}$ channel are shown in Figures 288 – 290.

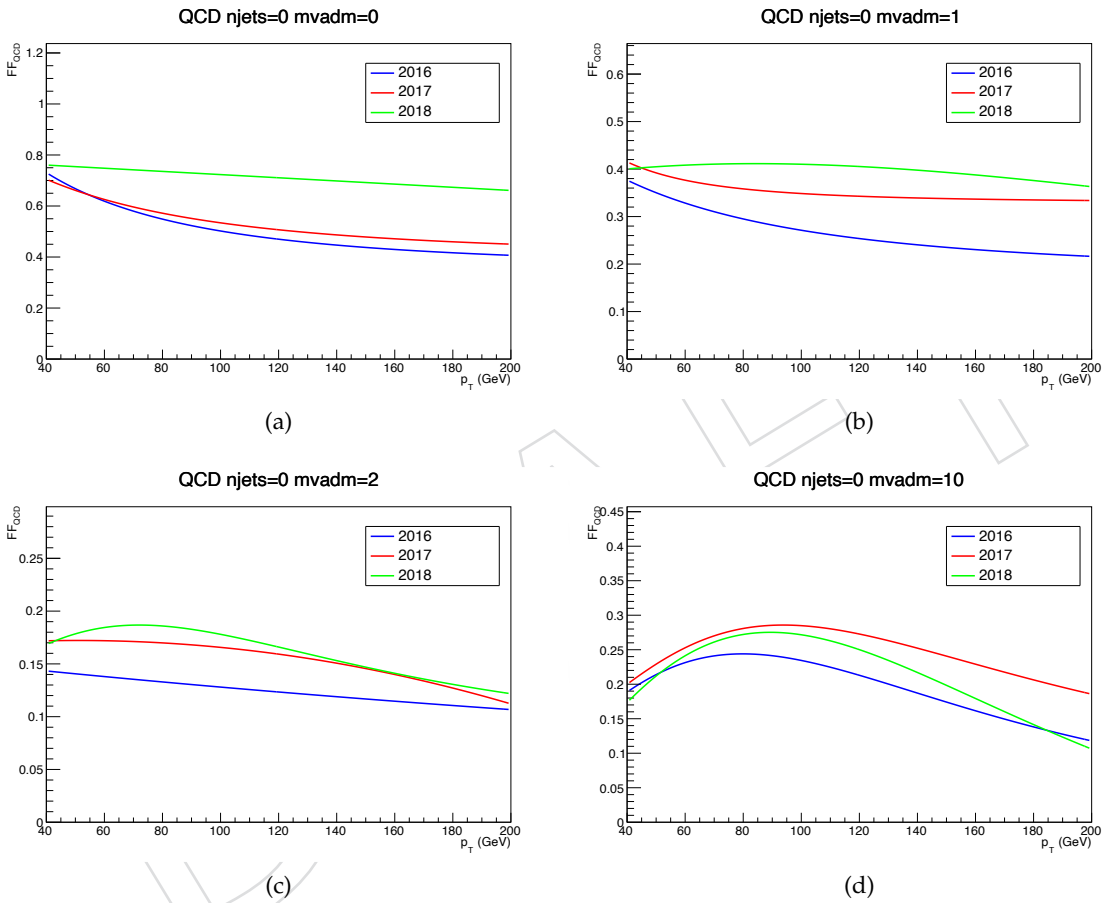

Figure 288: The fits of uncorrected QCD fake factors in the $\tau_\mathrm{h}\tau_\mathrm{h}$ channel for the $N_{jets} = 0$ bins. The fits for MVA-DM = 0, 1, 2, 10 τ_h candidates are shown in insets a, b, c, and d respectively.

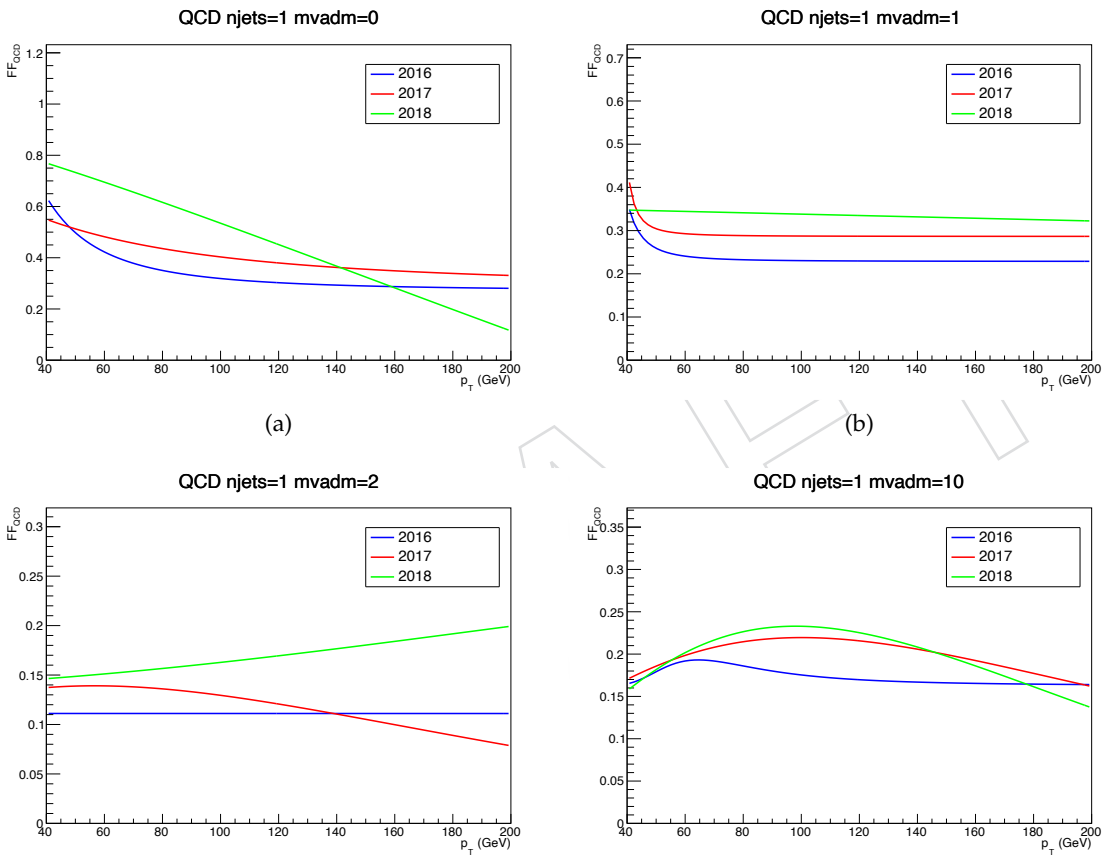

(a) (b) (c) (d)

Figure 289: The fits of uncorrected QCD fake factors in the $\tau_{\mathrm{h}}\tau_{\mathrm{h}}$ channel for the $N_{jets} = 1$ bins. The fits for MVA-DM = 0, 1, 2, 10 τ_{h} candidates are shown in insets a, b, c, and d respectively.

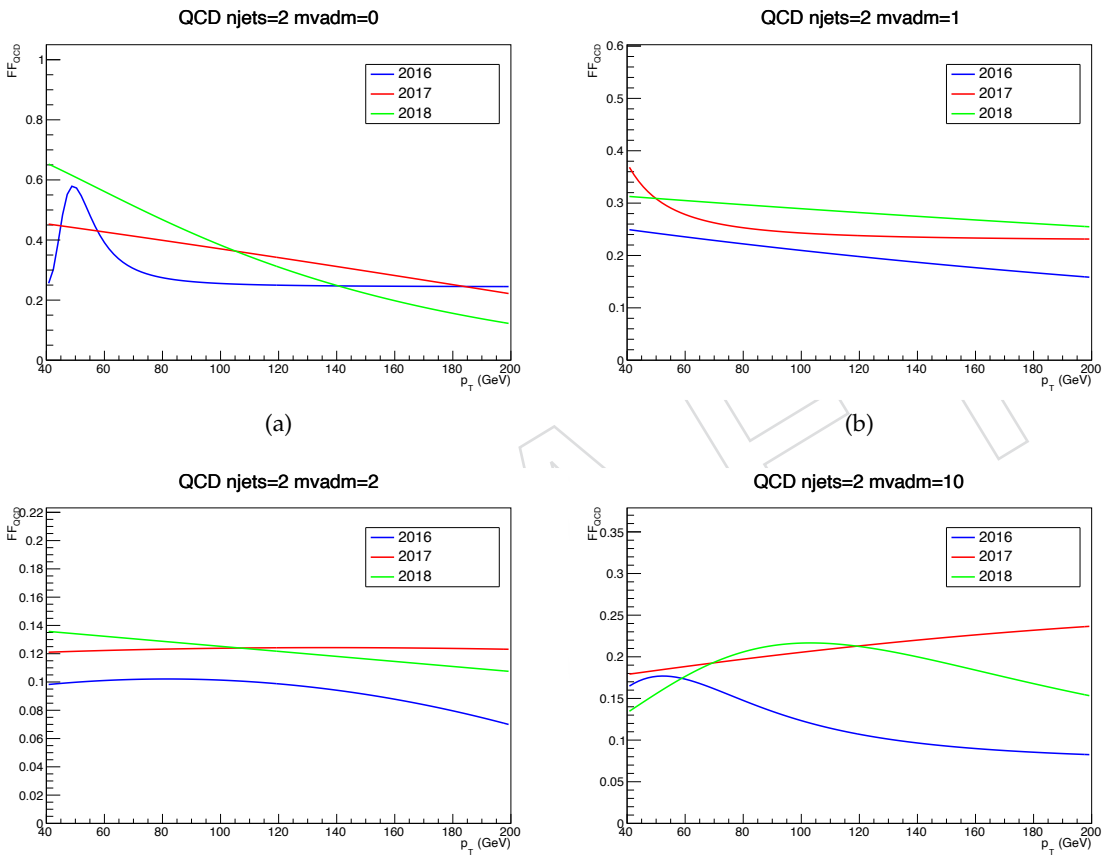

(a) (b) (c) (d)

Figure 290: The fits of uncorrected QCD fake factors in the $\tau_h\tau_h$ channel for the $N_{jets} \geq 2$ bins. The fits for MVA-DM = 0, 1, 2, 10 τ_h candidates are shown in insets a, b, c, and d respectively.

E.2 Raw fake factor fits in the $\tau_\mu \tau_h$ channel

The fits of the raw (un-corrected) QCD, W+jets, and $t\bar{t}$ fake factors in the $\tau_\mu \tau_\mathrm{h}$ channel are shown in Figures 291 – 293, 294 – 296, and 297 respectively.

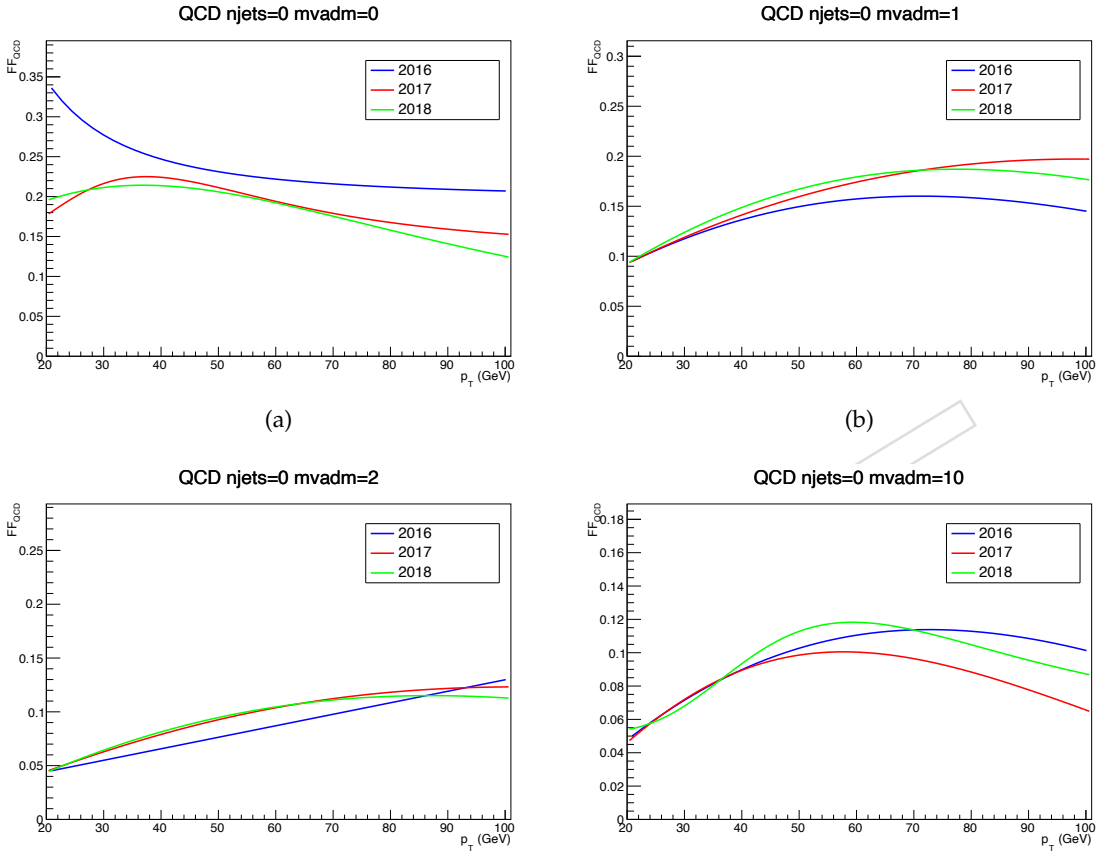

(a) (b) (c) (d)

Figure 291: The fits of uncorrected QCD fake factors in the $\tau_\mu \tau_\mathrm{h}$ channel for the $N_{jets} = 0$ bins. The fits for MVA-DM = 0, 1, 2, 10 τ_h candidates are shown in insets a, b, c, and d respectively.

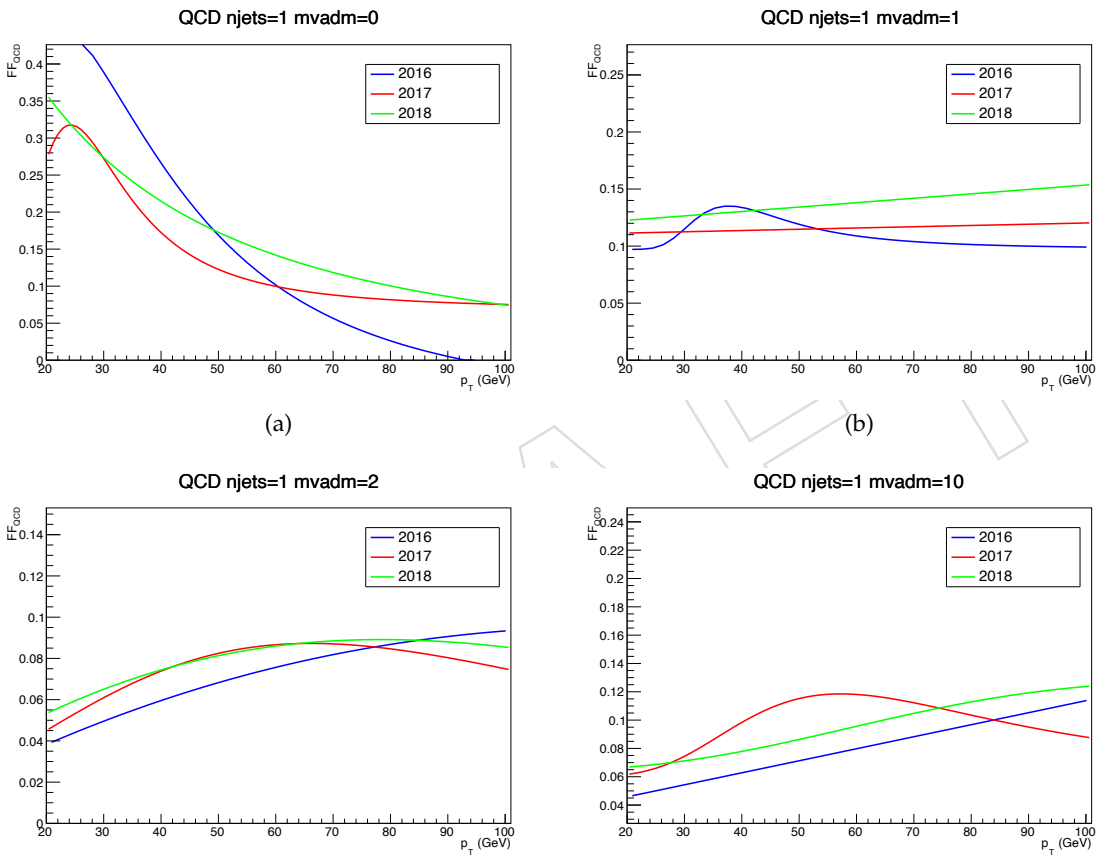

(a) (b) (c) (d)

Figure 292: The fits of uncorrected QCD fake factors in the $\tau_\mu \tau_\mathrm{h}$ channel for the $N_{jets} = 1$ bins. The fits for MVA-DM = 0, 1, 2, 10 τ_h candidates are shown in insets a, b, c, and d respectively.

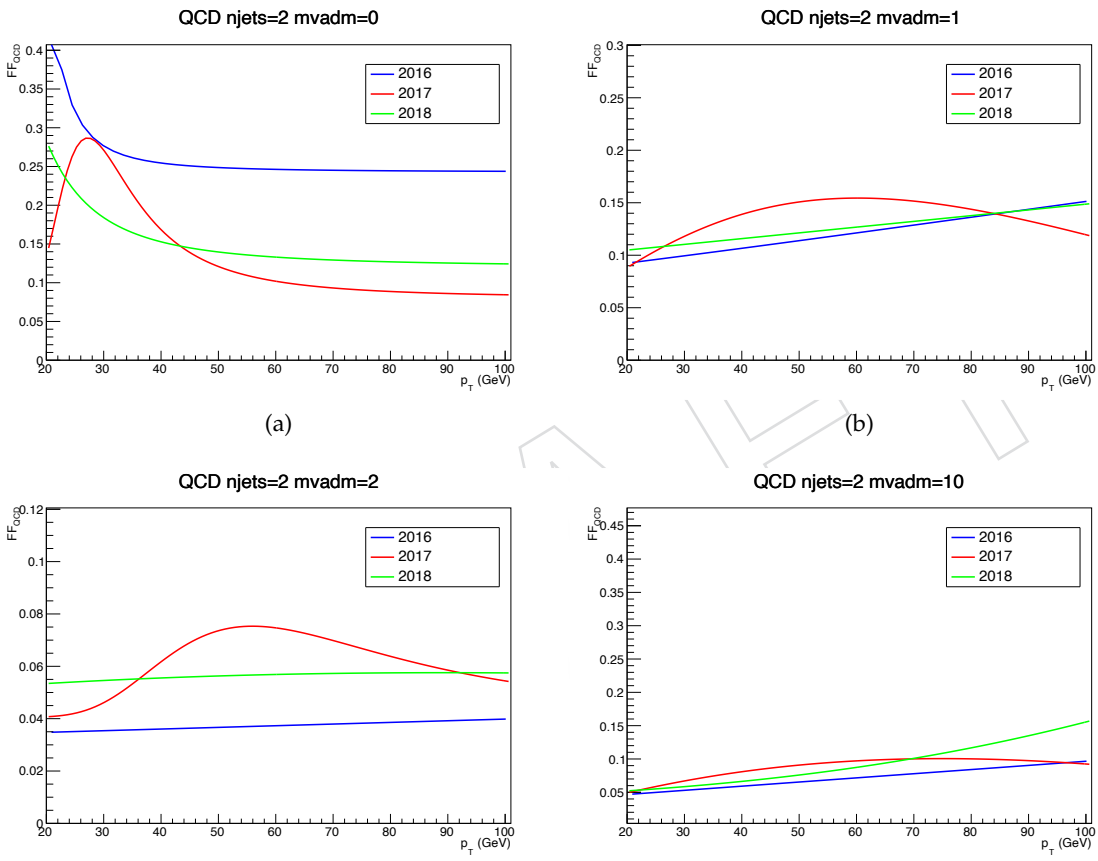

(a) (b) (c) (d)

Figure 293: The fits of uncorrected QCD fake factors in the $\tau_\mu \tau_\mathrm{h}$ channel for the $N_{jets} \geq 2$ bins. The fits for MVA-DM = 0, 1, 2, 10 τ_h candidates are shown in insets a, b, c, and d respectively.

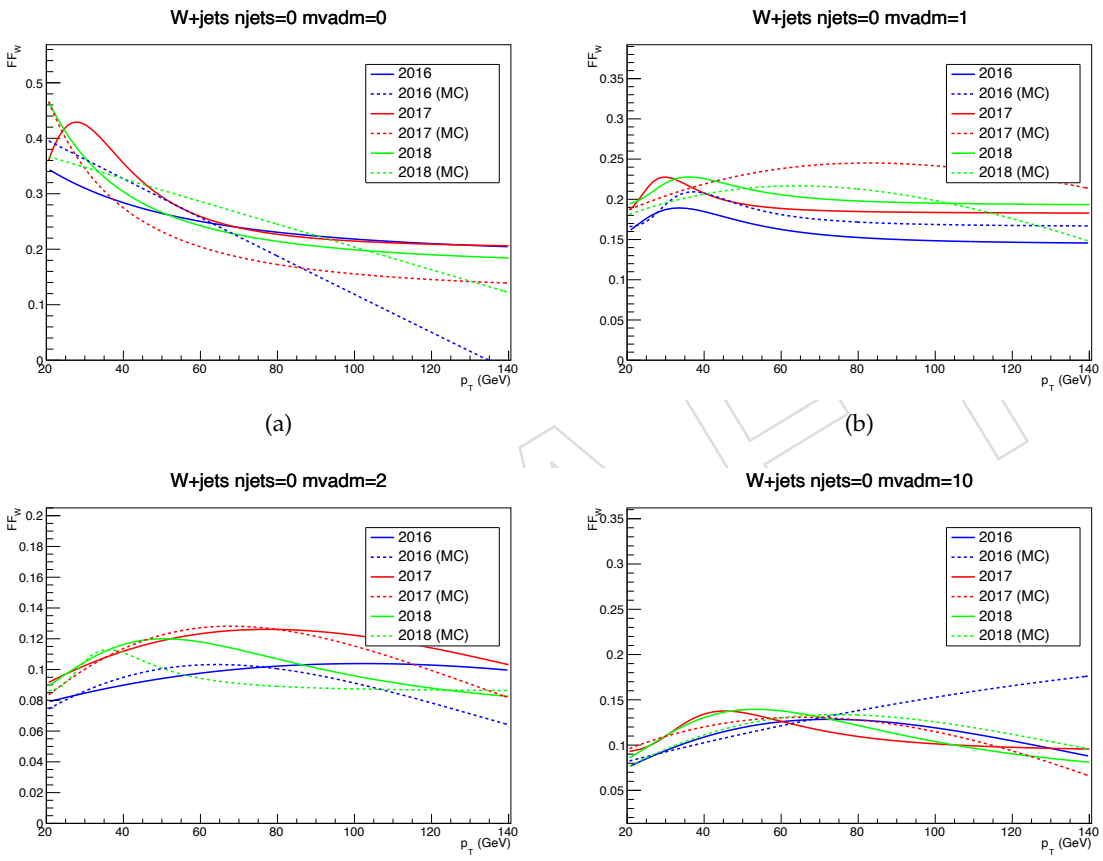

(a) (b) (c) (d)

Figure 294: The fits of uncorrected W+jets fake factors in the $\tau_\mu \tau_\mathrm{h}$ channel for the $N_{jets} = 0$ bins. The fits for MVA-DM = 0, 1, 2, 10 τ_h candidates are shown in insets a, b, c, and d respectively.

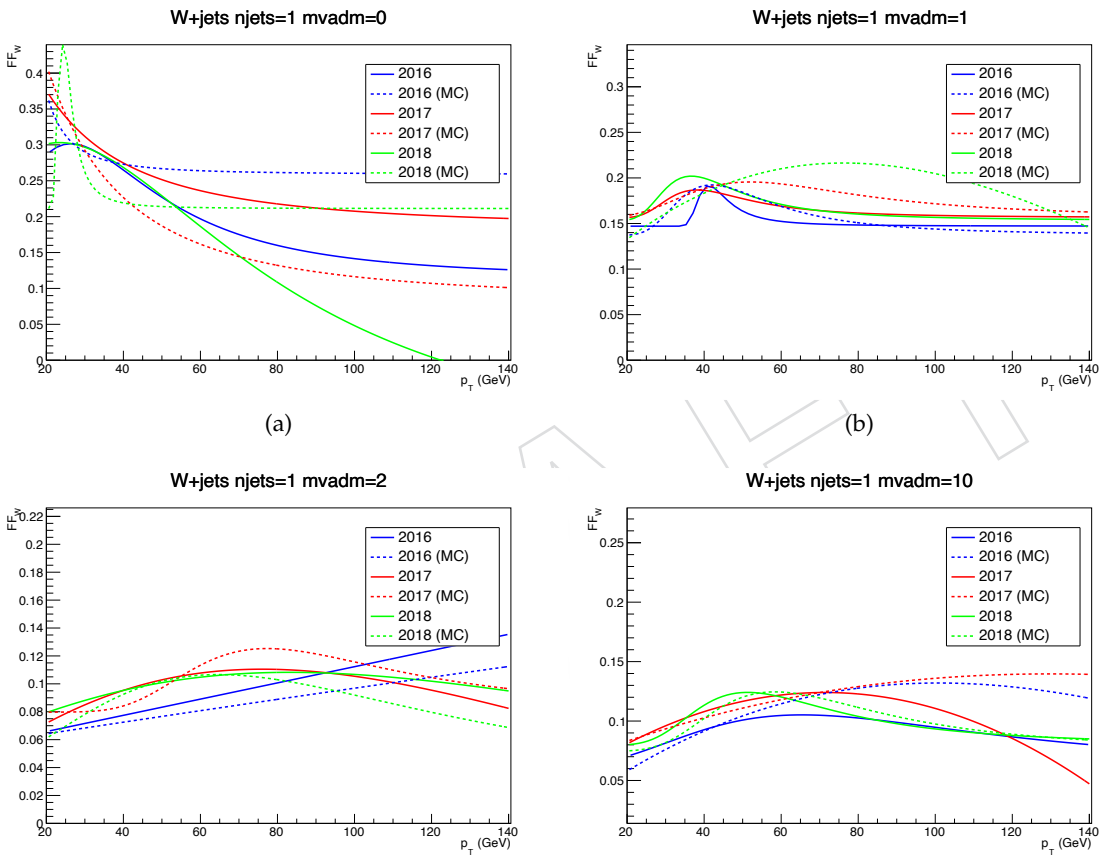

(a) (b) (c) (d)

Figure 295: The fits of uncorrected W+jets fake factors in the $\tau_\mu \tau_\mathrm{h}$ channel for the $N_{jets} = 1$ bins. The fits for MVA-DM = 0, 1, 2, 10 τ_h candidates are shown in insets a, b, c, and d respectively.

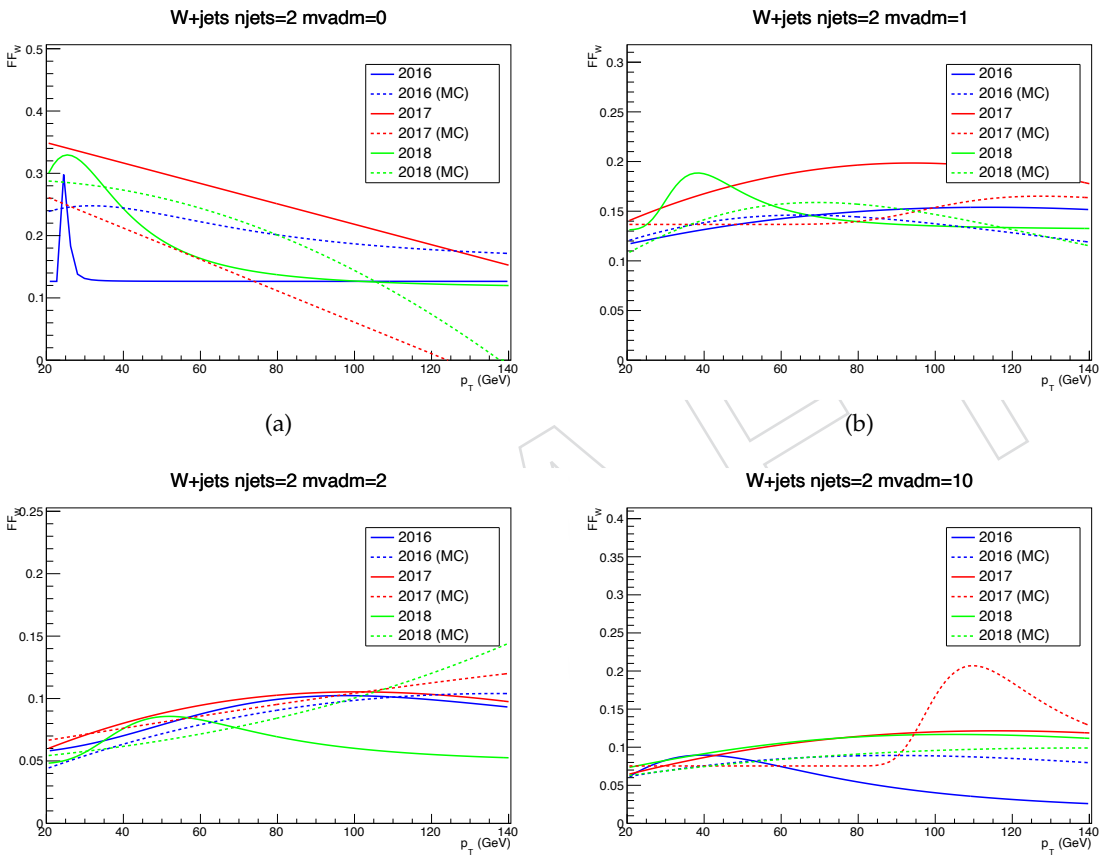

Figure 296: The fits of uncorrected W+jets fake factors in the $\tau_\mu \tau_\mathrm{h}$ channel for the $N_{jets} \geq 2$ bins. The fits for MVA-DM = 0, 1, 2, 10 τ_h candidates are shown in insets a, b, c, and d respectively.

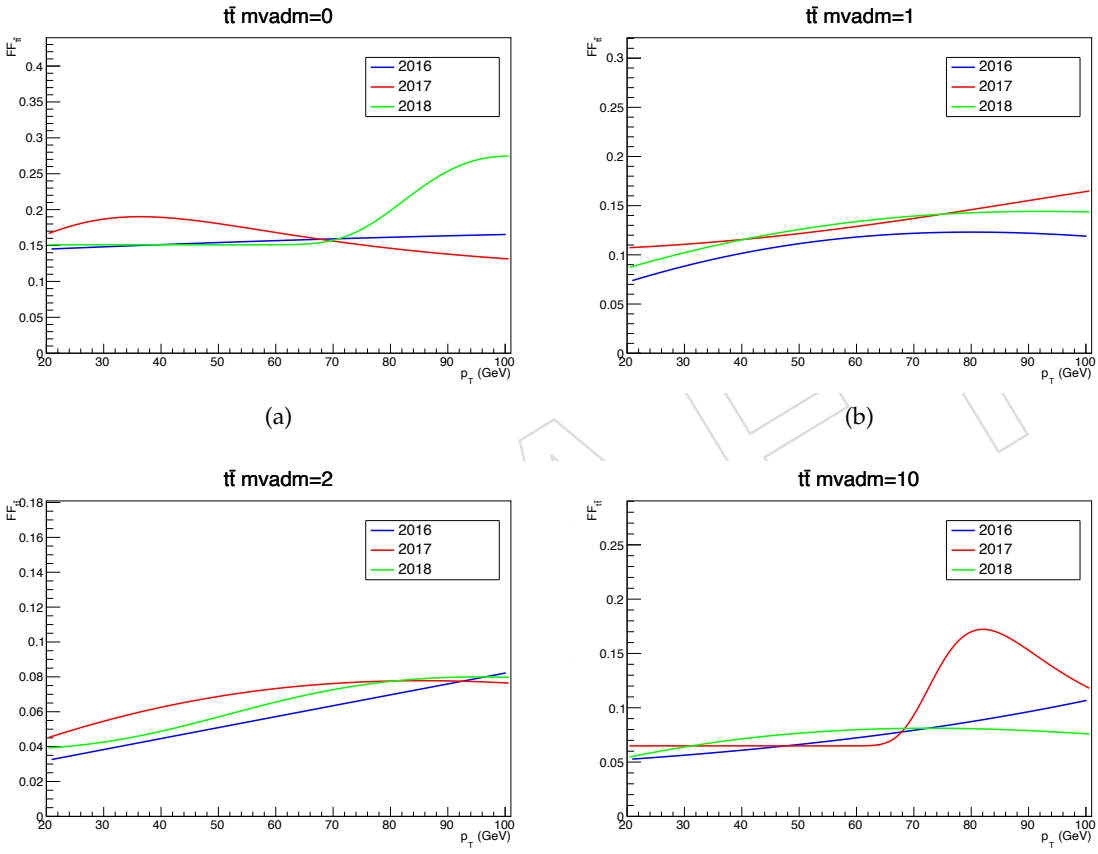

(a) (b) (c) (d)

Figure 297: The fits of uncorrected $t\bar{t}$ fake factors in the $\tau_\mu \tau_h$ channel. The fits for MVA-DM = 0, 1, 2, 10 τ_h candidates are shown in insets a, b, c, and d respectively.

E.3 Raw fake factor fits in the $\tau_e\tau_h$ channel

The fits of the raw (un-corrected) QCD, W+jets, and $t\bar{t}$ fake factors in the $\tau_e\tau_h$ channel are shown in Figures 298 – 300, 301 – 303, and 304 respectively.

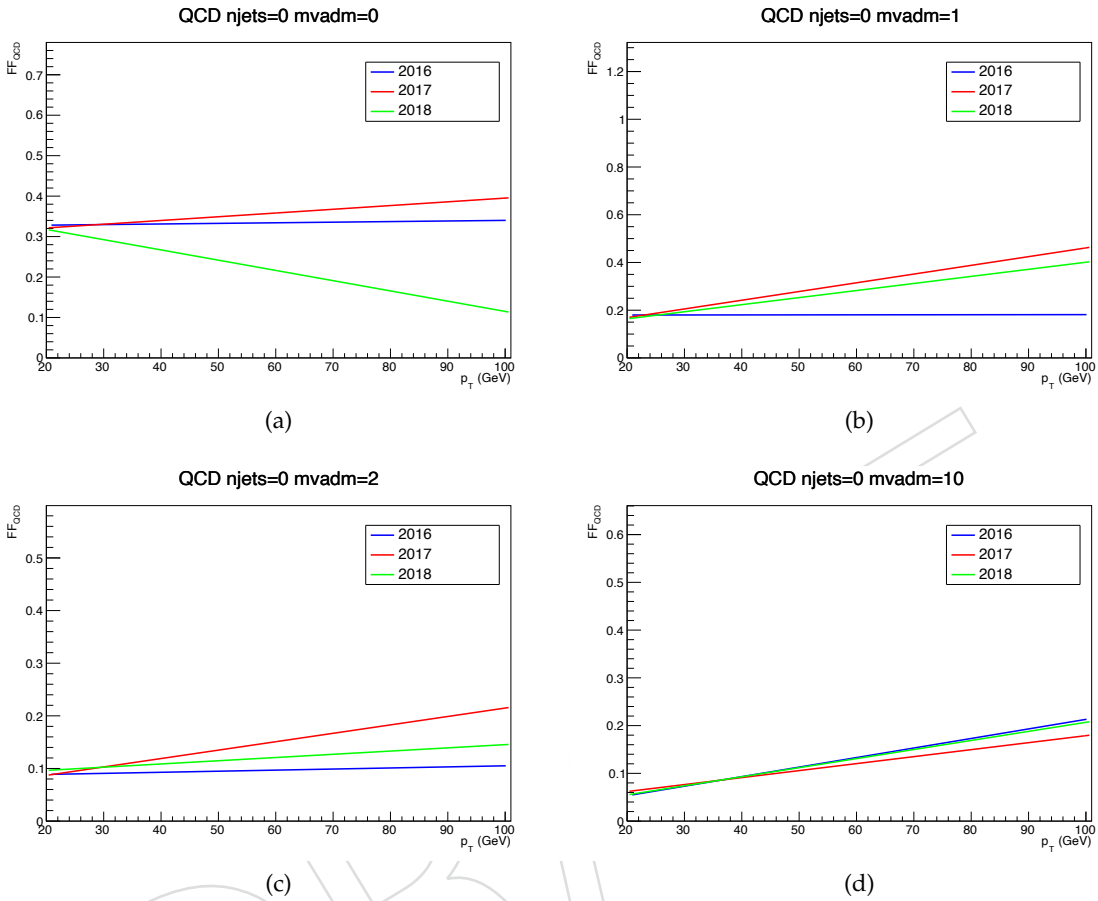

Figure 298: The fits of uncorrected QCD fake factors in the $\tau_e\tau_h$ channel for the $N_{jets} = 0$ bins. The fits for MVA-DM = 0, 1, 2, 10 τ_h candidates are shown in insets a, b, c, and d respectively.

E.4 Closure corrections in the $\tau_h\tau_h$ channel

The fits of the closure corrections used to correct the E_T^{miss} related variables in the $\tau_h\tau_h$ channel are shown in Figure 305.

E.5 Closure corrections in the $\tau_\mu\tau_h$ channel

The fits of the closure corrections used to correct the E_T^{miss} related variables for the QCD, W+jets, and $t\bar{t}$ fake factors in the $\tau_\mu\tau_h$ channel are shown in Figures 306, 307, and 308 respectively.

The fits of the closure corrections used to correct the E_T^{miss} related variables for the QCD and W+jets fake factors in the $\tau_\mu\tau_h$ channel are shown in Figures 309 and 310 respectively.

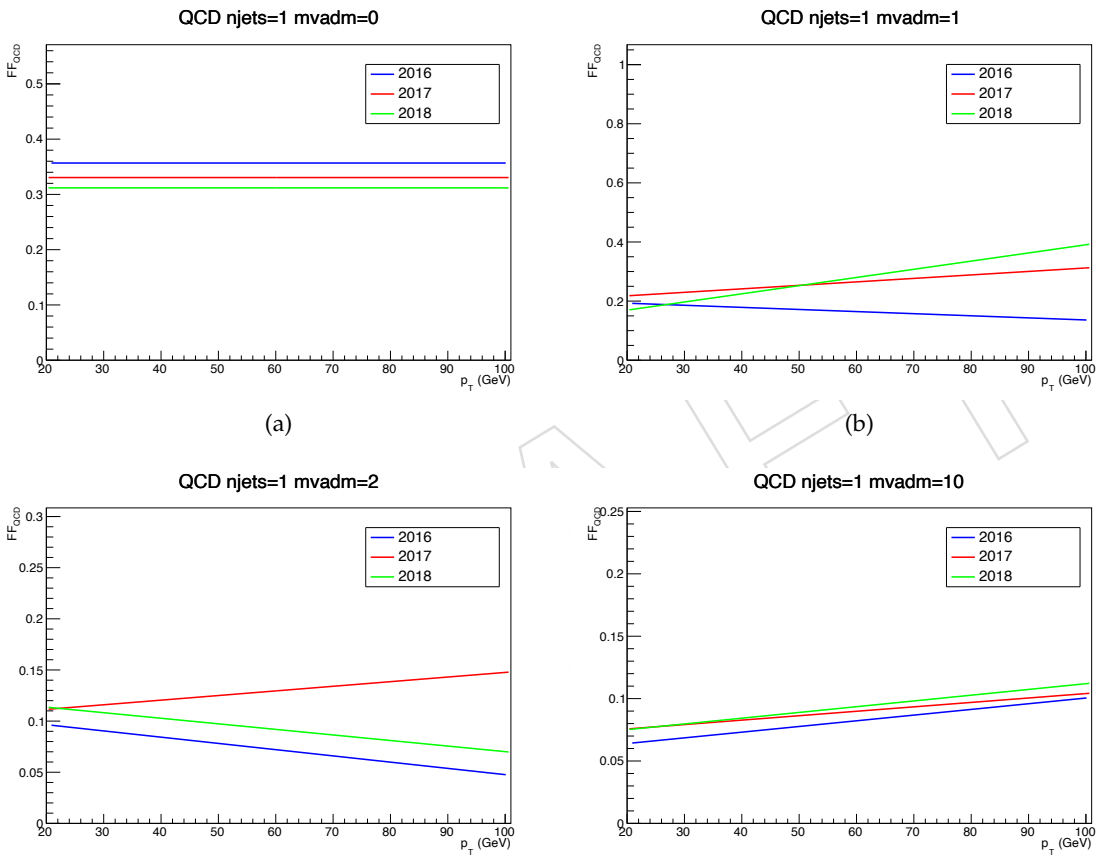

(a) (b) (c) (d)

Figure 299: The fits of uncorrected QCD fake factors in the $\tau_e \tau_\mathrm{h}$ channel for the $N_{jets} = 1$ bins. The fits for MVA-DM = 0, 1, 2, 10 τ_h candidates are shown in insets a, b, c, and d respectively.

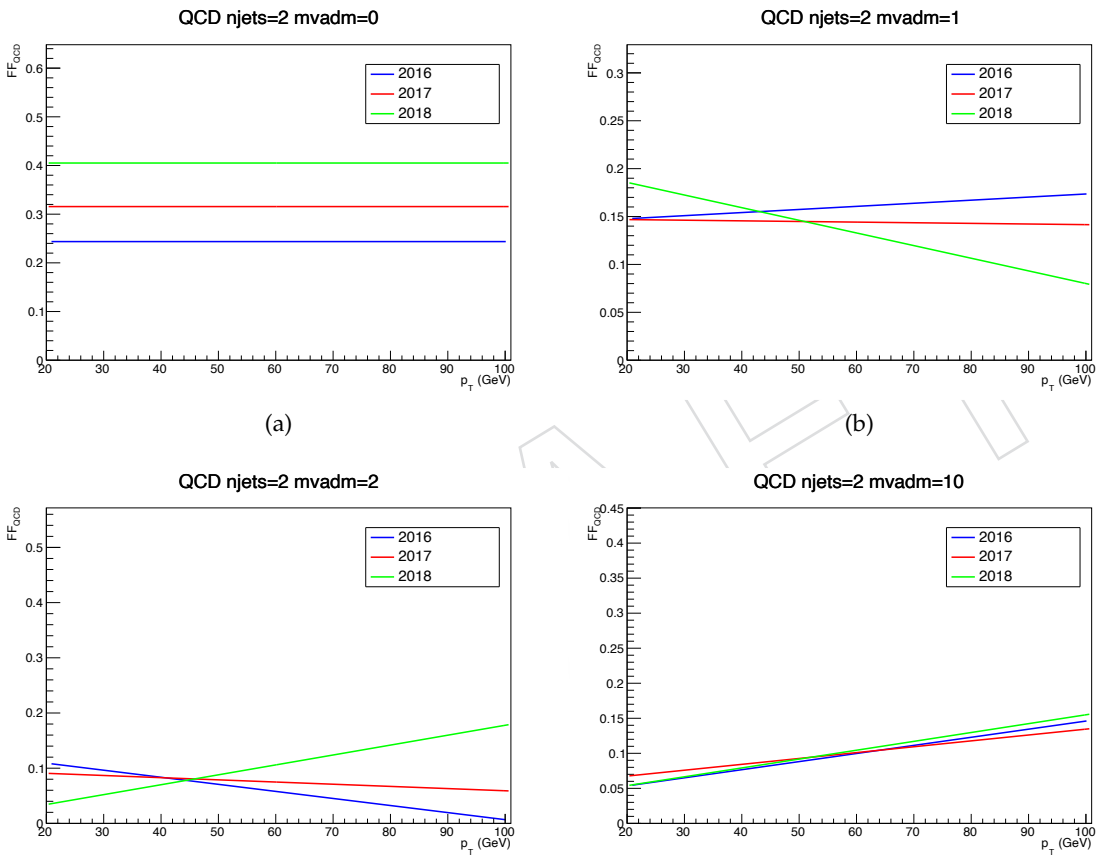

(a) (b) (c) (d)

Figure 300: The fits of uncorrected QCD fake factors in the $\tau_e\tau_\mathrm{h}$ channel for the $N_{jets} \geq 2$ bins. The fits for MVA-DM = 0, 1, 2, 10 τ_h candidates are shown in insets a, b, c, and d respectively.

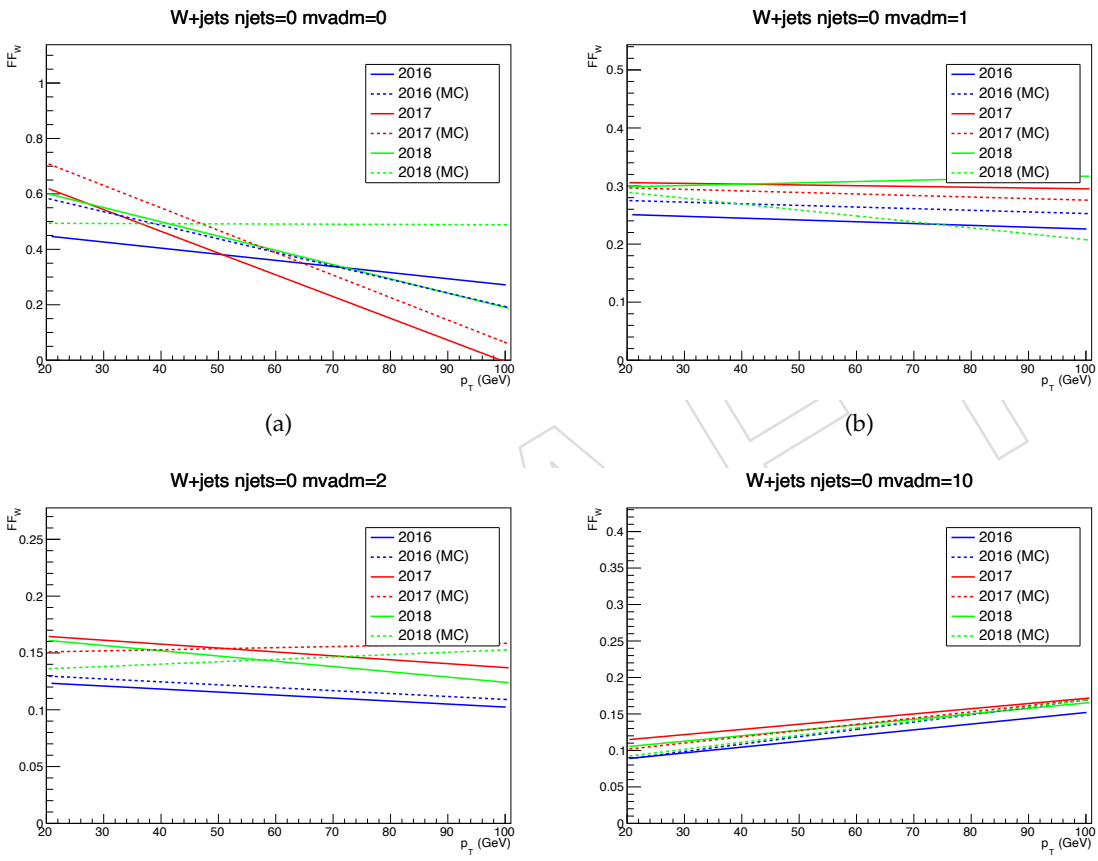

(a) (b) (c) (d)

Figure 301: The fits of uncorrected W+jets fake factors in the $\tau_e \tau_\mathrm{h}$ channel for the $N_{jets} = 0$ bins. The fits for MVA-DM = 0, 1, 2, 10 τ_h candidates are shown in insets a, b, c, and d respectively.

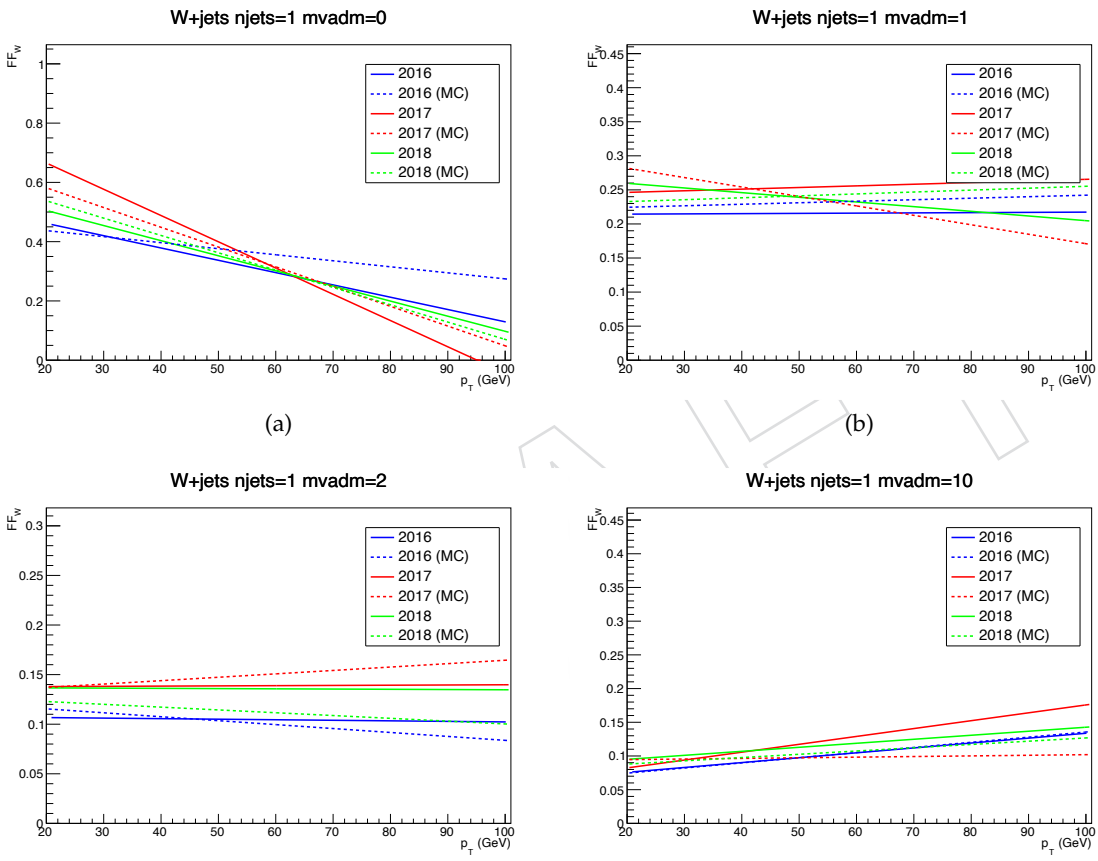

(a) (b) (c) (d)

Figure 302: The fits of uncorrected W+jets fake factors in the $\tau_e\tau_\mathrm{h}$ channel for the $N_{jets} = 1$ bins. The fits for MVA-DM = 0, 1, 2, 10 τ_h candidates are shown in insets a, b, c, and d respectively.

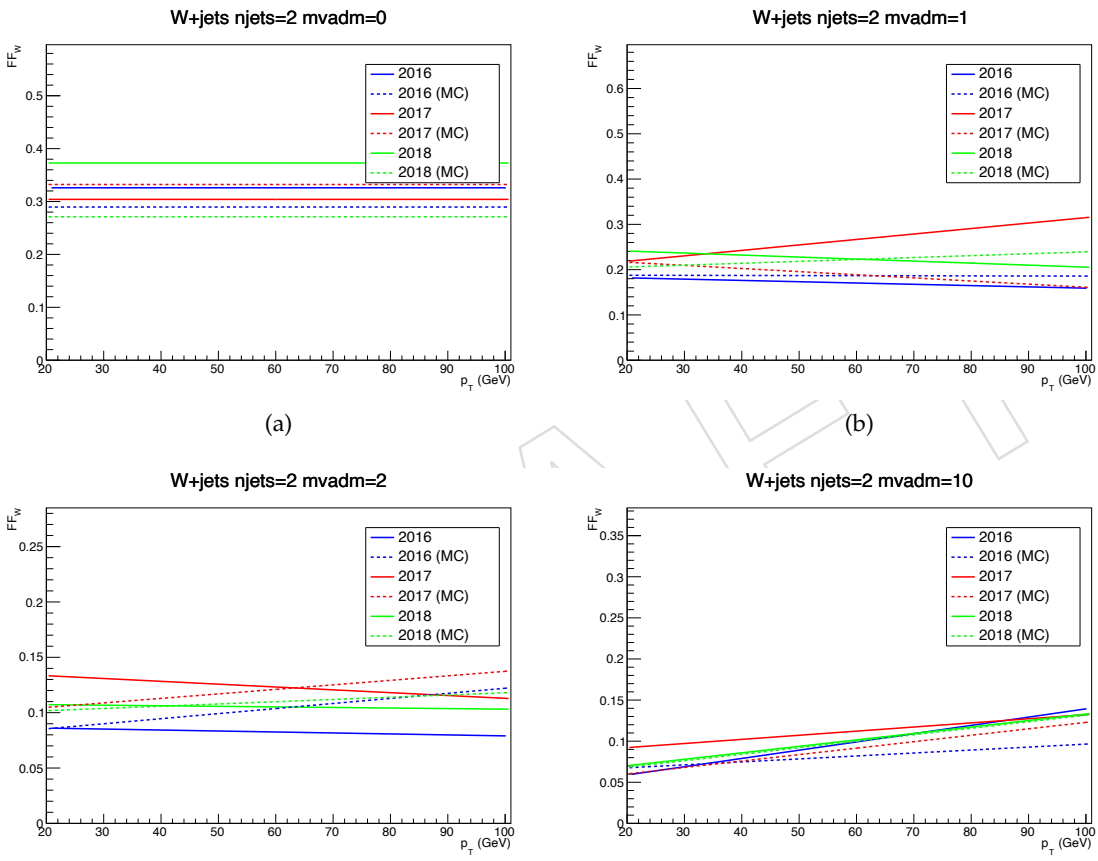

(a) (b) (c) (d)

Figure 303: The fits of uncorrected W+jets fake factors in the $\tau_e \tau_\mathrm{h}$ channel for the $N_{jets} \geq 2$ bins. The fits for MVA-DM = 0, 1, 2, 10 τ_h candidates are shown in insets a, b, c, and d respectively.

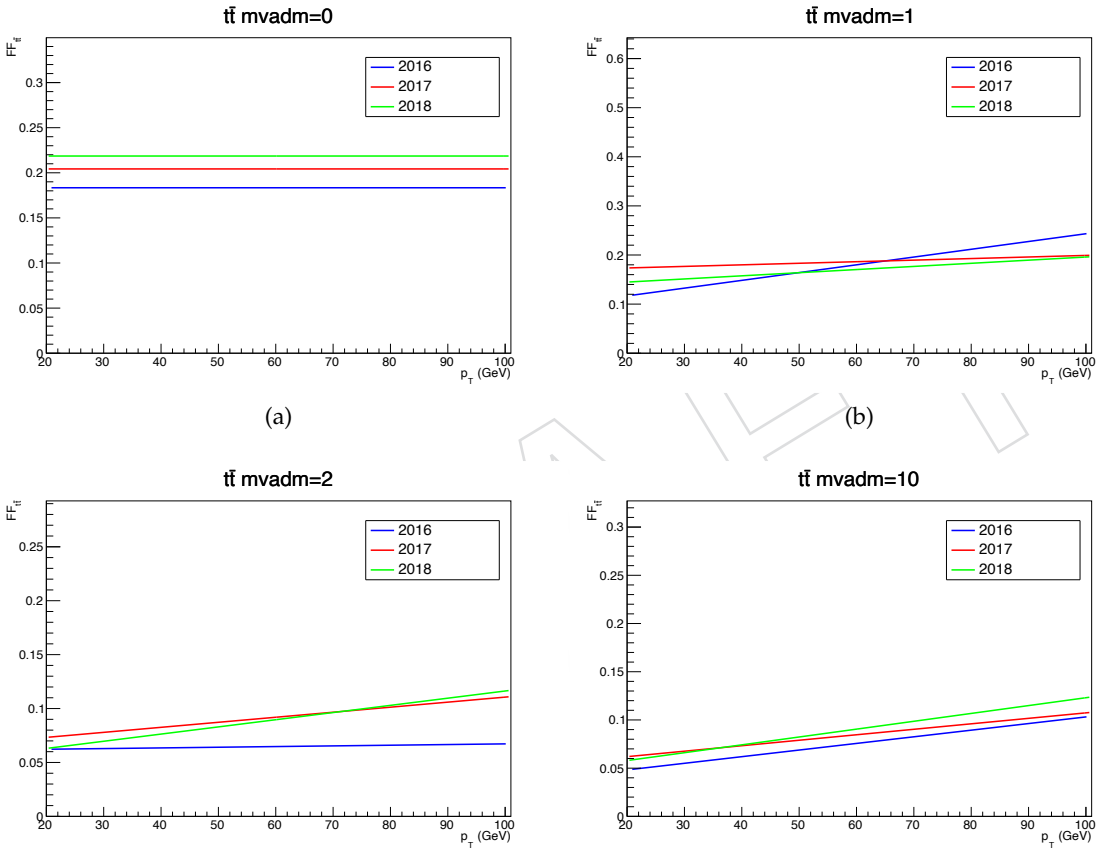

(a) (b) (c) (d)

Figure 304: The fits of uncorrected $t\bar{t}$ fake factors in the $\tau_e\tau_h$ channel. The fits for MVA-DM = 0, 1, 2, 10 τ_h candidates are shown in insets a, b, c, and d respectively.

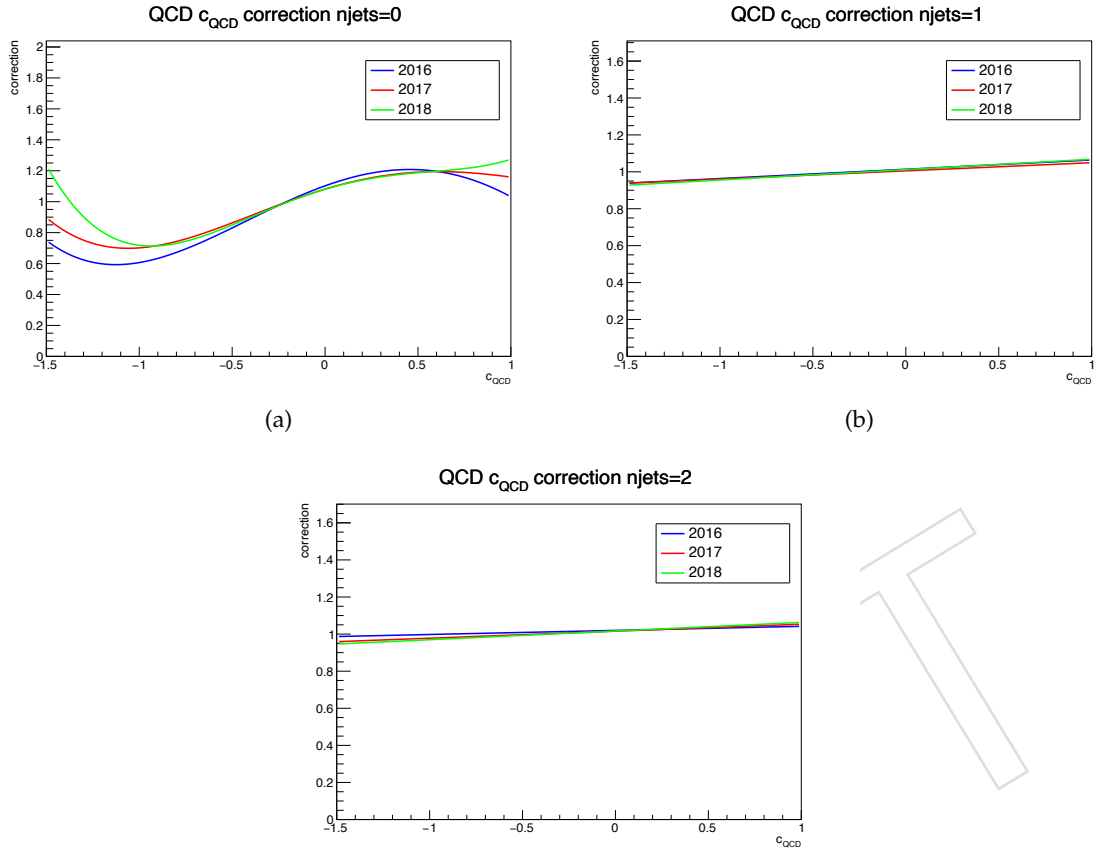

(a) (b)

(c)

Figure 305: The fits of E_T^{miss} closure corrections in the $\tau_h \tau_h$ channel. The fits are shown for events with 0, 1 and ≥ 2 jets in insets a, b, and c respectively.

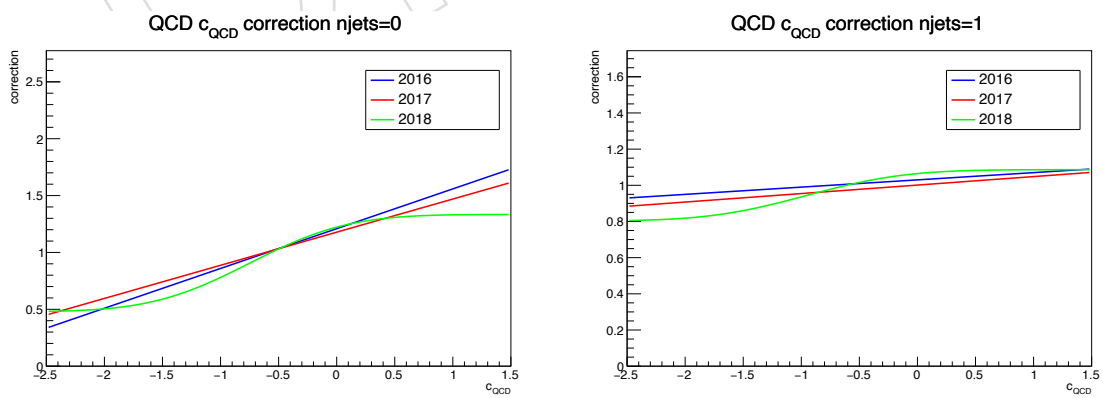

(a) (b)

Figure 306: The fits of E_T^{miss} closure corrections for the QCD fake factors in the $\tau_\mu \tau_h$ channel. The fits are shown for events with 0 and ≥ 1 jets in insets a and b respectively.

DRAFT

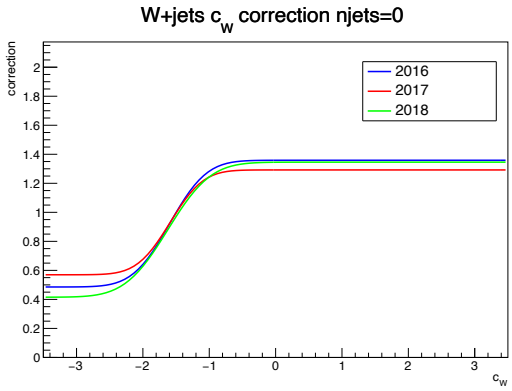

(a)

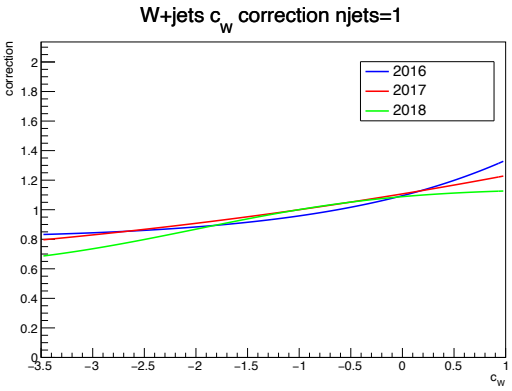

(b)

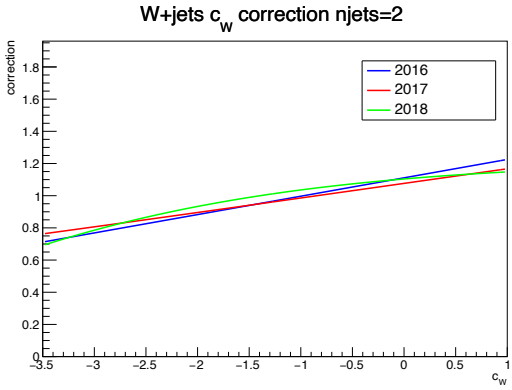

(c)

Figure 307: The fits of $E_{\mathrm{T}}^{\mathrm{miss}}$ closure corrections for the W+jets fake factors in the $\tau_\mu \tau_{\mathrm{h}}$ channel. The fits are shown for events with 0, 1 and ≥ 2 jets in insets a, b, and c respectively.

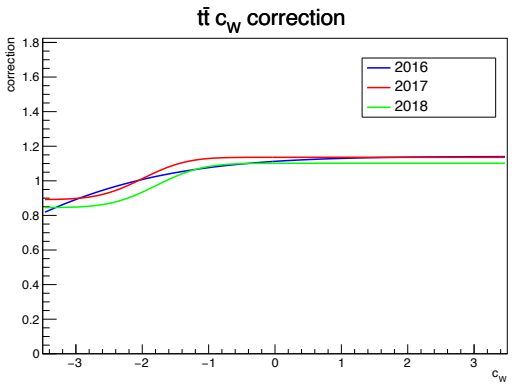

(a)

Figure 308: The fits of $E_{\mathrm{T}}^{\mathrm{miss}}$ closure corrections for the $t\bar{t}$ fake factors in the $\tau_\mu \tau_{\mathrm{h}}$ channel.

DRAFT

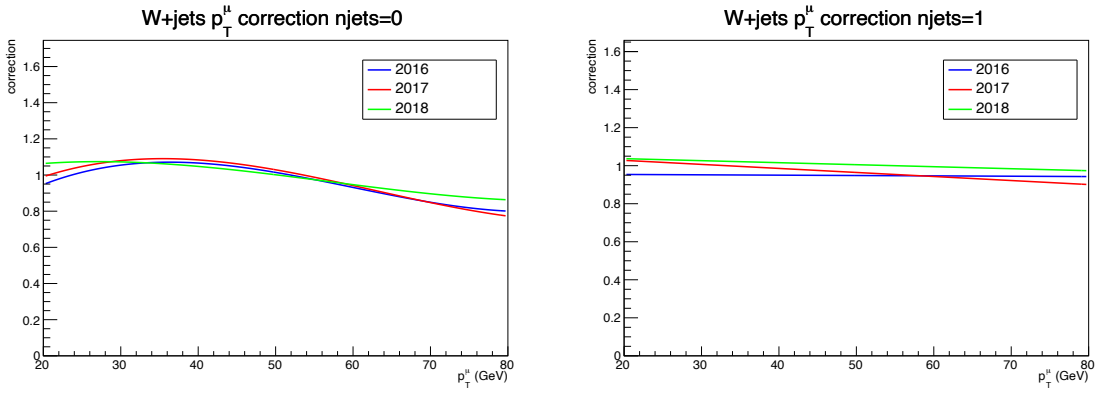

(a) (b)

Figure 309: The fits of p_T^μ closure corrections for the QCD fake factors in the $\tau_\mu \tau_h$ channel. The fits are shown for events with 0 and ≥ 1 jets in insets a and b respectively.

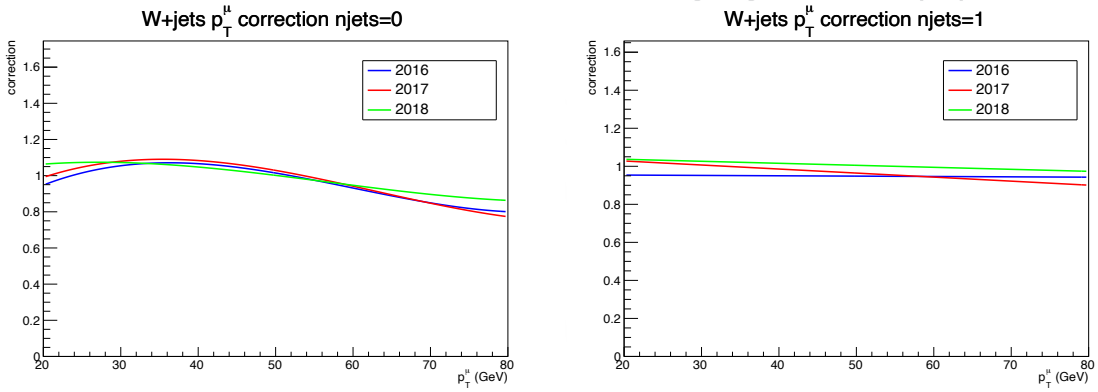

(a) (b)

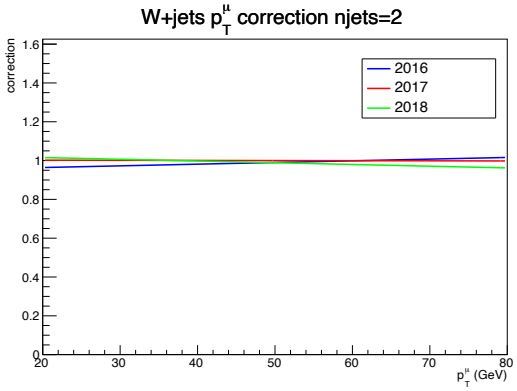

(c)

Figure 310: The fits of p_T^μ closure corrections for the W+jets fake factors in the $\tau_\mu \tau_h$ channel. The fits are shown for events with 0, 1 and ≥ 2 jets in insets a, b, and c respectively.

E.6 Closure corrections in the $\tau_e\tau_h$ channel

The fits of the closure corrections used to correct the $E_{\mathrm{T}}^{\mathrm{miss}}$ related variables for the QCD, W+jets, and $\mathrm{t\bar{t}}$ fake factors in the $\tau_e\tau_{\mathrm{h}}$ channel are shown in Figures 311, 312, and 313 respectively.

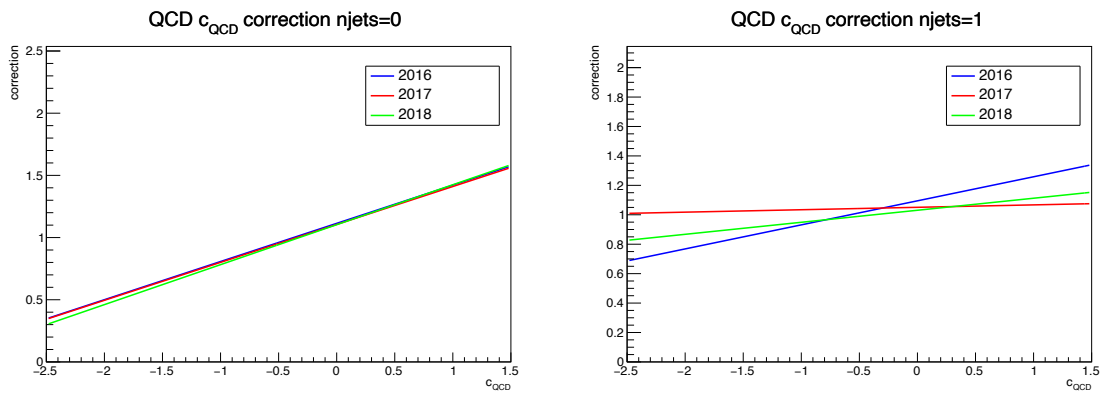

(a) (b)

Figure 311: The fits of $E_{\mathrm{T}}^{\mathrm{miss}}$ closure corrections for the QCD fake factors in the $\tau_e\tau_{\mathrm{h}}$ channel. The fits are shown for events with 0 and ≥ 1 jets in insets a and b respectively.

The fits of the closure corrections used to correct the $E_{\mathrm{T}}^{\mathrm{miss}}$ related variables for the QCD and W+jets fake factors in the $\tau_e\tau_{\mathrm{h}}$ channel are shown in Figures 314 and 315 respectively.

E.7 QCD DR→AR extrapolation corrections in the $\tau_\mu\tau_h$ channel

The fits of the OS/SS corrections used to correct the QCD fake factors in the $\tau_\mu\tau_{\mathrm{h}}$ channel are shown in Figure 316.

The fits of the anti-iso → iso corrections used to correct the QCD fake factors in the $\tau_\mu\tau_{\mathrm{h}}$ channel are shown in Figure 316.

E.8 W+jets DR→AR extrapolation corrections in the $\tau_\mu\tau_h$ channel

The fits of the high-m_{T} → low-m_{T} corrections used to correct the W+jets fake factors in the $\tau_\mu\tau_{\mathrm{h}}$ channel are shown in Figure 318.

E.9 $\mathrm{t\bar{t}}$ DR→AR extrapolation corrections in the $\tau_\mu\tau_h$ channel

The fits of the corrections used to account for differences in the $\mathrm{t\bar{t}}$ fake factors in data and simulation are shown in Figure 319 – 319.

E.10 QCD DR→AR extrapolation corrections in the $\tau_e\tau_h$ channel

The fits of the OS/SS corrections used to correct the QCD fake factors in the $\tau_e\tau_{\mathrm{h}}$ channel are shown in Figure 320.

The fits of the anti-iso → iso corrections used to correct the QCD fake factors in the $\tau_e\tau_{\mathrm{h}}$ channel are shown in Figure 320.

E.11 W+jets DR→AR extrapolation corrections in the $\tau_e\tau_h$ channel

The fits of the high-m_{T} → low-m_{T} corrections used to correct the W+jets fake factors in the $\tau_e\tau_{\mathrm{h}}$ channel are shown in Figure 322.

DRAFT

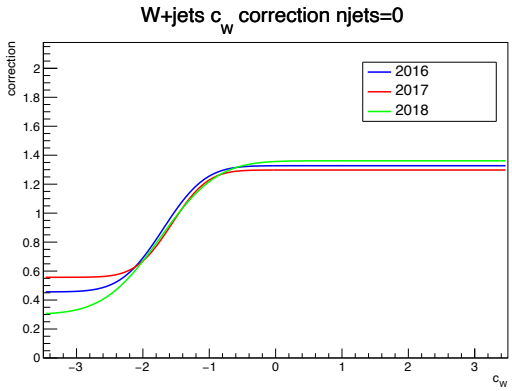

(a)

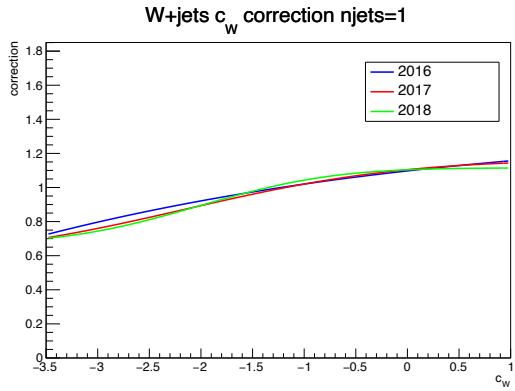

(b)

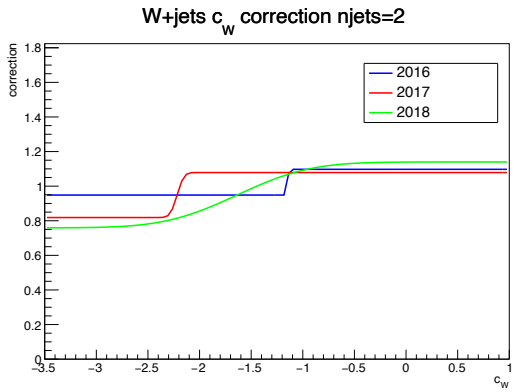

(c)

Figure 312: The fits of $E_{\mathrm{T}}^{\mathrm{miss}}$ closure corrections for the W+jets fake factors in the $\tau_e\tau_{\mathrm{h}}$ channel. The fits are shown for events with 0, 1 and ≥ 2 jets in insets a, b, and c respectively.

DRAFT

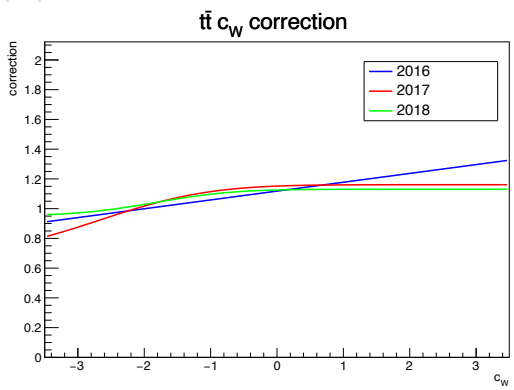

(a)

Figure 313: The fits of $E_{\mathrm{T}}^{\mathrm{miss}}$ closure corrections for the $\mathrm{t\bar{t}}$ fake factors in the $\tau_e\tau_{\mathrm{h}}$ channel.

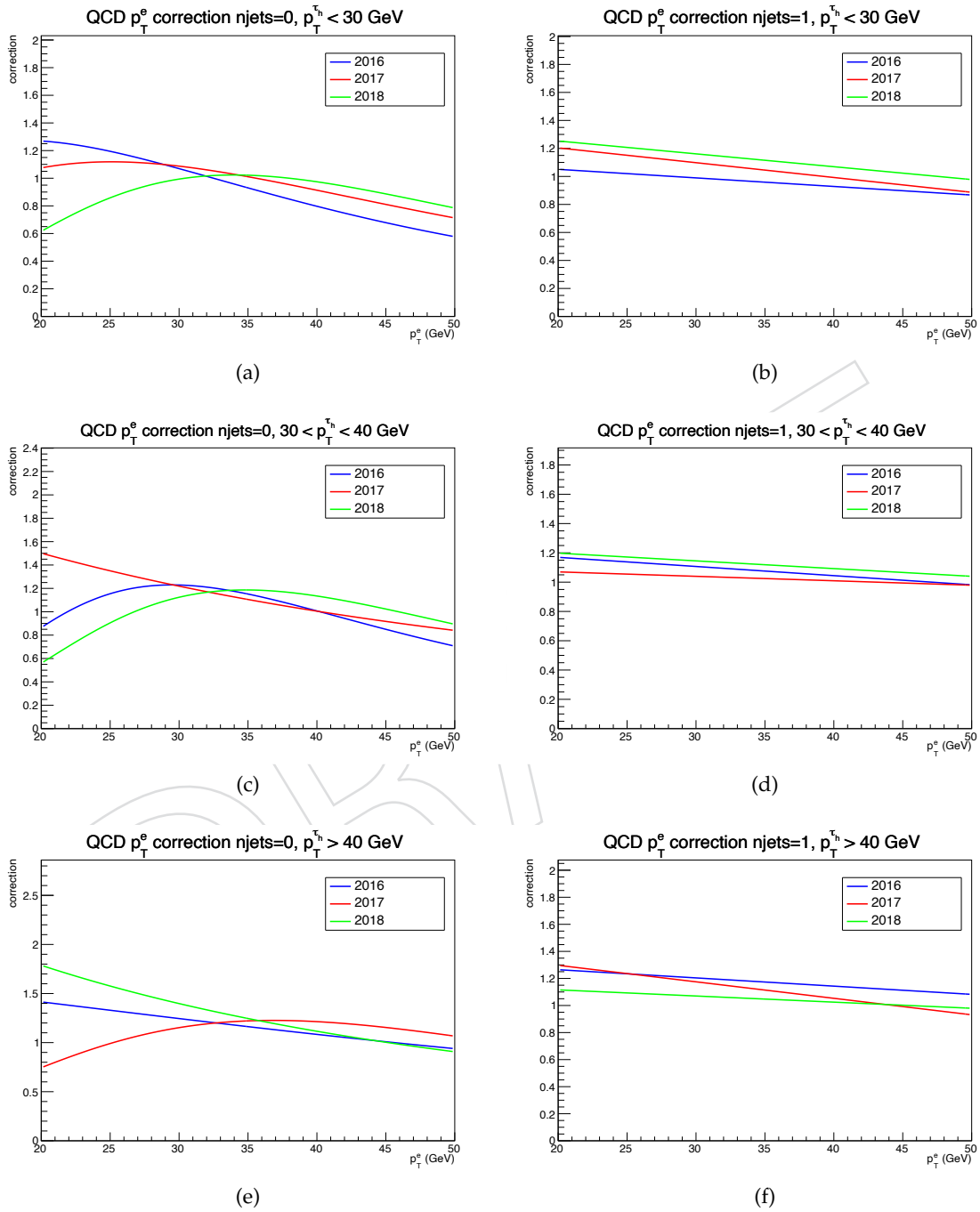

Figure 314: The fits of p_T^e closure corrections for the QCD fake factors in the $\tau_e\tau_h$ channel. The fits are shown for events with 0 and ≥ 1 jets in the left and right insets respectively.

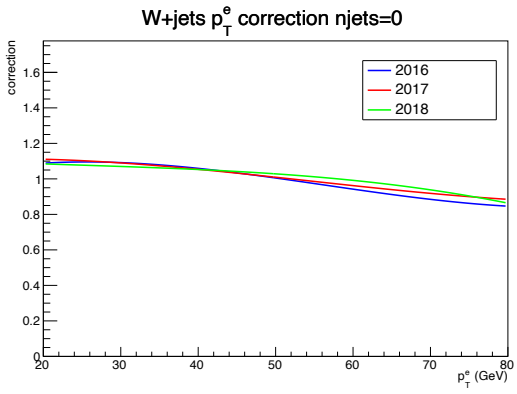

(a)

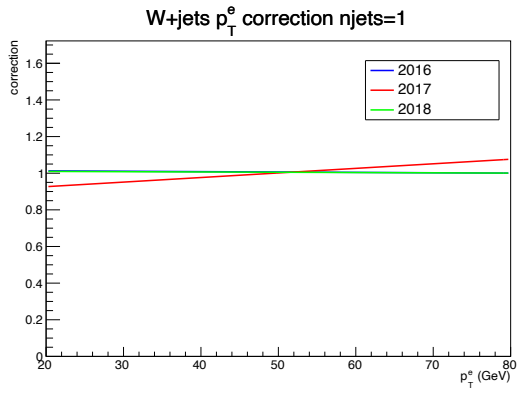

(b)

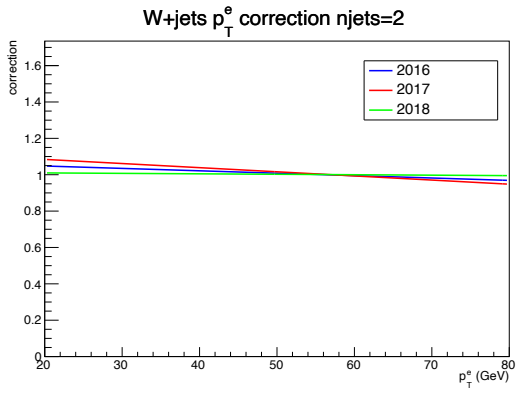

(c)

Figure 315: The fits of p_T^e closure corrections for the W+jets fake factors in the $\tau_e\tau_h$ channel. The fits are shown for events with 0, 1 and ≥ 2 jets in insets a, b, and c respectively.

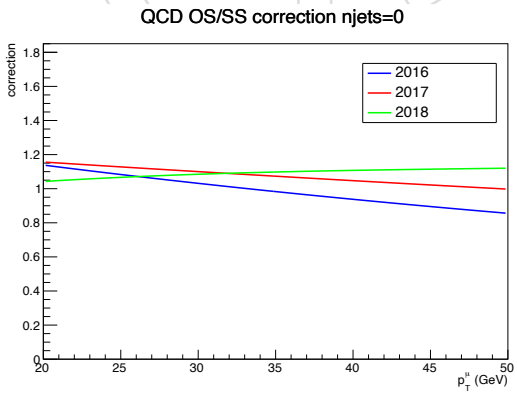

(a)

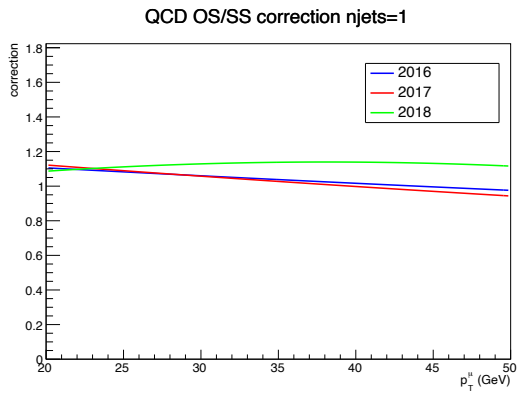

(b)

Figure 316: The fits of OS/SS QCD fake factor corrections in the $\tau_\mu\tau_h$ channel. The fits are shown for events with 0 and ≥ 1 jets in insets a and b respectively.

DRAFT

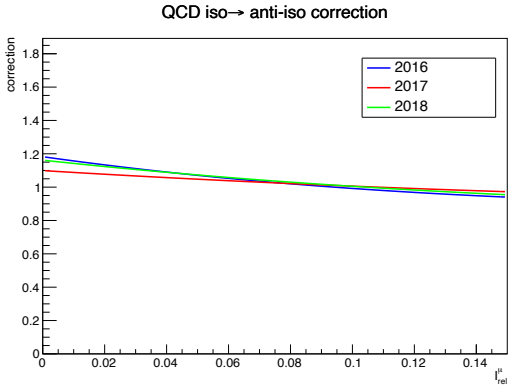

(a)

Figure 317: The fits of anti-iso → iso QCD fake factor corrections in the $\tau_\mu \tau_h$ channel.

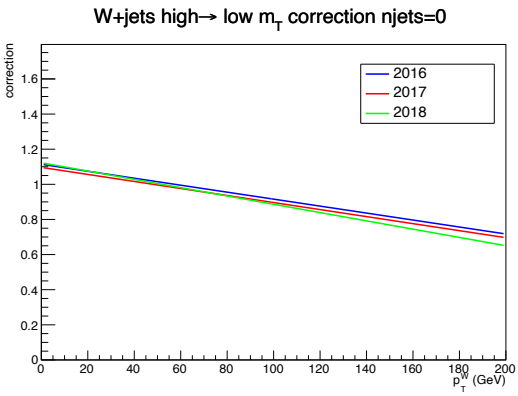

(a)

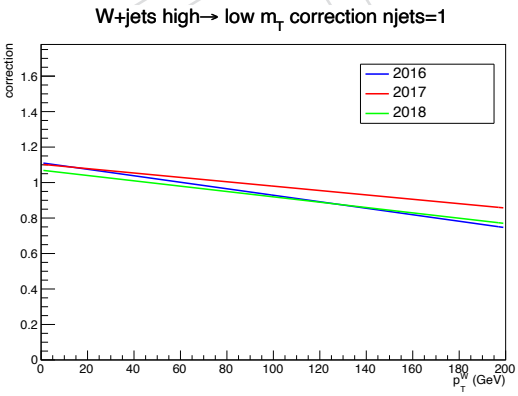

(b)

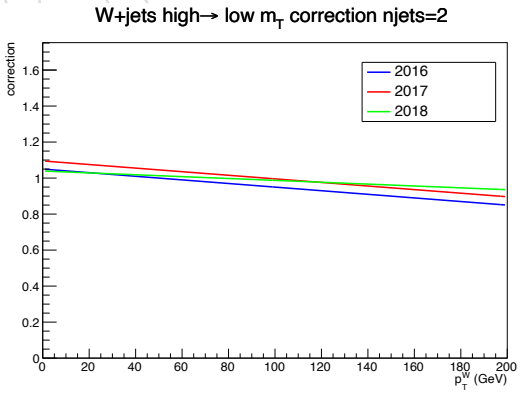

(c)

Figure 318: The fits of high-m_T → low-m_T W+jets fake factor corrections in the $\tau_\mu \tau_h$ channel. The fits are shown for events with 0, 1, and ≥ 2 jets in insets a, b, and c respectively.

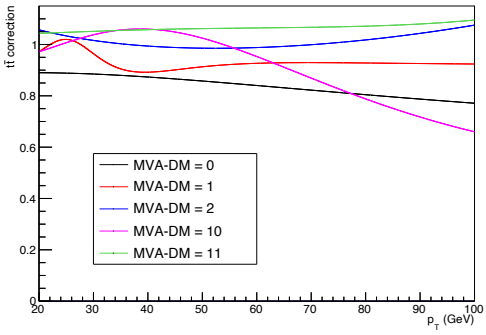

(a) 2016

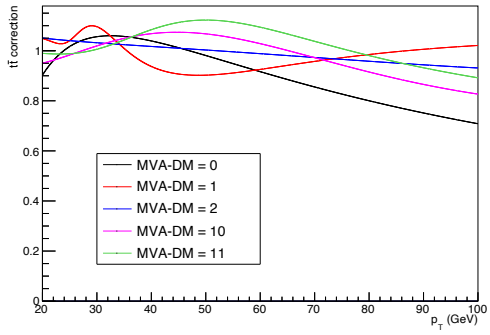

(b) 2017

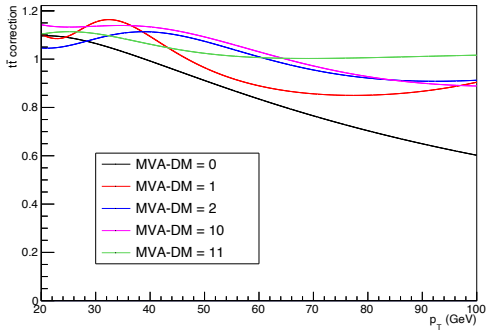

(c) 2018

Figure 319: The corrections applied to the $t\bar{t}$ fake factors to account for differences in fake rates in data and MC. The corrections are derived in bins of MVA-DM.

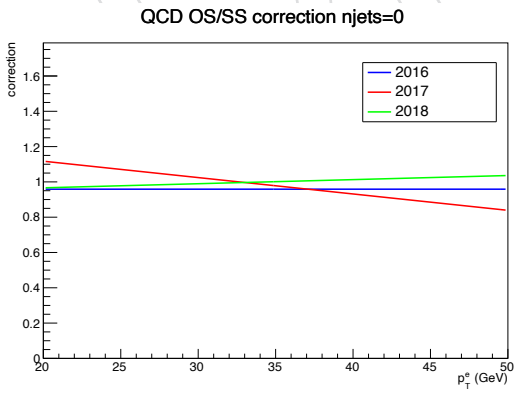

(a)

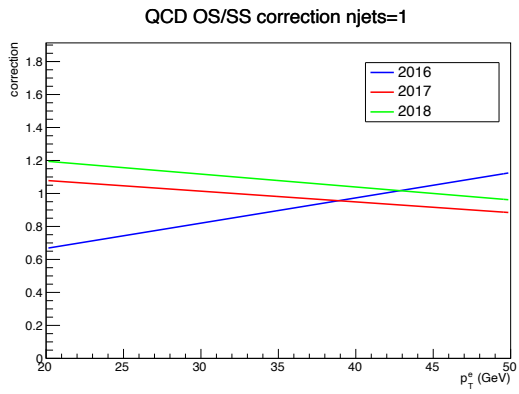

(b)

Figure 320: The fits of OS/SS QCD fake factor corrections in the $\tau_e\tau_h$ channel. The fits are shown for events with 0 and ≥ 1 jets in insets a and b respectively.

DRAFT

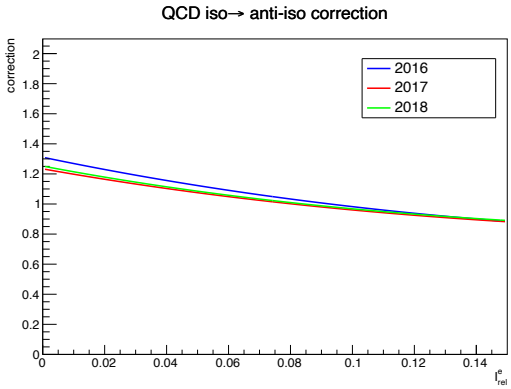

(a)

Figure 321: The fits of anti-iso → iso QCD fake factor corrections in the $\tau_e\tau_h$ channel.

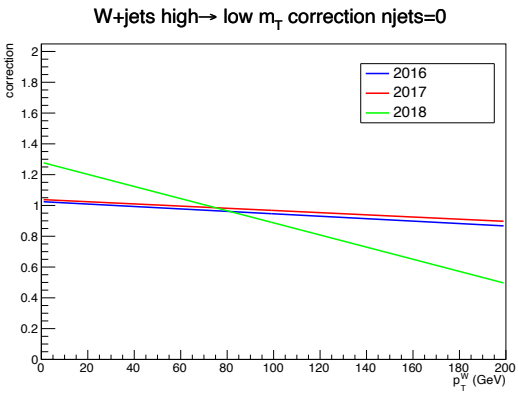

(a)

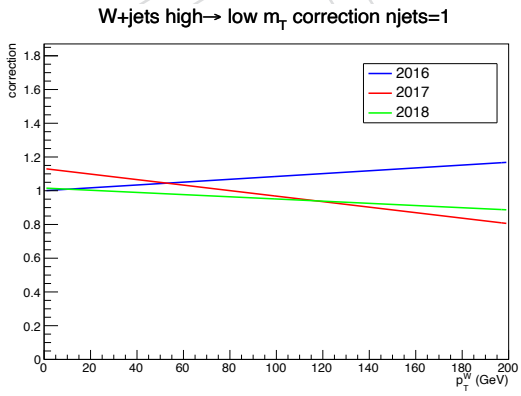

(b)

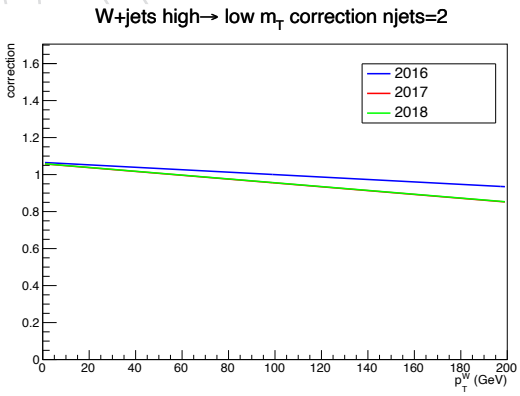

(c)

Figure 322: The fits of high-m_T → low-m_T W+jets fake factor corrections in the $\tau_e\tau_h$ channel. The fits are shown for events with 0, 1, and ≥ 2 jets in insets a, b, and c respectively.

E.12 $t\bar{t}$ DR→AR extrapolation corrections in the $\tau_e\tau_h$ channel

The fits of the corrections used to account for differences in the $t\bar{t}$ fake factors in data and simulation are shown in Figure 323 – 323.

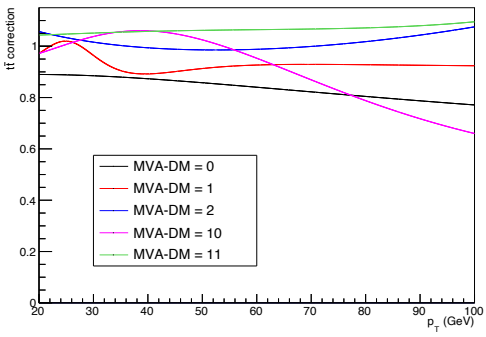

(a) 2016

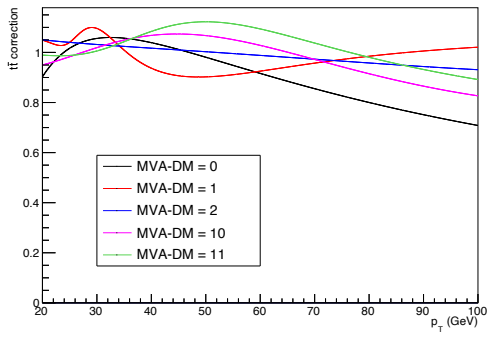

(b) 2017

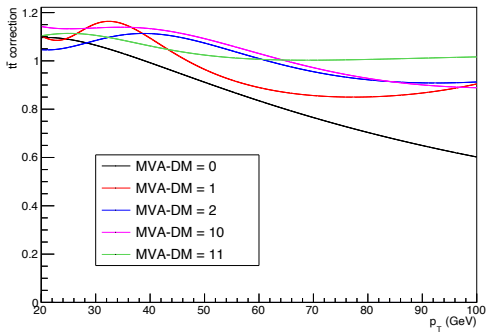

(c) 2018

Figure 323: The corrections applied to the $t\bar{t}$ fake factors to account for differences in fake rates in data and MC. The corrections are derived in bins of MVA-DM.

DRAFT

F CP measurement in the $a_1^{3pr} - a_1^{3pr}$ channel using the polarimetric vector method

The same selection criteria as for the decay plane method are applied for the polarimetric vector method, except that the presence of a secondary vertex is required for each tau. This allows to reconstruct precisely the tau momenta of the $a_1^{3pr} a_1^{3pr}$ decays as described in section 4.9. The event categorisation is applied as throughout the analysis and described in section 10.1. Each event is assigned to a category depending on the highest BDT score. BDT score distributions for the $a_1^{3pr} a_1^{3pr}$ channel can be found in Fig. 324 – 326.

Control plots for all variables used in the trainings of the BDT in the $a_1^{3pr} a_1^{3pr}$ channel are shown in Fig. 327– 330.

The three components of the vector constructed by the secondary and the primary vertex positions are shown in Fig. 331 – 333. $\mu\tau_h$ events are considered in order to check the modelling of secondary vertices for genuine hadronic taus. Similarly 334 – 336 show the same distributions for $a_1^{3pr} a_1^{3pr}$ channel which is dominated by fake taus. The agreement between data and simulation is found to be good.

As the QCD fake factors used were derived for the decay plane method, without requiring the presence of tau secondary vertices, same sign events, which are enriched in fake taus, are shown in Fig. 337 for the BDT score distributions of the fakes category. We observe that the yields agree when the additional SV requirement is added.

The set of prefit plots fitted in the analysis in the $a_1^{3pr} a_1^{3pr}$ channel for the polarimetric vector method are shown in Fig. 338 – 340. Other prefit plots which are not fitted (fully unblinded) are shown in Fig. 341 – 346 The sensitivity comparisons without shape systematics between the decay plane method and the polarimetric vector method are given in Fig. 347 – 348. Symmetrising is used for all signal and background templates (except anti-symmetrisation for the CP-mixed Higgs samples). For the full Run 2, the use of the polarimetric vector method for the $a_1^{3pr} a_1^{3pr}$ channel improves significantly the sensitivity, from 0.17σ to 0.28σ.

The impacts and constraints for the first 90 nuissance parameters are shown in Fig. 349 – 351. The goodness-of-fit (GOF) tests with a saturated model in the signal category for each year are in Fig. 352 – 354 and in the signal and backgrounds categories for the Run 2 in Fig. 355. The GOF tests are satisfactory. The observed likelihood scans for the parameters rates μ_{ggH} and μ_V, the common rate parameter μ_{tautau} and the angle α representing $\phi_{\tau\tau}$ are in Fig. 356 – 359. A $\phi_{\tau\tau}$ angle of $80.5^{\circ}{}^{+9.5^{\circ}}_{-35.6^{\circ}}$ is observed and can be explained by a high μ_{tautau} value and statistical fluctuations of data towards Higgs CP-odd. This measure should be constrained in the global fit.

DRAFT

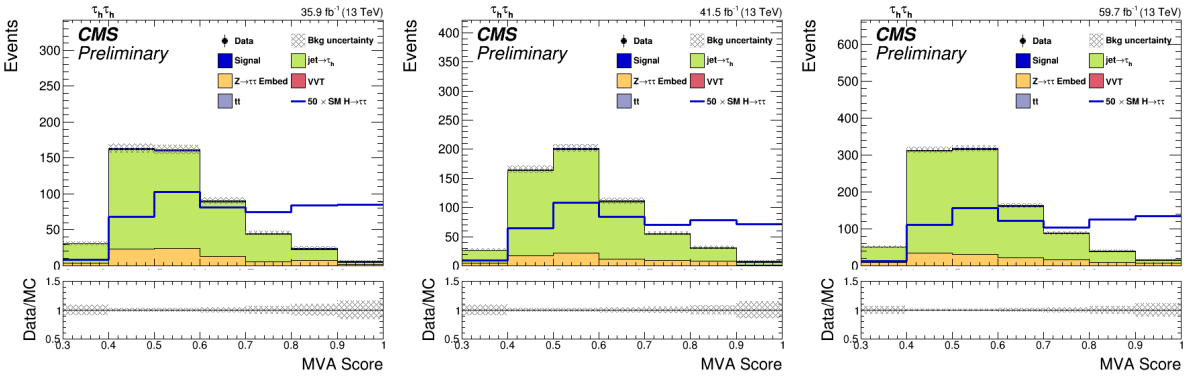

(a) 2016 (b) 2017 (c) 2018

Figure 324: Classification BDT scores in the higgs category of the $a_1^{3pr} a_1^{3pr}$ channel for 2016, 2017 and 2018. The signals are scaled by a factor of 50 and the uncertainty band considers only statistical uncertainty.

DRAFT

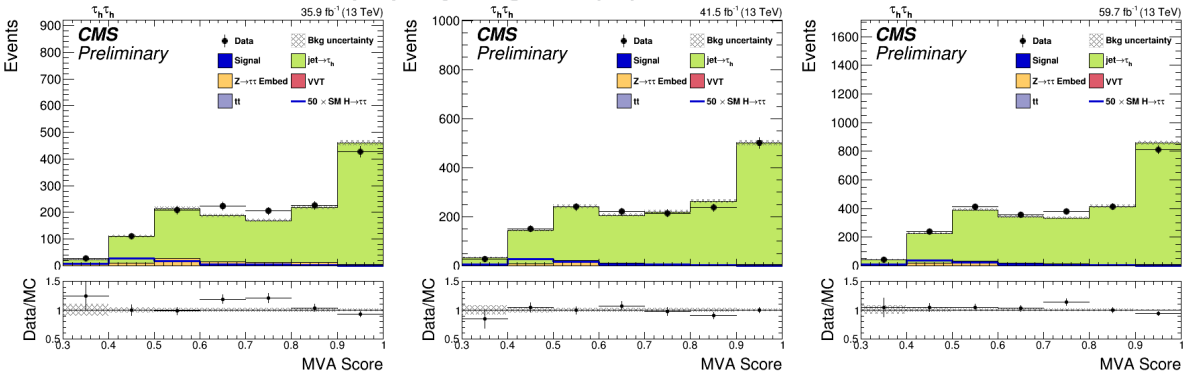

(a) 2016 (b) 2017 (c) 2018

Figure 325: Classification BDT scores in the jet fakes category of the $a_1^{3pr} a_1^{3pr}$ channel for 2016, 2017 and 2018. The signals are scaled by a factor of 50 and the uncertainty band considers only statistical uncertainty.

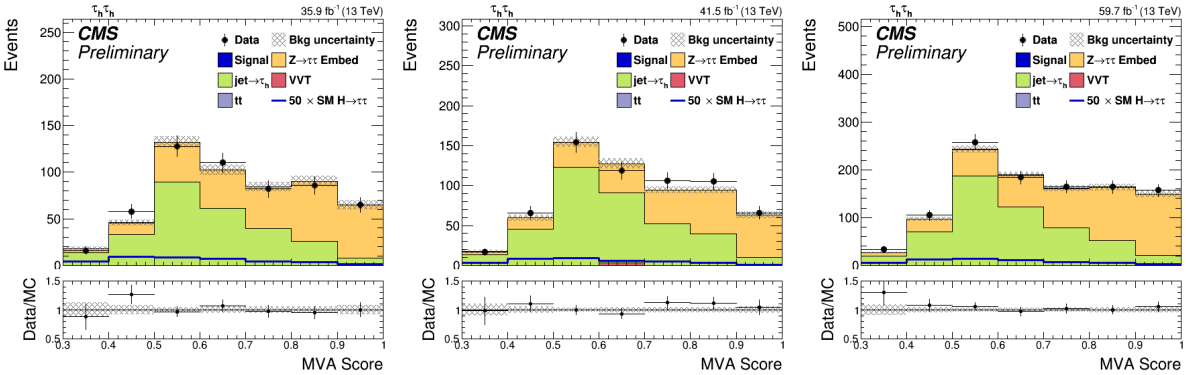

(a) 2016 (b) 2017 (c) 2018

Figure 326: Classification BDT scores in the $Z \to \tau\tau$ embedded category of the $a_1^{3pr} a_1^{3pr}$ channel for 2016, 2017 and 2018. The signals are scaled by a factor of 50 and the uncertainty band considers only statistical uncertainty.

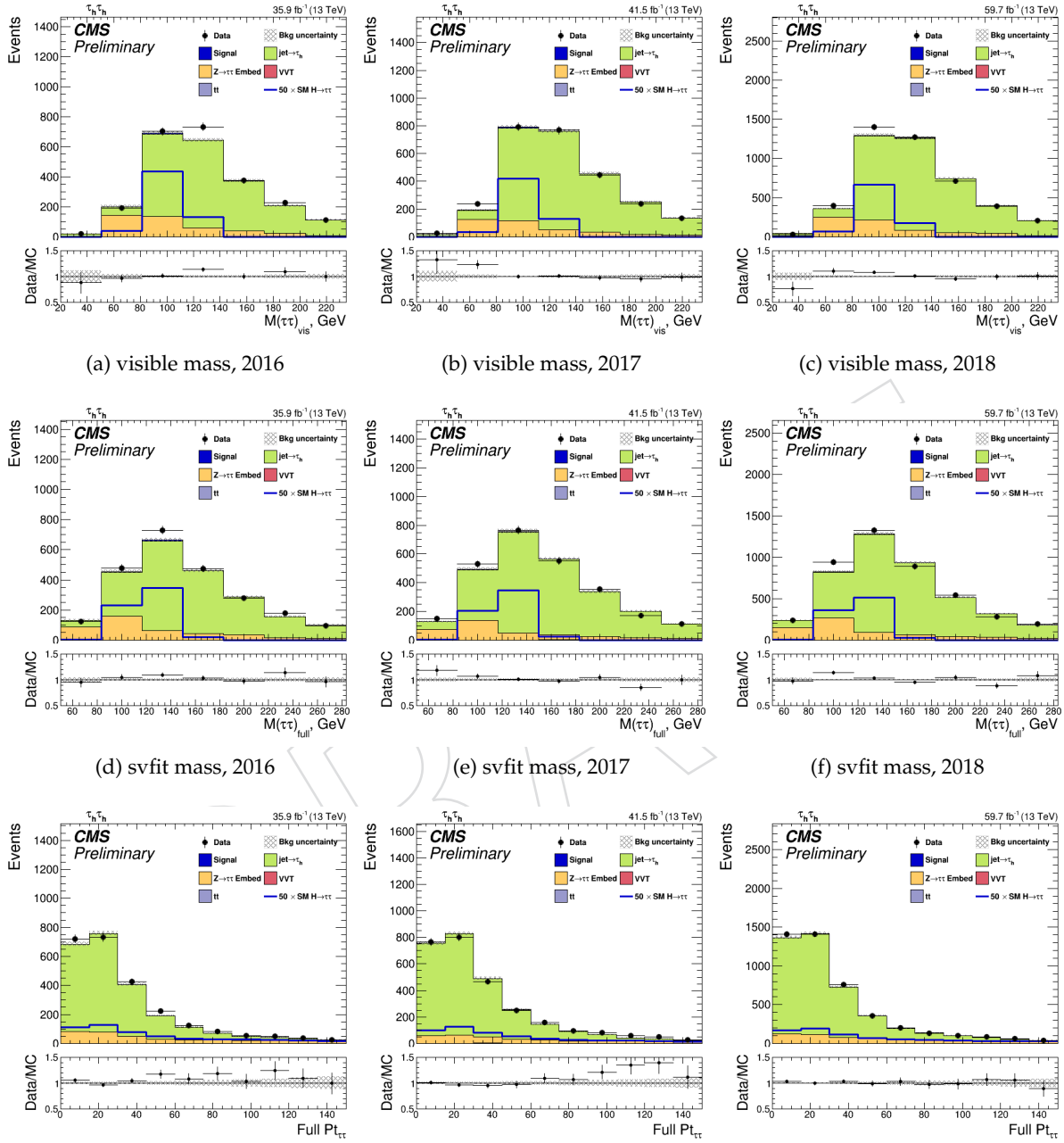

(a) visible mass, 2016 (b) visible mass, 2017 (c) visible mass, 2018

(d) svfit mass, 2016 (e) svfit mass, 2017 (f) svfit mass, 2018

(g) higgs p_T, 2016 (h) higgs p_T, 2017 (i) higgs p_T, 2018

Figure 327: Prefit plots for 2016, 2017 and 2018 of the input features to the BDT in the $a_1^{3pr} a_1^{3pr}$ channel. The signals are scaled by a factor of 50 and the uncertainty band considers only statistical uncertainty.

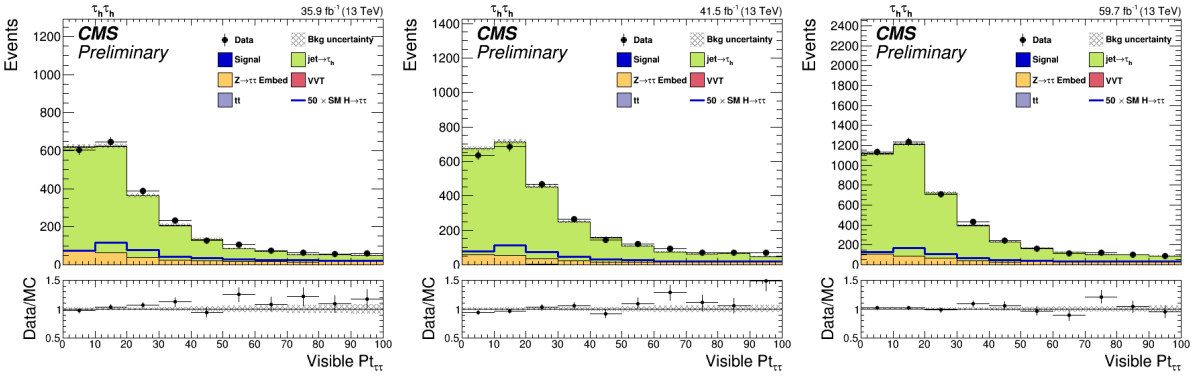

(a) visible p_T, 2016

(b) visible p_T, 2017

(c) visible p_T, 2018

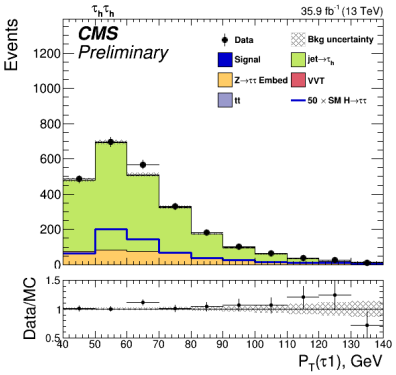

(d) τ p_T, 2016

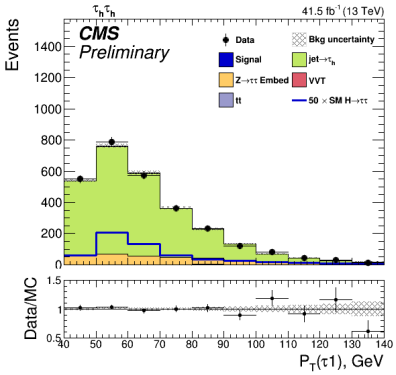

(e) τ p_T, 2017

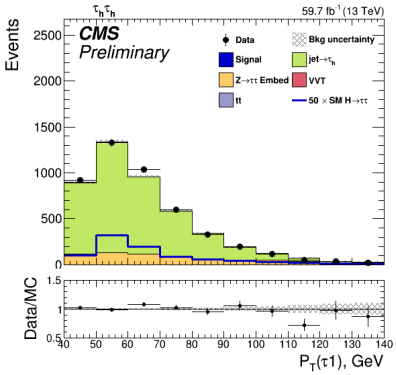

(f) τ p_T, 2018

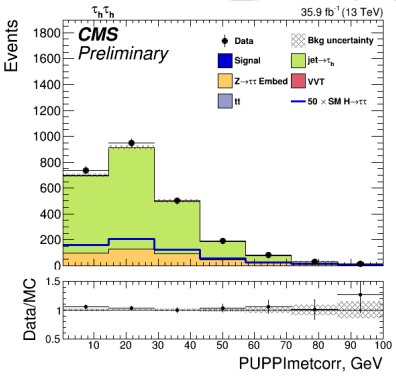

(g) p_T^{miss}, 2016

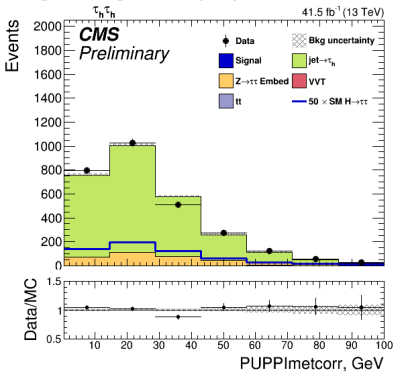

(h) p_T^{miss}, 2017

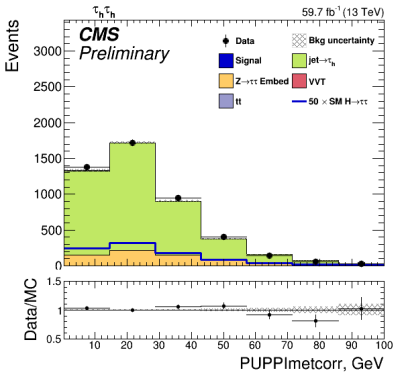

(i) p_T^{miss}, 2018

Figure 328: Prefit plots for 2016, 2017 and 2018 of the input features to the BDT in the $a_1^{3pr} a_1^{3pr}$ channel. The signals are scaled by a factor of 50 and the uncertainty band considers only statistical uncertainty.

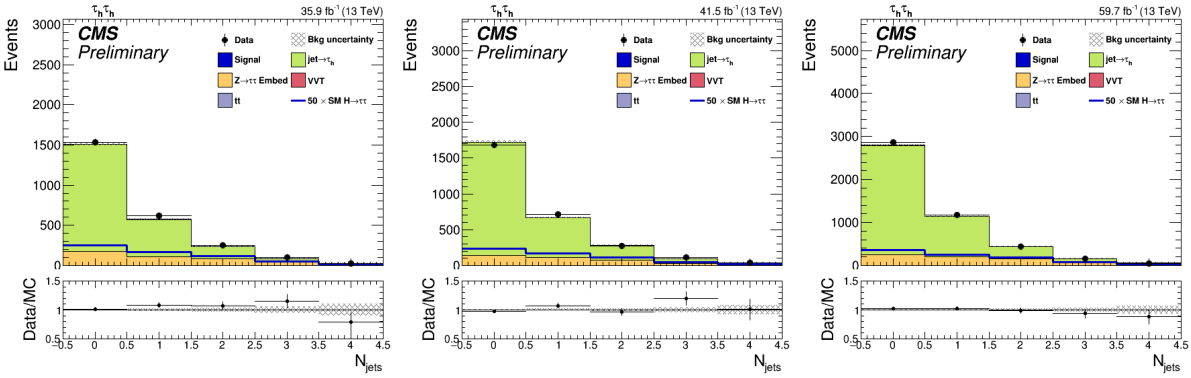

(a) number of jets, 2016

(b) number of jets, 2017

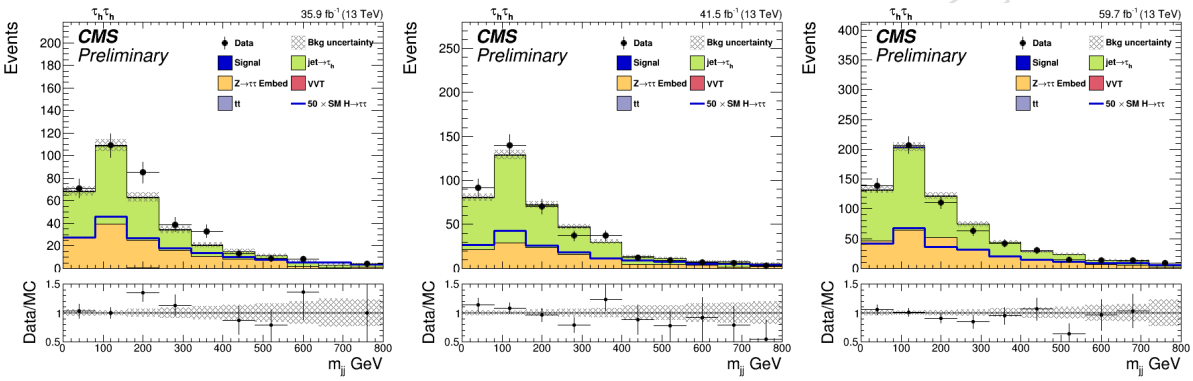

(c) number of jets, 2018

(d) dijet mass, 2016

(e) dijet mass, 2017

(f) dijet mass, 2018

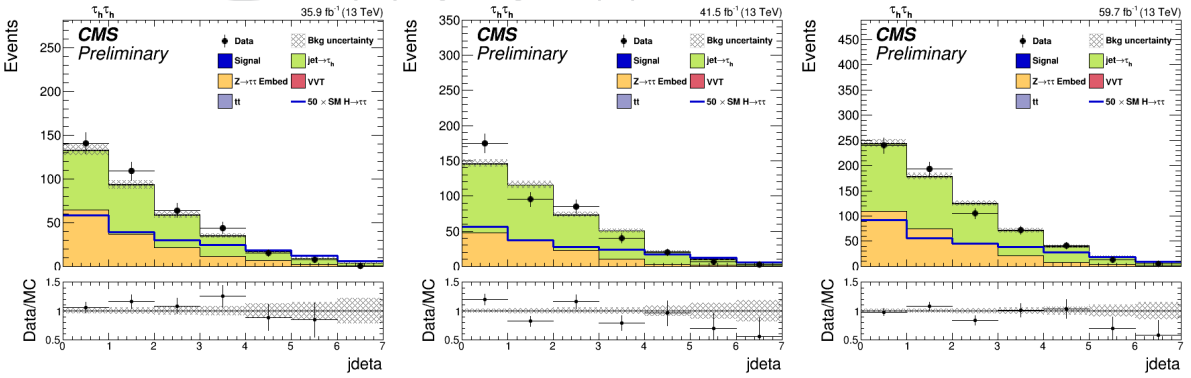

(g) $|\Delta\eta|$ of jets, 2016

(h) $|\Delta\eta|$ of jets, 2017

(i) $|\Delta\eta|$ of jets, 2018

Figure 329: Prefit plots for 2016, 2017 and 2018 of the input features to the BDT in the $a_1^{3pr} a_1^{3pr}$ channel. The signals are scaled by a factor of 50 and the uncertainty band considers only statistical uncertainty.

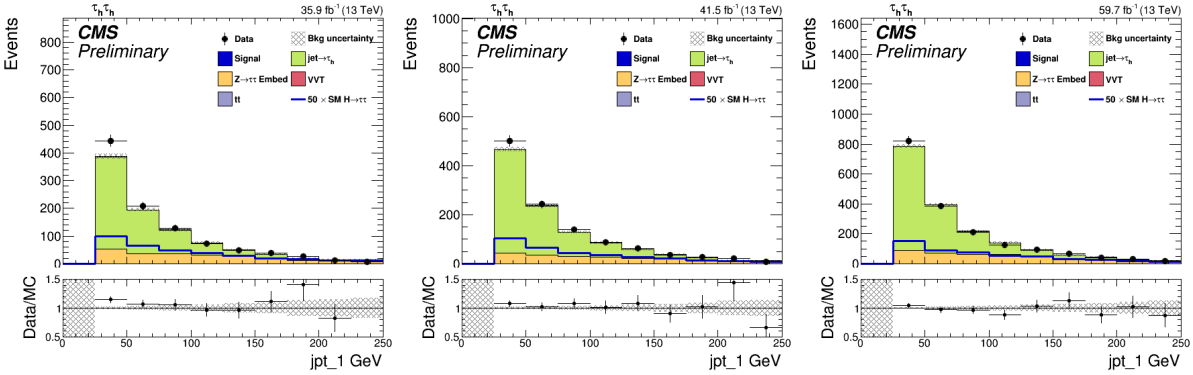

(a) leading jet p_T, 2016 (b) leading jet p_T, 2017 (c) leading jet p_T, 2018

Figure 330: Prefit plots for 2016, 2017 and 2018 of the input features to the BDT in the $a_1^{3pr} a_1^{3pr}$ channel. The signals are scaled by a factor of 50 and the uncertainty band considers only statistical uncertainty.

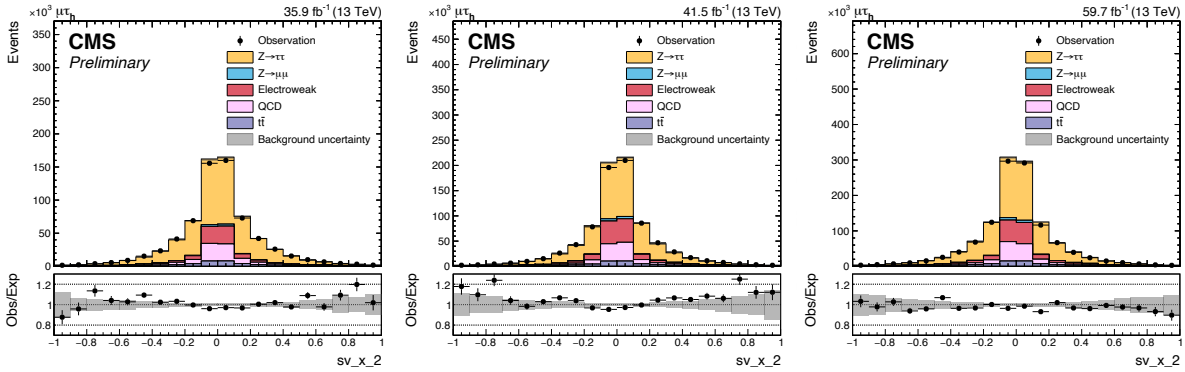

(a) 2016 (b) 2017 (c) 2018

Figure 331: Control plots for 2016, 2017 and 2018 of SV_x minus PV_x in the inclusive $\mu\tau_h$ channel. The uncertainty band considers only statistical uncertainty.

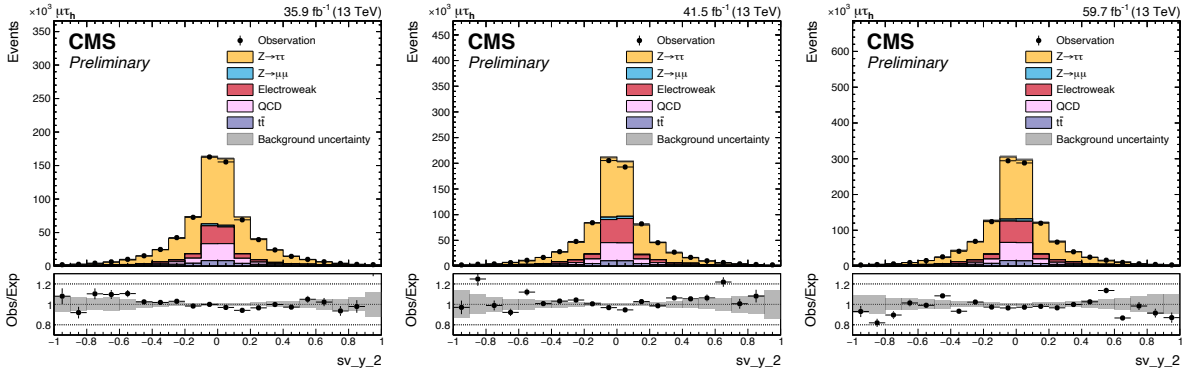

(a) 2016 (b) 2017 (c) 2018

Figure 332: Control plots for 2016, 2017 and 2018 of SV_y minus PV_y in the inclusive $\mu\tau_h$ channel. The uncertainty band considers only statistical uncertainty.

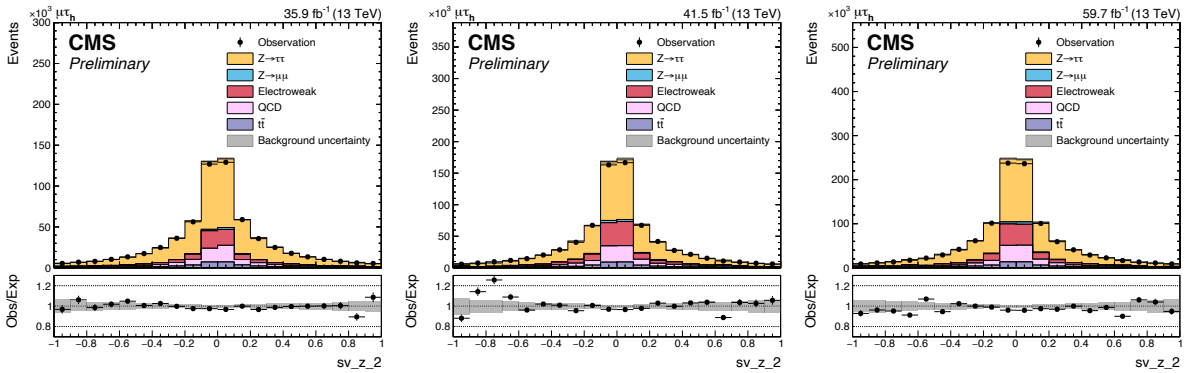

(a) 2016 (b) 2017 (c) 2018

Figure 333: Control plots for 2016, 2017 and 2018 of SV_z minus PV_z in the inclusive $\mu\tau_h$ channel. The uncertainty band considers only statistical uncertainty.

DRAFT

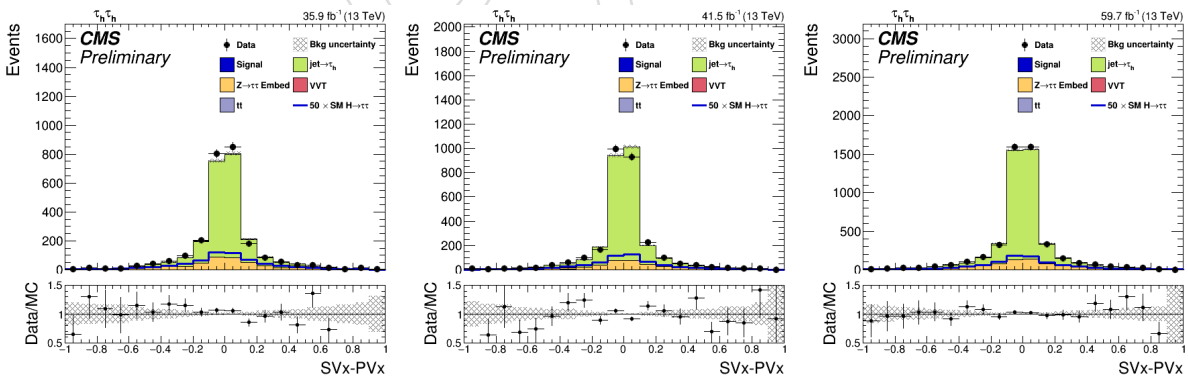

(a) 2016 (b) 2017 (c) 2018

Figure 334: Prefit plots for 2016, 2017 and 2018 of SV_x minus PV_x in the inclusive $a_1^{3pr}a_1^{3pr}$ channel for the subleading tau. The signals are scaled by a factor of 50 and the uncertainty band considers only statistical uncertainty.

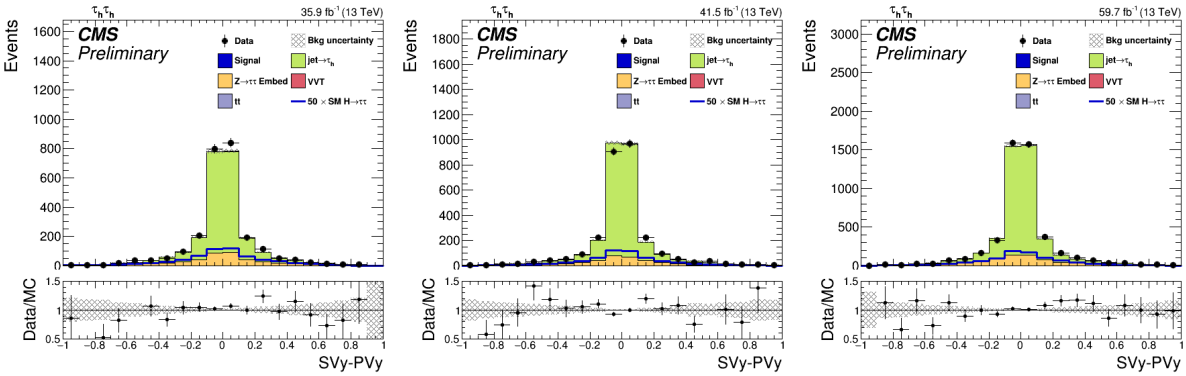

(a) 2016 (b) 2017 (c) 2018

Figure 335: Prefit plots for 2016, 2017 and 2018 of SV_y minus PV_y in the inclusive $a_1^{3pr} a_1^{3pr}$ channel for the subleading tau. The signals are scaled by a factor of 50 and the uncertainty band considers only statistical uncertainty.

DRAFT

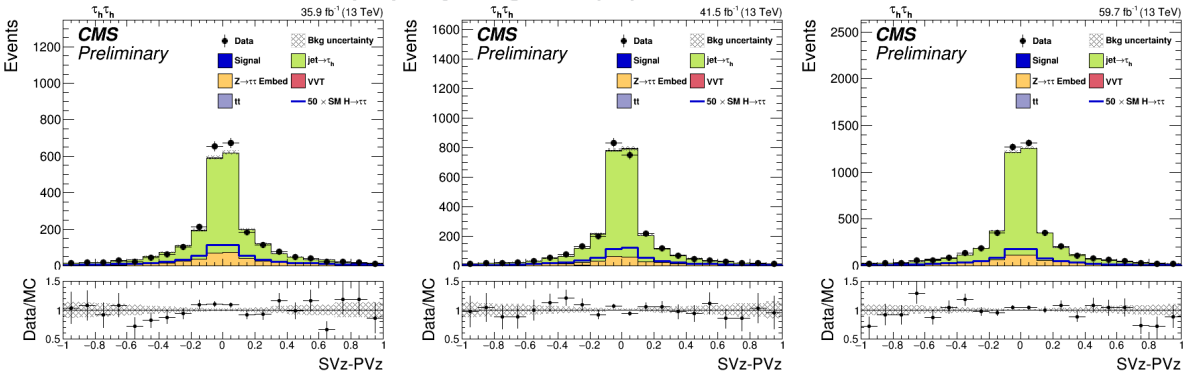

(a) 2016 (b) 2017 (c) 2018

Figure 336: Prefit plots for 2016, 2017 and 2018 of SV_z minus PV_z in the inclusive $a_1^{3pr} a_1^{3pr}$ channel for the subleading tau. The signals are scaled by a factor of 50 and the uncertainty band considers only statistical uncertainty.

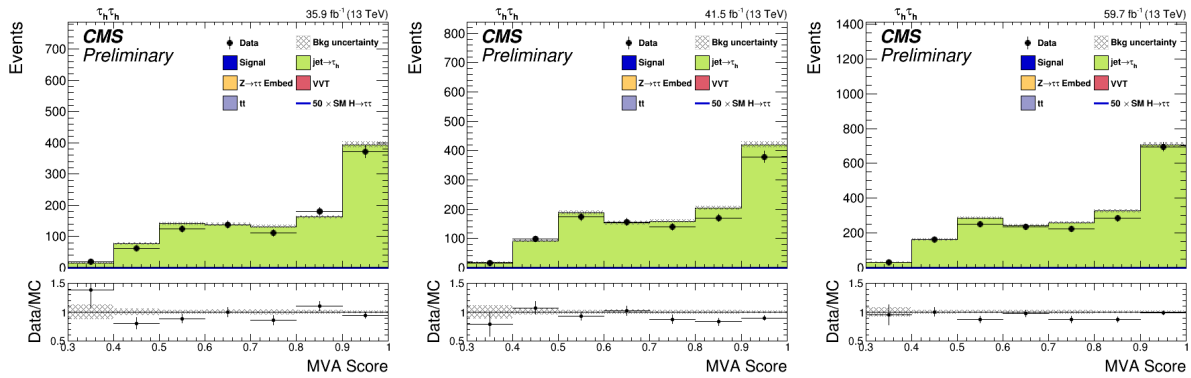

(a) 2016 (b) 2017 (c) 2018

Figure 337: Classification BDT scores in the jet fakes category of the $a_1^{3pr} a_1^{3pr}$ channel for 2016, 2017 and 2018 with same sign events. The signals are scaled by a factor of 50 and the uncertainty band considers only statistical uncertainty.

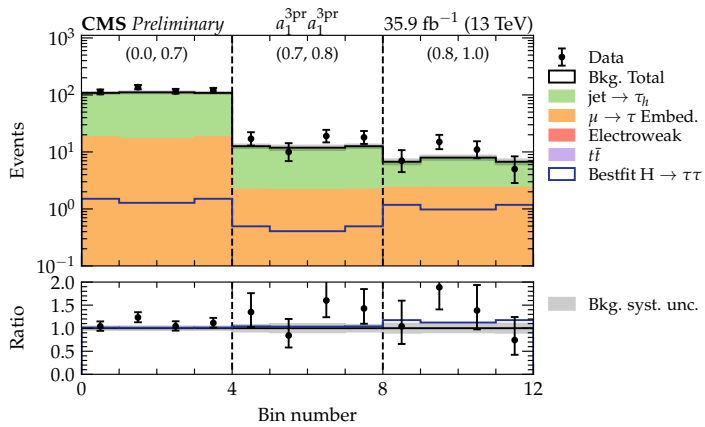

Figure 338: Distribution (prefit) of ϕ_{CP} of the $a_1^{3pr} a_1^{3pr}$ channel in the higgs category for 2016, in windows of increasing NN score. The x-axis represents the cyclic bins in ϕ_{CP} in the range of (0, 2π). The uncertainty band represents the full uncertainty.

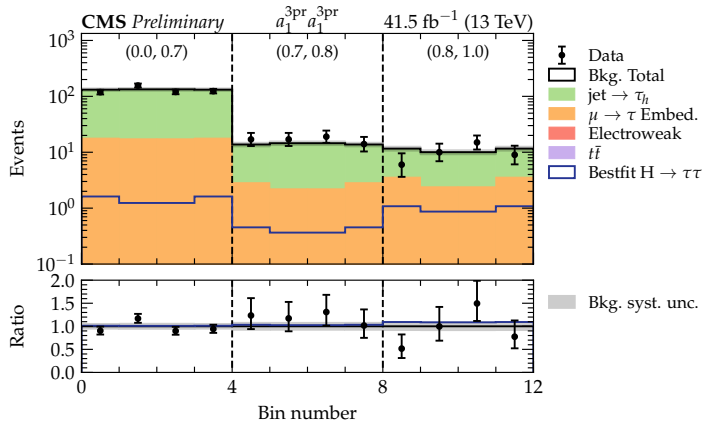

Figure 339: Distribution (prefit) of ϕ_{CP} of the $a_1^{3pr} a_1^{3pr}$ channel in the higgs category for 2017, in windows of increasing NN score. The x-axis represents the cyclic bins in ϕ_{CP} in the range of (0, 2π). The uncertainty band represents the full uncertainty.

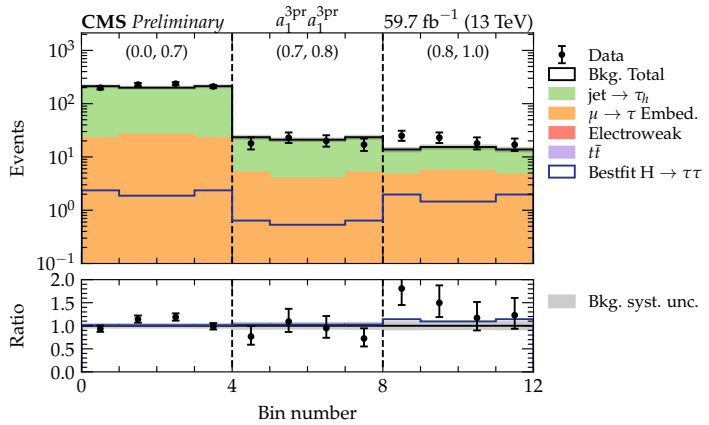

Figure 340: Distribution (prefit) of ϕ_{CP} of the $a_1^{3pr} a_1^{3pr}$ channel in the higgs category for 2018, in windows of increasing NN score. The x-axis represents the cyclic bins in ϕ_{CP} in the range of (0, 2π). The uncertainty band represents the full uncertainty.

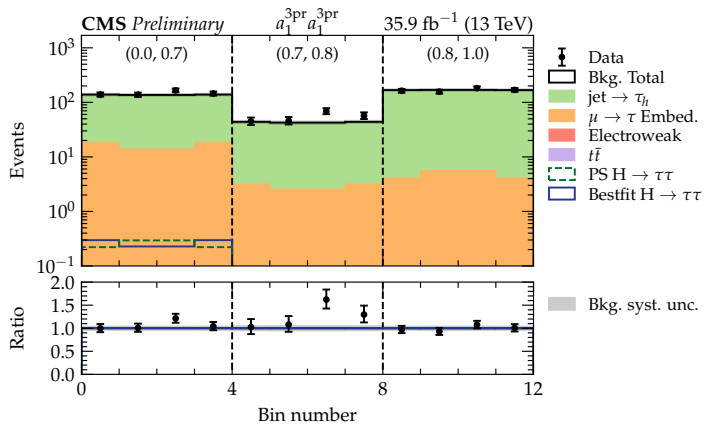

Figure 341: Distribution (prefit) of ϕ_{CP} of the $a_1^{3pr} a_1^{3pr}$ channel in the fakes category for 2016, in windows of increasing NN score. The x-axis represents the cyclic bins in ϕ_{CP} in the range of (0, 2π). The uncertainty band represents the full uncertainty.

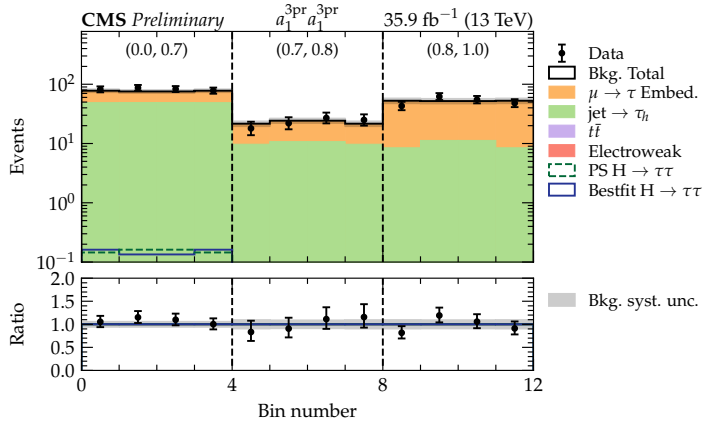

Figure 342: Distribution (prefit) of ϕ_{CP} of the $a_1^{3pr} a_1^{3pr}$ channel in the ztt for 2016, in windows of increasing NN score. The x-axis represents the cyclic bins in ϕ_{CP} in the range of $(0, 2\pi)$. The uncertainty band represents the full uncertainty.

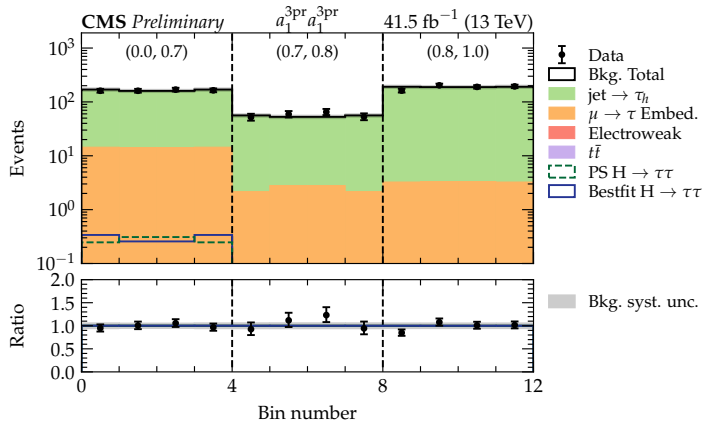

Figure 343: Distribution (prefit) of ϕ_{CP} of the $a_1^{3pr} a_1^{3pr}$ channel in the fakes for 2017, in windows of increasing NN score. The x-axis represents the cyclic bins in ϕ_{CP} in the range of $(0, 2\pi)$. The uncertainty band represents the full uncertainty.

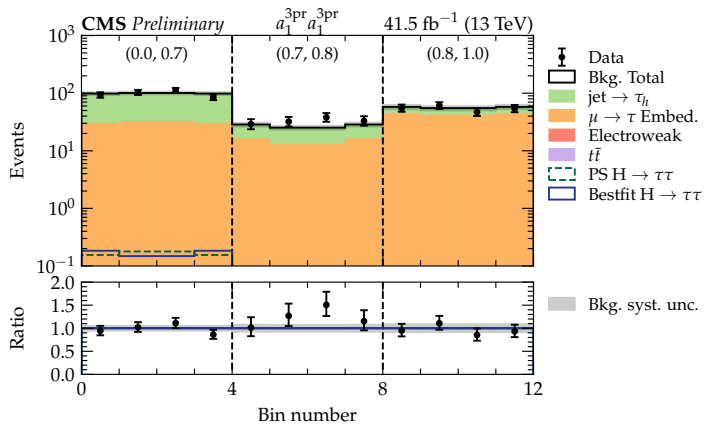

Figure 344: Distribution (prefit) of ϕ_{CP} of the $a_1^{3pr} a_1^{3pr}$ channel in the ztt for 2017, in windows of increasing NN score. The x-axis represents the cyclic bins in ϕ_{CP} in the range of $(0, 2\pi)$. The uncertainty band represents the full uncertainty.

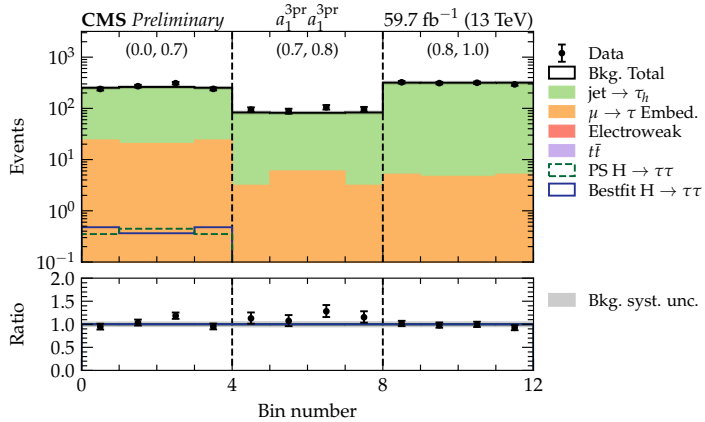

Figure 345: Distribution (prefit) of ϕ_{CP} of the $a_1^{3pr} a_1^{3pr}$ channel in the fakes for 2018, in windows of increasing NN score. The x-axis represents the cyclic bins in ϕ_{CP} in the range of $(0, 2\pi)$. The uncertainty band represents the full uncertainty.

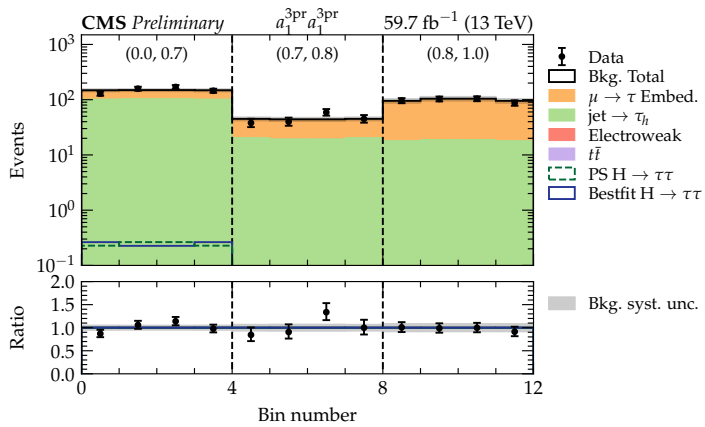

Figure 346: Distribution (prefit) of ϕ_{CP} of the $a_1^{3pr} a_1^{3pr}$ channel in the ztt for 2018, in windows of increasing NN score. The x-axis represents the cyclic bins in ϕ_{CP} in the range of $(0, 2\pi)$. The uncertainty band represents the full uncertainty.

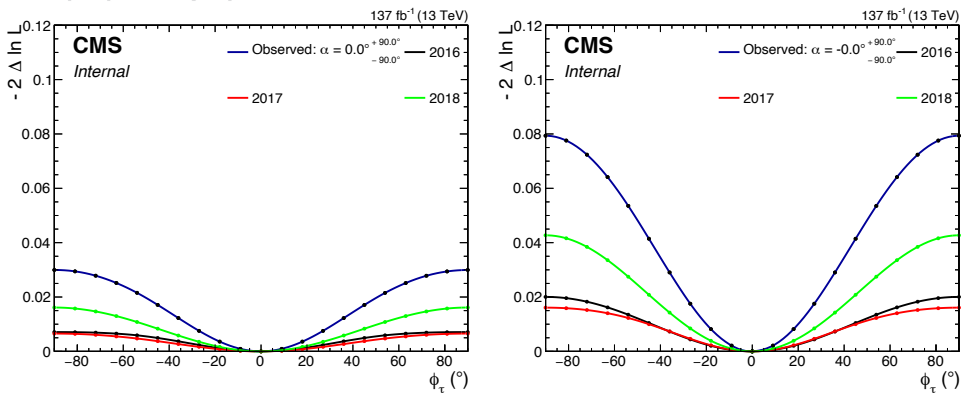

Figure 347: Sensitivities obtained for each year with the decay plane method (left) and the polarimetric vector method (right) in the $a_1^{3pr} a_1^{3pr}$ channel without shape systematics.

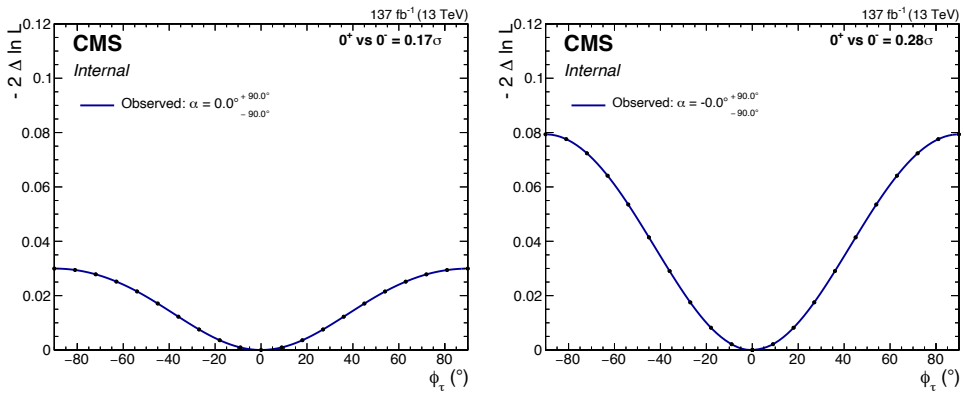

Figure 348: Sensitivities obtained for all years combined with the decay plane method (left) and the polarimetric vector method (right) in the $a_1^{3pr} a_1^{3pr}$ channel without shape systematics.

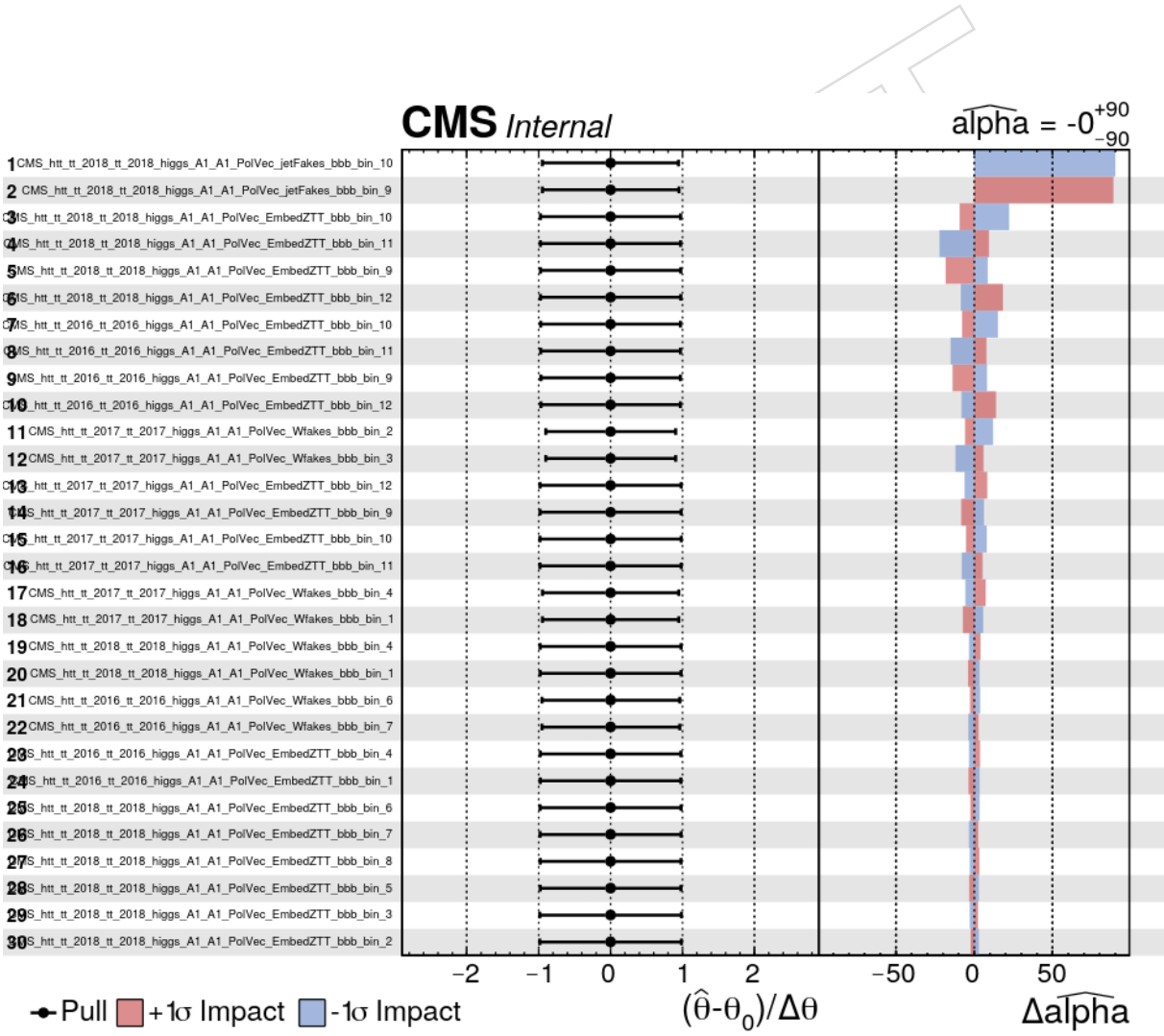

Figure 349: Impacts and constraints of the 1-30 ranked for nuissance parameters.

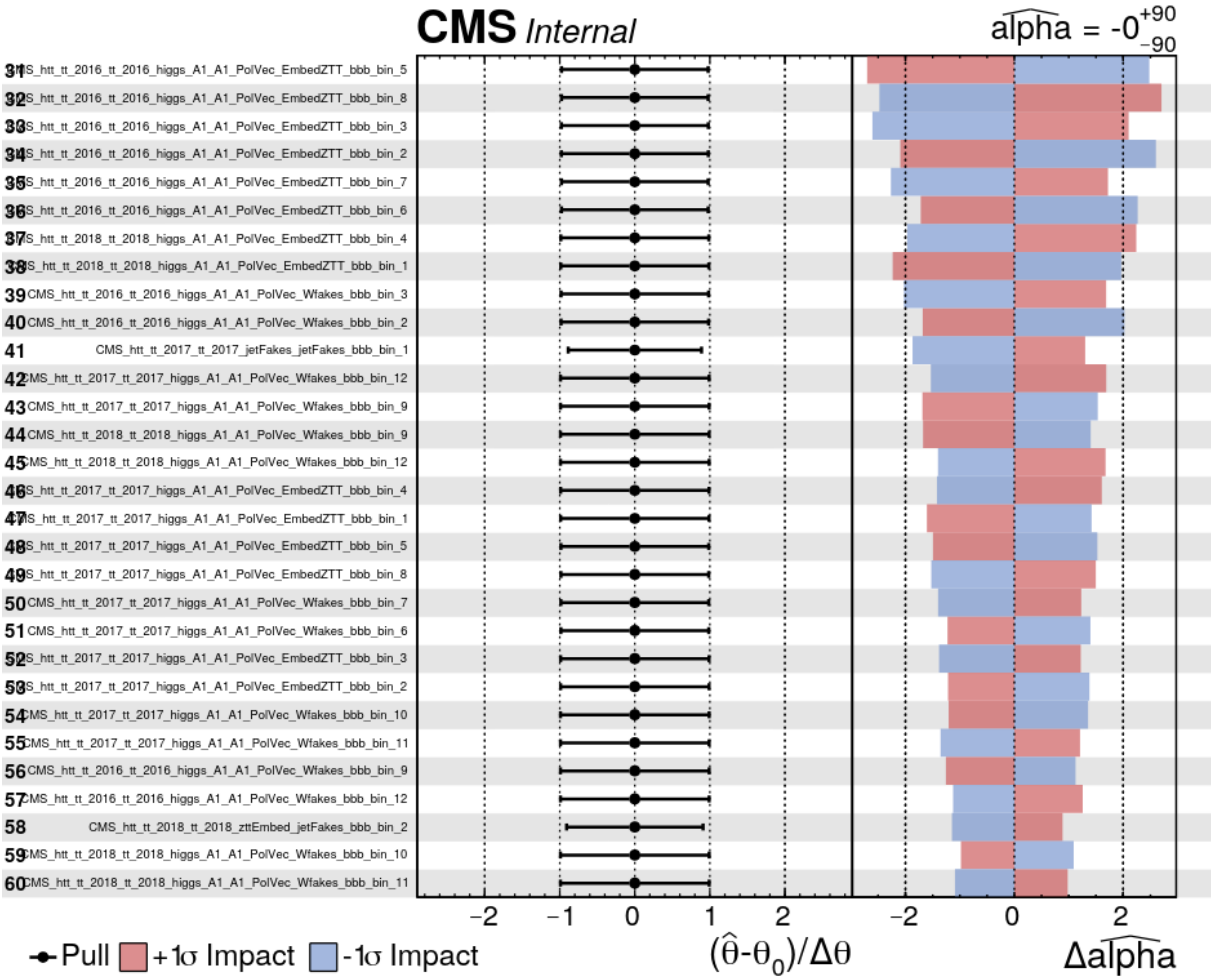

Figure 350: Impacts and constraints of the 31-60 ranked for nuissance parameters.

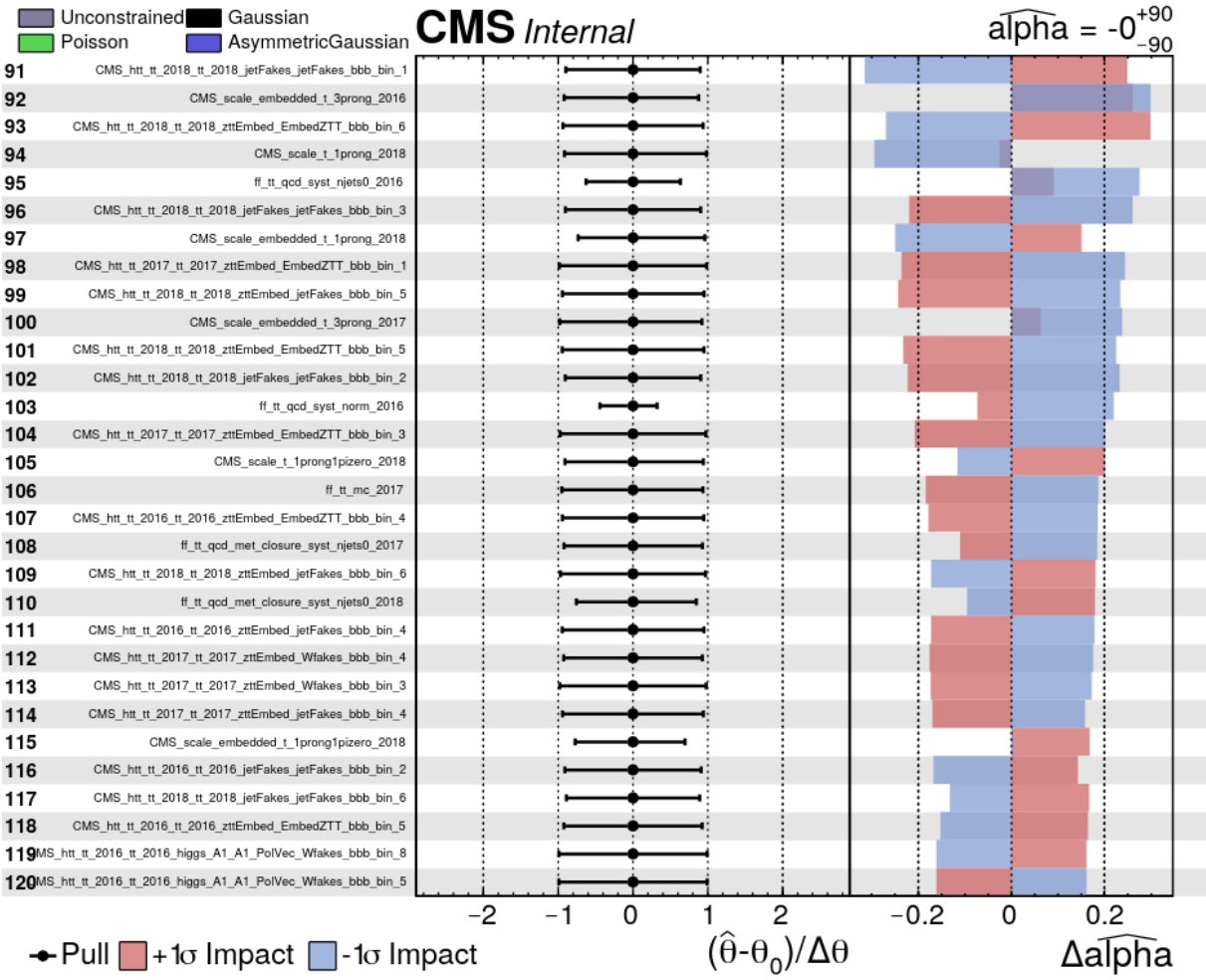

Figure 351: Impacts and constraints of the 61-90 ranked for nuissance parameters.

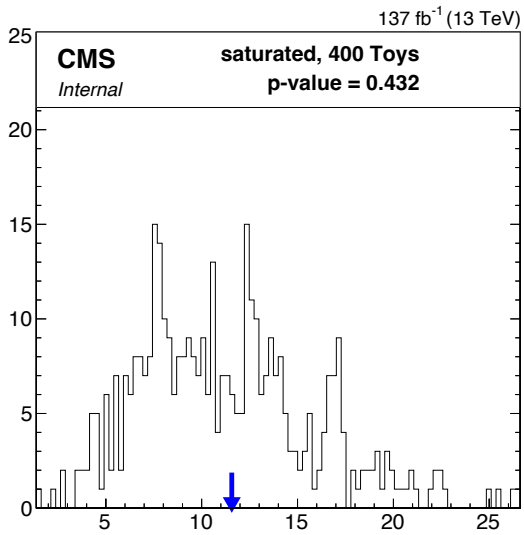

Figure 352: Goodness-of-fit test in the $a_1^{3pr} a_1^{3pr}$ category for 2016.

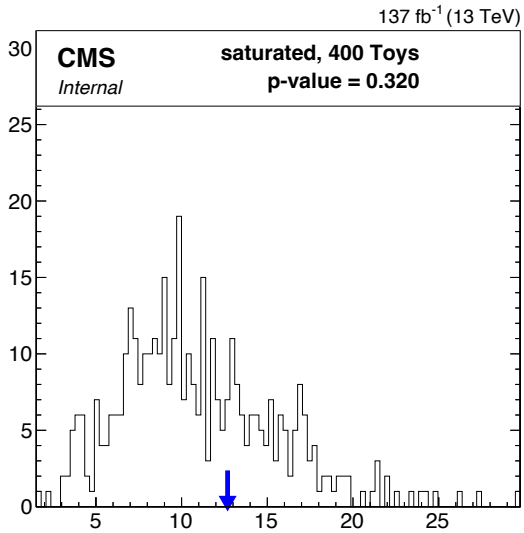

Figure 353: Goodness-of-fit test in the $a_1^{3pr} a_1^{3pr}$ category for 2017.

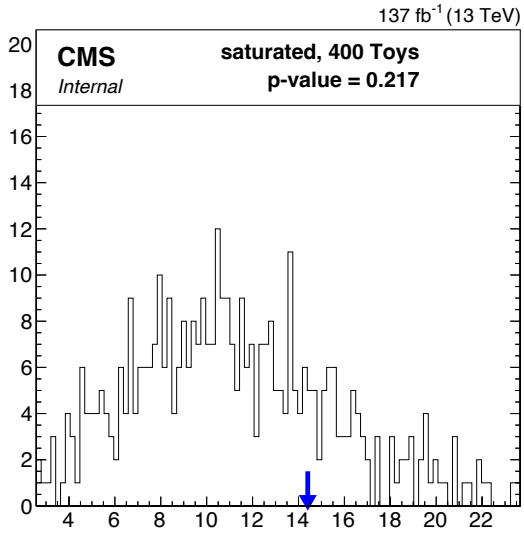

Figure 354: Goodness-of-fit test in the $a_1^{3pr} a_1^{3pr}$ category for 2018.

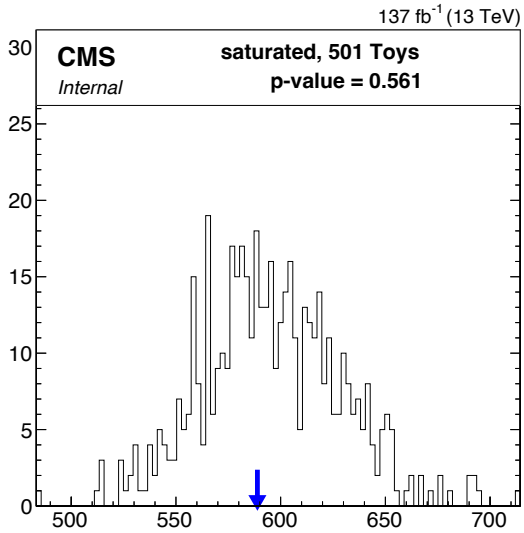

Figure 355: Goodness-of-fit test in the $a_1^{3pr} a_1^{3pr}$ and backgrounds categories for the Run 2.

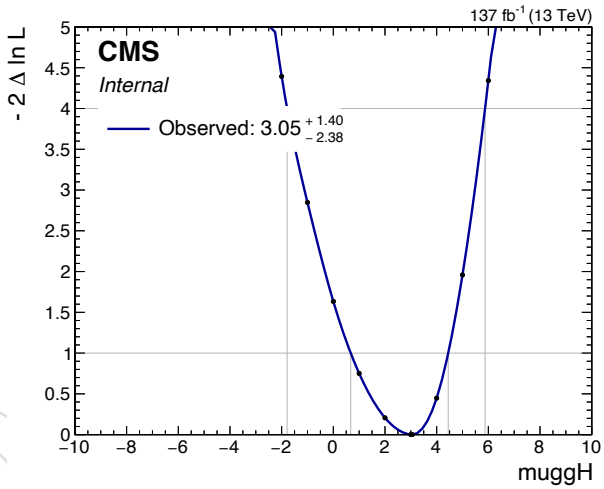

Figure 356: Observed likelihood scan of the μ_{ggH} rate parameter.

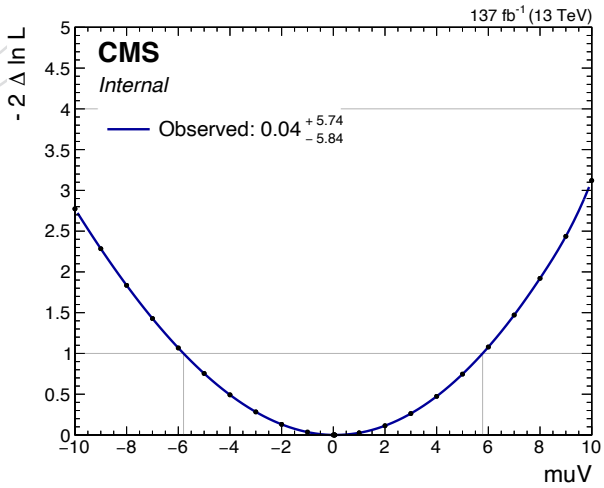

Figure 357: Observed likelihood scan of the μ_V rate parameter.

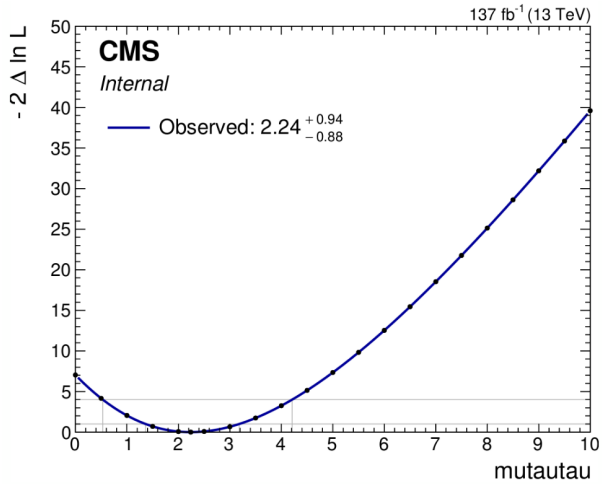

Figure 358: Observed likelihood scan of the μ_{tautau} rate parameter.

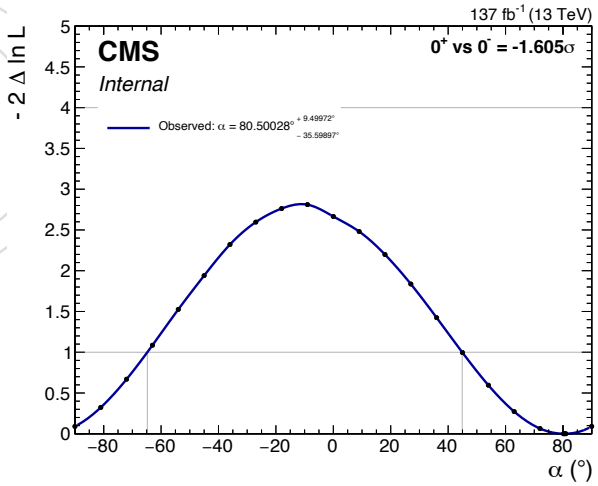

Figure 359: Observed likelihood scan of the α rate parameter.

DRAFT

Acknowledgments

DRAFT

References

[1] F. Englert and R. Brout, "Broken symmetry and the mass of gauge vector mesons", *Phys. Rev. Lett.* **13** (Aug, 1964) 321, doi:10.1103/PhysRevLett.13.321.

[2] P. W. Higgs, "Broken symmetries and the masses of gauge bosons", *Phys. Rev. Lett.* **13** (Oct, 1964) 508, doi:10.1103/PhysRevLett.13.508.

[3] G. S. Guralnik, C. R. Hagen, and T. W. B. Kibble, "Global conservation laws and massless particles", *Phys. Rev. Lett.* **13** (Nov, 1964) 585, doi:10.1103/PhysRevLett.13.585.

[4] G. Aad et al., "Observation of a new particle in the search for the Standard Model Higgs boson with the ATLAS detector at the LHC", *Physics Letters B* **716** (Sep, 2012) 1, doi:10.1016/j.physletb.2012.08.020, arXiv:12077214.

[5] S. Chatrchyan et al., "Observation of a new boson at a mass of 125 GeV with the CMS experiment at the LHC", *Physics Letters B* **716** (Sep, 2012) 30, doi:10.1016/j.physletb.2012.08.021, arXiv:12077235.

[6] A. Sirunyan et al., "Observation of the Higgs boson decay to a pair of τ leptons with the CMS detector", *Physics Letters B* **779** (Apr, 2018) 283, doi:10.1016/j.physletb.2018.02.004, arXiv:1708.00373.

[7] M. Aaboud et al., "Cross-section measurements of the Higgs boson decaying into a pair of τ-leptons in proton-proton collisions at a centre-of-mass energy of 13 TeV with the ATLAS detector", *Physical Review D* **99** (Apr, 2019) doi:10.1103/physrevd.99.072001, arXiv:1811.08856.

[8] S. Berge, W. Bernreuther, and S. Kirchner, "Determination of the Higgs CP-mixing angle in the tau decay channels at the LHC including the Drell–Yan background", *The European Physical Journal C* **74** (Nov, 2014) 3164, doi:10.1140/epjc/s10052-014-3164-0, arXiv:1408.0798.

[9] ATLAS Collaboration Collaboration, "Probing the $\mathcal{CP}$ nature of the Higgs boson coupling to τ leptons at HL-LHC", Technical Report ATL-PHYS-PUB-2019-008, CERN, Geneva, Mar, 2019.

[10] ATLAS Collaboration, "Evidence for the spin-0 nature of the Higgs boson using ATLAS data", *Phys. Lett. B* **726** (2013) 120, doi:10.1016/j.physletb.2013.08.026, arXiv:1307.1432.

[11] ATLAS Collaboration, "Study of the spin and parity of the Higgs boson in diboson decays with the ATLAS detector", *Eur. Phys. J. C* **75** (2015) 476, doi:10.1140/epjc/s10052-015-3685-1, arXiv:1506.05669.

[12] ATLAS Collaboration, "Test of CP Invariance in vector-boson fusion production of the Higgs boson using the Optimal Observable method in the ditau decay channel with the ATLAS detector", *Eur. Phys. J. C* **76** (2016) 658, doi:10.1140/epjc/s10052-016-4499-5, arXiv:1602.04516.

[13] ATLAS Collaboration, "Measurement of inclusive and differential cross sections in the $H \to ZZ^* \to 4\ell$ decay channel in pp collisions at $\sqrt{s} = 13$ TeV with the ATLAS detector", *JHEP* **10** (2017) 132, doi:10.1007/JHEP10(2017)132, arXiv:1708.02810.

DRAFT

[14] ATLAS Collaboration, "Measurement of the Higgs boson coupling properties in the $H \to ZZ^* \to 4\ell$ decay channel at $\sqrt{s}$ = 13 TeV with the ATLAS detector", *JHEP* **03** (2018) 095, doi:10.1007/JHEP03(2018)095, arXiv:1712.02304.

[15] ATLAS Collaboration, "Measurements of Higgs boson properties in the diphoton decay channel with 36 fb^{-1} of pp collision data at $\sqrt{s} = 13$ TeV with the ATLAS detector", *Phys. Rev. D* **98** (2018) 052005, doi:10.1103/PhysRevD.98.052005, arXiv:1802.04146.

[16] CMS Collaboration, "On the mass and spin-parity of the Higgs boson candidate via its decays to Z boson pairs", *Phys. Rev. Lett.* **110** (2013) 081803, doi:10.1103/PhysRevLett.110.081803, arXiv:1212.6639.

[17] CMS Collaboration, "Measurement of the properties of a Higgs boson in the four-lepton final state", *Phys. Rev. D* **89** (2014) 092007, doi:10.1103/PhysRevD.89.092007, arXiv:1312.5353.

[18] CMS Collaboration, "Constraints on the spin-parity and anomalous HVV couplings of the Higgs boson in proton collisions at 7 and 8 TeV", *Phys. Rev. D* **92** (2015) 012004, doi:10.1103/PhysRevD.92.012004, arXiv:1411.3441.

[19] CMS Collaboration, "Limits on the Higgs boson lifetime and width from its decay to four charged leptons", *Phys. Rev. D* **92** (2015) 072010, doi:10.1103/PhysRevD.92.072010, arXiv:1507.06656.

[20] CMS Collaboration, "Combined search for anomalous pseudoscalar HVV couplings in VH(H $\to b\bar{b}$) production and H $\to$ VV decay", *Phys. Lett. B* **759** (2016) 672, doi:10.1016/j.physletb.2016.06.004, arXiv:1602.04305.

[21] CMS Collaboration, "Constraints on anomalous Higgs boson couplings using production and decay information in the four-lepton final state", *Phys. Lett. B* **775** (2017) 1, doi:10.1016/j.physletb.2017.10.021, arXiv:1707.00541.

[22] S. Berge, W. Bernreuther, and S. Kirchner, "Prospects of constraining the higgs boson's cp nature in the tau decay channel at the lhc", *Physical Review D* **92** (Nov, 2015) doi:10.1103/physrevd.92.096012, arXiv:151003850.

[23] M. Krämer, J. Kühn, M. L. Stong, and P. M. Zerwas, "Prospects of measuring the parity of Higgs particles", *Zeitschrift für Physik C Particles and Fields* **64** (Mar, 1994) 21–30, doi:10.1007/bf01557231, arXiv:hep-ph/9404280.

[24] W. Bernreuther and S. Berge, "Figure used with permission of the authors".

[25] J. R. Dell'Aquila and C. A. Nelson, "Distinguishing a spin-0 technipion and an elementary Higgs boson: V_1V_2 modes with decays into $\mathrm{l}_a^- \boldsymbol{l}_b$ and/or $\mathrm{q}_a^- \boldsymbol{q}_b$", *Phys. Rev. D* **33** (Jan, 1986) 93, doi:10.1103/PhysRevD.33.93.

[26] S. Berge and W. Bernreuther, "Determining the cp parity of higgs bosons at the lhc in the τ to 1-prong decay channels", *Physics Letters B* **671** (Feb, 2009) 470, doi:10.1016/j.physletb.2008.12.065, arXiv:0812.1910.

[27] S. Berge, W. Bernreuther, B. Niepelt, and H. Spiesberger, "How to pin down the cp quantum numbers of a higgs boson in its τ decays at the lhc", *Physical Review D* **84** (Dec, 2011) doi:10.1103/physrevd.84.116003, arXiv:1108.0670.

DRAFT

[28] K. Desch, A. Imhof, Z. Was, and M. Worek, "Probing the cp nature of the higgs boson at linear colliders with τ spin correlations; the case of mixed scalar-pseudoscalar couplings", *Physics Letters B* **579** (Jan, 2004) 157, doi:10.1016/j.physletb.2003.10.074, arXiv:0307331.

[29] G. Bower, T. Pierzcha$\lesssim$, Z. Was, and M. Worek, "Measuring the higgs boson's parity using $\tau \to \rho\nu$", *Physics Letters B* **543** (Sep, 2002) 227–234, doi:10.1016/s0370-2693(02)02445-0, arXiv:hep-ph/0204292.

[30] M. Worek, "Higgs CP from H/A $\to$ tau tau decay", 2003.

[31] V. Cherepanov, E. Richter-Was, and Z. Was, "Monte Carlo, fitting and Machine Learning for Tau leptons", *SciPost Phys. Proc.* **1** (2019) 018, doi:10.21468/SciPostPhysProc.1.018, arXiv:1811.03969.

[32] V. Cherepanov and A. Zotz, "Kinematic reconstruction of $Z/H \to \tau\tau$ decay in proton-proton collisions", arXiv:1805.06988.

[33] S. Jadach, J. H. Kuhn, and Z. Was, "TAUOLA: A Library of Monte Carlo programs to simulate decays of polarized tau leptons", *Comput. Phys. Commun.* **64** (1990) 275–299, doi:10.1016/0010-4655(91)90038-M.

[34] M. Jezabek, Z. Was, S. Jadach, and J. H. Kuhn, "The tau decay library TAUOLA, update with exact O(alpha) QED corrections in tau $\to$ mu. (e) neutrino anti-neutrino decay modes", *Comput. Phys. Commun.* **70** (1992) 69–76, doi:10.1016/0010-4655(92)90092-D.

[35] S. Jadach, Z. Was, R. Decker, and J. H. Kuhn, "The tau decay library TAUOLA: Version 2.4", *Comput. Phys. Commun.* **76** (1993) 361–380, doi:10.1016/0010-4655(93)90061-G.

[36] T. Przedzinski, E. Richter-Was, and Z. Was, "Documentation of *TauSpinner* algorithms: program for simulating spin effects in τ -lepton production at LHC", *Eur. Phys. J.* **C79** (2019), no. 2, 91, doi:10.1140/epjc/s10052-018-6527-0, arXiv:1802.05459.

[37] CMS Collaboration Collaboration, "Performance of the DeepTau algorithm for the discrimination of taus against jets, electron, and muons",.

[38] CMS Collaboration. https://twiki.cern.ch/twiki/bin/view/CMS/JetID#Recommendations_for_13_TeV_data.

[39] CMS Collaboration. https://twiki.cern.ch/twiki/bin/view/CMS/JetMET.

[40] CMS Collaboration Collaboration, "Pileup mitigation at CMS in 13 TeV data", Technical Report CMS-PAS-JME-18-001, CERN, Geneva, 2019.

[41] CMS Collaboration, "Description and performance of track and primary-vertex reconstruction with the CMS tracker", *JINST* **9** (2014) P10009, doi:10.1088/1748-0221/9/10/P10009, arXiv:1405.6569.

[42] R. Frühwirth, W. Waltenberger, and P. Vanlaer, "Adaptive Vertex Fitting", Technical Report CMS-NOTE-2007-008, CERN, Geneva, Mar, 2007.

[43] R. Frühwirth, P. Kubinec, W. A. Mitaroff, and M. Regler, "Vertex reconstruction and track bundling at the LEP collider using robust algorithms", *Comput. Phys. Commun.* **96** (Mar, 1996) 189–208. 23 p, doi:10.1016/0010-4655(96)00040-9.

DRAFT

[44] A. Sirunyan et al., "Performance of reconstruction and identification of τ leptons decaying to hadrons and ν_τ in pp collisions at $\sqrt{s} = 13$ tev", *Journal of Instrumentation* **13** (2018).

[45] https://indico.cern.ch/event/894671/contributions/3775389/attachments/2000488/3343871/TauPOG-TauIDandTriggerSF-09March2020-MohammadHassanshahi_v2.pdf.

[46] C. Grimault, "unpublished Master 2 internship", 2018.

[47] Andrew Loeliger, Cecile Caillol, Abhi Mallampalli, Jithin Madhusudanan, Sridhara Dasu, Tulika Bose, Doyeong Kim, Tyler Mitchell, Yurii Maravin, Abdollah Mohammadi, Keti Kaadze, Senka Duric, Isobel Ojalvo, Sam Higginbotham, and Dan Marlow, "Measurement of higgs boson production and decay to a pair of tau leptons on the full run 2 data set using a cut-based approach", *CMS Note* **2019/019** (2019).

[48] CMS Collaboration, "Electron and muon scale factor measurements for Higgs to tau tau analyses". http://cms.cern.ch/iCMS/jsp/db_notes/noteInfo.jsp?cmsnoteid=CMS%20AN-2020/014.

[49] R. Barlow and C. Beeston, "Fitting using finite Monte Carlo samples", *Computer Physics Communications* **77** (1993) 219–228.

[50] J. S. Conway, "Incorporating Nuisance Parameters in Likelihoods for Multisource Spectra", (2011). arXiv:1103.0354. To be published in a CERN Yellow Report.

[51] https://indico.cern.ch/event/868279/contributions/3668554/attachments/1959280/3266317/2019-12-17_Tau_trigger_SF_for_DeepTau.pdf.

[52] CMS Collaboration, "Search for additional neutral MSSM Higgs bosons in the $\tau\tau$ final state in proton-proton collisions at $\sqrt{s} = 13$ TeV", *JHEP* **09** (2018) 007, doi:10.1007/JHEP09(2018)007, arXiv:1803.06553.

[53] CMS Collaboration Collaboration, "Measurement of the $z/\gamma^* \to \tau_h\tau_h$ cross section in pp collisions at $\sqrt{s}$ = 13 tev and validation of τ lepton analysis techniques", *European Physical Journal C* **78** (09, 2018).

[54] "CMS AN-2018/256 – Multi-class neural network architecture and training for measurements of Higgs(125) boson decays to two tau leptons". http://cms.cern.ch/iCMS/jsp/db_notes/noteInfo.jsp?cmsnoteid=CMS%20AN-2018/256.

[55] https://twiki.cern.ch/twiki/bin/viewauth/CMS/TWikiLUM.

[56] LHC Higgs Cross Section Working Group Collaboration, "Handbook of LHC Higgs Cross Sections: 4. Deciphering the Nature of the Higgs Sector", doi:10.23731/CYRM-2017-002, arXiv:1610.07922.

[57] CMS Collaboration. https://twiki.cern.ch/twiki/bin/viewauth/CMS/MissingETRun2Corrections#MET_Uncertainties.

[58] CMS Collaboration. https://twiki.cern.ch/twiki/bin/viewauth/CMS/TauTauEmbeddingSamples2016.

DRAFT

[59] CMS Collaboration. https://twiki.cern.ch/twiki/bin/viewauth/CMS/TauTauEmbeddingSamples2017.

[60] S. Mrenna and P. Skands, "Automated Parton-Shower Variations in Pythia 8", *Phys. Rev.* **D94** (2016), no. 7, 074005, doi:10.1103/PhysRevD.94.074005, arXiv:1605.08352.

[61] CMS Collaboration. https://cms-hcomb.gitbooks.io/combine/content/.

[62] CMS Collaboration, "Measurement of Higgs boson production and decay to a pair of tau leptons on the full Run 2 data set using a cut-based approach; Analysis note". http://cms.cern.ch/iCMS/jsp/db_notes/noteInfo.jsp?cmsnoteid=CMS%20AN-2019/109.

DRAFT